Functional π-Conjugated Nanomaterials via Living Crystallization-Driven Self-Assembly

by
Huda Shaikh

MChem, University of Warwick, 2017

A Dissertation Submitted for Fulfilment of the
Requirements for the Degree of

DOCTOR OF PHILOSOPHY

in the Department of Chemistry

Supervisory Committee

Functional π-Conjugated Nanomaterials via Living Crystallization-Driven Self-Assembly

by

Huda Shaikh

Supervisory Committee

Prof. Ian Manners, Department of Chemistry
Supervisor

Prof. Alexandre Brolo, Department of Chemistry
Departmental Member

Prof. Rustom Bhiladvala, Department of Mechanical Engineering
Outside Member

Abstract

Nature makes use of the bottom-up synthetic technique termed self-assembly to fabricate a vast array of complex materials that are integral to life. The self-assembly of block copolymers (BCPs) has been shown to be a versatile method for the preparation of a diverse range of nano- and micro-sized micelle morphologies. It has been demonstrated that crystallization of the micelle core-forming block of the BCP enables access to one-dimensional (1D) or two-dimensional (2D) micelle morphologies that are difficult to obtain exclusively via other synthetic strategies. Living crystallization-driven self-assembly (CDSA) presents a facile route towards preparing nanostructures with precisely controlled dimensions. This field of research is rapidly growing with the desire to use these intricate nanostructures for real-world applications. The work contained in this thesis focusses on the solution self-assembly of π-conjugated-based homopolymers and BCPs, with the broad aim of preparing functional nanostructures with controlled dimensions and desirable structural, optical and electronic properties.

Table of Contents

List of Figures

List of Schemes

List of Tables

List of Abbreviations

°	Degrees
°C	Degrees Celsius
1D	One-dimensional
^{1}H NMR	Proton nuclear magnetic resonance
2D	Two-dimensional
a_0	Area of solvophilic head group
Å	Angstrom
a.u.	Arbitrary units
Abs(λ)	Absorption
AFM	Atomic force microscopy
A_n	Number-average area
ATRP	Atom-transfer radical polymerization
A_w	Weight-average area
A_w/A_n	Area dispersity
-*b*-	Block
BCP	Block copolymer
ca.	Circa
CD	Circular dichroism
CDSA	Crystallization-driven self-assembly
cm	Centimetre
CTA	Chain transfer agent
CuAAc	Copper-catalyzed azide-alkyne cycloaddition click
Da	Dalton
diBCP	Diblock copolymer
$Đ_m$	Molecular mass dispersity
DMF	Dimethylformamide
DMSO	Dimethyl sulfoxide
DNA	Deoxyribose nucleic acid
DP	Degree of polymerization
DSC	Differential scanning calorimetry
E	Energy
E_F	Fermi energy
EtOH	Ethanol
eV	Electron volt
FRET	Förster resonance energy transfer
F(λ)	Coefficient of factors

g	Grams
GPC	Gel permeation chromatography
GRIM	Grignard metathesis
GSB	Ground-state bleach
h	Hour
H_2O	Water
HBC	Hexabenzocoronene
INCP	In-situ nanoparticlization of conjugated polymers
iPrOH	isopropanol
I(λ)	Excitation intensity
kDa	kilodalton
l	Solvophilic tail length
LAADF	low-angle annular dark-field
L_n	Number-average length
L_w	Weight-average length
L_w/L_n	Length dispersity
MALDI-ToF	Matrix-assisted laser-desorption/ionization time-of-flight
MeOH	Methanol
MeCN	Acetonitrile
MERS-CoV	Middle Eastern respiratory syndrome coronavirus
mg	Milligram
m	Metre
m/z	Mass over charge
min	Minute
mL	Millilitre
mmol	Millimole
M_n	Number average molecular weight
MOA	8-Mercaptooctanoic acid
mol	Mole
MUA	Mercaptoundecanoic acid
m_{unimer}/m_{seed}	Unimer-to-seed mass ratio
M_w	Weight-average molecular weight
M_w/M_n	Molecular weight dispersity
nm	Nanometre
NMR	Nuclear magnetic resonance
ns	Nanosecond
η(λ)	Energy transfer efficiency
OFET	Organic field-effect transistor

OLED	Organic light-emitting diode
OPV	Oligo (*p*-phenylenevinylene)
P	Packing parameter
P2VP	Poly(2-vinylpyridine)
P3HT	Poly(3-hexylthiophene)
P3EHT	Poly(3-(2'-ethylhexyl)thiophene)
P(3TEG)T	Poly(3-triethylene glycol thiophene)
PDHF	Poly(di-*n*-hexylfluorene)
PDCF	Poly(di-*n*-(3,7-dimethyoctane)fluorene)
PDI	Perylene diimide
PDMS	Poly(dimethylsiloxane)
PDOF	Poly(di-*n*-octylfluorene)
PEG	Poly(ethylene glycol)
PF	Polyfluorene
PFS	Poly(ferrocenyldimethylsilane)
PFTMC	Poly(spiro[fluorene-9,5'-[1,3]dioxin]-2'-one)
PL	Photoluminescence
PLE	Photoluminescence excitation
PLLA	Poly($_L$-lactide)
PMDETA	*N,N,N',N',N''*-pentamethyldiethylenetriamine
PNIPAm	Poly(*N*-isopropylacrylamide)
[PPh_3]Br	Triphenylphosphonium bromide
ppm	Parts per million
PPV	Poly(phenylene vinylene)
ps	picosecond
PT	Polythiophene
QD	Quantum dot
QPF	Quaternized polyfluorene
QPT	Quaternized polythiophene
QR	Quantum rod
Q(λ)	Quantum yield
RAFT	Reversible addition-fragmentation transfer
RI	Refractive index
RNA	Ribonucleic acid
s	second
SARS-CoV	Severe acute respiratory syndrome coronavirus
SEC	Size-exclusion chromatography
SEM-EDS	Scanning electron microscopy-energy dispersive x-ray spectroscopy

STED	Stimulation emission depletion microscopy
STEM	Scanning transmission electron microscopy
τ	Time period
TA	Transient absorption
T_c	Crystallization temperature
TEM	Transmission electron microscopy
T_g	Glass transition temperature
THF	Tetrahydrofuran
T_m	Melting point transition temperature
Tol	Toluene
triBCP	Triblock copolymer
UV	Ultraviolet
UV-vis	Ultraviolet/visible
v	Solvophobic tail volume
v/v	Volume by volume
WAXS	Wide-angle X-ray scattering
W_n	Number-average width
w.t%	Weight percentage
W_w	Weight-average width
W_w/W_n	Width dispersity
δ	Chemical shift
λ	Wavelength
λ_{abs}	Absorption wavelength
λ_{em}	Emission wavelength
λ_{ex}	Excitation wavelength
µm	Micrometre
σ	Standard deviation
χ	Flory-Huggins parameter

Acknowledgments

I am very grateful for all the support I have received throughout my PhD from my lovely family, friends and colleagues.

Firstly I would like to thank Prof Ian Manners for giving me the amazing opportunity to carry out my PhD in his research group at Bristol (Year 0 – 1.5) and then Victoria (Year 1.5 – 3.5). I have been given endless support from both Ian and Deborah O'Hanlon Manners over the past three and a half years, especially during challenging times. I would also like to thank Dr. George Whittell and Dr. Xu-Hui Jin for their guidance and advice at the start of my PhD at the University of Bristol and Dr. Yifan Zhang, Dr. Liam MacFarlane and Dr. Yuetong Kang for their advice and assistance throughout the last two years of my degree.

During my PhD, I have had an incredible time living in Bristol and Victoria. I have been very fortunate to have so many amazing and inspiring people surrounding me during my studies. There are too many people to individually list here, however I would like to give a special thanks to group members that have made my last few years really enjoyable: Ali, Charlotte, Diego G. H, Diego R. L, Horatio, Liam, Marcus, Matt, Mitch, Nikki, Sam, Steve, Tomoya, Vince, Yifan and Yuetong.

I would like to give a special thanks to Sam Pearce, whose support, risqué humour, and calming demeanour have kept me positive throughout all the challenging times over the last few years. It is difficult to imagine how I would have gotten to this stage in my education and life without the love, help and support from my family at home. In particular my mother, Bushra, my brother, Faysal, my step-father Wayne and my grandparents, Shamim and Zafar Vaince. My mum and grandfather have worked incredibly hard to ensure I have the best possible opportunities at every stage in my life so far and I hope to replicate their incredible kindness, charisma and intelligence.

Chapter 1 Introduction

Sections of this Introduction Chapter were adapted from:

MacFarlane, L. R.; Shaikh, H.; Garcia-Hernandez, J. D.; Vespa, M.; Fukui, T.; Manners, I., *Nat. Rev. Mat.* **2021**, *6*, 7-26

1.1. Nanomaterials: Inspiration from Nature

Life is reliant on a number of complex self-assembled systems that operate on different length scales. Strategies for the synthesis of complex materials have often drawn inspiration from nature,[1] which usually employs hierarchical self-assembly of components, from the molecular to the cosmological scale, to produce a range of bespoke and intricate systems. Examples include functional materials for use in areas from therapeutics to optoelectronics, in which the latest research efforts focus on nanostructured materials.[2,3] Thus, in the pursuit of biologically integrated electronic devices much inspiration comes from natural skin. Bottom-up strategies, including self-assembly, are important to mimic skin-like properties, such as stretchability and the ability to self-heal.[4–7] They also permit the construction of precisely ordered materials on small length scales (10^{-9} - 10^{-6} m) for which top-down methods may be unsuitable.[1,3,8–10]

1.1.1. Nanoscale and Microscale Ordered Materials in Nature

There are many natural materials whose functionality depend on the nano- and microscale structure. Iridescence observed on butterfly wings, and in many other insects and plants, is an example of such a phenomenon.[11–13] Iridescent materials can display multiple arrays of intense colors that are dependent on the vision angle. In *M. cypris* and *G. oto* butterfly wings, these visual effects stem from photonic crystal-like microstructures with ordered subwavelength structure that leads to the Bragg scattering of incident light over specific wavelengths (Figure 1. 1).[14] These microscale architectures are composed of punctuated nanolayers, concave pits and micro-ribs with nanoridges.[13,15] Mimicking the iridescence effect in synthetic materials would be useful for applications in the anti-counterfeiting and cosmetics industries.[16–18]

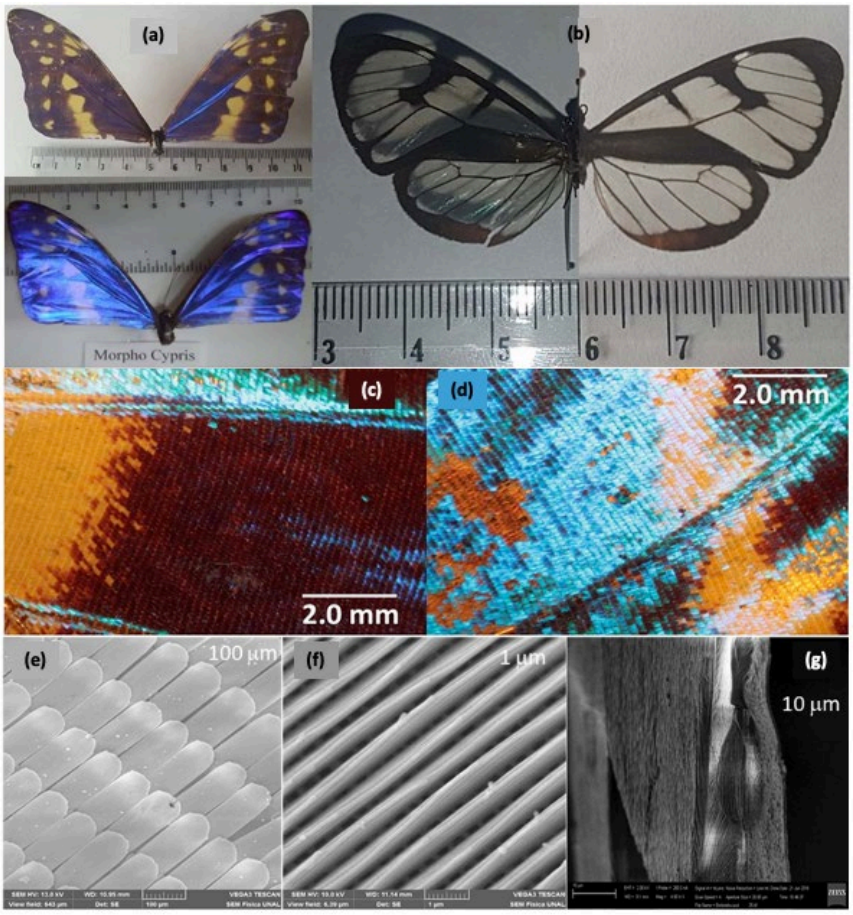

Figure 1. 1: Photonic Effects in Natural Nanostructures on Butterfly Wings. Photographs showing the iridescent effect of (a) *M. cypris* Colombian butterfly wings and (b) *G. oto* Colombian butterfly wings. Images of the *M. cypris* Colombian butterfly wing using an optical microscope with 1x magnification at (c) 0° and (d) 60° about the normal axis. SEM images at scales of (e) 100 µm and (f) 1 µm. SEM image of the lateral disposition at (g) 10 µm. Reproduced with permission from ref [14].

1.1.2. Self-Assembly and Hierarchy in Nature

Self-assembly and the hierarchical organization of matter are vital processes for nature's success at building important functional materials such as muscles, bone, and wood. Order is present across multiple length scales in these materials and this structural hierarchy produces enhanced physical properties when compared to their constituent components.[10]

Viruses represent one of the most famous examples of self-assembled nanoparticles that exist in nature and have evolved into highly efficient vessels for large-scale human infection. These intricate nanostructures can have remarkable infection efficacy and in recent times this has hugely impacted our daily lives.[19] The tobacco mosaic virus is composed of well-defined dimensions and presents a remarkable illustration of hierarchy in nature. The virus core is composed of an

RNA strand that is encased and protected by a protein coat (termed the capsid). The capsid is composed of subunits that assemble in a helical arrangement on binding to the RNA virus core.[20]

The current ongoing pandemic has been caused by the highly pathogenic virus SARS-CoV-2 (2020) from the coronavirus subfamily of RNA viruses. The name 'coronavirus' comes from their shape, which is spherical (ca. 80-220 nm in diameter) and has protein spikes on the periphery that form the characteristic corona (Figure 1. 2). In the novel SARS-CoV-2 virus, these spikes are coated with sugars that camouflage the virus from the human immune system enabling the virus to go undetected, a process termed glycan shielding.[21] Combined with the conformational masking effect exhibited by the spike glycoprotein trimers, which are responsible for cell entry, these behaviours account for a severe delay in the immune response of hosts. These properties are believed to be unique to the most pathogenic strains of coronavirus, such as SARS-CoV-2, SARS-CoV and MERS-CoV.[21]

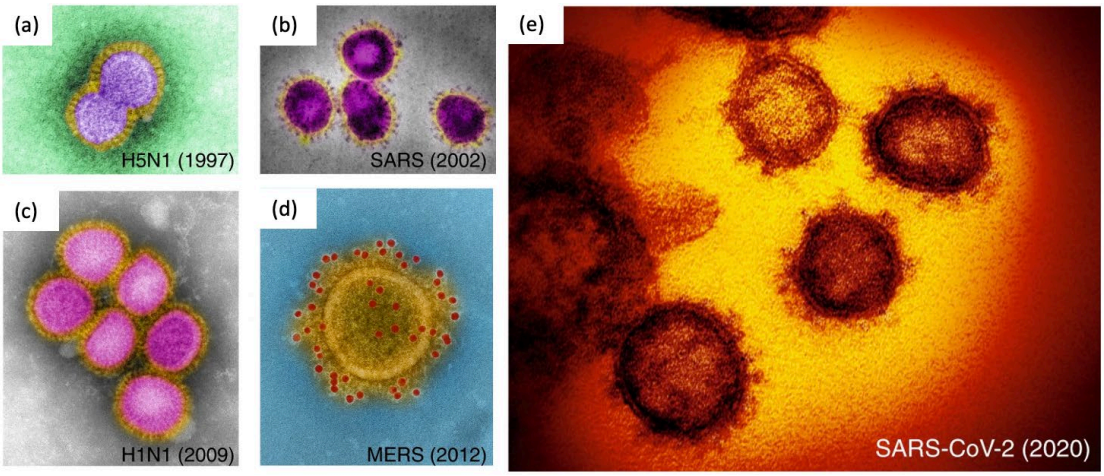

Figure 1. 2: False coloured images of (a) avian influenza virus (Hong Kong, 1997), (b) SARS coronavirus (China, 2002), (c) swine influenza virus (Mexico, 2009), (d) MERS coronavirus (Saudi Arabia, 2012) and (e) SARS-CoV-2 (China, 2020). Reproduced with permission from ref [19].

1.1.3. Synthetic Strategies using Supramolecular Self-Assembly

Biochemical species, such as chromosomes and enzymes, are critically dependent on the precise organization of smaller building blocks on a variety of length scales to achieve their function.[8,10] Self-assembly describes the spontaneous arrangement of preformed components into lower entropy structures by means of non-covalent interactions. Such non-covalent interactions

include hydrogen bonds, π-π stacking, Van der Waals, and electrostatic forces. Although these interactions may be individually weak compared to covalent bonds their sum is sufficient to create a stable assembly.[22]

There are two main types of self-assembly systems, dynamic and static.[1] Self-assembly systems that operate at a global or local equilibrium are described as static and examples include hemoglobin proteins and molecular crystals. Such assemblies are generally formed after an initial input of energy is supplied. In dynamic self-assembly, which works outside of thermodynamic equilibrium, the construction of stable structures is dependent on the continuous dissipation of energy. Fabrication of structures via dynamic self-assembly is less well developed but is a growing field for molecular systems.[23,24] Polymerizations driven by the Belousov-Zhabotinsky oscillatory reaction have been applied to produce dynamic assemblies capable of undergoing internal structural rearrangement or division.[25,26]

In the late 1970's, Jean-Marie-Lehn first introduced the term, '*supramolecular chemistry*', which describes the 'chemistry of molecular assemblies and of the intermolecular bond'.[27] A number of synthetic self-assembly systems have since been developed for the construction of supramolecular polymers from molecular and macromolecular-based building blocks (monomers). This approach has led to the creation of well-defined 1D functional structures, such as nanofibers, twisted nanoribbons, and nanotubes with biological, optical and electronics properties (Figure 1. 3). Supramolecular self-assembly is a continuously evolving field and current research efforts also extend to developing hybrid systems and multidimensional architectures that display unique functions. [28–31]

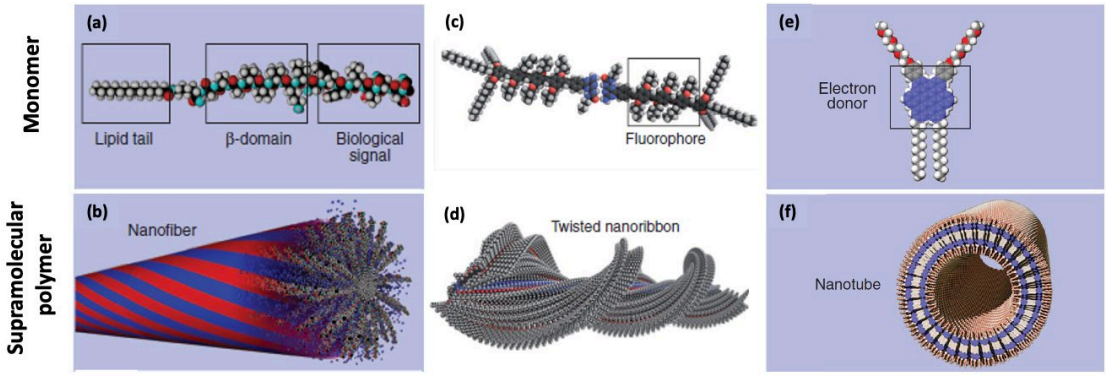

Figure 1. 3: Molecular representation of three monomers and their corresponding supramolecular polymers formed via self-assembly. (a)-(b) A peptide amphiphile monomer forms cylindrical nanofibers via β-sheet type hydrogen bonding and hydrophobic interactions. (c)-(d) Oligo (phenylene vinylene) substituted with alkyl groups and chiral centres forms a twisted ribbon with defined chirality via hydrogen bonding. (e)-(f) A monomer with a hexabenzocoronene core substituted with alkyl and ethylene glycol chains forms a nanotube via π-π stacking and hydrophobic interactions. Adapted with permission from ref [31].

1.2. Block Copolymer Self-Assembly

Building blocks capable of undergoing self-assembly typically consist of components with differing chemical or physical properties, most commonly polarity. These amphiphiles are diverse in composition, but the subsequent nature of their self-assembly behaviour shares many common features. Micellization arising from surfactant self-assembly is a well-explored process and offers a simple model to illustrate the general self-assembly of molecular and macromolecular amphiphiles. Surfactants are composed of a polar head group and a non-polar tail. In polar solvents micellization can occur to form different morphologies, including spheres and fibers, provided that the critical micelle concentration (CMC) is reached. The non-polar tails aggregate in polar media and form the micelle core, which is shielded by solvated polar head groups minimizing unfavourable exposure to the solvent media.

Block copolymers (BCPs) are much larger amphiphilic species than simple molecular amphiphiles and are constructed of two or more different polymer blocks with distinct physicochemical properties. Many synthetic strategies have been developed to afford BCPs with well-defined molecular weights, low molar mass dispersities, and different architectures. BCP self-assembly offers a versatile and efficient route for preparing discrete structural domains in the solid and solution state.[32]

1.2.1. Solid-State Block Copolymer Self-Assembly

Microphase separation of BCPs in the solid-state is dependent on the volume fractions of the incompatible coblocks (f) and the degree of segregation (χN) (Figure 1. 4a-b). The degree of segregation is determined by the degree of polymerization of the polymer coblocks (N) and the Flory-Huggins interaction parameter (χ) between them. From the theoretical phase diagram of a diblock copolymer there is a threshold value of χN above which phase separation can occur as the coblocks possess sufficient incompatibility ($\chi N \geq 10$).[33] Microphase segregated morphologies are typically accessed by heating the BCP to a temperature above the glass transition temperature (T_g) of the polymer blocks followed by rapid cooling. Typical morphologies that are accessible from the self-assembly of diblock copolymers include spheres, cylinders, lamellae and gyroids (Figure 1. 4c). Triblock or multiblock copolymers introduce further complexity to the theoretical phase diagram as even more morphologies can be prepared.[34,35]

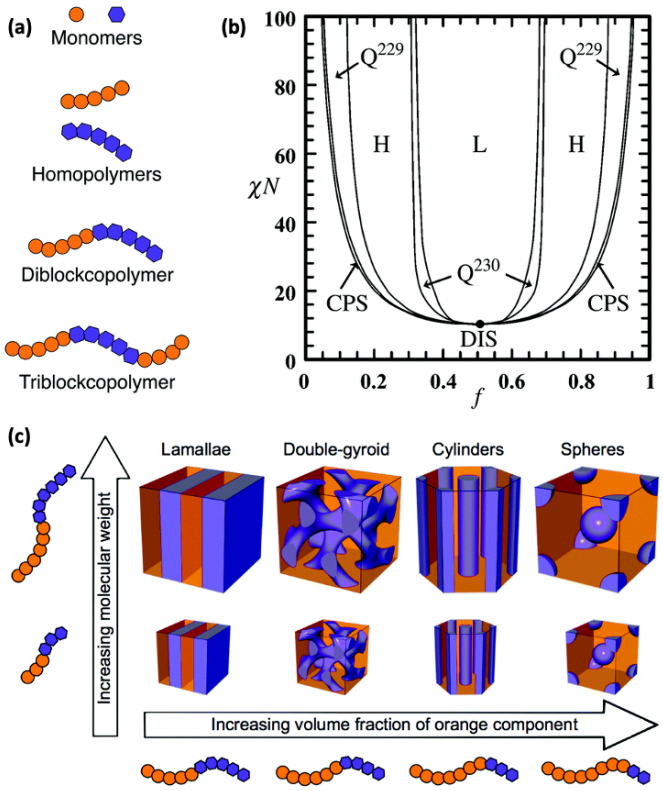

Figure 1. 4: Solid-State Self-Assembly of Diblock Copolymers. (a) Components of BCP building blocks. (b) Linear diblock copolymer theoretical phase diagram for block volume fraction (f) versus degree of segregation (χN). Morphologies are labelled as follows: lamellae (L), hexagonally packed cylinders (H), body-centred spheres (Q^{229}), double-gyroid phase (Q^{230}), close-packed spheres (CPS) and a disordered phase (DIS). (c) Cartoon illustration of the different morphologies accessible depending on the composition of the BCP building block. Adapted with permission from ref [36].

1.2.2. Solution-State Block Copolymer Self-Assembly

Many of the principles that govern surfactant self-assembly also apply to BCP self-assembly. However, the solution self-assembly of BCPs is a more complex process than surfactant solution self-assembly and BCP self-assembly in the solid state. Additional interactions between the BCP and solvent medium affect the ability to predict micelle morphology. The introduction of a selective solvent for one polymer block to a solution of dissolved BCP drives micelle formation via aggregation of the insoluble core-forming block. Several factors influence the self-assembly of amphiphiles in solution including the solvent medium, chemical composition of the amphiphile, concentration, temperature, and the presence of additional additives.[37,38] Micelle morphology can be tuned by altering the solvent system, degree of polymerisation, block ratio and chemical nature of the blocks and by introducing various chemical and physical stimuli.[39] Typically, for a given BCP, assemblies with higher core-corona interfacial curvature are obtained in solution than in bulk due to the repulsive interactions between the swollen solvated coronal chains, which therefore occupy a larger volume fraction.

Analogous to surfactant self-assembly, micelle morphology can be related to the packing parameter (P) for surfactants (Figure 1. 5) but the correlation is much less accurate.. The packing parameter illustrates how tuning the amphiphile structure influences the self-assembled morphology, $P = v/a_o l_c$, where v is the volume of hydrophobic block, a_o is the area of hydrophilic head group, and l_c is the length of the hydrophobic block.[40] In the case of amorphous BCPs, when $P \leq 1/3$ spherical micelles are formed, worm-like micelles can be prepared at $1/3 \leq P \leq 1/2$ and vesicular structures are favoured at $1/2 \leq P \leq 1$.[41] Even though the packing parameter has an influence on the solution self-assembly of BCPs, often this term is not very accurate for predicting specific micelle morphologies in solution. This is a complex challenge due to the swelling behaviour of the solvophilic corona-forming block. The degree of swelling of the corona-forming block directly affects the value of a_o and is dependent on the quality of the solvent. So for the same BCP, the solvent medium can influence the relative volume fractions of the solvophobic and solvophilic blocks.

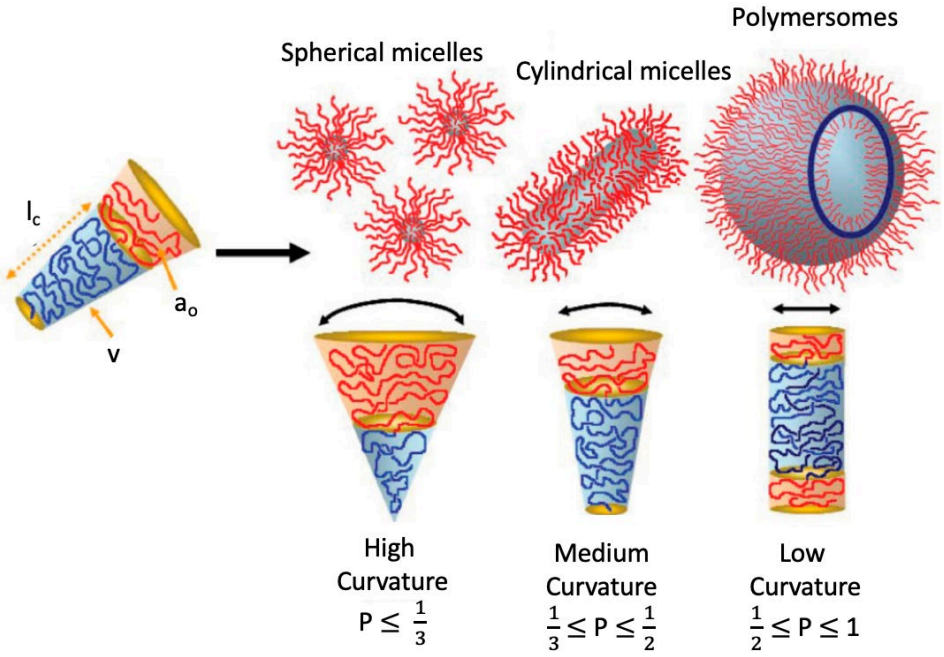

Figure 1. 5: Schematic depiction of polymer chain arrangements arising from different morphologies of AB di-blocks. Morphologies are predicted by the packing parameter (*P*) through the following equation, $P = v/a_o l_c$. Where *v* is the volume fraction of the solvophobic A block (blue chains), a_o is the area pf the solvophilic B block (red chains) and l_c is the length of the A block. The morphology changes from sphere to cylinder to polymersomes with an increasing value of *P* (*left to right*). Adapted with permission from ref [41].

For the case of many BCPs, self-assembly in selective solvents for one of the polymer blocks results in the formation of kinetically trapped morphologies, which can be attributed to the slow exchange of BCP unimers between micelles that prevents thermodynamic equilibrium from being reached. This is not normally the case for surfactant self-assembly, in which kinetically labile structures are formed in solution and the molecular amphiphiles are in rapid exchange between self-assembled micelles and dissolved surfactant amphiphiles (unimers). For BCPs, the free energy of the system governs the thermodynamically favoured morphology. Key contributions to the free energy include inter-chain repulsion between the coronal polymer chains, degree of chain-stretching in the core of the micelle, and interfacial energy between the solvent and the micelle core.[32]

In the mid 90's, pioneering work in this area by Eisenberg and coworkers focused on the solution self-assembly of polystyrene-*b*-poly(acrylic acid) (PS-*b*-PAA) BCPs. Low corona-to-core ratio BCPs were prepared that were capable of forming an array of "crew-cut" micelles.[42–44] The BCPs were dissolved in a common solvent for both polymer coblocks (dimethylformamide) then a selective

solvent for the PAA block (water) was added to induce aggregation of the PS block. Altering the degree of polymerization of the coblocks and also introducing additives capable of screening charge on the PAA coronal chains effectively changed the value of a_o, and thereby influenced the micelle morphology giving rise to a complex range of architectures (Figure 1. 6).[40]

Further complexity in nanostructure morphology is introduced when we consider the self-assembly of multiblock copolymers. The number of interaction parameters are increased due to the presence of additional polymer blocks. This makes it more difficult to predict micelle morphology. Complex architectures with multiple discrete core or corona domains can be prepared from the solution self-assembly of triblock terpolymers, namely multicompartment or "patchy" micelles.[45,46] Subsequent hierarchical organization of compartmentalized micelles can also be achieved by introducing additional stimuli that can trigger the aggregation of specific polymer segments of the pre-formed micelle, to afford supermicelle architectures.[45]

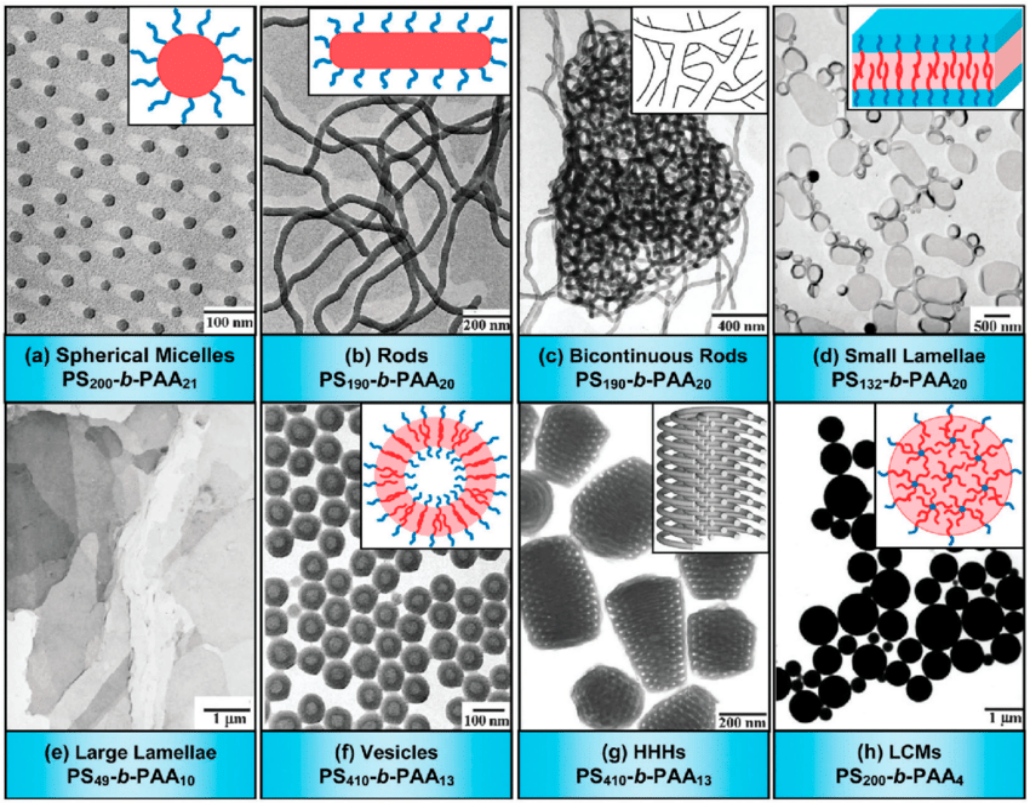

Figure 1. 6: Transmission electron microscopy (TEM) images and cartoon illustrations of micelle morphologies prepared by the solution self-assembly of PS_n-*b*-PAA_m. HHH = hexagonal hollow hoops, LCM = large compound micelles. In the cartoon illustrations red represents PS regions and blue represents PAA regions. Reproduced with permission from ref [40].

Fiber-like micelles, which possess a diameter or width on the nanoscale and a high aspect ratio, are currently under extensive investigation for applications in drug delivery and as templates for the alignment of metal nanoparticles.[47, 48] The fiber morphology is the most difficult to obtain in pure form through the self-assembly of BCPs with amorphous core-forming blocks, as the phase-space associated with their stability is generally very limited.

If crystallization of the core-forming block can be facilitated during the self-assembly of BCPs this provides an additional contribution to the free energy of the system and has an important influence on micelle morphology. The formation of micelles with low core-corona interfacial curvature are favoured by the self-assembly of BCPs with a crystallizable block, due to the high structural order and rigidity present in the crystalline micelle core. It is therefore possible to obtain pure fiber-like or platelet micelle morphologies.[32]

1.3. Crystallization-Driven Self-Assembly

Polymer crystallization in the solid state and solution occurs if there is sufficient alignment of polymer chains during aggregation.[49] Achieving single crystalline order in polymeric materials is highly challenging. Typically, a mixture of crystalline and amorphous domains is formed. Preparative methods that can yield highly crystalline materials are desirable for a range of applications including polymer-based electronic devices.[50]

In solution, the formation of micelles with low core-corona interfacial curvature is favoured for BCPs with a crystallizable core-forming block. Initial work focused on the self-assembly of BCPs with a crystallizable polyethylene oxide (PEO) segment. 2D platelet micelles with crystalline cores were prepared in solvent systems that were selective for the corona-forming block and sufficiently poor to allow for crystallization of PEO core-forming block in solution.[51,52]

The self-assembly of polyferrocenyldimethylsilane (PFDMS) BCPs has been explored and characterized in detail since preliminary work was instigated in the 1990's.[53,54] Various BCPs containing a PFDMS core-forming block are able to undergo self-assembly in solvents selective for the corona-forming block.[55] PFDMS BCPs can undergo core crystallization in solution with a preference to form morphologies with low core-corona interfacial curvature such as cylindrical micelles.[54] Solution self-assembly of non-crystallizable polyferrocenylsilanes,

with unsymmetrical substitution at silicon in the main chain, typically only forms spherical micelles. Optimization of the solvent systems used and the ratio of the degree of polymerization of polymer coblocks can yield morphologically pure fiber-like micelles (low core:corona ratio, ≥1:6) or platelet micelles (high core:corona ratio, e.g. 1:3).[56–58]

Polyethylene (PE) BCPs has been reported to undergo self-assembly to form a range of micelle morphologies with crystalline cores.[59,60] Depending on the degree of polymerization (DP) of the PE core-forming block, a range of low core-corona interfacial curvature structures can be prepared such as ellipsoidal micelles at low DPs of PE and fiber-like micelles at higher DPs.[59] The solvent systems were also found to have a key influence on the final micelle morphologies. In poor solvents for the PE core block a mixture of spherical and fiber-like micelles were observed.[60] When solvents that are slightly less poor for the core-forming block were used the exclusive formation of fiber-like micelles can be achieved.[60] It is clear that there needs to be a balance between solvent selectivity and crystallization rate to achieve pristine low core-corona interfacial curvature morphologies. The critical importance of core crystallization on the obtained micelle morphology has led to term crystallization-driven self-assembly (CDSA) being coined.[32]

In the last decade an array of BCPs containing a crystallizable block have also been shown to undergo CDSA including several polyferrocenylsilanes,[61,62] poly(ferrocenyldimethylgermane),[63] poly(L-lactic acid) (PLLA),[64–66] poly(ε-caprolactone),[67,68] polyacetylene,[69] poly(ethylene oxide),[70] poly(ethylenesulfide),[71] poly(acrylonitrile),[72] poly(3-hexylthiophene) (P3HT),[50,73,74] poly(3-heptylselenophene),[75,76] poly(3-octylthiophene),[77] poly(*p*-phenylene),[78] poly(*p*-phenylenevinylene) (PPV),[79,80] poly(*p*-phenyleneethynylene),[81,82] poly(di-*n*-dihexylfluorene) (PDHF),[83,84] polycarbonates,[85] poly(2-isopropyl-2-oxazoline),[86] poly(perfluoroethyloctyl-methacrylate),[87,88] and cyclic peptoids.[89]

Despite the CDSA protocol being a robust and versatile strategy to afford 1D fiber-like micelles and 2D platelets , it remains difficult to predict micelle morphology. Factors such as core-to-corona ratio or the percentage of common solvent can have different effects on obtained micelle morphologies depending on

the BCP system. For example, for PFDMS BCPs a high core to corona ratio can induce the formation of 2D platelets whereas for BCPs with a PLLA core-forming block a low core to corona ratio promotes the formation of analogous assemblies.[90,91]

1.3.1. Living CDSA: Routes to Nanostructures with Controlled Dimensions

Seeded growth strategies have been developed to prepare micelles with precisely controlled fiber length and platelet area.[92, 93] 'Living' CDSA offers a route to control the length of 1D micelles with crystalline cores. This methodology is analogous to living covalent polymerisation, wherein polymer chains can grow by further addition of monomers to reactive chain ends without termination or transfer events occurring. When all of the monomers are consumed in solution the chain ends still remain active and can continue growing if further monomer is added.[94] Similarly, the exposed crystal faces of the crystalline core in fiber-like micelles can seed the epitaxial growth of added solvated BCP (unimer). Sonication can be used to fragment the crystalline core micelles to afford short micelles that can act as seeds to promote epitaxial crystal growth in the presence of unimer. [95] As the seeds are typically very small in length and the rate of epitaxial growth from these seeds is equivalent, uniform micelles of low length dispersity and controlled dimensions can be achieved.

Based on these principles two main techniques have been developed to obtain low length dispersity micelles, termed seeded growth and self-seeding (Figure 1. 7).[96, 97] In the seeded growth method, pre-existing cylindrical micelles are used as seeds, further addition of molecularly dissolved unimers results in epitaxial growth from the crystalline faces of the core termini. The seed micelles are generated via vigorous sonication of polydisperse cylindrical micelles in a selective solvent for the corona block.[96] Epitaxial growth of added unimers is generally favoured over self-nucleation to afford low dispersity micelles with controllable lengths dependent on the unimer-to-seed ratio (Figure 1. 8).

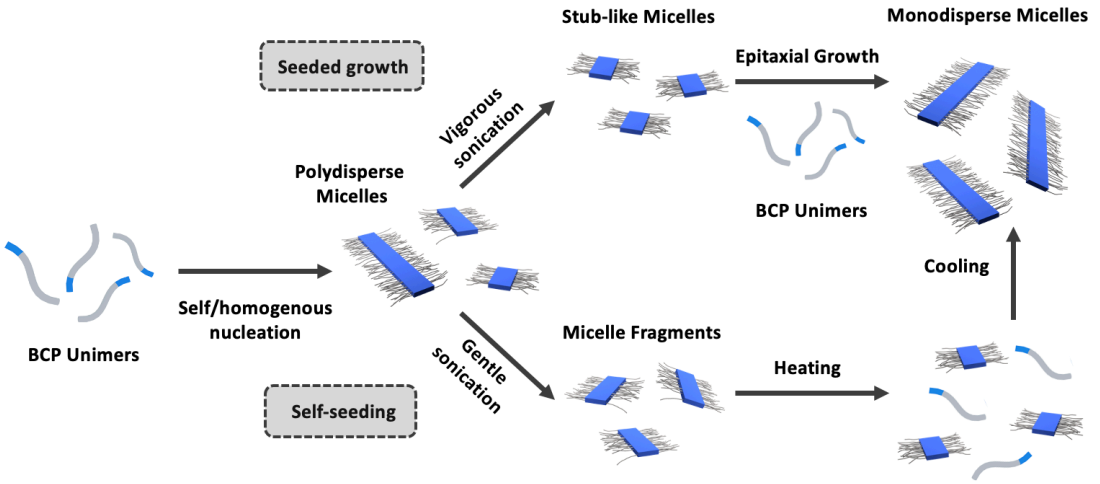

Figure 1. 7: Schematic diagram illustrating the two protocols used to obtain low-dispersity fiber-like micelles with a ribbon-like core, applicable to π-conjugated BCP systems. Seeded growth (top) and self-seeding methods (bottom). Adapted with permission from ref [98].

There are two main self-seeding protocols that can be adopted depending on the nature of the system that involve using heat or adjusting solvent ratios.[99] During a typical thermal self-seeding process, the sample is heated to dissolve regions of lower crystallinity and then cooled, which allows the dissolved polymer to recrystallize on the ends of the surviving micelle fragments of higher crystallinity. This step is performed under dilute conditions to avoid self-nucleation of the dissolved polymer, as a result the surviving seed crystallites are the only nuclei from which the unimer can grow.[99] In addition to the use of temperature, a solvent-based self-seeding method can be used.[97] A pre-annealing step can also be carried out that improves fiber crystallinity. This has been particularly beneficial for 'living' CDSA of polythiophene and polyselenophene BCPs.[97,99,100] 'Living' CDSA of π-conjugated polymers will be discussed in detail in section 1.5.

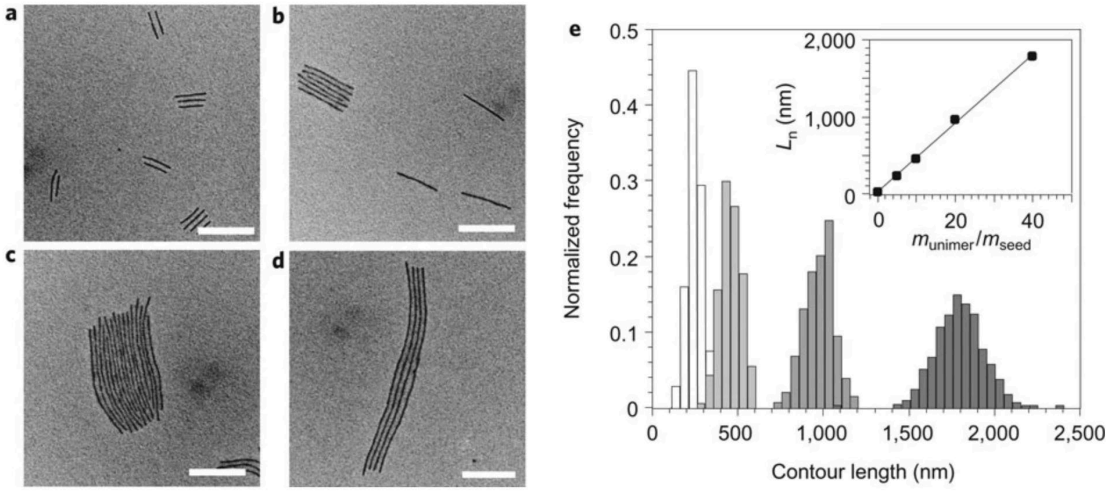

Figure 1. 8: a–d, TEM images of monodisperse cylindrical micelles of PI_{550}-*b*-PFS_{50} obtained by employing a seeded growth protocol. e, Histograms of the contour length distribution of samples a–d. The inset shows the linear dependence of the micelle contour length on the unimer-to-seed ratio. Scale bars, 500 nm. Reproduced with permission from ref [93].

Epitaxial growth of BCP unimer from seed micelles with different core and/or corona chemistries can be achieved under appropriate solvent conditions. In the case of heteroepitaxial growth the lattice mismatch between the seed and the epitaxially grown layer needs to be small (ca. < 15 %).[101] Seeded growth methods can produce uniform fiber-like micelles with segmented core or coronal chemistries, also termed block comicelles. Typically block comicelles are prepared with a B-A-B structure where A is the seed micelle and B represents the epitaxially grown segments.[93] Unidirectional growth from seed micelles is also possible and has been demonstrated with a PFDMS-based BCP system. First, B-A-B block comicelles were prepared, where A is a central PFDMS-*b*-poly(dimethylsiloxane) (PDMS) segment and the terminal B segments are composed of PFDMS-*b*-polyisoprene (PI).[102] The PI corona was then cross-linked and the central PFDMS-*b*-PDMS segments were dissolved to afford seed micelles containing only one exposed crystal face that can promote further epitaxial growth unidirectionally. Sequential addition of BODIPY dye functionalized PFMDS BCP unimer to the seeds micelles resulted in the formation of fluorescent nanopixel block comicelles with discrete segments containing different emission properties (Figure 1. 9f).[103]

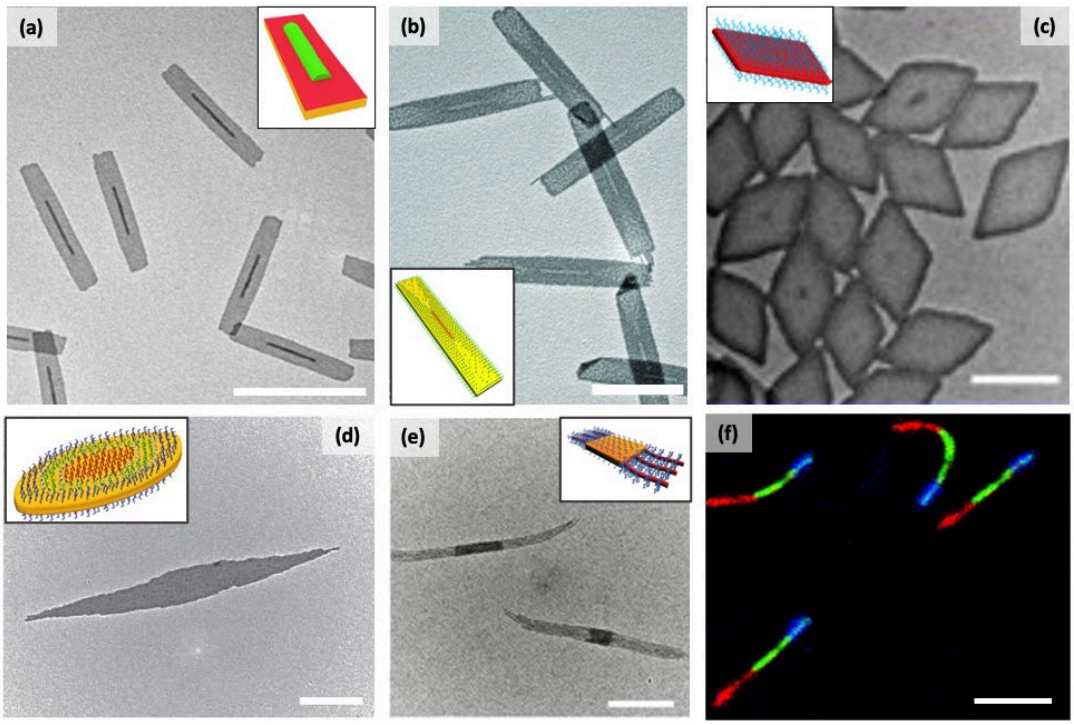

Figure 1. 9: 1D and 2D Architectures via CDSA of PFS Materials. (a) 2D rectangular platelets prepared by seeded growth of PFS[PPh_2Me]I unimers from PFS-*b*-P2VP cylindrical micelle seeds. Adapted with permission from ref [108]. (b) 2D rectangular platelet by seeded growth of a blend of PFS homopolymer and PFS-*b*-P2VP unimers from PFS-*b*-PDMS seeds. Adapted with permission from ref [104]. (c) 2D diamond platelets prepared by CDSA of PLLA-*b*-PDMAEMA. Adapted from ref [105]. (d) Lenticular platelet micelles by seeded growth of dye-functionalized PFS BCP unimers from PFS-*b*-PDMS seeds. Adapted with permission from ref [90]. (e) Scarf-like micelles by seeded growth of PFG-*b*-P2VP from PFS-*b*-P2VP seeds. Adapted with permission from ref [63]. (f) Fluorescent unidirectional 1D block comicelles prepared by seeded growth of different BODIPY dye-functionalized PDMS unimers from PFMDS-*b*-PMVS seeds. Adapted with permission from ref [103]. Scale bars: (a, b) 2 μm, (c) 1 μm, (d, e) 500 nm and (f) 5 μm.

A variety of architectures can be fabricated from the 'living' CDSA strategy, including 2D platelets, 1D branched micelles, 3D starlike micelles and scarf-like micelles,[63] composed of 2D platelet seed and multiple epitaxially grown 1D fiber-like micelles (Figure 1. 9e).[90,98,104,106] Initial work on 2D architectures via CDSA focused on using PFDMS BCPs with a core to corona ratio of 1:1, which possess a higher core to corona ratio compared to the materials used to prepare 1D cylindrical micelles. Lenticular platelets of controlled area and segmented fluorescent architectures could be prepared with these BCPs (Figure 1. 9d).[90] However, this strategy was limited in terms of the upper limit of size control and in the formation of ordered 2D structures like rectangular or square platelets. A robust strategy was developed to prepare large 2D rectangular platelets of controlled size that involves seeded growth of a 1:1 mass blend of PFDMS BCP and PFDMS homopolymer from 1D cylindrical micelle seeds (Figure 1. 9b).[104] The

latest synthetic strategy to prepare low dispersity 2D platelets focuses on the seeded growth of phosphonium or ammonium charge terminated PFDMS or PLLA homopolymers (Figure 1. 9a).[107,108] These synthetic strategies have also been applied to the heteroepitaxial growth of PFMDG-based materials from PFDMS seed micelles, to afford low dispersity segmented 1D cylindrical micelles and 2D platelets.[63,109]

In the last decade the 'living' CDSA methodology has also been applied to small molecular amphiphile systems, such as hexabenzocoronenes,[110,111] perylene diimides,[112] Zn porphyrins,[113] and Pt pincer complexes.[114] Similar to the 'living' CDSA of BCP-based materials, seeded growth of these small molecular amphiphile systems can yield kinetically trapped micelles of controlled dimensions and high functionality.

1.3.2. Routes to Hierarchical Architectures

Block comicelles with discrete coronal chemistries can undergo further self-assembly via additional non-covalent interactions when blended or in the presence of external stimuli. For instance, amphiphilic PFDMS-based B-A-B block comicelles with hydrophilic (P2VP) or hydrophobic (PDMS) coronal regions can undergo further self-assembly via aggregation of one of these segments upon adjusting the polarity of the solvent system.[115,116] If more selective solvent for the coronas on the terminal segments of the block comicelle is added, side-by-side stacking of the block comicelles occurs to afford 1D train-track structures (Figure 1. 10f). If more selective solvent for the corona on the central segment in the block comicelles is added, then end-to-end stacking occurs resulting in the formation of 3D multidimensional micelle networks or superlattices. Block comicelles or homopolymers containing segments with hydrogen bonding donor or acceptor moieties can also undergo co-assembly when blended to afford hierarchical supermicelles, with complex architectures such as wind-mills or shish-kebab structures (Figure 1. 10b-e).[117,118] The tunability and precise length control of the interacting segments achieved by 'living' CDSA was vital for achieving low dispersity complex supermicellar constructs.

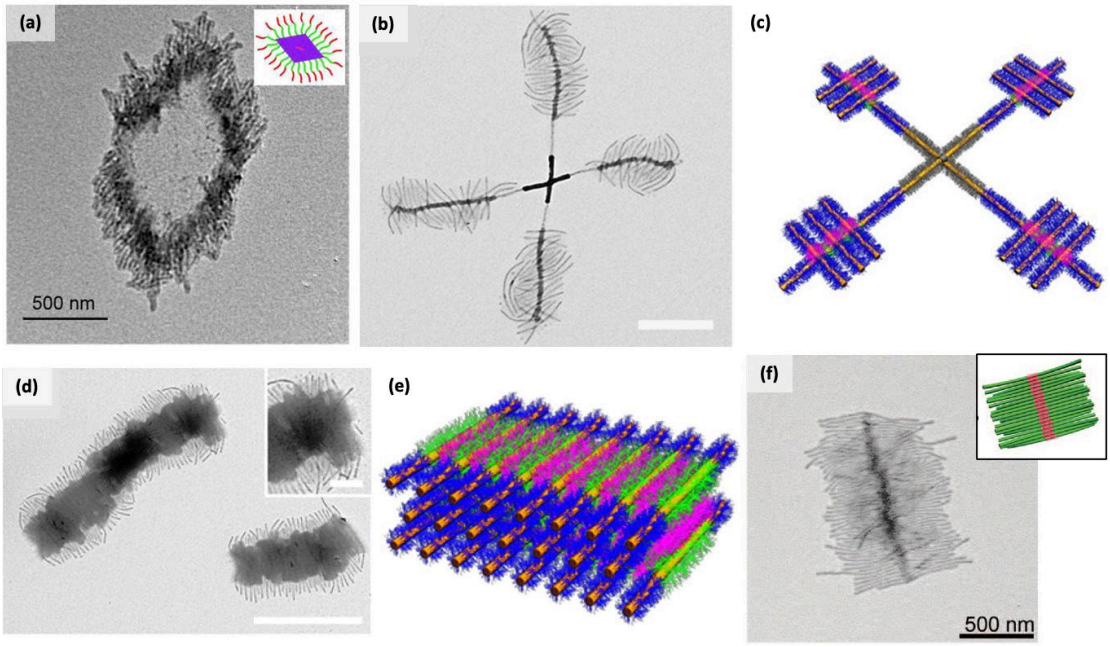

Figure 1. 10: Complex and hierarchical structures prepared from PLLA or PFDMS-based materials. (a) TEM image of diamond-fiber hybrid structures prepared from seeded growth of different PLLA BCP unimers from PLLA diamond platelets. Adapted with permission from ref [119]. TEM image (b) and corresponding (c) cartoon illustration of windmill-like supermicelles prepared via hydrogen-bonding interactions between PFDMS-based block comicelles, induced by solvent adjustment. Adapted with permission from ref [117]. TEM image (d) and corresponding (e) cartoon illustration of supermicellar "shish-kebab" structures via addition of homopolymer with hydrogen-bond donating moieties to PFDMS block comicelles with hydrogen-bond acceptor moieties. Adapted with permission from ref [118]. (f) TEM image and corresponding cartoon illustration of train-track structures prepared via hierarchical self-assembly of B-A-B amphiphilic PFMDS block comicelles, induced by solvent adjustment. Adapted with permission from ref [115].

1.4. π-Conjugated Polymers

π-Conjugated polymers can have semiconducting behaviour in the pristine state and possess a band-like structure due to the electronic delocalization present along the polymer backbone, typically composed of alternating σ- and π-bonds. This class of polymers has emerged as a promising candidate for numerous applications in organic electronics, biomedical imaging and therapy, and sensing technology.[120,121] Polyacetylene was the first conducting polymer synthesised in the 1970s[122,123], and the significance of this discovery was subsequently recognized with a Nobel Prize.[124–126] Since then a myriad of conductive π-conjugated polymers have been synthesized, including polythiophene, polyfluorene, and poly(phenylene vinylene).[127] The π-overlap of p_z atomic orbitals along the polymer backbone (π-conjugation) creates a number of π-states that leads to the formation of electronic bands with a π-band gap (Figure 1. 11).[128] This

π-electron system is responsible for the unique optoelectronic properties that π-conjugated polymers exhibit.

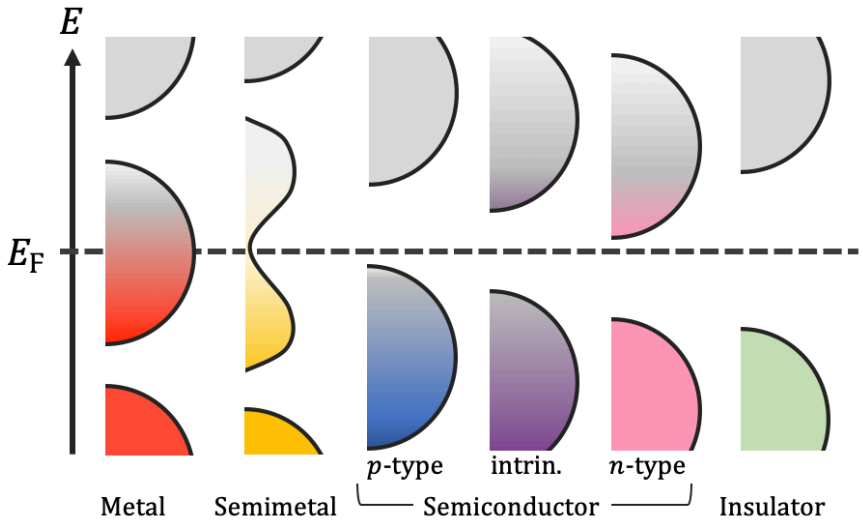

Figure 1. 11: Energy level diagram displaying the contrast in band structure of metals, semiconductors and insulators. The Fermi level (E_F) is labelled in the diagram and indicates the highest occupied energy level below which all energy levels are filled with electrons (at 0 K). The Fermi-Dirac distribution is illustrated by the colors, grey = empty states and all other colors = filled states. Insulators possess large bandgaps between the electron filled valence band (green) and the empty conduction band (grey). Metals and semimetals have merged valence (red/yellow) and conduction (grey) bands. Semiconductors have a smaller bandgap between the valence (blue/purple/pink) and conduction (grey) bands relative to insulators. Adapted from ref [129].

Conductivity in different materials can be explained through band theory. Metals are highly conductive as they possess overlapping valence and conduction bands that enables free movement of charge carriers. π-conjugated materials are semiconductors as a small bandgap (ca. 1.2-3.0 eV) exists between the filled valence band and empty conduction band. If sufficient energy is supplied, electrons can be excited from the valence band into conduction band. In the case of π-conjugated polymers the valence band is synonymous to the low energy π-bonding orbital (HOMO) and the conduction band is equivalent to the high energy π*-antibonding orbital (LUMO). When an electron is excited into the conduction band an exciton is formed that represents the bound state of the excited electron (now in the conduction band) and the electron hole (or simply "hole") created in the valence band. Excitons can be separated when their binding energy is overcome, for example separation can occur at an heterointerface with a material possessing a lower LUMO level. Generation of excitons and subsequent energy transfer are essential prerequisites for the operation of organic-based optoelectronic devices such as light emitting diodes.[130] The band gap in insulator

materials is too large (> 4 eV) for significant excitation of electrons into the conduction band at ambient temperature. Conductivity in conjugated polymers can be enhanced by doping via oxidation or reduction of the π-conjugated system (p-doping and n-doping) which generates additional charge carriers.[131]

In conjugated polymers π-electrons are involved in optical excitations and optical transitions occur between the HOMO and LUMO levels (i.e. the optical bandgap).[132] Therefore, the size of the optical bandgap plays an important role in the absorption and emission profiles of a conjugated polymer. Additionally, numerous studies have reported the key role of repeat unit coplanarity and inter-chain ordering on the optoelectronic properties of conjugated polymers.[133–135] π-electron delocalization enables conjugated polymers to absorb light in the UV-visible region. The absorption profile is often broad due to the presence of a wide distribution of conjugation lengths. Upon excitation, most conjugated polymers can emit light via fluorescence and some achieve remarkably high photoluminescence quantum efficiencies (e.g. 72 % for polyfluorene-based thin films, 0.72 photons emitted per absorbed photon). [136,137] Other possible transitions include exciton energy transfer which can occur between different chromophores (< 10 nm apart). Irradiation of a donor chromophore generates an exciton that can migrate along the polymer backbone and the exciton energy can be transferred though non-radiative dipole-dipole coupling to a lower energy acceptor chromophore. This results in a simultaneous decay of the donor emission and excitation of the acceptor, a process termed Förster resonance energy transfer (FRET).

Conjugated polymers are attractive materials for electronic applications mainly due to their tunable optoelectronic properties, flexibility and processability. The use of conjugated polymers for light-emitting diodes (LEDs) was investigated after the serendipitous discovery of electroluminescence behaviour in π-conjugated polymeric materials.[138,139] Conjugated polymers are also efficient at absorbing light, possess large absorption coefficients (ca. 10^5 cm^{-1}) and broad emission profiles making them ideal materials for use in photovoltaic devices and lasers.[140,141] Current research efforts focus on improving charge carrier mobilities and exciton diffusion behavior of π-conjugated polymeric materials to match that of silicon and small molecule organic-based technologies.

Applications of π-conjugated-based nanoparticles are discussed further in section 1.6.

1.4.1. Synthesis of π-Conjugated Polymers

Initial synthetic strategies for conjugated polymers involved the use of electrochemical and chemical oxidation reactions. However, the resulting materials often exhibit a high polydispersity and poorly controlled regiochemistry.[142,143] An alternative approach is Grignard metathesis (GRIM) polymerization, also known as Kumada catalyst-transfer polycondensation. This process is a living chain-growth polycondensation polymerization[144–146] that uses nickel-mediated cross-coupling reactions to produce materials with low polydispersity and high regioregularity.[147–150] The technique was initially developed for the synthesis of polythiophene but has since been used to synthesize various other materials, including well-defined polyfluorene, polyselenophene, polypyrrole, polycarbazole, and polytellurophene.[151] The living nature of the polymerization enables not only control over the molar mass and access to narrow molar-mass distributions, but also chain-end functionalization with high fidelity (Scheme 1. 1a).[152] Subsequently, BCPs can be directly or orthogonally synthesized from end-functionalized conjugated homopolymers. For example, BCPs can be obtained by polymerization of a second monomer from a macroinitiator[153,154] (Scheme 1. 1a) or by click reactions (Scheme 1. 1b), such as the copper-catalysed azide–alkyne cycloaddition.[74,155]

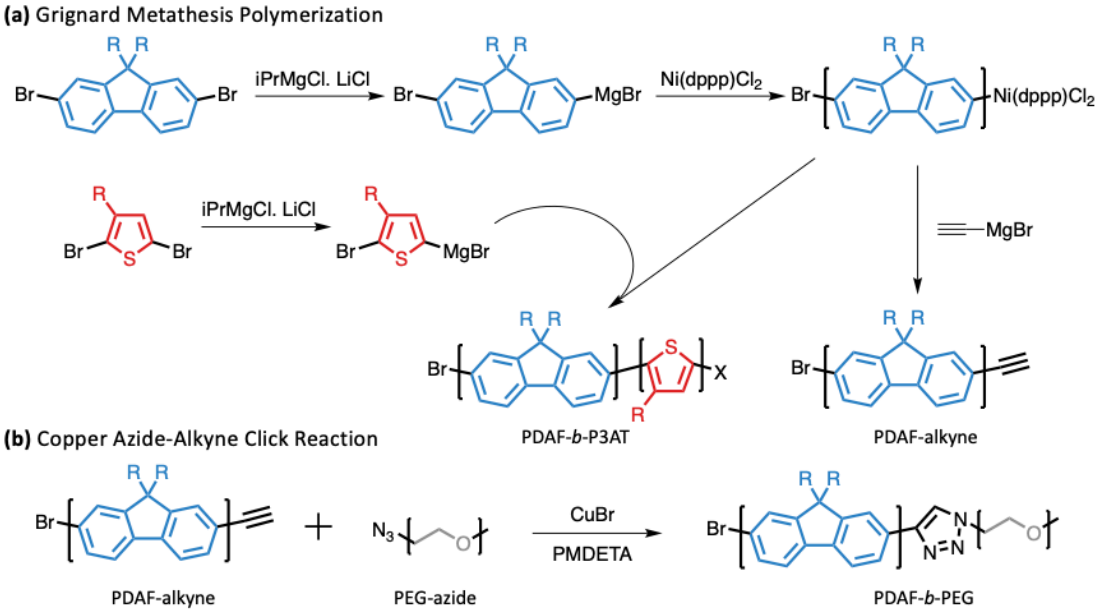

Scheme 1. 1: Example syntheses of (a) alkyne-terminated poly(di-*n*-alkylfluorene) (PDAF) or PDAF-*b*-poly(3-alkylthiophene) (P3AT) BCP by grignard metathesis polymerization and (b) PDAF-*b*-PEG by a copper azide-alkyne click reaction. R = alkyl side chain. iPrMgCl. LiCl = isopropylmagnesium chloride lithium chloride complex solution (turbo Grignard). Ni(dppp)Cl_2 = dichloro(1,3-bis(diphenylphosphino)propane)nickel. PMDETA = N,N.N',N''.N''-pentamethyldiethylenetriamine.

Other polymerization methods, such as Stille or Suzuki–Miyaura cross-coupling, can be applied to a wide range of monomers to yield conjugated polymers with a high molar mass. However, it is difficult to obtain materials with a targeted degree of polymerization or low dispersity. Applying the CDSA approach to π-conjugated core-forming BCPs is of particular interest in producing conductive and emissive nanowire structures that could be incorporated in devices.[156, 157, 158] Synthesis of low dispersity polymers with end-group functionality is essential to afford conjugated BCPs that can be used by 'living' CDSA methods to prepare colloidally stable, uniform nanowires.

1.4.2. P-type Conjugated Polymers

Although many different π-conjugated polymers have been synthesized, the majority of these materials are p-type semiconductors, possessing much better hole mobility than electron mobility (Figure 1. 12). PPVs are one of the most studied examples where typically side chains are attached to the aromatic ring to improve solubility and tune the emission behaviour (in the range of orange to green emission).[159] Additionally, poly(3-alkylthiophenes) have also been widely studied and the nature of side chains in these materials has been shown to have a

direct impact on conductivity. Some substituents can enhance conductivity by optimizing the crystallization kinetics of the polymer in solution. Substitution of the sulfur atom in polythiophene with selenium (to give polyselenophene) reduces the optical band gap from ca. 1.9 eV to 1.6 eV, and with tellurium (polytellurophene) to 1.4 eV.[160] Polyfluorenes have unique optoelectronic properties, and key structure-property relationships have been uncovered giving valuable insight into conjugated polymer electronics.[161] These materials typically absorb in the UV light region, possess efficient blue emission, large hole mobilities, and high thermal and light stability due to their conjugated polymer backbone. Phenylene rings are co-planarized by a bridging carbon atom, which is responsible for the large band gap and blue emission. Some polyfluorene derivatives can exhibit up to three different structural phases with distinct chain conformations that can influence the emission behaviour and packing of the polymer chains in the aggregated state. Co-polymerization of fluorene monomers with low-band gap monomers enables access to emission colors across the entire visible spectrum.[162]

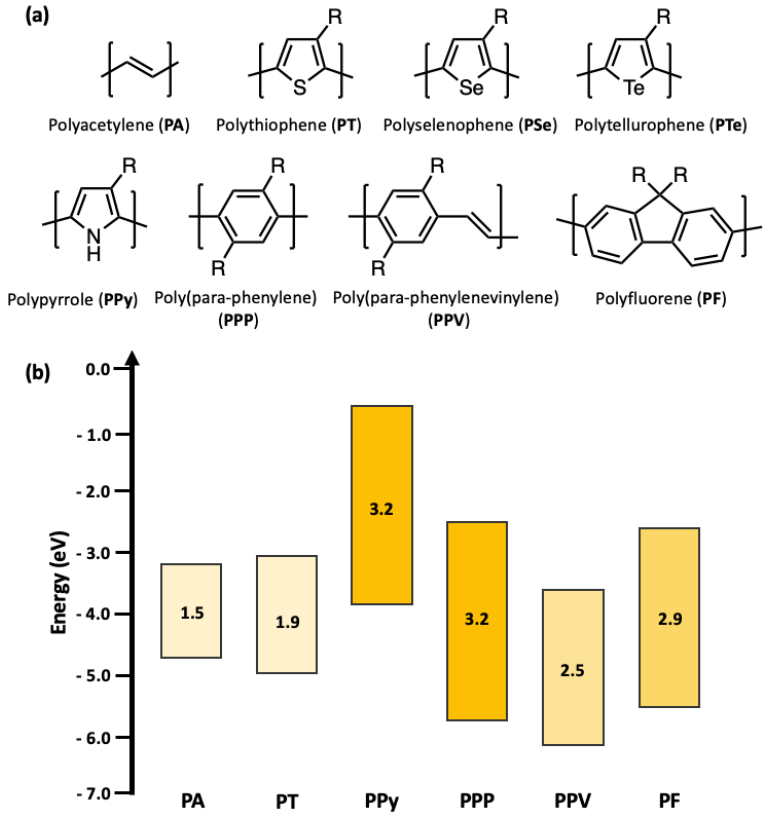

Figure 1. 12: (a) Chemical structures of key conjugated polymers. Positions where side chain substitution typically occurs are represented by the R group positions. (b) Energy level diagram showing the different bandgaps of key conjugated polymers. Band gap (eV) for each polymer is labelled within the band gap illustration. Adapted from ref [163].

1.4.3. Self-Assembly of π-Conjugated Polymers

The majority of reports on conjugated polymer nanoparticles are based on two main synthetic methods, namely, reprecipitation or the preparation of mini-emulsions. These methods typically yield spherical nanoparticles. More recent strategies, including solution self-assembly and microfluidic approaches, have emerged which provide access to low core-corona interfacial curvature morphologies such as 1D nanofibers and 2D platelets.[164–167] π-Conjugated polymers possess rod-like rigidity along the polymer backbone, which promotes π-π stacking interactions between polymer chains during aggregation. If this crystallization process is controlled this can lead to the formation of well-defined 1D nanowires. This will be discussed further in section 1.5.

As mentioned previously (start of section 1.4), some of the key features that make π-conjugated polymeric materials appealing, include their optical and electronic properties, facile processing in solution, compositional flexibility and tailorability, and low cost. The active layers in devices such as organic photovoltaics (OPVs), organic field-effect transistors (OFETs) and organic light-emitting diodes (OLEDs) are frequently produced by spin-coating a film of a molecularly dissolved conjugated polymer onto a substrate[168]. As the solvent evaporates, the conjugated polymer chains stack into crystalline domains that can transport charge carriers. The major limitation of this process is the resulting inhomogeneity of the resulting material which possesses both ordered and disordered regions, which can hinder exciton diffusion over long distances. However, assembling conjugated polymers into nanoparticles before casting the material onto a substrate allows for better control of the crystallization process with increased precision on the nanoscale[164]. Applications of functional nanoparticles prepared through π-conjugated polymer self-assembly will be discussed in section 1.6.

1.5. π-Conjugated Polymer Nanoparticles

1.5.1. Nanoparticles via Crystallization-Driven Self-Assembly

Control over the molecular packing and nanoscale morphology of conjugated polymers are essential prerequisites for optimising the optoelectronic properties of these materials and improving device performance. In particular, crystallization-driven self-assembly of π-conjugated BCPs provides a route to preparing nanofibers that possess exceptionally long exciton diffusion lengths due to the highly ordered crystalline fiber core created during the self-assembly process which involves epitaxial growth.[83] This process appears to provide a uniform energetic landscape, permitting exciton diffusion lengths an order of magnitude larger than typical values for bulk films. Assuming a realistic average absorption coefficient for conjugated polymers[169], a 200-nm-thick film of these nanofibers (commensurate with the measured exciton diffusion length) could absorb 98% of incoming photons, vital for highly efficient light-harvesting devices. Furthermore, devices could be based on a bilayer architecture, a simpler and more reproducible configuration than the bulk heterojunction, which is designed to mitigate the short exciton diffusion lengths of bulk conjugated polymer layers (Figure 1. 13).

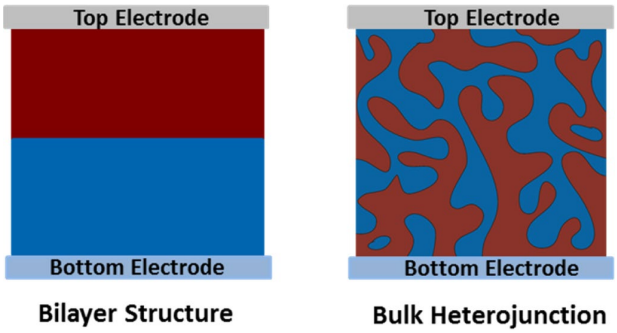

Figure 1. 13: Illustrations of a planar bilayer heterojunction (*left*) and a bulk heterojunction (*right*) as photoactive layers. Donor materials are represented by the red regions and acceptor materials are represented by the blue regions. Reproduced from ref [170].

A wide range of crystallizable core-forming blocks has been reported to undergo CDSA to yield 1D nanofibers, including conjugated polymers, such as polythiophene[59], polyselenophene[173], polyfluorene,[83,174], PPV[165] and polytellurophene.[175] The CDSA behaviour of P3HT BCPs has been studied in detail uncovering key structure-activity relationships. For example P3HT-*b*-P2VP BCPs

can form 1D nanofibers via CDSA in selective solvents for the P2VP corona-forming block.[176,177] Increasing the length of the corona-forming block or decreasing the P3HT regioregularity resulted in fiber-like micelles with more disordered crystalline cores. Attachment of CdSe quantum dots to either the P2VP corona or to amorphous regions in the P3HT core has been achieved. The attachment of quantum dots to the fiber cores also illustrated the order present in the cores for the different hybrid materials (Figure 1. 14).

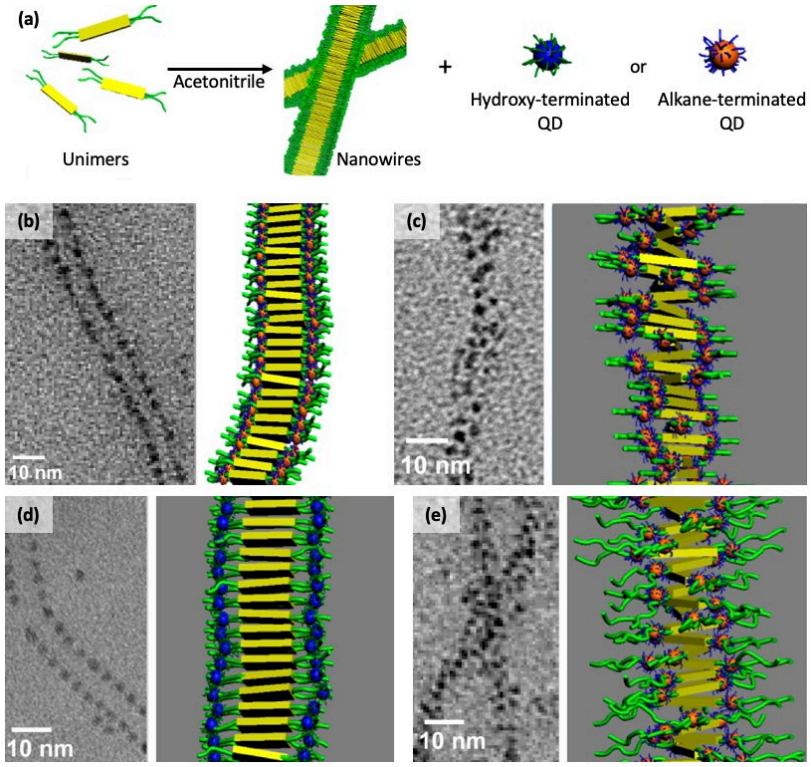

Figure 1. 14: Schematic illustration of the preparation of P3HT-*b*-P2VP nanofibers followed by attachment of CdSe quantum dots (QD) via non-covalent interactions. TEM image and corresponding cartoon illustration of (b) nanofibers with alkane-terminated QDs attached to the regions of the P3HT fiber core with low regioregularity, (c) nanofibers with reduced P3HT regioregularity with alkane-terminated QDs, (d) nanofibers with hydroxy-terminated QDs attached to the P2VP corona, and (e) nanofibers with longer coronas and decorated with alkane-terminated QDs. Scale bars: 10 nm. Adapted with permission from ref [178].

The solution-phase self-assembly of π-conjugated BCPs also provides a route to more complex nanoparticle morphologies. For example, poly(3-triethylene glycol thiophene) (P(3TEG)T) can form different intricate morphologies when used as either a core or corona block. As a core-forming block in water, P(3TEG)T-*b*-poly(ethylene glycol) (PEG) can aggregate into large ribbon-like structures through the interplay of hydrogen bonding and π–π stacking interactions (Figure 1. 15b).[179] As the corona-forming block in P3HT-*b*-P(3TEG)T,

helical fibers form upon the addition of K^+ ions,[180] which further assemble into superhelical bundles over time (Figure 1. 15c). Two-dimensional square platelet nanoparticles, a morphology not commonly observed for conjugated polymer nanoparticles, can be prepared through the self-assembly of PPV BCPs such as PPV-*b*-P2VP (Figure 1. 15a).[165] The particle dimensions could be controlled by altering the block ratio and by changing the concentration of the polymer solution for self-assembly.

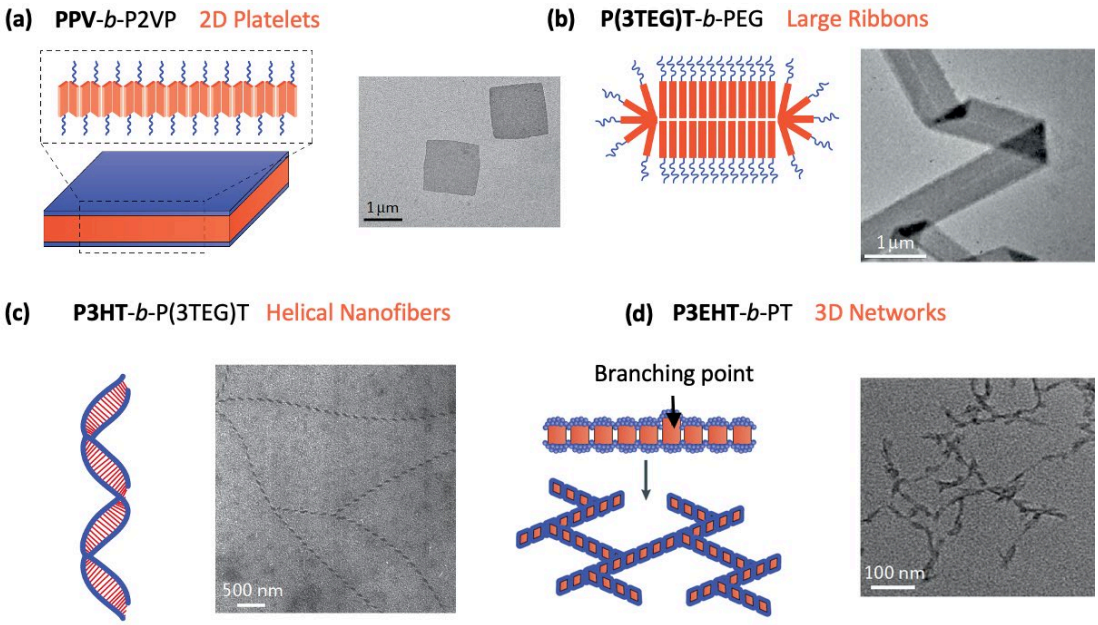

Figure 1. 15: Chemical structures, schematic representations and tunnelling electron microscopy images of amphiphilic π-conjugated block copolymer nanoparticles with different morphologies. (a) Self-assembly of poly(phenylene vinylene)-*b*-poly(2-vinylpyridine) (PPV-*b*-P2VP) in iPrOH to form 2D square platelets. Adapted with permission from ref [179]. (b) Stepwise self-assembly of poly(3-triethyleneglycol thiophene)-*b*-poly(ethylene glycol) (P(3TEG)T-*b*-PEG) in MeOH and then H_2O to produce ribbon-like structures. Adapted with permission from ref [180]. (c) Addition of KI salt to P3HT-*b*-P(3TEG)T in chloroform: acetonitrile (2.5:1, v/v) to form helical fibers. adapted from ref [165]. (d) In situ nanoparticlization of conjugated polymers in toluene to form fibrous branched polythiophene structures. Adapted with permission from ref [181].

1.5.2. Nanoparticles via Living Crystallization-Driven Self-Assembly

The initial extension of the living CDSA approach to π-conjugated BCPs focused on polythiophene-containing materials, in which fibers with controlled lengths of up to ~300 nm could be produced.[73] Thermally-induced self-seeding has since been shown to produce nanoparticles with a low length dispersity and length control of up to 1 µm (Figure 1. 16a).[50] However, obtaining fibers of a predetermined length using this method is more difficult than with seeded growth, owing to the sensitive exponential relationship between fiber length and

annealing temperature and also sample thermal-history effects. The living CDSA approach has been applied to a range of materials with different conjugated polymer core-forming blocks, such as polyfluorene, poly(3-decylselenophene) and PPV.[50,84,182] The living nature of this self-assembly method permits the formation of hierarchical block co-micelle architectures through the addition of unimers with a different corona-forming block. Furthermore, light can be used in certain cases to the control the living CDSA process (Figure 1. 16c).[183] PPV BCP nanofibers were self-assembled using photoisomerization of the core-forming block from a non-crystallizable cis form to a crystallizable trans form. This switchability gives control over the final fiber length and can be used to form segmented and gradient fiber structures.

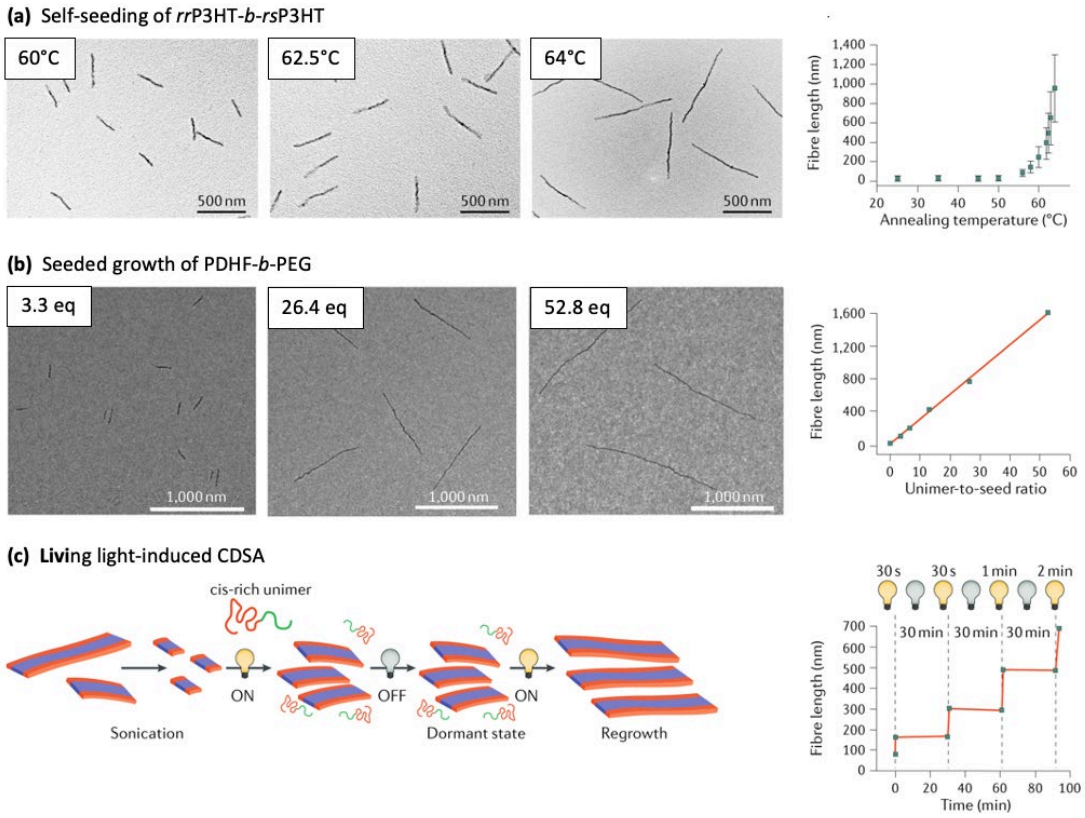

Figure 1. 16: Living CDSA for the preparation of conjugated polymer nanoparticles. (a) TEM images showing fibers of controlled lengths prepared by the self-seeding of *rr*P3HT-*b*-*rs*P3HT at different seed-annealing temperatures. The graph displays the relationship between fiber length and seed-annealing temperature. The error bars represent the standard deviation. (b) TEM images of fibers of controlled lengths produced by the seeded growth of PDHF-*b*-PEG using different unimer-to-seed ratios. The graph displays the relationship between fiber length and the unimer-to-seed mass ratio. (c) Process of living light-induced CDSA using a photoisomerizable poly(*p*-phenylenevinylene) core-forming block. The cis *p*-phenylenevinylene core-forming block in the unimer (green) is photoisomerized to the trans isomer (blue), which enables seeded growth, owing to its lower solubility. Reproduced with permission from ref [184].

We very recently reported the preparation of low dispersity nanowires with a crystalline PDHF core by the 'living' CDSA seeded growth method (Figure 1. 16b).[83] Due to the efficient epitaxial crystallization of PDHF inherent to the self-assembly method, the low dispersity nanowires possess a remarkably well-ordered core, which enables exciton diffusion lengths above 200 nm to be achieved. The value observed in these nanowires surpasses that typically observed for bulk processed conjugated polymer samples (< 10 nm) and is well above the critical length needed for virtually quantitative light absorption suggesting intriguing practical potential. Detailed photophysical measurements were performed on nanofibers that exhibit exciton energy-transfer from the donor crystalline PDHF core to the solvated lower-energy P3HT corona as an acceptor.[83]

1.5.3. Nanoparticles via In-Situ Nanoparticlization of Conjugated Polymers

Recently a technique termed in situ nanoparticlization of conjugated polymers (INCP) has been developed by Choi and coworkers, through which complex nanoparticles form spontaneously during polymerization through careful consideration of the polymerization solvent and polymer solubility (Figure 1. 15d). This process has been reported for BCPs with both polythiophene[181,185–187] and polyacetylene[188–190] core-forming blocks using GRIM and ring-opening metathesis polymerization, respectively. In a typical experiment, the different monomers are sequentially polymerized. The monomer that is polymerized at the end becomes insoluble as the chain length increases. Small aggregates with a crystalline core are formed that further assemble into linear, branched and bundled fibers, as well as platelet-like nanoparticles. This process is analogous to the polymerization-induced CDSA process subsequently reported for non-conjugated crystallizable BCPs[191,192] and that was previously developed for the preparation of amorphous BCP nanoparticles[193]. These self-assembly techniques present a promising scalable route for the preparation of conjugated polymer nanoparticles.

1.6. Applications of π-Conjugated Nanoparticles

1.6.1. Electronics and Optoelectronics

Studies into the self-assembly and optoelectronic properties of polythiophene-containing materials have revealed the importance of both the number of grain boundaries and film morphology in macroscopic charge-carrier mobility (Figure 1. 17).[172,194–196] The organization of conjugated polymer nanoparticles into thin films or higher-order structures is a key challenge with considerable potential for improving device performance and offering new applications. Aligned 1D conjugated polymer nanoparticles can be introduced into flexible devices, which may in the future be incorporated into our everyday lives as wearable technology.[197]

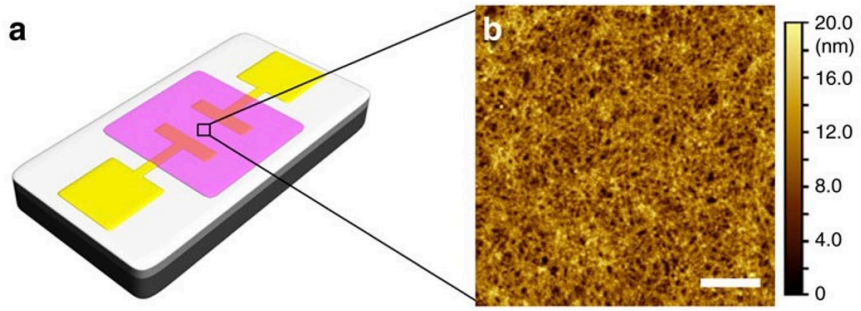

Figure 1. 17: (a) Schematic illustration of a bottom-gate, bottom-contact OFET device with semiconducting film made of nanowires. (b) AFM image of *rr*P3HT$_{106}$-*b*-*rs*P3HT$_{47}$ fibers (cast from solution). Scale bar: 1 μm. Adapted with permission from ref [50].

Organization of conjugated polymer nanoparticles to increase the alignment and packing density can improve bulk material performance.[164,198] Such organization has been achieved after deposition of nanoparticles on a substrate through processes such as thermal annealing and mechanical manipulation.[199–201] As an example, the packing density and spatial arrangement of red, green and blue fluorescent nanoparticles is important for the creation of white-light-emitting devices.[202] If the nanoparticles are too close in proximity, Förster-type energy transfer occurs, leading to quenching or non-white-light emission. This problem was overcome by intercalating the nanoparticles in an electrospun poly(ethylene oxide) matrix to provide sufficient spatial separation to suppress undesirable energy-transfer processes. This approach enabled white-light emission, potentially paving the way towards flexible white-light displays or fixtures.

Mechanical manipulation can also produce nanopatterned and micropatterned surfaces, which have potential applications in OFET and OLED devices.[203] Repetitive compression of a PPV nanoparticle film was used to form 3D nanopillars with a tunable bandgap for LEDs.[204] During compression, the nanoparticles hierarchically self-assemble into microdisks, which then further assemble into regularly spaced nanopillars. The optoelectronic properties of these structures depend on the polymer-chain packing induced by the mechanical forces. By controlling structure formation through selective compression, it has been suggested that it might be possible to form nanoscale heterojunctions by placing different morphologies, with different bandgaps, in close proximity. This level of control of the nanoscale morphology and electronic bandgap presents exciting opportunities for device fabrication.

1.6.2. Biomedical Applications

Conjugated polymer nanoparticles offer desirable properties for biomedical applications including biocompatibility, high functionalizability, and low toxicity (when not under light irradiation)[205]. Additionally, nanoparticles synthesized from biodegradable conjugated polymers are of particular interest, as they can possess high stability to clearance but can then undergo degradation followed by excretion after the desired therapeutic effect is achieved.[206]

Recently, polythiophene and polybenzothiadazole nanoparticles were used to produce 3D reconstructions of the brain blood vessel network with outstanding resolution at depths of 400 μm through an intact mouse skull.[207] The nanoparticles undergo two-photon excitation when irradiated with a near-infrared (NIR) laser, followed by detectable emission at 725 nm with a high signal-to-noise ratio and quantum yield of 20.6%. In addition to fluorescence imaging, conjugated polymer nanoparticles can be used for photoacoustic imaging, whereby absorbed light is converted into heat, which leads to thermoelastic expansion and consequently pressure spikes that create ultrasonic waves[208]. A probe composed of polythiophene and polybenzothiadiazole nanoparticles was designed for non-invasive, whole-body lymph-node photoacoustic imaging in living mice[209]. This nanoparticle system was also able to photoacoustically report

the levels of reactive oxygen species (for example, $O_2^{\bullet-}$ and $^{\bullet}OH$). Compared with single-walled carbon nanotubes and 1D gold nanoparticles, this system produced stronger photoacoustic signals in living mice.

1.6.3. Photocatalysis

The photophysical properties of conjugated polymers can be easily and precisely tuned through chemical modifications, offering opportunities for the use of rational design to improve photocatalytic activity.[210] Spherical nanoparticles (ca. 30 – 50 nm) composed of poly(fluorene-*co*-benzothiazole) (PFBT) copolymer have been shown to exhibit excellent hydrogen-generation performance upon photoirradiation without the assistance of a co-catalyst. The activity of the nanoparticles was enhanced by five orders of magnitude compared with a pristine PFBT polymer suspension owing to the larger surface area. [211] Slight modifications to the main chain of the conjugated polymer (poly(fluorene-*co*-dithienylbenzothiazole)) resulted in the formation of spherical nanoparticles that possess photocatalytic activity that was 15 times higher than that of PFBT-based nanoparticles. [212]

The light-harvesting capabilities of conjugated polymer nanoparticles have also been exploited to augment photosynthesis in chloroplasts.[213] The nanoparticles surround chloroplasts and convert the incoming UV light that is not well absorbed into longer wavelengths that are more readily absorbed. The absorption and re-emission by the nanoparticles allows the chloroplasts to capture a broader range of light to improve the photosynthetic efficiency. Although most current studies focus on the use of spherical nanoparticles, understanding the relationship between shape and photocatalytic activity is of particular interest and might be possible through the living CDSA approach.

1.6.4. Sensing

Conjugated polymers display coloured fluorescence emission throughout the visible spectrum with a high fluorescence quantum yield. Quenching in response to stimuli is a useful property in sensing applications. Photoresponsive conjugated polymer nanoparticles have been prepared by combining photochromic diarylethene side chains with π-conjugated main chains.[214] The emission of these nanoparticles is switched on or off by irradiation with visible or

UV light, respectively, causing the functional unit to undergo a reversible ring-closing reaction. This molecular design holds promise for the fabrication of photoresponsive optoelectronic devices based on conjugated polymer nanoparticles.

Furthermore, there is a growing need for new anti-counterfeiting materials that exhibit tunable optical properties when the material is dry in the solid state. In this regard, a supramolecular conjugated polymer nanoparticle-based system has been reported to display tunable full-colour fluorescence and white-light emission.[215] These nanoparticles were formed by non-covalent host–guest interactions, and display responsive behaviour when a dithienylethene-derived unit is incorporated. Aqueous solutions of the nanoparticles were painted on paper, and upon exposure to metal ions or UV light, the fluorescence of the ink is quenched. This is due to the complexation of the metal ions to the nanoparticles or the photoisomerization of the dithienylethene moieties, respectively (Figure 1. 18a-b). Additional information can be encoded by incorporating a chemiluminescent substrate that is responsive to hydrogen peroxide (Figure 1. 18c). Applications as security inks and anti-counterfeiting agents have been proposed for these materials.

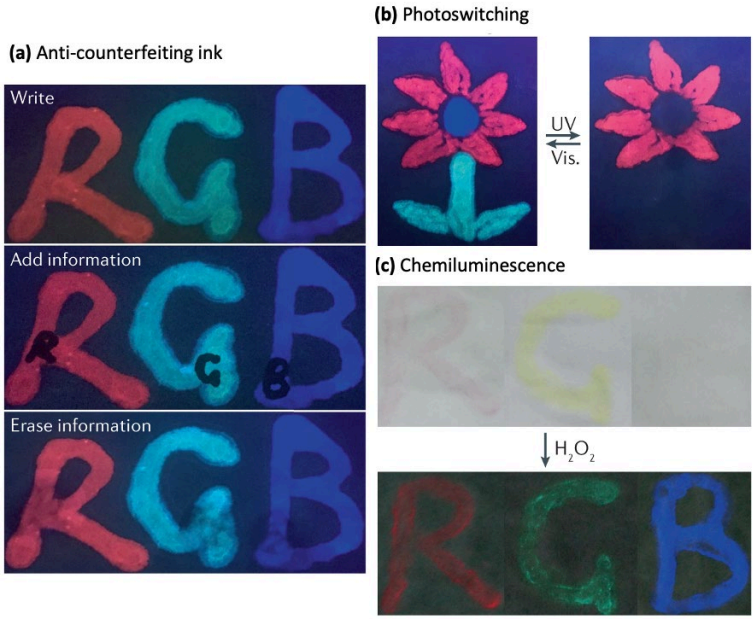

Figure 1. 18: Encoding information using fluorescent inks based on conjugated-polymer nanoparticles. (a) Addition of Fe^{3+} ions leads to fluorescence quenching. Information can, therefore, be encoded and then erased through the addition or removal, respectively, of Fe^{3+} ions. (b) The nanoparticle-based inks undergo reversible photoswitching upon irradiation with ultraviolet (UV) or visible (Vis.) light. (c) The nanoparticles can be designed to exhibit chemiluminescent behaviour on addition of H_2O_2. Adapted with permission from ref [215].

Detection of toxic chemicals and explosives is vital for addressing environmental pollution and security concerns. The detection of metallic pollutants, such as aqueous mercury contaminants, has been demonstrated using rhodamine-doped conjugated polymer nanoparticles.[216] Highly sensitive and selective detection of cyanide has also been achieved with nanoparticles made from a hyperbranched conjugated polymer.[217] Ultrasensitive detection of picric acid in aqueous and vapour phases by conjugated polymer nanoparticles via several different mechanisms, including aggregation-enhanced FRET and PET, has also been reported.[218,219] FRET-based detection by conjugated polymer nanoparticles has also been employed in singlet-oxygen sensing, providing a more rapid response compared with thin-film systems.[220] Other nanoparticles, such as spherical micelles, nanocaterpillars (worm-like micelles with an undulating height profile) and star-like micelles, prepared through the in situ nanoparticlization of conjugated polymers, have also achieved selective detection of 2,4,6-trinitrotoluene.[221]

1.7. Thesis Objectives

The introduction of this thesis has provided an overview of supramolecular and block copolymer self-assembly, with reference to specific examples of nanoparticles prepared by the self-assembly of π-conjugated polymers. Highly ordered crystalline core nanostructures of controlled dimensions have been prepared by implementing the 'living' CDSA approach. Research discussed in this thesis includes an investigation into the full scope of using 'living' CDSA to prepare functional nanomaterials that could potentially be integrated into electronic devices. The main objectives of this research are to investigate the scope of the 'living' crystallization-driven self-assembly of polyfluorene-based block copolymers and study the optoelectronic properties of these materials. Seeded growth methods will be used prepare a variety of nanostructures with desirable morphologies and electronic properties.

1.7.1. Construction of Different Types of Nanoscale Heterojunctions

Segmented heterojunction nanowires have been prepared via CDSA of polyfluorene BCPs. These materials have been shown to possess exceptional

electronic properties due to the highly ordered crystalline micelle cores. In this system, the fiber core composed of crystallized polyfluorene that acts as an energy-donor. Upon selective excitation, solvated coronal chains composed of quaternized polythiophene act as low energy-acceptor regions. The first two results chapters of this thesis will focus on the design of different types of nanoscale heterojunctions where polyfluorene-based crystalline core fibers are coupled with either crystalline polymeric acceptor materials (Chapter 2) or inorganic nanoparticle acceptors (Chapter 3).

1.7.2. Control the Formation of Different Micelle Morphologies via CDSA of Polyfluorene BCPs

Helical and 2D platelet micelle morphologies are of growing interest for possible application in electronic devices. These morphologies can be prepared by the CDSA of PFDMS or polythiophene-based BCPs. The aim of this research is to prepare these morphologies from the CDSA of polyfluorene-based materials. In Chapter 4 the synthesis of helical nanostructures from polyfluorene-based triblock copolymer materials is explored. In Chapter 5 the CDSA of polyfluorene homopolymers and diblock copolymers with charged terminal groups was investigated for the preparation of 1D fiber-like micelles and 2D platelets of controlled dimensions.

1.7.3. Explore the Scope of 'Living' CDSA of Polyfluorene BCPs

Throughout this thesis, the synthesis and self-assembly of a range of polyfluorene-based homopolymers with charged end groups, diblock copolymers, and triblock terpolymers has been described. Optimization of CDSA and seeded growth protocols has been carried out to uncover key trends in the solution self-assembly behaviour of these materials. For example, in Chapter 5 the propensity of polyfluorene homopolymers and diblock copolymers with charged terminal groups to form 1D fiber-like micelles and 2D platelets via solution self-assembly was explored. In Chapter 6 the self-assembly of poly(di-*n*-octylfluorene)-based BCPs, that can access the highly ordered β-phase, was studied.

1.8. Thesis Structure and Collaborator Acknowledgments

1.8.1. Thesis Structure

This thesis is comprised of different research projects all based on investigations of the self-assembly of polyfluorene-based materials. Five results chapters are presented with an additional chapter discussing the final thesis summary, conclusions and future directions for research built on this work. The contents of each chapter are listed here:

Chapter 2: Solid-State Donor-Acceptor Coaxial Heterojunction Nanowires via Living Crystallization-Driven Self-Assembly.

Chapter 3: Hybrid Nanowires: Energetically Coupled Polyfluorene-Containing Nanofibers and Inorganic Quantum Dots

Chapter 4: Uniform Helical Nanofibers of Controlled Handedness via Seeded Growth of Polyfluorene-Containing Block Copolymers

Chapter 5: Further Studies of the Solution Self-Assembly of Poly(*n*-dihexylfluorene) Homopolymers and Block Copolymers with Charged Terminal Groups.

Chapter 6: Solution Self-Assembly of Diblock Copolymers with a Crystallizable Poly(di-*n*-octylfluorene) Core-Forming Block and Investigation of β-phase Packing

1.8.2. Collaborator Acknowledgments

As is customary in Prof. Ian Manners group, each thesis chapter is self-contained with separate introduction and summary sections in a format that is suitable for publication as a research article. As part of a large research group with established international collaborators, a significant amount of the work presented in this thesis was produced in collaboration with internal and external colleagues.

Chapter 1: Sections of this introductory chapter were reproduced from *Nat. Rev. Mat*, **2021**, *6*, 7-26, which was co-written with Dr. Liam MacFarlane, Dr. Tomoya Fukui, J. Diego Garcia-Hernandez and Marcus Vespa. Insight and additional input was provided by Prof. Ian Manners. All contributions are from

current or former members of the Manner's research group at the University of Victoria.

Chapter 2: Reproduced from *Journal of the American Chemical Society*, **2020**, *142*, 13469-13480. Synthesis of polymers, self-assembly and seeded growth experiments, and optical spectroscopy characterization were conducted by Huda Shaikh. Segmented nanofiber self-assembly was conducted by Prof. Xu-Hui Jin (*University of Bristol*). AFM was conducted by Dr. Robert Harniman (*University of Bristol*). WAXS was conducted and analyzed in collaboration with Prof. Robert Richardson (*University of Bristol*). Initial scientific design of the experiments was conducted in calibration with Prof. Xu-Hui Jin. Research was conducted at the University of Bristol and University of Victoria.

Chapter 3: Polymer synthesis was conducted by Huda Shaikh and self-assembly and seeded growth experiments were conducted by Huda Shaikh and Dr. Yifan Zhang (*University of Victoria*). Functionalized quantum nanostructures were prepared by Dr. Yifan Zhang. Joint scientific input was contributed by Huda Shaikh and Dr. Yifan Zhang in the preparation of a manuscript based on this project. Transient absorption measurements were conducted by Alexander Sneyd (*University of Cambridge*). Useful scientific input was provided by our collaborators, the Prof. Richard Friend group (*University of Cambridge*). Research was conducted at the University of Bristol and University of Victoria.

Chapter 4: Synthesis of polymers and self-assembly and seeded growth experiments were conducted by Huda Shaikh. Characterization of helical nanofibers was conducted by Huda Shaikh. AFM was conducted by Dr. Robert Harniman (*University of Bristol*) and Dr. Yuetong Kang (*University of Victoria*). Initial scientific design of the experiments was conducted in calibration with Prof. Xu-Hui Jin and Dr. George Whittell. Research was conducted at the University of Bristol and University of Victoria.

Chapter 5: AFM was conducted by Dr. Yuetong Kang (*University of Victoria*). All other research presented in this Chapter was conducted by Huda Shaikh. Research was conducted at the University of Victoria.

Chapter 6: This research was solely conducted by Huda Shaikh. Research was conducted at the University of Bristol and University of Victoria.

Chapter 7: This work was solely conducted by Huda Shaikh.

1.9. References

(1) Whitesides, G. M.; Grzybowski, B. Self-Assembly at All Scales. *Science.* **2002**, *295* (5564), 2418–2421.

(2) Feynman, R. P. There's Plenty of Room at the Bottom. *Eng. Sci.* **1960**, *23* (5), 22–36.

(3) Lu, W.; Lieber, C. M. Nanoelectronics from the Bottom Up. *Nat. Mater.* **2007**, *6*, 841–850.

(4) Tee, B. C. K.; Wang, C.; Allen, R.; Bao, Z. An Electrically and Mechanically Self-Healing Composite with Pressure- and Flexion-Sensitive Properties for Electronic Skin Applications. *Nat. Nanotechnol.* **2012**, *7*, 825–832.

(5) Li, C. H.; Wang, C.; Keplinger, C.; Zuo, J. L.; Jin, L.; Sun, Y.; Zheng, P.; Cao, Y.; Lissel, F.; Linder, C.; You, X. Z.; Bao, Z. A Highly Stretchable Autonomous Self-Healing Elastomer. *Nat. Chem.* **2016**, *8*, 618–624.

(6) Son, D.; Kang, J.; Vardoulis, O.; Kim, Y.; Matsuhisa, N.; Oh, J. Y.; To, J. W.; Mun, J.; Katsumata, T.; Liu, Y.; McGuire, A. F.; Krason, M.; Molina-Lopez, F.; Ham, J.; Kraft, U.; Lee, Y.; Yun, Y.; Tok, J. B. H.; Bao, Z. An Integrated Self-Healable Electronic Skin System Fabricated via Dynamic Reconstruction of a Nanostructured Conducting Network. *Nat. Nanotechnol.* **2018**, *13*, 1057–1065.

(7) Liu, K.; Jiang, Y.; Bao, Z.; Yan, X. Skin-Inspired Electronics Enabled by Supramolecular Polymeric Materials. *CCS Chem.* **2019**, *1* (4), 431–447.

(8) Fratzl, P.; Weinkamer, R. Nature's Hierarchical Materials. *Prog. Mater. Sci.* **2007**, *52* (8), 1263–1334.

(9) Philp, D.; Fraser Stoddart, J. Self-Assembly in Natural and Unnatural Systems. *Angew. Chem. Int. Ed. Engl.* **1996**, *35* (11), 1154–1196.

(10) Lakes, R. Materials with Structural Hierarchy. *Nature* **1993**, *361*, 511–515.

(11) Vukusic, P.; Sambles, J. R.; Lawrence, C. R. Colour Mixing in Wing Scales of a Butterfly. *Nature* **2000**, *404*, 457.

(12) Vukusic, P.; Sambles, J. R. Photonic Structures in Biology. *Nature* **2003**, *424*, 852–855.

(13) Parker, A. R.; Townley, H. E. Biomimetics of Photonic Nanostructures. *Nat. Nanotechnol.* **2007**, *2*, 347–353.

(14) Barrera-Patiño, C. P.; Vollet-Filho, J. D.; Teixeira-Rosa, R. G.; Quiroz, H. P.; Dussan, A.; Inada, N. M.; Bagnato, V. S.; Rey-González, R. R. Photonic Effects in Natural Nanostructures on Morpho Cypris and Greta Oto Butterfly Wings. *Sci. Rep.* **2020**, *10*, 5786.

(15) Vukusic, P.; Sambles, J. R.; Lawrence, C. R.; Wootton, R. J. Now You See It - Now You Don't. *Nature* **2001**, *410*, 36.

(16) Engl, G.; Kolle, M.; Kim, P.; Khan, M.; Muñoz, P.; Mazur, E.; Aizenberg, J. Bioinspired Micrograting Arrays Mimicking the Reverse Color Diffraction Elements Evolved by the Butterfly Pierella Luna. *Proc. Natl. Acad. Sci. U. S. A.* **2014**, *111* (44), 15630–15634.

(17) Meng, Y.; Qiu, J.; Wu, S.; Ju, B.; Zhang, S.; Tang, B. Biomimetic Structural Color Films with a Bilayer Inverse Heterostructure for Anticounterfeiting Applications. *ACS Appl. Mater. Interfaces* **2018**, *10* (44), 38459–38465.

(18) Mihranyan, A.; Ferraz, N.; Strømme, M. Current Status and Future Prospects of Nanotechnology in Cosmetics. *Prog. Mater. Sci.* **2012**, *57* (5), 875–910.

(19) Kostarelos, K. Nanoscale Nights of COVID-19. *Nat. Nanotechnol.* **2020**, *15*, 343–344.

(20) Klug, A. The Tobacco Mosaic Virus Particle: Structure and Assembly. *Philos. Trans. R. Soc. B Biol. Sci.* **1999**, *354* (1383), 531–535.

(21) Walls, A. C.; Park, Y. J.; Tortorici, M. A.; Wall, A.; McGuire, A. T.; Veesler, D. Structure, Function, and Antigenicity of the SARS-CoV-2 Spike Glycoprotein. *Cell* **2020**, *181* (2), 281–292.

(22) Stupp, S. I.; Palmer, L. C. Supramolecular Chemistry and Self-Assembly in Organic Materials Design. *Chem. Mater.* **2014**, *26* (1), 507–518.

(23) Boekhoven, J.; Hendriksen, W. E.; Koper, G. J. M.; Eelkema, R.; Van Esch, J. H. Transient Assembly of Active Materials Fueled by a Chemical Reaction. *Science.* **2015**, *349* (6252), 1075–1079.

(24) Grzybowski, B. A.; Fitzner, K.; Paczesny, J.; Granick, S. From Dynamic Self-Assembly to Networked Chemical Systems. *Chem. Soc. Rev.* **2017**, *46*, 5647–5678.

(25) Cheng, G.; Perez-Mercader, J. Dissipative Self-Assembly of Dynamic Multicompartmentalized Microsystems with Light-Responsive Behaviors. *Chem* **2020**, *6* (5), 1160–1171.

(26) Bastakoti, B. P.; Perez-Mercader, J. Autonomous Ex Novo Chemical Assembly with Blebbing and Division of Functional Polymer Vesicles from a "Homogeneous Mixture." *Adv. Mater.* **2017**, *29* (43), 1704368.

(27) Lehn, J. M. Cryptates: The Chemistry of Macropolycyclic Inclusion Complexes. *Acc. Chem. Res.* **1978**, *11* (2), 49–57.

(28) Iqbal, P.; Preece, J. A.; Mendes, P. M. Nanotechnology: The "Top-Down" and "Bottom-Up" Approaches. In *Supramolecular Chemistry: From Molecules to Nanomaterials*; Gale, P., Steed, J., Eds.; Wiley, 2012.

(29) Zhang, S. Fabrication of Novel Biomaterials through Molecular Self-Assembly. *Nat. Biotechnol.* **2003**, *21* (10), 1171–1178.

(30) Lehn, J. M. Toward Self-Organization and Complex Matter. *Science.* **2002**, *295* (5564), 2400–2403.

(31) Aida, T.; Meijer, E. W.; Stupp, S. I. Functional Supramolecular Polymers. *Science.* **2012**, *335* (6070), 813–817.

(32) Tritschler, U.; Pearce, S.; Gwyther, J.; Whittell, G. R.; Manners, I. 50th Anniversary Perspective: Functional Nanoparticles from the Solution Self-Assembly of Block Copolymers. *Macromolecules* **2017**, *50* (9), 3439–3463.

(33) Segalman, R. A. Patterning with Block Copolymer Thin Films. *Mater. Sci. Eng. R Reports* **2005**, *48* (6), 191–226.

(34) Zheng, W.; Wang, Z. G. Morphology of ABC Triblock Copolymers. *Macromolecules* **1995**, *28*, 7215–7223.

(35) Tang, P.; Qiu, F.; Zhang, H.; Yang, Y. Morphology and Phase Diagram of Complex Block Copolymers: ABC Linear Triblock Copolymers. *Phys. Rev. E - Stat. Nonlinear, Soft Matter Phys.* **2004**, *69*, 031803.

(36) Dumanli, A. G.; Savin, T. Recent Advances in the Biomimicry of Structural Colours. *Chem. Soc. Rev.* **2016**, *45* (24), 6698–6724.

(37) Hamley, I. W. Nanotechnology with Soft Materials. *Angew. Chem. Int. Ed.* **2003**, *42* (15), 1692–1712.

(38) Israelachvili, J. N.; Mitchell, D. J.; Ninham, B. W. Theory of Self-Assembly of Hydrocarbon Amphiphiles into Micelles and Bilayers. *J. Chem. Soc. Faraday Trans. 2 Mol. Chem. Phys.* **1976**, *72*, 1525–1568.

(39) Zhang, L.; Eisenberg, A. Multiple Morphologies and Characteristics of "crew-Cut" Micelle-like Aggregates of Polystyrene-b-Poly(Acrylic Acid) Diblock Copolymers in Aqueous Solutions. *J. Am. Chem. Soc.* **1996**, *118* (13), 3168–3181.

(40) Mai, Y.; Eisenberg, A. Self-Assembly of Block Copolymers. *Chem. Soc. Rev.* **2012**, *41* (18), 5969.

(41) Blanazs, A.; Armes, S. P.; Ryan, A. J. Self-Assembled Block Copolymer Aggregates: From Micelles to Vesicles and Their Biological Applications. *Macromol. Rapid Commun.* **2009**, *30*, 267–277.

(42) Discher, D. E.; Eisenberg, A. Polymer Vesicles. *Science.* **2002**, *297* (5583), 967–973.

(43) Zhang, L.; Yu, K.; Eisenberg, A. Ion-Induced Morphological Changes in "crew-Cut" Aggregates of Amphiphilic Block Copolymers. *Science.* **1996**, *272* (5269), 1777–1779.

(44) Zhang, L.; Eisenberg, A. Multiple Morphologies of "Crew-Cut" Aggregates of Polystyrene-b-Poly(Acrylic Acid) Block Copolymers. *Science.* **1995**, *268* (5218), 1728–1731.

(45) Gröschel, A. H.; Schacher, F. H.; Schmalz, H.; Borisov, O. V.; Zhulina, E. B.; Walther, A.; Müller, A. H. E. Precise Hierarchical Self-Assembly of Multicompartment Micelles. *Nat. Commun.* **2012**, *3*, 710.

(46) Gröschel, A. H.; Müller, A. H. E. Self-Assembly Concepts for Multicompartment Nanostructures. *Nanoscale* **2015**, *7* (28), 11841–11876.

(47) Dalhaimer, P.; Engler, A. J.; Parthasarathy, R.; Discher, D. E. Targeted Worm Micelles. *Biomacromolecules* **2004**, *5* (5), 1714–1719.

(48) Yan, X.; Liu, G.; Haeussler, M.; Tang, B. Z. Water-Dispersible Polymer/Pd/Ni Hybrid Magnetic Nanofibers. *Chem. Mater.* **2005**, *17* (24), 6053–6059.

(49) Strobl, G. Crystallization and Melting of Bulk Polymers: New Observations, Conclusions and a Thermodynamic Scheme. *Prog. Polym. Sci.* **2006**, *31* (4), 398–442.

(50) Li, X.; Wolanin, P. J.; Macfarlane, L. R.; Harniman, R. L.; Qian, J.; Gould, O. E. C.; Dane, T. G.; Rudin, J.; Cryan, M. J.; Schmaltz, T.; Frauenrath, H.; Winnik, M. A.; Faul, C. F. J.; Manners, I. Uniform Electroactive Fibre-like Micelle Nanowires for Organic Electronics. *Nat. Commun.* **2017**, *8*, 15909.

(51) Lotz, B.; Kovacs, A. J.; Bassett, G. A.; Keller, A. Properties of Copolymers Composed of One Poly-Ethylene-Oxide and One Polystyrene Block - II. Morphology of Single Crystals. *Kolloid-Zeitschrift Zeitschrift für Polym.* **1966**, *209*, 115–128.

(52) Richter, D.; Schneiders, D.; Monkenbusch, M.; Willner, L.; Fetters, L. J.; Huang, J. S.; Lin, M.; Mortensen, K.; Farago, B. Polymer Aggregates with Crystalline Cores: The System Polyethylene-Poly(Ethylenepropylene). *Macromolecules* **1997**, *30* (4), 1053–1068.

(53) Massey, J.; Nicole Power, K.; Manners, I.; Winnik, M. A. Self-Assembly of a Novel Organometallic-Inorganic Block Copolymer in Solution and the Solid State: Nonintrusive Observation of Novel Wormlike Poly(Ferrocenyldimethylsilane)-b-Poly (Dimethylsiloxane) Micelles. *J. Am. Chem. Soc.* **1998**, *120* (37), 9533–9540.

(54) Massey, J. A.; Temple, K.; Cao, L.; Rharbi, Y.; Raez, J.; Winnik, M. A.; Manners, I. Self-Assembly of Organometallic Block Copolymers: The Role of Crystallinity of the Core-Forming Polyferrocene Block in the Micellar Morphologies Formed by Poly(Ferrocenylsilane-b-Dimethylsiloxane) in n-Alkane Solvents. *J. Am. Chem. Soc.* **2000**, *122* (47), 11577–11584.

(55) Hailes, R. L. N.; Oliver, A. M.; Gwyther, J.; Whittell, G. R.; Manners, I. Polyferrocenylsilanes: Synthesis, Properties, and Applications. *Chem. Soc. Rev.* **2016**, *45* (19), 5358–5407.

(56) Cao, L.; Manners, I.; Winnik, M. A. Influence of the Interplay of Crystallization and Chain Stretching on Micellar Morphologies: Solution Self-Assembly of Coil-Crystalline Poly(Isoprene-Block-Ferrocenylsilane). *Macromolecules* **2002**, *35* (22), 8258–8260.

(57) Massey, J. A.; Temple, K.; Cao, L.; Rharbi, Y.; Raez, J.; Winnik, M. A.; Manners, I. Self-Assembly of Organometallic Block Copolymers: The Role of Crystallinity of the Core-Forming Polyferrocene Block in the Micellar Morphologies Formed by Poly(Ferrocenylsilane-b-Dimethylsiloxane) in n-Alkane Solvents. *J. Am. Chem. Soc.* **2000**, *122* (47), 11577–11584.

(58) Wang, X.; Guerin, G.; Wang, H.; Wang, Y.; Manners, I.; Winnik, M. A. Cylindrical Block Copolymer Micelles and Co-Micelles of Controlled Length and Architecture. *Science.* **2007**, *317* (5838), 644–647.

(59) Yin, L.; Lodge, T. P.; Hillmyer, M. A. A Stepwise "Micellization-Crystallization" Route to Oblate Ellipsoidal, Cylindrical, and Bilayer Micelles with Polyethylene Cores in Water. *Macromolecules* **2012**, *45* (23), 9460–9467.

(60) Schmelz, J.; Karg, M.; Hellweg, T.; Schmalz, H. General Pathway toward Crystalline-Core Micelles with Tunable Morphology and Corona Segregation. *ACS Nano* **2011**, *5* (12), 9523–9534.

(61) Gädt, T.; Schacher, F. H.; McGrath, N.; Winnik, M. A.; Manners, I. Probing the Scope of Crystallization-Driven Living Self-Assembly: Studies of Diblock Copolymer Micelles with a Polyisoprene Corona and a Crystalline Poly(Ferrocenyldiethylsilane) Core-Forming

Metalloblock. *Macromolecules* **2011**, *44* (10), 3777–3786.

(62) Du, V. A.; Qiu, H.; Winnik, M. A.; Whittell, G. R.; Manners, I. Synthesis and Solution Self-Assembly of Polyisoprene-block-poly(Ferrocenylmethylsilane): A Diblock Copolymer with an Atactic but Semicrystalline Core-Forming Metalloblock. *Macromol. Chem. Phys.* **2016**, *217* (15), 1671–1682.

(63) Gädt, T.; Ieong, N. S.; Cambridge, G.; Winnik, M. A.; Manners, I. Complex and Hierarchical Micelle Architectures from Diblock Copolymers Using Living, Crystallization-Driven Polymerizations. *Nat. Mater.* **2009**, *8* (2), 144–150.

(64) Petzetakis, N.; Dove, A. P.; O'Reilly, R. K. Cylindrical Micelles from the Living Crystallization-Driven Self-Assembly of Poly(Lactide)-Containing Block Copolymers. *Chem. Sci.* **2011**, *2* (5), 955–960.

(65) Petzetakis, N.; Walker, D.; Dove, A. P.; O'Reilly, R. K. Crystallization-Driven Sphere-to-Rod Transition of Poly(Lactide)-b-Poly(Acrylic Acid) Diblock Copolymers: Mechanism and Kinetics. *Soft Matter* **2012**, *8* (28), 7408–7414.

(66) Sun, L.; Petzetakis, N.; Pitto-Barry, A.; Schiller, T. L.; Kirby, N.; Keddie, D. J.; Boyd, B. J.; O'Reilly, R. K.; Dove, A. P. Tuning the Size of Cylindrical Micelles from Poly(l-Lactide)-b-Poly(Acrylic Acid) Diblock Copolymers Based on Crystallization-Driven Self-Assembly. *Macromolecules* **2013**, *46* (22), 9074–9082.

(67) Du, Z. X.; Xu, J. T.; Fan, Z. Q. Micellar Morphologies of Poly(ε-Caprolactone)-b-Poly(Ethylene Oxide) Block Copolymers in Water with a Crystalline Core. *Macromolecules* **2007**, *40* (21), 7633–7637.

(68) He, W.-N.; Zhou, B.; Xu, J. T.; Du, B. Y.; Fan, Z. Q. Two Growth Modes of Semicrystalline Cylindrical Poly(ε-Caprolactone)-b -Poly(Ethylene Oxide) Micelles. *Macromolecules* **2012**, *45* (24), 9768–9778.

(69) Thakellapalli, H.; Li, S.; Farajidizaji, B.; Baughman, N. N.; Akhmedov, N. G.; Popp, B. V.; Wang, K. K. Synthesis and Properties of Conjugated Macrocycles Containing 2,7-Bis(2-Thienyl)-9H-Fluoren-9-One Units. *Org. Lett.* **2017**, *19* (10), 2674–2677.

(70) Mihut, A. M.; Drechsler, M.; Möller, M.; Ballauff, M. Sphere-to-Rod Transition of Micelles Formed by the Semicrystalline Polybutadiene-Block-Poly(Ethylene Oxide) Block Copolymer in a Selective Solvent. *Macromol. Rapid Commun.* **2010**, *31* (5), 449–453.

(71) Brubaker, C. E.; Velluto, D.; Demurtas, D.; Phelps, E. A.; Hubbell, J. A. Crystalline Oligo(Ethylene Sulfide) Domains Define Highly Stable Supramolecular Block Copolymer Assemblies. *ACS Nano* **2015**, *9* (7), 6872–6881.

(72) Lazzari, M.; Scalarone, D.; Vazquez-Vazquez, C.; López-Quintela, M. A. Cylindrical Micelles from the Self-Assembly of Polyacrylonitrile-Based Diblock Copolymers in Nonpolar Selective Solvents. *Macromol. Rapid Commun.* **2008**, *29* (4), 352–357.

(73) Gilroy, J. B.; Lunn, D. J.; Patra, S. K.; Whittell, G. R.; Winnik, M. A.; Manners, I. Fiber-like Micelles via the Crystallization-Driven Solution Self- Assembly of Poly(3-Hexylthiophene)-Block -Poly(Methyl Methacrylate) Copolymers. *J. Am. Chem. Soc.* **2012**, *45* (14), 5805–5815.

(74) Gwyther, J.; Gilroy, J. B.; Rupar, P. A.; Lunn, D. J.; Kynaston, E.; Patra, S. K.; Whittell, G. R.; Winnik, M. A.; Manners, I. Dimensional Control of Block Copolymer Nanofibers with a π-Conjugated Core: Crystallization-Driven Solution Self-Assembly of Amphiphilic Poly(3-Hexylthiophene)-b-Poly(2-Vinylpyridine). *Chem. - A Eur. J.* **2013**, *19* (28), 9186–9197.

(75) Kynaston, E. L.; Gould, O. E. C.; Gwyther, J.; Whittell, G. R.; Winnik, M. A.; Manners, I. Fiber-like Micelles from the Crystallization-Driven Self-Assembly of Poly(3-Heptylselenophene)-Block-Polystyrene. *Macromol. Chem. Phys.* **2015**, *216* (6), 685–695.

(76) Kynaston, E. L.; Nazemi, A.; MacFarlane, L. R.; Whittell, G. R.; Faul, C. F. J.; Manners, I.; Faul, C. F. J. Uniform Polyselenophene Block Copolymer Fiberlike Micelles and Block Co-Micelles via Living Crystallization-Driven Self-Assembly. *Macromolecules* **2018**, *51* (3), 1002–1010.

(77) Tritschler, U.; Gwyther, J.; Harniman, R. L.; Whittell, G. R.; Winnik, M. A.; Manners, I. Toward Uniform Nanofibers with a π-Conjugated Core: Optimizing the "Living" Crystallization-Driven Self-Assembly of Diblock Copolymers with a Poly(3-Octylthiophene) Core-Forming

Block. *Macromolecules* **2018**, *51* (14), 5101–5113.

(78) Lee, I.-H.; Amaladass, P.; Choi, T.-L. One-Pot Synthesis of Nanocaterpillar Structures via in Situ Nanoparticlization of Fully Conjugated Poly(p-Phenylene)-Block-Polythiophene. *Chem. Commun.* **2014**, *50* (59), 7945–7948.

(79) Mori, T.; Watanabe, T.; Minagawa, K.; Tanaka, M. Self-Assembly of Oligo(p-Phenylenevinylene)-Block-Poly(Ethylene Oxide) in Polar Media and Solubilization of an Oligo(p-Phenylenevinylene) Homooligomer inside the Assembly. *J. Polym. Sci. Part A Polym. Chem.* **2005**, *43* (8), 1569–1578.

(80) Tao, D.; Feng, C.; Cui, Y.; Yang, X.; Manners, I.; Winnik, M. A.; Huang, X. Monodisperse Fiber-like Micelles of Controlled Length and Composition with an Oligo(p-Phenylenevinylene) Core via "Living" Crystallization-Driven Self-Assembly. *J. Am. Chem. Soc.* **2017**, *139* (21), 7136–7139.

(81) Li, K.; Wang, Q. Multiple Self-Assembled Nanostructures from an Oligo(p-Phenyleneethynylene) Containing Rod-Coil-Rod Triblock Copolymer. *Chem. Commun.* **2005**, *38*, 4786–4788.

(82) Samorí, P.; Francke, V.; Müllen, K.; Rabe, J. P. Self-Assembly of a Conjugated Polymer: From Molecular Rods to a Nanoribbon Architecture with Molecular Dimensions. *Chem. - A Eur. J.* **1999**, *5* (8), 2312–2317.

(83) Jin, X.-H.; Price, M. B.; Finnegan, J. R.; Boott, C. E.; Richter, J. M.; Rao, A.; Menke, S. M.; Friend, R. H.; Whittell, G. R.; Manners, I. Long-Range Exciton Transport in Conjugated Polymer Nanofibers Prepared by Seeded Growth. *Science.* **2018**, *360* (6391), 897–900.

(84) Shaikh, H.; Jin, X. H.; Harniman, R. L.; Richardson, R. M.; Whittell, G. R.; Manners, I. Solid-State Donor-Acceptor Coaxial Heterojunction Nanowires via Living Crystallization-Driven Self-Assembly. *J. Am. Chem. Soc.* **2020**, *142* (31), 13469–13480.

(85) Finnegan, J. R.; He, X.; Street, S. T. G.; Garcia-Hernandez, J. D.; Hayward, D. W.; Harniman, R. L.; Richardson, R. M.; Whittell, G. R.; Manners, I. Extending the Scope of "Living" Crystallization-Driven Self-Assembly: Well-Defined 1D Micelles and Block Comicelles from Crystallizable Polycarbonate Block Copolymers. *J. Am. Chem. Soc.* **2018**, *140* (49), 17127–17140.

(86) Legros, C.; De Pauw-Gillet, M. C.; Tam, K. C.; Taton, D.; Lecommandoux, S. Crystallisation-Driven Self-Assembly of Poly(2-Isopropyl-2-Oxazoline)-Block-Poly(2-Methyl-2-Oxazoline) above the LCST. *Soft Matter* **2015**, *11* (17), 3354–3359.

(87) Gao, Y.; Li, X.; Hong, L.; Liu, G. Mesogen-Driven Formation of Triblock Copolymer Cylindrical Micelles. *Macromolecules* **2012**, *45* (3), 1321–1330.

(88) Li, X.; Jin, B.; Gao, Y.; Hayward, D. W.; Winnik, M. A.; Luo, Y.; Manners, I. Monodisperse Cylindrical Micelles of Controlled Length with a Liquid-Crystalline Perfluorinated Core by 1D "Self-Seeding." *Angew. Chem. Int. Ed.* **2016**, *55* (38), 11392–11396.

(89) Lee, C. U.; Smart, T. P.; Guo, L.; Epps, T. H.; Zhang, D. Synthesis and Characterization of Amphiphilic Cyclic Diblock Copolypeptoids from N-Heterocyclic Carbene-Mediated Zwitterionic Polymerization of N-Substituted N-Carboxyanhydride. *Macromolecules* **2011**, *44* (24), 9574–9585.

(90) Hudson, Z. M.; Boott, C. E.; Robinson, M. E.; Rupar, P. A.; Winnik, M. A.; Manners, I. Tailored Hierarchical Micelle Architectures Using Living Crystallization-Driven Self-Assembly in Two Dimensions. *Nat. Chem.* **2014**, *6* (10), 893–898.

(91) Yu, W.; Inam, M.; Jones, J. R.; Dove, A. P.; O'Reilly, R. K. Understanding the CDSA of Poly(Lactide) Containing Triblock Copolymers. *Polym. Chem.* **2017**, *8* (36), 5504–5512.

(92) Wang, H.; Lin, W.; Fritz, K. P.; Scholes, G. D.; Winnik, M. A.; Manners, I. Cylindrical Block Co-Micelles with Spatially Selective Functionalization by Nanoparticles. *J. Am. Chem. Soc.* **2007**, *129* (43), 12924–12925.

(93) Gilroy, J. B.; Gädt, T.; Whittell, G. R.; Chabanne, L.; Mitchels, J. M.; Richardson, R. M.; Winnik, M. A.; Manners, I. Monodisperse Cylindrical Micelles by Crystallization-Driven Living Self-Assembly. *Nat. Chem.* **2010**, *2* (7), 566–570.

(94) O'Shaughnessy, B.; Vavylonis, D. Dynamics of Living Polymers. *Eur. Phys. J. E* **2003**, *12* (3), 481–496.

(95) Guérin, G.; Wang, H.; Manners, I.; Winnik, M. A. Fragmentation of Fiberlike Structures: Sonication Studies of Cylindrical Block Copolymer Micelles and Behavioral Comparisons to Biological Fibrils. *J. Am. Chem. Soc.* **2008**, *130* (44), 14763–14771.

(96) Qian, J.; Guerin, G.; Cambridge, G.; Manners, I.; Winnik, M. A. Seeded Growth and Solvent-Induced Fragmentation of Fiberlike Polyferrocenylsilane – Polyisoprene Block Copolymer Micelles. *Macromol. Rapid Commun.* **2010**, *31* (9–10), 928–933.

(97) Qian, J.; Guerin, G.; Lu, Y.; Cambridge, G.; Manners, I.; Winnik, M. A. Self-Seeding in One Dimension: An Approach To Control the Length of Fiberlike Polyisoprene–Polyferrocenylsilane Block Copolymer Micelles. *Angew. Chem. Int. Ed.* **2011**, *50* (7), 1622–1625.

(98) Qiu, H.; Gao, Y.; Du, V. A.; Harniman, R.; Winnik, M. A.; Manners, I. Branched Micelles by Living Crystallization-Driven Block Copolymer Self-Assembly under Kinetic Control. *J. Am. Chem. Soc.* **2015**, *137* (6), 2375–2385.

(99) Qian, J.; Lu, Y.; Chia, A.; Zhang, M.; Rupar, P. A.; Gunari, N.; Walker, G. C.; Cambridge, G.; He, F.; Guerin, G.; Manners, I.; Winnik, M. A. Self-Seeding in One Dimension : A Route to Uniform Fiber-like Nanostructures from Block Copolymers with a Crystallizable Core-Forming Block. *ACS Nano* **2013**, *7* (5), 3754–3766.

(100) Qian, J.; Li, X.; Lunn, D. J.; Gwyther, J.; Hudson, Z. M.; Kynaston, E.; Rupar, P. A.; Winnik, M. A.; Manners, I. Uniform High Aspect Ratio Fiber-like Micelles and Block Co-Micelles with a Crystalline π - Conjugated Polythiophene Core by Self-Seeding. *J. Am. Chem. Soc.* **2014**, *136* (11), 4121–4124.

(101) Wittamann, J. C.; Lotz, B. Epitaxial Crystallization of Polyethylene on Organic Substrates: A Reappraisal of the Mode of Action of Selected Nucleating Agents. *J. Polym. Sci. Polym. Phys. Ed.* **1981**, *19* (12), 1837–1851.

(102) Rupar, P. A.; Chabanne, L.; Winnik, M. A.; Manners, I. Non-Centrosymmetric Cylindrical Micelles by Unidirectional Growth. *Science.* **2012**, *337* (6094), 559–562.

(103) Hudson, Z. M.; Lunn, D. J.; Winnik, M. A.; Manners, I. Colour-Tunable Fluorescent Multiblock Micelles. *Nat. Commun.* **2014**, *5*, 3372.

(104) Qiu, H.; Gao, Y.; Boott, C. E.; Gould, O. E. C.; Harniman, R. L.; Miles, M. J.; Webb, S. E. D.; Winnik, M. A.; Manners, I. Uniform Patchy and Hollow Rectangular Platelet Micelles from Crystallizable Polymer Blends. *Science.* **2016**, *352* (6286), 697–701.

(105) Inam, M.; Jones, J. R.; Pérez-Madrigal, M. M.; Arno, M. C.; Dove, A. P.; O'Reilly, R. K. Controlling the Size of Two-Dimensional Polymer Platelets for Water-in-Water Emulsifiers. *ACS Cent. Sci.* **2018**, *4* (1), 63–70.

(106) Qiu, H.; Cambridge, G.; Winnik, M. A.; Manners, I. Multi-Armed Micelles and Block Co-Micelles via Crystallization- Driven Self-Assembly with Homopolymer Nanocrystals as Initiators. *J. Am. Chem. Soc.* **2013**, *135* (33), 12180–12183.

(107) He, X.; Hsiao, M. S.; Boott, C. E.; Harniman, R. L.; Nazemi, A.; Li, X.; Winnik, M. A.; Manners, I. Two-Dimensional Assemblies from Crystallizable Homopolymers with Charged Termini. *Nat. Mater.* **2017**, *16* (4), 481–488.

(108) Pearce, S.; He, X.; Hsiao, M. S.; Harniman, R. L.; Macfarlane, L. R.; Manners, I. Uniform, High-Aspect-Ratio, and Patchy 2D Platelets by Living Crystallization-Driven Self-Assembly of Crystallizable Poly(Ferrocenyldimethylsilane)-Based Homopolymers with Hydrophilic Charged Termini. *Macromolecules* **2019**, *52* (16), 6068–6079.

(109) Nazemi, A.; He, X.; MacFarlane, L. R.; Harniman, R. L.; Hsiao, M. S.; Winnik, M. A.; Faul, C. F. J. J.; Manners, I. Uniform "Patchy" Platelets by Seeded Heteroepitaxial Growth of Crystallizable Polymer Blends in Two Dimensions. *J. Am. Chem. Soc.* **2017**, *139* (12), 4409–4417.

(110) Kang, J.; Miyajima, D.; Mori, T.; Inoue, Y.; Itoh, Y.; Aida, T. A Rational Strategy for the Realization of Chain-Growth Supramolecular Polymerization. *Science.* **2015**, *347* (6222),

646–651.

(111) Zhang, W.; Jin, W.; Fukushima, T.; Saeki, A.; Seki, S.; Aida, T. Supramolecular Linear Heterojunction Composed of Graphite-like Semiconducting Nanotubular Segments. *Science.* **2011**, *334* (6054), 340–343.

(112) Ogi, S.; Stepanenko, V.; Sugiyasu, K.; Takeuchi, M.; Würthner, F. Mechanism of Self-Assembly Process and Seeded Supramolecular Polymerization of Perylene Bisimide Organogelator. *J. Am. Chem. Soc.* **2015**, *137* (9), 3300–3307.

(113) Ogi, S.; Sugiyasu, K.; Manna, S.; Samitsu, S.; Takeuchi, M. Living Supramolecular Polymerization Realized through a Biomimetic Approach. *Nat. Chem.* **2014**, *6*, 188–195.

(114) Robinson, M. E.; Nazemi, A.; Lunn, D. J.; Hayward, D. W.; Boott, C. E.; Hsiao, M. S.; Harniman, R. L.; Davis, S. A.; Whittell, G. R.; Richardson, R. M.; De Cola, L.; Manners, I. Dimensional Control and Morphological Transformations of Supramolecular Polymeric Nanofibers Based on Cofacially-Stacked Planar Amphiphilic Platinum(II) Complexes. *ACS Nano* **2017**, *11* (9), 9162–9175.

(115) Qiu, H.; Hudson, Z. M.; Winnik, M. A.; Manners, I. Multidimensional Hierarchical Self-Assembly of Amphiphilic Cylindrical Block Comicelles. *Science.* **2015**, *347* (6228), 1329–1332.

(116) Li, X.; Gao, Y.; Boott, C. E.; Hayward, D. W.; Harniman, R.; Whittell, G. R.; Richardson, R. M.; Winnik, M. A.; Manners, I. " Cross " Supermicelles via the Hierarchical Assembly of Amphiphilic Cylindrical Triblock Comicelles. *J. Am. Chem. Soc.* **2016**, *138* (12), 4087–4095.

(117) Li, X.; Gao, Y.; Boott, C. E.; Winnik, M. A.; Manners, I. Non-Covalent Synthesis of Supermicelles with Complex Architectures Using Spatially Confined Hydrogen-Bonding Interactions. *Nat. Commun.* **2015**, *6*.

(118) Li, X.; Gao, Y.; Harniman, R.; Winnik, M.; Manners, I. Hierarchical Assembly of Cylindrical Block Comicelles Mediated by Spatially Confined Hydrogen-Bonding Interactions. *J. Am. Chem. Soc.* **2016**, *138* (39), 12902–12912.

(119) He, X.; He, Y.; Hsiao, M. S.; Harniman, R. L.; Pearce, S.; Winnik, M. A.; Manners, I. Complex and Hierarchical 2D Assemblies via Crystallization-Driven Self-Assembly of Poly(l -Lactide) Homopolymers with Charged Termini. *J. Am. Chem. Soc.* **2017**, *139* (27), 9221–9228.

(120) Günes, S.; Neugebauer, H.; Sariciftci, N. S. Conjugated Polymer-Based Organic Solar Cells. *Chem. Rev.* **2007**, *107* (4), 1324–1338.

(121) Guo, X.; Baumgarten, M.; Müllen, K. Designing π-Conjugated Polymers for Organic Electronics. *Prog. Polym. Sci.* **2013**, *38* (12), 1832–1908.

(122) Shirakawa, H.; Louis, E. J.; MacDiarmid, A. G.; Chiang, C. K.; Heeger, A. J. Synthesis of Electrically Conducting Organic Polymers: Halogen Derivatives of Polyacetylene, (CH)X. *J. Chem. Soc. Chem. Commun.* **1977**, No. 16, 578.

(123) Chiang, C. K.; Fincher, C. R.; Park, Y. W.; Heeger, A. J.; Shirakawa, H.; Louis, E. J.; Gau, S. C.; MacDiarmid, A. G. Electrical Conductivity in Doped Polyacetylene. *Phys. Rev. Lett.* **1977**, *39* (17), 1098–1101.

(124) Heeger, A. J. Semiconducting and Metallic Polymers: The Fourth Generation of Polymeric Materials (Nobel Lecture). *Angew. Chem. Int. Ed.* **2001**, *40* (14), 2591–2611.

(125) Shirakawa, H. The Discovery of Polyacetylene Film: The Dawning of an Era of Conducting Polymers (Nobel Lecture). *Angew. Chem. Int. Ed.* **2001**, *40* (14), 2574–2580.

(126) MacDiarmid, A. G. "Synthetic Metals": A Novel Role for Organic Polymers (Nobel Lecture). *Angew. Chem. Int. Ed.* **2001**, *40* (14), 2581–2590.

(127) Skotheim, T. A.; Reynolds, J. R. *Conjugated Polymers: Theory, Synthesis, Properties, and Characterization*; Taylor and Francis Group, 2007.

(128) Salaneck, W. R.; Friend, R. H.; Brédas, J. L. Electronic Structure of Conjugated Polymers: Consequences of Electron-Lattice Coupling. *Phys. Rep.* **1999**, *319* (6), 231–251.

(129) Band Filling Diagram https://upload.wikimedia.org/wikipedia/commons/9/9d/Band_filling_diagram.svg

(accessed Jan 19, 2021).

(130) Mikhnenko, O. V.; Blom, P. W. M.; Nguyen, T. Q. Exciton Diffusion in Organic Semiconductors. *Energy Environ. Sci.* **2015**, *8* (7), 1867–1888.

(131) Bredas, J. L.; Street, G. B. Polarons, Bipolarons, and Solitons in Conducting Polymers. *Acc. Chem. Res.* **1985**, *18* (10), 309–315.

(132) Geoghegan, M.; Hadziioannou, G. *Polymer Electronics*; 2013.

(133) Scherf, U.; List, E. J. W. Semiconducting Polyfluorenes - Towards Reliable Structure-Property Relationships. *Adv. Mater.* **2002**, *14* (7), 477–487.

(134) Andrew, T. L.; Swager, T. M. Structure-Property Relationships for Exciton Transfer in Conjugated Polymers. *J. Polym. Sci. Part B Polym. Phys.* **2011**, *49*, 476–498.

(135) Lei, T.; Wang, J. Y.; Pei, J. Design, Synthesis, and Structure-Property Relationships of Isoindigo-Based Conjugated Polymers. *Acc. Chem. Res.* **2014**, *47*, 1117–1126.

(136) Eggimann, H. J.; Le Roux, F.; Herz, L. M. How β-Phase Content Moderates Chain Conjugation and Energy Transfer in Polyfluorene Films. *J. Phys. Chem. Lett.* **2019**, *10* (8), 1729–1736.

(137) Soos, Z. G.; Galvão, D. S.; Etemad, S. Fluorescence and Excited-state Structure of Conjugated Polymers. *Adv. Mater.* **1994**, *6*, 280–287.

(138) Burroughes, J. H.; Bradley, D. D. C.; Brown, A. R.; Marks, R. N.; Mackay, K.; Friend, R. H.; Burns, P. L.; Holmes, A. B. Light-Emitting Diodes Based on Conjugated Polymers. *Nature* **1990**, *347* (6293), 539–541.

(139) Friend, R. H.; Gymer, R. W.; Holmes, A. B.; Burroughes, J. H.; Marks, R. N.; Taliani, C.; Bradley, D. D. C.; Dos Santos, D. A.; Brédas, J. L.; Lögdlund, M.; Salaneck, W. R. Electroluminescence in Conjugated Polymers. *Nature* **1999**, *397* (6715), 121–128.

(140) Heeger, A. J. Semiconducting Polymers: The Third Generation. *Chem. Soc. Rev.* **2010**, *39* (7), 2354–2371.

(141) Samuel, I. D. W.; Turnbull, G. A. Organic Semiconductor Lasers. *Chem. Rev.* **2007**, *107* (4), 1272–1295.

(142) Roncali, J. Conjugated Poly(Thiophenes): Synthesis, Functionalization, and Applications. *Chem. Rev.* **1992**, *92* (4), 711–738.

(143) Toshima, N.; Hara, S. Direct Synthesis of Conducting Polymers from Simple Monomers. *Prog. Polym. Sci.* **1995**, *20* (1), 155–183.

(144) Blackstone, V.; Lough, A. J.; Murray, M.; Manners, I. Probing the Mechanism of the PCl 5-Initiated Living Cationic Polymerization of the Phosphoranimine Cl 3P=NSiMe 3 Using Model Compound Chemistry. *J. Am. Chem. Soc.* **2009**, *131* (10), 3658–3667.

(145) Yokozawa, T.; Yokoyama, A. Chain-Growth Polycondensation: The Living Polymerization Process in Polycondensation. *Prog. Polym. Sci.* **2007**, *32* (1), 147–172.

(146) Yokozawa, T.; Ohta, Y. Transformation of Step-Growth Polymerization into Living Chain-Growth Polymerization. *Chem. Rev.* **2016**, *116* (4), 1950–1968.

(147) Loewe, R. S.; Ewbank, P. C.; Liu, J.; Zhai, L.; McCullough, R. D. Regioregular, Head-to-Tail Coupled Poly(3-Alkylthiophenes) Made Easy by the GRIM Method: Investigation of the Reaction and the Origin of Regioselectivity. *Macromolecules* **2001**, *34* (13), 4324–4333.

(148) Yokozawa, T.; Nanashima, Y.; Kohno, H.; Suzuki, R.; Nojima, M.; Ohta, Y. Catalyst-Transfer Condensation Polymerization for Precision Synthesis of π-Conjugated Polymers. *Pure Appl. Chem.* **2013**, *85* (3), 573–587.

(149) McKeown, G. R.; Ye, S.; Cheng, S.; Seferos, D. S. Homogenous Synthesis of Monodisperse High Oligomers of 3-Hexylthiophene by Temperature Cycling. *J. Am. Chem. Soc.* **2019**, *141*, 17053–17056.

(150) Ye, S.; Cheng, S.; Pollit, A. A.; Forbes, M. W.; Seferos, D. S. Isolation of Living Conjugated Polymer Chains. *J. Am. Chem. Soc.* **2020**, *142* (25), 11244–11251.

(151) Stefan, M. C.; Javier, A. E.; Osaka, I.; McCullough, R. D. Grignard Metathesis Method (GRIM): Toward a Universal Method for the Synthesis of Conjugated Polymers. *Macromolecules*

2009, *42* (1), 30–32.

(152) Jeffries-EL, M.; Sauvé, G.; McCullough, R. D. In-Situ End-Group Functionalization of Regioregular Poly(3-Alkylthiophene) Using the Grignard Metathesis Polymerization Method. *Adv. Mater.* **2004**, *16* (12), 1017–1019.

(153) Zhang, Y.; Tajima, K.; Hirota, K.; Hashimoto, K. Synthesis of All-Conjugated Diblock Copolymers by Quasi-Living Polymerization and Observation of Their Microphase Separation. *J. Am. Chem. Soc.* **2008**, *130* (25), 7812–7813.

(154) Stefan, M. C.; Bhatt, M. P.; Sista, P.; Magurudeniya, H. D. Grignard Metathesis (GRIM) Polymerization for the Synthesis of Conjugated Block Copolymers Containing Regioregular Poly(3-Hexylthiophene). *Polym. Chem.* **2012**, *3* (7), 1693–1701.

(155) Cosemans, I.; Vandenbergh, J.; D'Olieslaeger, L.; Ethirajan, A.; Lutsen, L.; Vanderzande, D.; Junkers, T. Synthesis of PPV-b-PEG Block Copolymers via CuAAC Conjugation. *Eur. Polym. J.* **2014**, *55* (1), 114–122.

(156) Wang, H.; Hau Wang, H.; Urban, V. S.; Littrell, K. C.; Thiyagarajan, P.; Yu, L. Syntheses of Amphiphilic Diblock Copolymers Containing a Conjugated Block and Their Self-Assembling Properties. *J. Am. Chem. Soc.* **2000**, *122* (29), 6855–6861.

(157) Wu, P.; Ren, G.; Li, C.; Mezzenga, R.; Jenekhe, S. A. Crystalline Diblock Conjugated Copolymers : Synthesis , Self-Assembly , and Microphase Separation of Poly (3-Butylthiophene) - b -Poly (3-Octylthiophene). *Macromolecules* **2009**, *42*, 2317–2320.

(158) Patra, S. K.; Ahmed, R.; Whittell, G. R.; Lunn, D. J.; Dunphy, E. L.; Winnik, M. A.; Manners, I. Cylindrical Micelles of Controlled Length with a π-Conjugated Polythiophene Core via Crystallization-Driven Self-Assembly. *J. Am. Chem. Soc.* **2011**, *133* (23), 8842–8845.

(159) Barth, S.; Bässler, H. Intrinsic Photoconduction in PPV-Type Conjugated Polymers. *Phys. Rev. Lett.* **1997**, *79* (22), 4445.

(160) Razzell-Hollis, J.; Fleischli, F.; Jahnke, A. A.; Stingelin, N.; Seferos, D. S.; Kim, J. S. Effects of Side-Chain Length and Shape on Polytellurophene Molecular Order and Blend Morphology. *J. Phys. Chem. C* **2017**, *121* (4), 2088–2098.

(161) McCullough, R. D.; Williams, S. P.; Lowe, R. D.; Jayaraman, M.; Tristram-Nagle, S. Self-Orienting Head-to-Tail Poly(3-Alkylthiophenes): New Insights on Structure-Property Relationships in Conducting Polymers. *J. Am. Chem. Soc.* **1993**, *115* (11), 4910–4911.

(162) Monkman, A.; Rothe, C.; King, S.; Dias, F. Polyfluorene Photophysics. In *Polyfluorenes*; Springer Berlin Heidelberg, 2008.

(163) Polyene Bandgaps http://cleanenergywiki.org/images/d/da/Polyene_bandgaps.png (accessed Jan 19, 2021).

(164) Persson, N. E.; Chu, P.-H.; McBride, M.; Grover, M.; Reichmanis, E. Nucleation, Growth, and Alignment of Poly(3-Hexylthiophene) Nanofibers for High-Performance OFETs. *Acc. Chem. Res.* **2017**, *50* (4), 932–942.

(165) Han, L.; Wang, M.; Jia, X.; Chen, W.; Qian, H.; He, F. Uniform Two-Dimensional Square Assemblies from Conjugated Block Copolymers Driven by π–π Interactions with Controllable Sizes. *Nat. Commun.* **2018**, *9* (1), 865.

(166) Gwyther, J.; Gilroy, J. B.; Rupar, P. A.; Lunn, D. J.; Kynaston, E.; Patra, S. K.; Whittell, G. R.; Winnik, M. A.; Manners, I. Dimensional Control of Block Copolymer Nanofibers with a π-Conjugated Core: Crystallization-Driven Solution Self-Assembly of Amphiphilic Poly(3-Hexylthiophene)- b -Poly(2-Vinylpyridine). *Chem. - A Eur. J.* **2013**, *19* (28), 9186–9197.

(167) Gilroy, J. B.; Lunn, D. J.; Patra, S. K.; Whittell, G. R.; Winnik, M. A.; Manners, I. Fiber-like Micelles via the Crystallization-Driven Solution Self-Assembly of Poly(3-Hexylthiophene)-Block -Poly(Methyl Methacrylate) Copolymers. *Macromolecules* **2012**, *45* (14), 5806–5815.

(168) Chang, C. C.; Pai, C. L.; Chen, W. C.; Jenekhe, S. A. Spin Coating of Conjugated Polymers for Electronic and Optoelectronic Applications. *Thin Solid Films* **2005**, *479* (1–2), 254–260.

(169) Vezie, M. S.; Few, S.; Meager, I.; Pieridou, G.; Dörling, B.; Ashraf, R. S.; Goñi, A. R.; Bronstein, H.; McCulloch, I.; Hayes, S. C.; Campoy-Quiles, M.; Nelson, J. Exploring the Origin of High

Optical Absorption in Conjugated Polymers. *Nat. Mater.* **2016**, *15* (7), 746–753.

(170) Wang, H. J.; Chen, C. P.; Jeng, R. J. Polythiophenes Comprising Conjugated Pendants for Polymer Solar Cells: A Review. *Materials (Basel).* **2014**, *7*, 2411–2439.

(171) Qian, J.; Li, X.; Lunn, D. J.; Gwyther, J.; Hudson, Z. M.; Kynaston, E.; Rupar, P. A.; Winnik, M. A.; Manners, I. Uniform, High Aspect Ratio Fiber-like Micelles and Block Co-Micelles with a Crystalline π-Conjugated Polythiophene Core by Self-Seeding. *J. Am. Chem. Soc.* **2014**, *136* (11), 4121–4124.

(172) Li, X.; Wolanin, P. J.; MacFarlane, L. R.; Harniman, R. L.; Qian, J.; Gould, O. E. C.; Dane, T. G.; Rudin, J.; Cryan, M. J.; Schmaltz, T.; Frauenrath, H.; Winnik, M. A.; Faul, C. F. J.; Manners, I. Uniform Electroactive Fibre-like Micelle Nanowires for Organic Electronics. *Nat. Commun.* **2017**, *8* (1), 15909.

(173) Kynaston, E. L.; Nazemi, A.; MacFarlane, L. R.; Whittell, G. R.; Faul, C. F. J.; Manners, I. Uniform Polyselenophene Block Copolymer Fiberlike Micelles and Block Co-Micelles via Living Crystallization-Driven Self-Assembly. *Macromolecules* **2018**, *51* (3), 1002–1010.

(174) Lin, C. H.; Tung, Y. C.; Ruokolainen, J.; Mezzenga, R.; Chen, W. C. Poly[2,7-(9,9-Dihexylfluorene)]-Block-Poly(2-Vinylpyridine) Rod-Coil and Coil-Rod-Coil Block Copolymers: Synthesis, Morphology and Photophysical Properties in Methanol/THF Mixed Solvents. *Macromolecules* **2008**, *41* (22), 8759–8769.

(175) Hicks, G. E. J. J.; Jarrett-Wilkins, C. N.; Panchuk, J. R.; Manion, J. G.; Seferos, D. S. Oxidation Promoted Self-Assembly of π-Conjugated Polymers. *Chem. Sci.* **2020**, *11* (25), 32–34.

(176) Kim, Y.-J.; Cho, C.-H.; Paek, K.; Jo, M.; Park, M.; Lee, N.-E.; Kim, Y.; Kim, B. J.; Lee, E. Precise Control of Quantum Dot Location within the P3HT- b -P2VP/QD Nanowires Formed by Crystallization-Driven 1D Growth of Hybrid Dimeric Seeds. *J. Am. Chem. Soc.* **2014**, *136* (7), 2767–2774.

(177) Jin, S.-M.; Kim, I.; Lim, J. A.; Ahn, H.; Lee, E. Interfacial Crystallization-Driven Assembly of Conjugated Polymers/Quantum Dots into Coaxial Hybrid Nanowires: Elucidation of Conjugated Polymer Arrangements by Electron Tomography. *Adv. Funct. Mater.* **2016**, *26* (19), 3226–3235.

(178) Kim, Y. J.; Cho, C. H.; Paek, K.; Jo, M.; Park, M. K.; Lee, N. E.; Kim, Y. J.; Kim, B. J.; Lee, E. Precise Control of Quantum Dot Location within the P3HT-b-P2VP/QD Nanowires Formed by Crystallization-Driven 1D Growth of Hybrid Dimeric Seeds. *J. Am. Chem. Soc.* **2014**, *136* (7), 2767–2774.

(179) Kamps, A. C.; Cativo, M. H. M.; Fryd, M.; Park, S.-J. Self-Assembly of Amphiphilic Conjugated Diblock Copolymers into One-Dimensional Nanoribbons. *Macromolecules* **2014**, *47* (1), 161–164.

(180) Lee, E.; Hammer, B.; Kim, J.-K.; Page, Z.; Emrick, T.; Hayward, R. C. Hierarchical Helical Assembly of Conjugated Poly(3-Hexylthiophene)-Block-Poly(3-Triethylene Glycol Thiophene) Diblock Copolymers. *J. Am. Chem. Soc.* **2011**, *133* (27), 10390–10393.

(181) Lee, I.-H.; Amaladass, P.; Yoon, K.-Y.; Shin, S.; Kim, Y.-J.; Kim, I.; Lee, E.; Choi, T.-L. Nanostar and Nanonetwork Crystals Fabricated by in Situ Nanoparticlization of Fully Conjugated Polythiophene Diblock Copolymers. *J. Am. Chem. Soc.* **2013**, *135* (47), 17695–17698.

(182) Tao, D.; Wang, Z.; Huang, X.; Tian, M.; Lu, G.; Manners, I.; Winnik, M. A.; Feng, C. Continuous and Segmented Semiconducting Fiber-like Nanostructures with Spatially Selective Functionalization by Living Crystallization-Driven Self-Assembly. *Angew. Chem. Int. Ed.* **2020**, *59* (21), 8232–8239.

(183) Shin, S.; Menk, F.; Kim, Y.; Lim, J.; Char, K.; Zentel, R.; Choi, T. L. Living Light-Induced Crystallization-Driven Self-Assembly for Rapid Preparation of Semiconducting Nanofibers. *J. Am. Chem. Soc.* **2018**, *140* (19), 6088–6094.

(184) MacFarlane, L. R.; Shaikh, H.; Garcia-Hernandez, J. D.; Vespa, M.; Fukui, T.; Manners, I. Functional Nanoparticles through π-Conjugated Polymer Self-Assembly. *Nat. Rev. Mater.* **2021**, *6*, 7–26.

(185) Lee, I. H.; Amaladass, P.; Choi, T. L. One-Pot Synthesis of Nanocaterpillar Structures via in

Situ Nanoparticlization of Fully Conjugated Poly(p-Phenylene)-Block-Polythiophene. *Chem. Commun.* **2014**, *50* (59), 7945–7948.

(186) Lee, I.-H.; Choi, T.-L. Importance of Choosing the Right Polymerization Method for in Situ Preparation of Semiconducting Nanoparticles from the P3HT Block Copolymer. *Polym. Chem.* **2016**, *7* (46), 7135–7141.

(187) Lee, I.-H.; Amaladass, P.; Choi, I.; Bergmann, V. W.; Weber, S. A. L.; Choi, T.-L. Preparing DNA-Mimicking Multi-Line Nanocaterpillars via in Situ Nanoparticlisation of Fully Conjugated Polymers. *Polym. Chem.* **2016**, *7* (7), 1422–1428.

(188) Yoon, K.-Y.; Shin, S.; Kim, Y.-J.; Kim, I.; Lee, E.; Choi, T.-L. One-Pot Preparation of 3D Nano- and Microaggregates via In Situ Nanoparticlization of Polyacetylene Diblock Copolymers Produced by ROMP. *Macromol. Rapid Commun.* **2015**, *36* (11), 1069–1074.

(189) Shin, S.; Yoon, K.-Y.; Choi, T.-L. Simple Preparation of Various Nanostructures via in Situ Nanoparticlization of Polyacetylene Blocklike Copolymers by One-Shot Polymerization. *Macromolecules* **2015**, *48* (5), 1390–1397.

(190) Yang, S.; Shin, S.; Choi, I.; Lee, J.; Choi, T.-L. Direct Formation of Large-Area 2D Nanosheets from Fluorescent Semiconducting Homopolymer with Orthorhombic Crystalline Orientation. *J. Am. Chem. Soc.* **2017**, *139* (8), 3082–3088.

(191) Boott, C. E.; Gwyther, J.; Harniman, R. L.; Hayward, D. W.; Manners, I. Scalable and Uniform 1D Nanoparticles by Synchronous Polymerization, Crystallization and Self-Assembly. *Nat. Chem.* **2017**, *9* (8), 785–792.

(192) Oliver, A. M.; Gwyther, J.; Boott, C. E.; Davis, S.; Pearce, S.; Manners, I. Scalable Fiber-like Micelles and Block Co-Micelles by Polymerization-Induced Crystallization-Driven Self-Assembly. *J. Am. Chem. Soc.* **2018**, *140* (51), 18104–18114.

(193) Canning, S. L.; Smith, G. N.; Armes, S. P. A Critical Appraisal of RAFT-Mediated Polymerization-Induced Self-Assembly. *Macromolecules* **2016**, *49* (6), 1985–2001.

(194) Zhang, R.; Li, B.; Iovu, M. C.; Jeffries-EL, M.; Sauvé, G.; Cooper, J.; Jia, S.; Tristram-Nagle, S.; Smilgies, D. M.; Lambeth, D. N.; McCullough, R. D.; Kowalewski, T. Nanostructure Dependence of Field-Effect Mobility in Regioregular Poly(3-Hexylthiophene) Thin Film Field Effect Transistors. *J. Am. Chem. Soc.* **2006**, *128* (11), 3480–3481.

(195) Kleinhenz, N.; Persson, N.; Xue, Z.; Chu, P. H.; Wang, G.; Yuan, Z.; McBride, M. A.; Choi, D.; Grover, M. A.; Reichmanis, E. Ordering of Poly(3-Hexylthiophene) in Solutions and Films: Effects of Fiber Length and Grain Boundaries on Anisotropy and Mobility. *Chem. Mater.* **2016**, *28* (11), 3905–3913.

(196) Crossland, E. J. W.; Tremel, K.; Fischer, F.; Rahimi, K.; Reiter, G.; Steiner, U.; Ludwigs, S. Anisotropic Charge Transport in Spherulitic Poly(3-Hexylthiophene) Films. *Adv. Mater.* **2012**, *24* (6), 839–844.

(197) Xu, J.; Wu, H.-C.; Zhu, C.; Ehrlich, A.; Shaw, L.; Nikolka, M.; Wang, S.; Molina-Lopez, F.; Gu, X.; Luo, S.; Zhou, D.; Kim, Y.-H.; Wang, G.-J. N.; Gu, K.; Feig, V. R.; Chen, S.; Kim, Y.; Katsumata, T.; Zheng, Y.-Q.; Yan, H.; Chung, J. W.; Lopez, J.; Murmann, B.; Bao, Z. Multi-Scale Ordering in Highly Stretchable Polymer Semiconducting Films. *Nat. Mater.* **2019**, *18* (6), 594–601.

(198) Cativo, M. H. M.; Kim, D. K.; Riggleman, R. A.; Yager, K. G.; Nonnenmann, S. S.; Chao, H.; Bonnell, D. A.; Black, C. T.; Kagan, C. R.; Park, S.-J. Air–Liquid Interfacial Self-Assembly of Conjugated Block Copolymers into Ordered Nanowire Arrays. *ACS Nano* **2014**, *8* (12), 12755–12762.

(199) Di Nuzzo, D.; Kulkarni, C.; Zhao, B.; Smolinsky, E.; Tassinari, F.; Meskers, S. C. J.; Naaman, R.; Meijer, E. W.; Friend, R. H. High Circular Polarization of Electroluminescence Achieved via Self-Assembly of a Light-Emitting Chiral Conjugated Polymer into Multidomain Cholesteric Films. *ACS Nano* **2017**, *11* (12), 12713–12722.

(200) Yi, Z.; Ni, W.; Zhang, Q.; Li, M.; Kan, B.; Wan, X.; Chen, Y. Effect of Thermal Annealing on Active Layer Morphology and Performance for Small Molecule Bulk Heterojunction Organic Solar Cells. *J. Mater. Chem. C* **2014**, *2* (35), 7247–7255.

(201) Vohra, V.; Anzai, T. Molecular Orientation of Conjugated Polymer Chains in Nanostructures

and Thin Films: Review of Processes and Application to Optoelectronics. *J. Nanomater.* **2017**, *2017*, 1–18.

(202) Kim, C.; Gwon, Y. J.; Kim, J.; Lee, T. S. Synthesis of Fluorescent Conjugated Polymer Nanoparticles and Their Immobilization on a Substrate for White Light Emission. *Polym. Chem* **2018**, *9*, 5671.

(203) Menard, E.; Meitl, M. A.; Sun, Y.; Park, J.-U.; Shir, D. J.-L.; Nam, Y.-S.; Jeon, S.; Rogers, J. A. Micro- and Nanopatterning Techniques for Organic Electronic and Optoelectronic Systems. *Chem. Rev.* **2007**, *107* (4), 1117–1160.

(204) Herrera, M.; Abdul-Moqueet, M.; Mahmoud, M. A. Conjugated Polymer Nanoparticles Having Modified Band Gaps Assembled into Nano- and Micropatterned Organic Light-Emitting Diodes. *ACS Appl. Nano Mater.* **2019**, *2* (1), 577–585.

(205) Feng, L.; Zhu, C.; Yuan, H.; Liu, L.; Lv, F.; Wang, S. Conjugated Polymer Nanoparticles: Preparation, Properties, Functionalization and Biological Applications. *Chem. Soc. Rev.* **2013**, *42* (16), 6620–6633.

(206) Repenko, T.; Rix, A.; Ludwanowski, S.; Go, D.; Kiessling, F.; Lederle, W.; Kuehne, A. J. C. Bio-Degradable Highly Fluorescent Conjugated Polymer Nanoparticles for Bio-Medical Imaging Applications. *Nat. Commun.* **2017**, *8* (1), 470.

(207) Wang, S.; Liu, J.; Feng, G.; Ng, L. G.; Liu, B. NIR-II Excitable Conjugated Polymer Dots with Bright NIR-I Emission for Deep In Vivo Two-Photon Brain Imaging Through Intact Skull. *Adv. Funct. Mater.* **2019**, *29* (15), 1808365.

(208) Wang, L. V; Hu, S. Photoacoustic Tomography: In Vivo Imaging from Organelles to Organs. *Science.* **2012**, *335* (6075), 1458–1462.

(209) Pu, K.; Shuhendler, A. J.; Jokerst, J. V.; Mei, J.; Gambhir, S. S.; Bao, Z.; Rao, J. Semiconducting Polymer Nanoparticles as Photoacoustic Molecular Imaging Probes in Living Mice. *Nat. Nanotechnol.* **2014**, *9* (3), 233–239.

(210) Vyas, V. S.; Lotsch, B. V. Organic Polymers Form Fuel from Water. *Nature* **2015**, *521* (7550), 41–42.

(211) Wang, L.; Fernández-Terán, R.; Zhang, L.; Fernandes, D. L. A.; Tian, L.; Chen, H.; Tian, H. Organic Polymer Dots as Photocatalysts for Visible Light-Driven Hydrogen Generation. *Angew. Chem. Int. Ed.* **2016**, *55* (40), 12306–12310.

(212) Pati, P. B.; Damas, G.; Tian, L.; Fernandes, D. L. A.; Zhang, L.; Pehlivan, I. B.; Edvinsson, T.; Araujo, C. M.; Tian, H. An Experimental and Theoretical Study of an Efficient Polymer Nano-Photocatalyst for Hydrogen Evolution. *Energy Environ. Sci.* **2017**, *10* (6), 1372–1376.

(213) Wang, Y.; Li, S.; Liu, L.; Lv, F.; Wang, S. Conjugated Polymer Nanoparticles to Augment Photosynthesis of Chloroplasts. *Angew. Chem. Int. Ed.* **2017**, *56* (19), 5308–5311.

(214) Watanabe, K.; Hayasaka, H.; Miyashita, T.; Ueda, K.; Akagi, K. Dynamic Control of Full-Colored Emission and Quenching of Photoresponsive Conjugated Polymers by Photostimuli. *Adv. Funct. Mater.* **2015**, *25* (19), 2794–2806.

(215) Zuo, M.; Qian, W.; Li, T.; Hu, X. Y.; Jiang, J.; Wang, L. Full-Color Tunable Fluorescent and Chemiluminescent Supramolecular Nanoparticles for Anti-Counterfeiting Inks. *ACS Appl. Mater. Interfaces* **2018**, *10* (45), 39214–39221.

(216) Childress, E. S.; Roberts, C. A.; Sherwood, D. Y.; LeGuyader, C. L. M.; Harbron, E. J. Ratiometric Fluorescence Detection of Mercury Ions in Water by Conjugated Polymer Nanoparticles. *Anal. Chem.* **2012**, *84* (3), 1235–1239.

(217) Li, H.; Wu, X.; Xu, Y.; Tong, H.; Wang, L. Dicyanovinyl-Functionalized Fluorescent Hyperbranched Conjugated Polymer Nanoparticles for Sensitive Naked-Eye Cyanide Ion Detection. *Polym. Chem.* **2014**, *5* (20), 5949–5956.

(218) Malik, A. H.; Hussain, S.; Kalita, A.; Iyer, P. K. Conjugated Polymer Nanoparticles for the Amplified Detection of Nitro-Explosive Picric Acid on Multiple Platforms. *ACS Appl. Mater. Interfaces* **2015**, *7* (48), 26968–26976.

(219) Wang, T.; Zhang, N.; Bai, R.; Bao, Y. Aggregation-Enhanced FRET-Active Conjugated Polymer

Nanoparticles for Picric Acid Sensing in Aqueous Solution. *J. Mater. Chem. C* **2018**, *6* (2), 266–270.

(220) Frausto, F.; Thomas, S. W. Ratiometric Singlet Oxygen Detection in Water Using Acene-Doped Conjugated Polymer Nanoparticles. *ACS Appl. Mater. Interfaces* **2017**, *9* (18), 15768–15775.

(221) Shin, S.; Lim, J.; Gu, M.-L.; Yu, C.-Y.; Hong, M.; Char, K.; Choi, T.-L. Dimensionally Controlled Water-Dispersible Amplifying Fluorescent Polymer Nanoparticles for Selective Detection of Charge-Neutral Analytes. *Polym. Chem.* **2017**, *8* (48), 7507–7514.

Chapter 2

Solid-State Donor-Acceptor Coaxial Heterojunction Nanowires via Living Crystallization-Driven Self-Assembly

This chapter has been adapted from:

Huda Shaikh,† Xu-Hui Jin,† Robert L. Harniman, Robert M. Richardson, George R. Whittell and Ian Manners, *J. Am. Chem. Soc*, **2020**, *142*, 13469-13480.

† Equal contribution

Contributions:

Synthesis of polymer materials, self-assembly and seeded growth experiments, and optical spectroscopy analysis of the triBCP-based nanofibers were conducted by Huda Shaikh. Segmented nanofiber self-assembly was conducted by Dr. Xu-Hui Jin (University of Bristol). Characterization by atomic force microscopy was conducted by Dr. Robert L. Harniman (University of Bristol). Characterization by wide-angle x-ray scattering was conducted and analyzed in collaboration with Prof. Robert M. Richardson and Dr. George R. Whittell (University of Bristol). Research was conducted at the University of Bristol and University of Victoria.

2.1. Abstract

The creation of organic heterojunctions from conjugated polymers on the nanoscale has attracted recent attention as a consequence of their considerable potential in optoelectronic devices. Herein, we report proof-of-concept results on a versatile synthetic strategy to access various linearly segmented nanowire heterojunctions with controlled dimensions using the seeded growth "living crystallization-driven self-assembly" method followed by a secondary crystallization step. Specifically, we describe the creation of coaxial and segmented coaxial B-A-B and A-B-A nanowires with a solvophilic poly(ethylene glycol) (PEG) corona, and an inner crystalline core that consists of poly(di-*n*-hexylfluorene) (PDHF), which functions as a donor, and an outer crystalline core of poly(3-(2'-ethyl)hexylthiophene) (P3EHT) which acts as an acceptor. The latter is present either along the entire length of the nanowire, solely in the central segment, or in the terminal blocks. These nanowires were created by the seeded growth of two types of π-conjugated polymeric building blocks: the triblock copolymer PDHF-*b*-P3EHT-*b*-PEG and the diblock copolymer PDHF-*b*-PEG, using fiber-like seeds derived from either material. The nanowires with both solid-state donor and acceptor blocks exhibit Förster resonance energy transfer (FRET) from the PDHF inner core to the P3EHT outer core, which was characterized by fluorescence spectroscopy and laser confocal scanning fluorescence microscopy (LCSM). The FRET in the solid-state coaxial heterojunctions with an inner PDHF core and an outer P3EHT core was enhanced relative to the directly analogous system in which the P3EHT block was solvated.

2.2. Introduction

Heterojunctions involving interfaces derived from organic materials with different band gaps have attracted widespread recent attention for potential electronics applications such as light-emitting diodes, transistors, and light-harvesting photovoltaic devices.[1] In organic electronic materials, the dissociation of excitons into electrons and holes at the heterojunction interface is essential. A typical system consists of a donor material (hole-transporting phase) with a higher LUMO than the acceptor (electron-transporting phase) to allow for efficient charge separation, combination, or energy transfer.[1–4] In comparison with solution-processed organic bulk heterojunctions with random, interpenetrating nanoscale phase-separated morphologies achieved by blending different types of semiconducting polymers and other electroactive species, the controlled formation of precisely defined heterojunction nanostructures from organic conjugated materials by bottom-up self-assembly methods is still underdeveloped. Although several impressive examples of organic heterojunctions have been reported, such as supramolecular heterojunctions derived from hexabenzocoronenes with different substituents[5] or oligo(*p*-phenylenevinylene) (OPV) and perylene diimide (PDI),[6] co-assembled materials formed from nanofibers based on n/p type molecules,[7] shish-kebab assemblies formed by secondary nucleation of poly(3-hexylthiophene) (P3HT) fibers by PDI nanowires,[8] co-assembled p- and n-type molecules,[9–11] bottom up strategies that allow precise control of the spatial structure and dimensions from π–conjugated polymers remain unexplored.

"Living" Crystallization-Driven Self-Assembly (CDSA) has recently emerged as an efficient seeded growth strategy for the preparation of morphologically pure low dispersity 1D fiber-like and 2D platelet micelles with controlled dimensions based on the seeded growth of crystallizable polymer based or molecular based amphiphiles. Initial work by ourselves and Winnik and co-workers focused on the use of crystallizable poly(ferrocenyldimethylsilane) block copolymers (BCPs)[12], control over fiber length from the nanometer to the micrometer scale, and the formation of block comicelles via the sequential seeded growth of BCPs with different coronal chemistries was achieved.[13–15] By altering the chemical nature of the crystallizable core-forming block and the core-corona

ratio, "living" CDSA has also been used to construct either 1D fibers[16–24] or two-dimensional (2D) platelets[25,26] as well as hierarchical materials.[27,28] Transposition of these concepts to π-stacking molecular amphiphiles has allowed the control of the dimensions of 1D and 2D supramolecular assemblies.[29–37]

A recent focus has involved formation of well-defined nanowires via the living CDSA of crystallizable π-conjugated core-forming blocks such as P3HT[38–40], OPV[41–44], poly(cyclopentenylene-vinylene)[45], polyselenophene[46] and polytellurophene[47]. Uniform fibers with a P3HT core prepared via this method have been incorporated into OFET devices.[48] The ability to study nanofibers with controlled lengths has allowed key structure-properties relationships to be established; for example, that increased fiber length results in higher charge carrier mobilities.[48]

We very recently reported the preparation of low dispersity nanowires with a crystalline poly(di-*n*-hexylfluorene) (PDHF) core by "living" CDSA.[49] Due to the efficient epitaxial crystallization of PDHF inherent to the self-assembly method, the low dispersity nanowires possess a remarkably well-ordered core, which enables exciton diffusion lengths above 200 nm to be achieved. The value observed in these nanowires surpasses that typically observed for bulk processed conjugated polymer samples (< 10 nm) and is well above the critical length needed for virtually quantitative light absorption suggesting intriguing practical potential. Detailed photophysical measurements were performed on nanofibers which exhibit exciton energy-transfer from the donor crystalline PDHF core to the solvated lower-energy P3HT corona as an acceptor. However, for the ultimate creation of devices, heterojunctions in which both the donor and acceptor exist in the solid-state are desirable.[50] With this in mind, we report herein proof-of-concept results on a new versatile approach to prepare π-conjugated polymer heterojunction nanowires in which the acceptor also exists in the crystalline state rather than solvated in solution. This involves the use of "Living" CDSA combined with a subsequent crystallization step for the acceptor material. This approach allows access to both coaxial and segmented conjugated polymer heterojunction nanowires which exhibit Förster resonance energy transfer (FRET) between the crystalline donor and acceptor regions.

2.3. Results and Discussion

2.3.1. Synthesis and Characterization of PDHF BCPs

In this work poly(di-*n*-hexylfluorene) (PDHF) was selected as the donor domain and the underlying inner crystalline core of the nanofibers. In order to form the heterojunction nanofibers, we chose poly(3-(2'-ethyl)hexylthiophene) (P3EHT) as the second crystallizable core-forming block.[51–53] The branched side chains on the thiophene unit offers different solubility characteristics to PDHF and relatively slow crystallization kinetics compared to P3HT with linear side chains.[53,54] We have previously reported that P3HT-based block copolymers can undergo CDSA in a range of different THF:MeOH solvent mixtures.[39] We hypothesized that a more soluble P3EHT segment should not aggregate in solutions with high contents of THF but would be expected to aggregate and crystallize in solutions rich in a polar solvent such as methanol. In addition, P3EHT was also selected as the acceptor polymer over the quaternized polythiophene (QPT) acceptor copolymer in our previous report[49] as it is crystallizable whereas QPT is not. As a result, a detailed comparison between this work and our previously reported system is not possible. Instead, we aim to provide a direct comparison of the energy transfer behavior for fibers made from the same polymer with either a PDHF-donor crystalline core and solvated P3EHT acceptor or a dual PDHF-donor and P3EHT-acceptor crystalline core.

The fluorescence emission of PDHF is in the 400-500 nm range and possesses good overlap with the absorption of P3EHT in THF:MeOH solvent mixtures (λ_{max} = 440-480 nm) (Figure S2. 4), indicating Förster resonance energy transfer (FRET) between the core-forming blocks of PDHF and P3EHT would be expected. Hydrophilic PEG was chosen as the corona-forming block to afford colloidally stable nanofibers. This choice also allows the use of a polar solvent for self-assembly that is unfavorable for both the PDHF and P3EHT blocks, facilitating CDSA in solution.

High purity and low dispersity PDHF$_8$-*b*-P3EHT$_{25}$-*b*-PEG$_{113}$ triblock copolymer used for stepwise CDSA studies was synthesized by employing a copper-catalyzed azide-alkyne cycloaddition click reaction (CuAAc) with azido-terminated PEG$_{113}$ and alkyne-terminated PDHF$_8$-*b*-P3EHT$_{25}$ (Scheme S2. 1). The

core-forming diblock of $PDHF_8$-*b*-$P3EHT_{25}$ was synthesized via sequential Grignard metathesis (GRIM) polymerization of 2-bromo-7-iodo-9,9-bis-*n*-hexylfluorene and 2,5-dibromo-3-(2'-ethyl)hexyl thiophene followed by addition of ethynyl magnesium bromide to quench the polymerization and afford alkyne-terminated diblock copolymer. The PDHF-*b*-P3EHT BCP was subsequently purified by Soxhlet extraction to afford low molecular mass dispersity ($Đ_m$ = 1.24) and the final PDHF-*b*-P3EHT-*b*-PEG triblock copolymer was purified by silica gel chromatography ($Đ_m$ = 1.17). An aliquot from the GRIM polymerization before the addition of the activated 2,5-dibromo-3-(2'-ethyl)hexyl thiophene was collected to characterize the PDHF block. From matrix-assisted laser desorption/ionization time-of-flight (MALDI-TOF) mass spectrometry the degree of polymerization of the PDHF block was calculated to be 8 and a number-average molecular mass (M_n) of 2738 Da was found (Figure S2. 1). Analysis of the ^{1}H NMR spectrum of PDHF-*b*-P3EHT-*b*-PEG triblock copolymer, allowed for the determination of the ratio of the PEG_{113} block to the PDHF and P3EHT blocks, which allowed for the degree of polymerization for each block to be determined as 8 for the PDHF block (consistent with MALDI-TOF analysis) and 25 for the P3EHT block (Figure S2. 2). Analysis by gel permeation chromatography (GPC) showed that all the materials synthesized are of high purity and low molecular mass dispersity ($Đ_m \leq 1.24$) (Figure S2. 3). The chemical structure of the materials studied are described in Scheme 2. 1 and Table S2. 1, respectively.

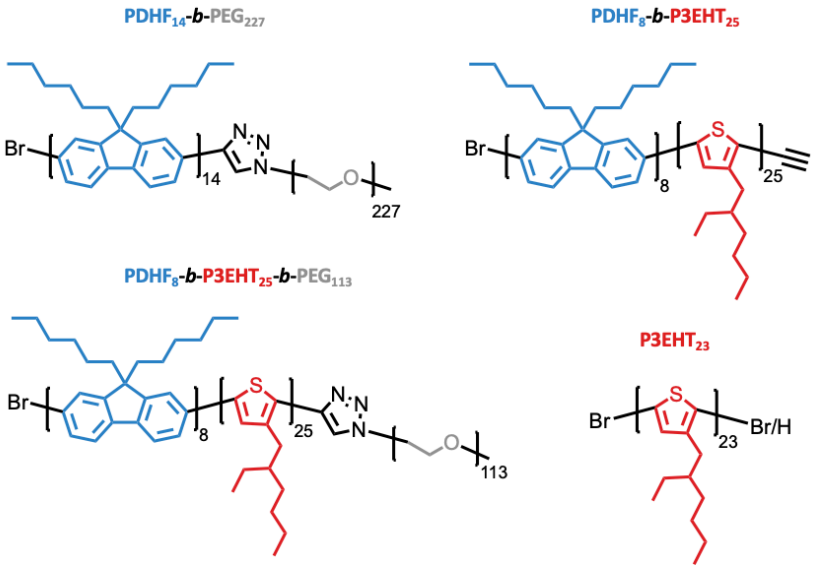

Scheme 2. 1: Chemical structures of $PDHF_{14}$-*b*-PEG_{227}, $PDHF_8$-*b*-$P3EHT_{25}$, $PDHF_8$-*b*-$P3EHT_{25}$-*b*-PEG_{113} and $P3EHT_{23}$.

2.3.2. Self-assembly and Seeded Growth of PDHF-*b*-P3EHT-*b*-PEG to form fiber-like micelles with a PDHF core

The creation of nanowires with an inner PDHF core, an outer P3EHT core and a PEG corona required careful choice of solvents and the use of a two-step self-assembly strategy. Prior to attempting the preparation of nanowires with a crystalline core composed of both PDHF and P3EHT, the self-assembly conditions for both PDHF and P3EHT were considered separately. We have previously shown that $PDHF_{14}$-*b*-PEG_{227} can self-assemble into 1D nanowires with a crystalline core of PDHF in a mixed solvent system of tetrahydrofuran (THF) and methanol (MeOH) (1:1, v/v), using MeOH as a selective solvent for the PEG block (Figure 2. 1a, c).[49] In comparison to the PDHF repeat unit with linear sidechains, P3EHT has branched sidechains. As a result, P3EHT was expected to possess different solubility behavior and reduced crystallization kinetics compared to PDHF. To test this hypothesis, MeOH was added dropwise to solvated $P3EHT_{23}$ homopolymer in THF until a ratio of THF:MeOH (1:1, v/v) was reached. After 24 h no observable aggregation was detected by either the Tyndall effect or by transmission electron microscopy (TEM) analysis (Figure S2. 5). In addition, the UV-vis spectrum of this solution in THF:MeOH (1:1, v/v) resembled that of the dissolved $P3EHT_{23}$ homopolymer in THF (Figure S2. 5). These results strongly indicate that in THF:MeOH (1:1, v/v), P3EHT blocks should remain solvated whereas PDHF blocks will precipitate.

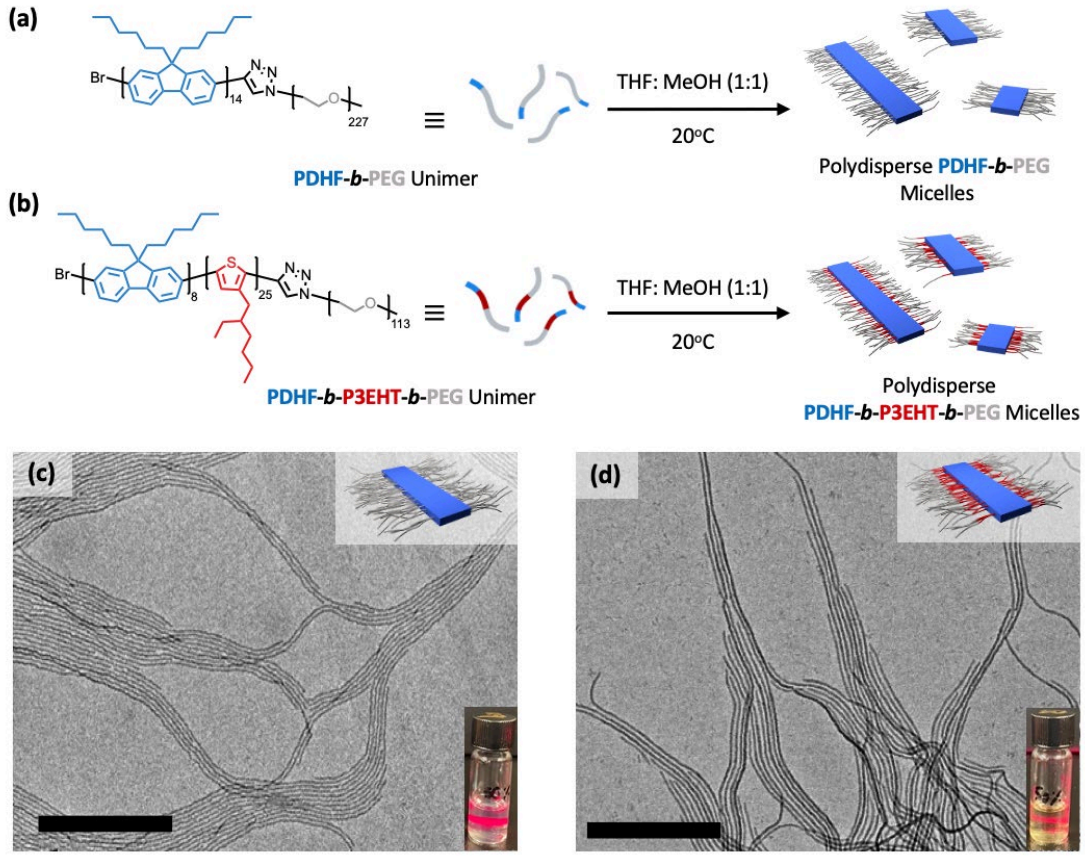

Figure 2. 1: Chemical structure and schematic illustration of the self-assembly of (a) $PDHF_{14}$-*b*-PEG_{227} in THF:MeOH (1:1, v/v) to form nanofibers with a PDHF crystalline core and (b) $PDHF_8$-*b*-$P3EHT_{25}$-*b*-PEG_{113} in THF:MeOH (1:1, v/v) to form nanofibers with a PDHF crystalline core. (c-d) TEM images of (c) $PDHF_{14}$-*b*-PEG_{227} and (d) $PDHF_8$-*b*-$P3EHT_{25}$-*b*-PEG_{113} nanofibers. Scale bars: 1 µm. Insets: schematic illustration of the nanofibers (*top right*) and a photograph of the solution of self-assembled nanofibers pointed at with a laser pen (wavelength ca. 650 nm) showing a strong Tyndall effect (*bottom right*).

The self-assembly behavior of the triblock copolymer $PDHF_8$-*b*-$P3EHT_{25}$-*b*-PEG_{113} was therefore studied under the same solvent conditions, THF:MeOH (1:1, v/v). The tri-BCP was dissolved in THF and then MeOH was added dropwise (over ca. 2 minutes) to reach a 1:1 ratio. The dropwise methanol addition is preferred over direct addition as this process leads to more controlled aggregation and facilitates crystallization. After 5 minutes, a strong Tyndall effect was observed for the solution of $PDHF_8$-*b*-$P3EHT_{25}$-*b*-PEG_{113} in THF:MeOH (1:1, v/v) which suggests some aggregation has already occurred (Figure 2. 1d). This was also observed for $PDHF_{14}$-*b*-PEG_{227} (Figure 2. 1c). After aging for 24 h, TEM analysis of aliquots after solvent evaporation demonstrated the exclusive formation of long fiber-like micelles (ca. 8 µm) which were polydisperse in length. The absence of a detectable thin film on the substrate attributable to residual molecularly dissolved

BCP (unimer) suggested that all of the unimer was consumed (Figure 2. 1b, d). As the P3EHT polymer does not aggregate under these solvent conditions, the self-assembly of the triblock copolymer should be exclusively driven by the precipitation and crystallization of the core-forming PDHF block. The UV-vis spectrum for $PDHF_8$-*b*-$P3EHT_{25}$-*b*-PEG_{113} fibers in THF:MeOH (1:1, v/v) displayed broadened peaks, relative to the peaks in the UV-vis spectrum of the unimer solution in THF (Figure S2. 6). A new, slightly blue-shifted peak was observed at 370 nm compared to the peak at 390 nm in THF, which can be attributed to H-like aggregate behavior for the PDHF block.[55–57] In addition, the intensities of the peaks at 430 and 470 nm were enhanced compared to unimer solution in THF. This indicates the presence of interchain π-π stacking interactions between P3EHT blocks. Under the same conditions, no evidence for similar interactions with the $P3EHT_{23}$ homopolymer was apparent as the UV-vis spectrum of the THF:MeOH (1:1, v/v) solution was identical to the UV-vis spectrum in THF (Figure S2. 5).

As selective precipitation of the PDHF core-forming block in the triblock copolymer was achieved in THF:MeOH (1:1, v/v), living CDSA was also investigated in this solvent system (Figure 2. 2a). The initial polydisperse fibers ca. 8 μm (Figure 1d) formed from CDSA of $PDHF_8$-*b*-$P3EHT_{25}$-*b*-PEG_{113} in THF:MeOH (1:1, v/v) were subjected to vigorous sonication for 2 h at 0°C followed by annealing at 45°C for 3 h to further increase the crystallinity of the fiber cores, and then slow cooling to 20°C. This resulted in low dispersity seed micelles (L_n = 68 nm, L_w/L_n = 1.08, where L_w is the weight-average length and L_n is the number-average length) confirmed by TEM (Figure S2. 7). To hinder the possibility of competitive homogenous nucleation, seeded growth experiments were performed at 30°C, the temperature at which the $PDHF_8$-*b*-$P3EHT_{25}$-*b*-PEG_{113} unimer solution is more colloidally stable. These experiments involved addition of $PDHF_8$-*b*-$P3EHT_{25}$-*b*-PEG_{113} unimer (in THF) to the seed micelle solution in THF:MeOH (1:1, v/v) followed by rapid shaking for 10 s and aging at 30°C for 24 h.

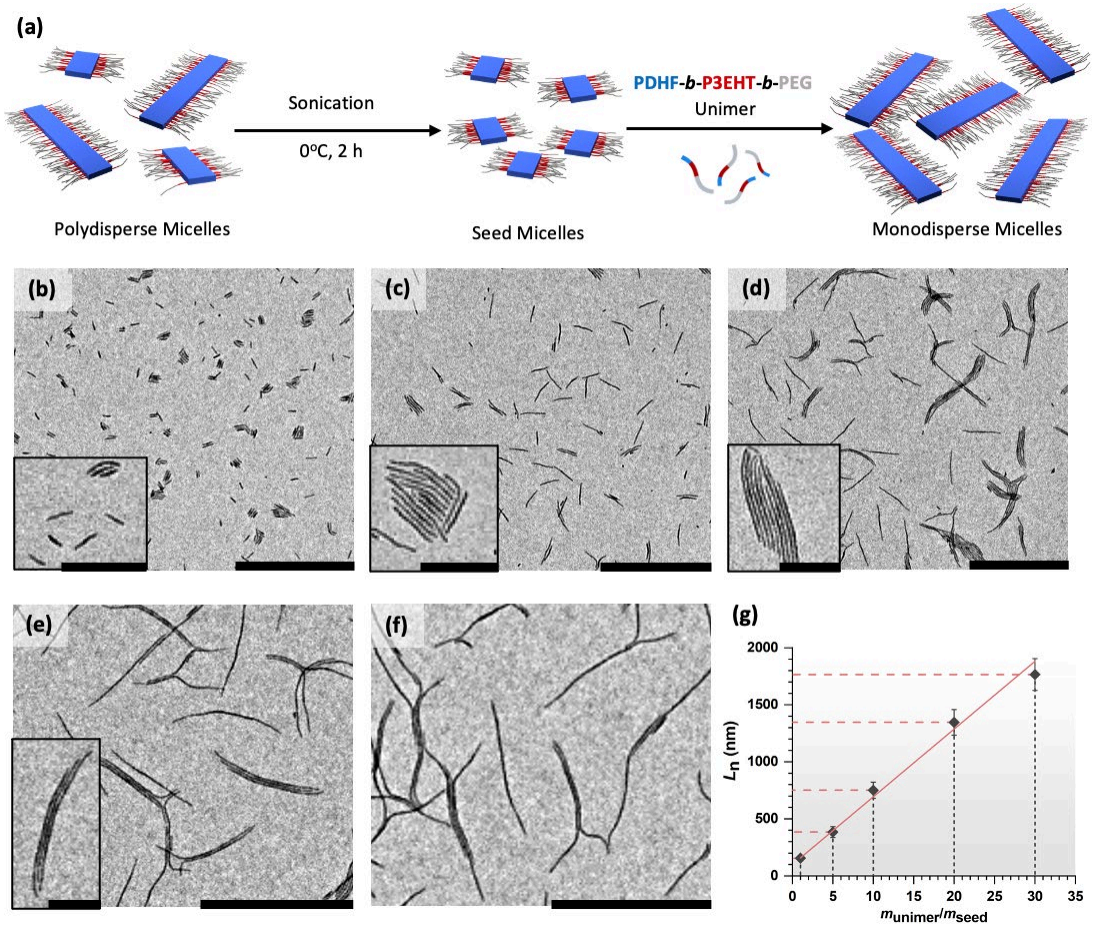

Figure 2. 2: Schematic illustration of the seeded growth protocol employed to prepare low dispersity PDHF$_8$-*b*-P3EHT$_{25}$-*b*-PEG$_{113}$ nanofibers in THF:MeOH (1:1, v/v). The unimer was added as a solution in THF. TEM images of nanofibers of controlled length prepared by seeded growth of PDHF$_8$-*b*-P3EHT$_{25}$-*b*-PEG$_{113}$ BCPs from seed micelles (L_n= 68 nm, L_w/L_n= 1.08) with m_{unimer}/m_{seed} values of (b) 1, (c) 5, (d) 10, (e) 20 and (f) 30. Scale bars: 2 µm, Inset scale bars: 500 nm. (g) Graph of micelle number-average length (L_n) against unimer-to-seed ratio (m_{unimer}/m_{seed}) showing a linear correlation.

This seeded growth protocol was repeated at a range of different unimer-to-seed ratios, m_{unimer}/m_{seed}, by varying the volume of unimer solution added. After 24 h, TEM analysis confirmed the formation of a range of uniform nanofibers of controlled length, from 155 to 1765 nm (Figure 2. 2b-f, Figure S2. 8). The length dispersity of the fibers was calculated by dividing the weight-average length (L_w) by the number-average length (L_n); all the fibers prepared using different m_{unimer}/m_{seed} ratios had low length dispersities ($L_w/L_n \leq 1.03$) (Table S2. 2). Well-behaved living CDSA behavior was apparent as the L_n values for the fiber-like micelles showed a linear dependence on the m_{unimer}/m_{seed} value (Figure 2. 2g) and the lengths observed up to a m_{unimer}/m_{seed} of 20 were consistent within experimental error with those predicted based on a seed length of 68 nm assuming no change in the core dimensions. However, at a m_{unimer}/m_{seed} ratio of

30, the experimentally obtained length of the fibers (L_n = 1765 nm) diverged significantly from the theoretically predicted value (L_n = 2110 nm). This indicated that epitaxial growth was not as well-controlled when unimer-to-seed ratios above 20 were employed. Lower experimental values for L_n compared to theory are consistent with the presence of competitive homogeneous nucleation at high unimer concentrations.[39] From TEM analysis there is evidence of some self-nucleation events as a very small amount (< 1%) of short fibers were detected (length ca. 300 nm) (Figure S2. 9). Nevertheless, the amount of self-nucleation appears small as the observed fiber length (L_n = 1765 nm) would correspond to an effective seed length of 57 nm, which is still within one standard deviation (σ) of the experimentally obtained value for the seeds (L_n = 68 nm, σ = 20 nm).

2.3.3. Templated crystallization of P3EHT on the inner PDHF core

Next, we attempted to crystallize the acceptor P3EHT segment as an outer core-forming block by using the underlying donor PDHF core-forming block as a template. The templated crystallization of block copolymer segments via the use of preformed crystallized blocks as lamellar substrates has been previously reported in solution.[58] In our case, based on previous work on analogous nanofibers from the diblock copolymer $PDHF_{14}$-*b*-PEG_{227}, the fiber-like nanowires in THF:MeOH (1:1, v/v) were anticipated to possess a rectangular PDHF core where the width of the fiber represents the extended chain length of the PDHF block and the coronal chains flank the parallel interfaces either side.[49] When the THF:MeOH ratio of a solution of $PDHF_8$-*b*-$P3EHT_{25}$-*b*-PEG_{113} nanofibers with a PDHF core was increased from 1:1 to 1:9, by dropwise MeOH addition over ca. 2 minutes at 20°C followed by ageing for 24 h, aggregation of the P3EHT block to produce heterojunction nanofibers with cores comprising both crystalline PDHF and also P3EHT was detected (Figure 2. 3a) (vide infra).

TEM analysis (Figure 2. 1d and Figure S2. 10) allowed a comparison of the number-average fiber widths (W_n) and weight-average fiber widths (W_w) for the fibers formed in THF:MeOH (1:1, v/v) and (1:9, v/v) and provided evidence that the P3EHT block had also formed part of the core in the latter case (**Figure S2. *11***). In each case the width detected by TEM was expected to represent the electron dense core region. PDHF is a rigid rod polymer and as the degree of

polymerization is relatively low, a fully chain extended conformation is expected. As noted above, we have previously shown this to be the case for nanofibers with a $PDHF_{14}$ core[49]. For example, fiber-like micelles of $PDHF_{14}$-*b*-PEG_{227} possessed a width of 12.9 nm, in good agreement with that for an expected extended $PDHF_{14}$ chain (12.5 nm) with a repeat unit length of 0.89 nm.[49] The analogous length of a fully extended $PDHF_8$ chain is estimated to be ca. 7.1 nm. However, the width of the fibers prepared in THF:MeOH (1:1, v/v) determined via TEM (W_n = 14 nm, W_n/W_w = 1.04) was double this value. This indicated that aggregation and potentially some crystallization of P3EHT at the locally parallel interfaces each side of the inner PDHF core presumably occurs upon solvent evaporation. In the case of regioregular poly(3-alkylthiophene)s the critical molecular weight below which polymer chains are fully extended is ca. 10 kDa (for P3EHT the critical chain length is ~ 52 repeat units).[59,60] Assuming a length of 0.387 nm for a single monomer unit of P3EHT,[61,62] the contour length of a fully extended $P3EHT_{25}$ chain is estimated to be ca. 10 nm, which is far greater than the additional width unaccounted for (ca. 3.5 nm) flanking each side of the inner PDHF core. Assuming that the PDHF exists in a chain extended state as previously detected,[49] this indicates that on drying the P3EHT has aggregated around the PDHF core, presumably without significant crystallization, and that this component only makes a relatively small but significant contribution to the observed width by TEM.

For the nanofibers subjected to a slow increase in MeOH concentration from THF:MeOH 1:1 to 1:9 (v/v), if the P3EHT has also aggregated, the core should consist of an inner PDHF region with an additional outer flanking core of P3EHT on each side. If both the $PDHF_8$ and $P3EHT_{25}$ blocks are crystallized and the polymer chains exist in the fully extended conformations the observed fiber width should be ca. 27 nm (PDHF = 7 nm; P3EHT = 2 x 10 nm). From TEM analysis, the fiber width in THF:MeOH (1:9, v/v) is W_n = 24 nm (W_n/W_w = 1.02). This value is substantially larger than that in THF:MeOH (1:1, v/v) (W_n = 14 nm, W_n/W_w = 1.04) and is similar to the expected extended chain length of one $PDHF_8$ block and the two outer $P3EHT_{25}$ blocks (ca. 27 nm). This data is consistent with precipitation and crystallization of the P3EHT block on the outer edges of the PDHF inner crystalline core.

Further evidence for the aggregation and crystallization of the P3EHT segment was provided by UV-vis spectroscopy and wide-angle X-ray scattering (WAXS). A red-shifted shoulder (ca. λ_{abs} = 500-550 nm) on the UV-vis absorbance peak of P3EHT was observed (in THF:MeOH 1:9, v/v). This vibronic peak has been attributed to solid-state aggregation and ordering of the P3EHT chains[63,64] (Figure S2. 6). A similar peak was detected in the UV-vis spectrum of P3EHT homopolymer in the same MeOH rich solvent medium where this material forms a red precipitate (Figure S2. 5). The $PDHF_8$-*b*-$P3EHT_{25}$-*b*-PEG_{113} nanofibers in THF:MeOH (1:9, v/v) appeared colloidally stable (Figure 2. 3c and Figure S2. 10) and exhibited significantly quenched fluorescence (ca. 90 %, 0.01 mg mL^{-1}) compared to the fibers with a solvated P3EHT block in THF:MeOH (1:1, v/v) (Figure S2. 12). As poly(3-alkylthiophene)s exhibit significant quenching of fluorescence in the solid-state relative to the solvated state, attributed to non-radiative decay via strong interchain interactions, polaron formation upon light absorption or intersystem crossing (heavy atom sulfur), this observation suggests the presence of interactions between the P3EHT chains and is consistent with their aggregation[65–67]. WAXS was performed on $PDHF_8$-*b*-$P3EHT_{25}$-*b*-PEG_{113} nanofibers (L_n = 1132 nm, L_w/L_n = 1.01) in THF:MeOH (1:9, v/v). The WAXS pattern of the nanofibers in solution exhibited weak Bragg peaks at q values of 0.56, 0.78, 1.09 and 1.24 $Å^{-1}$ that were superimposed on the amorphous solvent scattering peak (Figure S2. 13a). These observed peaks are all in close agreement with previously measured Bragg peaks of crystalline P3EHT in the solid-state.[68] For the crystalline PDHF inner core region, Bragg peaks would be anticipated at q values of 0.41, 0.71 and 1.35 $Å^{-1}$.[49] However, no peaks corresponding to these values could be detected, presumably as a result of dilution, the low degree of polymerization of the $PDHF_8$ block, and background scattering of the solvent. WAXS analysis of a bulk sample of $PDHF_8$-*b*-$P3EHT_{25}$ revealed Bragg peaks corresponding to both crystalline PDHF[49] (q = 0.41, 0.71 and 1.37 $Å^{-1}$) and P3EHT[68] (q = 0.82, 0.97, 1.15, 1.47, 1.64 and 1.76 $Å^{-1}$) domains (Figure S2. 13b). Overall these results indicate that both the PDHF and P3EHT blocks crystallized in the core of the nanofibers in THF:MeOH (1:9, v/v).

2.3.4. Energy transfer between the inner PDHF and outer P3EHT cores

In order to explore the behavior of the nanowires as heterojunctions, the potential for energy transfer between the donor PDHF inner core and the acceptor P3EHT outer core was investigated by fluorescence spectroscopy (Figure 2. 3d). First, to ensure that fluorescence data collected for the fibers in THF:MeOH (1:1, v/v) can be directly compared to fluorescence data for fibers in THF:MeOH (1:9, v/v) we needed to rule out the presence of residual unimer. In the seeded growth experiments in THF:MeOH (1:1, v/v) discussed previously, the observed fiber lengths matched those expected based on the unimer-to-seed ratio which was consistent with complete unimer consumption. To further ensure no unimer is present in fiber solutions in THF:MeOH (1:1, v/v), methanol was added to low-dispersity PDHF$_8$-*b*-P3EHT$_{25}$-*b*-PEG$_{113}$ nanofibers (L_n = 527 nm, L_w/L_n = 1.02) until a ratio of THF:MeOH (1:9, v/v) was reached. After ageing for 5 days, no significant change in fiber length (L_n = 524 nm, L_w/L_n = 1.03) was detected by TEM (Figure S2. 14). This observation strongly indicates that no remaining unimer was present in the original solution otherwise an increase in fiber length would have transpired. Furthermore, dialysis of the fiber solutions in THF:MeOH (1:1, v/v) and THF:MeOH (1:9, v/v) into the same solvent systems for 2 days was also carried out to ensure the removal of any residual unimer.

Normalized fluorescence spectra of PDHF$_8$-*b*-P3EHT$_{25}$-*b*-PEG$_{113}$ unimers in THF and the nanofiber solution (L_n = 751 nm, L_w/L_n = 1.01) in THF:MeOH (1:1, v/v) showed that the majority of the fluorescence corresponds to the PDHF $I_{0\text{-}0}$ vibronic band (λ_{max} = 416 nm)[69,70] when the PDHF core is selectively excited at 380 nm (Figure 2. 3b). In THF, where both PDHF and P3EHT blocks are solvated, there was only a small fluorescence contribution from the P3EHT segment (λ_{max} = 562 nm). However, in THF:MeOH (1:1, v/v) an increased contribution to the fluorescence from the P3EHT was observed. This is indicative of enhanced FRET occurring from the crystalline PDHF core, which functions as a donor, to the solvated acceptor P3EHT corona leading to quenching of the PDHF emission. In THF:MeOH (1:9, v/v), where the P3EHT forms an outer-crystalline core, the major contribution to the emission was from the P3EHT (λ_{max} = 580 nm) as this block becomes more ordered and the FRET from the PDHF is increased. The slight shift in the P3EHT emission was also observed for the homopolymer in THF:MeOH (1:9,

v/v) relative to the emission peaks in THF and THF:MeOH (1:1, v/v) (Figure S2. 15). In addition, significant quenching of the emission was also observed in THF:MeOH (1:9, v/v) compared to THF:MeOH (1:1, v/v) which is also indicative of P3EHT aggregation (Figure S2. 12). The relative FRET efficiency (E_{rel}) of the donor-acceptor system can be estimated from the fluorescence spectra. This is calculated by dividing the emission intensity of the acceptor (P3EHT, λ_{max} = 562-580 nm) by the total emission intensities of the donor and acceptor (PDHF-donor, λ_{max} = 416 nm; P3EHT-acceptor, λ_{max} = 562-580 nm). The smallest relative FRET efficiency was observed for the unimers in THF (E_{rel} = 0.09). This was increased for the nanofibers with a PDHF core in THF:MeOH (1:1, v/v) (E_{rel} = 0.28) and further enhanced with the nanofibers with a PDHF-*b*-P3EHT core in THF:MeOH (1:9, v/v) (E_{rel} = 0.62). Overall, these observations suggest the presence of ordered P3EHT domains in THF:MeOH (1:9, v/v) which improves the efficiency of the energy transfer form PDHF donor to the P3EHT acceptor.

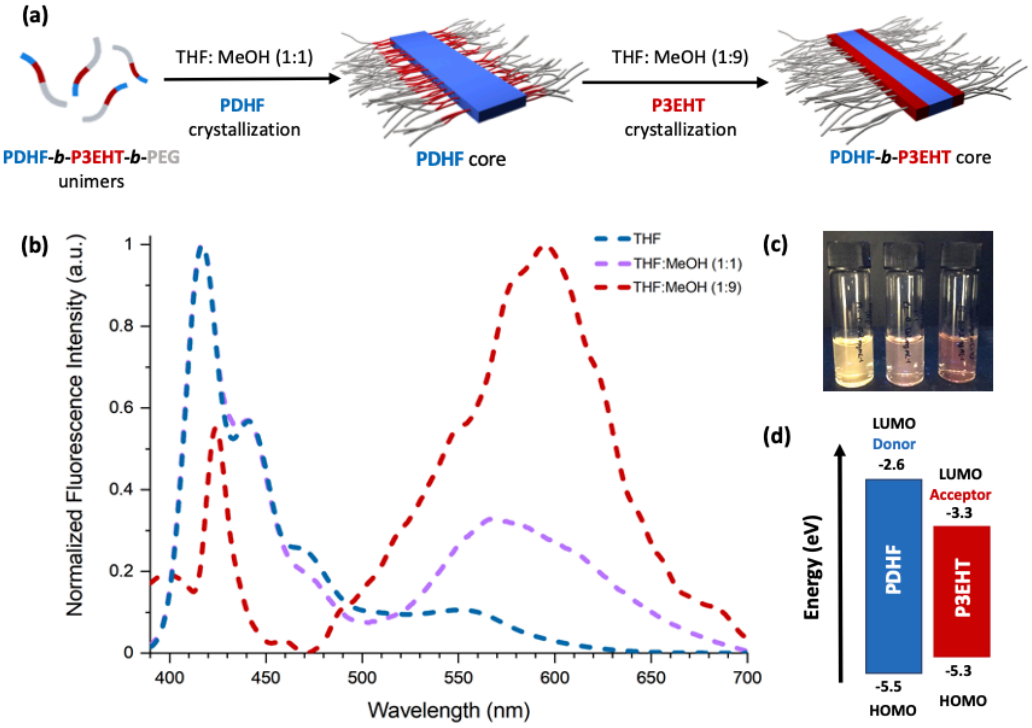

Figure 2. 3: (a) Schematic illustration of the living CDSA protocol employed to prepare low dispersity nanofibers with a crystalline inner PDHF and outer P3EHT core. (b) Normalized solution-state photoluminescence spectra of $PDHF_8$-*b*-$P3EHT_{25}$-*b*-PEG_{113} unimers in THF Normalized solution-state photoluminescence spectra of $PDHF_8$-*b*-$P3EHT_{25}$-*b*-PEG_{113} unimers in THF (blue trace) and nanofibers (L_n = 751 nm, L_w/L_n = 1.01) in THF:MeOH (1:1, v/v) (purple trace) and in THF:MeOH (1:9, v/v) (red trace) after dialysis (2 days, dialysis tubing molecular weight cut-off = 14,000 kDa) to remove any residual unimer. For Photoluminescence spectra, λ_{ex} = 380 nm. (c) Photograph of $PDHF_8$-*b*-$P3EHT_{25}$-*b*-PEG_{113} (from left to right) in THF, THF:MeOH (1:1, v/v) and THF:MeOH (1:9, v/v) under UV light (365 nm). (d) Energy level diagram of PDHF[71] and P3EHT.[72]

2.3.5. Formation of A-B-A and B-A-B segmented heterojunction nanowires

Finally, we explored the formation of uniform 1D segmented nanofibers via the "living" CDSA process. Segmented nanowires with a continuous PDHF-donor core and either a P3EHT-*b*-PEG-acceptor corona or an electronically insulating PEG corona were prepared by the stepwise co-assembly of BCPs via living CDSA. Subsequent addition of further PEG selective solvent was then used to induce aggregation and crystallization of the P3EHT acceptor block to afford solid-state heterojunction nanowires.

We have previously reported that an all-π-conjugated donor-acceptor diblock copolymer comprising a PDHF core-forming block and a quaternized polythiophene corona–forming block could undergo epitaxial growth from the termini of low dispersity $PDHF_{14}$-*b*-PEG_{227} nanofibers to form uniform segmented nanowires.[49] Although $PDHF_8$-*b*-$P3EHT_{25}$-*b*-PEG_{113} contains two types of core-forming blocks, the PDHF block should selectively grow from the core termini of the $PDHF_{14}$-*b*-PEG_{227} nanofibers under solvent conditions in which the P3EHT block is solvated (THF:MeOH, 1:1, v/v). To prepare nanowires with terminal crystalline heterojunction segments, $PDHF_8$-*b*-$P3EHT_{25}$-*b*-PEG_{113} unimer in THF was rapidly added to uniform $PDHF_{14}$-*b*-PEG_{227} fibers in THF:MeOH (1:1, v/v) (L_n = 247 nm, L_w/L_n = 1.04) at 30°C, shaken for 10 s and aged at 30°C for 1 day (Figure 2. 4a). Subsequently the PEG-selective solvent MeOH was slowly added over several minutes until a ratio of 1:9 (v/v) of THF:MeOH was reached.

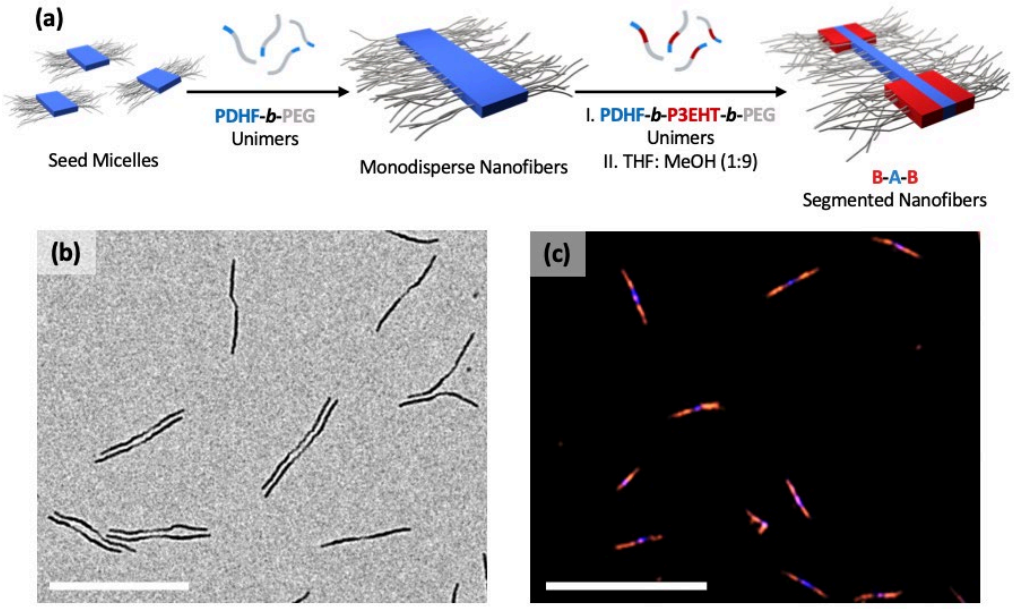

Figure 2. 4: (a) Schematic illustration of the preparation of low dispersity B-A-B segmented nanofibers with a central $PDHF_{14}$-*b*-PEG_{227} segment (A) and terminal $PDHF_8$-*b*-$P3EHT_{25}$-*b*-PEG_{113} segments (B). (b) TEM image of B-A-B segmented nanofibers (L_n = 739 nm, L_w/ L_n = 1.02) in THF:MeOH (1:9, v/v) prepared from the epitaxial growth of $PDHF_8$-*b*-$P3EHT_{25}$-*b*-PEG_{113} unimers from $PDHF_{14}$-*b*-PEG_{227} seed micelles (L_n = 247 nm, L_w/L_n = 1.04). (c) LCSM image of B-A-B segmented nanofibers (L_n= 3473 nm, L_w/ L_n = 1.03) in THF:MeOH (1:9, v/v) prepared from the epitaxial growth of $PDHF_8$-*b*-$P3EHT_{25}$-*b*-PEG_{113} unimers from $PDHF_{14}$-*b*-PEG_{227} seed micelles (L_n= 972 nm, L_w/ L_n= 1.02). LCSM image was taken with both blue (PDHF) and red (P3EHT) channels. Scale bars: (b) 1 µm and (c) 10 µm.

From TEM analysis, uniform B-A-B (A = $PDHF_{14}$-*b*-PEG_{227}, B = $PDHF_8$-*b*-$P3EHT_{25}$-*b*-PEG_{113}) segmented nanofibers (L_n = 739 nm, L_w/ L_n = 1.02) with distinct segments could be detected with the visibly thicker terminal B segments flanking the 247 nm long A $PDHF_{14}$-*b*-PEG_{227} segment (Figure 2. 4b). This would be expected based on the presence of a coaxial core in the B segments containing both crystalline PDHF and P3EHT. Although the unimers possessed a significantly smaller degree of polymerization compared to the seeds (8 vs 14), no branched micelle formation was detected. The electron density contrast with the carbon film substrate was sufficient for quantification measurements which gave larger fiber widths for the terminal B regions (W_n = 24 nm, W_n/W_w = 1.01) compared to the A segments (W_n = 14 nm, W_n/W_w = 1.04) (Figure S2. 16). These widths are similar to those expected based on the extended chain lengths for $PDHF_{14}$ (12.5 nm)[49] for the A segment and, as discussed earlier, for $PDHF_8$ (7 nm) and $P3EHT_{25}$ (10 nm) for the B segment. The corresponding values for the B and A segments would be predicted to be 27 nm and 12.5 nm, respectively. Furthermore, atomic force microscopy (AFM) analysis also showed that the fiber width for the terminal B

segments (ca. 23 nm) was also larger than for the central A segment (ca. 17 nm). Both of these values include a contribution from the PEG corona. Interestingly, the height of the terminal B segments (ca. 10 nm) was found to be substantially larger than that of the central A segment (ca. 5 nm) (Figure 2. 5a-b and Figure S2. 17). This observation suggests that some of the coronal PEG chains may have aggregated on top of the PDHF/P3EHT core during the drying process. The presence of the wider PDHF/P3EHT core present in the B segments appears to be the decisive factor underlying this phenomenon despite the smaller degree of polymerization of the PEG corona relative to the A segments. To investigate this possibility, the adhesion profile was determined (Figure 2. 5c-d and Figure S2. 18). This AFM data was consistent with the PEG coronas flanking the fiber core which, based on the height and width data, has a ribbon-like morphology. Moreover, from the adhesion profile, higher adhesion on the edges of the micelle core (ca. 100 mV) was detected on the terminal B segments compared to the central A segment (ca. 50 mV) (Figure 2. 5d). This suggests that PEG corona may partially reside on top of P3EHT blocks in the B segments, which may also account for their increased height.

To visualize the different segments by laser confocal scanning microscopy (LCSM) imaging, long B-A-B segmented fibers were prepared where the length of the A segments (L_n= 972 nm, L_w/ L_n= 1.02) exceeds the length over which efficient exciton diffusion occurs for PDHF cores (ca. 200 nm) .[49] For this reason, some PDHF emission from the central A segment was anticipated as well as orange emission for the terminal segments with an acceptor P3EHT outer core. LCSM imaging of B-A-B segmented nanofibers (A: L_n= 972 nm, L_w/ L_n= 1.02; B-A-B: L_n= 3473 nm, L_w/ L_n = 1.03) in THF:MeOH (1:9, v/v) confirmed the formation of segmented heterojunction nanofibers (Figure 2. 4c). Segments with different fluorescence emission were observed; the central A segment possessing a PDHF crystalline core displayed blue emission and the terminal B segments with a PDHF-*b*-P3EHT crystalline core showed red/orange emission from the outer P3EHT segment due to FRET.

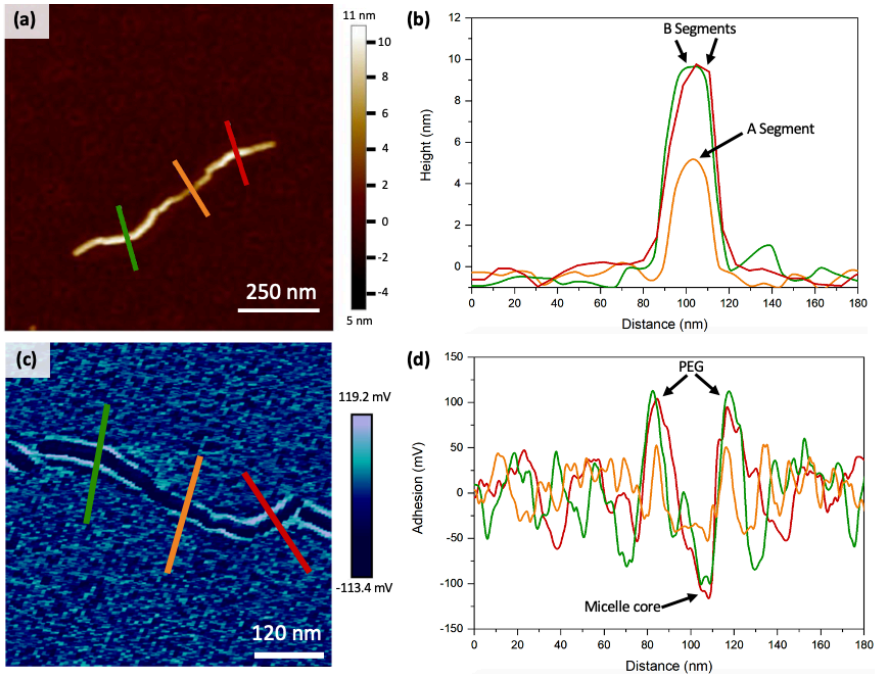

Figure 2. 5: AFM images of low-dispersity B-A-B segmented nanofibers (A: L_n = 247 nm, L_w/L_n = 1.04; B-A-B: (L_n = 739 nm, L_w/L_n = 1.02) drop cast from THF:MeOH (1:9, v/v) on to mica. (a) Height image of B-A-B segmented nanofibers and (b) corresponding height traces. (c) Adhesion image of B-A-B segmented nanofibers and (d) corresponding adhesion profile traces. The central A segment analysis is collected from the orange trace and terminal B segments analyses were collected from the green and red traces.

To prepare nanowires with an "inverse" A-B-A structure with a central crystalline heterojunction B segment (Figure 2. 6a), PDHF$_{14}$-*b*-PEG$_{227}$ unimers in THF was added to uniform PDHF$_8$-*b*-P3EHT$_{25}$-*b*-PEG$_{113}$ fibers in THF:MeOH (1:1, v/v) (L_n = 396 nm, L_w/L_n = 1.01) at 30°C. The resulting solution was shaken for 10 s and then aged at 30°C for 1 day. The PEG-selective solvent MeOH was subsequently added to obtain a ratio of 1:9 (v/v) of THF:MeOH. The resulting uniform nanofibers (L_n= 2785 nm, L_w/L_n= 1.04) were characterized by TEM analysis (Figure S2. 19). Interestingly, despite the larger degree of polymerization for the unimer compared to the seeds (14 vs 8), epitaxial growth proceeded in normal fashion. Fiber core widths for the central B segment (W_n = 27 nm, W_n/W_w = 1.02) were found to be significantly larger than for the terminal A segments (W_n = 17 nm, W_n/W_w = 1.03) (Figure S2. 20). The value for the central B segment is close to the sum of the extended PDHF and P3EHT chain lengths (ca. 27 nm) but that for the terminal A segments is larger than anticipated (ca. 12.5 nm for PDHF$_{14}$). The discrepancy in the latter case may arise from the difficulty in precisely assigning the position of the core-corona interface and highlights the

likely scenario that errors are inherent to these measurements on organic components which differ only slightly in terms of their electron density. LCSM imaging of A-B-A segmented nanofibers in THF:MeOH (1:9, v/v) (B: L_n= 1237 nm, L_w/ L_n= 1.05; A-B-A: L_n= 6296 nm, L_w/ L_n = 1.07) further confirmed the presence of A-B-A segmented nanofibers with distinct segments with different fluorescence emission. The central B segment consists of a 1237 nm long PDHF-*b*-P3EHT crystalline core (predominantly red/orange P3EHT emission) and the long A segments (2530 nm each) consist of only a PDHF crystalline core, which are longer than the exciton diffusion length (ca. 200 nm) and which therefore give rise to blue emission (Figure 2. 6b-d). When only the blue emission channel is viewed this residual PDHF fluorescence can be detected (Figure 2. 6c).

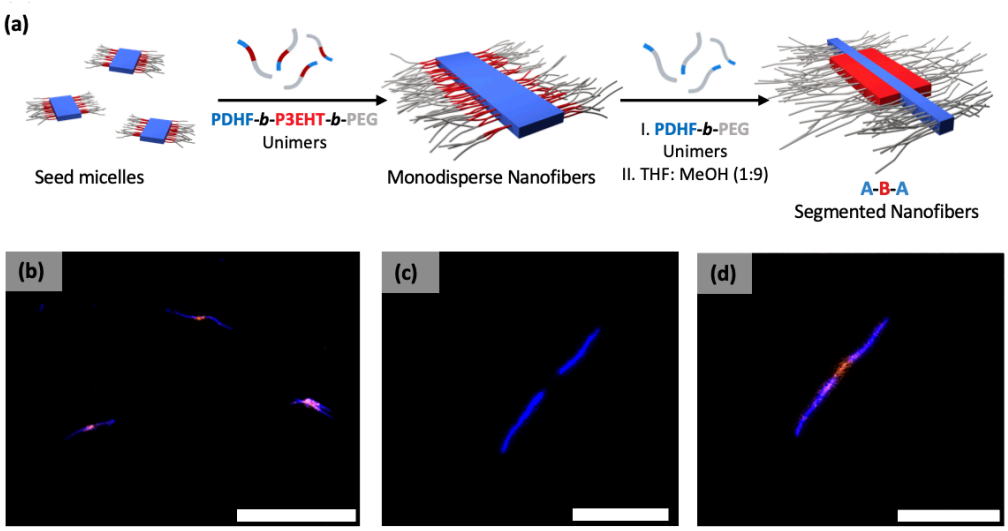

Figure 2. 6: (a) Schematic illustration of the preparation of low dispersity A-B-A segmented nanofibers with a central $PDHF_8$-*b*-$P3EHT_{25}$-*b*-PEG_{113} segment (B) and terminal $PDHF_{14}$-*b*-PEG_{227} segments (A). LCSM images (b), (c) and (d) of A-B-A segmented nanofibers (L_n= 6296 nm, L_w/ L_n = 1.07) prepared from the epitaxial growth of $PDHF_{14}$-*b*-PEG_{227} unimers from $PDHF_8$-*b*-$P3EHT_{25}$-*b*-PEG_{113} seed micelles (L_n= 1237 nm, L_w/L_n= 1.05) in THF:MeOH (1:9, v/v). LCSM images (b) and (d) were taken with both blue (PDHF) and red (P3EHT) channels and (c) only with the blue channel. Scale bars: (b) 10 µm and (c), (d) 4 µm.

2.4. Summary

For polymer-based heterojunction nanowires of potential use in optoelectronic devices, solid-state donor and acceptor materials are desirable. In this proof-of-concept work we have successfully addressed this challenge via the use of the living CDSA seeded growth method accompanied by an additional crystallization step to create coaxial heterojunctions with controlled dimensions and a crystalline energy-accepting outer core-forming P3EHT block surrounding a crystalline PDHF inner core-forming block which functions as an energy donor.[49] Enhanced FRET from the PDHF inner core to the lower energy ordered P3EHT outer core was detected compared to the directly analogous coaxial structure in which the latter block was solvated. We have also shown that the "living" CDSA approach can be applied to the preparation of uniform B-A-B and A-B-A segmented nanofibers with precise control over the coaxial heterojunction location along the crystalline nanofibers.

This work demonstrates a new approach to make various polymer-based coaxial heterojunctions which may prove useful for the fabrication of organic optoelectronic devices. Ongoing work is focused on detailed investigations of the properties of these heterojunction nanowires, including studies of the energy-transfer mechanism. We are also exploring the extension of this method to other crystallizable p- and n-type π-conjugated polymers to create solid-state donor-acceptor nanowires with tunable properties and enhanced exciton transport and FRET efficiency and also their fabrication into devices, including those associated with light harvesting, current rectification, and transistor behavior.

2.5. Supporting Information

2.5.1. Materials and Methods

All reagents used for polymers synthesis were of reagent grade and were used as received unless otherwise stated. The synthesis of $PDHF_{14}$-*b*-PEG_{227} has been reported elsewhere[1] and is not described here. The synthesis of $P3EHT_{23}$ homopolymer has been reported elsewhere,[53] the experimental protocol was not modified further and the degree of polymerization (23) and the number-average molecular weight (M_n = 4452 Da) was determined by Matrix-Assisted Laser Desorption/Ionization Time-Of-Flight Mass Spectrometry (MALDI-TOF MS). Poly(ethylene glycol) methyl ether tosylate (M_n = 5000 Da, degree of polymerization, DP = 113) was purchased from Sigma Aldrich and used as received in the synthesis of PEG_{113}-azide. All chemicals were used as received, 2-bromo-7-iodofluorene was purchased from Fluorochem and all other chemicals were purchased from Sigma Aldrich. For self-assembly experiments, reagent grade solvents were filtered via a polytetrafluoroethylene membrane (0.2 μm pores).

Nuclear magnetic resonance (NMR). ^{1}H NMR spectra were taken with a Varian 400 MHz spectrometer; chemical shifts were referenced to the residual solvent peak ($CHCl_3$, δ = 7.26 ppm).

Gel Permeation Chromatography (GPC). Measurements were conducted using a Viscotek GPC_{max} equipped with a UV detector operating at 400 nm and a differential refractometer. Measurements were carried out at 1.0 mL min^{-1} with THF containing [*n*Bu_4N]Br (0.1% w/w) as the eluent at 35˚C, results were measured against polystyrene standards (Viscotek). Samples were dissolved in THF containing [*n*Bu_4N]Br (0.1% w/w) at 0.2 mg mL^{-1} and 2 mg mL^{-1} and filtered prior to analysis with syringe filters (polytetrafluoroethylene membrane, 0.2 μm pores).

Matrix-Assisted Laser Desorption/Ionization Time-Of-Flight Mass Spectrometry (MALDI-TOF MS). Measurements were conducted on a Bruker Ultraflex II ToF spectrometer under the reflector positive ion regime. Samples were prepared with a 9:1 ratio of *trans*-2-[3-(4- *tert*-butylphenyl)-2-methyl-2-propenylidene]malonitrile matrix (20 mg mL^{-1} in THF) to polymer solution (0.2

mg mL^{-1} in THF). An aliquot of the resulting sample solution (ca. 2 µL) was deposited onto the sample plate and dried under ambient conditions before analysis.

Transmission Electron Microscopy (TEM). Samples were prepared by drop casting 10 µL of a nanofiber solution onto a carbon-coated copper grid (Agar Scientific, mesh size 200). Bright-field TEM micrographs were taken using a JEOL JEM 1400 EX microscope operating at 120 kV, equipped with a Gatan Orius SC1000 CCD camera. Micelle length distributions were determined using the software program ImageJ developed at US National Institute of Health. A minimum of 300 micelles were traced to determine their contour length and construct histograms of the length distributions. This data allows for calculation of the number average length (L_n), weight average length (L_w) for each sample, this is calculated as shown below (L = length of fiber, N = number).

$$L_n = \frac{\sum_{i=1}^{n} N_i L_i}{\sum_{i=1}^{n} N_i} \qquad L_w = \frac{\sum_{i=1}^{n} N_i {L_i}^2}{\sum_{i=1}^{n} N_i L_i}$$

Atomic Force Microscopy (AFM). Samples were prepared by drop casting 10 µL of a nanofiber solution onto a carbon-coated mica. Imaging was taken using a Bruker Multimode VIII atomic force microscope equipped with a ScanAsyst-HR fast scanning module and a ScanAsyst-Air-HR probe (tip radius, 2 nm), under ambient conditions utilising peak force feedback control.

Spectroscopic Measurements. UV/vis data were obtained on a Lambda 35 Spectrometer employing quartz cells (1 cm x 1 cm) from 200 to 800 nm. Fluorescence spectra were obtained on a PTI QM40 Spectrofluorometer using an excitation wavelength of λ_{ex} = 380 nm. Dialysis was performed using tubing with a molar mass cut-off of 14,000 $gmol^{-1}$.

Laser confocal scanning microscopy (LCSM). Images were obtained using Leica SP5 system equipped with a Leica DMI6000 inverted epifluorescence microscope (100 x (NA 1.4) oil immersion objective lens). A UV diode laser (at 405 nm), was used to excite the nanofibers and the digital false-color images obtained were color coded (PDHF = blue, P3EHT = red). Sample concentrations ranged from 0.005 mg mL^{-1} to 0.02 mg mL^{-1} in THF:MeOH (1:1, v/v) or THF:MeOH (1:9, v/v).

Wide-Angle X-ray Scattering (WAXS). Sample nanofiber solutions were prepared by self-assembly at 0.5 mg mL^{-1} in THF:MeOH (1:1, v/v) then changing

the solvent system to THF:MeOH (1:9, v/v) via MeOH addition. These samples were then concentrated to ca. 100 mg mL^{-1} (>99 % solvent removal) under a nitrogen stream then sealed in a quartz capillary tube (1.5 mm diameter) with epoxy resin. Solid-state samples were drop cast onto mica or Kapton® film. A Ganesha SAXS/WAXS apparatus (SAXSLAB, Denmark) was used and a Pilatus 300K 2D X-Ray Detector (Dectris, Switzerland) was used to measure the scattering pattern.

2.5.2. Synthesis of alkyne-terminated PDHF-*b*-P3EHT

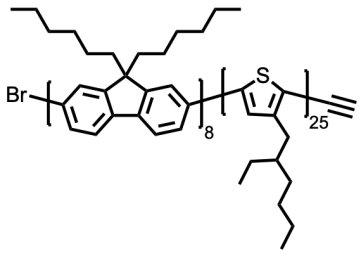

Alkyne-terminated $PDHF_8$-*b*-$P3EHT_{25}$ was synthesized by sequential Grignard Metathesis polymerization (GRIM). 2-Bromo-7-iodo-9,9-bis-*n*-hexylfluorene and 2,5-Dibromo-3-(2'-ethyl)hexyl thiophene were synthesised according to reported procedures.[73,53] 2-Bromo-7-iodo-9,9-bis-*n*-hexylfluorene (203 mg, 0.38 mmol) and 2,5-Dibromo-3-(2'-ethylhexyl) thiophene (267 mg, 0.75 mmol) were separately dissolved in 10 mL of anhydrous THF. The solution of 2-bromo-7-iodo-9,9-bis-*n*-hexylfluorene was cooled to -20˚C before 1.3 M *i*PrMgCl.LiCl (1 eq.) was added dropwise then the resulting solution was left to stir for 90 min at -78˚C. To the solution of 2,5-dibromo-3-(2'-ethylhexyl) thiophene, 1.3 M iPrMgCl.LiCl (1 eq.) was added dropwise at 20˚C then the resulting solution was left to stir for 110 min at 20˚C. The activated fluorene monomer was added in one rapid injection to a solution of $Ni(dppp)Cl_2$ (10 mg, 0.019 mmol) and anhydrous THF (100 mL) at 0˚C. After 20 minutes of stirring, the activated thiophene monomer solution was then added in one quick injection to the reaction mixture. After 2 h, 0.5 M ethynylmagnesium bromide (3 mL) was added to the reaction mixture which was then stirred for 10 min. The resultant mixture was then precipitated into methanol, giving a red solid.

Further purification by Soxhlet extraction in ethyl acetate, methanol then chloroform followed by removal of solvent *in vacuo* and then repeated precipitation into cold methanol (0°C) gave the purified polymer (red solid, yield: 97 mg, 43 %). The degree of polymerisation of the PDHF aliquot was calculated to be 8 and M_n = 2738 Da by MALDI-TOF with a 9:1 ratio of matrix to polymer solution (0.5 mg mL^{-1} in THF). Molecular mass dispersity ($Đ_m = M_w / M_n$) of 1.27 was determined by GPC analysis for the $PDHF_8$ homopolymer (M_w= 14, 103 Da and M_n= 11, 072 Da). A molar mass dispersity ($Đ_m$) of 1.24 was determined by GPC analysis for the $PDHF_8$-*b*-$P3EHT_{25}$ diblock copolymer (M_w= 18, 311 Da and M_n= 14, 735 Da).

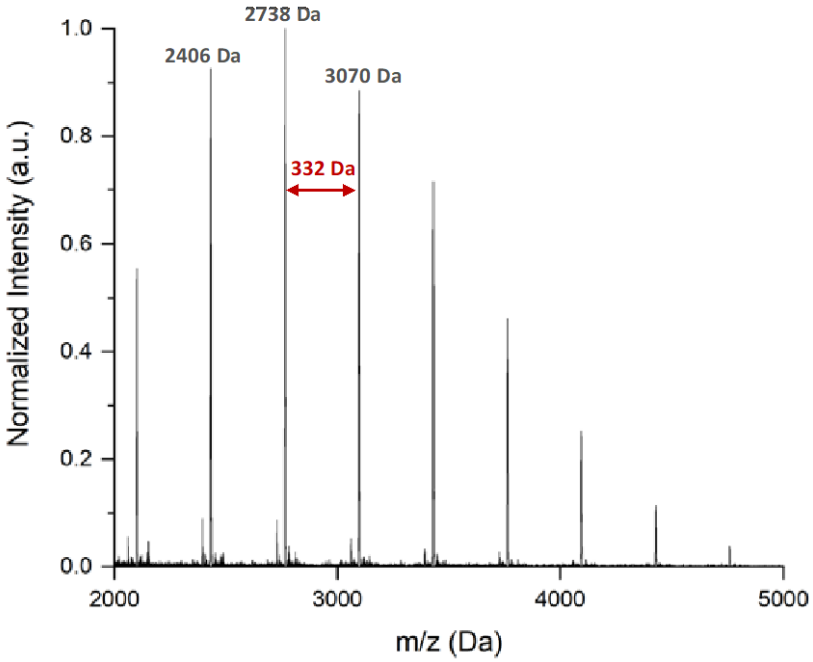

Figure S2. 1: MALDI-TOF mass spectrum of Br/H-capped $PDHF_8$ homopolymer aliquot, M^+ = 2738 Da. The low intensity peak distribution corresponds to H/H-capped $PDHF_8$ homopolymer. The mass of each PDHF repeat unit is 332 g mol^{-1}.

2.5.3. Synthesis of PDHF-*b*-P3EHT-*b*-PEG

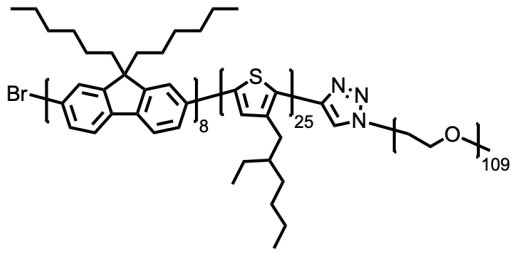

Alkyne-terminated $PDHF_8$-*b*-$P3EHT_{25}$ (30 mg, 0.0039 mmol) and azide-terminated PEG_{113} (25 mg, 0.0052 mmol) were dissolved in 3 mL of THF and subjected to three consecutive freeze-pump-thaw cycles. Azide-terminated PEG_{113} was synthesized according to a previously reported procedure.[74] CuBr (5.3 mg, excess) and PMDETA (8 μL, excess) were premixed and dissolved in 1 mL anhydrous THF then added to the polymer solution under N_2. The reaction mixture was then heated to 45˚C and stirred for 48 h. The polymers were then purified by passing the reaction mixture through a basic alumina column to remove Cu/PMDETA. Volatiles were removed *in vacuo* followed by repeated precipitation into cold methanol to remove excess PEG_{113}-N_3. Residual alkyne-terminated $PDHF_8$-*b*-$P3EHT_{25}$ was removed by silica gel chromatography (eluent chloroform 100 %), then the triblock copolymer was collected using chloroform and methanol (9:1, v/v) as the eluent. One of the collected fractions was used for further studies and was precipitated into cold methanol, this gave the product as a red solid (yield: 21 mg, 43 %). A molar mass dispersity ($Đ_m$) of 1.17 was determined by GPC analysis for the $PDHF_8$-*b*-$P3EHT_{25}$-*b*-PEG_{113} polymer (M_w= 27, 353 Da and M_n= 23, 322 Da). ^{1}H NMR (400 MHz, $CDCl_3$) δ (ppm) = 7.62-7.85 (m, 50 H, polyfluorene aromatic x 6), 6.94 (s, 25 H, polythiophene aromatic x 1), 3.64 (s, 452 H, polyethylene glycol-(C*H*$_2$) x 2), 3.38 (s, 3 H, polyethylene glycol-C*H*$_3$), 2.73 (d, 52 H, polythiophene-C*H*$_2$), 2.12 (brs, 34 H, polyfluorene-(C*H*$_2$) x 2), 1.69 (brs, 27 H, polythiophene-C*H*), 1.19-1.40 (m, 342 H, polyfluorene-(CH_2(C*H*$_2$)$_4$) x 2 and polythiophene-CH_2(C*H*$_2$) x 4), 0.75-0.93 (m, 223 H, polyfluorene-(C*H*$_3$) x 2 and polythiophene-(C*H*$_3$) x 2).

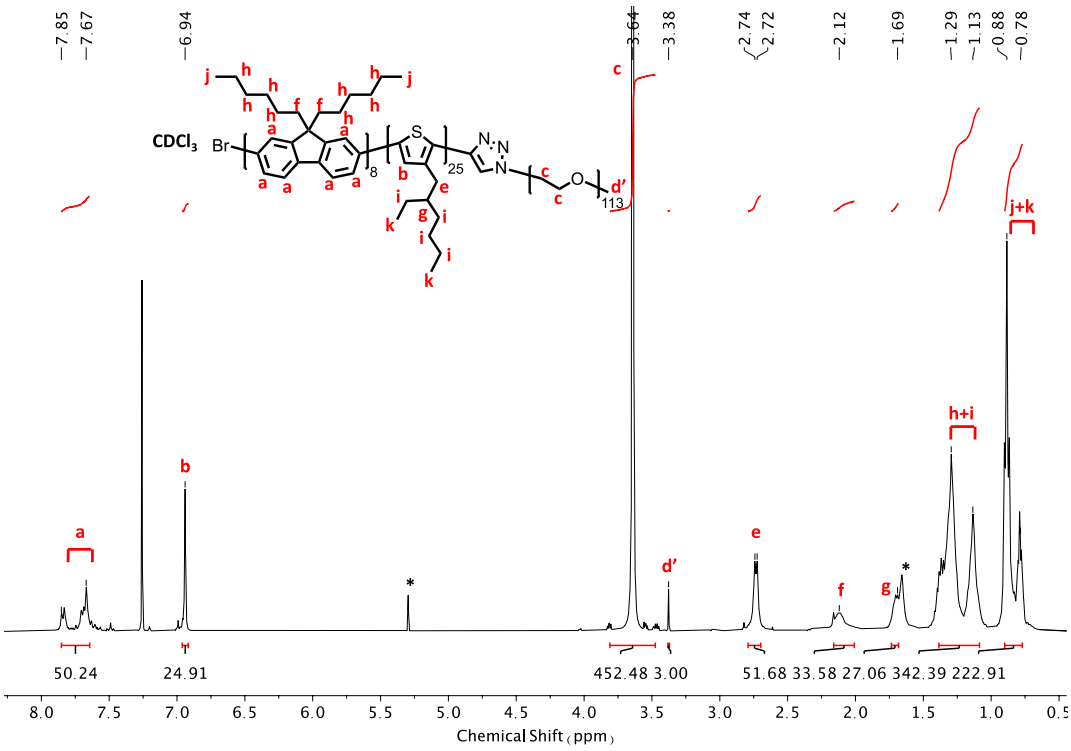

Figure S2. 2: ^{1}H NMR spectrum of PDHF$_8$-*b*-P3EHT$_{25}$-*b*-PEG$_{113}$ (400 MHz, $CDCl_3$). Residual CH_2Cl_2 (δ = 5.30 ppm) and H_2O (δ = 1.56 ppm) are marked with an *.

Integration of the ^{1}H NMR spectrum of PDHF-*b*-P3EHT-*b*-PEG, allowed the determination of the block ratio of the PEG to the PDHF and P3EHT blocks. Comparing the aliphatic protons of PEG (δ = 3.64 ppm) to the aromatic protons of PDHF (δ = 7.85-7.62 ppm) and the aromatic protons of P3EHT (δ = 6.94 ppm), the block ratio of PEG: PDHF: P3EHT was estimated to be 1: 0.07: 0.22. A DP of 8 for the PDHF block and 25 for the P3EHT block was subsequently determined from the known DP of the PEG block (113). The DP of the PDHF block based on MALDI-TOF analysis was also 8.

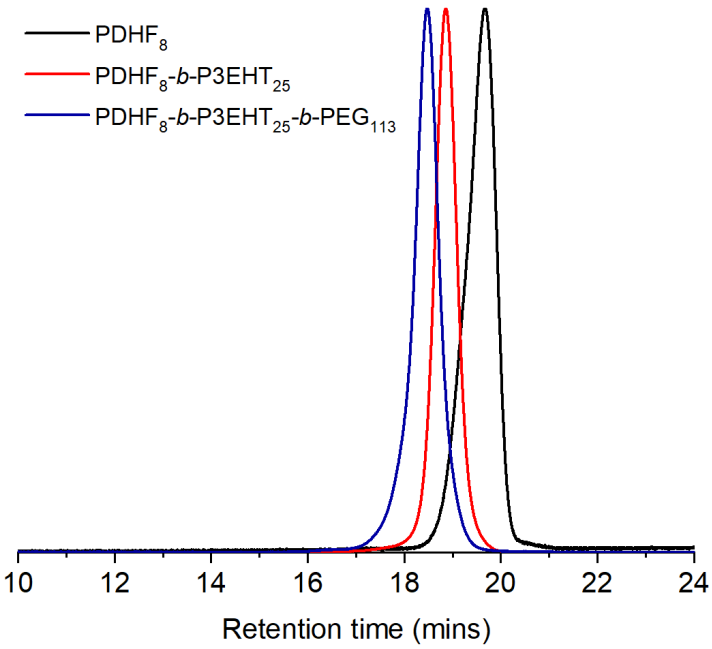

Figure S2. 3: GPC traces (UV response at λ = 400 nm) eluted in THF containing [*n*Bu$_4$N]Br (0.1 % w/w) (1 mL min^{-1}) at 35°C of PDHF$_8$ homopolymer (black trace), alkyne-terminated PDHF$_8$-b-P3EHT$_{25}$ diblock copolymer (red trace) and PDHF$_8$-*b*-P3EHT$_{25}$-*b*-PEG$_{113}$ triblock copolymer (blue trace).

2.5.4. CDSA of PDHF-*b*-P3EHT-*b*-PEG

Preparation of polydisperse PDHF-*b*-P3EHT-*b*-PEG nanofibers

In an example self-assembly protocol, 200 µL of methanol (MeOH) was added dropwise to 200 µL of a 0.6 mg mL^{-1} solution of PDHF$_8$-*b*-P3EHT$_{25}$-*b*-PEG$_{113}$ block copolymer in THF at 30°C resulting in a final concentration of 0.3 mg mL^{-1}and a ratio of THF to MeOH of 1:1 (v/v). The mixture was then shaken manually for 10 s and aged at 30°C for 24 h before analysis by TEM imaging to confirm the formation of polydisperse nanofibers of PDHF$_8$-*b*-P3EHT$_{25}$-*b*-PEG$_{113}$.

Preparation of Seed Micelles

Seed micelles of PDHF$_8$-*b*-P3EHT$_{25}$-*b*-PEG$_{113}$ block copolymers were prepared by sonication of a 0.3 mg mL^{-1} solution in THF:MeOH (1:1, v/v) of polydisperse nanofibers in an ultrasonic bath at 0°C for 2 h. To further increase the crystallinity, after sonication the resulting solutions were heated to 45°C for 3 h then subsequently cooled slowly to 20°C and aged for 24 h. The samples were then analysed by TEM imaging.

Preparation of low dispersity PDHF-*b*-P3EHT-*b*-PEG nanofibers by seeded growth

Seeded growth experiments were conducted by quickly injecting a known volume of $PDHF_8$-*b*-$P3EHT_{25}$-*b*-PEG_{113} unimer (in THF, 3 mg mL^{-1}, between 1-15μL) to a solution of seed micelles in THF:MeOH (1:1, v/v) of a known concentration (either 0.015 mg mL^{-1} or 0.0075 mg mL^{-1}). The samples were then shaken for 10 s and aged at 30°C for 24 h before analysis by TEM. The contour lengths of at least 300 micelles were measured from several TEM images of each sample.

Preparation of low dispersity PDHF-*b*-P3EHT-*b*-PEG nanofibers with a dual PDHF/P3EHT core

The THF:MeOH ratio of a solution of nanofibers with a PDHF core was increased from 1:1 to 1:9 by dropwise MeOH addition over ca. 2 minutes at 20°C followed by ageing for 24 h. Aggregation of the P3EHT block to produce heterojunction nanofibers with cores comprising both crystalline PDHF and also P3EHT was detected. The dropwise methanol addition was preferred over direct addition as this process should lead to more controlled aggregation and crystallization.

Preparation of B-A-B segmented nanofibers by seeded growth

.1. Preparation of low dispersity nanofibers from $PDHF_{14}$-b-PEG_{227} (A segment)

Seed micelles of $PDHF_{14}$-*b*-PEG_{227} were prepared by sonication (0°C for 2 h in an ultrasonic bath) of polydisperse fibers in THF:MeOH (1:1, v/v). A 20 μL solution of these seed micelles (0.6 mg mL^{-1}, L_n=21 nm, L_w/L_n= 1.08) was diluted with 600 μL of THF:MeOH (1:1, v/v). Then 20 μL of unimer $PDHF_{14}$-*b*-PEG_{227} unimer solution (THF, 3 mg mL^{-1}) was added to the dilute seed solution at 30°C. The resulting mixture was shaken for 10 s and aged for 24 h at 30°C. Uniform $PDHF_{14}$-*b*-PEG_{227} nanowires (L_n= 124 nm, L_w/L_n= 1.05) were observed by TEM analysis.

.2. Formation of low dispersity B-A-B segmented nanowires from living CDSA of PDHF$_8$-b-P3EHT$_{25}$-b-PEG$_{113}$ (B segments) from PDHF$_{14}$-b-PEG$_{227}$ seeds (A segment)

A 12 µL solution of PDHF$_{14}$-*b*-PEG$_{227}$ nanofibers (0.11 mg ml^{-1}, L_n= 124 nm, L_w/L_n= 1.05) in THF: MeOH (1:1, v/v) was diluted with 100 µL THF:MeOH (1:1, v/v). Subsequently, 3 µL of PDHF$_8$-*b*-P3EHT$_{25}$-*b*-PEG$_{113}$ unimer solution (THF, 2 mg mL^{-1}) was quickly injected into the dilute solution of PDHF$_{14}$-*b*-PEG$_{227}$ nanofibers at 30°C. The resulting mixture was shaken for 10 s and aged for 24 h at 30°C. The solvent system was then adjusted until a ratio of 1:9 (v/v) of THF:MeOH was achieved and aged for a further 24 h. Uniform B-A-B segmented nanofibers (L_n=507 nm, L_w/L_n= 1.02) were observed TEM analysis.

Preparation of A-B-A segmented nanofibers by seeded growth

1. Preparation of low dispersity nanofibers from PDHF$_8$-b-P3EHT$_{25}$-b-PEG$_{113}$ (B segment)

A 10 µL solution of PDHF$_8$-*b*-P3EHT$_{25}$-*b*-PEG$_{113}$ seed micelles (0.2 mg mL^{-1}, L_n= 87 nm, L_w/L_n= 1.05) in THF:MeOH (1:1, v/v) was diluted with 200 µL of THF:MeOH (1:1, v/v). Then 3 µL of PDHF$_8$-*b*-P3EHT$_{25}$-*b*-PEG$_{113}$ unimer solution (THF, 2 mg mL^{-1}) was added to the dilute seed solution at 30°C. The resulting mixture was shaken for 10 s and aged for 24 h at 30°C. Uniform PDHF$_8$-*b*-P3EHT$_{25}$-*b*-PEG$_{113}$ nanofibers (L_n= 396 nm, L_w/L_n= 1.05) were observed TEM analysis.

2. Formation of low dispersity A-B-A segmented nanowires from living CDSA of PDHF$_{14}$-b-PEG$_{227}$ (A segments) from PDHF$_8$-b-P3EHT$_{25}$-b-PEG$_{113}$ seeds (B segment)

A 20 µL solution of PDHF$_8$-*b*-P3EHT$_{25}$-*b*-PEG$_{113}$ nanofibers (0.038 mg ml^{-1}, L_n= 396 nm, L_w/L_n= 1.05) in THF:MeOH (1:1, v/v) was diluted with 200 µL of THF:MeOH (1:1, v/v). Then 2 µL of PDHF$_{14}$-*b*-PEG$_{227}$ unimer solution (THF, 3 mg mL^{-1}) was added to the dilute seed solution at 30°C. The resulting mixture was shaken for 10 s and aged for 24 h at 30°C. The solvent system was then adjusted until a ratio of 1:9 (v/v) of THF:MeOH was achieved and aged for a further 24 h. Uniform A-B-A segmented nanofibers (L_n= 2785 nm, L_w/L_n= 1.04) were observed by TEM analysis.

2.5.5. Supplementary Figures

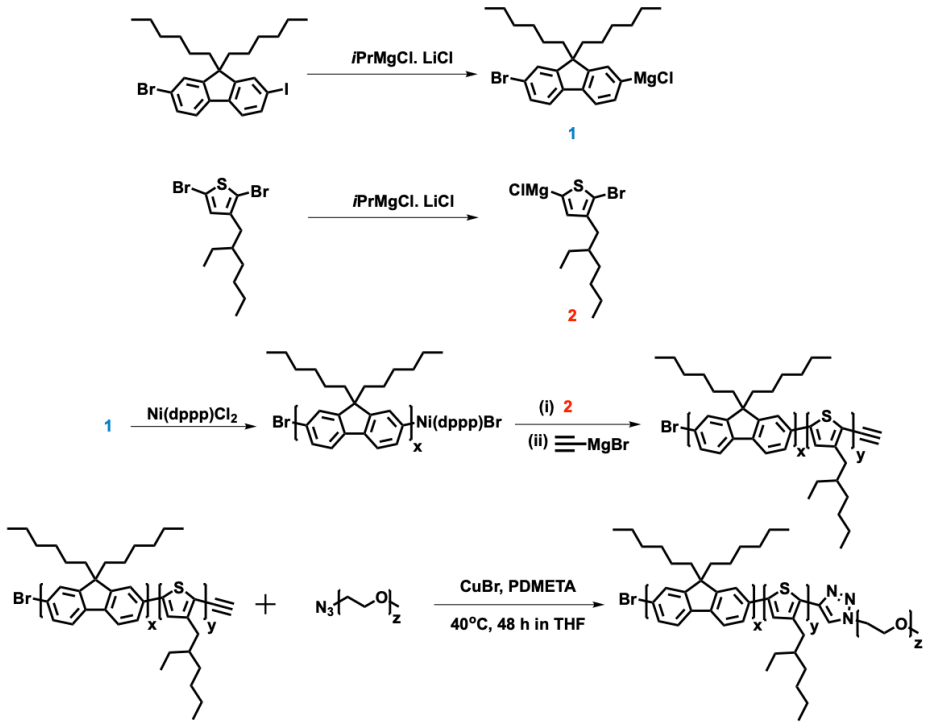

Scheme S2. 1: Synthesis of PDHF-*b*-P3EHT-*b*-PEG. dppp = 1,3-bis(diphenylphosphino)propane. PMDETA=*N,N,N',N'',N''*-pentamethyldiethylenetriamine.

Table S2. 1: Characterization data for PDHF homopolymer and PDHF-based block copolymers

Material Composition	M_n (kg mol^{-1})	M_w [c] (kg mol^{-1})	$Đ_m$ [c]
$PDHF_8$ [a]	11.1[c]	14.1	1.27
$PDHF_8$-*b*-$P3EHT_{25}$ [b]	14.7[c]	18.3	1.24
$PDHF_8$-*b*-$P3EHT_{25}$-*b*-PEG_{113} [b]	23.3[c]	27.4	1.17
$PDHF_{14}$-*b*-PEG_{227} [b]	27.9[c]	32.1	1.15

Data obtained by [a] MALDI-ToF, [b] ^{1}H NMR and [c] GPC (THF containing [nBu$_4$N]Br (0.1% w/w)). Molecular mass dispersity = $Đ_m$ (M_w/M_n).

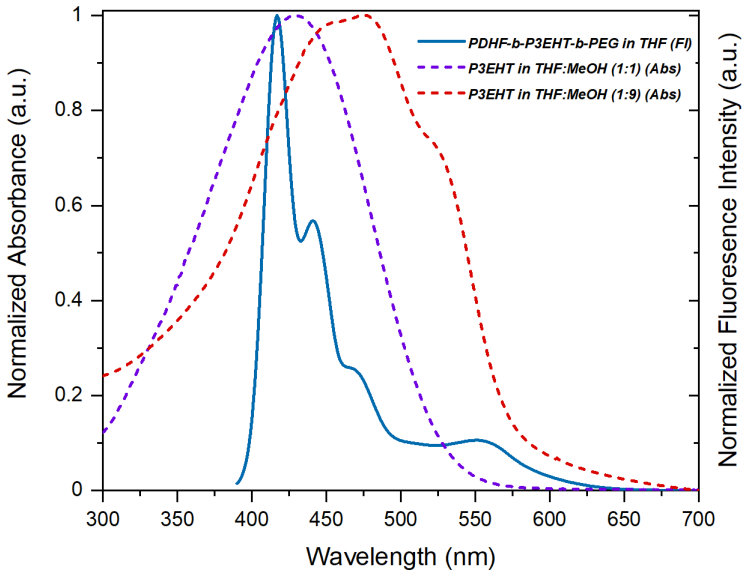

Figure S2. 4: Normalized solution-state UV-vis spectra of $P3EHT_{25}$ homopolymer in THF:MeOH (1:1, v/v) (purple trace) and in THF:MeOH (1:9, v/v) (red trace) and normalized solution-state photoluminescence spectrum of $PDHF_8$-*b*-$P3EHT_{25}$-*b*-PEG_{113} unimers in THF (blue trace, marked FI = fluorescence intensity), λ_{ex} = 380 nm. The spectrum in THF:MeOH (1:9, v/v) was obtained rapidly after dilution of the THF:MeOH (1:1, v/v) sample with MeOH and before precipitation occurred.

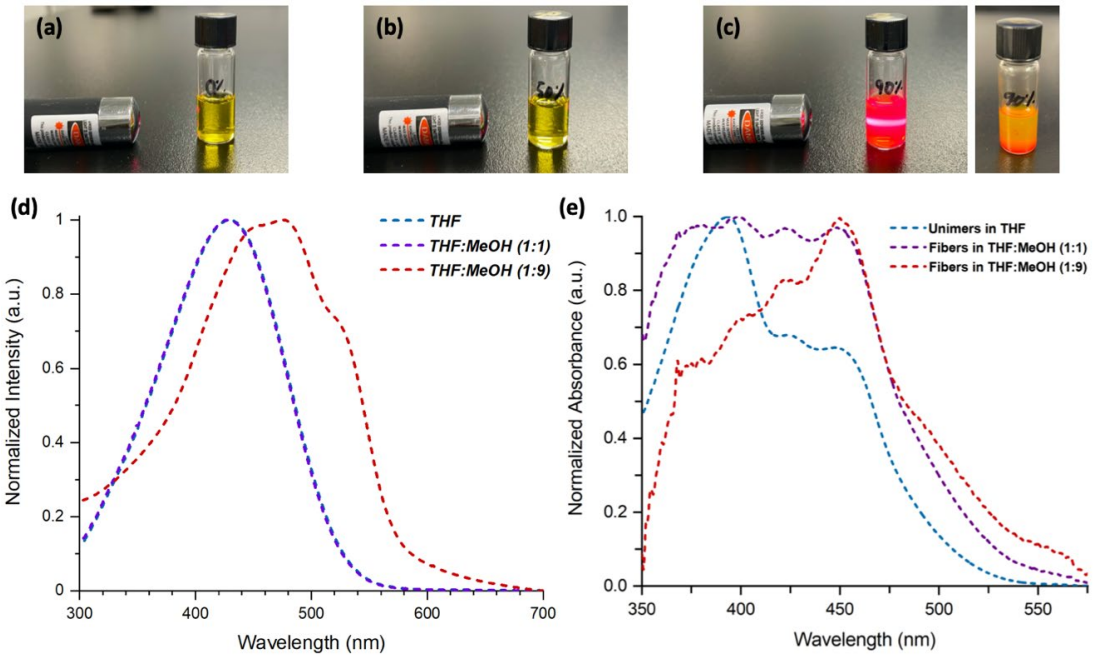

Figure S2. 5: Photographs of a solution of $P3EHT_{23}$ homopolymer in (a) THF, (b) THF:MeOH (1:1, v/v) and (c) THF:MeOH (1:9, v/v) with a laser pen to monitor the Tyndall effect. The Tyndall effect was only observed in THF:MeOH (1:9, v/v). (d) Solution-state UV-vis spectra of $P3EHT_{23}$ homopolymer in THF (blue trace) and THF:MeOH (1:1, v/v) (purple trace) and as a colloidal suspension in THF:MeOH (1:9, v/v) (red trace). (e) Solution-state UV-vis spectra of $PDHF_8$-*b*-$P3EHT_{25}$-*b*-PEG_{113} in THF (blue trace), THF:MeOH (1:1, v/v) (purple trace) and in THF:MeOH (1:9, v/v) (red trace).

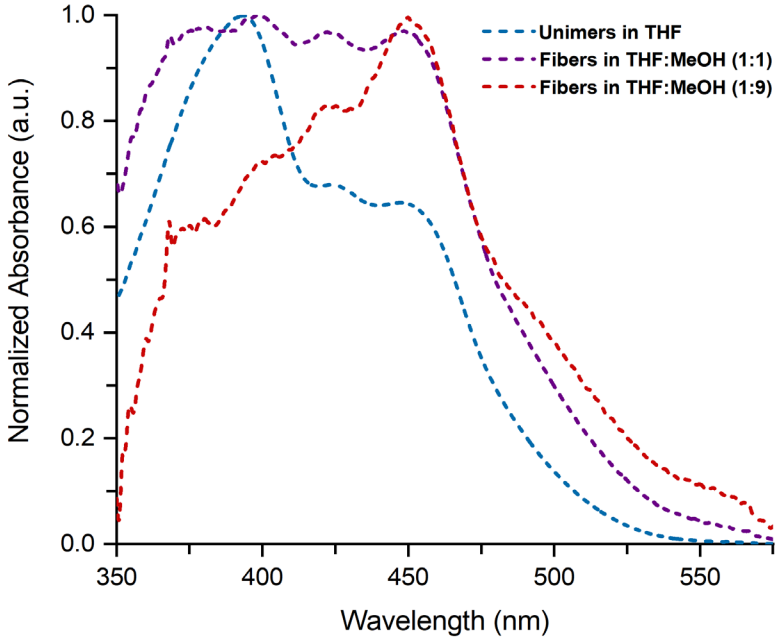

Figure S2. 6: Normalized solution-state UV-vis spectra of $PDHF_8$-*b*-$P3EHT_{25}$-*b*-PEG_{113} unimers in THF (blue trace) and nanofibers in THF:MeOH (1:1, v/v) (purple trace) and in THF:MeOH (1:9, v/v) (red trace).

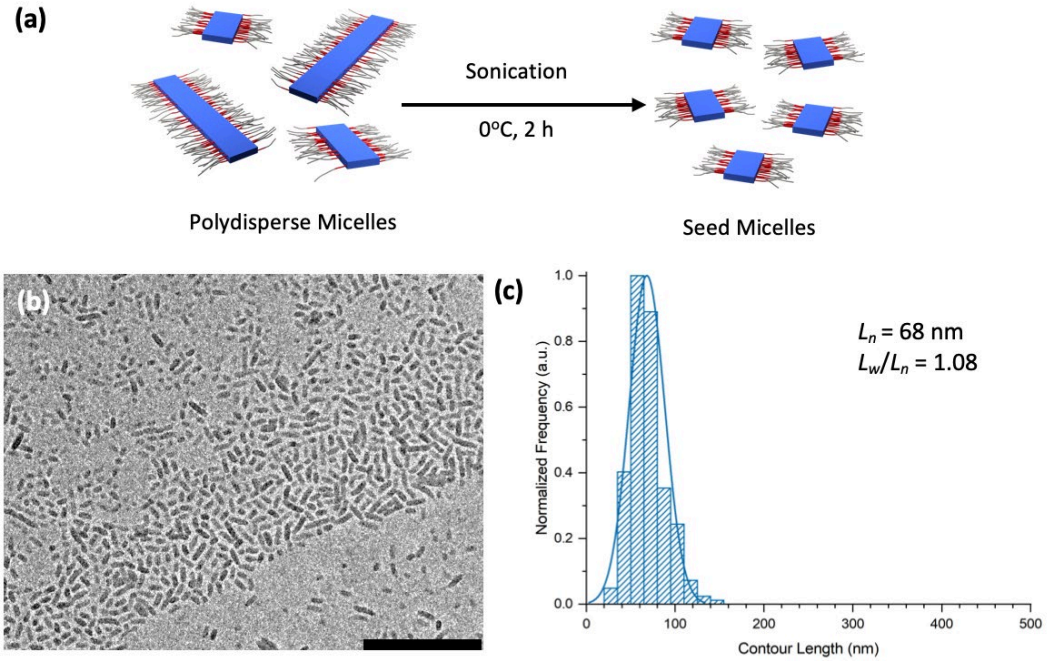

Figure S2. 7: (a) Schematic illustration of the preparation of $PDHF_8$-*b*-$P3EHT_{25}$-*b*-PEG_{113} seed micelles in THF:MeOH (1:1, v/v). (b) TEM image of $PDHF_8$-*b*-$P3EHT_{25}$-*b*-PEG_{113} seed micelles (L_n = 68, L_w/L_n = 1.08) prepared by sonication of polydisperse micelles in THF:MeOH (1:1, v/v). Scale bar: 500 nm. (c) Histogram of the contour length distribution of $PDHF_8$-*b*-$P3EHT_{25}$-*b*-PEG_{113} seed micelles.

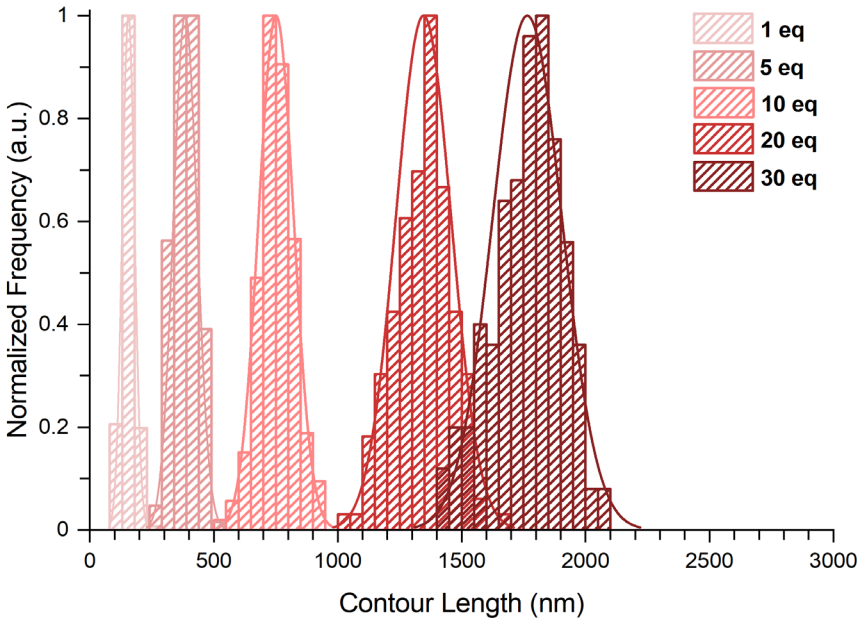

Figure S2. 8: Histograms representing contour length distributions of nanofibers prepared by the seeded growth of $PDHF_8$-*b*-$P3EHT_{25}$-*b*-PEG_{113}. Inset legend shows the mass equivalents of unimer added to seed micelles.

Table S2. 2: Contour length data of nanofibers prepared by seeded growth of $PDHF_8$-*b*-$P3EHT_{25}$-*b*-PEG_{113} in THF:MeOH (1:1, v/v) using seeded growth. Seed micelles are represented in the table as 0 equivalents of unimer-to-seed.

	Unimer-to-Seed Ratio					
	0	**1**	**5**	**10**	**20**	**30**
L_n **(nm)**	68	155	384	751	1346	1765
L_w **(nm)**	73	159	390	758	1355	1776
L_w/L_n	1.08	1.03	1.02	1.01	1.01	1.01
σ (nm)	20	25	48	71	112	140
σ/ L_n	0.29	0.16	0.12	0.09	0.08	0.08

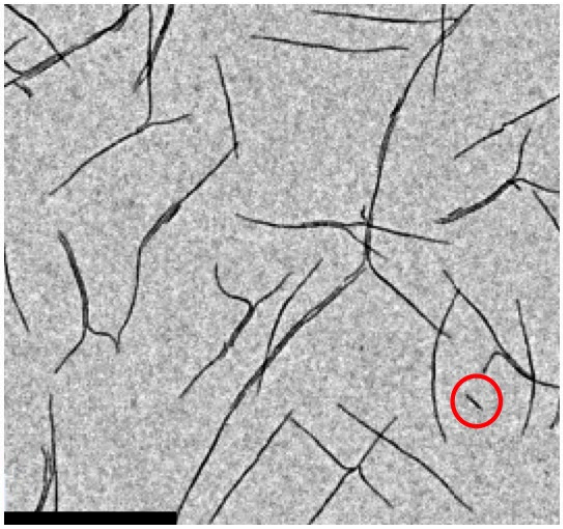

Figure S2. 9: TEM image of nanofibers of controlled length (L_n= 1765 nm, L_w/L_n= 1.01) prepared by seeded growth of PDHF$_8$-*b*-P3EHT$_{25}$-*b*-PEG$_{113}$ BCPs from seed micelles (L_n= 68 nm, L_w/L_n= 1.08) with m_{unimer}/m_{seed} values of 30. Scale bar: 2 µm. A fiber presumably formed by self-nucleation (ca. 300 nm) is circled in red.

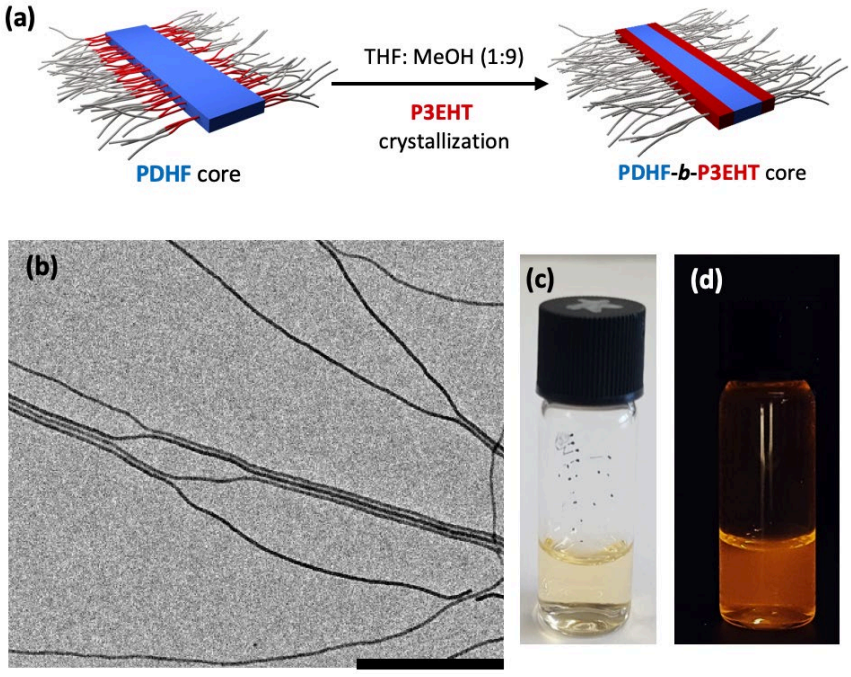

Figure S2. 10: (a) Schematic illustration of the secondary crystallization of P3EHT in THF:MeOH (1:9, v/v). TEM image of (b) PDHF-*b*-P3EHT-core forming nanofibers in THF:MeOH (1:9, v/v). Scale bar: 1 µm. Photograph of a solution of PDHF$_8$-*b*-P3EHT$_{25}$-*b*-PEG$_{113}$ nanofibers in THF:MeOH (1:9, v/v) under (c) visible light and (d) UV light (365 nm).

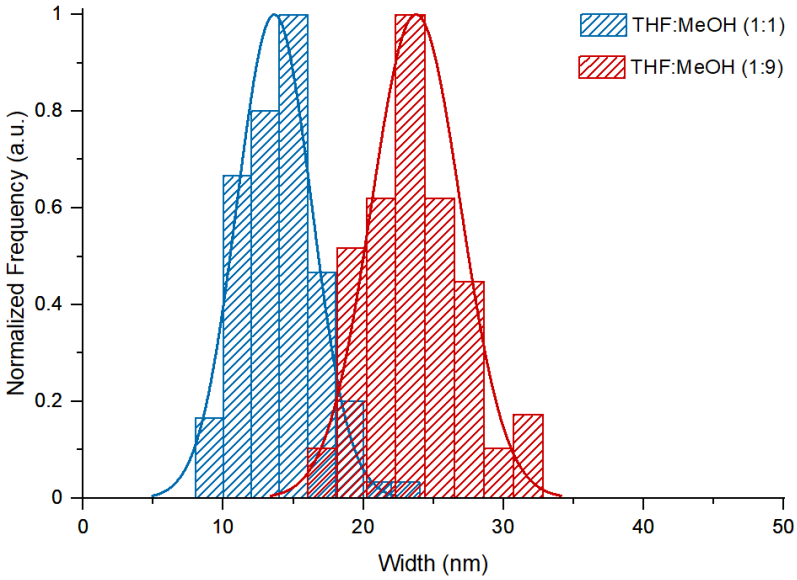

Figure S2. 11: Histograms representing fiber width distributions of PDHF$_8$-*b*-P3EHT$_{25}$-*b*-PEG$_{113}$ nanofibers in THF:MeOH (1:1, v/v) (blue) and THF:MeOH (1:9, v/v) (red). In THF:MeOH (1:1, v/v) W_n = 14 nm, W_n/W_w = 1.04 and in THF:MeOH (1:9, v/v) W_n = 24 nm, W_n/W_w = 1.02.

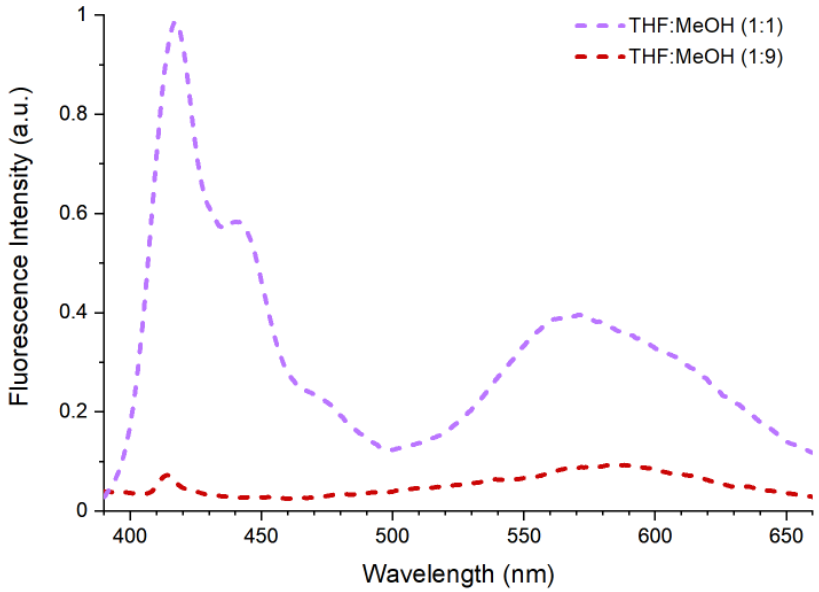

Figure S2. 12: Solution-state photoluminescence spectra of PDHF$_8$-*b*-P3EHT$_{25}$-*b*-PEG$_{113}$ nanofibers in THF:MeOH (1:1, v/v) (purple trace) and in THF:MeOH (1:9, v/v) (red trace) after dialysis, concentration = 0.01 mg mL^{-1}. λ_{ex} = 380 nm.

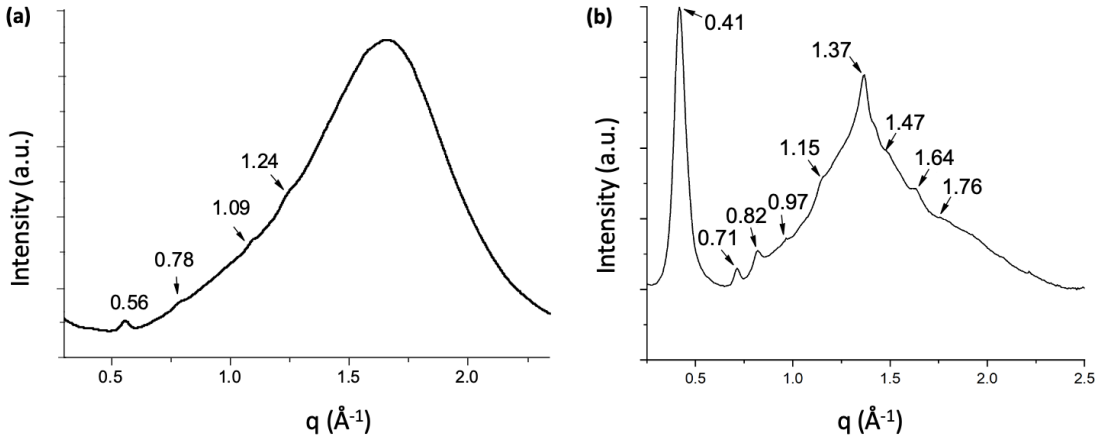

Figure S2. 13: (a) Solution-state WAXS spectrum of PDHF$_8$-*b*-P3EHT$_{25}$-*b*-PEG$_{113}$ nanofibers in THF:MeOH (1:9, v/v). The large broad background peak arises from solvent scattering. Experimental observed q values were assigned to previously reported q values for crystalline P3EHT shown in brackets,[68] at q = 0.56 (0.63), 0.78 (0.84), 1.09 (1.19), 1.24 (1.30) Å^{-1}. The discrepancies are attributed to the location of the peaks for the BCP on the slope of the broad background peak. Peaks for the inner crystalline PDHF core were not detected presumably due to the low volume fraction. (b) Solid-state WAXS spectrum of bulk PDHF$_8$-*b*-P3EHT$_{25}$ BCP. Experimental q values are assigned to previously reported q values for crystalline PDHF shown in brackets,[1] at q = 0.41 (0.41), 0.71 (0.71) and 1.37 (1.35) Å^{-1}. Experimental observed q values are assigned to previously reported q values for crystalline P3EHT shown in brackets,[5] at q = 0.82 (0.84), 0.97 (1.01), 1.15 (1.19), 1.47 (1.50), 1.64 (1.61) and 1.76 (1.78) Å^{-1}. The discrepancies are attributed to the location of the peaks for the BCP on the slope of the broad amorphous halo. Previously reported P3EHT q values are quoted from Table S1.[5]

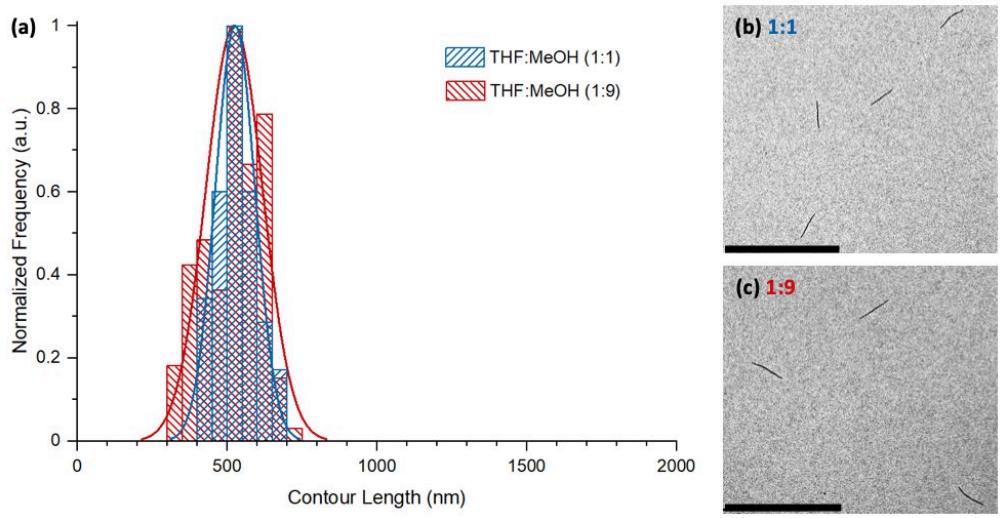

Figure S2. 14: (a) Histograms representing fiber length distributions of PDHF$_8$-*b*-P3EHT$_{25}$-*b*-PEG$_{113}$ nanofibers in THF:MeOH (1:1, v/v) (blue) and THF:MeOH (1:9, v/v) (red). TEM images of low dispersity PDHF$_8$-*b*-P3EHT$_{25}$-*b*-PEG$_{113}$ nanofibers in THF:MeOH (1:1, v/v) L_n = 527 nm, L_n/L_w = 1.02 and in THF:MeOH (1:9, v/v) L_n = 524 nm, L_n/L_w = 1.03. Scale bars: 2 µm.

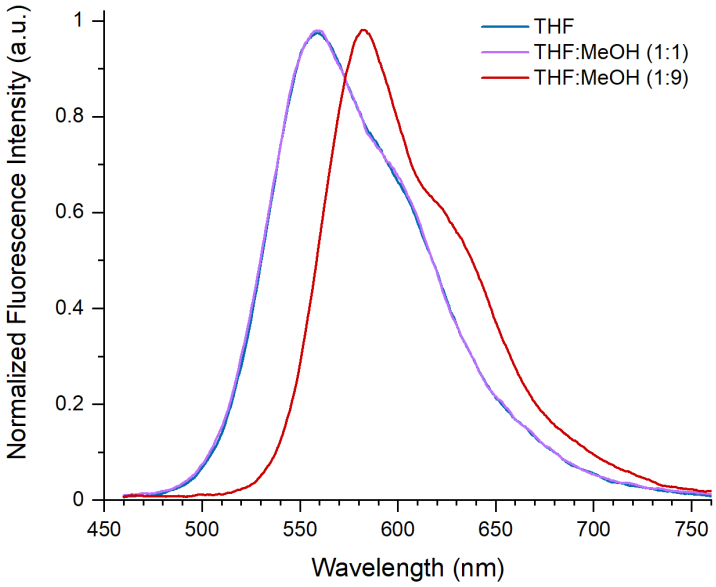

Figure S2. 15: Normalized solution-state photoluminescence spectra of $P3EHT_{23}$ homopolymer in THF (blue trace), in THF:MeOH (1:1, v/v) (purple trace) and in THF:MeOH (1:9, v/v) (red trace) . For the photoluminescence spectra, λ_{ex} = 380 nm. The spectrum in THF:MeOH (1:9, v/v) was obtained rapidly after dilution of the THF:MeOH (1:1, v/v) sample with MeOH and before precipitation occurred.

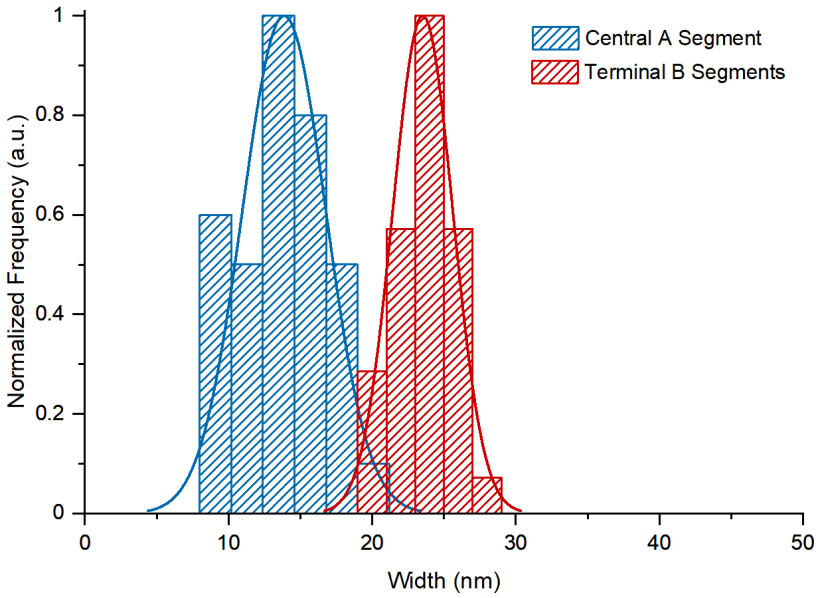

Figure S2. 16: Histograms representing fiber width distributions of B-A-B segmented nanofibers (A: L_n = 124 nm, L_w/L_n = 1.05; B-A-B: L_n = 507 nm, L_w/L_n = 1.02) in THF:MeOH (1:9, v/v). For the central A segment (blue) W_n = 14 nm, W_n/W_w = 1.04 and for the terminal B segments (red) W_n = 24 nm, W_n/W_w = 1.01.

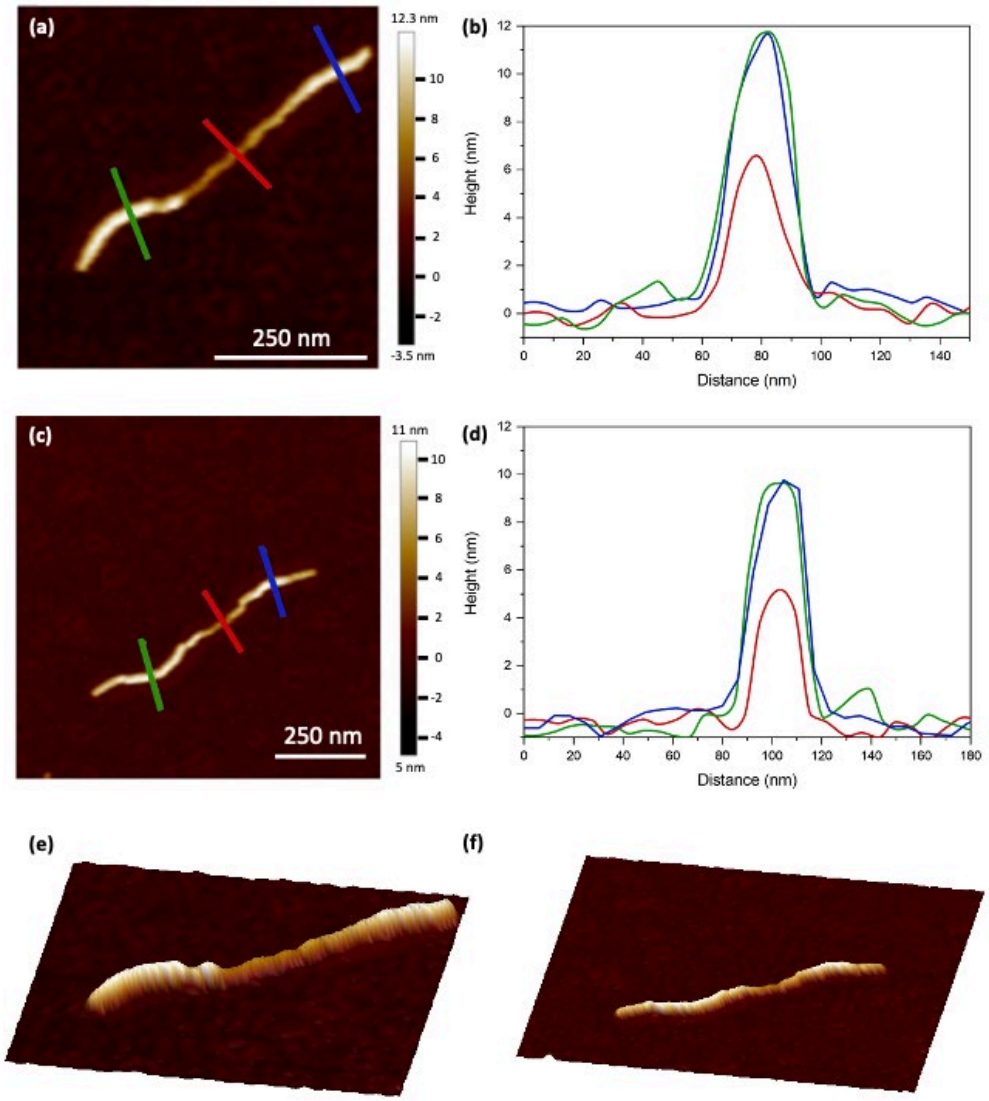

Figure S2. 17: (a), (c) AFM images of uniform B-A-B segmented nanofibers (A: L_n = 247 nm, L_w/L_n = 1.04; B-A-B: L_n = 739 nm, L_w/ L_n = 1.02) drop cast from THF:MeOH (1:9, v/v) on to mica. (b), (d) Height traces corresponding with AFM images in (a) and (c) respectively. (e), (f) 3D rendering of topological data.

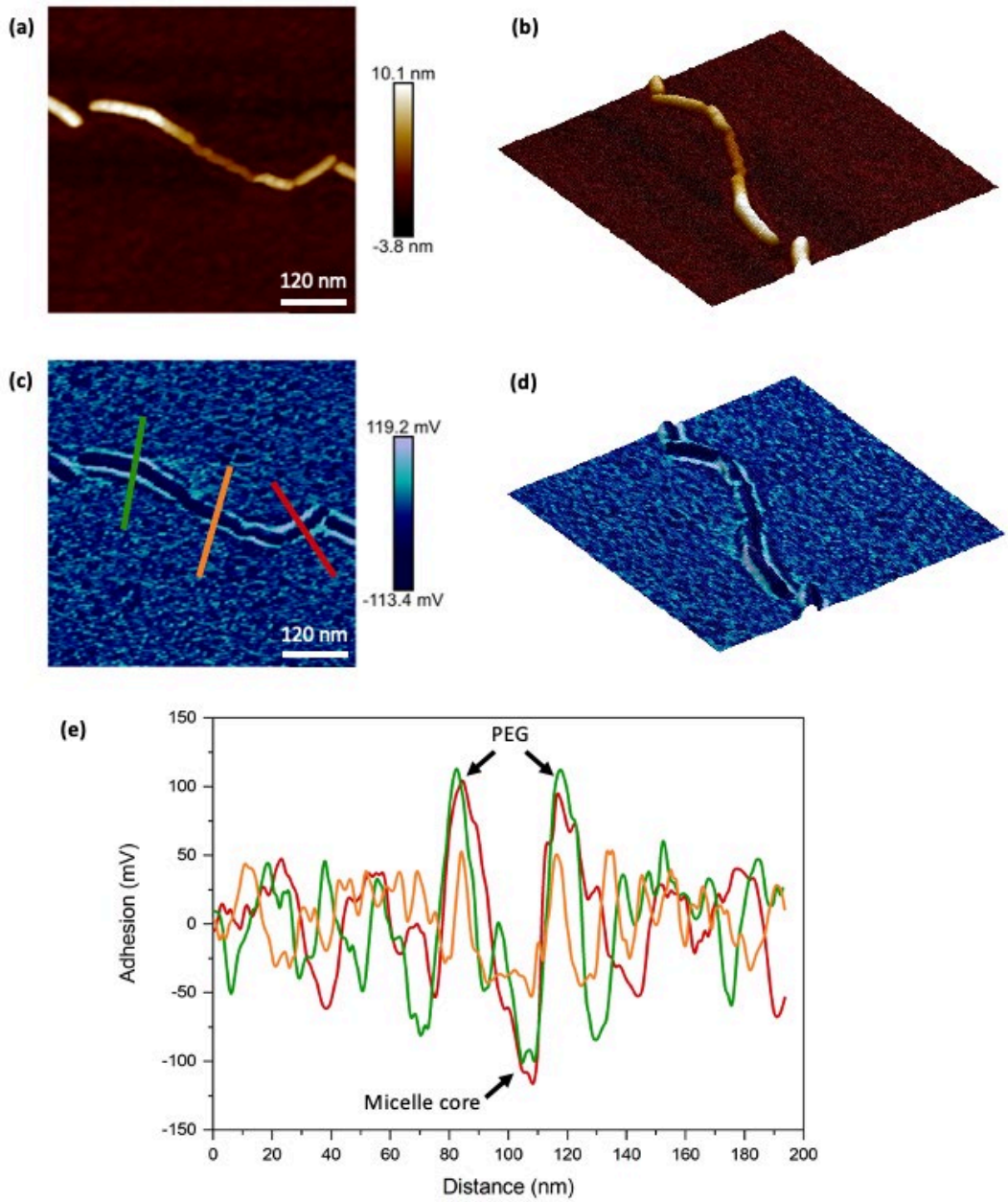

Figure S2. 18: (a) AFM height image and (c) adhesion profile image of uniform B-A-B segmented nanofibers (A: L_n = 124 nm, L_w/L_n = 1.05; B-A-B: L_n = 507 nm, L_w/L_n = 1.02) drop cast from THF:MeOH (1:9, v/v) on to mica. (b), (d) 3D rendering of topological data of (a) and (c) respectively. (e) Adhesion profile traces corresponding with AFM image (c).

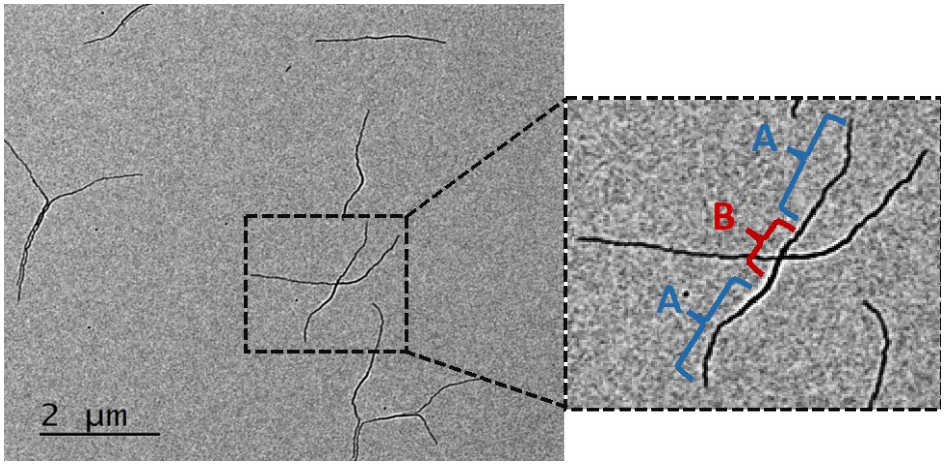

Figure S2. 19: TEM image of uniform A-B-A segmented nanofibers (B: L_n= 396 nm, L_w/ L_n= 1.05; A-B-A: L_n= 2785 nm, L_w/ L_n = 1.04) drop cast from THF:MeOH (1:9, v/v). Right inset highlights the different segments, A = $PDHF_{14}$-*b*-PEG_{227} and B = $PDHF_8$-*b*-$P3EHT_{25}$-*b*-PEG_{113}.

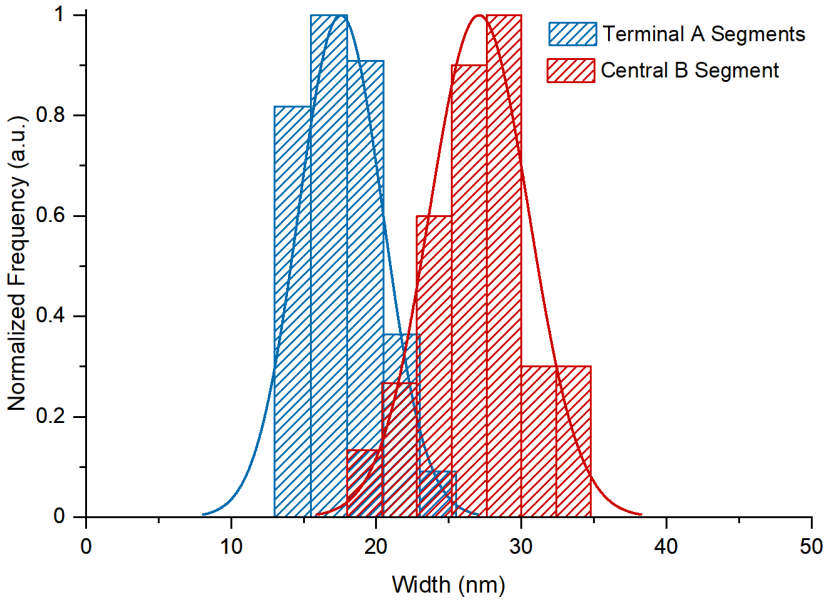

Figure S2. 20: Histograms representing fiber width distributions of A-B-A segmented nanofibers (B: L_n= 396 nm, L_w/ L_n= 1.05; A-B-A: L_n= 2785 nm, L_w/ L_n = 1.04) in THF:MeOH (1:9, v/v). For the terminal A segments (blue) W_n = 17 nm, W_n/W_w = 1.03 and for the central B segment (red) W_n = 27 nm, W_n/W_w = 1.02.

2.6. References

(1) Mazzio, K. A.; Luscombe, C. K. The Future of Organic Photovoltaics. *Chem. Soc. Rev.* **2015**, *44* (1), 78–90.

(2) Huang, J. S.; Goh, T.; Li, X.; Sfeir, M. Y.; Bielinski, E. A.; Tomasulo, S.; Lee, M. L.; Hazari, N.; Taylor, A. D. Polymer Bulk Heterojunction Solar Cells Employing Förster Resonance Energy Transfer. *Nat. Photonics* **2013**, *7* (6), 479–485.

(3) Fahlman, M.; Fabiano, S.; Gueskine, V.; Simon, D.; Berggren, M.; Crispin, X. Interfaces in Organic Electronics. *Nat. Rev. Mater.* **2019**, *4*, 627–650.

(4) Zhang, L.; Zhong, X.; Pavlica, E.; Li, S.; Klekachev, A.; Bratina, G.; Ebbesen, T. W.; Orgiu, E.; Samorì, P. A Nanomesh Scaffold for Supramolecular Nanowire Optoelectronic Devices. *Nat. Nanotechnol.* **2016**, *11* (10), 900–906.

(5) Zhang, W.; Jin, W.; Fukushima, T.; Saeki, A.; Seki, S.; Aida, T. Supramolecular Linear Heterojunction Composed of Graphite-like Semiconducting Nanotubular Segments. *Science.* **2011**, *334* (6054), 340–343.

(6) Würthner, F.; Chen, Z.; Hoeben, F. J. M.; Osswald, P.; You, C. C.; Jonkheijm, P.; Herrikhuyzen, J. V.; Schenning, A. P. H. J.; Van Der Schoot, P. P. A. M.; Meijer, E. W.; Beckers, E. H. A.; Meskers, S. C. J.; Janssen, R. A. J. Supramolecular P-n-Heterojunctions by Co-Self-Organization of Oligo(p-Phenylene Vinylene) and Perylene Bisimide Dyes. *J. Am. Chem. Soc.* **2004**, *126* (34), 10611–10618.

(7) López-Andarias, J.; Rodriguez, M. J.; Atienza, C.; López, J. L.; Mikie, T.; Casado, S.; Seki, S.; Carrascosa, J. L.; Martín, N. Highly Ordered n/p-Co-Assembled Materials with Remarkable Charge Mobilities. *J. Am. Chem. Soc.* **2015**, *137* (2), 893–897.

(8) Bu, L.; Pentzer, E.; Bokel, F. A.; Emrick, T.; Hayward, R. C. Growth of Polythiophene/Perylene Tetracarboxydiimide Donor/Acceptor Shish-Kebab Nanostructures by Coupled Crystal Modification. *ACS Nano* **2012**, *6* (12), 10924–10929.

(9) Ajayaghosh, A.; Vijayakumar, C.; Praveen, V. K.; Babu, S. S.; Varghese, R. Self-Location of Acceptors as "Isolated" or "Stacked" Energy Traps in a Supramolecular Donor Self-Assembly: A Strategy to Wavelength Tunable FRET Emission. *J. Am. Chem. Soc.* **2006**, *128* (22), 7174–7175.

(10) Ardona, H. A. M.; Draper, E. R.; Citossi, F.; Wallace, M.; Serpell, L. C.; Adams, D. J.; Tovar, J. D. Kinetically Controlled Coassembly of Multichromophoric Peptide Hydrogelators and the Impacts on Energy Transport. *J. Am. Chem. Soc.* **2017**, *139* (25), 8685–8692.

(11) Prasanthkumar, S.; Ghosh, S.; Nair, V. C.; Saeki, A.; Seki, S.; Ajayaghosh, A. Organic Donor-Acceptor Assemblies Form Coaxial p-n Heterojunctions with High Photoconductivity. *Angew. Chem. Int. Ed.* **2015**, *54* (3), 946–950.

(12) Hailes, R. L. N.; Oliver, A. M.; Gwyther, J.; Whittell, G. R.; Manners, I. Polyferrocenylsilanes: Synthesis, Properties, and Applications. *Chem. Soc. Rev.* **2016**, *45* (19), 5358–5407.

(13) Massey, J. A.; Temple, K.; Cao, L.; Rharbi, Y.; Raez, J.; Winnik, M. A.; Manners, I. Self-Assembly of Organometallic Block Copolymers: The Role of Crystallinity of the Core-Forming Polyferrocene Block in the Micellar Morphologies Formed by Poly(Ferrocenylsilane-b-Dimethylsiloxane) in n-Alkane Solvents. *J. Am. Chem. Soc.* **2000**, *122* (47), 11577–11584.

(14) Wang, X.; Guerin, G.; Wang, H.; Wang, Y.; Manners, I.; Winnik, M. A. Cylindrical Block

Copolymer Micelles and Co-Micelles of Controlled Length and Architecture. *Science.* **2007**, *317* (5838), 644–647.

(15) Gilroy, J. B.; Gädt, T.; Whittell, G. R.; Chabanne, L.; Mitchels, J. M.; Richardson, R. M.; Winnik, M. A.; Manners, I. Monodisperse Cylindrical Micelles by Crystallization-Driven Living Self-Assembly. *Nat. Chem.* **2010**, *2* (7), 566–570.

(16) Inam, M.; Cambridge, G.; Pitto-Barry, A.; Laker, Z. P. L.; Wilson, N. R.; Mathers, R. T.; Dove, A. P.; O'Reilly, R. K. 1D: Vs. 2D Shape Selectivity in the Crystallization-Driven Self-Assembly of Polylactide Block Copolymers. *Chem. Sci.* **2017**, *8* (6), 4223–4230.

(17) Arno, M. C.; Inam, M.; Coe, Z.; Cambridge, G.; Macdougall, L. J.; Keogh, R.; Dove, A. P.; O'Reilly, R. K. Precision Epitaxy for Aqueous 1D and 2D Poly(ϵ -Caprolactone) Assemblies. *J. Am. Chem. Soc.* **2017**, *139* (46), 16980–16985.

(18) Finnegan, J. R.; He, X.; Street, S. T. G.; Garcia-Hernandez, J. D.; Hayward, D. W.; Harniman, R. L.; Richardson, R. M.; Whittell, G. R.; Manners, I. Extending the Scope of "Living" Crystallization-Driven Self-Assembly: Well-Defined 1D Micelles and Block Comicelles from Crystallizable Polycarbonate Block Copolymers. *J. Am. Chem. Soc.* **2018**, *140* (49), 17127–17140.

(19) He, Y.; Eloi, J. C.; Harniman, R. L.; Richardson, R. M.; Whittell, G. R.; Mathers, R. T.; Dove, A. P.; O'Reilly, R. K.; Manners, I. Uniform Biodegradable Fiber-Like Micelles and Block Comicelles via "Living" Crystallization-Driven Self-Assembly of Poly(l -Lactide) Block Copolymers: The Importance of Reducing Unimer Self-Nucleation via Hydrogen Bond Disruption. *J. Am. Chem. Soc.* **2019**, *141* (48), 19088–19098.

(20) Schmelz, J.; Schedl, A. E.; Steinlein, C.; Manners, I.; Schmalz, H. Length Control and Block-Type Architectures in Worm-like Micelles with Polyethylene Cores. *J. Am. Chem. Soc.* **2012**, *134* (34), 14217–14225.

(21) Jin, B.; Sano, K.; Aya, S.; Ishida, Y.; Gianneschi, N.; Luo, Y.; Li, X. One-Pot Universal Initiation-Growth Methods from a Liquid Crystalline Block Copolymer. *Nat. Commun.* **2019**, *10* (1), 2397.

(22) Schöbel, J.; Karg, M.; Rosenbach, D.; Krauss, G.; Greiner, A.; Schmalz, H. Patchy Wormlike Micelles with Tailored Functionality by Crystallization-Driven Self-Assembly: A Versatile Platform for Mesostructured Hybrid Materials. *Macromolecules* **2016**, *49* (7), 2761–2771.

(23) Du, Z. X.; Xu, J. T.; Fan, Z. Q. Micellar Morphologies of Poly(ε-Caprolactone)-b-Poly(Ethylene Oxide) Block Copolymers in Water with a Crystalline Core. *Macromolecules* **2007**, *40* (21), 7633–7637.

(24) He, W. N.; Zhou, B.; Xu, J. T.; Du, B. Y.; Fan, Z. Q. Two Growth Modes of Semicrystalline Cylindrical Poly(ε-Caprolactone)-b -Poly(Ethylene Oxide) Micelles. *Macromolecules* **2012**, *45* (24), 9768–9778.

(25) He, X.; Hsiao, M. S.; Boott, C. E.; Harniman, R. L.; Nazemi, A.; Li, X.; Winnik, M. A.; Manners, I. Two-Dimensional Assemblies from Crystallizable Homopolymers with Charged Termini. *Nat. Mater.* **2017**, *16* (4), 481–488.

(26) Qiu, H.; Gao, Y.; Boott, C. E.; Gould, O. E. C.; Harniman, R. L.; Miles, M. J.; Webb, S. E. D.; Winnik, M. A.; Manners, I. Uniform Patchy and Hollow Rectangular Platelet Micelles from Crystallizable Polymer Blends. *Science.* **2016**, *352* (6286), 697–701.

(27) Qiu, H.; Hudson, Z. M.; Winnik, M. A.; Manners, I. Multidimensional Hierarchical Self-

Assembly of Amphiphilic Cylindrical Block Comicelles. *Science.* **2015**, *347* (6228), 1329–1332.

(28) Li, X.; Gao, Y.; Boott, C. E.; Hayward, D. W.; Harniman, R.; Whittell, G. R.; Richardson, R. M.; Winnik, M. A.; Manners, I. " Cross " Supermicelles via the Hierarchical Assembly of Amphiphilic Cylindrical Triblock Comicelles. *J. Am. Chem. Soc.* **2016**, *138* (12), 4087–4095.

(29) Robinson, M. E.; Lunn, D. J.; Nazemi, A.; Whittell, G. R.; De Cola, L.; Manners, I. Length Control of Supramolecular Polymeric Nanofibers Based on Stacked Planar Platinum (Ii) Complexes by Seeded-Growth. *Chem. Commun.* **2015**, *51* (88), 15921–15924.

(30) Ogi, S.; Sugiyasu, K.; Manna, S.; Samitsu, S.; Takeuchi, M. Living Supramolecular Polymerization Realized through a Biomimetic Approach. *Nat. Chem.* **2014**, *6* (3), 188–195.

(31) Ogi, S.; Stepanenko, V.; Sugiyasu, K.; Takeuchi, M.; Würthner, F. Mechanism of Self-Assembly Process and Seeded Supramolecular Polymerization of Perylene Bisimide Organogelator. *J. Am. Chem. Soc.* **2015**, *137* (9), 3300–3307.

(32) Aliprandi, A.; Mauro, M.; De Cola, L. Controlling and Imaging Biomimetic Self-Assembly. *Nat. Chem.* **2016**, *8* (1), 10–15.

(33) Matern, J.; Dorca, Y.; Sánchez, L.; Fernández, G. Revising Complex Supramolecular Polymerization under Kinetic and Thermodynamic Control. *Angew. Chem. Int. Ed.* **2019**, *58* (47), 16730–16740.

(34) Hartlieb, M.; Mansfield, E. D. H.; Perrier, S. A Guide to Supramolecular Polymerizations. *Polym. Chem.* **2020**, *11* (6), 1083–1110.

(35) Wehner, M.; Würthner, F. Supramolecular Polymerization through Kinetic Pathway Control and Living Chain Growth. *Nat. Rev. Chem.* **2020**, *4*, 38–53.

(36) Fukui, T.; Kawai, S.; Fujinuma, S.; Matsushita, Y.; Yasuda, T.; Sakurai, T.; Seki, S.; Takeuchi, M.; Sugiyasu, K. Control over Differentiation of a Metastable Supramolecular Assembly in One and Two Dimensions. *Nat. Chem.* **2017**, *9* (5), 493–499.

(37) Sarkar, A.; Sasmal, R.; Empereur-mot, C.; Bochicchio, D.; Kompella, S. V. K.; Sharma, K.; Dhiman, S.; Sundaram, B.; Agasti, S. S.; Pavan, G. M.; George, S. J. Self-Sorted, Random, and Block Supramolecular Copolymers via Sequence Controlled, Multicomponent Self-Assembly. *J. Am. Chem. Soc.* **2020**, *142* (16), 7606–7617.

(38) Patra, S. K.; Ahmed, R.; Whittell, G. R.; Lunn, D. J.; Dunphy, E. L.; Winnik, M. A.; Manners, I. Cylindrical Micelles of Controlled Length with a π-Conjugated Polythiophene Core via Crystallization-Driven Self-Assembly. *J. Am. Chem. Soc.* **2011**, *133* (23), 8842–8845.

(39) Gwyther, J.; Gilroy, J. B.; Rupar, P. A.; Lunn, D. J.; Kynaston, E.; Patra, S. K.; Whittell, G. R.; Winnik, M. A.; Manners, I. Dimensional Control of Block Copolymer Nanofibers with a π-Conjugated Core: Crystallization-Driven Solution Self-Assembly of Amphiphilic Poly(3-Hexylthiophene)-b-Poly(2-Vinylpyridine). *Chem. - A Eur. J.* **2013**, *19* (28), 9186–9197.

(40) Qian, J.; Li, X.; Lunn, D. J.; Gwyther, J.; Hudson, Z. M.; Kynaston, E.; Rupar, P. A.; Winnik, M. A.; Manners, I. Uniform High Aspect Ratio Fiber-like Micelles and Block Co-Micelles with a Crystalline π - Conjugated Polythiophene Core by Self-Seeding. *J. Am. Chem. Soc.* **2014**, *136* (11), 4121–4124.

(41) Shin, S.; Menk, F.; Kim, Y.; Lim, J.; Char, K.; Zentel, R.; Choi, T. L. Living Light-Induced Crystallization-Driven Self-Assembly for Rapid Preparation of Semiconducting Nanofibers.

J. Am. Chem. Soc. **2018**, *140* (19), 6088–6094.

(42) Han, L.; Wang, M.; Jia, X.; Chen, W.; Qian, H.; He, F. Uniform Two-Dimensional Square Assemblies from Conjugated Block Copolymers Driven by π-π Interactions with Controllable Sizes. *Nat. Commun.* **2018**, *9*, 865.

(43) Tao, D.; Feng, C.; Cui, Y.; Yang, X.; Manners, I.; Winnik, M. A.; Huang, X. Monodisperse Fiber-like Micelles of Controlled Length and Composition with an Oligo(p-Phenylenevinylene) Core via "Living" Crystallization-Driven Self-Assembly. *J. Am. Chem. Soc.* **2017**, *139* (21), 7136–7139.

(44) Tao, D.; Wang, Z.; Huang, X.; Tian, M.; Lu, G.; Manners, I.; Winnik, M. A.; Feng, C. Continuous and Segmented Semiconducting Fiber-like Nanostructures with Spatially Selective Functionalization by Living Crystallization-Driven Self-Assembly. *Angew. Chem. Int. Ed.* **2020**, *59* (21), 8232–8239.

(45) Yang, S.; Kang, S. Y.; Choi, T. L. Morphologically Tunable Square and Rectangular Nanosheets of a Simple Conjugated Homopolymer by Changing Solvents. *J. Am. Chem. Soc.* **2019**, *141* (48), 19138–19143.

(46) Kynaston, E. L.; Nazemi, A.; MacFarlane, L. R.; Whittell, G. R.; Faul, C. F. J.; Manners, I. Uniform Polyselenophene Block Copolymer Fiberlike Micelles and Block Co-Micelles via Living Crystallization-Driven Self-Assembly. *Macromolecules* **2018**, *51* (3), 1002–1010.

(47) Hicks, G. E. J.; Jarrett-Wilkins, C. N.; Panchuk, J. R.; Manion, J. G.; Seferos, D. S. Oxidation Promoted Self-Assembly of π-Conjugated Polymers. *Chem. Sci.* **2020**. https://doi.org/10.1039/d0sc00806k.

(48) Li, X.; Wolanin, P. J.; Macfarlane, L. R.; Harniman, R. L.; Qian, J.; Gould, O. E. C.; Dane, T. G.; Rudin, J.; Cryan, M. J.; Schmaltz, T.; Frauenrath, H.; Winnik, M. A.; Faul, C. F. J.; Manners, I. Uniform Electroactive Fibre-like Micelle Nanowires for Organic Electronics. *Nat. Commun.* **2017**, *8*, 15909.

(49) Jin, X.; Price, M. B.; Finnegan, J. R.; Boott, C. E.; Richter, J. M.; Rao, A.; Menke, M. S.; Friend, R. H.; Whittell, G. R.; Manners, I. Long-Range Exciton Transport in Conjugated Polymer Nanofibers Prepared by Seeded Growth. *Science.* **2018**, *360*, 897–900.

(50) Le, T. P.; Smith, B. H.; Lee, Y.; Litofsky, J. H.; Aplan, M. P.; Kuei, B.; Zhu, C.; Wang, C.; Hexemer, A.; Gomez, E. D. Enhancing Optoelectronic Properties of Conjugated Block Copolymers through Crystallization of Both Blocks. *Macromolecules* **2020**, *53* (6), 1967–1976.

(51) Loewe, R. S.; Khersonsky, S. M.; McCullough, R. D. A Simple Method to Prepare Head-to-Tail Coupled, Regioregular Poly(3-alkylthiophenes) Using Grignard Metathesis. *Adv. Mater.* **1999**, *11* (3), 250–253.

(52) Loewe, R. S.; Ewbank, P. C.; Liu, J.; Zhai, L.; McCullough, R. D. Regioregular, Head-to-Tail Coupled Poly(3-Alkylthiophenes) Made Easy by the GRIM Method: Investigation of the Reaction and the Origin of Regioselectivity. *Macromolecules* **2001**, *34* (13), 4324–4333.

(53) Ho, V.; Boudouris, B. W.; Segalman, R. A. Tuning Polythiophene Crystallization through Systematic Side Chain Functionalization. *Macromolecules* **2010**, *43* (19), 7895–7899.

(54) Ho, V.; Boudouris, B. W.; McCulloch, B. L.; Shuttle, C. G.; Burkhardt, M.; Chabinyc, M. L.; Segalman, R. A. Poly(3-Alkylthiophene) Diblock Copolymers with Ordered Microstructures and Continuous Semiconducting Pathways. *J. Am. Chem. Soc.* **2011**, *133* (24), 9270–9273.

(55) Deng, Y.; Yuan, W.; Jia, Z.; Liu, G. H- and J-Aggregation of Fluorene-Based Chromophores. *J. Phys. Chem. B* **2014**, *118* (49), 14536–14545.

(56) Spano, F. C.; Silva, C. H- and J-Aggregate Behavior in Polymeric Semiconductors. *Annu. Rev. Phys. Chem.* **2014**, *65* (1), 477–500.

(57) Hestand, N. J.; Spano, F. C. Molecular Aggregate Photophysics beyond the Kasha Model: Novel Design Principles for Organic Materials. *Acc. Chem. Res.* **2017**, *50* (2), 341–350.

(58) Agbolaghi, S.; Zenoozi, S.; Hosseini, Z.; Abbasi, F. Scrolled/Flat Crystalline Structures of Poly(3-Hexylthiophene) and Poly(Ethylene Glycol) Block Copolymers Subsuming Unseeded Half-Ring-Like and Seeded Cubic, Epitaxial, and Fibrillar Crystals. *Macromolecules* **2016**, *49* (24), 9531–9541.

(59) Liu, J.; Arif, M.; Zou, J.; Khondaker, S. I.; Zhai, L. Controlling Poly(3-Hexylthiophene) Crystal Dimension: Nanowhiskers and Nanoribbons. *Macromolecules* **2009**, *42* (24), 9390–9393.

(60) Davidson, E. C.; Segalman, R. A. Thermal Control of Confined Crystallization within P3EHT Block Copolymer Microdomains. *Macromolecules* **2017**, *50* (20), 8097–8105.

(61) Tashiro, K.; Ono, K.; Minagawa, Y.; Kobayashi, M.; Kawai, T.; Yoshino, K. Structure and Thermochromic Solid-state Phase Transition of Poly (3-alkylthiophene). *J. Polym. Sci. Part B Polym. Phys.* **1991**, *29* (10), 1223–1233.

(62) McCulloch, B.; Ho, V.; Hoarfrost, M.; Stanley, C.; Do, C.; Heller, W. T.; Segalman, R. A. Polymer Chain Shape of Poly(3-Alkylthiophenes) in Solution Using Small-Angle Neutron Scattering. *Macromolecules* **2013**, *46* (5), 1899–1907.

(63) Fei, Z.; Boufflet, P.; Wood, S.; Wade, J.; Moriarty, J.; Gann, E.; Ratcliff, E. L.; McNeill, C. R.; Sirringhaus, H.; Kim, J. S.; Heeney, M. Influence of Backbone Fluorination in Regioregular Poly(3-Alkyl-4-Fluoro)Thiophenes. *J. Am. Chem. Soc.* **2015**, *137* (21), 6866–6879.

(64) Yu, L.; Davidson, E.; Sharma, A.; Andersson, M. R.; Segalman, R.; Müller, C. Isothermal Crystallization Kinetics and Time-Temperature-Transformation of the Conjugated Polymer: Poly(3-(2′-Ethyl)Hexylthiophene). *Chem. Mater.* **2017**, *29* (13), 5654–5662.

(65) Cook, S.; Furube, A.; Katoh, R. Analysis of the Excited States of Regioregular Polythiophene P3HT. *Energy Environ. Sci.* **2008**, *1* (2), 294–299.

(66) Li, Y.; Vamvounis, G.; Holdcroft, S. Tuning Optical Properties and Enhancing Solid-State Emission of Poly(Thiophene)s by Molecular Control: A Postfunctionalization Approach. *Macromolecules* **2002**, *35* (18), 6900–6906.

(67) Perepichka, I. F.; Perepichka, D. F.; Meng, H.; Wudl, F. Light-Emitting Polythiophenes. *Adv. Mater.* **2005**, *17* (19), 2281–2305.

(68) Davidson, E. C.; Beckingham, B. S.; Ho, V.; Segalman, R. A. Confined Crystallization in Lamellae Forming Poly(3-(2′-Ethyl)Hexylthiophene) (P3EHT) Block Copolymers. *J. Polym. Sci. Part B Polym. Phys.* **2016**, *54* (2), 205–215.

(69) Fukuda, M.; Sawada, K.; Yoshino, K. Synthesis of Fusible and Soluble Conducting Polyfluorene Derivatives and Their Characteristics. *J. Polym. Sci. Part A Polym. Chem.* **1993**, *31* (10), 2465–2471.

(70) Klaerner, G.; Miller, R. D. Polyfluorene Derivatives: Effective Conjugation Lengths from Well-Defined Oligomers. *Macromolecules* **1998**, *31* (6), 2007–2009.

(71) Yang, C. H.; Bhongale, C. J.; Chou, C. H.; Yang, S. H.; Lo, C. N.; Chen, T. M.; Hsu, C. S. Synthesis and Light Emitting Properties of Sulfide-Containing Polyfluorenes and Their Nanocomposites with CdSe Nanocrystals: A Simple Process to Suppress Keto-Defect. *Polymer.* **2007**, *48* (1), 116–128.

(72) Burkhart, B.; Khlyabich, P. P.; Thompson, B. C. Influence of the Ethylhexyl Side-Chain Content on the Open-Circuit Voltage in Rr-Poly(3-Hexylthiophene- Co -3-(2-Ethylhexyl)Thiophene) Copolymers. *Macromolecules* **2012**, *45* (9), 3740–3748.

(73) Peterson, J. J.; Werre. M.; Simon, Y. C.; Coughlin, E. B.; Carter, K. R. Carborane-Containing Polyfluorene: *o*-Carborane in the Main Chain. *Macromolecules*. **2009**, *42* (22), 8594-8598

(74) Deng, J.; Luo, Y.; Zhang, L. PEGylated polyamidoamine dendron-assisted encapsulation of plasmid DNA into *in situ* forming supramolecular hydrogel. *Soft Matter*. **2011**, *7*, 5944-5947

Chapter 3

Efficient Energy Funneling in Spatially Tailored Segmented Conjugated Block Copolymer Nanofiber – Quantum Dot or Rod Conjugates

This chapter has been adapted from:

Yifan Zhang,† Huda Shaikh,† Alexander Sneyd,† Jia Tian, James Xiao, Arthur Blackburn, Akshay Rao, Richard H. Friend, and Ian Manners, *J. Am. Chem. Soc*, Submission ID: ja-2021-01571b

† Equal contribution

Contributions:

Synthesis of polymers was conducted by Huda Shaikh. Synthesis of quantum nanostructures was conducted by Dr. Yifan Zhang and Dr. Jia Tian (University of Victoria). Self-assembly and related characterization were conducted jointly by Huda Shaikh and Dr. Yifan Zhang. Photophysical measurements were conducted by Dr. Yifan Zhang and Huda Shaikh. Transient absorption spectroscopy measurements were conducted by Alexander Sneyd (University of Cambridge). Research was conducted at the University of Bristol, University of Victoria and University of Cambridge.

3.1. Abstract

Hybrid systems composed of conjugated polymers and inorganic semiconductor nanocrystals such as quantum dots (QDs) and nanorods (QRs) represent highly desirable multifunctional materials for applications from energy harvesting to light emission and sensing. Herein, we describe energy transfer studies between low dispersity segmented conjugated polymer micellar nanofibers integrated with quantum dots that are spatially confined to discrete regions in the hybrid assembly *via* non-covalent interactions. The nanofibers were prepared from diblock copolymers with a crystallizable poly(di-*n*-hexylfluorene) (PDHF) core-forming block and different corona-forming blocks using the seeded-growth 'living' crystallization-driven self-assembly method. The highly ordered crystalline PDHF core in the fibers functions as a donor and permits long range exciton transport (> 200 nm). Energy can therefore be funneled through the fiber core to QDs and QRs that function as acceptor materials and which are non-covalently bound to spatially-defined coronal regions of poly(2-vinylpyridine) (P2VP) or quaternized polyfluorene (QPF). Using steady-state and time-resolved spectroscopy, we demonstrate that efficient energy transfer (over 70%) occurs from the crystalline PDHF donor core to the acceptor CdSe QRs attached at the fiber termini. The emission of the PDHF donor in the hybrid conjugate was extensively quenched (by 84 %), and a subsequent 4-fold enhancement of the QR emission in solution was observed. These results indicate that the conjugates prepared in this work show promise for potential applications in fields such as light-emitting diodes, photovoltaics, chemical sensors, and photocatalysis.

3.2. Introduction

Hybrid multifunctional materials which take advantage of the unique but complementary properties of their components are of growing interest for the development of next generation energy storage or conversion materials.[1–5] For example, resonant energy coupling between π-conjugated polymers and quantum dots (QDs) and nanorods (QRs), derived from inorganic semiconductors, enables the construction of efficient photonic devices.[6–11] These hybrid materials allow for the integration of the narrow absorption and large optical oscillator strengths of conjugated polymers[12] to be combined with the high quantum yield and wavelength-tunable emission of quantum nanostructures in one material.[13] In such hybrid nanowires, π-conjugated polymeric materials may act as efficient antenna delivering absorbed energy to nearby inorganic quantum nanostructures. This can enhance photoluminescence emission or can be used for other functions like chemical sensing or photocatalysis.[14–17] A key challenge for the creation of efficient π-conjugated polymer-based hybrid systems is that, upon excitation, the diffusion of Frenkel excitons[18] is normally limited to a short distance.[19,20] The majority of photoinduced excitons are therefore quenched before reaching the dissociation interface with the acceptor material.

Over the past decade the seeded growth method termed 'living' crystallization-driven self-assembly (CDSA) has been shown to allow the facile preparation of low dispersity, size-tunable 1D[21–30] and 2D[31–35] nanostructures with crystalline cores from polymeric or π-stacking[36–38]molecular amphiphiles. Moreover, sequential addition of different amphiphiles to the seeds using the living CDSA approach also enables the formation of segmented micellar nanoparticles with different core or coronal chemistries, and thereby spatial-selective functionalization.[39,40] Recently, we have used this approach to fabricate low dispersity conjugated block copolymer (BCP) nanofibers with a donor poly(di-*n*-hexylfluorene) (PDHF) core and spatially segmented acceptor coronal regions that revealed the existence of long-range exciton transport along the fiber core (> 200 nm).[41] This is believed to arise from the epitaxial nature of the 'living' CDSA growth process which leads to a highly ordered crystalline core with a uniform energetic landscape.[42,43] The creation of emissive coaxial nanowires with an inner donor PDHF core and an outer acceptor core and the attachment of QDs to specific

coronal regions of segmented π-conjugated nanofibers also been described.[44,45] Optimization of the π-conjugated polymer nanofiber length to match the maximum exciton diffusion length along the fiber core was expected to make the most efficient use of the light-absorbing antenna effect that could significantly enhance the optical performance of a hybrid system. In this Chapter we report studies of the Förster resonance energy transfer (FRET) in conjugates comprised of tailored segmented PDHF nanofibers and CdSe quantum nanostructures such as QDs and QRs.

3.3. Results and Discussion

Segmented nanofibers were prepared *via* the 'living' CDSA method and consist of a continuous crystalline PDHF core with spatially distinct coronal segments (Figure 3. 1a, c). Functionalized coronas, poly(2-vinylpyridine) (P2VP) or quaternized polyfluorene (QPF), allowed for the decoration with mercaptoundecanoic acid coated QDs (MUA-QDs) and 8-mercaptooctanoic acid coated QRs (MOA-QRs) *via* non-covalent interactions (Figure 3. 1b). Spatial-selective decoration of the segmented PDHF nanofibers with QDs or QRs was realized by the use of either hydrogen bonding (MUA-QDs and P2VP) or electrostatic interactions (MOA-QRs and QPF) between the grafted corona and ligand coating on the surface of quantum nanostructures.[46,47] Moreover, the density of the attached QDs and QRs was tailorable by varying the mass equivalents and tuning the length of the segments with the functionalized (P2VP or QPF) grafted coronas

3.3.1. Preparation of Segmented Nanofibers

Block copolymers (BCPs) containing a crystallizable PDHF block and various corona-forming blocks, including polyethylene glycol (PEG), P2VP or QPF, were synthesized. Alkyne-capped PDHF homopolymer and PDHF-*b*-QPF diblock copolymer were prepared *via* Grignard Metathesis polymerization (GRIM) (Scheme S3. 1) and P2VP was prepared *via* reversible-addition fragmentation-transfer polymerization (RAFT). The PDHF core-forming block was coupled with the azido-functionalized P2VP and PEG corona-forming blocks by employing copper-catalyzed azide-alkyne cycloaddition click reactions (CuAAc). For a detailed account of the synthesis and characterization of the polymers, see Supporting information (Table S3. 1 and Figure S3. 1-8). CdSe quantum nanostructures with different surface functionalities including MUA-QDs (diameter = 4 ± 0.5 nm) and MOA-QRs (length = 12 ± 2 nm, and width = 4 ± 1 nm) were synthesized according to literature procedures (Figure 3. 1b, Figure S3. 9-10).[48,49]

Segmented nanofibers with a continuous PDHF core and PEG corona located in the central block and either a P2VP or QPF corona located on the terminal regions were prepared *via* 'living' CDSA (Figure 3. 1c). Low-dispersity

PDHF-*b*-PEG nanofibers (Material A, Figure 3. 1a) of different lengths were prepared by rapid addition of PDHF-*b*-PEG unimers dissolved in THF to seed solutions in THF:MeOH (1:1, v/v).[41] Different unimer-to-seed mass ratios were employed using this seeded growth protocol to prepare a range of low dispersity samples with fiber lengths from ca. 100 nm up to ca. 900 nm (Figure S3. 11 and Table S3. 2). Additionally, different samples of low dispersity PDHF-*b*-P2VP nanofibers (Material B, Figure 3. 1a) of length ca. 100 nm to 700 nm were prepared using an identical protocol (Figure S3. 13 and Table S3. 3) and a clear linear dependence of the unimer-to seed ratio on the number average length (L_n) was observed (Figure S3. 12). The longer fibers were used to create segmented block nanofibers and hybrid materials with QDs and QRs that were used for detailed structural characterization. The shorter fibers were used to create segmented fibers of length up to 200 nm for in depth photophysical measurements based on the comparable, previously determined[41] exciton diffusion lengths for the crystalline PDHF core.

B-A-B segmented triblock nanofibers with a central PDHF-*b*-PEG segment (A) and terminal PDHF-*b*-P2VP (B) segments were prepared by the addition of PDHF-*b*-P2VP unimer to PDHF-*b*-PEG seed solutions in THF:MeOH (1:1, v/v) (Figure 3. 1d, Figure S3. 15 and Table S3. 4). A linear dependence of the unimer-to seed ratio on the L_n (Figure S3. 14) was observed. C-A-C segmented triblock nanofibers with a central PDHF-*b*-PEG segment (A) and terminal PDHF-*b*-QPF (C) segments were prepared by an analogous approach involving addition of PDHF-*b*-QPF unimer to PDHF-*b*-PEG seeds solutions in THF:EtOH (1:1, v/v) (Figure S3. 16 and Table S3. 5). Furthermore, C-B-A-B-C pentablock segmented nanofibers were prepared *via* the addition of addition of PDHF-*b*-QPF unimers to B-A-B triblock segmented nanofiber solutions in THF:EtOH (1:1, v/v) (Figure 3. 1e, Figure S3. 17 and Table S3. 6).

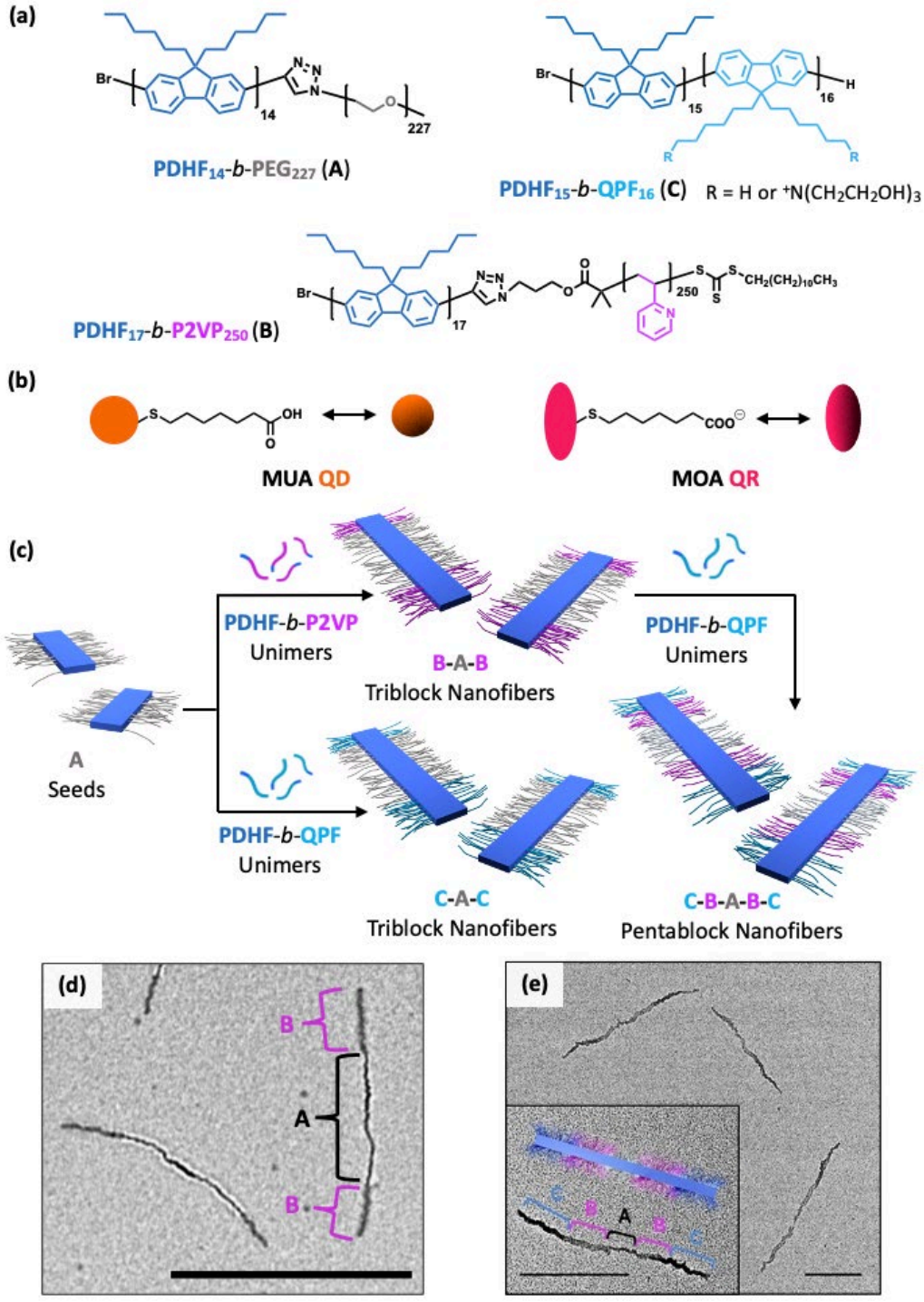

Figure 3. 1: (a) Structures of $PDHF_{14}$-*b*-PEG_{227} (A), $PDHF_{17}$-*b*-PEG_{250} (B) and $PDHF_{15}$-*b*-QPF_{16} (C). (b) Schematic illustration of ligand coated CdSe quantum nanostructures. (c) Schematic illustration of the preparation of length controlled triblock nanofibers and pentablock nanofibers via seeded growth from A nanofibers and triblock nanofiber seeds, respectively. Bright-field TEM images of typical (d) triblock B-A-B nanofibers (A: L_n = 497 nm, L_w/L_n = 1.05; B-A-B: L_n = 823 nm, L_w/L_n = 1.06). and (e) segmented pentablock C-B-A-B-C nanofibers (B-A-B seeds: L_n = 532 nm, L_w/L_n = 1.06; C-B-A-B-C: L_n = 1021 nm, L_w/L_n = 1.06). L_w = weight average length. Scale bars: (d) 1 μm and (e) 500 nm.

3.3.2. Preparation of Segmented Nanofibers with Spatial-Selective QD/QR Attachment

Next, spatial-selective decoration of the triblock nanofibers with QDs and rods was attempted. Segmented nanofibers were first dialyzed against a water/ethanol (H_2O:EtOH, 1:1 v/v) mixture to prevent precipitation of the quantum nanostructures in THF:MeOH/EtOH mixtures. Then a small aliquot of the MUA-QD or MOA-QR solutions in H_2O was rapidly added to the segmented nanofibers in H_2O:EtOH (1:1 v/v). QDs with MUA ligands interact with P2VP coronas *via* hydrogen-bonding and the negatively charged QRs with MOA ligands interact with the positively charged QPF coronas (Figure 3. 2a, b). From the bright-field, low-angle annular dark-field (LAADF) STEM images and energy dispersive X-Ray Spectroscopy (SEM-EDS) analysis, QDs attachment to PDHF-*b*-P2VP nanofibers (Figure 3. 2c, Figure S3. 18-19) was visible and the QDs were also shown to be selectively attached to the PDHF-*b*-P2VP segment in the triblock B-A-B nanofibers (Figure 3. 2d and Figure S3. 20). The selective attachment of MOA-QRs to C-A-C nanofibers was also confirmed by bright-field TEM, LAADF STEM images, and by SEM-EDS analysis (Figure 3. 2e and Figure S3. 21). The entire triblock C-A-C nanofiber was visible by the elemental mapping of carbon (Figure 3. 2j). Elemental maps of selenium (Figure 3. 2h) and cadmium (Figure 3. 2i) show that Se and Cd are clearly present at the nanofiber termini where the CdSe QRs is shown to be attached (Figure 3. 2g). Characterization of the spatial-selective attachment of QRs and QDs on C-B-A-B-C nanofibers by STEM and SEM-EDS (Figure 3. 2f and Figure S3. 22-25) showed the QDs selectively attached to B blocks while QRs are selectively attached to C blocks. In addition, different volumes of a 1 mg mL^{-1} solution of MOA-QRs in H_2O were rapidly added under stirring (600 rpm) to C-A-C nanofibers in H_2O:EtOH (1:1, v/v, 0.1 mg mL^{-1}). After ageing for 4 h, hybrid triblock segmented nanofibers with different quantities of QRs attached were obtained (Figure S3. 26).

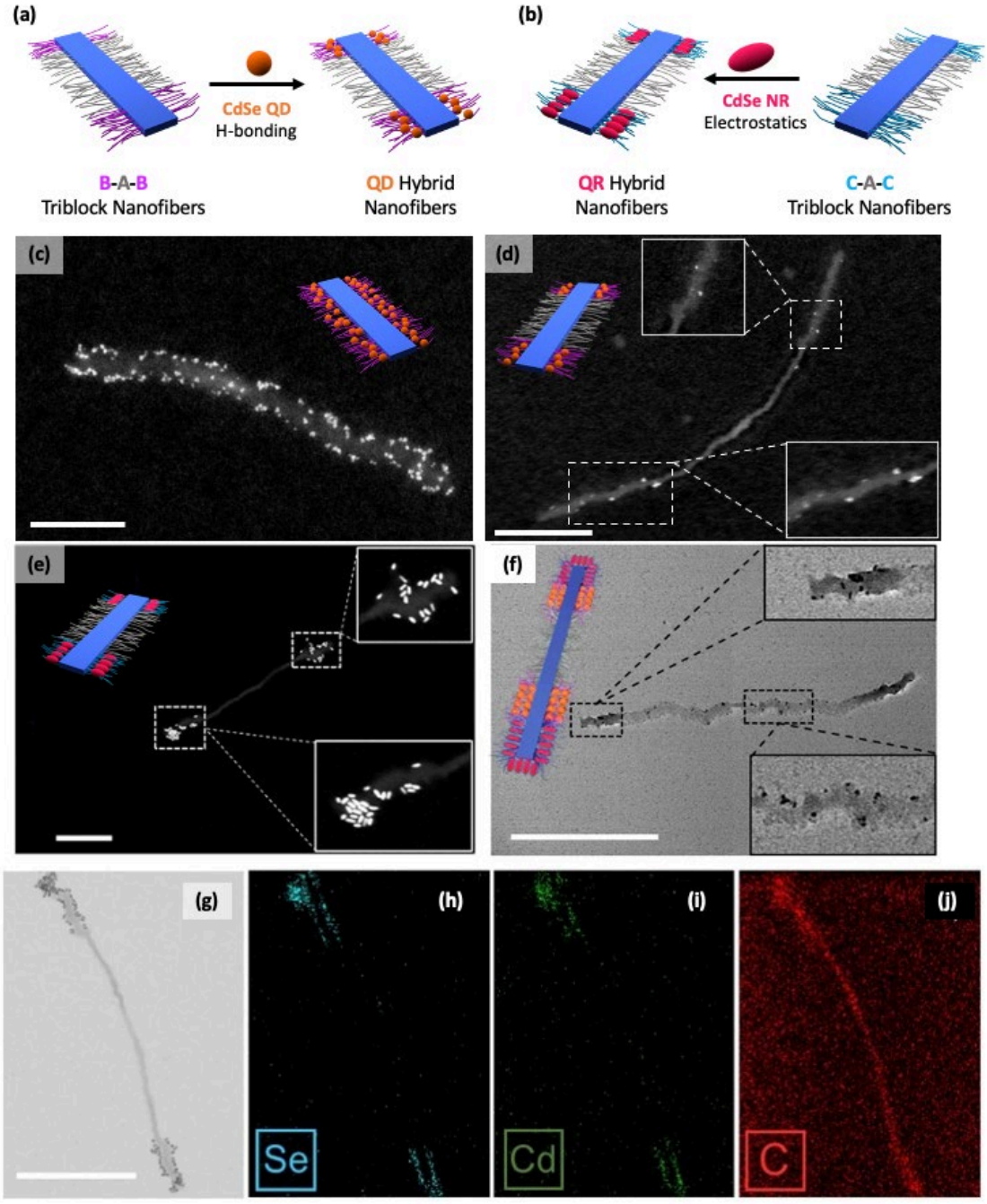

Figure 3. 2: (a) Schematic illustration of the preparation of hybrid B-A-B segmented nanofibers with spatial-selective attachment of CdSe QDs and (b) hybrid C-A-C segmented nanofibers with spatial-selective attachment of CdSe QRs. (b) STEM image of CdSe QDs attached to $PDHF_{17}$-*b*-$P2VP_{250}$ nanofibers (L_n = 377 nm, L_w/L_n = 1.10). Scale bar: 100 nm. (d) STEM image of CdSe QDs attached to B segments in B-A-B triblock nanofibers (A: L_n = 497 nm, L_w/L_n = 1.05; B-A-B: L_n = 823 nm, L_w/L_n = 1.06). Scale bar = 200 nm. (e) STEM image of CdSe QRs attached to C segments in C-A-C nanofibers (A: L_n = 330 nm, L_w/L_n = 1.06; C-A-C: L_n = 510 nm, L_w/L_n = 1.06). Scale bar: 100 nm. (f) STEM image of CdSe QDs and QRs selectively attached to the C-B-A-B-C pentablock nanofibers (A: L_n = 109 nm, L_w/L_n = 1.06; B-A-B: L_n = 793 nm, L_w/L_n = 1.06, C-B-A-B-C: L_n = 875 nm, L_w/L_n = 1.07). Scale bar = 500 nm. (g) STEM image and SEM-EDS mapping images of the elementary distribution of (h) Selenium (Se), (i) Cadmium (Cd), and (j) Carbon (C) of hybrid C-A-C nanofibers (A: L_n = 330 nm, L_w/L_n = 1.06; C-A-C: L_n = 510 nm, L_w/L_n = 1.06). Scale bar = 200 nm.

3.3.3. Photophysical Studies of Segmented Nanofibers-QD and QR Conjugates

Upon selective excitation of the crystalline PDHF-donor core, we postulate that the absorbed energy will be able to travel through the fiber core and transfer to the quantum nanostructure acceptors spatial-selective attached on the fiber termini. This occurs *via* FRET and should result in quenching of the donor PDHF emission and subsequent enhancement of the acceptor QR emission. The preparation of hybrid segmented nanofibers opens up the possibility to construct efficient photonic conjugates that facilitate energy transfer from the donor crystalline PDHF fiber core to spatial-attached acceptor CdSe QDs and QRs (Figure 3. 3a). Prior to an investigation of the energy funneling between the segmented nanofibers and QDs and QRs, the optical properties of the two separate subsystems were studied. From the absorption spectra, a broad peak at 390 nm was observed for the PDHF-*b*-PEG unimers in THF but for fibers in THF:MeOH (1:1, v/v) a slightly red-shifted peak at 400 nm and a slight blue-shifted peak at 381 nm were observed indicative of mixed H- and J- like aggregate characteristics (Figure 3. 3b).[12,50] The appearance of well-resolved vibronic peaks is indicative of high crystalline order in the PDHF core. Aggregation of the PDHF block was also confirmed from the fluorescence spectra, a slightly red-shifted emission was observed in the spectrum of the PDHF-*b*-PEG nanofibers compared to PDHF-*b*-PEG unimer solution. More defined vibronic coupling and a higher ratio of the $I_{0\text{-}1}$ (λ_{max} = 442 and 437 nm) to $I_{0\text{-}0}$ (λ_{max} = 412 and 417 nm) vibronic band in the PL spectra of the PDHF-*b*-PEG nanofibers compared to that of the unimers indicated a decreased Huang-Rhys parameter, thereby assigned to a smaller configurational relaxation upon excitation.[12] The absorption of the acceptor QRs solution and the emission of the donor PDHF-based nanofibers show significant spectral overlap, and gave a calculated Förster transfer radius of 4.9 nm (for details, see supporting information). This value would be expected to facilitate FRET from the crystalline core of the PDHF nanofiber to the spatial-selective attached CdSe QRs (Figure 3. 3c).

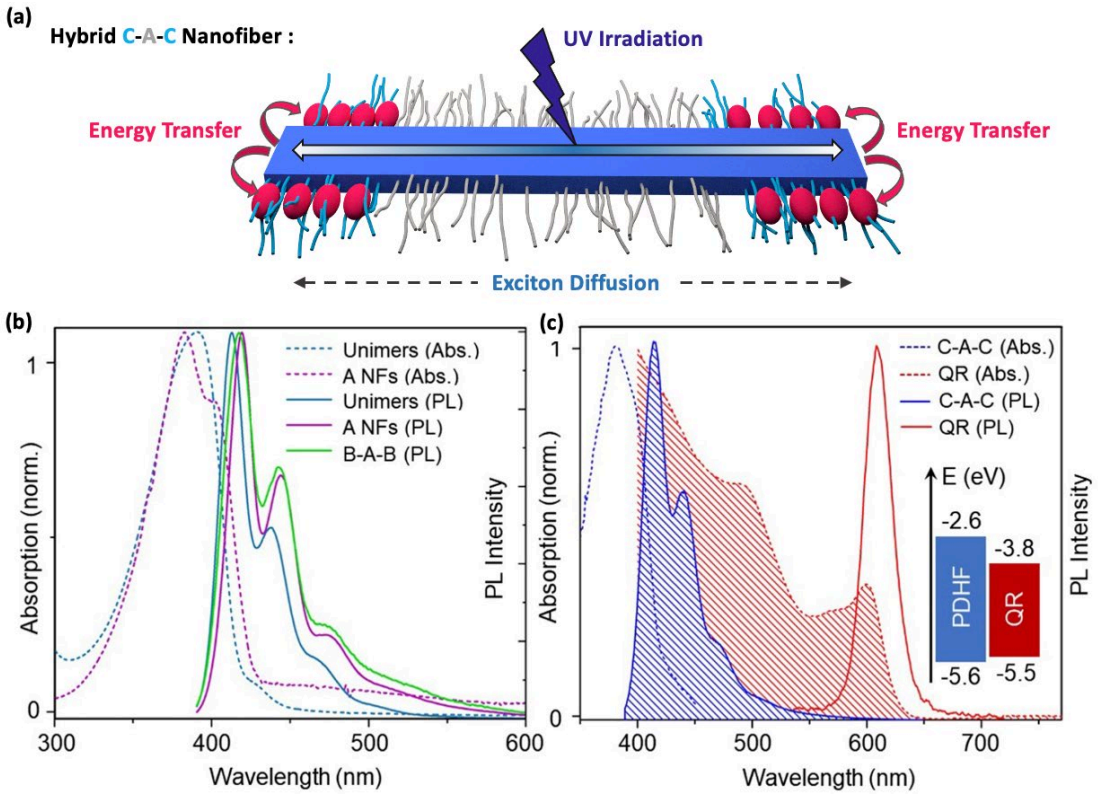

Figure 3. 3: (a) Schematic illustration of the exciton diffusion pathway in a hybrid C-A-C nanofiber upon excitation (λ_{exc} = 385 nm). (b) Normalized UV-vis absorption (*dashed traces*) and photoluminescence (PL) emission spectra (*solid traces*) of unimers in THF (*blue traces*), A (PDHF-*b*-PEG) nanofibers in H_2O:MeOH (1:1, v/v) (*purple traces*), and B-A-B nanofibers (A: L_n = 97 nm, L_w/L_n = 1.05; B-A-B: L_n = 191 nm, L_w/L_n = 1.07) in H_2O:MeOH (1:1, v/v) (*green traces*). (c) Normalized UV-vis (*dashed traces*) and PL emission spectra (*solid traces*) of C-A-C nanofibers (*blue traces*, L_n = 191 nm, L_w/L_n = 1.07), CdSe QR in H_2O:MeOH (1:1, v/v) (*red traces*). The inset shows the energy levels of PDHF and the CdSe QRs.

Energy transfer in the hybrid C-A-C nanofiber system, from the segmented PDHF nanofibers to the QRs, was studied in detail by fluorescence spectroscopy and imaging. Upon selective excitation of the PDHF donor (λ_{exc} = 385 nm), the fluorescence spectrum of the C-A-C nanofiber solution (2 mL, 0.1 mg mL^{-1}, A: L_n = 97 nm, L_w/L_n = 1.05; C-A-C: L_n = 191 nm, L_w/L_n = 1.07) in H_2O:MeOH (1:1, v/v) showed that the fluorescence is dominated by the PDHF $I_{0\text{-}0}$ vibronic band (λ_{max} = 430 nm). However, significant quenching of the PDHF donor (λ_{max} = 430 nm) and simultaneous enhancement of CdSe QR emission (λ_{max} = 610 nm) was observed for the fluorescence spectrum of the C-A-C nanofibers decorated with QRs (Figure 3. 4a). With increased loading of CdSe QRs, these effects were amplified and the highest quenching (84%) of PDHF emission occurred when 50 wt.% CdSe QRs (100 µL, 1 mg mL^{-1}) were attached to the C-A-C nanofibers (Figure 3. 4a). We have shown the spatial-selective attachment of CdSe QRs to the PDHF-*b*-QPF (C)

segments of the hybrid C-A-C nanofibers (Figure S3. 26). To confirm the quenching of PDHF emission from the entire crystalline fiber core including segment A, a control fluorescence study involving the addition of CdSe QRs to a mixture of individual A and C nanofibers was performed. The overall lengths of individual A and C fibers, relative ratio, and overall concentration match that of the C-A-C triblock nanofiber sample was studied. This comprised of a 1:1 mixture of A nanofibers (L_n = 41 nm, L_w/L_n = 1.06) and C nanofibers (L_n = 51 nm, L_w/L_n = 1.07). An equivalent amount of CdSe QRs that was used for the preparation of the hybrid C-A-C fibers (50 wt. % CdSe QDs attachment) was added to a mixture of A nanofibers (L_n = 41 nm, L_w/L_n = 1.06) and C nanofibers (L_n = 51 nm, L_w/L_n = 1.07). However, the fluorescence spectrum showed only a 40 % quenching of the PDHF donor emission (Figure S3. 27). The additional (up to ca. 44 %) quenching of the PDHF emission that was detected for the hybrid C-A-C nanofibers compared is attributed to the transfer of excitons generated along the entire crystalline PDHF C-A-C nanofiber core to the QRs attached to the corona of the terminal C segments. The quenching effect observed for the crystalline PDHF core emission and enhancement of the attached CdSe QRs emission can be directly visualized as a variation in emission color of the hybrid assembled solutions upon 365 nm excitation was observed at different QR concentrations (Figure 3. 4b).

To further investigate the energy transfer from the PDHF crystalline core to the attached QRs, we performed photoluminescence excitation (PLE) experiments on the hybrid C-A-C nanofibers at 610 nm (Figure 3. 4c). The PLE profile displayed a characteristic feature resembling the cumulative absorption of PDHF nanofibers and the QRs (Figure 3. 4c). Specifically, the PLE spectrum of hybrid C-A-C nanofibers at 610 nm can be expressed as[8]:

$$I(\lambda) = \left[Abs_{fiber}(\lambda) \times \eta(\lambda) + Abs_{QR}(\lambda)\right] \times Q(\lambda) \times F(\lambda) \quad (1)$$

The $I(\lambda)$ is the excitation intensity at 610 nm emission, $Abs_{fiber}(\lambda)$ and $Abs_{QR}(\lambda)$ are the absorption of PDHF nanofiber and QRs respectively; $\eta(\lambda)$ is the energy transfer efficiency; $Q(\lambda)$ is the quantum yield; $F(\lambda)$ is the coefficient including all other factors such as instrumentation response, systematic error, *etc.* By quantitative analysis of the PLE spectrum of hybrid C-A-C nanofibers, we can

extract the energy transfer efficiency η(λ). By referring the PLE profile of the QRs solution at 0.02 mg mL^{-1}, the Q(λ) × F(λ) values can be obtained, thereby generating the effective absorption spectrum of hybrid C-A-C nanofibers (Figure 3. 4d). The contribution of direct PDHF emission at 610 nm in PLE spectrum of hybrid C-A-C nanofibers has been subtracted (for detailed discussion, see Figure S3. 28) to yield the effective absorption spectrum ($Abs_{effective}$), which is equivalent to:

$$\mathrm{Abs}_{effective}(\lambda) = \mathrm{Abs}_{fiber}(\lambda) \times \eta(\lambda) + \mathrm{Abs}_{QR}(\lambda) \quad (2)$$

Therefore, the efficiency of energy transfer η(λ) can be obtained from the above equation (Figure 3. 4e). The calculated energy transfer efficiency at different wavelengths indicated up to 78% of the photons absorbed by the PDHF crystalline core reach the attached CdSe QRs at both fiber termini, which is consistent with the extensive quenching of the PDHF emission (84%). Moreover, the measured photoluminescence quantum yield (PLQY) of the hybrid C-A-C nanofibers at 610 nm was ca. 1.5% (excited at 405 nm; only emission from QRs is considered; for details see Table S3. 7), which is ca. 4 times higher than that of pure CdSe QRs (0.4%, Table S3. 7), confirming the efficient energy transfer between the PDHF crystalline core and attached QRs. In addition, to exclude the possible aggregation of hybrid C-A-C nanofibers when loaded with large amounts of CdSe QRs, stimulation emission depletion (STED) super-resolution microscopy was used to visualize the well dispersed hybrid C-A-C nanofibers sample. Upon 405 nm excitation (Figure 3. 4f, g), different lengths of low-dispersity hybrid C-A-C nanofibers (L_n = 3221 nm, L_w/L_n = 1.10 in Figure 4f, and, L_n = 561 nm, L_w/L_n = 1.08 in Figure 3. 4g), blue emission was observed from the crystalline PDHF core in the central A segment and red emission from the selectively attached CdSe QRs on both terminal C segments was observed.

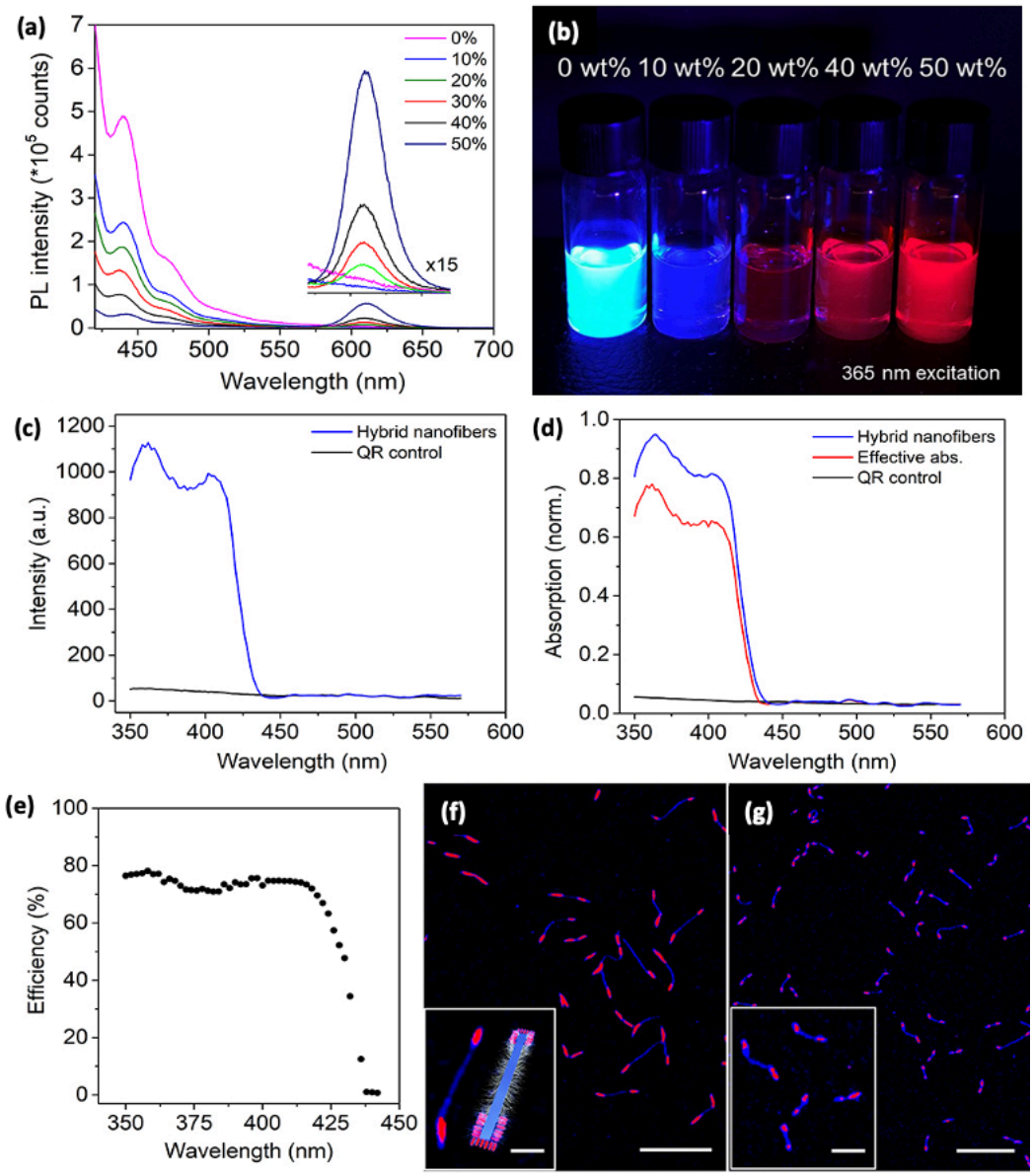

Figure 3. 4: (a) Fluorescence spectra of hybrid C-A-C nanofibers (A: L_n = 167 nm, L_w/L_n = 1.06; C-A-C: L_n = 191 nm, L_w/L_n = 1.07) with different added amounts of CdSe QRs (0 to 50 wt. %, relative to nanofibers). (b) Photograph of hybrid C-A-C nanofibers with different loadings of QRs in solution upon 365 nm excitation. (c) PLE spectrum of hybrid C-A-C nanofibers (blue) and QDs (black) in H_2O:MeOH (1:1, v/v) detected at 610 nm emission. (d) Absorption profiles of hybrid C-A-C nanofibers (blue line), effective hybrid C-A-C nanofibers (red line), and QRs control (black line). (e) Calculated C-A-C PDHF nanofibers to QR energy transfer efficiency η(λ). Superimposed STED images including both blue and red channels of different low-dispersity hybrid C-A-C nanofibers (f), A: L_n = 2511 nm, L_w/L_n = 1.10; C-A-C: L_n = 3221 nm, L_w/L_n = 1.10, or g, A: L_n = 417 nm, L_w/L_n = 1.07; C-A-C: L_n = 561 nm, L_w/L_n = 1.08). Scale bar (f) = 5 μm, inset = 1 μm. Scale bar (g) = 5 μm, inset = 500 nm.

3.3.4. Time-Resolved Spectroscopic Studies of Segmented Nanofibers-QR Conjugates

In order to elucidate the energy transfer process from the PDHF crystalline core to the attached QRs in the hybrid C-A-C nanofibers, we performed transient-

absorption (TA) spectroscopy. A representative TA map is given in Figure 3. 5a. Using an excitation wavelength of 400 nm, which generates excitons in both the PDHF and QRs, we see clear spectral signatures associated with each material. The broad photoinduced absorption from 650-900 nm is mainly due to the PDHF, while the Gaussian-like peak at 590 nm (which becomes much more prominent at later times) is due to a ground-state bleach (GSB) of the QRs. These assignments are confirmed by individual measurement of the PDHF and QRs separately (Figure S3. 29, 30). The rise of the signal associated with the QRs is demonstrative of energy transfer to the QRs from the PDHF. To quantify this transfer, we deconvolve each TA spectrum at each time delay into the linear sum of two spectral components: the individual spectra associated with the PDHF and QRs respectively (see Supporting Information and Figure S3. 29-34 for more details). We subsequently extract out the exciton population kinetics in each material over time for the overall hybrid system (Figure 3. 5b and Figure S3. 33). This extraction is repeated for the hybrid system excited at 460 nm (which selectively excites the QRs) to yield the intrinsic QR exciton decay, as well as for the *unloaded* C-A-C nanofibers to yield the intrinsic PDHF exciton decay. We find that the PDHF exciton population decays more quickly in the hybrid system than in the unloaded C-A-C nanofibers, with characteristic time constants of 90 ps and 270 ps, respectively. This is indicative of energy transfer from the PDHF to the QRs. We also see that the QR population in the hybrid exhibits a large rise over time when excited at 400 nm; a rise that is not observed when exciting the hybrid at 460 nm. This further confirms energy transfer.

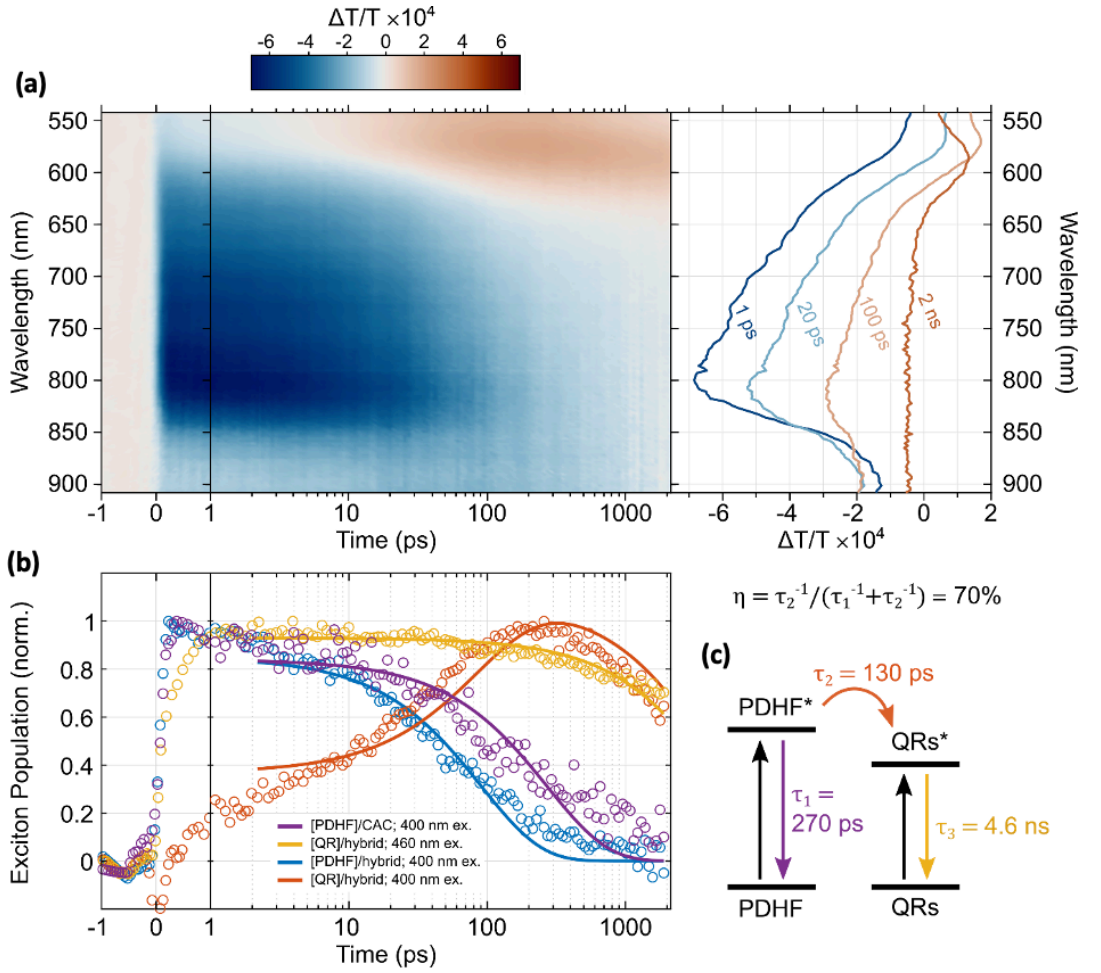

Figure 3. 5: (a) left panel: representative TA map of hybrid C-A-C nanofibers (A: L_n = 87 nm, L_w/L_n = 1.05; C-A-C: L_n = 152 nm, L_w/L_n = 1.07) with 50 wt. % loading of CdSe QRs relative to nanofibers. Right panel: associated spectra averaged over the time delays of 0.1-2.1 ps, 10-30 ps, 50-150 ps, and 1.8-2.2 ns. We observe a clear change in the TA signal over time. (b) Extracted exciton population kinetics of: PDHF in (unloaded) C-A-C nanofibers with 400 nm excitation (purple trace), giving the intrinsic PDHF dynamics; QRs in hybrid C-A-C nanofibers after 460 nm excitation (yellow trace), giving the intrinsic QR dynamics; PDHF in hybrid C-A-C nanofibers upon 400 nm excitation (blue trace), showing shortened lifetime due to energy transfer; and QRs in hybrid C-A-C nanofibers (orange trace), with the rise over time demonstrating energy transfer from PDHF to the QRs. The fluence with 400 nm excitation was 3 μJ/cm^2/s in each case, and at 460 nm a fluence of 4 μJ/cm^2/s was used to account for the QRs' lower absorption at 460 nm, and so that the maximum QR exciton concentration in each case was equal. Global fits are shown in each case using a 3-parameter model. The global fits are applied from 2 ps onwards to avoid fitting the QRs' hot-carrier cooling in the first 2 ps. (c) Illustration of 3-parameter model labelled with extracted time constants from (b). The system shows high transfer efficiency (70±10 %), and excitons are funneled to the QRs with a time constant of 130 ps.

To model the energy transfer to the QRs we employ a simple 3-parameter model:

$$\frac{d[PDHF]}{dt} = -\left(\frac{1}{\tau_1} + \frac{1}{\tau_2}\right)[PDHF] \tag{3}$$

$$\frac{d[QR]}{dt} = \frac{1}{\tau_2}[PDHF] - \frac{1}{\tau_3}[QR] \tag{4}$$

where τ_1 is the intrinsic decay time of the PDHF, τ_2 is the PDHF-to-QR transfer rate, and τ_3 is the intrinsic decay of the QRs. We then globally fit this system-of-equations to the four-population kinetics shown in Figure 3. 5b (note that for the *unloaded* C-A-C nanofiber system τ_2^{-1} is set to zero as there are no QRs present). The global fit models the data well, despite being highly constrained and with only 3 input kinetic parameters, which validates our approach. From the fit we extract a transfer time constant of $\tau_2 = 130$ ps. This transfer rate is understandable given that a large proportion of the PDHF excitons must diffuse through the PDHF core towards the QRs to be close enough for energy transfer. Given our systems of equations (3) and (4), the energy transfer efficiency can then be expressed as:

$$\eta = \frac{\tau_2^{-1}}{\tau_1^{-1} + \tau_2^{-1}} \tag{5}$$

Given that $\tau_1 = 270$ ps, we hence find that $\eta = 70\%$ with an estimated uncertainty of $\pm 10\%$. This value agrees with the calculated energy transfer efficiency from steady-state spectra (Figure 3. 4e). Another figure of merit is the number of additional excitons each QR receives in the hybrid ensemble due to energy transfer from PDHF. This in effect describes the effective increase in the QRs' oscillator strength. By simply considering the initial and maximum values in the QR concentration profile when the hybrid is excited at 400 nm in Figure 3. 5 (and by assuming that $\tau_3^{-1} \ll \tau_1^{-1} + \tau_2^{-1}$) we find that each QR (on average) receives roughly 4 times the excitons it would have absorbed in the absence of the PDHF. The value agrees well with the equivalent four-fold enhancement in the effective PLQY of the QRs when in the hybrid ensemble.

Interestingly, our TA data also suggests that the funneling of energy does not stop once the excitons in the PDHF have been efficiently transferred to the QRs; energy is in fact funneled further *amongst the QRs themselves*. Figure S3. 30 and Figure S3. 35 demonstrate that the GSB of the QRs exhibits a ~15 nm red-shift over 2 ns when selectively excited at 460 nm. This red-shift is entirely absent when the same batch of QRs are measured in a pure, dilute solution. This suggests that because the QRs are close to one another in the nanofibers, excitons may hop between QRs via FRET, with a preference to transfer to sites with the lowest band-

gaps as has been observed previously.[51] This QR-to-QR transfer occurs with a characteristic time constant of $\tau_r = 510$ ps, which is slower than the PDHF-to-QR energy transfer rate of $\tau_2 = 130$ ps. However, we note that the QRs have a significantly longer intrinsic lifetime than PDHF as expected for this family of inorganic materials, and so energy funneling amongst the QRs can still take place; given the QR lifetime of $\tau_3 = 4.6$ ns, we expect ~90% of excitons in the QRs to transfer to the lowest-energy QR in the locally accessible vicinity. Notably, this energy funneling between the QRs is *multiplicative* with the PDHF-to-QR energy funneling; a hypothetical five-fold concentration factor due to QRs residing on average in clusters of five would result in an overall 20-fold concentration factor when combined with four-fold concentration factor due to the PDHF. Future work will therefore explore tuning the polydispersity, lifetime, and clustering of the inorganic species in the hybrid ensembles to leverage the multiplicative energy funneling for applications such as upconversion or multi-electron catalysis.

3.4. Summary

Exciton-coupled conjugates composed of low-dispersity π-conjugated polymer nanofibers and spatial-defined semiconducting QDs and QRs were successfully prepared. Low-dispersity segmented nanofibers were prepared *via* seeded growth and comprised a continuous crystalline PDHF core with various grafted functional coronas provided sites for spatial-selective decoration with CdSe QDs and QRs. Upon PDHF-donor excitation, the segmented nanofibers can funnel absorbed energy along the PDHF crystalline core with a long exciton diffusion length towards the spatial-selective attached CdSe QRs on the fiber termini. By careful selection of the bandgap of the QRs as acceptor, effective energy transfer can be realized to have 4-fold enhancement of the QRs emission. This work provides a tunable platform with which to construct tailored conjugated polymer nanofiber/quantum dot and rod hybrid materials for enhanced photonic performance, with potential applications as sensors,[4] in bioimaging,[52,53] in photocatalysis,[10,54] as light-emitting diodes,[55,56] and as solar devices.[7,57]

3.5. Supporting Information

3.5.1. Materials and Methods

All reagents and solvents used for polymers synthesis were of reagent grade, and unless otherwise stated and were used as received. Solvents for self-assembly were of HPLC grade and filtered using 0.2 μm syringe filters prior to use. The synthesis of $PDHF_{14}$-*b*-PEG_{227} has been reported elsewhere and is not described here.[41]

Nuclear magnetic resonance (NMR). ^1H NMR spectra were taken with a Bruker 500 MHz spectrometer; chemical shifts were referenced to the residual solvent peak ($CHCl_3$, δ = 7.26 ppm).

Gel Permeation Chromatography (GPC). measurements were conducted on Viscotek GPC_{max} equipped with a UV detector operating at 400 nm and a refractometer. Measurements were carried out at 1.0 mL min^{-1} with THF containing [*n*Bu_4N]Br (0.1% w/w) as the eluent at 35 ˚C, results were measured against polystyrene standards (Viscotek).

Matrix-Assisted Laser Desorption/Ionization Time-Of-Flight Mass Spectrometry (MALDI-TOF MS). Measurements were conducted on a Bruker Ultraflex II ToF spectrometer under the reflector positive ion regime. Samples were prepared with a 9:1 ratio of *trans*-2-[3-(4-*tert*-butylphenyl)-2-methyl-2-propenylidene]malonitrile matrix (20 mg mL^{-1} in THF) to polymer solution (0.2 mg mL^{-1} in THF), then 5 μL of the sample was deposited onto the sample plate and dried under ambient conditions.

Transmission Electron Microscopy (TEM). Samples were prepared by drop casting 10 μL of the nanofiber solution onto a carbon-coated copper grid (Agar Scientific, mesh size 200). Bright-field TEM micrographs were taken using a JEOL TEM 1011EX microscope operating at 80 kV, equipped with a 11M pixel CCD camera. Micelle length distributions were determined using the software program ImageJ developed at US National Institute of Health. A minimum of 300 micelles are traced to determine their contour length and histograms of the length distributions obtained. This data allows for calculation of the number average length (L_n), weight average length (L_w) for each sample, this is calculated as shown below (L = length of fiber, N = number).

$$L_n = \frac{\sum_{i=1}^{n} N_i L_i}{\sum_{i=1}^{n} N_i} \qquad L_w = \frac{\sum_{i=1}^{n} N_i {L_i}^2}{\sum_{i=1}^{n} N_i L_i} \tag{1}$$

Spectroscopic Measurements. UV/vis data was obtained on a Lambda 35 Spectrometer employing quartz cells (1 cm × 1 cm). Fluorescence data was obtained on a PTI QM40 Spectrofluorometer using an excitation wavelength of 385 nm. Photoluminescence excitation spectrum was obtained on a PTI QM40 Spectrofluorometer using an emission wavelength of 610 nm.

Scanning Transmission Electron Measurements. STEM and low-angle annular dark-field measurements were performed on a HITACHI SU9000 cold field emission scanning electron microscope where the accelerating voltage and the current were set as 10 kV and 10 μA. Samples for STEM measurements were prepared by drop-casting 10 μL of nanofiber samples onto a carbon film coated copper grid.

Scanning Electron Microscopy-Energy Dispersive Measurements. SEM-EDS measurements were performed on a HITACHI SU9000 low kV cold field emission scanning electron microscope coupled with an Oxford AztecEnergy with X-MaxN 100 LE-100 mm^2 windowless Ultra Large Solid Angle SDD detector. The accelerating voltage and the current were set as 10 kV and 10 μA, the scanning resolution and collection time were set as 512∗512 and 10 μs/point. The quantitative elementary analysis and elementary distribution imaging were analysed by a comprehensive Energy Dispersive X-ray Microanalysis system.

Photoluminescence Quantum Yield (PLQY) Measurement. PLQY measurements were performed following the reported method. Materials were prepared in solution and dispensed into 1 mm cuvettes for characterization. Materials where excited with ∼400 μW of continuous wave laser excitation (405 and 520 nm) with an excitation spot of ∼0.3 mm^2, resulting in low excitation densities. Measurements were repeated several times to determine if there any uncertainties and to avoid variations in the laser power. The Rhodamine 6G solutions were used as a reference to confirm the measured PLQY value relative to the reported value.

3.5.2. Polymer Synthesis

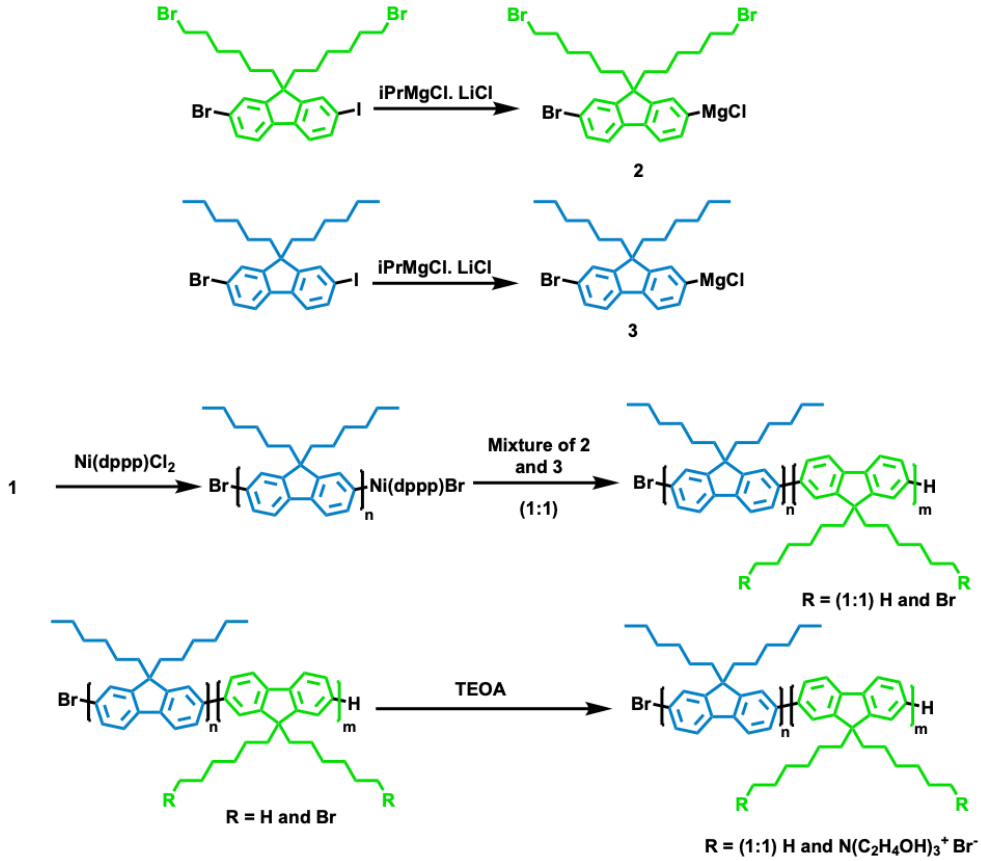

Scheme S3. 1: Synthesis of PDHF-*b*-QPF. PMDETA = N,N,N',N''-pentamethyldiethylenetriamine. dppp = 1,3-bis(diphenylphosphino)propane. TEOA = triethanolamine.

Table S3. 1: Characterization data of PDHF homopolymer and PDHF-based block copolymers. [a] DP determined by MALDI-ToF. [b] Block ratio determined by comparative integration of ^{1}H NMR peaks relative to the DP of PDHF blocks determined from MALDI-TOF. [c] M_n, M_w and $Đ_m$ determined by GPC analysis (THF containing [nBu$_4$N]Br (0.1% w/w)). Molecular mass dispersity = $Đ_m$ (M_w/M_n).

Material Composition	M_n (kg mol^{-1})	M_w [c] (kg mol^{-1})	$Đ_m$ [c]
$PDHF_{17}$ [a]	11.1	13.1	1.18
$PDHF_{17}$-*b*-$P2VP_{250}$ [b]	14.7	18.3	1.24
$PDHF_{14}$-*b*-PEG_{227} [b]	29.3	32.4	1.11
$PDHF_{15}$ [a]	11.5	14.6	1.27
$PDHF_{15}$-*b*-$PDHF_8$-*r*-$PDBHF_8$ [b]	13.8	17.8	1.29

Synthesis of Alkyne-terminated $PDHF_{17}$

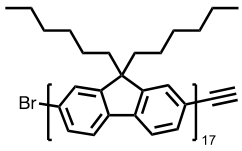

Alkyne-terminated $PDHF_{17}$ was synthesized by Grignard Metathesis polymerization (GRIM). 2-Bromo-7-iodo-9,9-bis-*n*-hexylfluorene was synthesised according to a reported procedure. 2-Bromo-7-iodo-9,9-bis-*n*-hexylfluorene (435 mg, 0.81 mmol) was dissolved in 10 mL of anhydrous THF. The solution of 2-bromo-7-iodo-9,9-bis-*n*-hexylfluorene was cooled to -20˚C before 1.3 M *i*PrMgCl.LiCl (0.62 mL, 0.81 mmol) was added dropwise then the resulting solution was left to stir for 90 min at -78˚C. The activated fluorene monomer was added in one quick injection to a solution of $Ni(dppp)Cl_2$ (22 mg, 0.041 mmol) and anhydrous THF (100 mL) at 0˚C. After 15 min, 0.5 M ethynylmagnesium bromide (3 mL, excess) was added to the reaction mixture which was then stirred for 1 h. The resultant mixture was then precipitated into methanol, giving a yellow solid. Further purification by Soxhlet extraction in ethyl acetate, methanol then chloroform followed by removal of solvent *in vacu*o gave the purified polymer (yellow solid, yield: 145 mg, 53 %). Degree of polymerisation of the alkyne-capped PDHF homopolymer was calculated to be 17 and M_n = 5758 Da by MALDI-TOF with a 9:1 ratio of matrix to polymer solution (0.5 mg mL^{-1} in THF). Molar mass dispersity ($Đ_m = M_w/ M_n$) of 1.18 was determined by GPC analysis for the $PDHF_{17}$ homopolymer (M_w= 13, 101 Da and M_n= 11, 120 Da). ^1H NMR (500 MHz, $CDCl_3$) δ (ppm) = 7.62-7.91 (m, 6 H, polyfluorene aromatic), 3.16 (s, alkyne), 2.13 (brs, 4 H, polyfluorene-(CH_2)x2), 1.33-0.61 (m, 30 H, polyfluorene-($CH_2(CH_2)_4$)x2 and polyfluorene-(CH_3)x2).

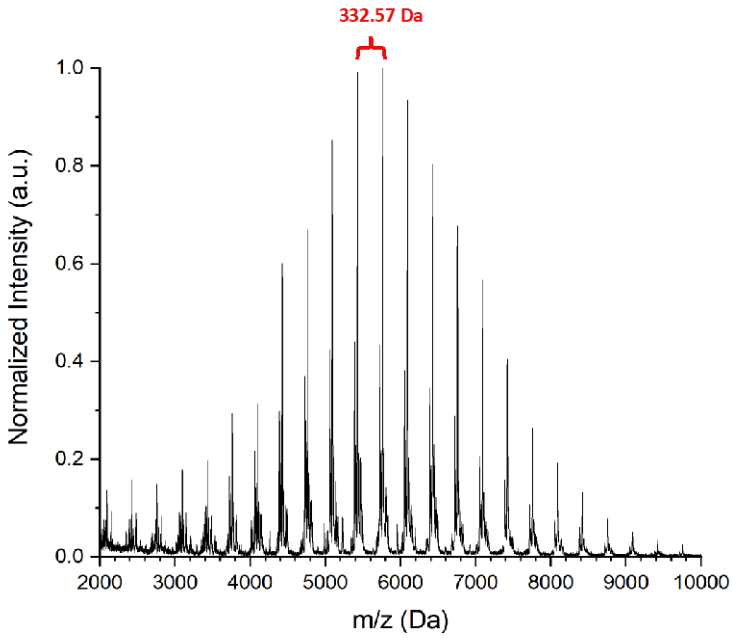

Figure S3. 1: MALDI-TOF mass spectrum of alkyne-capped $PDHF_{17}$, M^+ = 5758 Da. The mass of each PDHF repeat unit is 332 g mol^{-1}.

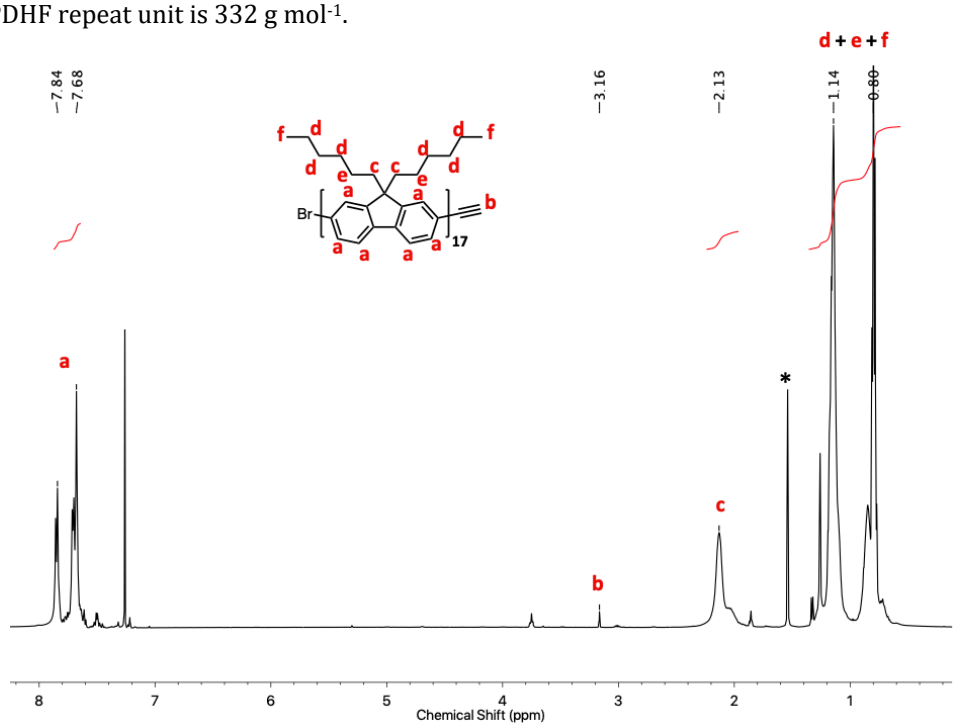

Figure S3. 2: ^1H NMR spectrum of alkyne-terminated $PDHF_{17}$ (500 MHz, $CDCl_3$). Residual H_2O is marked with an *.

Synthesis of Azido-terminated P2VP$_{250}$

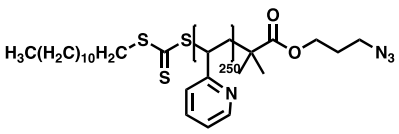

The RAFT CTA 2-(dodecylthiocarbonothioylthio)-2-methylpropionic acid 3-azido-1-propanol ester (17 mg, 0.038 mmol), 2-vinylpyridine (1 g, 9.51 mmol) and AIBN (1.24 mg, 0.0076 mmol) were dissolved in 3 mL of DMF then subjected to three consecutive freeze-pump-thaw cycles. The mixture was then stirred at 80°C for 20 h before being cooled to room temperature and diluted with THF to quench the polymerization. The resultant mixture was then precipitated into cold diethyl ether and purified further by repeated precipitation into cold hexanes to afford a white solid (341 mg, yield: 34 %). ^{1}H NMR (500 MHz, $CDCl_3$) ppm δ = 8.47-8.04 (m, 251 H, C*H*-N aromatic), 7.24-6.17 (m, 751 H, C*H* x 3 aromatic), 3.53 (brs, 2 H, CH_2-O) and 3.20 (brs, 2 H, CH_2-N_3),

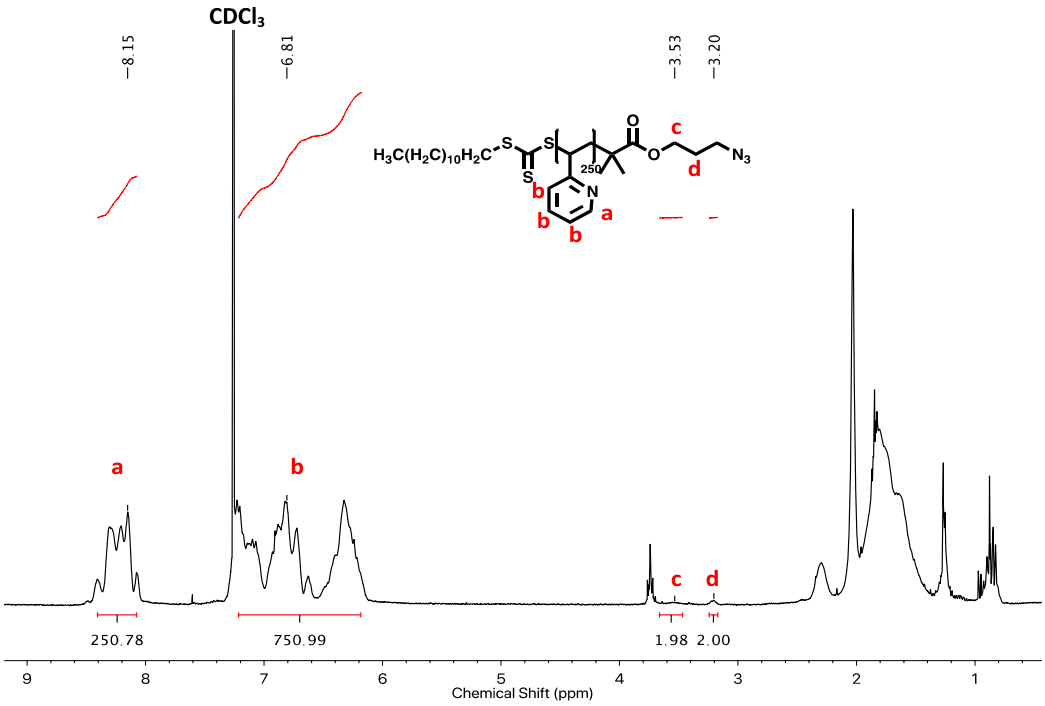

Figure S3. 3: ^{1}H NMR spectrum of azido terminated P2VP$_{250}$ (500 MHz, $CDCl_3$). NMR solvent residual signal marked by a $CDCl_3$ label.

Synthesis of $PDHF_{17}$-*b*-$P2VP_{250}$

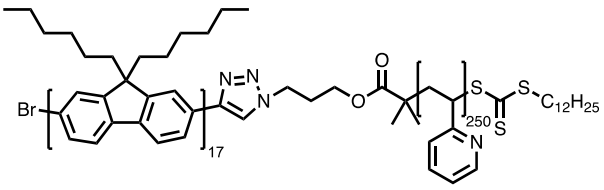

Alkyne-terminated $PDHF_{17}$ (30 mg, 0.0052 mmol) and azide-terminated $P2VP_{250}$ (167 mg, 0.0062 mmol) were dissolved in 3 mL of THF and subjected to three consecutive freeze-pump-thaw cycles. Azide-terminated $P2VP_{250}$ was synthesized according to a previously reported procedure. CuBr (10 mg, excess) and PMDETA (20 μL, excess) were dissolved in 1 mL anhydrous THF then added to polymer solution. The reaction mixture was heated to 40˚C and stirred for 48 h. The polymers were then purified by passing the reaction mixture through a basic alumina column to remove Cu/PMDETA. Volatiles were concentrated *in vacuo* followed by precipitation into hexanes. The polymers were subsequently dissolved in THF and dilute HCl was added to protonate the P2VP block resulting in precipitation of PDHF-*b*-P2VP diblock copolymers and residual P2VP homopolymers with any PDHF homopolymer impurities residing in the supernatant. The collected precipitate was then dissolved in chloroform/triethylamine and precipitated into hexanes. To remove any P2VP homopolymer, the solids were then washed with acetone three times affording the purified diblock copolymer as a yellow solid (yield: 43 mg, 30 %). Polydispersity of 1.24 was determined by GPC analysis for the $PDHF_{17}$-*b*-$P2VP_{250}$ polymers (M_w= 18, 273 Da and M_n= 14, 738 Da). ^{1}H NMR (500 MHz, $CDCl_3$) δ (ppm) = 8.73-7.57 (m, 363 H, polyfluorene aromatic x 6 and poly(2-vinyl pyridine) C*H*-N aromatic), 7.57-6.09 (m, 724 H, poly(2-vinyl pyridine) C*H* x 3 aromatic) and 3.51 (brs, 2 H, RAFT CTA CH_2-O).

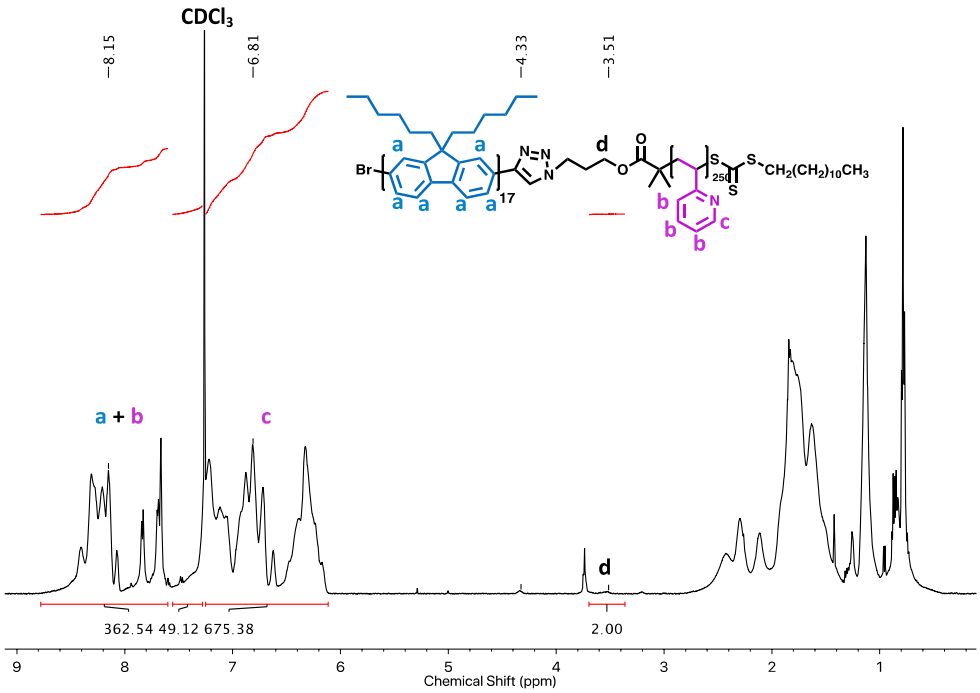

Figure S3. 4: ^{1}H NMR spectrum of PDHF$_{17}$-*b*-P2VP$_{250}$ (500 MHz, $CDCl_3$). NMR solvent residual signal marked by a $CDCl_3$ label.

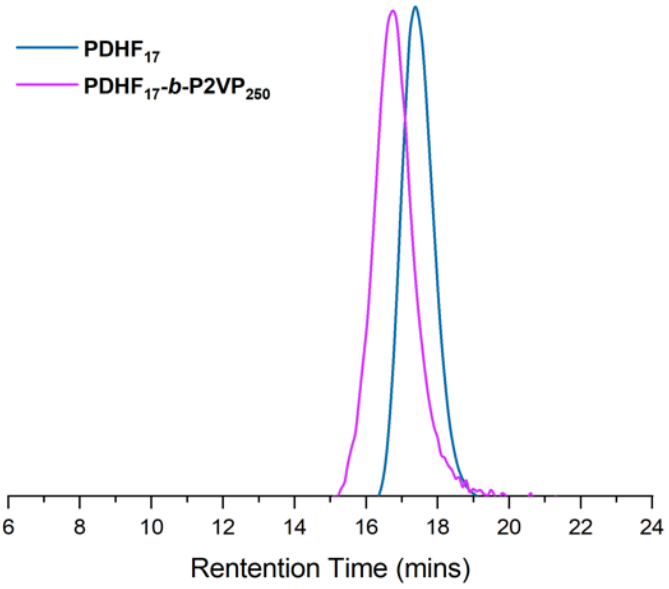

Figure S3. 5: GPC traces (UV response at λ = 380 nm) eluted in THF containing [*n*Bu$_4$N]Br (0.1 % w/w) (1 mL min^{-1}) at 35 °C of PDHF$_{17}$ homopolymer (blue trace) and PDHF$_{17}$-*b*-P2VP$_{250}$ (purple trace).

Synthesis of $PDHF_{15}$-*b*-$PDHF_8$-*r*-$PDBHF_8$

Alkyne-terminated $PDHF_{15}$-*b*-$PDHF_8$-*r*-$PDBHF_8$ was synthesized by sequential Grignard Metathesis polymerization (GRIM). 2-Bromo-7-iodo-9,9-bis-*n*-hexylfluorene and 2-Bromo-7-iodo-9,9-bis-*n*-dibromohexylfluorene were synthesised according to reported procedures. 2-Bromo-7-iodo-9,9-bis-*n*-hexylfluorene (300 mg, 0.56 mmol) and a 1:1 mixture of 2-Bromo-7-iodo-9,9-bis-*n*-dibromohexylfluorene (193 mg, 0.28 mmol) and -Bromo-7-iodo-9,9-bis-*n*-hexylfluorene (150 mg, 0.28 mmol) were separately dissolved in 10 mL of anhydrous THF. The two separate solutions were cooled to -20˚C before 1.3 M *i*PrMgCl.LiCl (1 eq.) was added dropwise and the resulting solutions were left to stir for 90 min at -78˚C. The activated 2-Bromo-7-iodo-9,9-bis-*n*-hexylfluorene monomer was added in one quick injection to a solution of Ni(dppp)Cl_2 (15.1 mg, 0.028 mmol) and anhydrous THF (100 mL) at 0˚C. After 15 minutes of stirring, the activated mixture of fluorene monomers was added in one quick injection to the reaction mixture. After 16 hours, the resultant mixture was then precipitated into methanol, giving a yellow-green solid. Further purification by Soxhlet extraction in ethyl acetate, methanol then chloroform followed by removal of solvent *in vacu*o gave the purified polymer (bright yellow solid, yield: 178 mg, 63 %). Degree of polymerisation of the PDHF aliquot was calculated to be 15 and M_n = 5083Da by MALDI-TOF with a 9:1 ratio of matrix to polymer solution (0.5 mg mL^{-1} in THF). Polydispersity (M_w/ M_n) of 1.27 was determined by GPC analysis for the $PDHF_{15}$ homopolymer (M_w= 14, 693 Da and M_n= 11, 572 Da). Polydispersity of 1.29 was determined by GPC analysis for the $PDHF_8$- *b*-$PDHF_8$-*r*-$PDBHF_8$ polymers (M_w= 17, 841 Da and M_n= 13, 835 Da). ^{1}H NMR (500 MHz, $CDCl_3$) δ (ppm) = 3.30 (s, 0.23 H, CH_2Br x 2), 2.13 (brs, 1 H, polyfluorene-(CH_2) x 2) and 1.70 (CH_2 CH_2Br x 2).

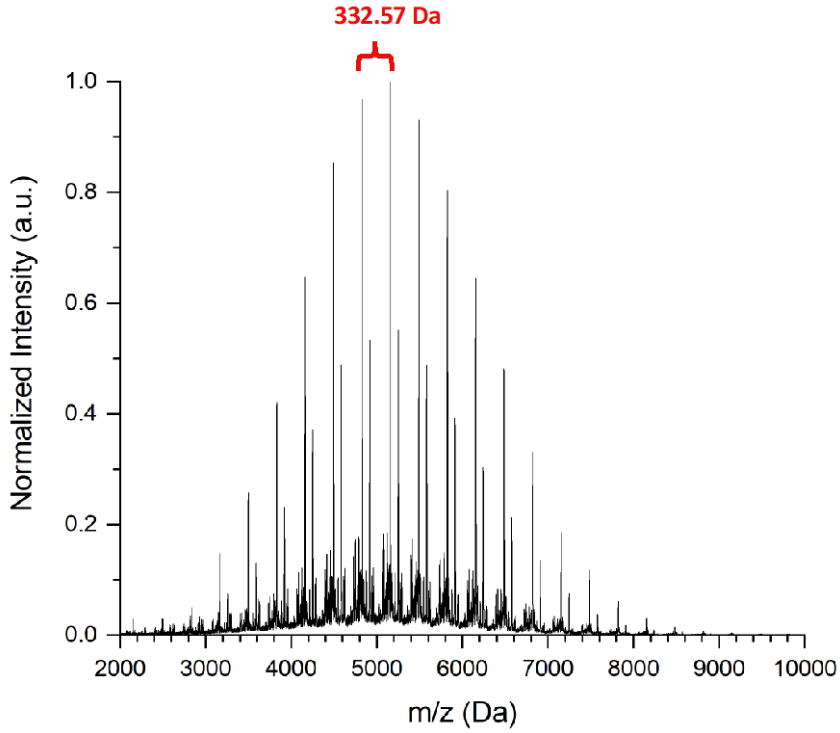

Figure S3. 6: MALDI-TOF mass spectrum of proton-capped $PDHF_{15}$ homopolymer aliquot. The mass of each PDHF repeat unit is 332 g mol^{-1}.

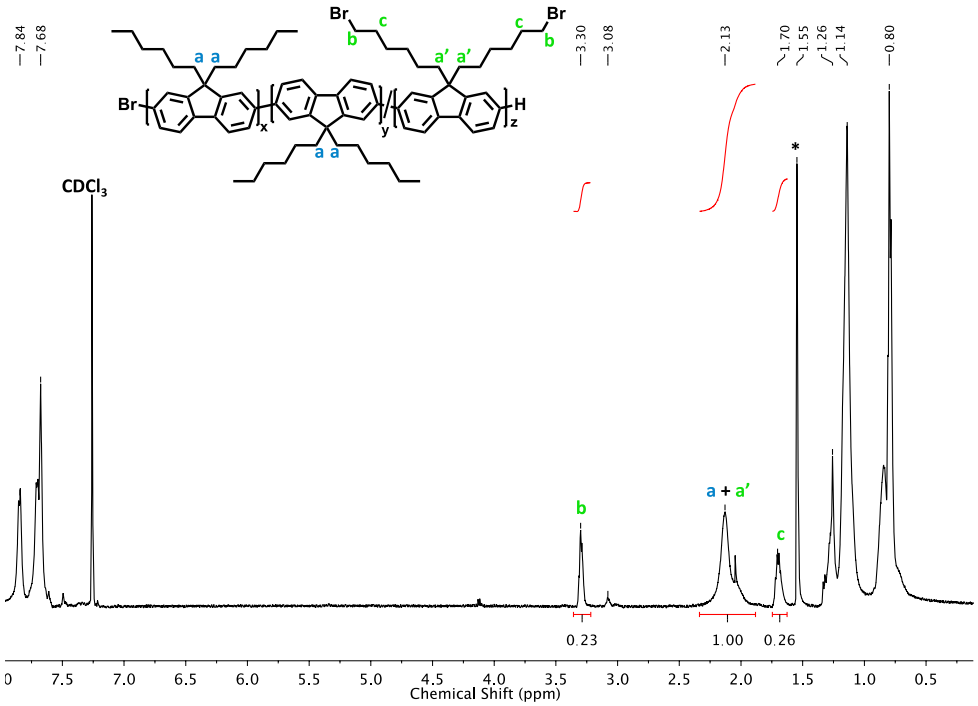

Figure S3. 7: ^{1}H NMR spectrum of PDHF-*b*-PDHF-*r*-PDBHF (500 MHz, $CDCl_3$). NMR solvent residual signal marked by a $CDCl_3$ label and residual H_2O is marked with an *.

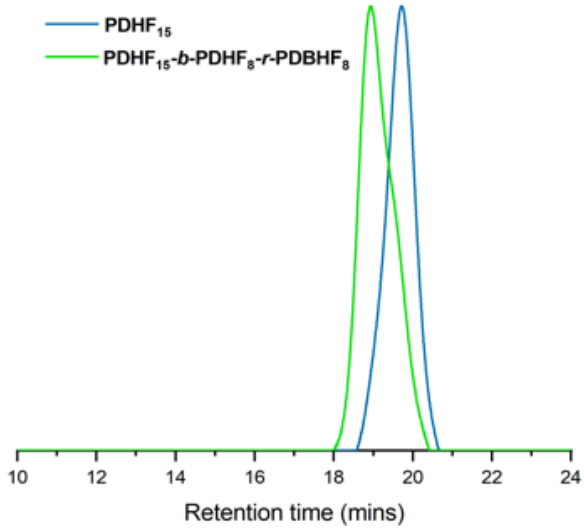

Figure S3. 8: GPC traces (UV response at λ = 380 nm) eluted in THF containing [*n*Bu$_4$N]Br (0.1 % w/w) (1 mL/min) at 35 °C of PDHF$_{15}$ homopolymer (blue trace) and PDHF-*b*-PDHF-*r*-PDBHF (green trace).

Synthesis of PDHF$_{15}$-*b*-QPF$_{16}$

PDHF$_{15}$-*b*-PDHF$_8$-*r*-PDBHF$_8$ (35 mg, 0.0030 mmol) was dissolved was dissolved in 20 mL of DMF/THF (1:1 v/v) mixed solvent and 1 mL (excess) of Triethanolamine (TEOA) was added dropwise. The resulting mixture was then heated under reflux for 24 h. Volatiles were subsequently removed *in vacuo* and the polymers were then dissolved in DCM and washed with Methanol three times then with a saturated brine solution before drying with anhydrous $MgSO_4$. DCM was removed *in vacuo* and the polymers were then dissolved in THF and precipitated into cold methanol to afford a pure yellow solid (yield: 27.6 mg, 77 %). The degree of quaternization of the copolymeric block was estimated to be ca. 48% by ^{1}H NMR in $CDCl_3$ by integration of the 3.30 ppm (C*H*$_2$Br x 2) and 3.09 ppm (C*H*$_2$-TEOA$^+$ x 2) resonances.

3.5.3. Synthesis of CdSe Quantum Nanostructures

Synthesis of CdSe quantum nanorods (QRs)

Synthesis of CdSe quantum nanorods were conducted according to a modified literature procedure.[58] All preparative procedures were conducted using standard Schlenk-line techniques under N_2. In a typical synthesis, 105 mg of CdO, 449 mg of tetradecylphosphonic acid (TDPA) and tri-n-octylphosphine oxide (TOPO, 1.5 g) were combined and heated to 100 °C and degassed for 30 min, and

then heated to 300 °C until becoming clear under N_2. The CdSe precursor was cooled to room temperature and aged for 24h under N_2. After that, the solution was heated to 320 °C, a solution of Se (31 mg) of Se in 300 μL toluene was injected. The reacting mixture was cooled to 250 °C and kept the temperature for 0.5 h. After cooling down to room temperature, crude solution was mixed with absolute ethanol and centrifuged. The precipitate was dispersed in n-hexane to form a stable solution. The dimensions of the synthesized CdSe QRs were 12 ± 2 nm in length and 4 ± 1 nm in width, which were characterized by bright-field TEM (Figures S9a and S9b).

Preparation of mercaptoundecanoic acid coated quantum dots (MUA-QDs)

20 mg of MUA were placed in a vial and 15 mL of toluene were added. 20 mg of commercial CdSe QDs were dissolved in the mixture (Figure S10a), and the vial was placed under nitrogen flow. The mixture was heated at 65 °C overnight. The reaction was stopped and allowed to cool to ~28 °C, removed from rotary evaporation, and kept out of the light. QDs in 2 mL aliquots were precipitated with ethyl acetate and ether and followed dissolved in methanol for three times. The final MUA-QDs were dried 5 min in a vacuum oven and dissolved in 400 μL of water. The resulting geometry of the MUA-QDs were remained unaltered (Figure S10b).

Preparation of 8-Mercaptooctanoic acid coated quantum nanorods (MOA-QRs)

CdSe quantum rods (20 mg) synthesized as described above were stirred in refluxing anhydrous toluene (2 mL) for 24 h under nitrogen. Most of the toluene was removed by a vacuum, and the quantum rods were precipitated in methanol. The CdSe quantum rods were washed twice with methanol to remove residual ligands and then transferred to a reaction tube. Anhydrous THF (2 mL) and 8-Mercaptooctanoic acid (200 mg) were introduced, and the mixture was refluxed under nitrogen for 12 h. The quantum rods were precipitated in THF during this period, indicating successful functionalization of the quantum rods with 8-Mercaptooctanoic acid. The MOA-QRs were further washed by dissolution in methanol and precipitation in THF. The pH of the solution was adjusted to ~11 by

adding 25% methanolic solution of NMe_4OH. The resulting geometry of the MOA-QRs were remained unaltered characterized by bright-field TEM (Figures S9c and S9d).

3.5.4. Block Copolymer Self-Assembly

Preparation of polydisperse PDHF-*b*-PEG nanofibers

In an example protocol, 500 µL of methanol (MeOH) was added dropwise to 500 µL of a 0.4 mg mL^{-1} solution of $PDHF_{14}$-*b*-PEG_{227} unimers in THF, resulting in a final concentration of 0.2 mg mL^{-1}. The mixture was then shaken manually for 10 s and aged at 30°C for 24 h before analysis by TEM imaging to confirm the formation of $PDHF_{14}$-*b*-PEG_{227} polydisperse nanofibers.

Preparation of PDHF-*b*-PEG seed micelles

Seed micelles were prepared by sonication of a 0.2 mg mL^{-1} solution in THF: MeOH (1:1, v/v) of polydisperse $PDHF_{14}$-*b*-PEG_{227} nanofibers in an ultrasonic bath at 0°C for 2 h. After sonication, the resulting solutions were heated to 45°C for 3 h then subsequently cooled slowly to 20°C and aged for 24 h. The samples were then analysed by TEM imaging.

Preparation of monodisperse PDHF-*b*-PEG nanofibers by seeded growth

Seeded growth experiments were conducted by quickly injecting a known volume of $PDHF_{14}$-*b*-PEG_{227} unimer (in THF, 2 mg mL^{-1}, between 20-30 µL) to a solution of seed micelles in THF:MeOH (1:1, v/v) of a known concentration. The samples were then shaken for 10 s and aged at 30°C for 24 h before analysis by TEM. The contour lengths of at least 300 micelles were measured from several TEM images of each sample.

Preparation of polydisperse PDHF-*b*-P2VP nanofibers

In an example protocol, 500 µL of methanol was added dropwise to 500 µL of a 0.4 mg mL^{-1} solution of $PDHF_{17}$-*b*-$P2VP_{250}$ unimers in THF, resulting in a final concentration of 0.2 mg mL^{-1}. The mixture was then shaken manually for 10 s and

aged at 30°C for 24 h before analysis by TEM imaging to confirm the formation of $PDHF_{17}$-*b*-$P2VP_{250}$ polydisperse nanofibers.

Preparation of PDHF-*b*-P2VP seed micelles

Seed micelles were prepared by sonication of a 0.2 mg mL^{-1} solution in THF: MeOH (1:1, v/v) of polydisperse $PDHF_{17}$-*b*-$P2VP_{250}$ nanofibers in an ultrasonic bath at 0°C for 2 h. After sonication the resulting solutions were heated to 45°C for 3 h then subsequently cooled slowly to 20°C and aged for 24 h. The samples were then analysed by TEM imaging.

Preparation of monodisperse PDHF-*b*-P2VP nanofibers by seeded growth

Seeded growth experiments were conducted by quickly injecting a known volume of $PDHF_{17}$-*b*-$P2VP_{250}$ unimer (in THF, 2 mg mL^{-1}, between 22-33 µL) to a solution of seed micelles in THF:MeOH (1:1, v/v) of a known concentration. The samples were then shaken for 10 s and aged at 30°C for 24 h before analysis by TEM. The contour lengths of at least 300 micelles were measured from several TEM images of each sample.

Preparation of B-A-B segmented nanofibers (A= PDHF-*b*-PEG, B= PDHF-*b*-P2VP)

A 200 µL solution of $PDHF_{14}$-*b*-PEG_{227} nanofiber seeds (0.2 mg mL^{-1}, L_n= 109 nm, L_w/L_n= 1.09) in THF:MeOH (1:1, v/v) was diluted with 500 µL MeOH and 460 µL of THF. Then different volume of $PDHF_{17}$-*b*-$P2VP_{250}$ unimer solution (2 mg mL^{-1}) in THF was added to the dilute seed solution at 30°C. The resulting solution in THF:MeOH (1:1, v/v) (0.1 mg mL^{-1}) was shaken for 10 s and aged for 24 h at 30°C. Uniform B-A-B segmented nanofibers were observed by TEM analysis.

Preparation of C-A-C segmented nanofibers (A= PDHF-*b*-PEG, C= PDHF-*b*-QPF)

A 50 µL solution of $PDHF_{14}$-*b*-PEG_{227} nanofiber seeds (0.2 mg mL^{-1}, L_n= 109 nm, L_w/L_n= 1.09) in THF:MeOH (1:1, v/v) was diluted with 100 µL MeOH and 100 µL of THF. Then different volume of $PDHF_{17}$-b-QPF_{16} unimer solution (2 mg mL^{-1}) in THF was added in one shot to the dilute seed solution at 30°C under stir (400

rpm). The resulting solution in THF:MeOH (1:1, v/v) was shaken for another 10 s and aged for 24 h at 30°C. Uniform C-A-C segmented nanofibers were observed by TEM analysis.

Preparation of C-B-A-B-C segmented nanofibers (A= PDHF-*b*-PEG, B= PDHF-*b*-P2VP, C = PDHF-*b*-QPF)

A 50 μL solution of B-A-B seeds (0.1 mg mL^{-1}, L_n= 523 nm, L_w/L_n= 1.05) in THF:MeOH (1:1, v/v) was diluted with 100 μL MeOH and 100 μL of THF. Then, different volume of $PDHF_{17}$-*b*-QPF_{16} unimer solution (1 mg mL^{-1}) in THF was added in one shot to the dilute seed solution at 30°C under stir (400 rpm). The resulting solution in THF:MeOH (1:1, v/v) was shaken for another 10 s and aged for 24 h at 30°C. Uniform C-B-A-B-C segmented nanofibers were observed by TEM analysis.

3.5.5. Cooperative Assembly of Segmented Nanofibers and QDs/QRs

Preparation of hybrid B-A-B nanofibers

In an example protocol, 20 μL of 0.1 mg mL^{-1} QDs solution (water) was added dropwise to 500 μL of a 0.1 mg mL^{-1} solution of B-A-B segmented nanofibers in THF:MeOH (1:1, v/v) under stir (250 rpm), resulting in a final 4 wt.% hybrid B-A-B nanofiber solution. The mixture was then aged at room temperature for 1 h before analysis by TEM imaging to confirm the resulting geometry of the hybrid B-A-B nanofibers.

Preparation of hybrid C-A-C nanofibers

In an example protocol, 20 μL of 0.1 mg mL^{-1} QRs solution (water) was added dropwise to 500 μL of a 0.1 mg mL^{-1} solution of C-A-C segmented nanofibers in H_2O:MeOH (1:1, v/v) under stir (250 rpm), resulting in a final 4 wt.% hybrid C-A-C nanofiber solution. The mixture was then aged at room temperature for 1 h before analysis by TEM imaging to confirm the resulting geometry of the hybrid C-A-C nanofibers.

Preparation of hybrid C-B-A-B-C nanofibers

In an example protocol, 20 μL of 0.1 mg mL^{-1} QDs solution (water) and 20 μL of 0.1 mg mL^{-1} QRs solution (water) was sequentially added dropwise to 500 μL of a 0.1 mg mL^{-1} solution of C-B-A-B-C segmented nanofibers in THF:MeOH (1:1, v/v) under stir (250 rpm), resulting in a final hybrid C-B-A-B-C nanofiber solution. The mixture was then aged at room temperature for 1 h before analysis by TEM imaging to confirm the resulting geometry of the hybrid C-B-A-B-C nanofibers.

Calculations of the Förster radius (R_0)

The Förster radius (R_0) of triblock C-A-C nanofiber and CdSe QR was calculated following the equation below:[41,59]

$$R_0 = \frac{9\eta\boldsymbol{\kappa}^2}{128\pi^5 n^4}\int \lambda^4 F_D(\lambda)\sigma_A(\lambda)\, d\lambda \qquad (2)$$

Where η is the emission efficiency of the triblock C-A-C nanofiber from the energy donor (measured to be 73±10%), $\boldsymbol{\kappa}$ is the dipole-dipole orientation factor taken to be $\sqrt{2/3}$ for a randomly orientated dynamic average, n is the refractive index of the donor medium taken to be 2.3±1,[60,61] $F_D(\lambda)$ is the area normalized donor emission spectrum (see Figure 3b in the main text) and $\sigma_A(\lambda)$ is obtained by normalizing our experimental spectra to the literature crystal size dependent peak absorption coefficient.[62] Based on these, the Förster transfer radius (R_0) was calculated to be 4.93 nm.

3.5.6. Supplementary Figures

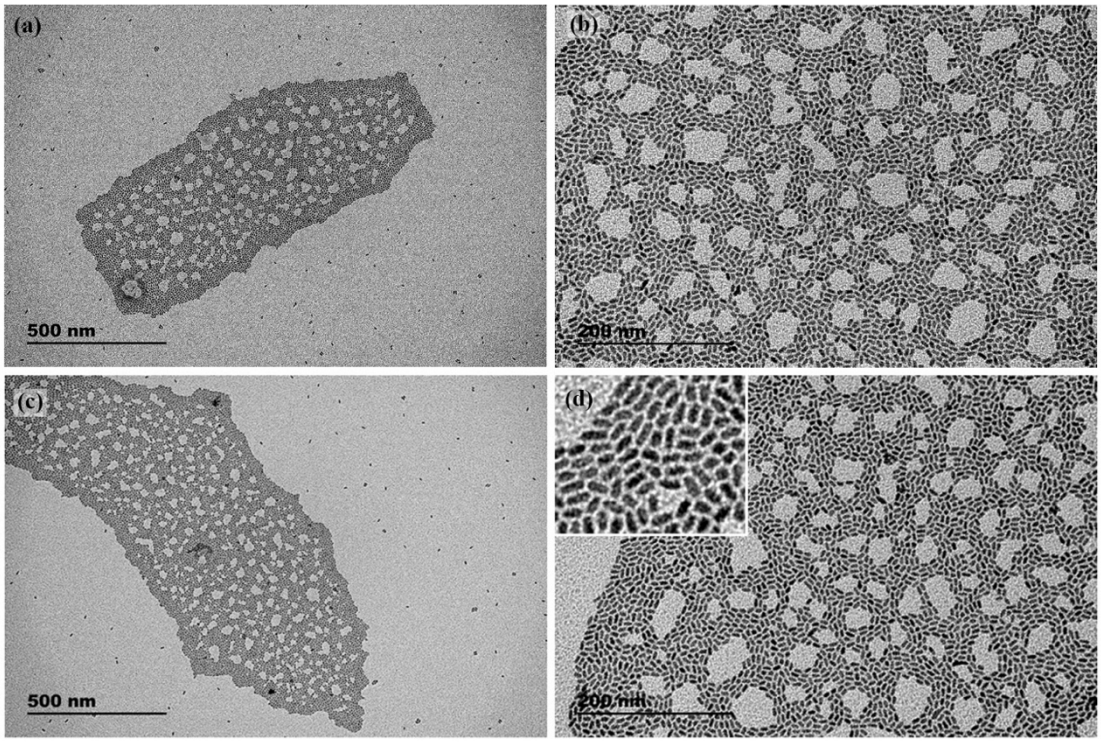

Figure S3. 9: (a), (b) Bright-field TEM images of synthesized CdSe QRs. The CdSe QRs have dimensions of 12 ± 2 nm in length, and 4 ± 1 nm in width. (c), (d) Bright-field TEM images of MOA-CdSe QRs, indicating no observable change after ligand exchange process.

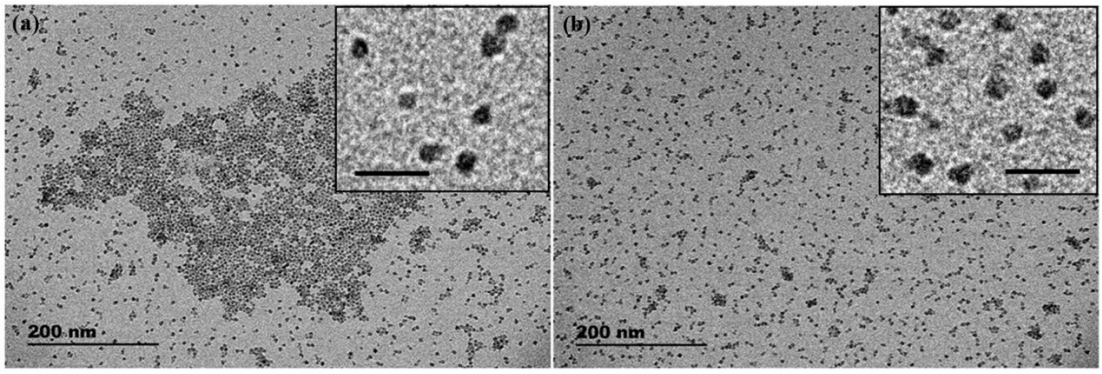

Figure S3. 10: (a) Bright-field TEM images of commercial CdSe QDs. The diameter of CdSe QDs is 4 ± 0.5 nm. Scale bar = 20 nm (inlet). (b) Bright-field TEM images of MUA-CdSe QDs, indicating no observable change after ligand exchange process. Scale bar = 20 nm (inset).

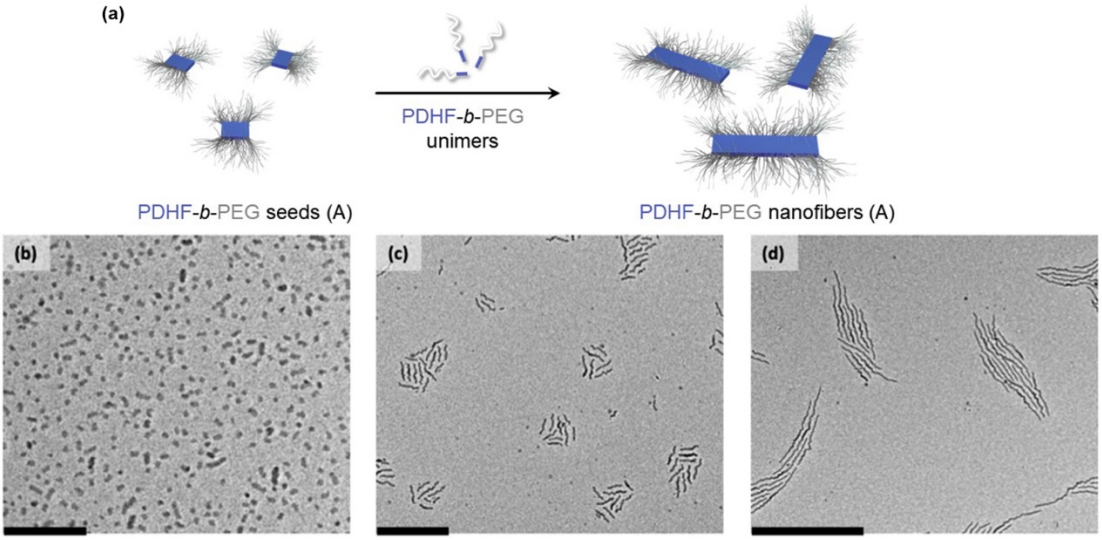

Figure S3. 11: Schematic illustration of the seeded growth protocol employed to prepare monodisperse nanofibers of from $PDHF_{14}$-*b*-PEG_{227} block copolymers in THF: MeOH (1:1, v/v). TEM images of (b) seed nanofibers and (c), (d) monodisperse nanofibers of controlled length prepared by seeded growth of $PDHF_{14}$-*b*-PEG_{227} block copolymers. (b) L_n = 22 nm, L_w/L_n = 1.13. (c) (L_n = 109 nm, L_w/L_n = 1.09). (d) L_n = 497 nm, L_w/L_n = 1.05. Scale bars: (b) 250 nm, (c) 500 nm and (d) 1 μm.

Table S3. 2: Contour length data from TEM analysis of nanofibers prepared by seeded growth of $PDHF_{14}$-*b*-PEG_{227} from $PDHF_{14}$-*b*-PEG_{227} seed micelles (L_n = 45 nm, L_w/L_n = 1.11; L_n = 22 nm, L_w/L_n = 1.13) in THF: MeOH (1:1, v/v) using seeded growth. Seed micelles used for different seeded growth experiments are represented in the table as 0 equivalents of unimer-to seed.

	Unimer-to-Seed Ratio							
	Exp. 1					**Exp. 2**		
	0	**2**	**5**	**10**	**20**	**0**	**4**	**8**
L_n (nm)	45	102	227	497	935	22	109	254
L_w (nm)	50	112	242	523	987	25	119	269
L_w/L_n	1.11	1.09	1.07	1.05	1.06	1.13	1.09	1.06
σ (nm)	16	31	58	115	221	7	33	62
σ/ L_n	0.36	0.30	0.26	0.23	0.24	0.32	0.31	0.24

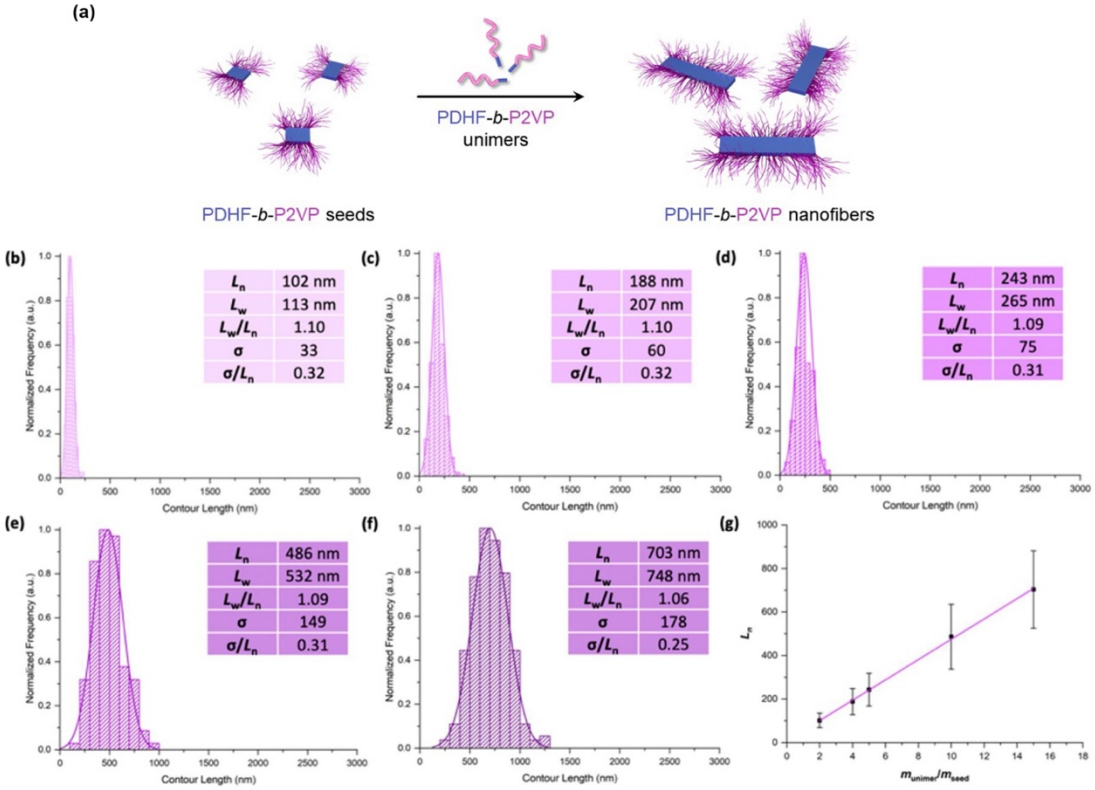

Figure S3. 12: Schematic illustration of the seeded growth protocol employed to prepare monodisperse nanofibers of $PDHF_{17}$-*b*-$P2VP_{250}$ block copolymers in THF: MeOH (1:1, v/v). Histograms representing contour length distributions of nanofibers prepared by the seeded growth of $PDHF_{17}$-*b*-$P2VP_{250}$ with m_{unimer}/m_{seed} values of (b) 2, (c) 4, (d) 5, (e) 10 and (f) 15. (g) Graph of micelle length (L_n) against unimer-to-seed ratio (m_{unimer}/m_{seed}) showing a linear correlation.

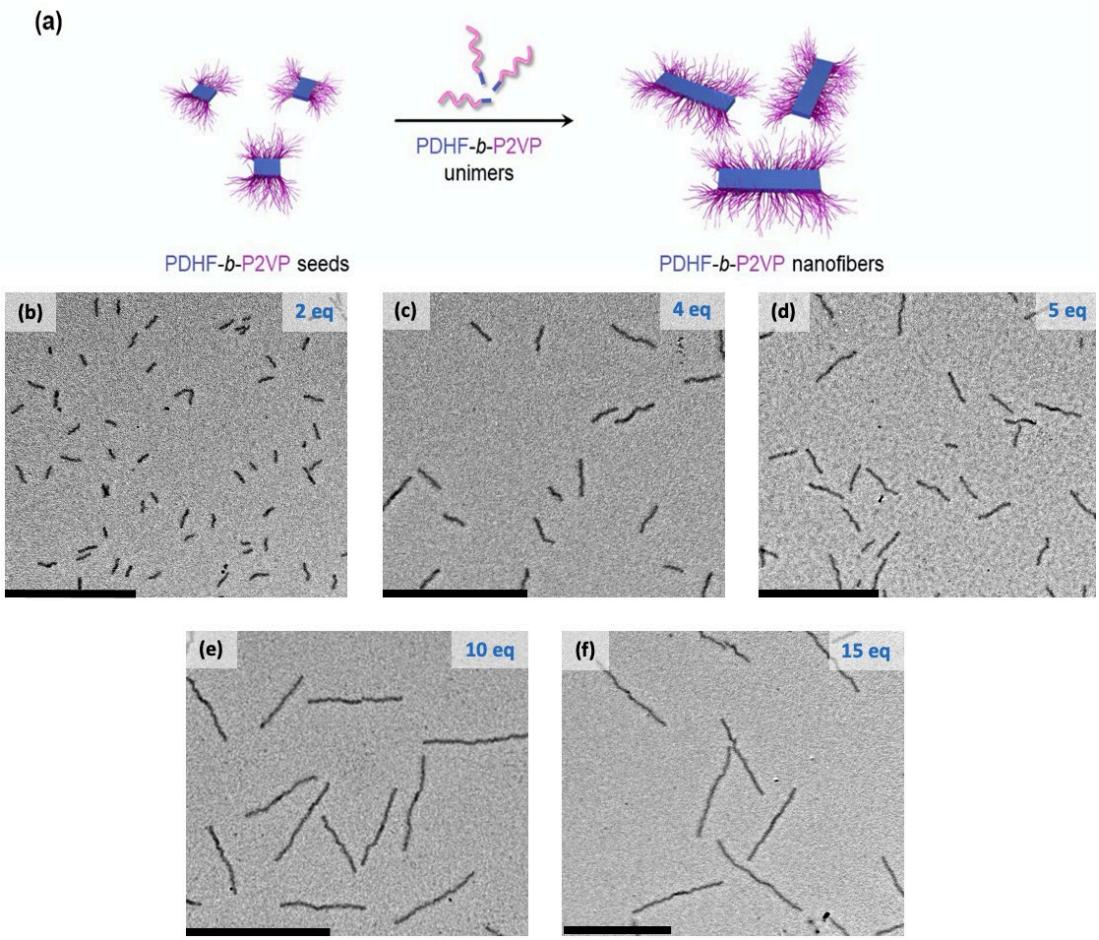

Figure S3. 13: Schematic illustration of the seeded growth protocol employed to prepare monodisperse nanofibers of $PDHF_{17}$-*b*-$P2VP_{250}$ in THF: MeOH (1:1, v/v). Bright-field TEM images of nanofibers prepared by the seeded growth of $PDHF_{17}$-*b*-$P2VP_{250}$ with m_{unimer}/m_{seed} values of (b) 2, (c) 4, (d) 5, (e) 10 and (f) 15. Scale bars: 1 μm.

Table S3. 3: Contour length data from TEM analysis of nanofibers prepared by seeded growth of $PDHF_{17}$-*b*-$P2VP_{250}$ from $PDHF_{17}$-*b*-$P2VP_{250}$ seed micelles (L_n = 40 nm, L_w/L_n = 1.15) in THF:MeOH (1:1, v/v) using seeded growth. Seed micelles used for the seeded growth experiment are represented in the table as 0 equivalents of unimer-to seed.

	Unimer-to-Seed Ratio					
	0	**2**	**4**	**5**	**10**	**15**
L_n **(nm)**	40	102	188	243	486	703
L_w **(nm)**	46	113	207	265	532	748
L_w/L_n	1.15	1.10	1.10	1.09	1.09	1.06
σ (nm)	15	33	60	75	149	178
σ/ L_n	0.38	0.32	0.32	0.31	0.31	0.25

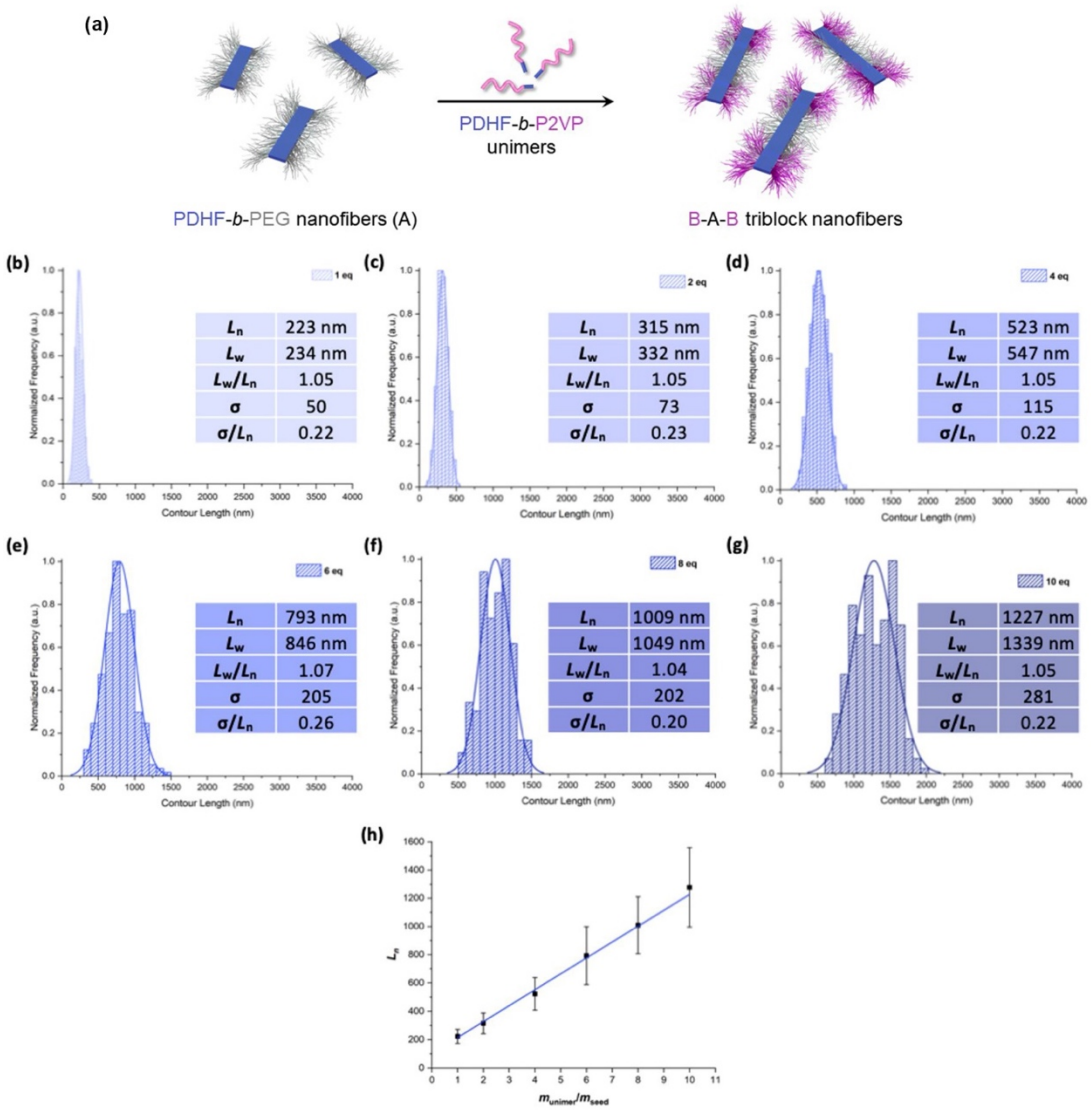

Figure S3. 14: Schematic illustration of the seeded growth protocol employed to prepare monodisperse B-A-B nanofibers of $PDHF_{17}$-*b*-$P2VP_{250}$ (B) from $PDHF_{14}$-*b*-PEG_{227} (A) in THF: MeOH (1:1, v/v). Histograms representing contour length distributions of nanofibers prepared by the seeded growth of $PDHF_{17}$-*b*-$P2VP_{250}$ with m_{unimer}/m_{seed} values of (b) 1, (c) 2, (d) 4, (e) 6, (f) 8 and (g) 10. (h) Graph of micelle length (L_n) against unimer-to-seed ratio (m_{unimer}/m_{seed}) showing a linear correlation.

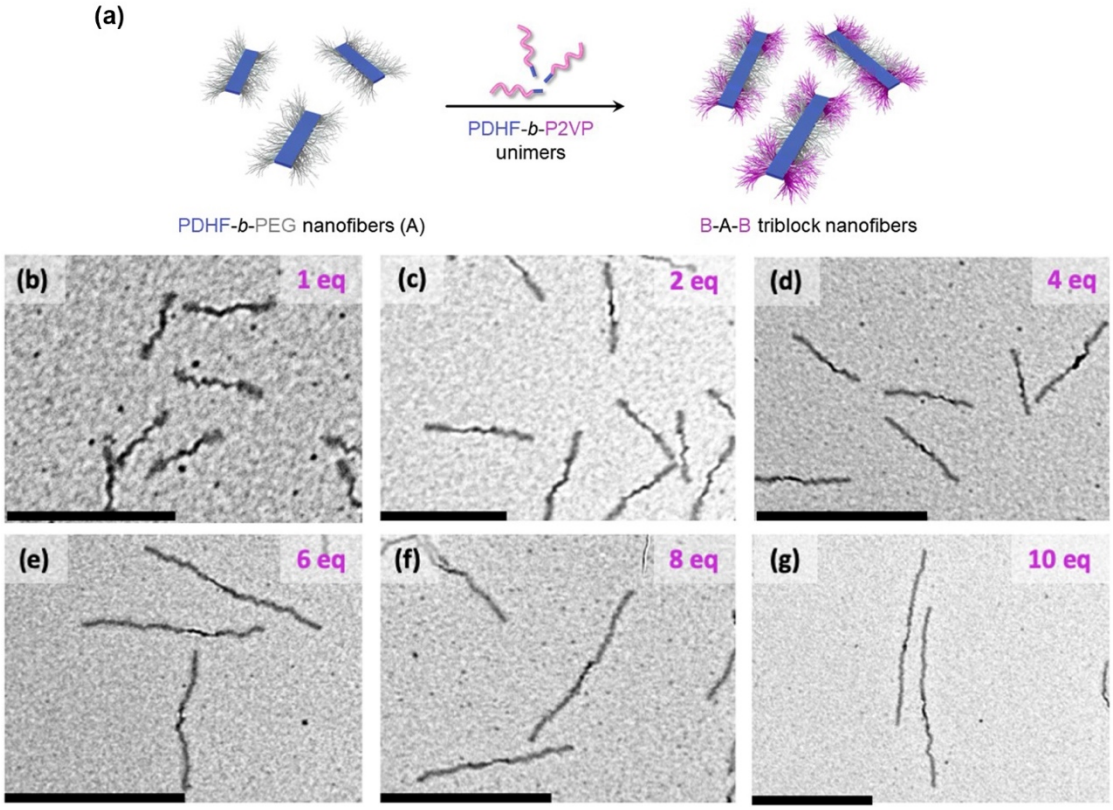

Figure S3. 15: Schematic illustration of the seeded growth protocol employed to prepare monodisperse B-A-B nanofibers of $PDHF_{17}$-*b*-$P2VP_{250}$ from $PDHF_{14}$-*b*-PEG_{227} in THF: MeOH (1:1, v/v). TEM images of nanofibers prepared by the seeded growth of $PDHF_{17}$-*b*-$P2VP_{250}$ with m_{unimer}/m_{seed} values of (b) 1, (c) 2, (d) 4, (e) 6, (f) 8 and (g) 10. Scale bars: (b)-(c) 500 nm and (d)-(g) 1 μm.

Table S3. 4: Contour length data from TEM analysis of nanofibers prepared by seeded growth of $PDHF_{17}$-*b*-$P2VP_{250}$ from $PDHF_{17}$-*b*-PEG_{227} seed micelles (L_n = 109 nm, L_w/L_n = 1.09) in THF: MeOH (1:1, v/v) using seeded growth. Seed micelles used for the seeded growth experiment are represented in the table as 0 equivalents of unimer-to seed.

	Unimer-to-Seed Ratio						
	0	**1**	**2**	**4**	**6**	**8**	**10**
L_n **(nm)**	109	223	315	523	793	1009	1277
L_w **(nm)**	119	234	332	547	846	1049	1339
L_w/L_n	1.09	1.05	1.05	1.05	1.07	1.04	1.05
σ (nm)	33	50	73	115	205	202	281
σ/ L_n	0.31	0.22	0.23	0.22	0.26	0.20	0.22

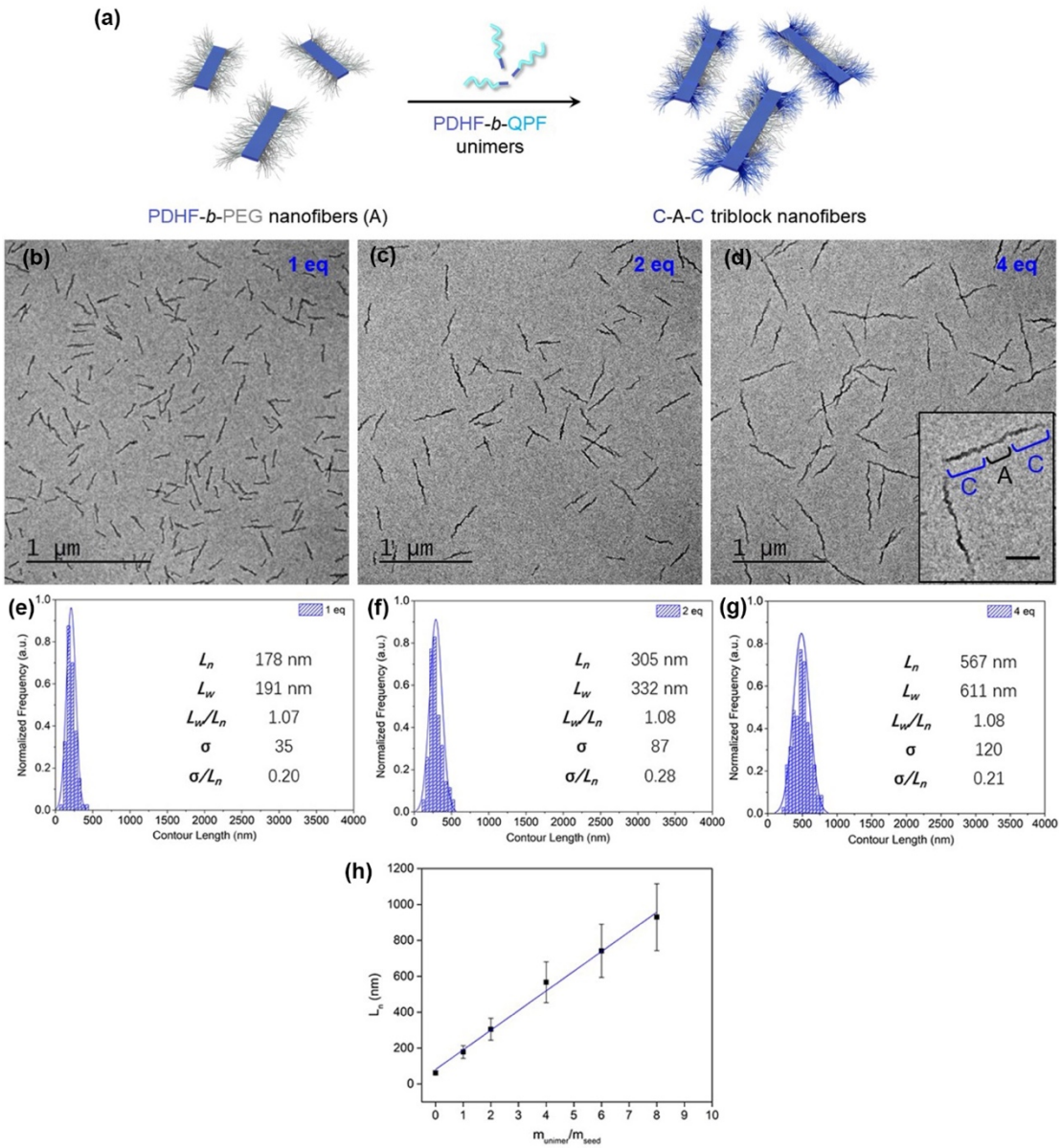

Figure S3. 16: (a) Schematic illustration of the seeded growth protocol employed to prepare monodisperse B-A-B nanofibers of $PDHF_{15}$-*b*-QPF_{16} from $PDHF_{14}$-*b*-PEG_{227} in THF: MeOH (1:1, v/v). Bright-field TEM images of nanofibers prepared by the seeded growth of $PDHF_{17}$-*b*-QPF_{16} with m_{unimer}/m_{seed} values of (b) 1, (c) 2, (d) 4. Scale bar = 200 nm (inset). Histograms representing contour length distributions of nanofibers prepared by the seeded growth of $PDHF_{15}$-*b*-QPF_{16} with m_{unimer}/m_{seed} values of (e) 1, (f) 2, and (g) 4. (h) Graph of micelle length (L_n) against unimer-to-seed ratio (m_{unimer}/m_{seed}) showing a linear correlation.

Table S3. 5: Contour length data from TEM analysis of nanofibers prepared by seeded growth of $PDHF_{15}$-*b*-QPF_{16} from $PDHF_{17}$-*b*-PEG_{227} seed micelles (L_n = 62 nm, L_w/L_n = 1.06) in THF: EtOH (1:1, v/v) using seeded growth. Seed micelles used for the seeded growth experiment are represented in the Table as 0 equivalents of unimer-to seed.

	Unimer-to-Seed Ratio					
	0	**1**	**2**	**4**	**6**	**8**
L_n **(nm)**	62	178	305	567	742	936
L_w **(nm)**	66	191	332	611	801	1011
L_w/L_n	1.06	1.07	1.08	1.08	1.08	1.08
σ (nm)	15	35	87	120	195	234
σ/ L_n	0.24	0.20	0.28	0.21	0.26	0.25

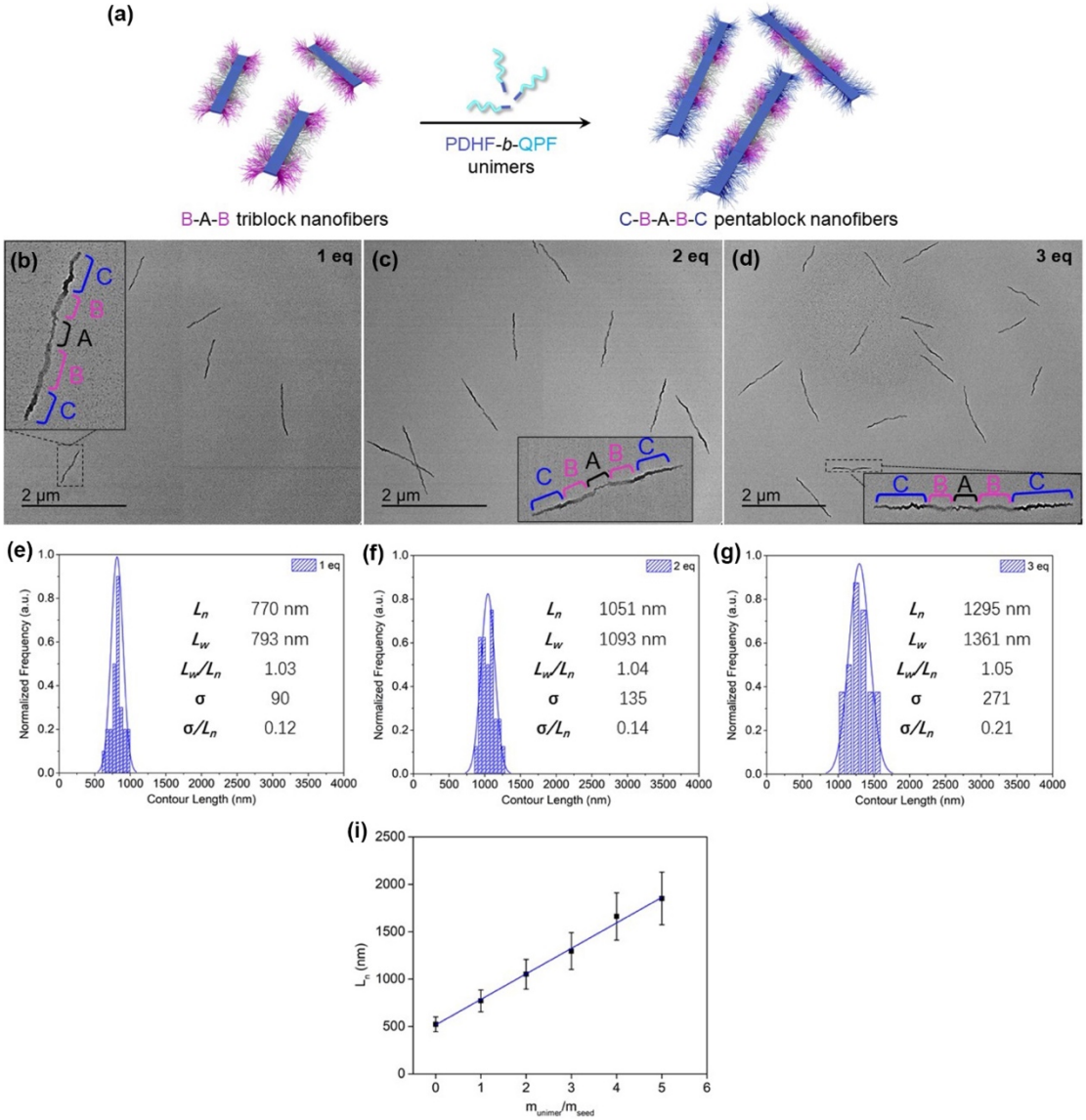

Figure S3. 17: (a) Schematic illustration of the seeded growth protocol employed to prepare monodisperse C-B-A-B-C nanofibers of $PDHF_{15}$-*b*-QPF_{16} from B-A-B seeds in THF: MeOH (1:1, v/v). TEM images of nanofibers prepared by the seeded growth of $PDHF_{17}$-*b*-QPF_{16} with m_{unimer}/m_{seed} values of (b) 1, (c) 2, (d) 3. Histograms representing contour length distributions of nanofibers prepared by the seeded growth of $PDHF_{15}$-*b*-QPF_{16} with m_{unimer}/m_{seed} values of (e) 1, (f) 2, and (g) 3. (h) Graph of micelle length (L_n) against unimer-to-seed ratio (m_{unimer}/m_{seed}) showing a linear correlation.

Table S3. 6: Contour length data from TEM analysis of nanofibers prepared by seeded growth of $PDHF_{15}$-*b*-QPF_{16} from C-B-A-B-C seed micelles (L_n = 523 nm, L_w/L_n = 1.05) in THF: EtOH (1:1, v/v) using seeded growth. Seed micelles used for the seeded growth experiment are represented in the table as 0 equivalents of unimer-to-seed.

	Unimer-to-Seed Ratio					
	0	**1**	**2**	**3**	**4**	**5**
L_n **(nm)**	523	770	1051	1295	1661	1851
L_w **(nm)**	547	793	1093	1361	1768	1962
L_w/L_n	1.05	1.03	1.04	1.05	1.06	1.06
σ (nm)	115	90	135	271	382	407
σ/ L_n	0.22	0.12	0.14	0.21	0.23	0.22

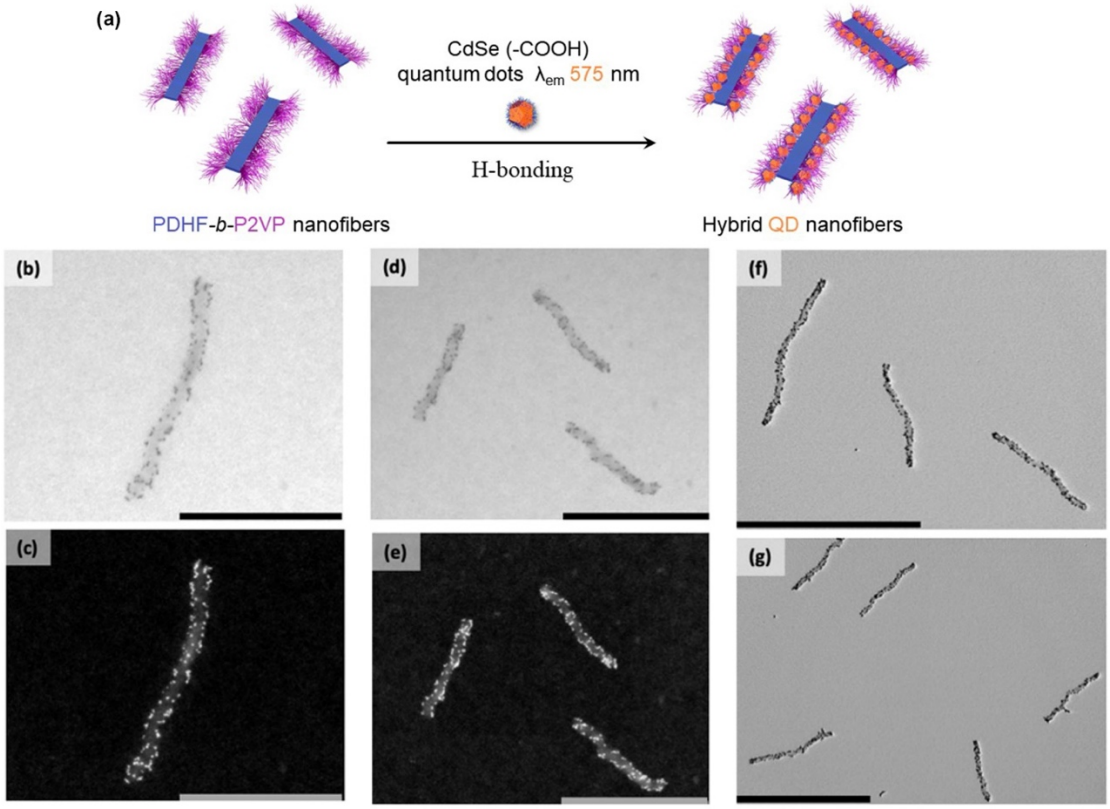

Figure S3. 18: (a) Schematic illustration of the decoration of monodisperse $PDHF_{17}$-*b*-$P2VP_{250}$ nanofibers with CdSe QDs (λ_{em}=575 nm). (b), (d) Bright-Field STEM and (c), (e) Low-Angle Annular Dark-Field (LAADF) STEM images of CdSe QDs decorated $PDHF_{17}$-*b*-$P2VP_{250}$ nanofibers (L_n = 377 nm, L_w/L_n = 1.10). (f), (g) TEM images of CdSe QDs decorated $PDHF_{17}$-*b*-$P2VP_{250}$ nanofibers (L_n = 653 nm, L_w/L_n = 1.10). Scale bars (b) and (c): 300 nm; (d) and (e) 400 nm; (f) and (g) 1 μm.

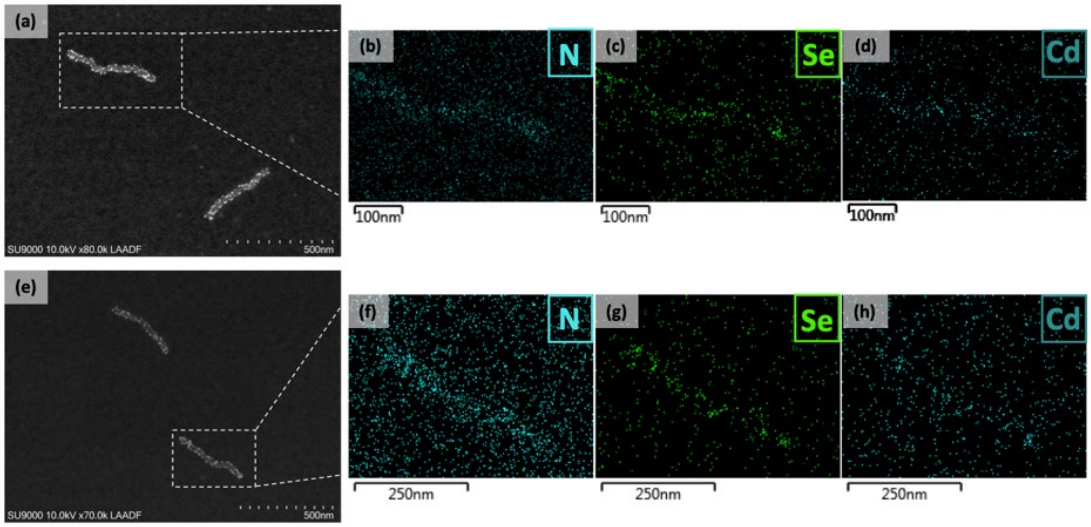

Figure S3. 19: (a), (e) LAADF STEM images of CdSe QDs decorated PDHF$_{17}$-*b*-P2VP$_{250}$ nanofibers (L_n = 377 nm, L_w/L_n = 1.10). SEM-EDS mapping images of the elementary distribution of (b), (f) Nitrogen, (c), (g) Selenium and (d), (h) Cadmium.

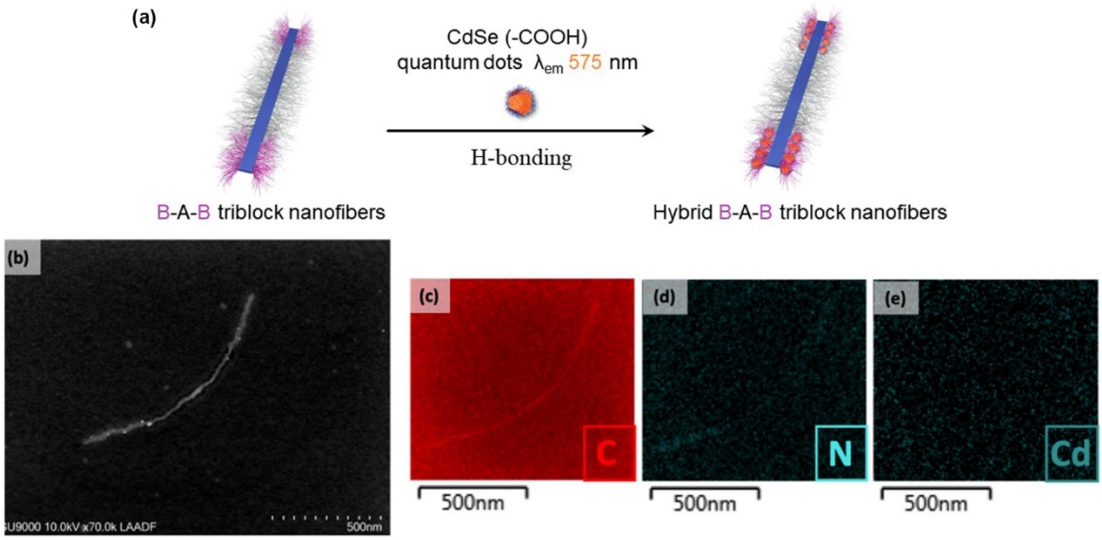

Figure S3. 20: (a) Schematic illustration of the decoration of monodisperse B-A-B nanofibers with CdSe QDs (λ_{em}=575 nm). (b) LAADF STEM images of CdSe QDs decorated B-A-B nanofibers (A: L_n = 497 nm, L_w/L_n = 1.05; B-A-B: L_n = 823 nm, L_w/L_n = 1.06). SEM-EDS mapping images of the elementary distribution of (c) Carbon, (d) Nitrogen and (e) Cadmium. The SEM-EDS mapping image of Cadmium is below the detection limit for the CdSe QDs.

Table S3. 7: Photoluminescence quantum yield (PLQY) measurements of different materials.

Material	PLQY (405 nm excitation)
CdSe QRs[+]	0.4±0.1 %
Hybrid C-A-C nanofibers[+]	1.5±0.1 %
Rhodamine 6G solution*	54±3 %

[+] the emission wavelength range used to calculate the PLQY is 580-650 nm, where there is negligible PL emission from PDHF. * Rhodamine 6G ethanol solution is used for reference.

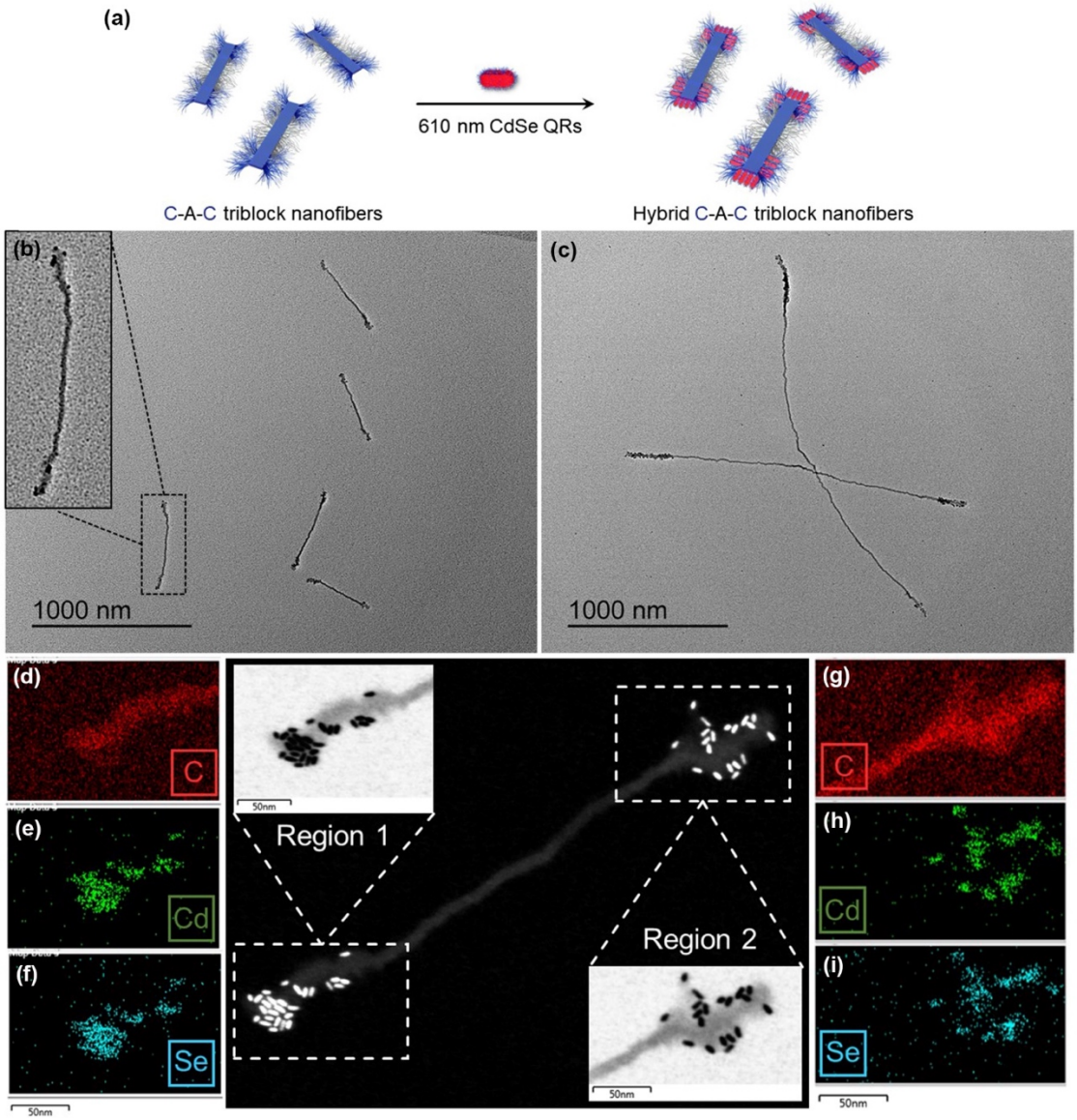

Figure S3. 21: (a) Schematic illustration of the decoration of monodisperse C-A-C nanofibers with CdSe QRs (λ_{em} = 610 nm). Bright-field TEM images of hybrid C-A-C nanofibers (b, A: L_n = 330 nm, L_w/L_n = 1.06; C-A-C: L_n = 510 nm, L_w/L_n = 1.06, c, A: L_n = 2110 nm, L_w/L_n = 1.06; C-A-C: L_n = 2285 nm, L_w/L_n = 1.07). LAADF STEM and SEM-EDS mapping images of hybrid C-A-C nanofibers (A: L_n = 330 nm, L_w/L_n = 1.06; C-A-C: L_n = 510 nm, L_w/L_n = 1.06). Elementary distribution of (d), (g), Carbon, (e), (h), Cadmium, and (f), (i), Selenium in region 1, 2 of the hybrid C-A-C nanofiber, respectively.

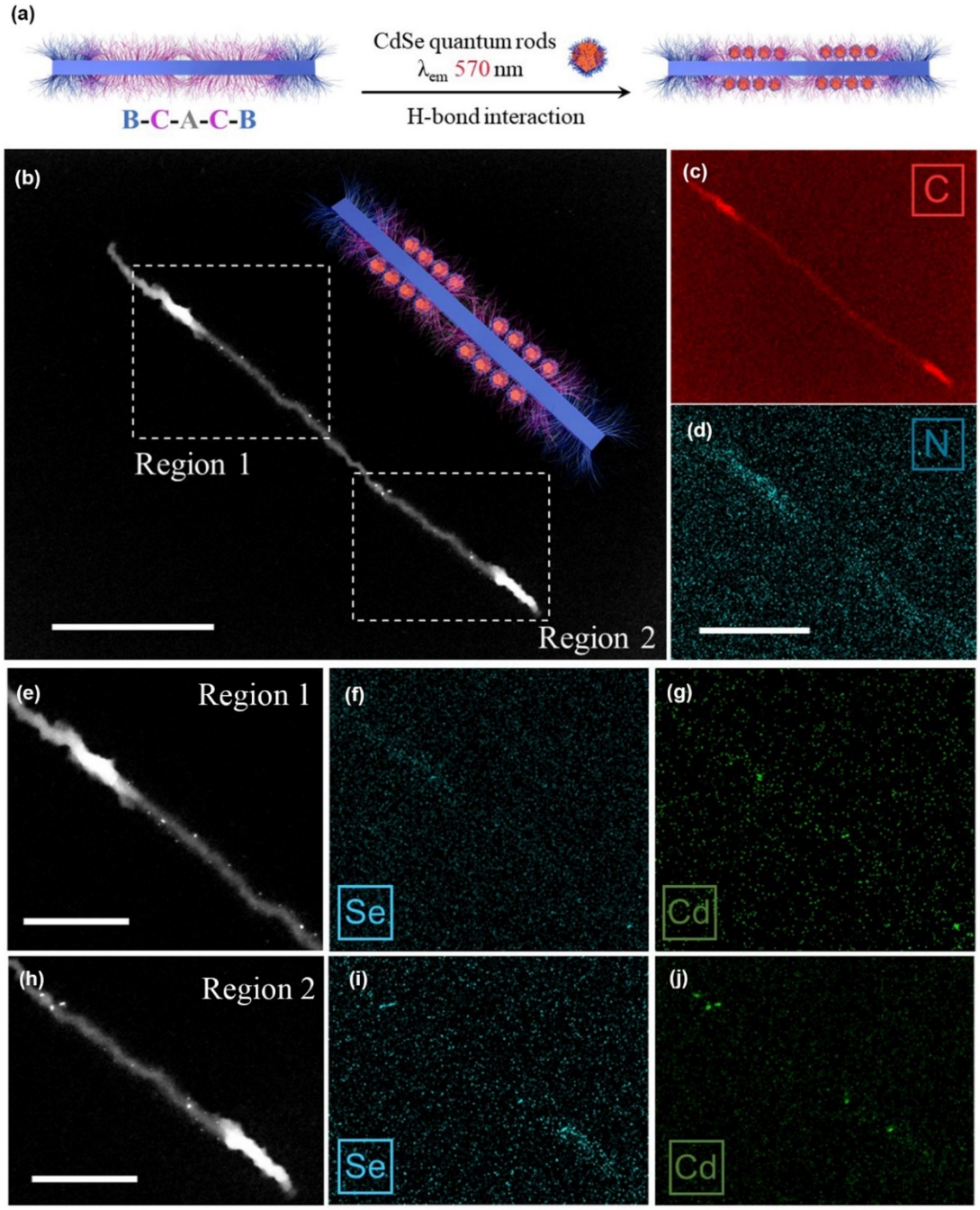

Figure S3. 22: (a) Schematic illustration of the selective decoration of monodisperse C-B-A-B-C nanofibers with CdSe QDs (λ_{em} = 570 nm) on B segments. (b), (e), (h) LAADF STEM images of a typical hybrid C-B-A-B-C nanofiber (A: L_n = 109 nm, L_w/L_n = 1.06; B-A-B: L_n = 793 nm, L_w/L_n = 1.07, C-B-A-B-C: L_n = 1135 nm, L_w/L_n = 1.07). Scale bar = 300 nm (b), 100 nm (e), (h). SEM-EDS elementary distribution mapping images of (c) Carbon and (d) Nitrogen of the hybrid C-B-A-B-C nanofiber. Scale bar = 300 nm. SEM-EDS elementary distribution mapping images of (f), (i), Selenium, and (g), (j), Cadmium in region 1 and 2 of the hybrid C-B-A-B-C nanofiber, respectively. Scale bar = 100 nm.

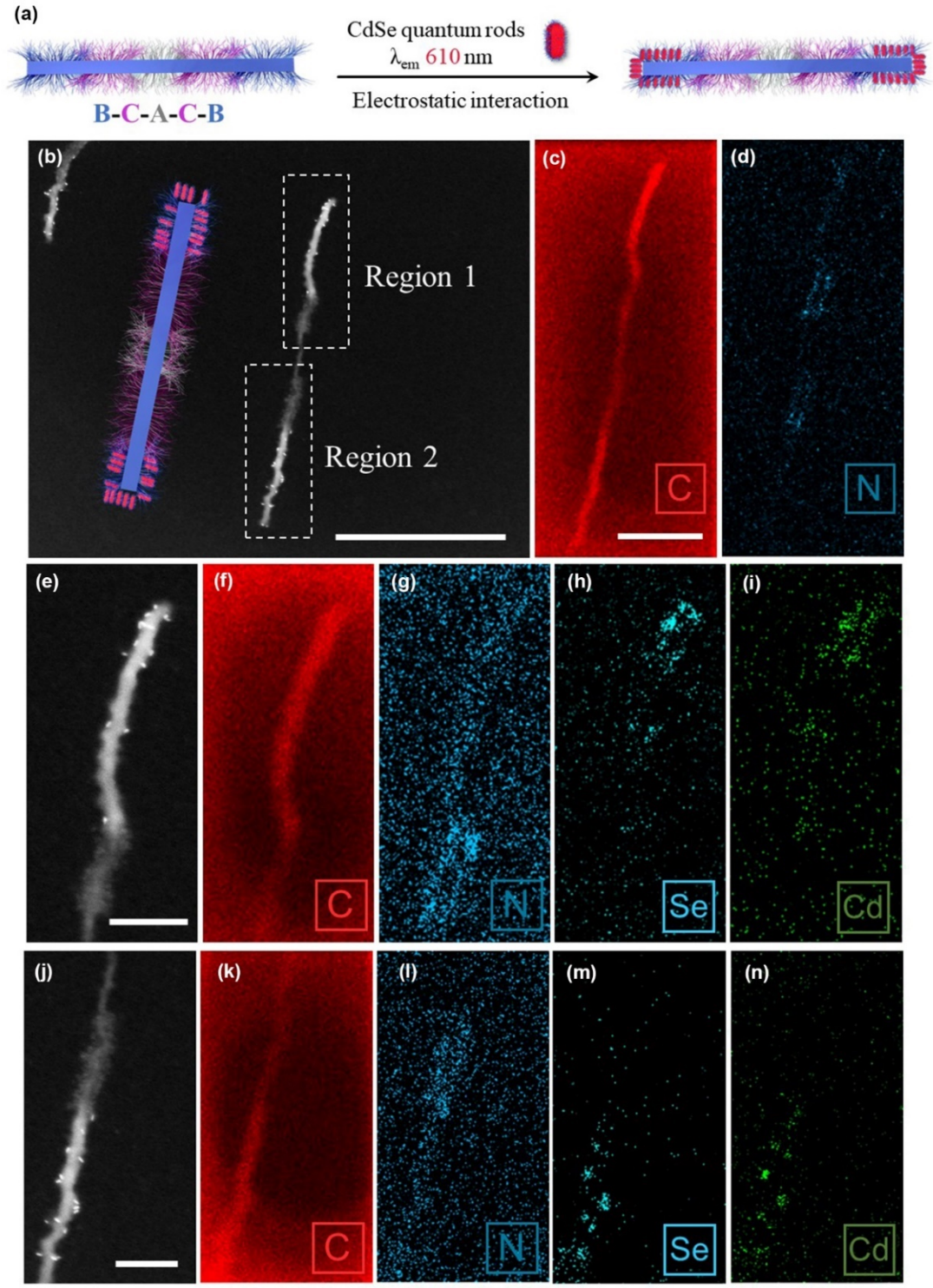

Figure S3. 23: (a) Schematic illustration of the selective decoration of monodisperse C-B-A-B-C nanofibers with CdSe QRs (λ_{em} = 610 nm) on C segments. (b), (e), (j), LAADF STEM images of a typical hybrid C-B-A-B-C nanofibers (A: L_n = 109 nm, L_w/L_n = 1.06; B-A-B: L_n = 315 nm, L_w/L_n = 1.06, C-B-A-B-C: L_n = 615 nm, L_w/L_n = 1.07). Scale bar = 300 nm (a), 100 nm (e), (j). SEM-EDS mapping elementary distribution images of (c) Carbon and (d) Nitrogen of the hybrid C-B-A-B-C nanofiber. Scale bar = 100 nm. SEM-EDS elementary distribution mapping images of (f), (k), Carbon, (g), (i), Nitrogen, (h), (m), Selenium, and (i), (n), Cadmium in region 1 and 2 of the hybrid C-B-A-B-C nanofiber, respectively. Scale bar = 100 nm.

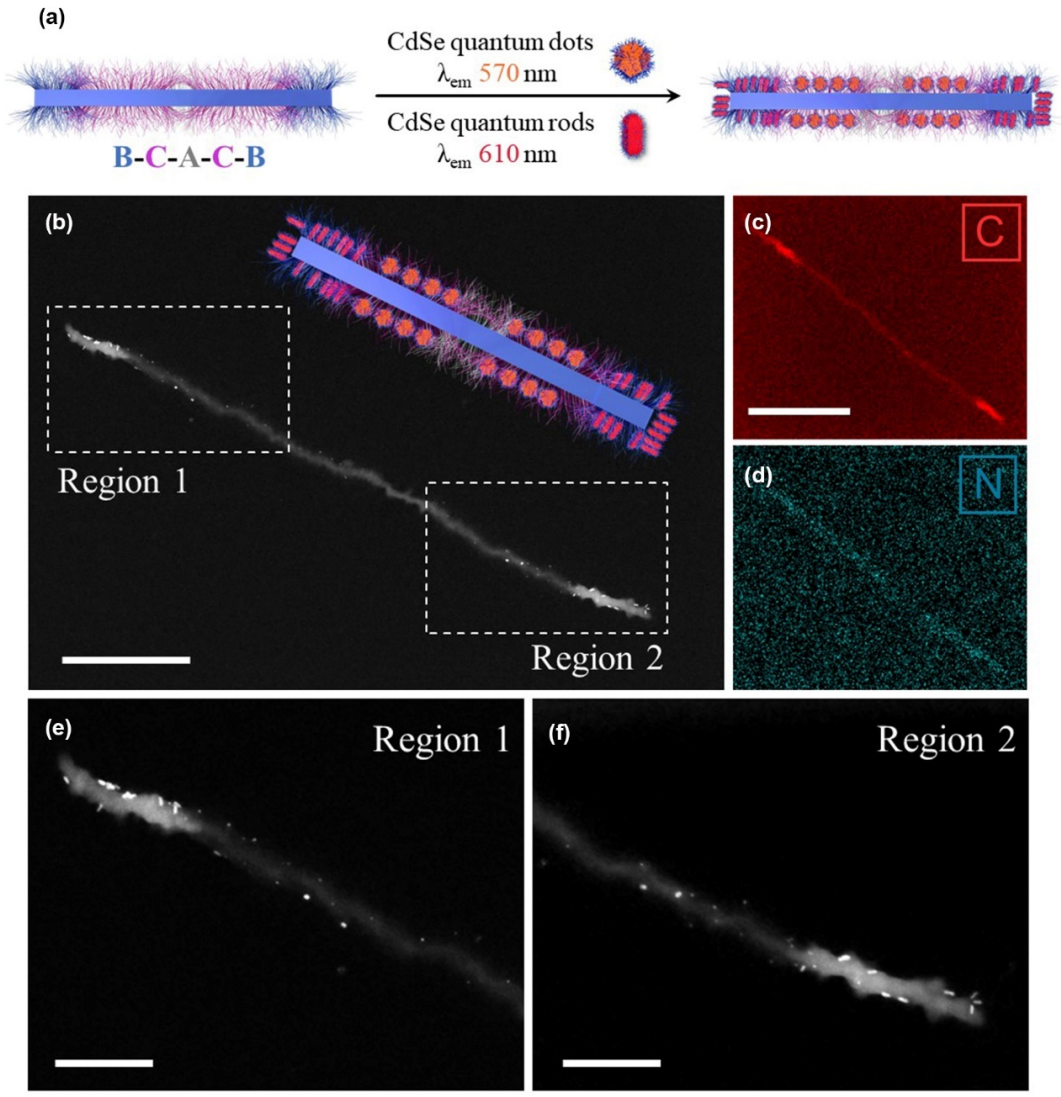

Figure S3. 24: (a) Schematic illustration of the selective decoration of monodisperse C-B-A-B-C nanofibers with CdSe QDs and QRs on different segments. (b), (e), (f) LAADF STEM image of a typical hybrid C-B-A-B-C nanofiber (A: L_n = 109 nm, L_n = 793 nm, L_w/L_n = 1.07, C-B-A-B-C: L_n = 1135 nm, L_w/L_n = 1.07). Scale bar = 300 nm (b), 100 nm (e), (f). SEM-EDS elementary distribution mapping images of (c) Carbon and (d) Nitrogen of the hybrid C-B-A-B-C nanofiber, showing the QDs and QRs attached to the B and C segments respectively. Scale bar = 100 nm.

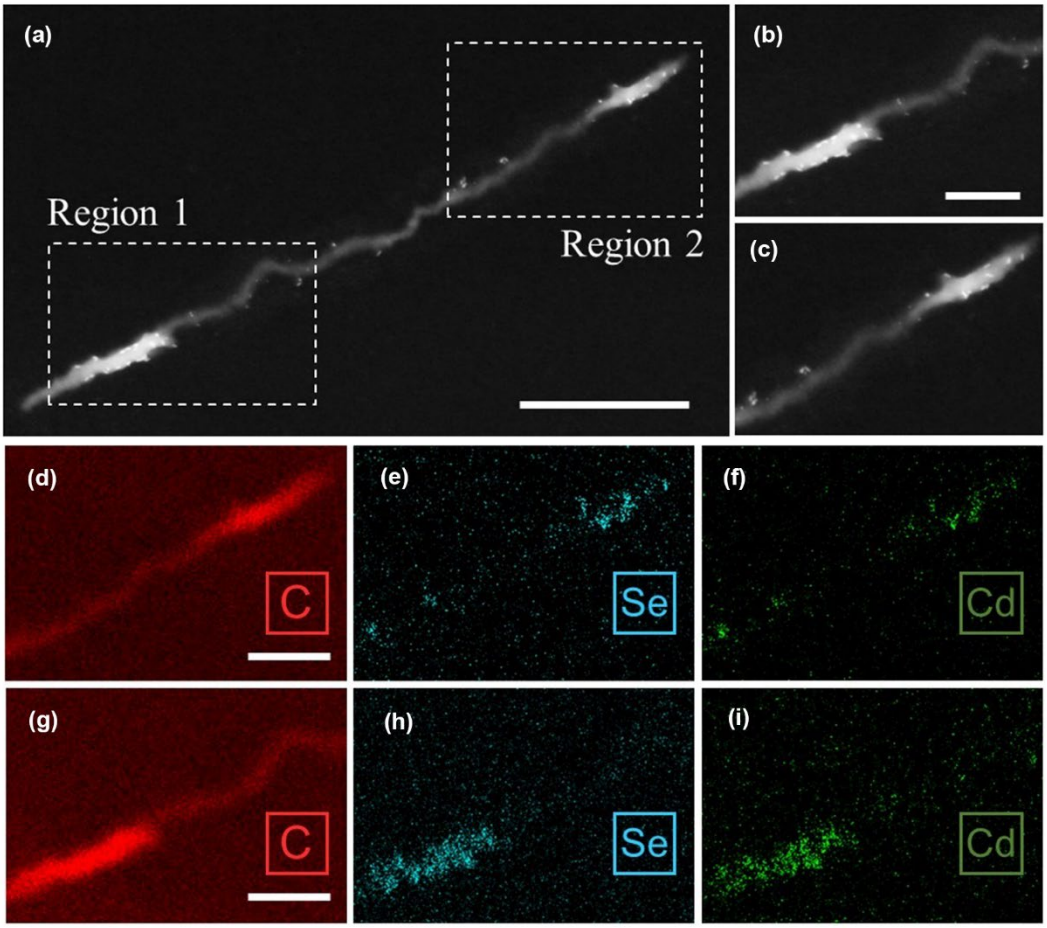

Figure S3. 25: (a), (b), (c) LAADF STEM images of a typical hybrid C-B-A-B-C nanofibers (A: L_n = 109 nm, L_n = 793 nm, L_w/L_n = 1.07, C-B-A-B-C: L_n = 1135 nm, L_w/L_n = 1.07). Scale bar = 300 nm (a), 100 nm (b, c). SEM-EDS elementary distribution mapping images of (d), (g), Carbon, (e), (h), Selenium, and (f), (i), Cadmium in region 1 and 2 of the hybrid C-B-A-B-C nanofiber, respectively. Scale bar = 100 nm.

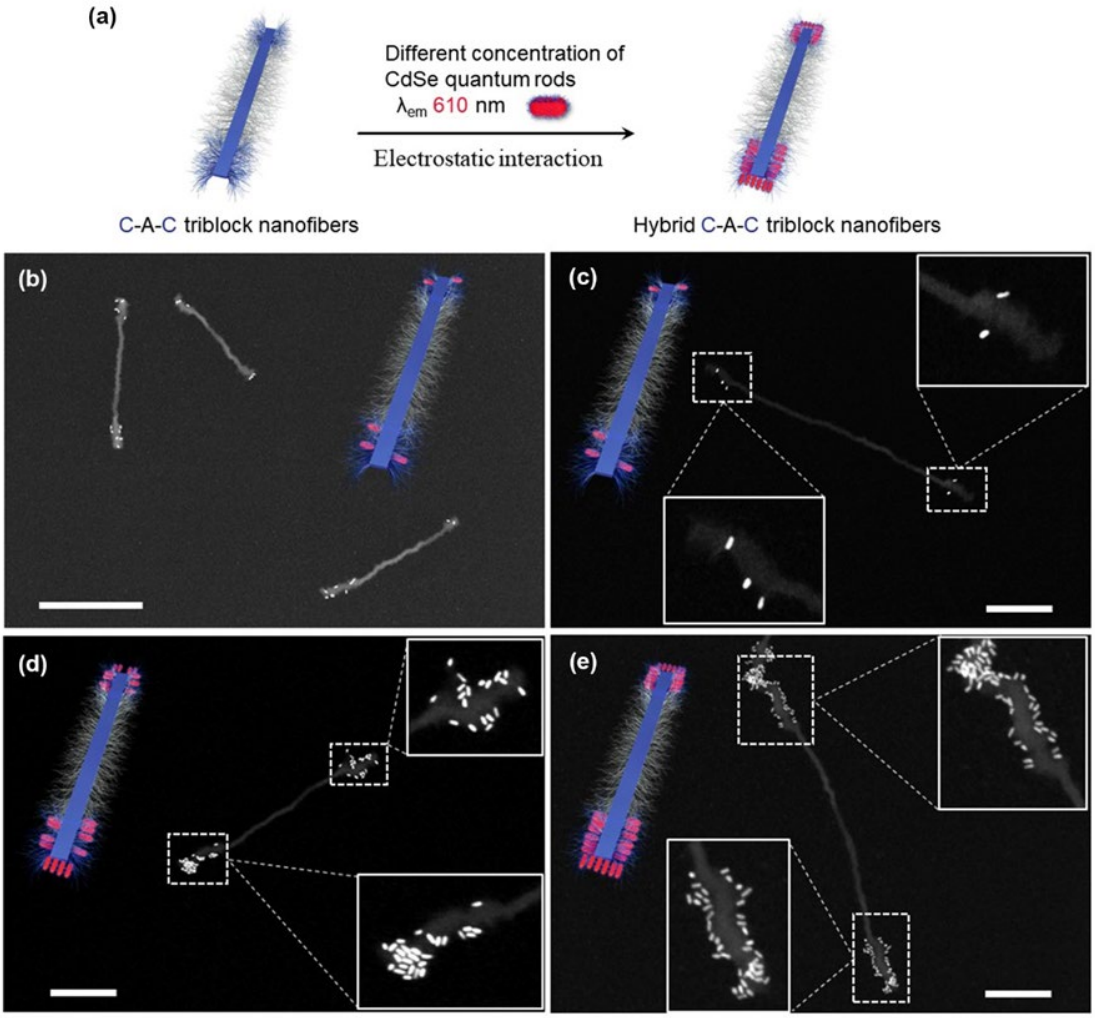

Figure S3. 26: (a) Schematic illustration of the decoration of monodisperse C-A-C nanofibers with CdSe QRs (λ_{em}=610 nm). (b) LAADF STEM images of CdSe QRs decorated triblock hybrid C-A-C nanofibers (L_n = 510 nm, L_w/L_n = 1.06). Scale bar, 500 nm. STEM images of the triblock hybrid C-A-C decorated nanofiber with different quantities of CdSe QRs prepared from (c) adding 2 µL, 1 mg mL^{-1} CdSe QRs in H_2O:EtOH (1:1, v/v) to 1 mL 0.1 mg mL^{-1} triblock hybrid C-A-C nanofiber, (d) adding 20 µL, 1 mg mL^{-1} CdSe QRs in H_2O:EtOH (1:1, v/v) to 1 mL 0.1 mg mL^{-1} triblock hybrid C-A-C nanofiber, and (e) adding 40 µL, 1 mg mL^{-1} CdSe QRs in H_2O:EtOH (1:1, v/v) to 1 mL 0.1 mg mL^{-1} triblock hybrid C-A-C nanofiber. Scale bar, 200 nm.

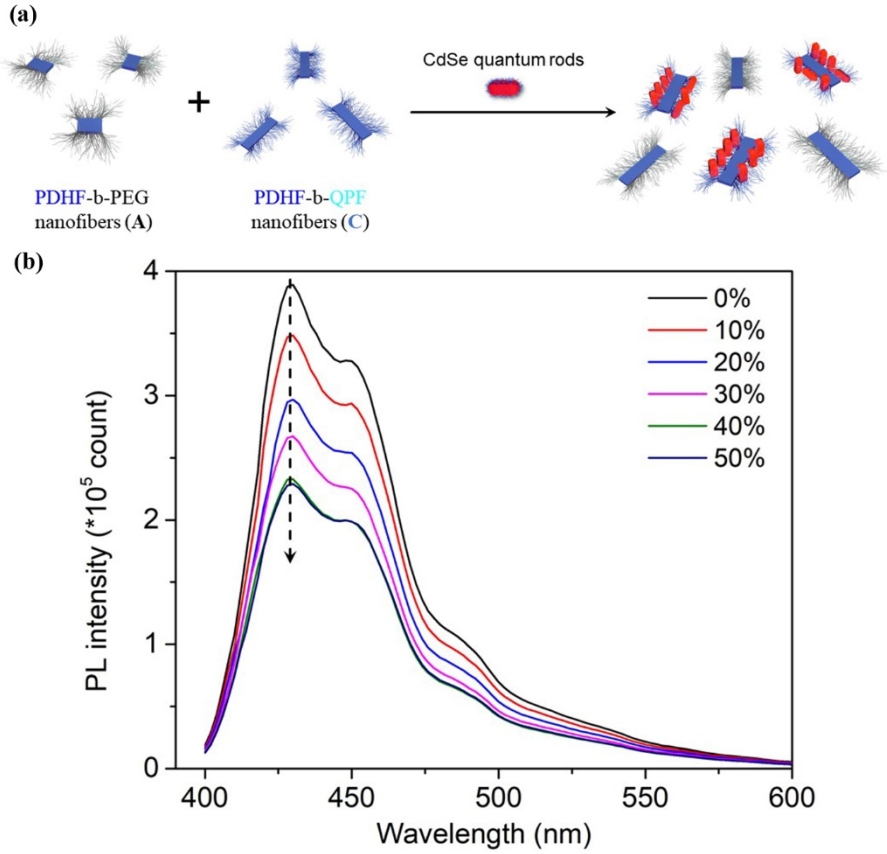

Figure S3. 27: (a) Schematic illustration of the addition of CdSe QRs to a mixture of PDHF-b-PEG (A) nanofibers and PDHF-*b*-QPF (C) nanofibers in Water: EtOH (1:1, v/v). (b) Fluorescence spectra of a mixture of PDHF-*b*-PEG nanofibers (L_n = 41 nm, L_w/L_n = 1.06) and PF-*b*-QPF nanofibers (L_n = 51 nm, L_w/L_n = 1.07) with different added amounts of CdSe QRs (0 to 50 wt. % relative to nanofibers), indicating the maximum quenching of PDHF crystalline core donor emission (40 %).

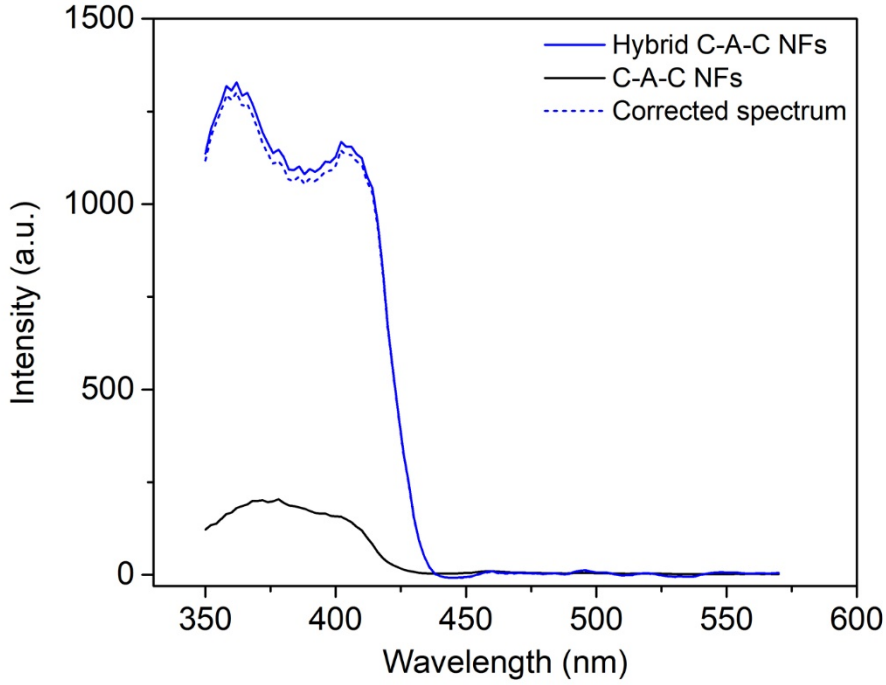

Figure S3. 28: PLE spectrum of hybrid C-A-C nanofibers (solid blue trace, 0.1 mg mL^{-1}) and a control sample of C-A-C triblock nanofibers (solid black trace, 0.1 mg mL^{-1}) without QRs attached as quenchers in H_2O:MeOH (1:1, v/v) detected at 610 nm emission. The spectrum shows that a proportion of the excitation spectrum of the hybrid C-A-C nanofibers originates from the direct emission of PDHF. As indicated in Figure 4a, the emission of PDHF from the hybrid C-A-C nanofiber samples can be quenched ca. 85%. This means the contribution of direct polyfluorene emission at 610 nm in PLE spectrum of hybrid C-A-C nanofibers equals to ca. 15% intensity of the PLE spectrum from the C-A-C nanofibers (0.1 mg mL^{-1}). The spectrum is corrected (dashed blue trace) by deduction of the direct emission from PDHF, which is used to calculate the absorption spectrum of effective hybrid C-A-C nanofibers in Figure 4d.

3.5.7. Transient-Absorption Spectroscopy of C-A-C Nanofibers

In this technique a pump pulse generates photoexcitations within the solutions, which are then probed at later times using a broadband probe pulse. Transient absorption spectra were recorded over short (-10 ps - 2 ns) time delays. The femtosecond transient absorption experiments are performed using a Yb-based amplifying system, Light Conversion PHAROS with 400 µJ per pulse at 1030 nm with a repetition rate of 38 kHz. The laser output is modified using a 4mm YAG substrate to produce the probe beam from 520 to 950 nm. Using a narrow band optical parametric oscillator system (ORPHEUS- LYRA, Light conversion) with 1030 nm seed, the pump beam is generated at 400 and 460 nm (full-width at half-maximum 250 fs). The probe pulse is delayed using a computer controlled mechanical delay-stage (Newport) and the on-off pump pulses are generated by means of a mechanical chopper (Thorlabs) before hitting the sample. The pump

and probe beams are focused with sizes 210x210 µm and 100x100 µm respectively, at the sample position. The probe pulse transmitted through the 1 mm sample cuvette is collected using a silicon line scan camera (AViiVA EM2/EM4) with a visible monochromator 550 nm blazed grating.

TA data of loaded and unloaded C-A-C nanofibers

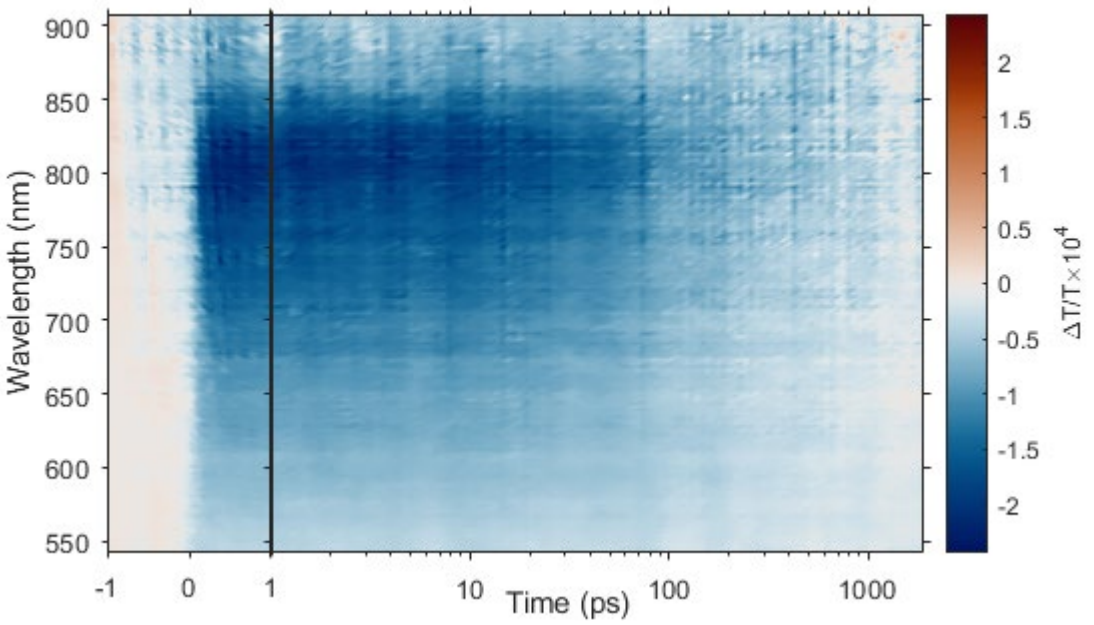

Figure S3. 29: TA map of unloaded C-A-C nanofibers (A: L_n = 87 nm, L_w/L_n = 1.05; C-A-C: L_n = 152 nm, L_w/L_n = 1.07). The pump wavelength is 400 nm, with an excitation fluence of 3μJ/cm^2. data has been background-corrected, chirp-corrected, and a bilateral filter with a Gaussian kernel has been used to remove excessive noise.

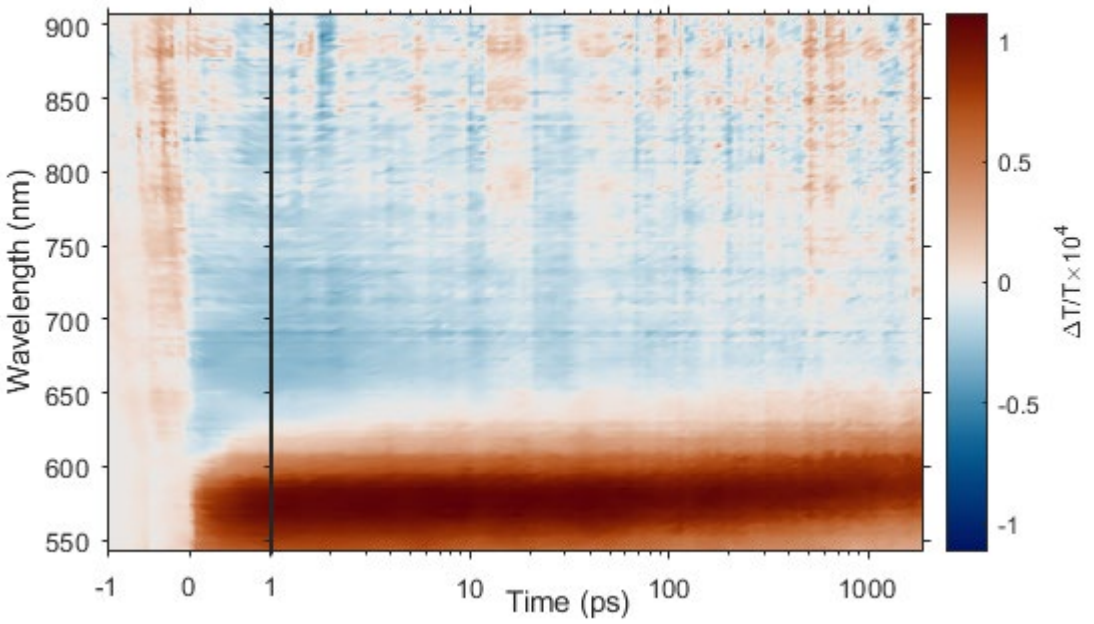

Figure S3. 30: TA map of C-A-C nanofibers (A: L_n = 87 nm, L_w/L_n = 1.05; C-A-C: L_n = 152 nm, L_w/L_n = 1.07) with 50 wt. % loading of CdSe QRs relative to nanofibers. The pump wavelength is 460 nm, with an excitation fluence of 4μJ/cm^2 to account for the lower absorption of the QRs at 460 nm versus 400 nm. This fluence results in roughly the same maximum QR exciton density being reached when the hybrid ensemble is excited at 400 nm. (see Figure S3. 31). The data has been background-corrected, chirp-corrected, and a bilateral filter with a Gaussian kernel has been used to remove excessive noise.

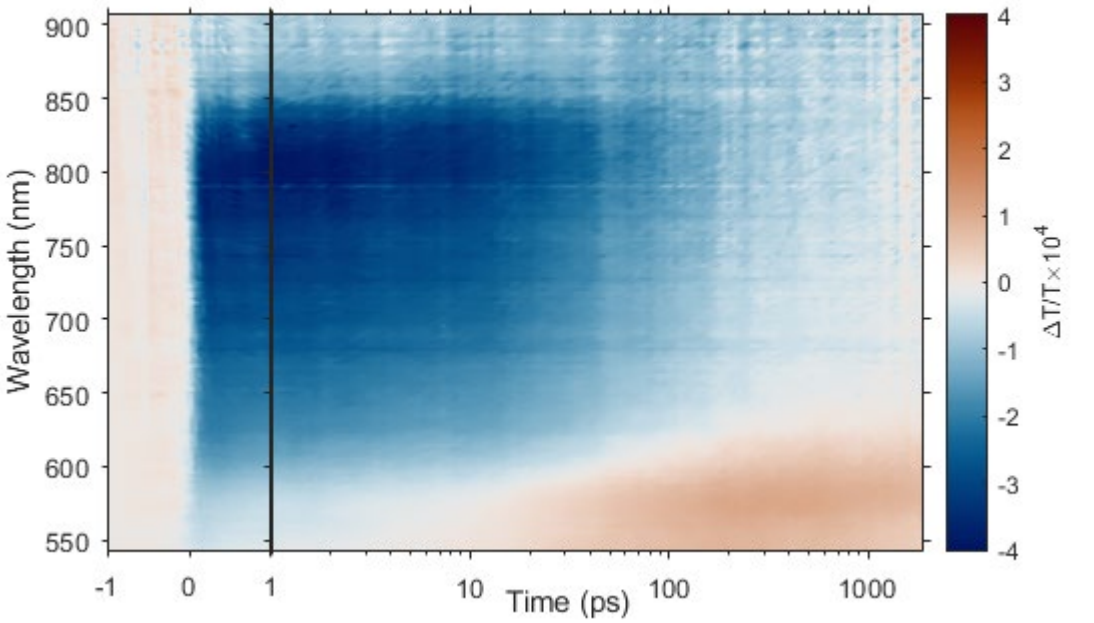

Figure S3. 31: TA map of C-A-C nanofibers (A: L_n = 87 nm, L_w/L_n = 1.05; C-A-C: L_n = 152 nm, L_w/L_n = 1.07) with 50 wt. % loading of CdSe QRs relative to nanofibers. The pump wavelength is 400 nm, with an excitation fluence of 3μJ/cm^2. The data has been background-corrected, chirp-corrected, and a bilateral filter with a Gaussian kernel has been used to remove excessive noise.

Modelling of energy transfer from TA data

To model the energy transfer in the TA data we employ a linear regression method for its simplicity, repeatability, ability to find global minima, and for the fact that it allows for the quantitative extraction of population kinetics. To begin, we find the individual spectra associated with the PDHF and QRs respectively – see Figure S3. 32.

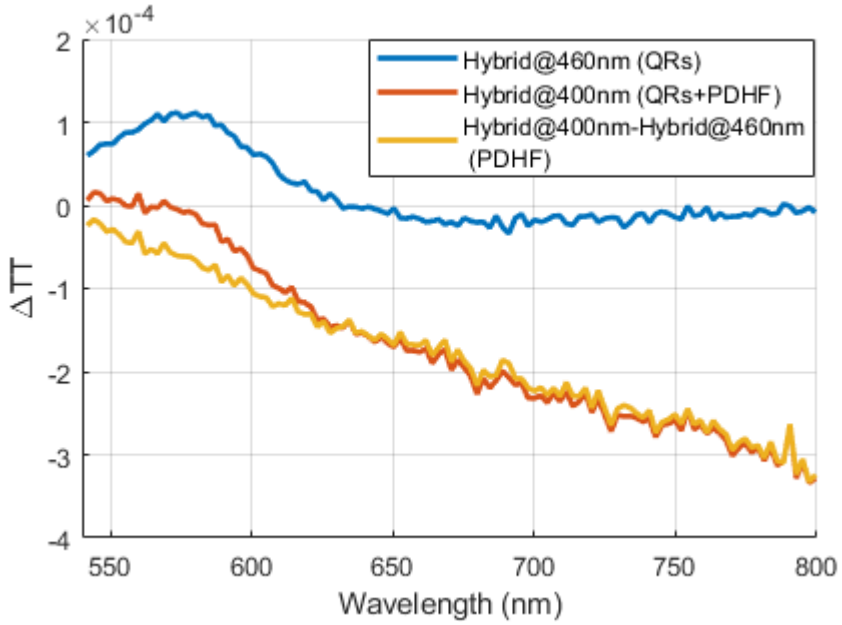

Figure S3. 32: Blue line: TA spectra (averaged from 1-50 ps) of hybrid ensemble excited at 460 nm (figure S30), giving the QR TA spectrum. Orange line: TA spectra (averaged from 1-50 ps) of hybrid ensemble excited at 400 nm (figure S31). Yellow line: orange spectrum minus ½ × blue spectrum, with factor of ½ to account for the slightly higher QR exciton density at 1-50 ps with 460 nm excitation. This yellow spectrum gives the PDHF spectrum. The PDHF spectrum was extracted this way since the intrinsic PDHF TA spectrum may be slightly different in the loaded nanofibers versus the unloaded nanofibers, and so the subtraction method used here gives the most physically realistic results for the hybrid ensemble.

We then assume that the TA of the hybrid can be represented by two species (the PDHF and QR components):

$$TA(\lambda, t) = Spectra(\lambda) \times Concentrations(t) \quad (3)$$

where $TA(\lambda, t)$ is the TA data (Figure S3. 29-31), $Spectra(\lambda)$ are the PDHF and QR spectra shown in Figure S3. 32, and $Concentrations(t)$ are the unknown parameters. This be written more explicitly in matrix form as:

$$\begin{pmatrix} TA(\lambda_1,t_1) & TA(\lambda_1,t_2) & \cdots \\ TA(\lambda_2,t_1) & TA(\lambda_2,t_2) & \vdots \\ \vdots & \cdots & \ddots \end{pmatrix} = \begin{pmatrix} TA_{PF}(\lambda_1) & TA_{QR}(\lambda_1) \\ TA_{PF}(\lambda_2) & TA_{QR}(\lambda_2) \\ \vdots & \vdots \end{pmatrix} \times \begin{pmatrix} Conc_{PF}(t_1) & Conc_{PF}(t_2) & \cdots \\ Conc_{QR}(t_1) & Conc_{QR}(t_2) & \cdots \end{pmatrix} \quad (4)$$

We then use linear regression to the PDHF and QR concentrations at each time using the "mldivide" function in Matlab R2018b. This is equivalent to finding the concentrations of the PDHF and QR at each time, that, when multiplied with their respective spectra, the sum of which most closely matches the TA spectrum at that time point (i.e. the residuals are minimized). This means that each spectral slice in the TA map is treated separately from every other spectral slice at different timepoints. We apply this linear regression analysis using two species to the hybrid excited at 400 nm (Figure S3. 31), using 1 species (QRs) to the hybrid excited at 460 nm (Figure S3. 30) and using 1 species (PDHF) to the unloaded C-A-C nanofibers excited at 400 nm (Figure S3. 29). The results for the concentrations in each case are shown in Figure S3. 33.

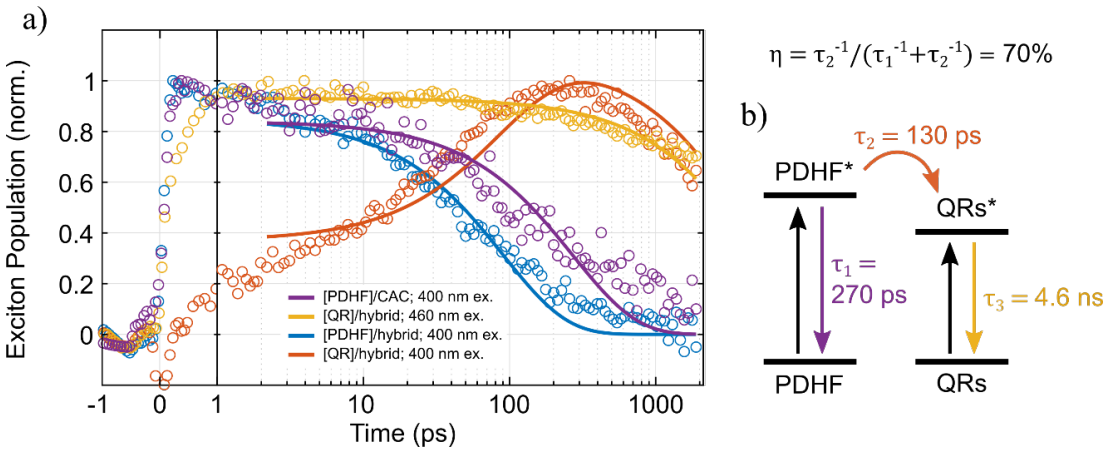

Figure S3. 33: (a) Extracted exciton population kinetics of: PDHF in (unloaded) C-A-C nanofibers with 400 nm excitation (purple), giving the intrinsic PDHF dynamics; QRs in hybrid C-A-C nanofibers after 460 nm excitation (yellow), giving the intrinsic QR dynamics; PDHF in hybrid C-A-C nanofibers upon 400 nm excitation (blue), showing shortened lifetime due to energy transfer; and QRs in hybrid C-A-C nanofibers (orange), with the rise over time demonstrating energy transfer from PDHF to the QRs. The fluence with 400 nm excitation was 3 μJ/cm2/s in each case, and at 460 nm a fluence of ~4 μJ/cm^2/s was used to account for the QRs' lower absorption at 460 nm, and so that the maximum QR exciton concentration in each case was equal. Global fits are shown in each case using a 3-parameter model i.e. by using equations 7, 8, 9, and 10 for the purple, orange, yellow, and blue lines respectively. (b) Illustration of 3-parameter model labelled with extracted time constants from (a). The system shows high transfer efficiency (70±10 %), and excitons are funnelled to the QRs with a time constant of 130 ps.

To assess whether linear regression with two species accurately models the data we compare the LHS of equation (4) – the real data – with the RHS of equation (4) – the intrinsic spectra multiplied by the extracted concentrations (i.e. the reconstruction of the data set). The comparison shown in Figure S3. 34 clearly shows linear regression with two species accurately models the data.

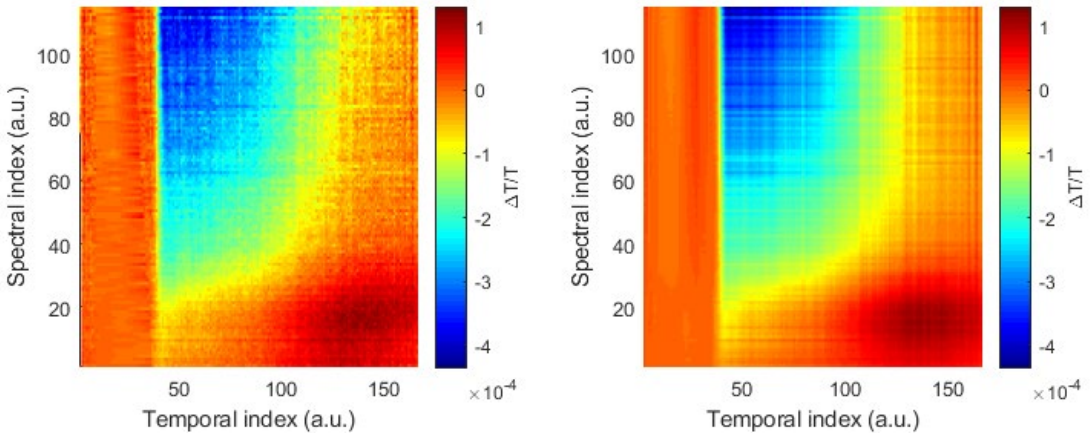

Figure S3. 34: Left panel: TA data of loaded hybrid ensemble excited at 400 nm. Right panel: reconstruction of data set in left panel using linear regression. An excellent match between the data and its reconstruction is found.

We next normalize the concentrations at 2 ps by using their average value from 1.5 to 2.5 ps. This value of 2 ps was used because there is an ultrafast rise in the QR signal (and hence the *extracted* exciton population) in the first 2 ps due to cooling of hot carriers to the band edge. This cooling was judged to have fully finished by 2 ps. Next, we scale the exciton populations to reflect the fact that we initially create more carriers in the PDHF than the QRs due to the higher absorption of PDHF at 400 nm. Finally, we need to model the energy transfer in the hybrid nanofibers. We do this by assuming a 3-parameter model:

$$\frac{d[PDHF]}{dt} = -\left(\frac{1}{\tau_1} + \frac{1}{\tau_2}\right)[PDHF] \tag{5}$$

$$\frac{d[QR]}{dt} = \frac{1}{\tau_2}[PDHF] - \frac{1}{\tau_3}[QR] \tag{6}$$

where τ_1 is the intrinsic decay time of the PDHF, τ_2 is the PDHF-to-QR transfer rate, and τ_3 is the intrinsic decay of the QRs. This simple model was used to avoid

over-fitting the data, and because it still accurately models the data. A graphical representation of this model is shown in Figure S3. 33. The solutions to the system-of-equations (5, 6) are the following:

$$[PF] = [PF]_0 e^{-(k_1+k_2)t} \tag{7}$$

$$[QR] = \frac{e^{-(k_1+k_2)t}\left(-k_2[PF]_0 + e^{k_4 t}(k_2[PF]_0 + k_4[QR]_0)\right)}{k_4} \tag{8}$$

where we have defined $k_4 \equiv k_1 + k_2 - k_3$, and $k_i \equiv \tau_i$. Note that for the case of 460 nm excitation, $[PF]_0 = 0$ and we can write:

$$[QR] = [QR]_0 e^{-k_3 t} \tag{9}$$

Furthermore, for the case of the unloaded C-A-C nanofibers where $k_2 = 0$ we can write:

$$[PF] = [PF]_0 e^{-k_1 t} \tag{10}$$

We then globally fit equations 7-10 to the exciton populations shown in Figure S3. 33. This was done by using the "fminsearch" function in Matlab R2018b. In the global minimization we also optimize the initial starting values for each exciton population. Also note that we only fit from 2 ps onwards to avoid fitting the hot-carrier cooling in the QRs as previously mentioned. Overall, we find that the equations model the data well, despite the low number of parameters employed (and hence there being no possibility for the occurrence of over-fitting). Finally, to find the energy transfer rate we take

$$\eta = \frac{\tau_2^{-1}}{\tau_1^{-1} + \tau_2^{-1}} \tag{11}$$

This gives an energy transfer rate of $70 \pm 10\%$. The uncertainty in this case is conservatively estimated as $\pm 10\,\%$ since the "fminsearch" algorithm does not output an uncertainty.

Red-shift of QR TA signal

As can be noticed in Figure S3. 30, there is red-shift in the ground-state-bleach (GSB) of the QR signal when excited at 460 nm. Discounting the first 2 ps where analysis of the GSB peak is complicated by carrier-cooling, we observe a ~15 nm red-shift over 2 ns. Alternatively, there is negligible peak-shift for a pure solution of the QRs (despite these QRs originating from the same batch). The explanation we give for this is that the QRs in the C-A-C hybrid nanofibers are relatively close to one another, allowing for Förster energy transfer of excitons between the QRs themselves. Since there will be some degree of polydispersity, excitons will therefore hop preferentially to the QRs with the lowest bandgaps, resulting in an overall red-shift in the GSB. This effect has been observed previously.[51] In solution however, the QRs are too far away from one another for energy transfer to occur, and therefore the GSB peak position stays constant. To model the rate of red-shift we employ a simple exponential rate i.e. that the peak position E_{GSB} follows:

$$E_{GSB}(t) = E_0 e^{-k_r t} + E_\infty \tag{12}$$

From this we find that the rate of red shifting has a characteristic time constant of $\frac{1}{k_r} \equiv \tau_r = 510 \pm 80$ ps. Note that this time constant is found by fitting in units of energy, not wavelength. We interpret this rate of red-shifting as the QR-to-QR energy transfer rate.

Another notable feature is that initial peak position of the QRs in the pure solution is higher (by ~10 nm) versus that of the QRs the hybrid nanofibers. Since the QRs originate from the same initial batch, this indicates there is some slight preferential incorporation of smaller QRs with larger bandgaps into the hybrid nanofibers.

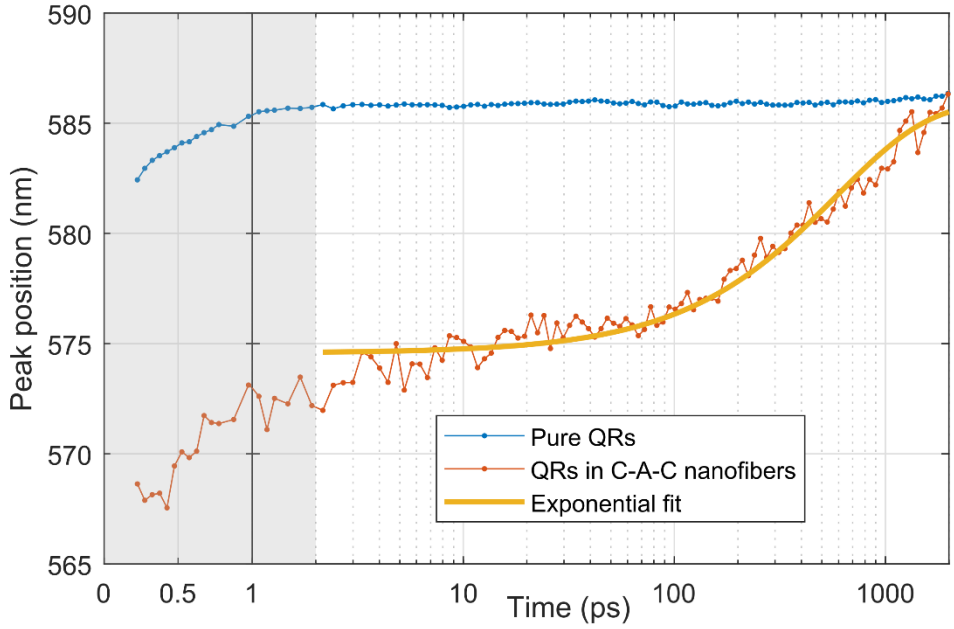

Figure S3. 35: Peak position of ground-state-bleach (GSB) of QRs in TA for pure solution of QRs (in EtOH) and for the QRs in the hybrid ensemble (when selectively excited at 460 nm). The peak position is extracted by Gaussian fitting plus a constant of the GSB. The yellow line is an exponential fit to the C-A-C QR redshift from 2 ps onwards. The grey shaded area highlights the initial period of carrier cooling in the QRs in the first 2 ps, complicating any interpretation of this region. However, past 2 ps, the GSB of the QRs in the hybrid nanofibers show a significant red-shift over time, despite the QRs originating from the same QR batch as that of the solution.

3.6. References

(1) Reddy, A. L. M.; Gowda, S. R.; Shaijumon, M. M.; Ajayan, P. M. Hybrid Nanostructures for Energy Storage Applications. *Adv. Mater.* **2012**, *24* (37), 5045–5064.

(2) Costi, R.; Saunders, A. E.; Banin, U. Colloidal Hybrid Nanostructures: A New Type of Functional Materials. *Angew. Chem. Int. Ed.* **2010**, *49* (29), 4878–4897.

(3) Yu, G.; Xie, X.; Pan, L.; Bao, Z.; Cui, Y. Hybrid Nanostructured Materials for High-Performance Electrochemical Capacitors. *Nano Energy* **2013**, *2* (2), 213–234.

(4) Hildebrandt, N.; Spillmann, C. M.; Russ Algar, W.; Pons, T.; Stewart, M. H.; Oh, E.; Susumu, K.; Díaz, S. A.; Delehanty, J. B.; Medintz, I. L. Energy Transfer with Semiconductor Quantum Dot Bioconjugates: A Versatile Platform for Biosensing, Energy Harvesting, and Other Developing Applications. *Chem. Rev.* **2017**, *117* (2), 536–711.

(5) Agranovich, V. M.; Gartstein, Y. N.; Litinskaya, M. Hybrid Resonant Organic-Inorganic Nanostructures for Optoelectronic Applications. *Chem. Rev.* **2011**, *111* (9), 5179–5214.

(6) Colvin, V. L.; Schlamp, M. C.; Alivisatos, A. P. Light-Emitting Diodes Made from Cadmium Selenide Nanocrystals and a Semiconducting Polymer. *Nature* **1994**, *370*, 354–357.

(7) Huynh, W. U.; Dittmer, J. J.; Alivisatos, A. P. Hybrid Nanorod-Polymer Solar Cells. *Science.* **2002**, *295* (5564), 2425–2427.

(8) Zhang, Q.; Atay, T.; Tischler, J. R.; Bradley, M. S.; Bulović, V.; Nurmikko, A. V. Highly Efficient Resonant Coupling of Optical Excitations in Hybrid Organic/Inorganic Semiconductor Nanostructures. *Nat. Nanotechnol.* **2007**, *2* (9), 555–559.

(9) Medintz, I. L.; Clapp, A. R.; Mattoussi, H.; Goldman, E. R.; Fisher, B.; Mauro, J. M. Self-Assembled Nanoscale Biosensors Based on Quantum Dot FRET Donors. *Nat. Mater.* **2003**, *2*, 630–638.

(10) Su, Y. W.; Lin, W. H.; Hsu, Y. J.; Wei, K. H. Conjugated Polymer/Nanocrystal Nanocomposites for Renewable Energy Applications in Photovoltaics and Photocatalysis. *Small* **2014**, *10* (22), 4427–4442.

(11) Kango, S.; Kalia, S.; Celli, A.; Njuguna, J.; Habibi, Y.; Kumar, R. Surface Modification of Inorganic Nanoparticles for Development of Organic-Inorganic Nanocomposites - A Review. *Prog. Polym. Sci.* **2013**, *38* (8), 1232–1261.

(12) Monkman, A. P.; Rothe, C.; King, S.; Dias, F. Polyfluorene Photophysics. In *Polyfluorenes*; Scherf, U., Neher, D., Eds.; Springer Berlin Heidelberg, 2008; pp 187-225.

(13) Alivisatos, A. P. Semiconductor Clusters, Nanocrystals, and Quantum Dots. *Science.* **1996**, *271* (5251), 933–937.

(14) Scholes, G. D.; Fleming, G. R.; Olaya-Castro, A.; Van Grondelle, R. Lessons from Nature about Solar Light Harvesting. *Nat. Chem.* **2011**, *3* (10), 763–774.

(15) Kriete, B.; Lüttig, J.; Kunsel, T.; Malý, P.; Jansen, T. L. C.; Knoester, J.; Brixner, T.; Pshenichnikov, M. S. Interplay between Structural Hierarchy and Exciton Diffusion in Artificial Light Harvesting. *Nat. Commun.* **2019**, *10* (1), 4615.

(16) Zhu, X.; Lin, Y.; Sun, Y.; Beard, M. C.; Yan, Y. Lead-Halide Perovskites for Photocatalytic α-Alkylation of Aldehydes. *J. Am. Chem. Soc.* **2019**, *141* (2), 733–738.

(17) Duan, J.; Chen, S.; Jaroniec, M.; Qiao, S. Z. Porous C3N4 Nanolayers@n-Graphene Films as Catalyst Electrodes for Highly Efficient Hydrogen Evolution. *ACS Nano* **2015**, *9* (1), 931–940.

(18) Frenkel, J. On the Transformation of Light into Heat in Solids. I. *Phys. Rev.* **1931**, *37* (1).

(19) Mikhnenko, O. V.; Blom, P. W. M.; Nguyen, T. Q. Exciton Diffusion in Organic Semiconductors. *Energy Environ. Sci.* **2015**, *8* (7), 1867–1888.

(20) Peumans, P.; Yakimov, A.; Forrest, S. R. Small Molecular Weight Organic Thin-Film Photodetectors and Solar Cells. *J. Appl. Phys.* **2003**, *93* (7), 3693–3723.

(21) Wang, X.; Guerin, G.; Wang, H.; Wang, Y.; Manners, I.; Winnik, M. A. Cylindrical Block Copolymer Micelles and Co-Micelles of Controlled Length and Architecture. *Science.* **2007**, *317* (5838), 644–647.

(22) Boott, C. E.; Gwyther, J.; Harniman, R. L.; Hayward, D. W.; Manners, I. Scalable and Uniform 1D Nanoparticles by Synchronous Polymerization, Crystallization and Self-Assembly. *Nat. Chem.* **2017**, *9* (8), 785–792.

(23) Schöbel, J.; Karg, M.; Rosenbach, D.; Krauss, G.; Greiner, A.; Schmalz, H. Patchy Wormlike Micelles with Tailored Functionality by Crystallization-Driven Self-Assembly: A Versatile Platform for Mesostructured Hybrid Materials. *Macromolecules* **2016**, *49* (7), 2761–2771.

(24) Schmelz, J.; Karg, M.; Hellweg, T.; Schmalz, H. General Pathway toward Crystalline-Core Micelles with Tunable Morphology and Corona Segregation. *ACS Nano* **2011**, *5* (12), 9523–9534.

(25) Tao, D.; Feng, C.; Cui, Y.; Yang, X.; Manners, I.; Winnik, M. A.; Huang, X. Monodisperse Fiber-like Micelles of Controlled Length and Composition with an Oligo(p-Phenylenevinylene) Core via "Living" Crystallization-Driven Self-Assembly. *J. Am. Chem. Soc.* **2017**, *139* (21), 7136–7139.

(26) Arno, M. C.; Inam, M.; Coe, Z.; Cambridge, G.; Macdougall, L. J.; Keogh, R.; Dove, A. P.; O'Reilly, R. K. Precision Epitaxy for Aqueous 1D and 2D Poly(ϵ -Caprolactone) Assemblies. *J. Am. Chem. Soc.* **2017**, *139* (46), 16980–16985.

(27) Yang, S.; Choi, T. L. Rapid Formation and Real-Time Observation of Micron-Sized Conjugated Nanofibers with Tunable Lengths and Widths in 20 Minutes by Living Crystallization-Driven Self-Assembly. *Chem. Sci.* **2020**, *11* (32), 8416–8424.

(28) Hicks, G. E. J. J.; Jarrett-Wilkins, C. N.; Panchuk, J. R.; Manion, J. G.; Seferos, D. S. Oxidation Promoted Self-Assembly of π-Conjugated Polymers. *Chem. Sci.* **2020**, *11* (25), 32–34.

(29) Qi, R.; Zhu, Y.; Han, L.; Wang, M.; He, F. Rectangular Platelet Micelles with Controlled Aspect Ratio by Hierarchical Self-Assembly of Poly(3-Hexylthiophene)- b-Poly(Ethylene Glycol). *Macromolecules* **2020**, *53* (15), 6555–6565.

(30) Shin, S.; Menk, F.; Kim, Y.; Lim, J.; Char, K.; Zentel, R.; Choi, T. L. Living Light-Induced Crystallization-Driven Self-Assembly for Rapid Preparation of Semiconducting Nanofibers. *J. Am. Chem. Soc.* **2018**, *140* (19), 6088–6094.

(31) He, X.; Hsiao, M. S.; Boott, C. E.; Harniman, R. L.; Nazemi, A.; Li, X.; Winnik, M. A.; Manners, I. Two-Dimensional Assemblies from Crystallizable Homopolymers with Charged Termini. *Nat. Mater.* **2017**, *16* (4), 481–488.

(32) Qiu, H.; Gao, Y.; Boott, C. E.; Gould, O. E. C.; Harniman, R. L.; Miles, M. J.; Webb, S. E. D.; Winnik, M. A.; Manners, I. Uniform Patchy and Hollow Rectangular Platelet Micelles from Crystallizable Polymer Blends. *Science.* **2016**, *352* (6286), 697–701.

(33) Han, L.; Wang, M.; Jia, X.; Chen, W.; Qian, H.; He, F. Uniform Two-Dimensional Square Assemblies from Conjugated Block Copolymers Driven by π-π Interactions with Controllable Sizes. *Nat. Commun.* **2018**, *9*, 865.

(34) Arno, M. C.; Inam, M.; Weems, A. C.; Li, Z.; Binch, A. L. A.; Platt, C. I.; Richardson, S. M.; Hoyland, J. A.; Dove, A. P.; O'Reilly, R. K. Exploiting the Role of Nanoparticle Shape in Enhancing Hydrogel Adhesive and Mechanical Properties. *Nat. Commun.* **2020**, *11*, 1420.

(35) Merg, A. D.; Van Genderen, E.; Bazrafshan, A.; Su, H.; Zuo, X.; Touponse, G.; Blum, T. B.; Salaita, K.; Abrahams, J. P.; Conticello, V. P. Seeded Heteroepitaxial Growth of Crystallizable Collagen Triple Helices: Engineering Multifunctional Two-Dimensional Core-Shell Nanostructures. *J. Am. Chem. Soc.* **2019**, *141* (51), 20107–20117.

(36) Ogi, S.; Sugiyasu, K.; Manna, S.; Samitsu, S.; Takeuchi, M. Living Supramolecular Polymerization Realized through a Biomimetic Approach. *Nat. Chem.* **2014**, *6*, 188–195.

(37) Zhang, W.; Jin, W.; Fukushima, T.; Saeki, A.; Seki, S.; Aida, T. Supramolecular Linear Heterojunction Composed of Graphite-like Semiconducting Nanotubular Segments. *Science.* **2011**, *334* (6054), 340–343.

(38) Aliprandi, A.; Mauro, M.; De Cola, L. Controlling and Imaging Biomimetic Self-Assembly. *Nat. Chem.* **2016**, *8* (1), 10–15.

(39) Wang, H.; Lin, W.; Fritz, K. P.; Scholes, G. D.; Winnik, M. A.; Manners, I. Cylindrical Block Co-Micelles with Spatially Selective Functionalization by Nanoparticles. *J. Am. Chem. Soc.* **2007**, *129* (43), 12924–12925.

(40) Mann, S.; Manners, I.; Patil, A. J.; Winnik, M. A.; Manners, I.; Wang, H.; Liu, K.; Petrov, S. Fabrication of Continuous and Segmented Polymer/ Metal Oxide Nanowires Using Cylindrical Micelles and Block Comicelles as Templates. *Adv. Mater.* **2009**, *21* (18), 1805–1808.

(41) Jin, X.-H.; Price, M. B.; Finnegan, J. R.; Boott, C. E.; Richter, J. M.; Rao, A.; Menke, S. M.; Friend, R. H.; Whittell, G. R.; Manners, I. Long-Range Exciton Transport in Conjugated Polymer Nanofibers Prepared by Seeded Growth. *Science.* **2018**, *360* (6391), 897–900.

(42) MacFarlane, L. R.; Shaikh, H.; Garcia-Hernandez, J. D.; Vespa, M.; Fukui, T.; Manners, I. Functional Nanoparticles through π-Conjugated Polymer Self-Assembly. *Nat. Rev. Mater.* **2021**, *6*, 7–26.

(43) Gilroy, J. B.; Rupar, P. A.; Whittell, G. R.; Chabanne, L.; Terrill, N. J.; Winnik, M. A.; Manners, I.; Richardson, R. M. Probing the Structure of the Crystalline Core of Field-Aligned, Monodisperse, Cylindrical Polyisoprene-Block-Polyferrocenylsilane Micelles in Solution Using Synchrotron Small- and Wide-Angle X-Ray Scattering. *J. Am. Chem. Soc.* **2011**, *133* (42), 17056–17062.

(44) Shaikh, H.; Jin, X. H.; Harniman, R. L.; Richardson, R. M.; Whittell, G. R.; Manners, I. Solid-State Donor-Acceptor Coaxial Heterojunction Nanowires via Living Crystallization-Driven Self-Assembly. *J. Am. Chem. Soc.* **2020**, *142* (31), 13469–13480.

(45) Tao, D.; Wang, Z.; Huang, X.; Tian, M.; Lu, G.; Manners, I.; Winnik, M. A.; Feng, C. Continuous and Segmented Semiconducting Fiber-like Nanostructures with Spatially Selective Functionalization by Living Crystallization-Driven Self-Assembly. *Angew. Chem. Int. Ed.*

2020, *59* (21), 8232–8239.

(46) Kim, Y. J.; Cho, C. H.; Paek, K.; Jo, M.; Park, M. K.; Lee, N. E.; Kim, Y. J.; Kim, B. J.; Lee, E. Precise Control of Quantum Dot Location within the P3HT-b-P2VP/QD Nanowires Formed by Crystallization-Driven 1D Growth of Hybrid Dimeric Seeds. *J. Am. Chem. Soc.* **2014**, *136* (7), 2767–2774.

(47) Jin, S. M.; Kim, I.; Lim, J. A.; Ahn, H.; Lee, E. Interfacial Crystallization-Driven Assembly of Conjugated Polymers/Quantum Dots into Coaxial Hybrid Nanowires: Elucidation of Conjugated Polymer Arrangements by Electron Tomography. *Adv. Funct. Mater.* **2016**, *26* (19), 3226–3235.

(48) Zhang, Q.; Russell, T. P.; Emrick, T. Synthesis and Characterization of CdSe Nanorods Functionalized with Regioregular Poly(3-Hexylthiophene). *Chem. Mater.* **2007**, *19* (15), 3712–3716.

(49) Aldana, J.; Wang, Y. A.; Peng, X. Photochemical Instability of CdSe Nanocrystals Coated by Hydrophilic Thiols. *J. Am. Chem. Soc.* **2001**, *123* (36), 8844–8850.

(50) Spano, F. C.; Silva, C. H- and J-Aggregate Behavior in Polymeric Semiconductors. *Annu. Rev. Phys. Chem.* **2014**, *65* (1), 477–500.

(51) Davis, N. J. L. K.; Allardice, J. R.; Xiao, J.; Karani, A.; Jellicoe, T. C.; Rao, A.; Greenham, N. C. Improving the Photoluminescence Quantum Yields of Quantum Dot Films through a Donor/Acceptor System for near-IR LEDs. *Mater. Horizons* **2019**, *6*, 137–143.

(52) Wolfbeis, O. S. An Overview of Nanoparticles Commonly Used in Fluorescent Bioimaging. *Chem. Soc. Rev.* **2015**, *44* (14), 4743–4768.

(53) Kim, S.; Lim, Y. T.; Soltesz, E. G.; De Grand, A. M.; Lee, J.; Nakayama, A.; Parker, J. A.; Mihaljevic, T.; Laurence, R. G.; Dor, D. M.; Cohn, L. H.; Bawendi, M. G.; Frangioni, J. V. Near-Infrared Fluorescent Type II Quantum Dots for Sentinel Lymph Node Mapping. *Nat. Biotechnol.* **2004**, *22* (1), 93–97.

(54) Liras, M.; Barawi, M.; De La Peña O'Shea, V. A. Hybrid Materials Based on Conjugated Polymers and Inorganic Semiconductors as Photocatalysts: From Environmental to Energy Applications. *Chem. Soc. Rev.* **2019**, *48* (22), 5454–5487.

(55) Kim, D. Y.; Cho, H. N.; Kim, C. Y. Blue Light Emitting Polymers. *Prog. Polym. Sci.* **2000**, *25* (8), 1089–1139.

(56) Wood, V.; Bulović, V. Colloidal Quantum Dot Light-Emitting Devices. *Nano Rev.* **2010**, *1* (1), 5202.

(57) McHale, J. L. Hierarchal Light-Harvesting Aggregates and Their Potential for Solar Energy Applications. *J. Phys. Chem. Lett.* **2012**, *3* (5), 587–597.

(58) Peng, Z. A.; Peng, X. Formation of High-Quality CdTe, CdSe, and CdS Nanocrystals Using CdO as Precursor [6]. *J. Am. Chem. Soc.* **2001**, *123* (1), 183–184.

(59) Pope, M.; Swenberg, C. E. Electronic Processes in Organic Solids. *Annu. Rev. Phys. Chem.* **1984**, *35*, 613.

(60) Morawska, P. O.; Wang, Y.; Ruseckas, A.; Orofino-Penia, C.; Kanibolotsky, A. L.; Santhanagopal, R.; Fröhlich, N.; Fritsch, M.; Allard, S.; Scherf, U.; Skabara, P. J.; Samuel, I. D. W.; Turnbull, G. A. Side-Chain Influence on the Mass Density and Refractive Index of

Polyfluorenes and Star-Shaped Oligofluorene Truxenes. *J. Phys. Chem. C* **2015**, *119*, 22102–22107.

(61) Campoy-Quiles, M.; Heliotis, G.; Xia, R.; Ariu, M.; Pintani, M.; Etchegoin, P.; Bradley, D. D. C. Ellipsometric Characterization of the Optical Constants of Polyfluorene Gain Media. *Adv. Funct. Mater.* **2005**, *15*, 925–933.

(62) Yu, W. W.; Qu, L.; Guo, W.; Peng, X. Experimental Determination of the Extinction Coefficient of CdTe, CdSe, and CdS Nanocrystals. *Chem. Mater.* **2003**, *15*, 2854–2860.

Chapter 4

Helical Nanofibers of Controlled Handedness via Crystallization-Driven Self-Assembly of Polyfluorene-Based Block Copolymers

Contributions:

Initial scientific design of the experiments was conducted in calibration with Dr. Xu-Hui Jin and Dr. George Whittell (University of Bristol). Characterization by atomic force microscopy was conducted by Dr. Robert Harniman (University of Bristol) and Dr. Yuetong Kang (University of Victoria). All other work performed in this Chapter was carried out by Huda Shaikh. Research was conducted at the University of Bristol and University of Victoria.

4.1. Abstract

Understanding and controlling chirality on the nanoscale is of widespread interest in developing complex functional materials for a number of current and emerging electronic, sensing and biological applications. The construction of helical nanostructures through self-assembly methods has predominantly focused on small molecules and few reports have looked at macromolecular building blocks. Herein, the preparation of helical nanofibers via crystallization-driven self-assembly (CDSA) of various polyfluorene-based block copolymer is described, including (*S*-) poly(di-*n*-(3,7-dimethyoctane)fluorene)-*b*-poly(di-*n*-hexylfluorene)[PPh_3]Br ((*S*-) PDCF-*b*-PDHF[PPh_3]Br, (*S*-) PDCF-*b*-PDHF-*b*-poly(*N*-isopropylacrylamide) ((*S*-) PDCF-*b*-PDHF-*b*-PNIPAm), (*R*-) PDCF-*b*-PDHF[PPh_3]Br and (*R*-) PDCF-*b*-PDHF-*b*-poly(ethylene glycol) ((*R*-) PDCF-*b*-PDHF-*b*-PEG). Single-handed helical nanofibers were formed, composed of a central crystalline PDHF core, a chiral (*S*-)/(*R*-) PDCF π-conjugated block and a solvophilic corona-forming block. Helicity of the self-assembled micelles was probed in solution by circular dichroism (CD) spectroscopy and in the dried state by transmission electron microscopy (TEM) and atomic force microscopy (AFM). Seeded growth afforded control over the length of the helical nanofibers prepared by the self-assembly of the triblock copolymer (*S*-) PDCF-*b*-PDHF-*b*-PNIPAm.

4.2. Introduction

In nature, homochirality is abundant and critical for key biological functions for example DNA and RNA are predominately composed of D-sugars and in proteins the major building blocks are L-amino acids. Additionally, chirality can be present on numerous hierarchical levels from the sub-atomic to the macroscopic[1,2] and even galactic scales.[3,4] Significant research has focused on using self-assembly methods to fabricate highly complex and controlled helical structures. Chiral components can generate higher order helical structures via chiral amplification.[3,5,6] Chirality in a material can directly influence the desired functionality such as enhancing hole mobility.[7] Several emerging areas where chiral structures hold intriguing potential include solar-energy conversion, photonics, and plasmonics.[8]

The construction of chiral nanomaterials with controlled dimensions and handedness via self-assembly of small molecules has attracted substantial interest.[9,10] Recent work in this field has been expanded to include the use of semiconducting polymers as building blocks for the formation of size-controlled helical structures for tailored optoelectronic devices, including responsive liquid crystal displays and advanced organic photovoltaics. Solution self-assembly of amphiphilic block copolymers (BCPs) with a crystallizable π-conjugated polymer block can be used to prepare highly ordered structures with low curvature at the core-to-corona interface. [11–20]

Micelles formed through crystallization-driven self-assembly (CDSA) possess crystal faces that can undergo further epitaxial growth in the presence of added BCP unimer. Fragmentation of the micelles via sonication yields short micelles that can act as seeds to prepare a variety of controlled length fibers. This seeded epitaxial growth process is termed 'living' CDSA and bears resemblance to living covalent polymerization. Investigations into the exciton diffusion properties of crystalline core micelles prepared by seeded growth of poly(di-*n*-hexylfluorene)-based BCPs were recently reported. [21] It was revealed that the micelle cores possessed near single crystal-like order enabling access to exceptionally long exciton diffusion lengths (> 200 nm).[21] Although fiber-like micelles can be prepared through the CDSA of a variety of π-conjugated materials,

the preparation of other micelle morphologies and their inherent electronic properties remains limited.[15,22,23]

Helical fibers can be prepared by the self-assembly of polythiophene (PT)-containing BCPs, hexabenzocoronene (HBC)- or perylenediimide (PDI)-based molecular amphiphiles.[23–27] In the case of PT-based helical fibers, helicity was achieved either by complexation of ethylene glycol chains in the corona-forming block and potassium ions or by use of an optically active helical poly(phenyl isocyanide) corona-forming block.[23,24] Seeded growth strategies have been developed using helical HBC- or PDI-based seeds.[25,26] The helicity of the supramolecular polymers is controlled by the helical seeds and it can be induced in the newly formed segments composed of achiral monomers. Very recently, control over the helical fiber lengths via 'living' CDSA has been reported using PT-containing BCPs.[23]

In this Chapter, we report the preparation of controlled uniform one-handed helical nanowires through the CDSA of polyfluorene-based block copolymers (Figure 4. 1). Poly(di-*n*-hexylfluorene) (PDHF) was used as the crystallizable central core-forming block of the nanofibers. A chiral polyfluorene with (*S*-) or (*R*-) enantiomerically enriched side chains, poly(di-*n*-(3,7-dimethyoctane)fluorene) (PDCF), was used as a corona-forming block, to enable a twist in the nanofibers. Self-assembled nanofibers of these materials were characterized by transmission electron microscopy (TEM), atomic force microscopy (AFM) and circular dichroism (CD) spectroscopy.

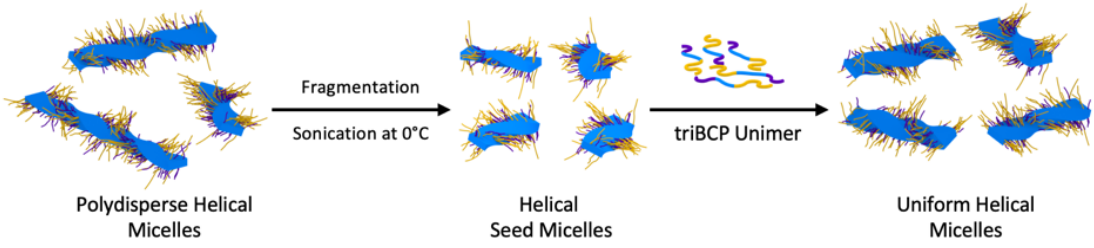

Figure 4. 1: Schematic illustration of the preparation of low-dispersity helical micelles via CDSA of (*S*-) $PDCF_6$-*b*-$PDHF_{10}$-*b*-$PNIPAm_{68}$ triBCPs containing a central crystallizable PDHF core-forming block (blue regions), a chiral PDCF corona-forming block (purple regions), and an additional polar PNIPAm corona-forming block (yellow regions) for colloidal stabilization of the micelles in solution.

4.3. Results and Discussion

4.3.1. Chiral Polyfluorene-based BCP Material Design and Synthesis

A fluorene polymer with (*S*-) or (*R*-) enantiomerically enriched side chains was selected as a chiral corona-forming block, poly(di-*n*-(3,7-dimethyoctane)) (PDCF) to enable the formation of helical nanofibers. Poly(di-*n*-hexylfluorene) (PDHF) was used as the crystallizable core-forming block and an additional corona-forming block was used that could be solvated in poor solvents for the PDHF block. The formation of colloidally stable helical nanostructures was expected to depend on the solvent medium and chemical nature of the stabilizing corona-forming blocks hence a range of coronas were investigated that could favour self-assembly in different polar solvents all of which are favourable for the crystallization of the PDHF block. Polyethylene glycol (PEG), poly(N-isopropylacrylamide) (PNIPAm), and a charged small molecule (triphenyl phosphonium bromide, $[PPh_3]Br$) were chosen as the corona-forming blocks. This choice enables the use of polar solvent systems for self-assembly which typically enable crystallization-driven self-assembly of PDHF BCPs.

Synthesis of the polyfluorene-based materials was achieved by employing a copper-catalyzed azide-alkyne cycloaddition click reactions (CuAAc) with alkyne-terminated (*S*-) or (*R*-) PDCF-*b*-PDHF and azido-terminated PEG, PNIPAm, and $[PPh_3]Br$ (Scheme S4. 1). The polyfluorene diblock copolymers were synthesized via sequential Grignard metathesis (GRIM) polymerization. First. 2-bromo-7-iodo-9,9-bis-*n*-(3,7-dimethyoctane)fluorene then 2-bromo-7-iodo-9,9-bis-*n*-hexylfluorene was subsequently polymerized from the (*S*-) or (*R*-) PDCF homopolymer block. The polymerization was quenched with ethynyl magnesium bromide to afford alkyne-terminated polymers. Subsequent purification by Soxhlet extraction in methanol, ethyl acetate and chloroform resulted in the purified polymers with low-dispersity molecular weight distributions ($Đ_m \leq 1.22$). Furthermore, the polymerization sequence could not be reversed to obtain alkyne-terminated PDHF-*b*-(*S*-) or (*R*-) PDCF BCPs. In the first step PDHF homopolymer was synthesized but addition of 2-bromo-7-iodo-9,9-bis-*n*-(3,7-dimethyoctane)fluorene monomer did not result in chain extension. The added monomer self-polymerized possibly because the π-complex of Ni (0) and PDHF

chain was weaker than that of the Ni (0) and the added monomer. Therefore the BCPs used for CDSA studies have a A-*b*-B-*b*-C architecture, where segments A and C are corona-forming blocks and segment B is the crystallizable core-forming block.

Tosylate-terminated PEG and (3-bromopropyl) triphenylphosphonium bromide were azido-functionalized by a substitution reaction with sodium azide and azido-functionalized PNIPAm was prepared by reversible addition-fragmentation transfer (RAFT) polymerization using an azido-functionalized chain transfer agent. Employing the CuAAc reaction with the azido-terminated polymers or charged small molecule and the alkyne-terminated polyfluorene diblock copolymers, afforded the final materials that were subsequently purified by silica gel chromatography to give low dispersity products ($Đ_m$ < 1.2).

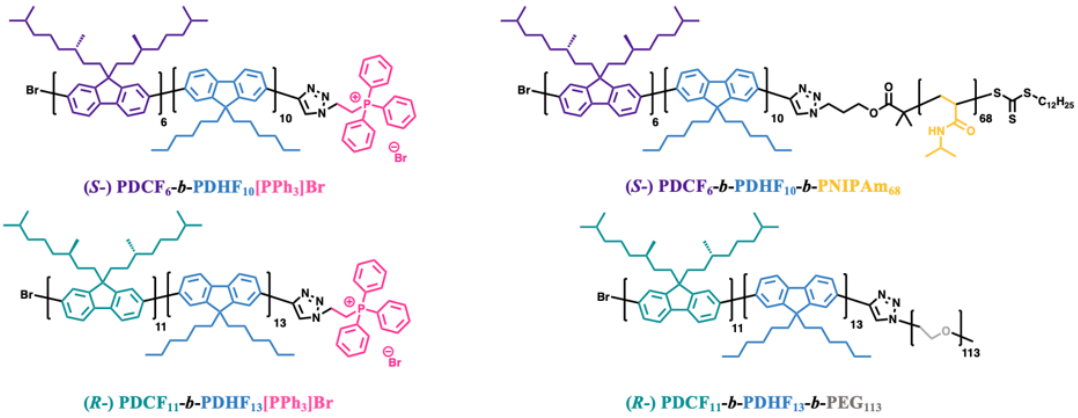

Scheme 4. 1: Chemical structures of the chiral-based materials synthesized. (*S*-) $PDCF_6$-b-$PDHF_{10}[PPh_3]Br$, (*S*-) $PDCF_6$-*b*-$PDHF_{10}$-*b*-$PNIPAm_{68}$, (*R*-) $PDCF_{11}$-*b*-$PDHF_{13}[PPh_3]Br$, (*R-)* $PDCF_{11}$-*b*-$PDHF_{13}$-*b*-PEG_{113}. The central crystallizable PDHF core-forming block is highlighted in blue, the chiral PDCF corona forming blocks in purple and teal, and the polar solvophilic corona-forming blocks in pink, yellow and grey.

The degree of polymerization for the (*S*-) or (*R*-) PDCF blocks were calculated from matrix-assisted laser desorption/ionization time-of-flight (MALDI-TOF) mass spectrometry analysis, whereby the number-average molecular mass (M_n) of the homopolymer aliquot from the GRIM polymerization is found (Figure S4. 1-2). Analysis of the ^1H NMR spectrum of the triblock copolymers allowed for determination of the ratio of the blocks, which allowed for the degree of polymerization for each block to be determined (Figure S4. 3-6). The weight-average molecular mass (M_w) and molecular mass dispersity ($Đ_m$) for all materials were determined by gel permeation chromatography (GPC) (Figure S4.

7-9). The chemical structure of each material used in this work is shown in Scheme 4. 1 and the degree of polymerization for each block in the copolymers is described in Table 4. 1.

Table 4. 1: Characterization data for PDHF-based block copolymers.

Material Composition [a, b]	M_n (kDa) [c]	M_w (kDa) [c]	$Đ_m$ [c]
(*S*-) $PDCF_6$ [a]	10.3	11.8	1.15
(*R*-) $PDCF_{11}$ [a]	11.0	13.3	1.21
(*S*-) $PDCF_6$-*b*-$PDHF_{10}$	18.9	22.6	1.19
(*R*-) $PDCF_{11}$-*b*-$PDHF_{13}$	29.1	35.6	1.22
(*S*-) $PDCF_6$-*b*-$PDHF_{10}[PPh_3]Br$	19.2	23.3	1.19
(*S*-) $PDCF_6$-*b*-$PDHF_{10}$-*b*-$PNIPAm_{68}$	25.1	29.6	1.18
(*R*-) $PDCF_{11}$-*b*-$PDHF_{13}[PPh_3]Br$	30.3	35.9	1.18
(*R*-) $PDCF_{11}$-*b*-$PDHF_{13}$-*b*-PEG_{113}	31.7	36.7	1.16

Degree of polymerization determined by [a] MALDI-ToF and [b] ^1H NMR. Number-average molecular weight (M_n), weight-average molecular weight (M_w) and molecular mass dispersity ($Đ_m = M_w/M_n$) values determined by [c] GPC (THF containing $[nBu_4N]Br$ (0.1% w/w)) calibrated against polystyrene standards.

4.3.2. Preparation of Helical PF Nanofibers via CDSA

CDSA of polyfluorene-based PF BCPs can be achieved in mixed THF and alcohol solvent systems. First, PF polymers (Hildebrand solubility parameter, δ_{PF} = 18.6-19.0 $MPa^{1/2}$) were dissolved in THF, the tyndall phenomenon was not observed for these solutions and UV-vis spectroscopy provided further evidence of the formation of molecularly dissolved BCP unimers by the presence of a broad vibronic peak at 390 nm. Selective solvent for the corona-forming blocks PEG (δ_{PEG5k} = 21.4 $MPa^{1/2}$), PNIPAm (δ_{PNIPAm} = 24.8 $MPa^{1/2}$), P2VP (δ_{P2VP} = 21.3 $MPa^{1/2}$) and $[PPh_3]Br$, such as methanol (MeOH, δ_{MeOH} = 29.7 $MPa^{1/2}$), ethanol (EtOH, δ_{EtOH} = 26.2 $MPa^{1/2}$) or isopropanol (iPrOH, δ_{iPrOH} = 23.5 $MPa^{1/2}$) were added slowly to the unimer solution in THF to promote homogenous self-nucleation of the PDHF block. Self-assembly behavior of the (*S*-) PDCF-*b*-PDHF-based triblock copolymers were studied with varying ratios of THF:MeOH/EtOH/iPrOH at 0.3 mg mL^{-1} at 20°C and aged for 24 h before TEM imaging.

In the case of (*S*-) $PDCF_6$-*b*-$PDHF_{10}[PPh_3]Br$, after aging for 24 h, TEM analysis showed the aggregation had occurred in THF:iPrOH solvent systems

(Figure S4. 10). Significantly, the self-assembly of triblock copolymer was extremely sensitive to the ratio of common solvent for all blocks (THF) to the selective solvent for the [PPh_3]Br group (iPrOH). In THF:iPrOH (11:9, v/v), small irregular aggregates (< 50 nm) are observed suggestive of some aggregation of the PDHF block. On increasing the poor solvent for the PDHF block, predominantly long fiber-like micelles with polydisperse lengths were observed from self-assembly in THF:iPrOH (1:1, v/v) and THF:iPrOH (9:11, v/v). With the inclusion of more polar solvent, in THF:iPrOH (2:3, v/v), THF:iPrOH (7:13, v/v) and THF:iPrOH (3:7, v/v) irregular and large aggregates were formed as a result of faster aggregation of the PDHF block. These results indicated that THF:iPrOH (1:1, v/v) and THF:iPrOH (9:11, v/v) are the most promising systems to facilitate efficient CDSA of the (*S*-) $PDCF_6$-*b*-$PDHF_{10}$[PPh_3]Br triblock copolymer in solution. However, some small irregular aggregates were still observed in these solvent systems, so a post-annealing step was added to attain morphologically pure fiber-like micelles, this involved heating the fiber solution to 50 °C for 2 h, followed by slow cooling to 20 °C and ageing for 24 h (Figure 4. 2a, c).

Next, self-assembly of (*S*-) $PDCF_6$-*b*-$PDHF_{10}$[PPh_3]Br was investigated in solvent mixtures containing polar aprotic solvents such as DMF and DMSO (Figure S4. 11). Adding DMF/DMSO dropwise to a unimer solution in THF at 20 °C led to precipitation of the polymer or the formation of irregular clustered aggregates. A direct dissolution method was used next in which a suspension of (*S*-) $PDCF_6$-*b*-$PDHF_{10}$[PPh_3]Br in a THF:DMF/DMSO mixture was heated at 140 °C for 30 mins followed by slow cooling and ageing at 20 °C for 24 h before imaging. In THF:DMF mixtures with a DMF content of ≤ 60 % a mixture of short and long fiber-like micelles (> 3 μm) (Figure S4. 11a-c). Fibrous bundles were prepared by self-assembly in higher contents of DMF (70 %) (Figure S4. 11d). Interestingly, in THF:DMSO mixtures large 2D platelets could be prepared with either a hexagonal (DMSO 50 %) or rectangular (DMSO 70 %) shape (Figure S4. 11e, f). Additionally, the large 2D platelets appear to spiral up layer by layer to a central peak. Each layer in the spiral structures possessed the same shape and a gradient in the electron contrast from the bottom to the top layer was observed. This suggests that screw dislocations occurred during the formation of the polydisperse platelets that then led to construction of the three-dimensional spiral

architectures. Similar structures have been reported based on poly(*p*-phenylenevinylene)-based BCPs that undergo self-assembly in solution driven via intermolecular π-π stacking and screw dislocations.[28] Investigations into preparing 2D platelets by CDSA of other phosphonium-capped PDHF polymers and using 'living' CDSA to obtain low area dispersity platelets is discussed further in Chapter 5.

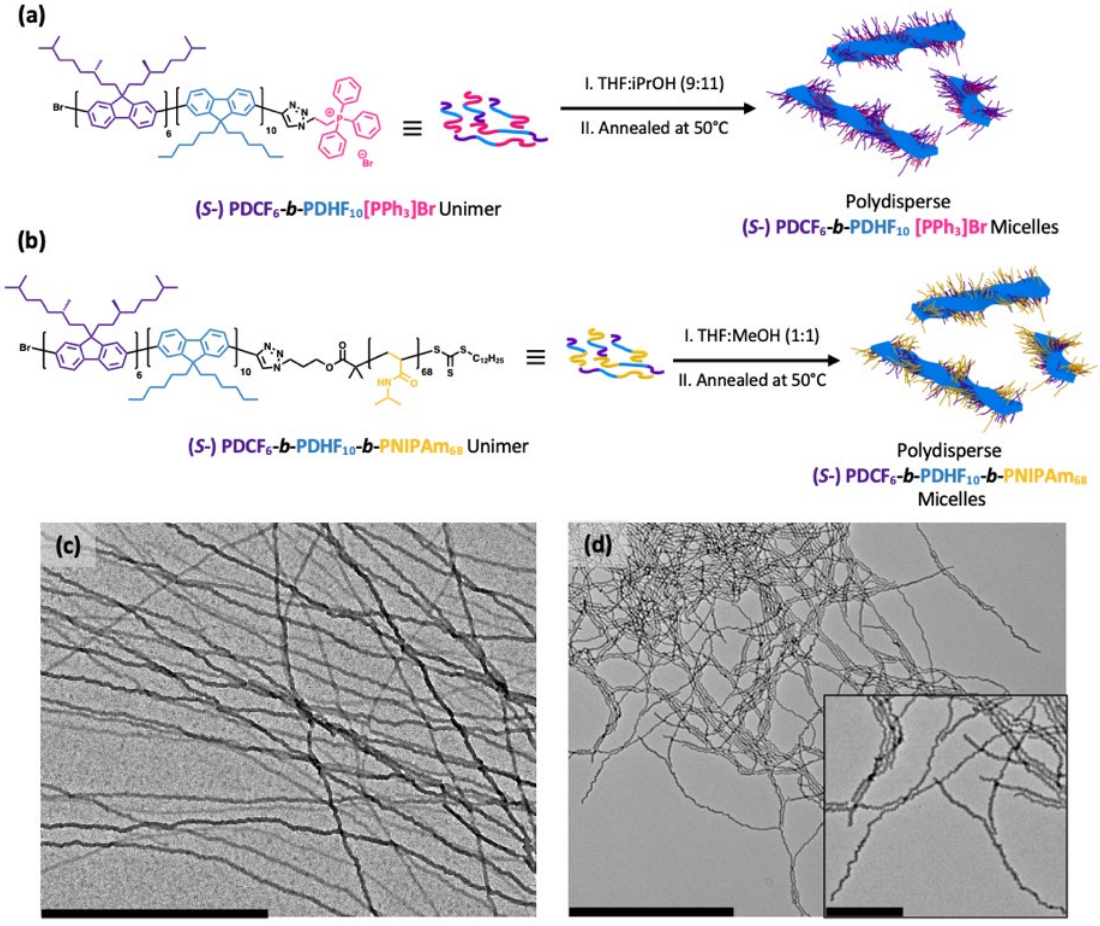

Figure 4. 2: (a) Self-assembly of (*S*-) PDCF$_6$-*b*-PDHF$_{10}$[PPh$_3$]Br in THF:iPrOH (9:11, v/v) to form helical nanofibers. Chemical structure of (*S*-) PDCF$_6$-*b*-PDHF$_{10}$[PPh$_3$]Br and schematic illustration of the nanofiber preparation. (b) Self-assembly of (*S*-) PDCF$_6$-*b*-PDHF$_{10}$-*b*-PNIPAm$_{68}$ in THF:MeOH (1:1, v/v) to form helical nanofibers. Chemical structure of (*S*-) PDCF$_6$-*b*-PDHF$_{10}$-*b*-PNIPAm$_{68}$ and schematic illustration of the nanofiber preparation. (c) TEM image of (*S*-) PDCF$_6$-*b*-PDHF$_{10}$[PPh$_3$]Br nanofibers drop cast from THF:iPrOH (9:11, v/v). Scale bar: 1 μm. (d) TEM image of (*S*-) PDCF$_6$-*b*-PDHF$_{10}$-*b*-PNIPAm$_{68}$ nanofibers drop cast from THF:MeOH (1:1, v/v). Scale bar: 2 μm. Inset scale bar: 500 nm.

Using a polymeric corona-forming block (PNIPAm) instead of the smaller [PPh$_3$]Br group, also resulted in crystallization of the core-forming PDHF block. In the case of (*S*-) PDCF$_6$-*b*-PDHF$_{10}$-*b*-PNIPAm$_{68}$, TEM analysis showed that aggregation of PDHF occurred in THF:iPrOH, THF:EtOH and THF:MeOH solvent systems. In THF:MeOH (1:1, v/v), predominantly long polydisperse fiber-like

micelles are formed but also some small aggregates were detected. Increasing the amount of MeOH (55 and 60 %) resulted in the formation of shorter fiber-like micelles and predominantly small irregular aggregates (ca. < 50 nm). The fibers prepared THF:MeOH (1:1, v/v) were subsequently annealed at 50 °C for 2 h resulting in morphologically pure fiber-like micelles (Figure 4. 2b, d). Moreover, multiple twists in the fibers are clearly visible from the TEM image (Figure 4. 2d).

The self-assembly of BCP materials composed of a chiral polyfluorene block with the opposite R chiral center ((*R*-) PDCF) was studied to determine the influence of the different enantiomers on the self-assembly and handedness of helical fibers formed. Similar to the (*S*-) analogue, (*R*-) $PDCF_{11}$-*b*-$PDHF_{13}[PPh_3]Br$ can also form fibers in THF:iPrOH solvent mixtures. The slightly longer degree of polymerization of the core-forming block in this (*R*-)-based polymer meant that the ideal solvent system to form fibers required more common solvent (THF) than what was needed for the (*S*-)-based analogue. Annealing the fibers prepared by self-assembly of (*R*-) $PDCF_{11}$-*b*-$PDHF_{13}[PPh_3]Br$ in THF:iPrOH (11:9) at 50 °C for 2 h followed by slow cooling and ageing at 20 °C was carried out (Figure 4. 3a). This was necessary to re-dissolve the small irregular aggregates formed by rapid precipitation at 20 °C (Figure 4. 3c). Using PEG as a polar corona-forming block was also successful in the preparation of nanofibers via CDSA. In solvent mixtures with high contents (90 %) of polar solvent (iPrOH, EtOH or MeOH) mainly small irregular aggregates were observed (< 50 nm) (Figure S4. 12a-c). Fibers were exclusively obtained in THF:EtOH (1:1, v/v) (Figure 4. 3b, d).

The absorption spectra for the different (*S*-)- and (*R*-)-based materials in THF display a broad peak at ca. 390 nm typical for solvated poly(di-*n*-alkylfluorene) materials (Figure S4. 13a-c).[29] For the fibers formed via CDSA of the phosphonium-capped (*R*-) $PDCF_{11}$-*b*-$PDHF_{13}$ and (*S*-) $PDCF_6$-*b*-$PDHF_{10}$ BCPs in THF:iPrOH solvent mixtures a slightly red-shifted shoulder at 410 nm and a blue-shifted maxima at 380 nm was observed in the absorption spectra (Figure S4. 13b, c). This is attributed to mixed H- and J- like aggregate characteristics.[30,31] However, for the fibers formed by CDSA of (*S*-) $PDCF_6$-*b*-$PDHF_{10}$-*b*-$PNIPAm_{68}$ in THF:MeOH (1:1, v/v) a significant blue-shifted maximum absorption peak at 352 nm and a small red-shifted shoulder at 400 nm were detected (Figure S4. 13a). This suggests that H-like aggregation is predominant which could be a result of

aggregation of the (*S*-) PDCF block in the more polar solvent system (MeOH vs iPrOH). Similar to the emission profiles of fibers prepared by CDSA of PDHF-based BCPs presented in Chapters 2 and 3, the emission spectra for the fibers composed of the (*S*-)- and (*R*-)-based materials also display defined vibronic features with a ratio of 1.7:1 of the $I_{0\text{-}0}$ band (λ_{max} = 412-417 nm) to the $I_{0\text{-}1}$ band (λ_{max} = 442nm) (Figure S4. 13d).

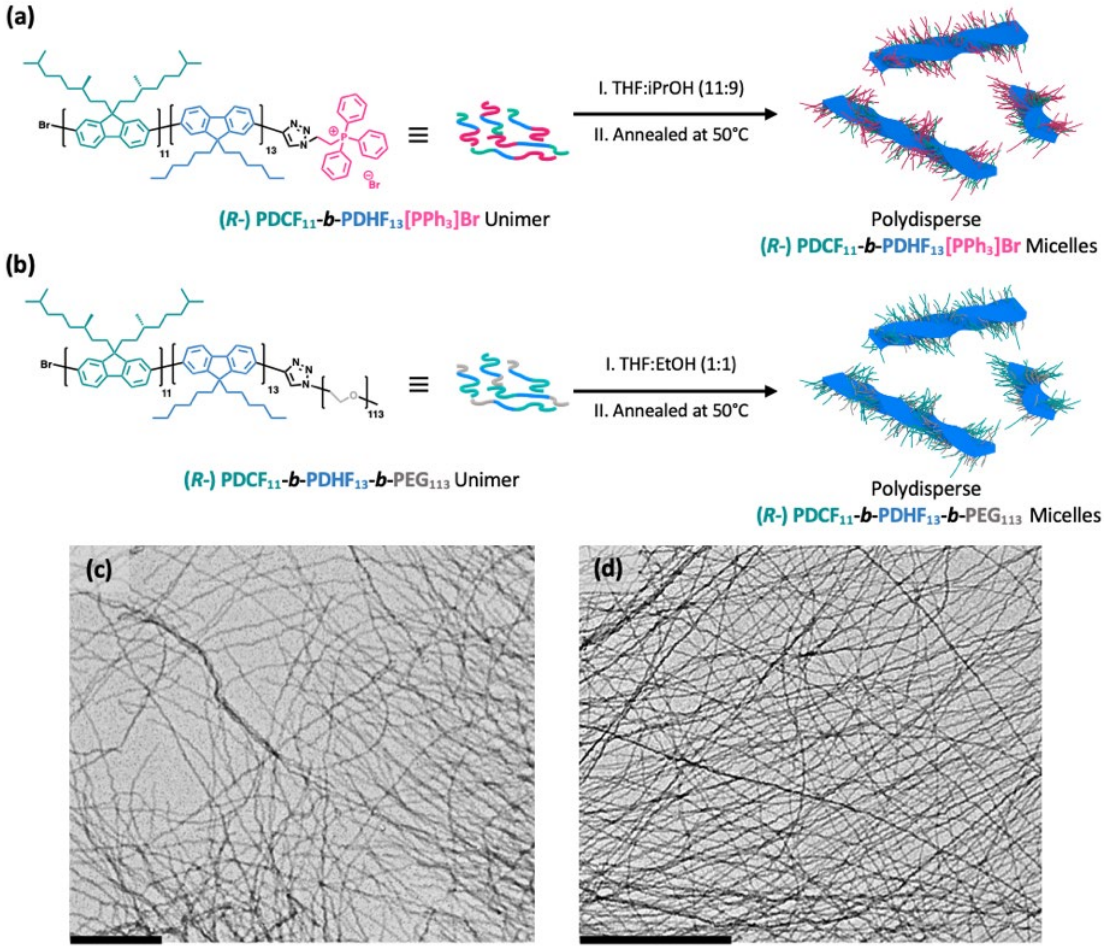

Figure 4. 3: (a) Self-assembly of (*R*-) $PDCF_{11}$-*b*-$PDHF_{13}[PPh_3]Br$ in THF:iPrOH (11:9, v/v) to form helical nanofibers. Chemical structure of (*R*-) $PDCF_{11}$-*b*-$PDHF_{13}[PPh_3]Br$ and schematic illustration of the nanofiber preparation. (b) Self-assembly of (*R*-) $PDCF_{11}$-*b*-$PDHF_{13}$-*b*-PEG_{113} in THF:EtOH (1:1, v/v) to form helical nanofibers. Chemical structure of (*R*-) $PDCF_{11}$-*b*-$PDHF_{13}$-*b*-PEG_{113} and schematic illustration of the nanofiber preparation. (c) TEM image of (*R*-) $PDCF_{11}$-*b*-$PDHF_{13}[PPh_3]Br$ nanofibers drop cast from THF:iPrOH (11:9, v/v). Scale bar: 1 µm. (d) TEM image of (*R*-) $PDCF_{11}$-*b*-$PDHF_{13}$-*b*-PEG_{113} nanofibers drop cast from THF:EtOH (1:1, v/v). Scale bar: 1 µm.

4.3.3. Characterization of Nanofiber Helicity

Characterizing helical nanofiber structures is a challenge as helicity may be present on different length scales, this affects which analytical technique is able to efficiently characterize and observe the helical conformation.[32] CD spectroscopy

is the most used technique for probing the helicity of nanofibers in solution but a racemic mix of left- and right-handed helices would not be detected. AFM can be used to probe the helicity of the nanofibers in the dried state. Helical nanofibers should be identified by the presence of visible periodic and angled striping along the nanofiber. The height or phase profile will give information on the size of the helical pitch and the angle of the striping will indicate the handedness. Overall there are many challenges in probing the helicity of nanofibers, for CD spectroscopy artifacts can hinder the validity of the measurements. For AFM, the nanofibers will need to possess a helical pitch of several nanometers to be visible, additionally the helical structure of the nanofiber maybe shielded by large solubilizing coronal chains on the periphery that could render the helix structure invisible from the AFM tip.[32]

CD spectroscopy experiments were conducted to obtain evidence of helicity in the nanofibers prepared by CDSA of (*S*-) or (*R*-) PDCF-*b*-PDHF based materials. We needed to also determine the origin of helicity and rule out any potential contributions to the CD spectra from isolated molecules or non-fibrous aggregates. Absorption and CD spectra were conducted in tandem to ensure the samples were of a sufficient concentration to detect a CD signal and to determine whether any CD signal observed also corresponds to the absorption peaks for polyfluorene. The CD spectrum of (*R*-) $PDCF_{11}$-*b*-$PDHF_{13}[PPh_3]Br$ unimers in THF showed no active signal (Figure 4. 4a) nor was a signal detected for the (*R*-) $PDCF_{11}$ homopolymer in THF:iPrOH (11:9, v/v) (Figure S4. 14a). A clear CD signal was detected for the fibers formed from CDSA of (*R*-) $PDCF_{11}$-*b*-$PDHF_{13}[PPh_3]Br$ in THF:iPrOH (9:11, v/v). The minima of the negative CD signal corresponds to the maximum absorption peak (λ_{max} = 384 nm) for the fiber sample. A shoulder trough in the CD signal is observed also associated with the absorption peak observed at 400 nm for the fibers. Therefore we can attribute the CD signal to helicity present due to the fiber conformation. Additionally, the presence of a CD signal also indicates that the fibers formed have a preferential twist direction.

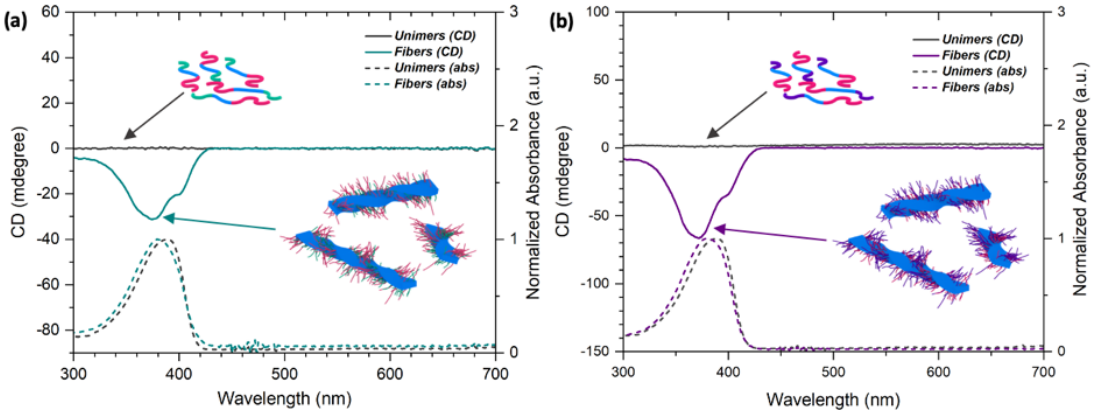

Figure 4. 4: (a) CD and absorption spectra of (*R*-) PDCF$_{11}$-*b*-PDHF$_{13}$[PPh$_3$]Br unimers in THF (grey traces) and fibers in THF:iPrOH (11:9, v/v) (teal traces). Inset: cartoon illustrations of the (*R*-) PDCF$_{11}$-*b*-PDHF$_{13}$[PPh$_3$]Br unimers and helical nanofibers. (b) CD and absorption spectra of (*S*-) PDCF$_6$-*b*-PDHF$_{10}$[PPh$_3$]Br unimers in THF (grey traces) and fibers in THF:iPrOH (9:11, v/v) (purple traces). Inset: cartoon illustrations of the (*S*-) PDCF$_6$-*b*-PDHF$_{10}$[PPh$_3$]Br unimers and helical nanofibers. Sample concentrations: 0.02 mg mL^{-1}.

For the (*S*-)-based analogue, (*S*-) PDCF$_6$-*b*-PDHF$_{10}$[PPh$_3$]Br, the CD spectra collected for the unimers in THF and fibers in THF:iPrOH (9:11, v/v) matched the spectra obtained for (*R*-) PDCF$_{11}$-*b*-PDHF$_{13}$[PPh$_3$]Br. The negative monosignate Cotton effect observed for the two enantiomers suggest that both materials have a preference to form helical nanofibers of the same handedness via twisting of the ribbon-like PDHF fiber cores. A bisignate cotton effect would indicate chiral aggregation of the (*S*-) or (*R*-) PDCF blocks.[33] For the fibers formed via CDSA of (*S*-) PDCF$_6$-*b*-PDHF$_{10}$-*b*-PNIPAm$_{68}$ in THF:MeOH (1:1, v/v) a bisignate cotton effect was observed which suggests that some chiral aggregation of the (S-) PDCF block occurred during self-assembly. This could be due to the more selective solvent used for this material (MeOH) compared to that used in the preparation of the (*S*-)/(*R*-) PDCF-*b*-PDHF[PPh$_3$]Br fibers (iPrOH) (Figure S4. 15).

AFM height imaging was used next to probe the helicity of the fibers in the dried state. For these experiments the phosphonium-capped BCP materials are more suitable for analysis to probe the helical pitch. Initial attempts at probing the helicity of the triblock copolymer materials were unsuccessful due to the large polymeric corona-forming block which shielded the helical pitch in the fibers from the AFM tip. However, AFM height analysis of the (*S*-) PDCF$_6$-*b*-PDHF$_{10}$[PPh$_3$]Br fibers, drop cast from THF:iPrOH (9:11, v/v) on to carbon-coated mica, revealed a periodic dip in height along the fiber core and along the coronal chains flanking

the core (Figure 4. 5a). A pitch of ca. 20 nm was observed along the fiber core (Figure 4. 5b).

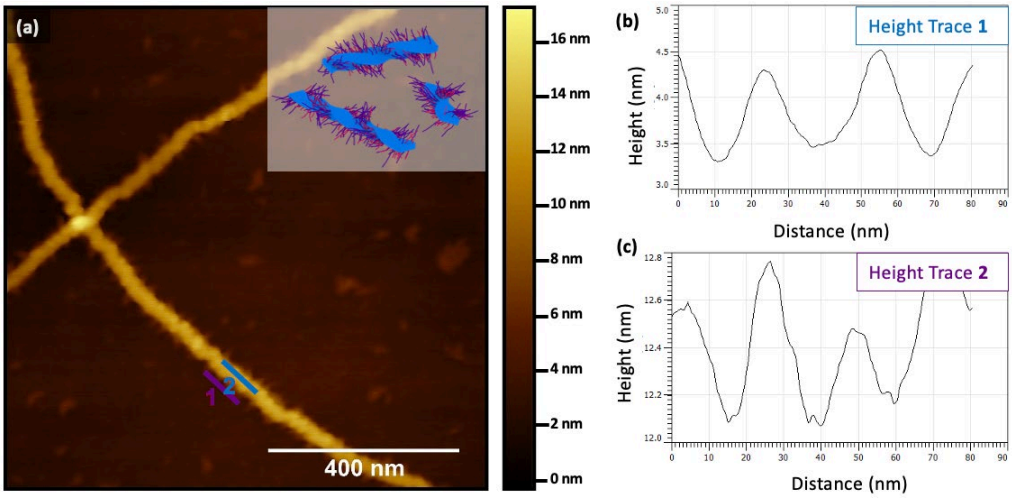

Figure 4. 5: (a) AFM height image of helical fibers prepared by the CDSA of (*S*-) $PDCF_6$-*b*-$PDHF_{10}[PPh_3]Br$ in THF:iPrOH (9:11, v/v) drop cast on to a carbon-coated copper mica. Scale bar: 400 nm. Inset: cartoon of (*S*-) $PDCF_6$-*b*-$PDHF_{10}[PPh_3]Br$ helical fibers. Corresponding height traces for the AFM image along (b) coronal region and (c) fiber core.

4.3.4. Seeded Growth: Living CDSA of Chiral PF Block Copolymers

Seeded growth of the phosphonium-capped (*S*-) or (*R*-) PDCF-*b*-PDHF BCPs was investigated in an attempt to prepare low length dispersity helical micelles. (*R*-) $PDCF_{11}$-*b*-$PDHF_{13}[PPh_3]Br$ seed micelles (L_n = 143 nm, L_w/L_n = 1.10, where L_n is the number-average length and L_w is the weight-average length) were prepared by sonication of polydisperse fibers at 0 °C for 1 h in THF:iPrOH (11:9, v/v) (Figure S4. 16a). Unimer in THF (5 mass equivalents) was added in one rapid injection at 20 °C to the seed sample (Figure S4. 16b). Some epitaxial growth was observed resulting in longer fiber-like micelles (up to 1 μm long), however a substantial amount of small irregular aggregates were also observed similar to that detected for the sample of the initial (*R*-) $PDCF_{11}$-*b*-$PDHF_{13}[PPh_3]B$ polydisperse fibers prepared at 20 °C before annealing. Seeded growth was next conducted at an elevated temperature (40 °C) to minimize the formation of these small aggregates but not sufficiently high enough to cause self-seeding of the pre-existing seed micelles. No small irregular aggregates were detected in this seeded growth experiment. Low-length dispersity micelles were obtained (L_n = 1072 nm, L_w/L_n = 1.10) however significant aggregation, branching and bundling of the fibers were evident from TEM analysis (Figure S4. 16c). Similar limitations were also observed for the phosphonium-capped (*S*-) BCP analogue. These results suggest

that the (*S*-)/(*R*-) PDCF-*b*-PDHF[PPh_3]Br micelles have limited colloidal stability and the materials exhibit rapid crystallization kinetics in solvents that are poor for PDHF. The molecular composition of the BCP material may be the origin of these issues as the chiral PDCF block is on one end of the crystallizable PDHF block and the phosphonium group is on the other end. The resulting micelles formed via CDSA contain the small phosphonium group flanking the micelle core and also (*S*-)/(*R*-) PDCF coronal chains that are fully exposed to the solvent. The solubilizing phosphonium group may be shielded from the solvent by the (*S*-)/(*R*-) PDCF coronal chains which therefore limits the colloidal stability of the micelles and leads to possible aggregation between the (*S*-)/(*R*-) PDCF chains.

Living CDSA for the triblock copolymer (triBCP) (*S*-) $PDCF_6$-*b*-$PDHF_{10}$-*b*-$PNIPAm_{68}$ was explored next (Figure 4. 6a). The substantially longer solubilizing PNIPAm block was expected to overcome the seeded growth limitations experienced by the (*S*-)/(*R*-) PDCF-*b*-PDHF[PPh_3]Br materials. Sonication of the polydisperse fibers formed in THF:MeOH (1:1, v/v) (Figure 4. 6b)at 0 °C for 1 h led to the formation of short seed micelles (L_n = 38 nm, L_w/L_n = 1.08) (Figure 4. 6c). In a typical seeded growth experiment a small volume of triBCP unimer in THF was added to the seeds in THF:MeOH (1:1, v/v) at 20 °C. The samples were immediately stirred for 10 s before ageing at 20 °C for 24 h before TEM imaging. Following solvent evaporation of the samples cast on to a carbon-coated copper mesh grid the micelles initially appeared aggregated (Figure 4. 6e, f). However, no branched structures or irregular aggregates were observed, and the micelle contour lengths could be easily traced. A linear dependence on the L_n and the unimer-to-seed ratio (m_{unimer}/m_{seed}) used in the seeded growth experiment was observed (Figure 4. 6g). Fiber lengths between 72 nm to 704 nm with low length dispersities (L_w/L_n < 1.08) were obtained (Figure S4. 17). AFM height imaging provided a clearer visualization of the individual fibers obtained via seeded growth, this could be due to the different substrate (carbon-coated copper grid vs silicon wafer) and drying process (air-drying vs drying under a N_2 stream) used for TEM and AFM imaging (Figure 4. 6d).

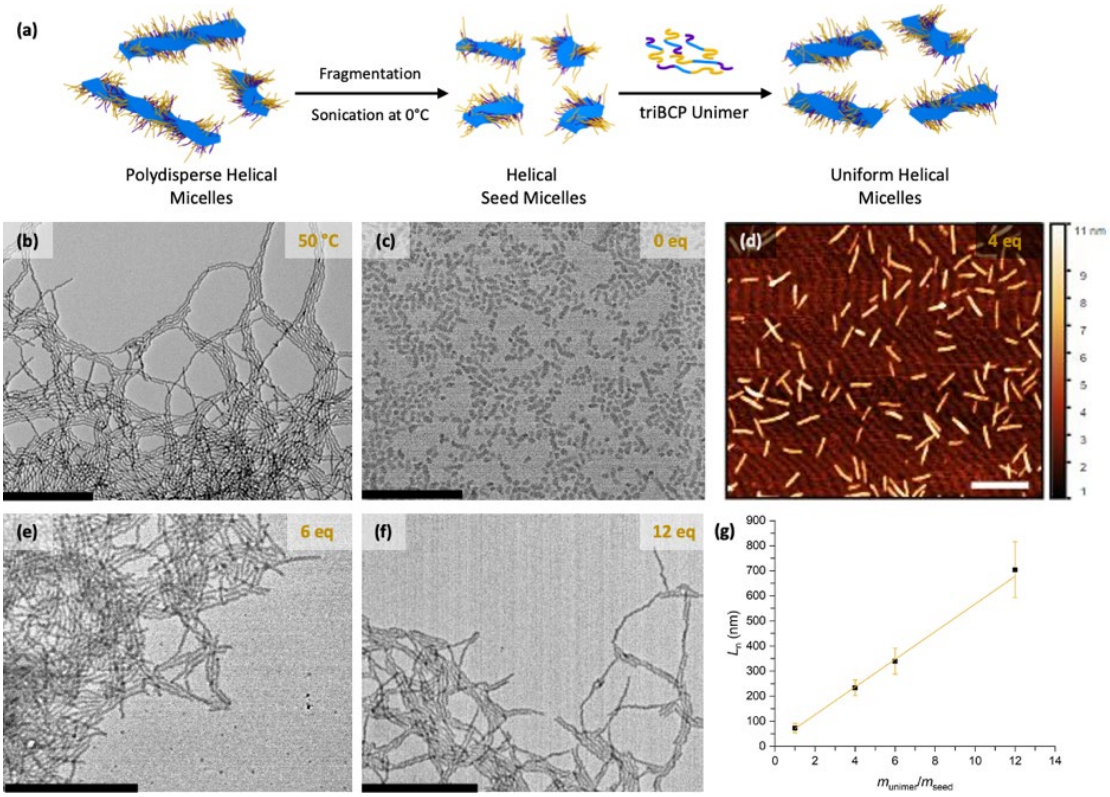

Figure 4. 6: Schematic illustration of the seeded growth protocol employed to prepare low dispersity (*S*-) PDCF$_6$-*b*-PDHF$_{10}$-*b*-PNIPAm$_{68}$ nanofibers in THF:MeOH (1:1, v/v). TEM images of the (b) polydisperse helical fibers prepared in THF:MeOH (1:1, v/v) and (c) the seed micelles (L_n = 38 nm, L_w/L_n= 1.08) prepared by sonication of the polydisperse fibers at 0 °C for 1 h. The unimer was added as a solution in THF. AFM and TEM images of nanofibers of controlled length prepared by the seeded growth of (*S*-) PDCF$_6$-*b*-PDHF$_{10}$-*b*-PNIPAm$_{68}$ BCPs from seed micelles with m_{unimer}/m_{seed} values of (d) 4, (e) 6 and (f) 12. Scale bars: (b), (e), (f) 1 µm, (c), (d) 500 nm. (g) Graph of micelle number-average length (L_n) against unimer-to-seed ratio (m_{unimer}/m_{seed}) showing a linear correlation.

4.4. Summary

In this Chapter, the synthesis and solution self-assembly of (*S*-)/(*R*-) PDCF-*b*-PDHF diblock and triblock copolymers is presented. These materials were synthesized via a combination of sequential GRIM polymerization, RAFT polymerization and click chemistry. Fiber formation was observed in mixed solvent systems containing common solvent and coronal selective polar protic solvents. Additionally, 3D spiral platelet structures were also observed from the self-assembly of phosphonium-capped (*S*-) PDCF-*b*-PDHF BCP in THF and DMSO solvent mixtures. We report that the fibers formed via CDSA of these materials have a helical conformation, characterized by CD spectroscopy or AFM microscopy. Through a seeded growth protocol, low length dispersity fibers ($L_w/L_n < 1.08$) of tunable lengths for the (*S*-) $PDCF_6$-*b*-$PDHF_{10}$-*b*-$PNIPAm_{68}$ triBCP were obtained. However, seeded growth approaches were not successful for the preparation of uniform (*S*-)/(*R*-) PDCF-*b*-PDHF[PPh_3]Br fibers. This observation suggested that the small phosphonium group enabled rapid aggregation of added unimer and the lack of a large polymeric corona prevented the formation of uniform fibers via living CDSA.

Future work will focus on investigating the solution self-assembly of materials with (*S*-) or (*R*-) PDCF as the core-forming block. The branched side-chains on the fluorene repeat unit offer slower crystallization kinetics crystallinity than that of the PDHF. This could enable the formation of helical micelles with nematic liquid crystalline core.[34] Furthermore, the helical nanofibers presented in this report could be used as templates for the preparation of chiral hybrid plasmonic materials via attachment of inorganic nanostructures (coated with alkyl ligands) to the (*S*-)/(*R*-) PDCF block.[35–37]

4.5. Supporting Information

4.5.1. Materials and Methods

All reagents and solvents used for polymers synthesis were of reagent grade, and unless otherwise stated were used as received. Solvents for self-assembly were of HPLC grade and filtered using 0.2 μm syringe filters prior to use.

Nuclear magnetic resonance (NMR). ^{1}H NMR spectra were taken with a Varian 400 MHz spectrometer or a Bruker 500 MHz spectrometer; chemical shifts were referenced to the residual solvent peak ($CHCl_3$ δ = 7.26 ppm).

Gel Permeation Chromatography (GPC). measurements were conducted on Viscotek GPC_{max} equipped with a UV detector at 400 nm and a refractometer. Measurements were carried out at 1.0 mL min^{-1} with THF containing [*n*Bu4N]Br (0.1% w/w) as the eluent at 35 °C, results were measured against polystyrene standards (Viscotek).

Matrix-Assisted Laser Desorption/Ionization Time-Of-Flight Mass Spectrometry (MALDI-TOF MS). Measurements were conducted on a Bruker Ultraflex II ToF spectrometer under the reflector positive ion regime. Samples were prepared with a 9:1 ratio of *trans*-2-[3-(4- *tert*-butylphenyl)-2-methyl-2-propenylidene]malonitrile matrix (20 mg ml^{-1} in THF) to polymer solution (1 mg ml^{-1} in THF). A 5 μL of the sample was deposited onto the sample plate and dried under ambient conditions.

Transmission Electron Microscopy (TEM). Samples were prepared by drop casting 10 μl of the nanofiber solution onto a carbon-coated copper grid (Agar Scientific, mesh size 200). Bright-field TEM micrographs were taken using a JEOL JEM 1400 EX microscope operating at 120 kV, equipped with a Gatan Orius SC1000 CCD camera. Micelle length distributions were determined using the software program ImageJ developed at US National Institute of Health. A minimum of 200 micelles are traced to determine their contour length and histograms of the length distributions obtained. This data allows for calculation of the number average length (L_n), weight average length (L_w) for each sample, this is calculated as shown below (L = length of fiber, N = number).

$$L_n = \frac{\sum_{i=1}^{n} N_i L_i}{\sum_{i=1}^{n} N_i} \qquad L_w = \frac{\sum_{i=1}^{n} N_i {L_i}^2}{\sum_{i=1}^{n} N_i L_i}$$

Atomic Force Microscopy (AFM). Samples were prepared by drop casting 10 µl of the nanofiber solution onto a carbon-coated mica or onto a silicon wafer. Imaging was taken using a Bruker Multimode VIII atomic force microscope equipped with a ScanAsyst-HR fast scanning module and a ScanAsyst-Air-HR probe (tip radius, 2 nm), under ambient conditions utilising peal force feedback control. Imaging was also obtained by Agilent Technologies 5500 Scanning Probe Microscope operating by tapping-mode.

Spectroscopic Measurements. UV/vis data were obtained on a Lambda 35 Spectrometer employing glass cells (1 cm x 1 cm) from 200 to 800 nm. Fluorescence data were obtained on a JASCO FP-6500 Spectrofluorometer using an excitation wavelength of λ_{ext} = 380 nm. CD spectra were obtained using a JASCO J-810 spectropolarimeter using a quartz cuvette with a 1 cm path length.

4.5.2. Synthesis of alkyne-terminated (S-) PDCF-b-PDHF and (R-) PDCF-b-PDHF

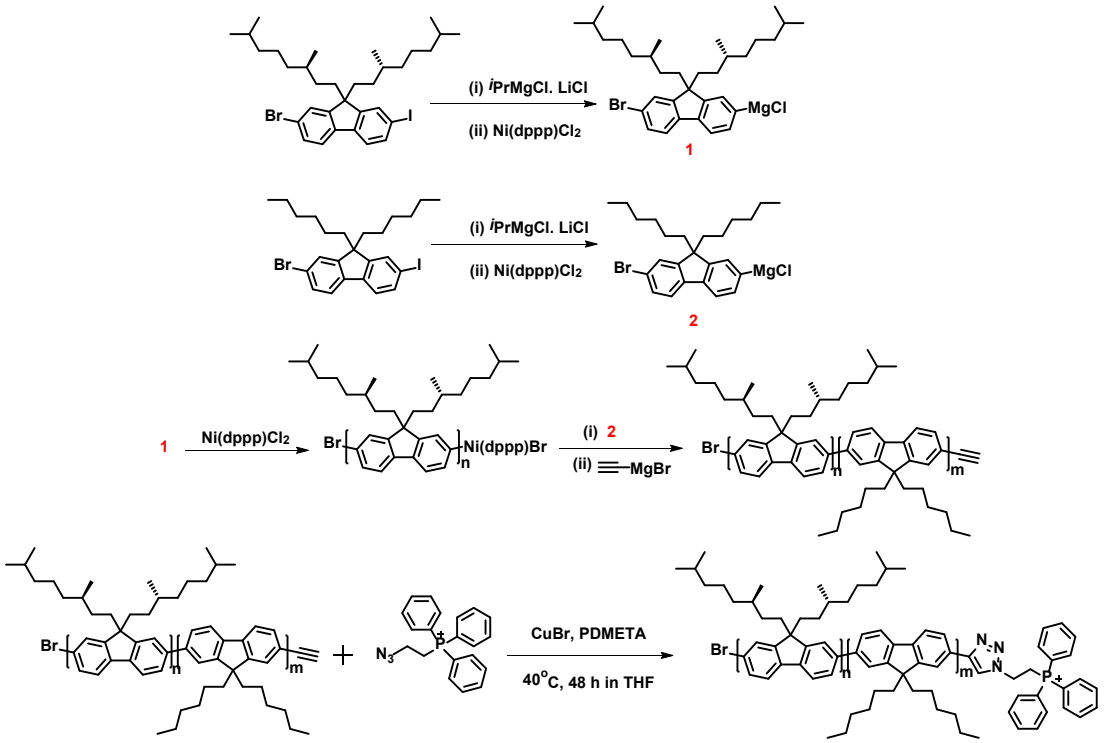

Scheme S4. 1: Synthesis of charge capped chiral polyfluorene diblock copolymers e.g. (*R*-) PDCF-*b*-PDHF[PPh_3]Br. PMDETA = *N,N,N′,N″,N‴*-pentamethyldiethylenetriamine

Alkyne-terminated (*S*-) PDCF-*b*-PDHF and (*R*-) PDCF-*b*-PDHF were synthesized by sequential Grignard Metathesis polymerization (GRIM).[38] 2-Bromo-7-iodo-9,9-bis-*n*-hexylfluorene and 2-Bromo-7-iodo-9,9-bis-*n*-(3,7-

dimethyoctane) were synthesised according to literature procedures. 2-Bromo-7-iodo-9,9-bis-*n*-hexylfluorene (479 mg, 0.89 mmol) and 2-Bromo-7-iodo-9,9-bis-*n*-(3,7-dimethyoctane) fluorene (553 mg, 0.86 mmol) were separately dissolved in 10 mL of anhydrous THF. Both solutions were cooled to -20˚C before 1.3 M *i*PrMgCl.LiCl (1 eq.) was added dropwise then the resulting solution were left to stir for 90 min at -78˚C. The activated solution of 2-Bromo-7-iodo-9,9-bis-*n*-(3,7-dimethyoctane) fluorene monomer was added in one quick injection to a solution of Ni(dppp)Cl_2 (24 mg, 0.044 mmol) and anhydrous THF (100 mL) at 0˚C. After 20 minutes of stirring, the activated 2-bromo-7-iodo-9,9-bis-*n*-hexylfluorene monomer was added to in one quick injection to the reaction mixture. After 30 mins, 0.5 M ethynylmagnesium bromide (3 mL) was added to the reaction mixture which was then stirred for 16 h. The resultant mixture was then precipitated into methanol, giving a yellow solid. Further purification by Soxhlet extraction in ethyl acetate and in chloroform gave the purified polymers.

The degree of polymerisation of all (*S*-) PDCF and (*R*-) PDCF homopolymer aliquots was calculated by MALDI-TOF MS with a 9:1 ratio of matrix to polymer solution (0.2 mg mL^{-1} in THF). The polydispersity (M_w/M_n) was determined by GPC (THF containing [*n*Bu_4N]Br (0.1 % w/w)).

(*S*-) $PDCF_6$-*b*-$PDHF_{10}$-yne

Alkyne-terminated (*S*-) $PDCF_6$-*b*-$PDHF_{10}$-yne was synthesized by an analogous method to that mentioned above. Yield = 139 mg, 41 %. GPC of (*S*-) $PDCF_6$ (THF containing [*n*Bu_4N]Br (0.1 % w/w), 1 mL min^{-1}): M_n = 10.3 kDa, M_w = 11.8 kDa, M_w/M_n = 1.15. GPC of (*S*-) $PDCF_6$-*b*-$PDHF_{10}$ (THF containing [*n*Bu_4N]Br (0.1 % w/w), 1 mL min^{-1}): M_n = 18.9 kDa, M_w = 22.6 kDa, M_w/M_n = 1.19.

(*R*-) $PDCF_{11}$-*b*-$PDHF_{13}$-yne

Alkyne-terminated (*R*-) $PDCF_{11}$-*b*-$PDHF_{13}$-yne was synthesized by an analogous method to that mentioned above. Yield = 155 mg, 48 %. GPC of (*R*-) $PDCF_{11}$ (THF containing [*n*Bu_4N]Br (0.1 % w/w), 1 mL min^{-1}): M_n = 11.0 kDa, M_w = 13.3 kDa, M_w/M_n = 1.21. GPC of (*R*-) $PDCF_{11}$-*b*-$PDHF_{13}$ (THF containing [*n*Bu_4N]Br (0.1 % w/w), 1 mL min^{-1}): M_n = 29.1 kDa, M_w = 35.6 kDa, M_w/M_n = 1.22.

4.5.3. Synthesis of azido-terminated PNIPAm

Azido-terminated $PNIPAm_{68}$ was prepared by RAFT polymerization. RAFT CTA 2-(dodecylthiocarbonothioylthio)-2-methylpropionic acid 3-azido-1-propanol ester (39.6 mg, 0.35 mmol), *N*-Isopropylacrylamide (2 g, 17.67 mmol) and AIBN (11.6 mg, 0.0071 mmol) were dissolved in 4 mL of DMF then the resulting solution was sparged with N_2 for 15 mins. The mixture was then stirred at 70 °C for 20 h before being cooled to room temperature and diluted with THF to quench the polymerization. The resultant mixture was then precipitated into cold diethyl ether and purified further by repeated precipitation into cold hexanes to afford a white solid (658 mg, yield: 33 %). GPC (THF containing [nBu$_4$N]Br (0.1 % w/w), 1 mL min^{-1}): M_n = 9.8 kDa, M_w = 11. 5 kDa, M_w/M_n = 1.17.

4.5.4. Synthesis of block copolymers via CuAAC click reactions

Alkyne- and azido-terminated homopolymers and block copolymers were coupled using copper-catalyzed azide-alkyne cycloaddition (CuAAc) click reactions. UV traces obtained from GPC analysis display a significant shift in molecular weight of the final π-conjugated diblock or triblock copolymer and the alkyne-terminated π-conjugated homopolymer or diblock copolymer starting material. High purity of the coupled block copolymer is made evident by the presence of a single monomodal distribution in the UV trace.

(*S*-) $PDCF_6$-*b*-$PDHF_{10}$[PPh_3]Br

Alkyne-terminated (*S*-) $PDCF_6$-*b*-$PDHF_{10}$ (50 mg, 9.72 x 10^{-6} mmol) and 2-azido-2-triphenylphosphonium bromide (10 mg, 1.05 x 10^{-5} mmol) were dissolved in THF (4 mL) and subjected to three consecutive freeze-pump-thaw cycles. CuBr (5 mg, excess) and PMDETA (10 µl, excess) were dissolved in 1 mL anhydrous THF then added to polymer solution. The reaction mixture was heated to 45^{o}C and stirred for 48 h. The polymers were then purified by passing the reaction mixture through a basic alumina column to remove Cu/PMDETA. Volatiles were removed *in vacuo* followed by washing with methanol to remove residual 2-azido-2-triphenylphosphonium bromide. Residual alkyne-terminated (*S*-) $PDCF_6$-*b*-$PDHF_{10}$ was removed by silica gel chromatography (eluent chloroform 100 %), (*S*-) $PDCF_6$-*b*-$PDHF_{10}$[PPh_3]Br was collected by using

chloroform and methanol (9:1 v/v) as the eluent to give the product as a yellow solid (21 mg, 42 %). GPC (THF containing [*n*Bu$_4$N]Br (0.1 % w/w), 1 mL min^{-1}): M_n = 19.2 kDa, M_w = 23.3 kDa, M_w/M_n = 1.19.

(*S*-) PDCF$_6$-*b*-PDHF$_{10}$-*b*-PNIPAm$_{68}$

Alkyne-terminated (*S*-) PDCF$_6$-*b*-PDHF$_{10}$ (60 mg, 0.011 mmol) and azido-terminated PNIPAm (168 mg, 0.012 mmol) were dissolved in THF (4 mL) and subjected to three consecutive freeze-pump-thaw cycles. CuBr (5 mg, excess) and PMDETA (10 μl, excess) were dissolved in 1 mL anhydrous THF then added to polymer solution. The reaction mixture was heated to 45 °C and stirred for 48 h. The polymers were then purified by passing the reaction mixture through a basic alumina column to remove Cu/PMDETA. Volatiles were removed *in vacuo* followed by washing with methanol to remove residual azido-terminated PNIPAm. Residual alkyne-terminated (*S*-) PDCF$_6$-*b*-PDHF$_{10}$ was removed by silica gel chromatography (eluent chloroform 100 %), (*S*-) PDCF$_6$-*b*-PDHF$_{10}$-*b*-PNIPAM$_{68}$ was collected by using chloroform and methanol (9:1 v/v) as the eluent to give the product as a yellow solid (23 mg, 38 %). GPC (THF containing [*n*Bu$_4$N]Br (0.1 % w/w), 1 mL min^{-1}): M_n = 25.1 kDa, M_w = 29.6 kDa, M_w/M_n = 1.18.

(*R*-) PDCF$_{11}$-*b*-PDHF$_{13}$[PPh$_3$]Br

Alkyne-terminated (*R*-) PDCF$_{11}$-*b*-PDHF$_{13}$ was synthesized by an analogous method to that described for (*S*-) PDCF$_6$-*b*-PDHF$_{10}$[PPh$_3$]Br earlier. Yield: (22 mg, 44 %). GPC (THF containing [*n*Bu$_4$N]Br (0.1 % w/w), 1 mL min^{-1}): M_n = 30.3 kDa, M_w = 35.9 kDa, M_w/M_n = 1.18.

(*R*-) PDCF$_{11}$-*b*-PDHF$_{13}$-*b*-PEG$_{113}$

(*R*-) PDCF$_{11}$-*b*-PDHF$_{13}$-*b*-PEG$_{113}$ was synthesized by an analogous method to that used to prepare PDCF$_6$-*b*-PDHF$_{10}$-*b*-PNIPAM$_{68}$. Yield: (18 mg, 32 %). GPC (THF containing [*n*Bu$_4$N]Br (0.1 % w/w), 1 mL min^{-1}): M_n = 31.7 kDa, M_w = 36.7 kDa, M_w/M_n = 1.16.

4.5.5. Supplementary Figures

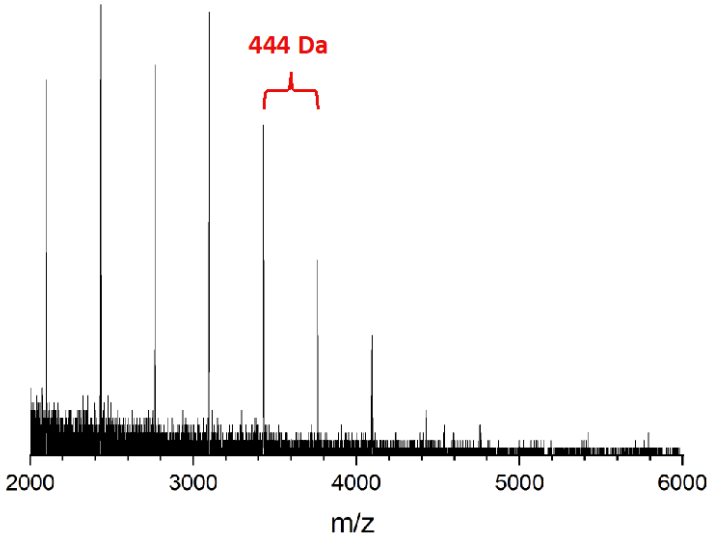

Figure S4. 1: MALDI-TOF mass spectrum of H/H-capped (*S*-) $PDCF_6$ homopolymer aliquot, M^+ = 2667 Da. The mass of each (*S*-) PDCF repeat unit is 444 g mol^{-1}.

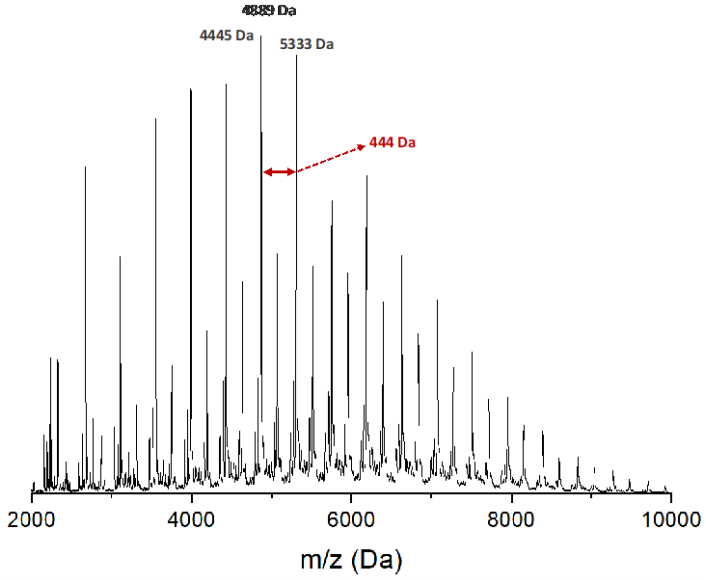

Figure S4. 2: MALDI-TOF mass spectrum of H/H-capped (*R*-) $PDCF_{11}$ homopolymer aliquot, M^+ = 4889 Da. The low intensity peak distribution corresponds to Br/Br-capped (*R*-) $PDCF_{11}$ homopolymer. The mass of each (*R*-) PDCF repeat unit is 444 g mol^{-1}.

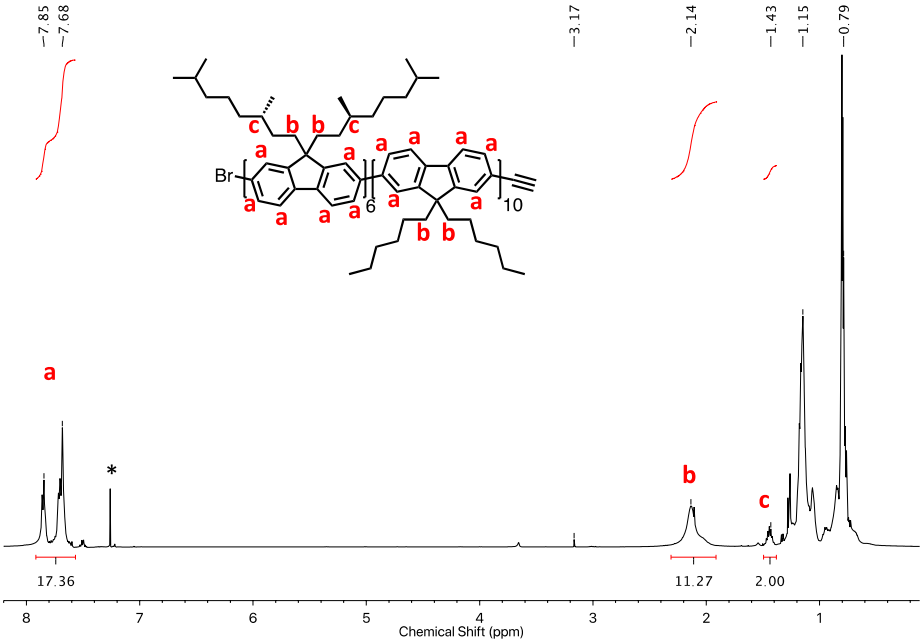

Figure S4. 3: ^{1}H NMR spectrum of (*S*-) PDCF$_{6}$-*b*-PDHF$_{10}$-yne (500 MHz, $CDCl_3$). $CDCl_3$ (δ = 7.26 ppm) is marked with an *.

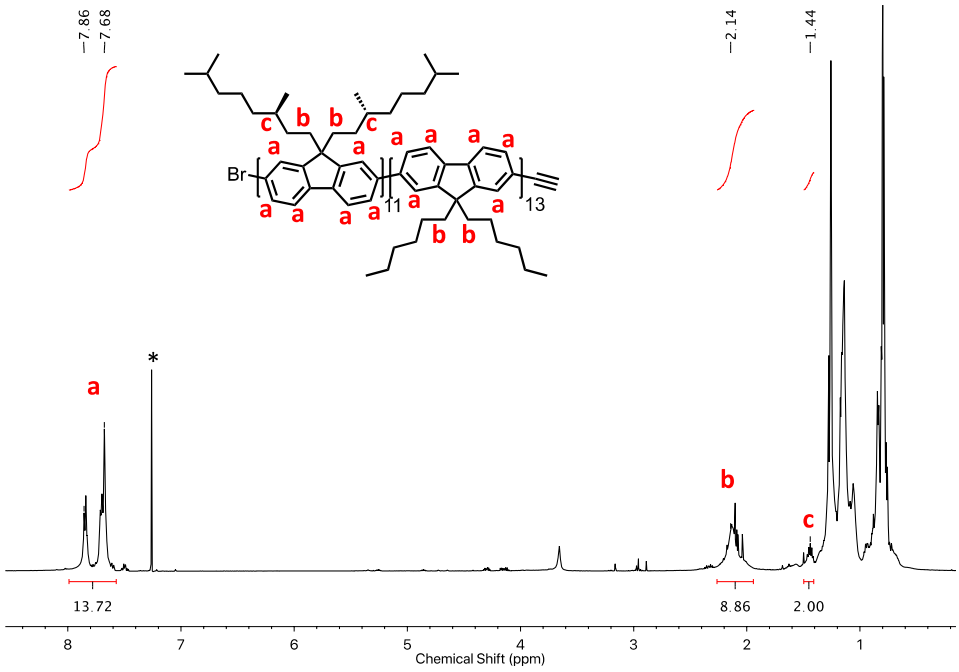

Figure S4. 4: ^{1}H NMR spectrum of (*R*-) PDCF$_{11}$-*b*-PDHF$_{13}$-yne (500 MHz, $CDCl_3$). $CDCl_3$ (δ = 7.26 ppm) is marked with an *.

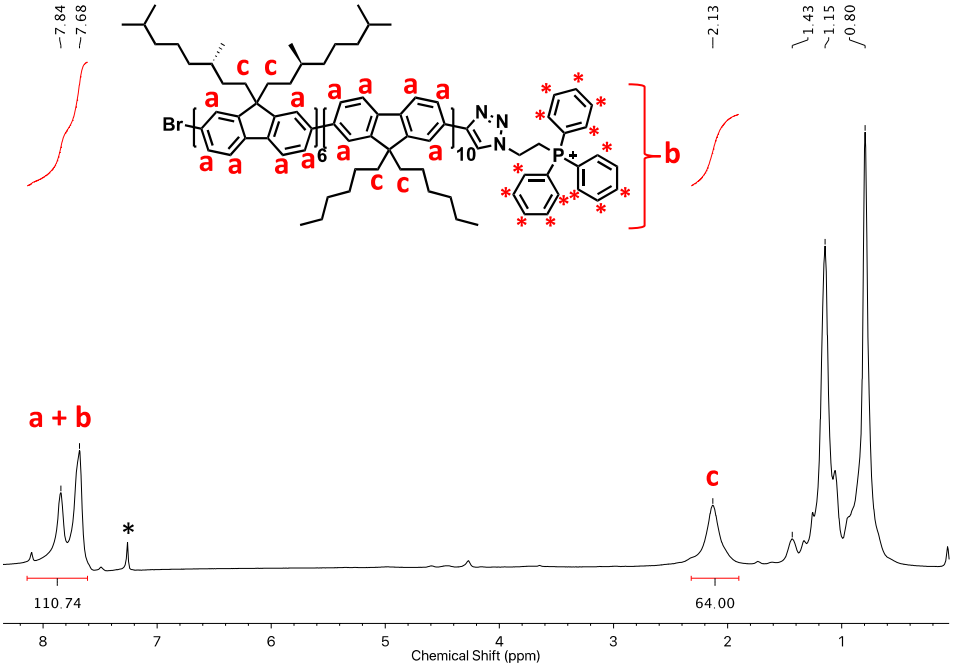

Figure S4. 5: ^{1}H NMR spectrum of (*S*-) PDCF$_6$-*b*-PDHF$_{10}$[PPh$_3$]Br (500 MHz, CDCl$_3$). CDCl$_3$ (δ = 7.26 ppm) is marked with an *.

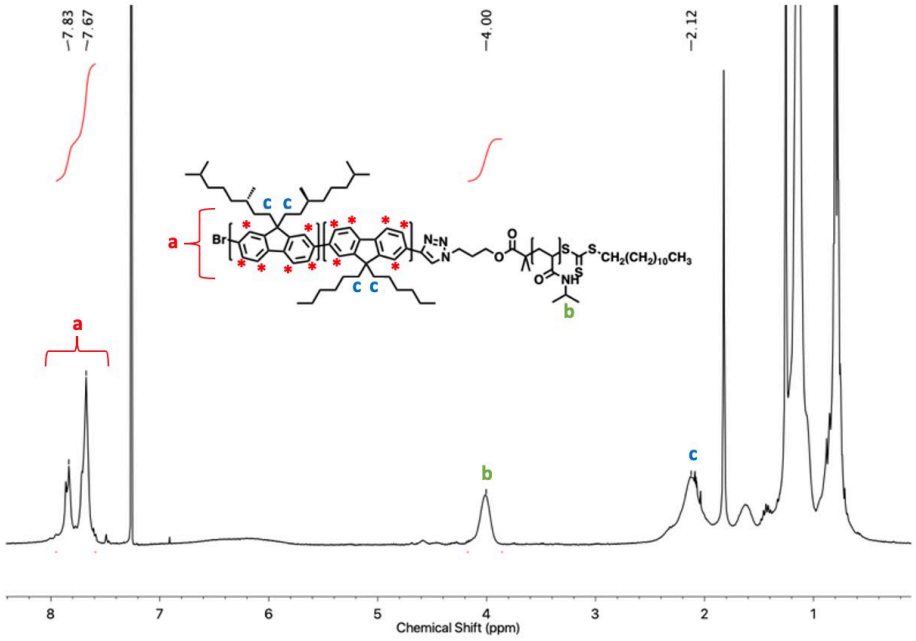

Figure S4. 6: ^{1}H NMR spectrum of (*S*-) PDCF$_6$-*b*-PDHF$_{10}$-*b*-PNIPAm$_{68}$ (500 MHz, CDCl$_3$).

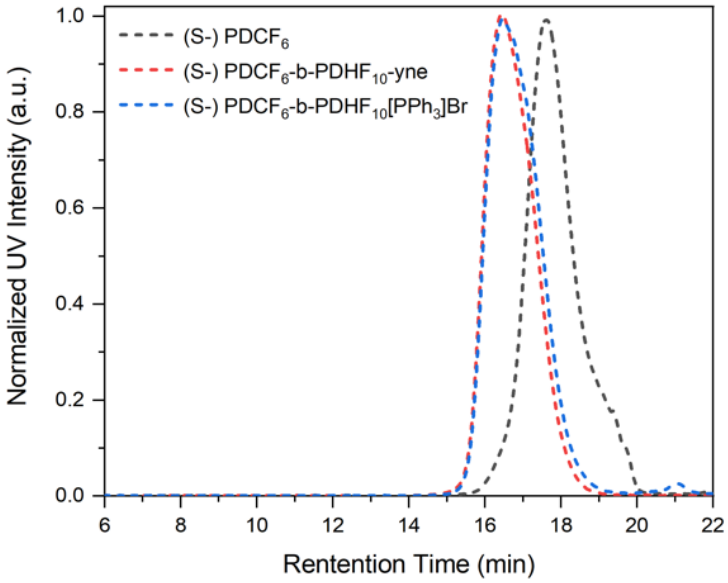

Figure S4. 7: GPC traces (UV response at λ = 400 nm) eluted in THF containing [*n*Bu$_4$N]Br (0.1 % w/w) (1 mL min^{-1}) at 35 ˚C of (*S*-) PDCF$_6$ homopolymer (*grey trace*), alkyne-terminated (*S*-) PDCF$_6$-*b*-PDHF$_{10}$ diblock copolymer (*red trace*) and (*S*-) PDCF$_6$-*b*-PDHF$_{10}$[PPh$_3$]Br (*blue trace*).

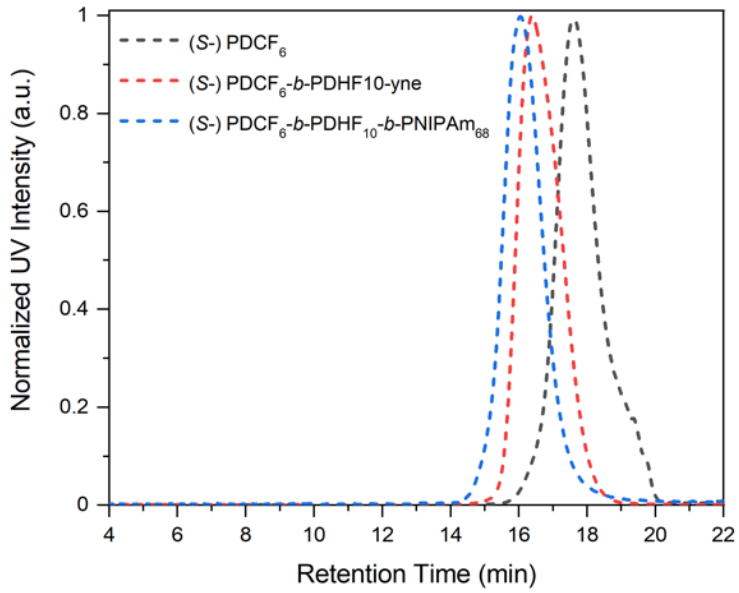

Figure S4. 8: GPC traces (UV response at λ = 400 nm) eluted in THF containing [*n*Bu$_4$N]Br (0.1 % w/w) (1 mL min^{-1}) at 35 ˚C of (*S*-) PDCF$_6$ homopolymer (*grey trace*), alkyne-terminated (*S*-) PDCF$_6$-*b*-PDHF$_{10}$ diblock copolymer (*red trace*) and (*S*-) PDCF$_6$-*b*-PDHF$_{10}$-*b*-PNIPAm$_{68}$ triblock copolymer (*blue trace*).

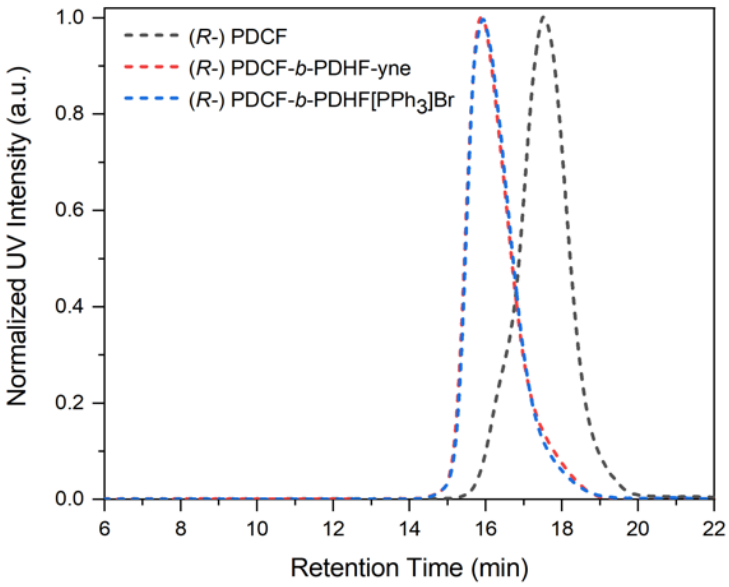

Figure S4. 9: GPC traces (UV response at λ = 400 nm) eluted in THF containing [*n*Bu$_4$N]Br (0.1 % w/w) (1 mL min^{-1}) at 35 ˚C of (*R*-) PDCF$_{11}$ homopolymer (*grey trace*), alkyne-terminated (R-) PDCF$_{11}$-*b*-PDHF$_{13}$ diblock copolymer (*red trace*) and (*R*-) PDCF$_{11}$-*b*-PDHF$_{13}$[PPh$_3$]Br (*blue trace*).

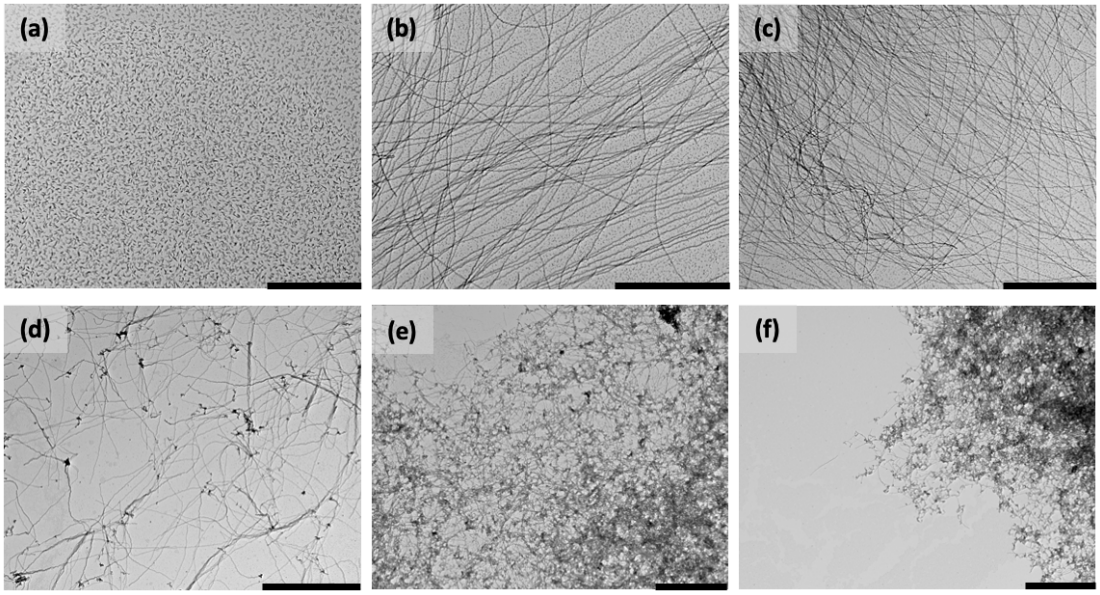

Figure S4. 10: TEM images of (*S*-) PDCF$_6$-*b*-PDHF$_{10}$[PPh$_3$]Br samples prepared by the dropwise addition of iPrOH to the unimer solution in THF until a final amount of (a) 45 %, (b) 50 %, (c), 55 %, (d) 60 %, (e) 65 % and (f) 70 % of iPrOH was reached. Samples were prepared at 0.1 mg mL^{-1} and aged for 24 h at 20 °C before imaging. Scale bars: 2 μm.

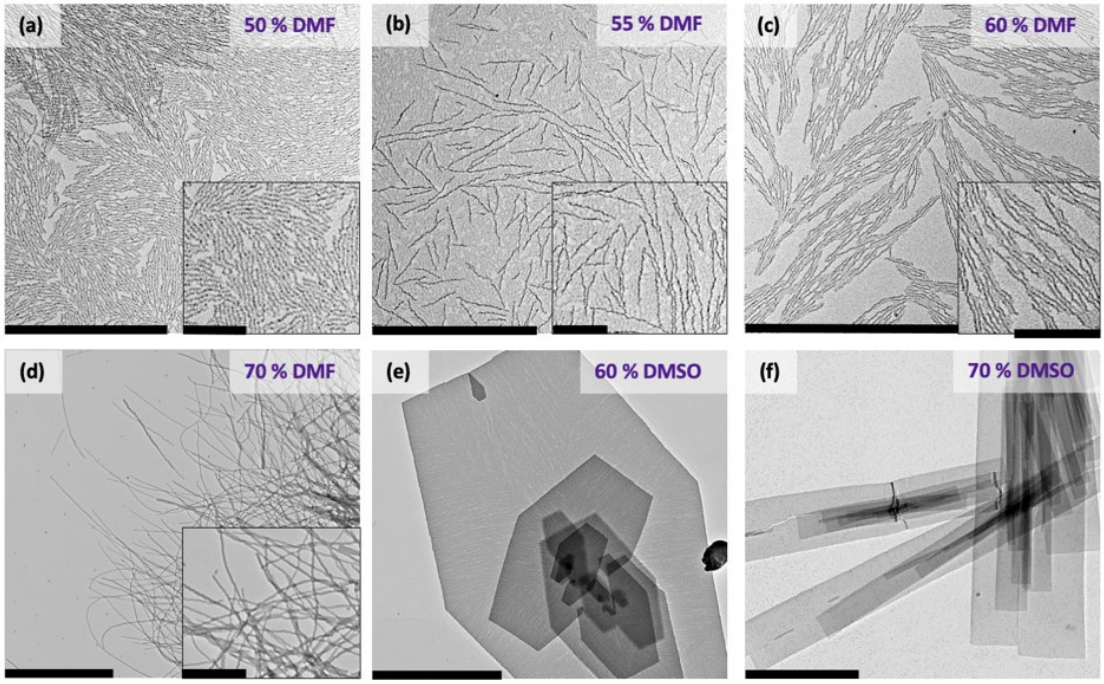

Figure S4. 11: TEM images of (*S*-) $PDCF_6$-*b*-$PDHF_{10}[PPh_3]Br$ samples prepared in THF and (a) 50 % DMF, (b) 55 % DMF, (c), 60 % DMF, (d) 70 % DMF, (e) 60 % DMSO and (f) 70 % DMSO. Samples were heated to 140 °C for 30 min followed by slow cooling and ageing for 24 h at 20 °C before imaging. Scale bars: 2 µm.

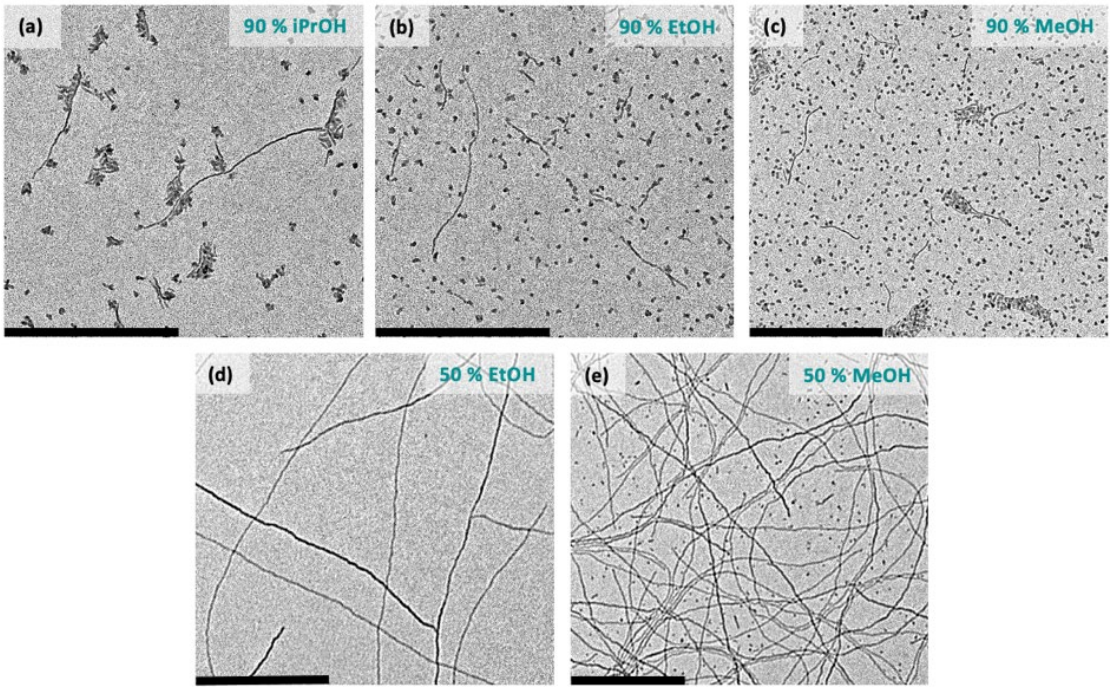

Figure S4. 12: TEM images of (*R*-) $PDCF_{11}$-*b*-$PDHF_{13}[PPh_3]Br$ samples prepared in THF and (a) 90 % iPrOH, (b) 90 % EtOH, (c), 90 % MeOH, (d) 50 % EtOH and (e) 50 % MeOH. Scale bars: 1 µm.

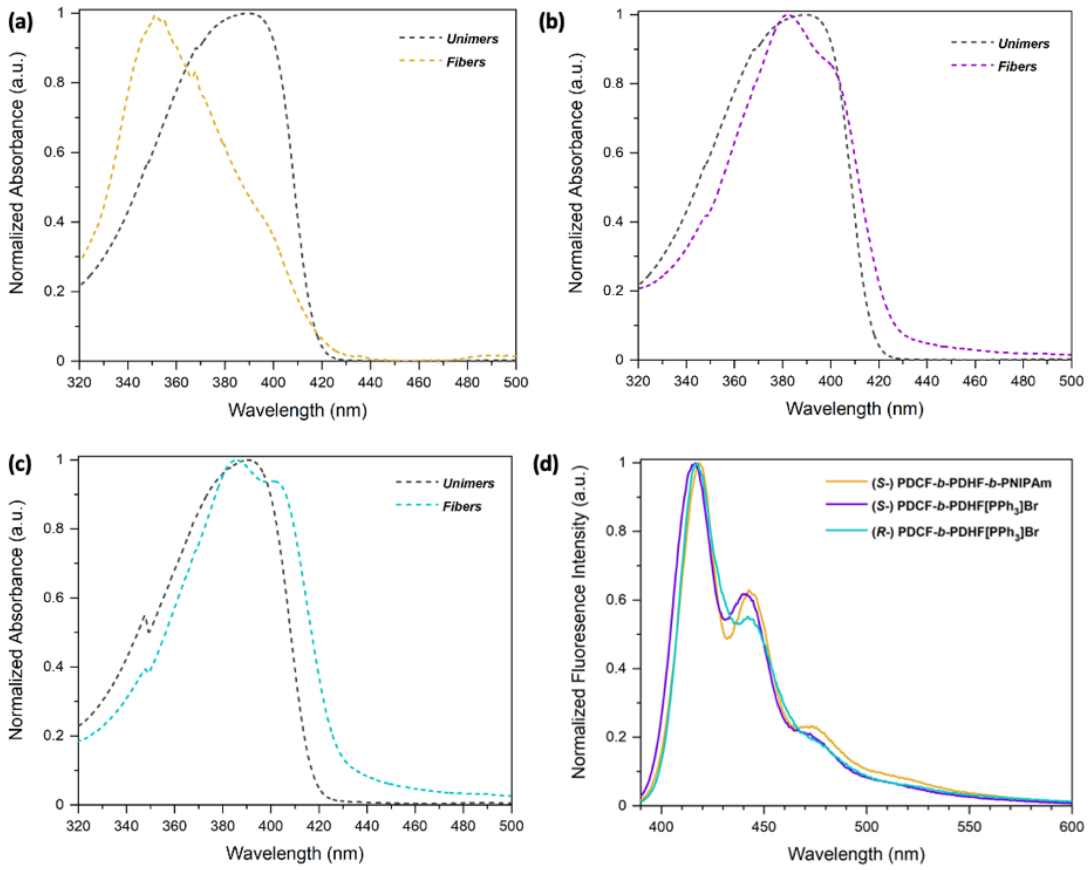

Figure S4. 13: Normalized UV-Vis spectra of (a) (*S*-) $PDCF_6$-*b*-$PDHF_{10}$-*b*-$PNIPAm_{68}$, (b) (*S*-) $PDCF_6$-*b*-$PDHF_{10}[PPh_3]Br$ and (c) (*R*-) $PDCF_{11}$-*b*-$PDHF_{13}[PPh_3]Br$ in THF (*grey traces*) and (*S*-) $PDCF_6$-*b*-$PDHF_{10}$-*b*-$PNIPAm_{68}$ fibers in THF:MeOH (1:1, v/v) (*yellow trace*), (*S*-) $PDCF_6$-*b*-$PDHF_{10}[PPh_3]Br$ fibers in THF:iPrOH (9:11, v/v) (*purple trace*) and (*R*-) $PDCF_{11}$-*b*-$PDHF_{13}[PPh_3]Br$ fibers in THF:iPrOH (11:9, v/v) (*teal trace*). (d) Photoluminescence spectra of (*S*-) $PDCF_6$-*b*-$PDHF_{10}$-*b*-$PNIPAm_{68}$ fibers in THF:MeOH (1:1, v/v) (*yellow trace*), (*S*-) $PDCF_6$-*b*-$PDHF_{10}[PPh_3]Br$ fibers in THF:iPrOH (9:11, v/v) (*purple trace*) and (*R*-) $PDCF_{11}$-*b*-$PDHF_{13}[PPh_3]Br$ fibers in THF:iPrOH (11:9, v/v) (*teal trace*). λ_{ex} = 380 nm.

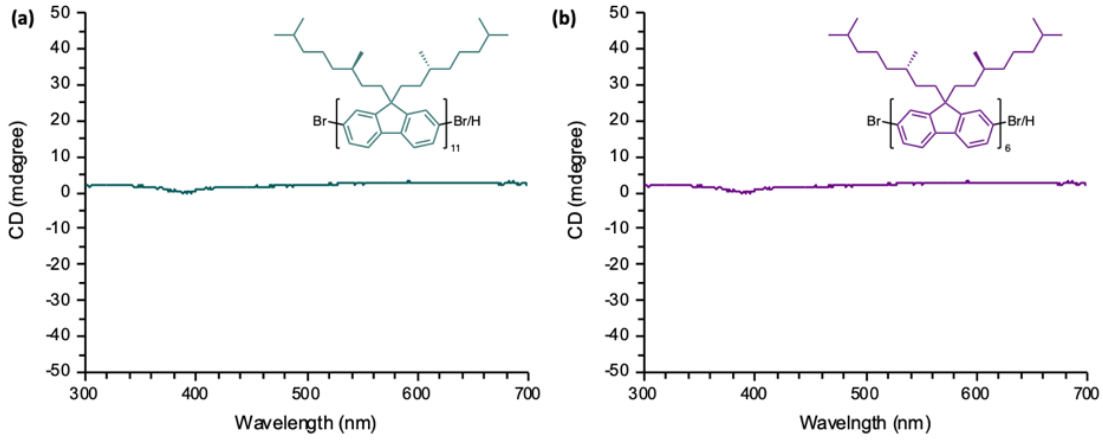

Figure S4. 14: (a) CD spectra of (*R*-) $PDCF_{11}$ unimers in THF and (b) (*S*-) $PDCF_6$ unimers in THF.

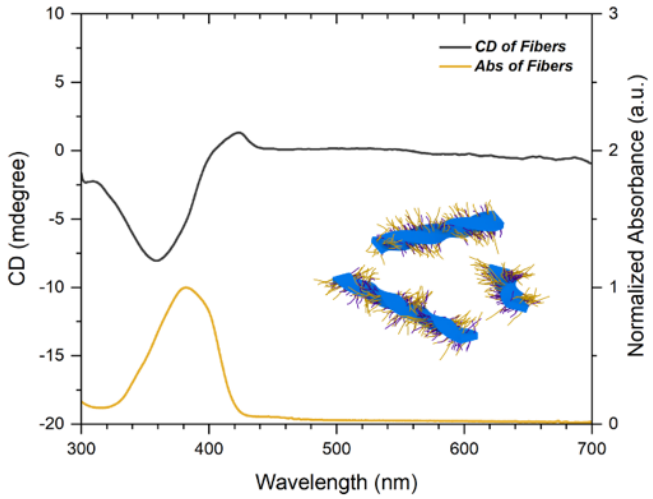

Figure S4. 15: CD (*grey trace*) and absorption (*yellow trace*) spectra of (*S*-) $PDCF_6$-*b*-$PDHF_{10}$-*b*-$PNIPAm_{68}$ fibers in THF:MeOH (1:1, v/v).

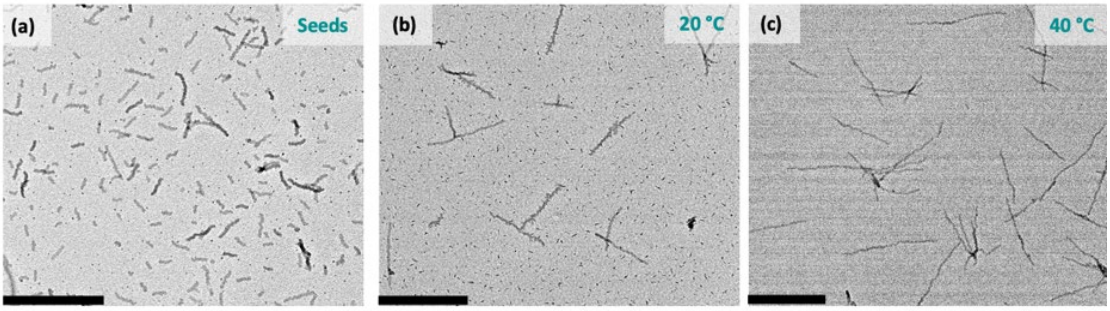

Figure S4. 16: Attempted seeded growth of (*R*-) $PDCF_{11}$-*b*-$PDHF_{13}[PPh_3]Br$ in THF:iPrOH (11:9, v/v). (a) TEM image of seed micelles prepared by sonication of polydisperse fibers at 0 °C for 1 h. TEM image of fibers obtained by the seeded growth of (*R*-) $PDCF_{11}$-*b*-$PDHF_{13}[PPh_3]Br$ BCPs from seed micelles with m_{unimer}/m_{seed} values of 5 at (b) 20 °C and (c) 40 °C. Scale bars: 1 µm.

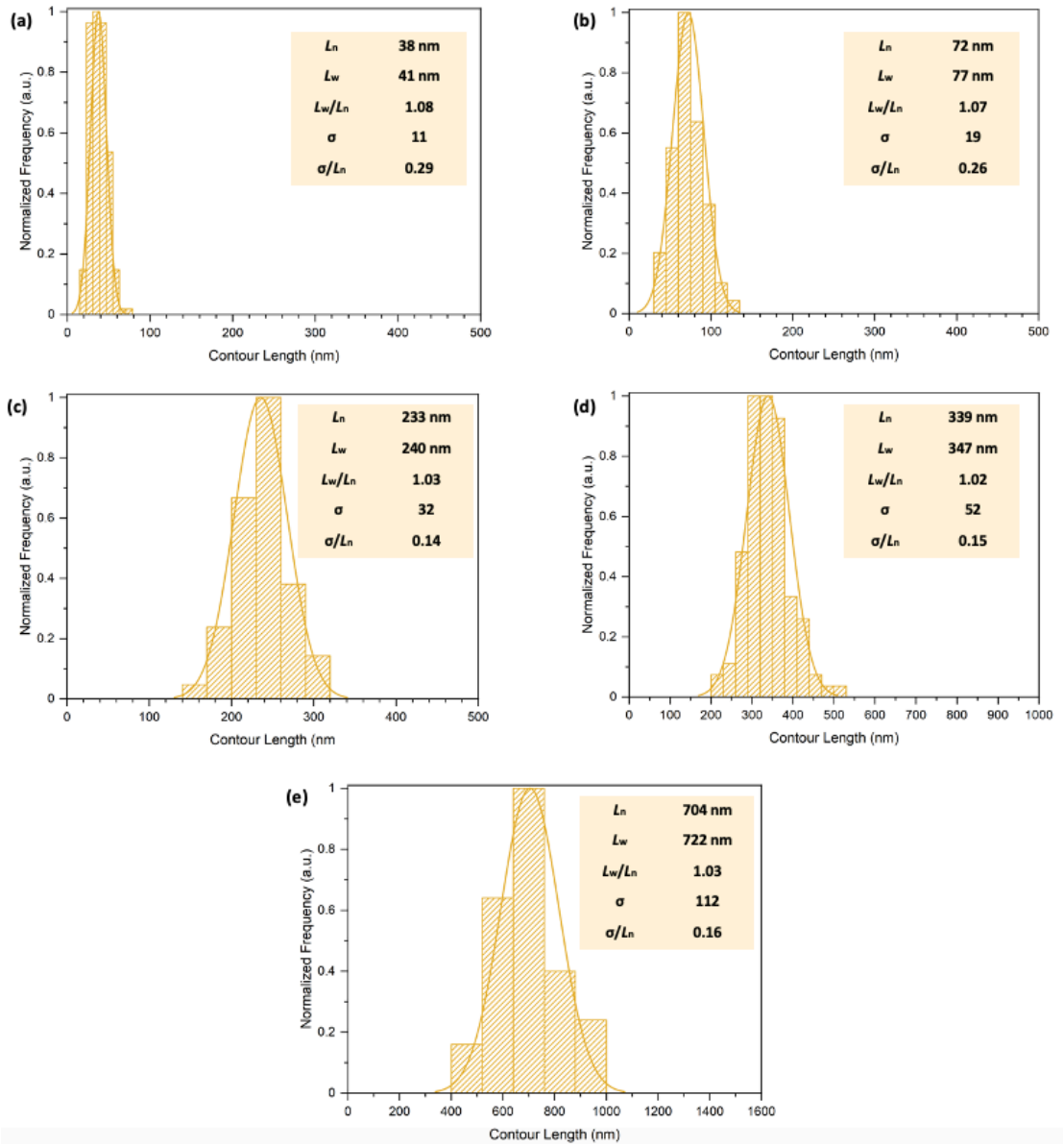

Figure S4. 17: Contour length distributions of (a) (*S*-) PDCF$_6$-*b*-PDHF$_{10}$-*b*-PNIPAm$_{68}$ seed micelles (L_n = 38 nm, L_w/L_n= 1.08) and nanofibers of controlled length prepared by the seeded growth of (*S*-) PDCF$_6$-*b*-PDHF$_{10}$-*b*-PNIPAm$_{68}$ BCPs from seed micelles with m_{unimer}/m_{seed} values of (b) 1, (c) 4, (d) 6, and (e) 12.

4.6. References

(1) Green, M. M.; Park, J.-W.; Sato, T.; Teramoto, A.; Lifson, S.; Selinger, R. L. B.; Selinger, J. V. The Macromolecular Route to Chiral Amplification. *Angew. Chem. Int. Ed.* **1999**, *38* (21), 3138–3154.

(2) Green, M. M.; Peterson, N. C.; Sato, T.; Teramoto, A.; Cook, R.; Lifson, S. A Helical Polymer with a Cooperative Response to Chiral Information. *Science.* **1995**, *268* (5219), 1860–1866.

(3) Liu, M.; Zhang, L.; Wang, T. Supramolecular Chirality in Self-Assembled Systems. *Chem. Rev.* **2015**, *115* (15), 7304–7397.

(4) Hegstrom, R. A.; Kondepudi, D. K. The Handedness of the Universe. *Sci. Am.* **1990**, 108–115.

(5) Green, M. M.; Reidy, M. P.; Johnson, R. J.; Darling, G.; O'Leary, D. J.; Willson, G. Macromolecular Stereochemistry: The Out-of-Proportion Influence of Optically Active Comonomers on the Conformational Characteristics of Polyisocyanates. The Sergeants and Soldiers Experiment. *J. Am. Chem. Soc.* **1989**, *111* (16), 6452–6454.

(6) Palmans, A. R. A.; Meijer, E. W. Amplification of Chirality in Dynamic Supramolecular Aggregates. *Angew. Chem. Int. Ed.* **2007**, *46* (47), 8948–8968.

(7) Yang, Y.; Rice, B.; Shi, X.; Brandt, J. R.; Correa Da Costa, R.; Hedley, G. J.; Smilgies, D. M.; Frost, J. M.; Samuel, I. D. W.; Otero-De-La-Roza, A.; Johnson, E. R.; Jelfs, K. E.; Nelson, J.; Campbell, A. J.; Fuchter, M. J. Emergent Properties of an Organic Semiconductor Driven by Its Molecular Chirality. *ACS Nano* **2017**, *11* (8), 8329–8338.

(8) Scanga, R.; Reuther, J. Helical Polymer Self-Assembly and Chiral Nanostructure Formation. *Polym. Chem.* **2021**, Accepted Manuscript.

(9) Amabilino, D. B.; Smith, D. K.; Steed, J. W. Supramolecular Materials. *Chem. Soc. Rev.* **2017**, *46*, 2404–2420.

(10) Yashima, E.; Ousaka, N.; Taura, D.; Shimomura, K.; Ikai, T.; Maeda, K. Supramolecular Helical Systems: Helical Assemblies of Small Molecules, Foldamers, and Polymers with Chiral Amplification and Their Functions. *Chem. Rev.* **2016**, *116*, 13752–13990.

(11) Patra, S. K.; Ahmed, R.; Whittell, G. R.; Lunn, D. J.; Dunphy, E. L.; Winnik, M. A.; Manners, I. Cylindrical Micelles of Controlled Length with a π-Conjugated Polythiophene Core via Crystallization-Driven Self-Assembly. *J. Am. Chem. Soc.* **2011**, *133* (23), 8842–8845.

(12) Gwyther, J.; Gilroy, J. B.; Rupar, P. A.; Lunn, D. J.; Kynaston, E.; Patra, S. K.; Whittell, G. R.; Winnik, M. A.; Manners, I. Dimensional Control of Block Copolymer Nanofibers with a π-Conjugated Core: Crystallization-Driven Solution Self-Assembly of Amphiphilic Poly(3-Hexylthiophene)-b-Poly(2-Vinylpyridine). *Chem. - A Eur. J.* **2013**, *19* (28), 9186–9197.

(13) Qian, J.; Li, X.; Lunn, D. J.; Gwyther, J.; Hudson, Z. M.; Kynaston, E.; Rupar, P. A.; Winnik, M. A.; Manners, I. Uniform High Aspect Ratio Fiber-like Micelles and Block Co-Micelles with a Crystalline π - Conjugated Polythiophene Core by Self-Seeding. *J. Am. Chem. Soc.* **2014**, *136* (11), 4121–4124.

(14) Shin, S.; Menk, F.; Kim, Y.; Lim, J.; Char, K.; Zentel, R.; Choi, T. L. Living Light-Induced Crystallization-Driven Self-Assembly for Rapid Preparation of Semiconducting Nanofibers. *J. Am. Chem. Soc.* **2018**, *140* (19), 6088–6094.

(15) Han, L.; Wang, M.; Jia, X.; Chen, W.; Qian, H.; He, F. Uniform Two-Dimensional Square Assemblies from Conjugated Block Copolymers Driven by π-π Interactions with Controllable Sizes. *Nat. Commun.* **2018**, *9*, 865.

(16) Tao, D.; Feng, C.; Cui, Y.; Yang, X.; Manners, I.; Winnik, M. A.; Huang, X. Monodisperse Fiber-like Micelles of Controlled Length and Composition with an Oligo(p-Phenylenevinylene) Core via "Living" Crystallization-Driven Self-Assembly. *J. Am. Chem. Soc.* **2017**, *139* (21), 7136–7139.

(17) Tao, D.; Wang, Z.; Huang, X.; Tian, M.; Lu, G.; Manners, I.; Winnik, M. A.; Feng, C. Continuous and Segmented Semiconducting Fiber-like Nanostructures with Spatially Selective Functionalization by Living Crystallization-Driven Self-Assembly. *Angew. Chem. Int. Ed.* **2020**, *59* (21), 8232–8239.

(18) Yang, S.; Kang, S. Y.; Choi, T. L. Morphologically Tunable Square and Rectangular Nanosheets of a Simple Conjugated Homopolymer by Changing Solvents. *J. Am. Chem. Soc.* **2019**, *141* (48), 19138–19143.

(19) Kynaston, E. L.; Nazemi, A.; MacFarlane, L. R.; Whittell, G. R.; Faul, C. F. J.; Manners, I.; Faul, C. F. J. Uniform Polyselenophene Block Copolymer Fiberlike Micelles and Block Co-Micelles via Living Crystallization-Driven Self-Assembly. *Macromolecules* **2018**, *51* (3), 1002–1010.

(20) Hicks, G. E. J. J.; Jarrett-Wilkins, C. N.; Panchuk, J. R.; Manion, J. G.; Seferos, D. S. Oxidation Promoted Self-Assembly of π-Conjugated Polymers. *Chem. Sci.* **2020**, *11* (25), 32–34.

(21) Jin, X.-H.; Price, M. B.; Finnegan, J. R.; Boott, C. E.; Richter, J. M.; Rao, A.; Menke, S. M.; Friend, R. H.; Whittell, G. R.; Manners, I. Long-Range Exciton Transport in Conjugated Polymer Nanofibers Prepared by Seeded Growth. *Science.* **2018**, *360* (6391), 897–900.

(22) Qi, R.; Zhu, Y.; Han, L.; Wang, M.; He, F. Rectangular Platelet Micelles with Controlled Aspect Ratio by Hierarchical Self-Assembly of Poly(3-Hexylthiophene)- b-Poly(Ethylene Glycol). *Macromolecules* **2020**, *53* (15), 6555–6565.

(23) Xu, L.; Wang, C.; Li, Y. X.; Xu, X. H.; Zhou, L.; Liu, N.; Wu, Z. Q. Crystallization-Driven Asymmetric Helical Assembly of Conjugated Block Copolymers and the Aggregation Induced White-Light Emission and Circularly Polarized Luminescence. *Angew. Chem. Int. Ed.* **2020**, *59* (38), 16675–16682.

(24) Lee, E.; Hammer, B.; Kim, J.-K.; Page, Z.; Emrick, T.; Hayward, R. C. Hierarchical Helical Assembly of Conjugated Poly(3-Hexylthiophene)- Block -Poly(3-Triethylene Glycol Thiophene) Diblock Copolymers. *J. Am. Chem. Soc.* **2011**, *133* (27), 10390–10393.

(25) Zhang, W.; Jin, W.; Fukushima, T.; Mori, T.; Aida, T. Helix Sense-Selective Supramolecular Polymerization Seeded by a One-Handed Helical Polymeric Assembly. *J. Am. Chem. Soc.* **2015**, *137* (43), 13792–13795.

(26) Ma, X.; Zhang, Y.; Zhang, Y.; Liu, Y.; Che, Y.; Zhao, J. Fabrication of Chiral-Selective Nanotubular Heterojunctions through Living Supramolecular Polymerization. *Angew. Chem. Int. Ed.* **2016**, *128*, 9691–9695.

(27) Hu, K.; Liu, Y.; Xiong, W.; Gong, Y.; Che, Y.; Zhao, J. Fabrication of Single-Handed Nanocoils with Controlled Length via a Living Supramolecular Self-Assembly. *Chem. Mater.* **2019**, *31*, 1403–1407.

(28) Zhu, Y.; Han, L.; Fan, H.; Wang, M.; Qi, R.; Zhao, Y.; He, F. Three-Dimensional Spirals of Conjugated Block Copolymers Driven by Screw Dislocation. *Macromolecules* **2020**, *53* (8), 3217–3223.

(29) Klaerner, G.; Miller, R. D. Polyfluorene Derivatives: Effective Conjugation Lengths from Well-Defined Oligomers. *Macromolecules* **1998**, *31* (6), 2007–2009.

(30) Monkman, A. P.; Rothe, C.; King, S.; Dias, F. Polyfluorenes. *Science.* **2008**, *297* (5583), 187.

(31) Spano, F. C.; Silva, C. H- and J-Aggregate Behavior in Polymeric Semiconductors. *Annu. Rev. Phys. Chem.* **2014**, *65* (1), 477–500.

(32) Lee, C. C.; Grenier, C.; Meijer, E. W.; Schenning, A. P. H. J. Preparation and Characterization of Helical Self-Assembled Nanofibers. *Chem. Soc. Rev.* **2009**, *38* (3), 671–683.

(33) Van Den Bergh, K.; Cosemans, I.; Verbiest, T.; Koeckelberghs, G. Expression of Supramolecular Chirality in Block Copoly(Thiophene)S. *Macromolecules* **2010**, *43*, 3794–3800.

(34) Kulkarni, C.; Di Nuzzo, D.; Meijer, E. W.; Meskers, S. C. J. Pitch and Handedness of the Cholesteric Order in Films of a Chiral Alternating Fluorene Copolymer. *J. Phys. Chem. B* **2017**, *121*, 11520–11527.

(35) Kim, Y. J.; Cho, C. H.; Paek, K.; Jo, M.; Park, M. K.; Lee, N. E.; Kim, Y. J.; Kim, B. J.; Lee, E. Precise Control of Quantum Dot Location within the P3HT-b-P2VP/QD Nanowires Formed by Crystallization-Driven 1D Growth of Hybrid Dimeric Seeds. *J. Am. Chem. Soc.* **2014**, *136* (7), 2767–2774.

(36) Hentschel, M.; Schäferling, M.; Duan, X.; Giessen, H.; Liu, N. Chiral Plasmonics. *Sci. Adv.* **2017**, *3*, e1602735.

(37) Cheng, G.; Xu, D.; Lu, Z.; Liu, K. Chiral Self-Assembly of Nanoparticles Induced by Polymers Synthesized via Reversible Addition-Fragmentation Chain Transfer Polymerization. *ACS Nano* **2019**, *13*, 1479–1489.

(38) Loewe, R. S.; Ewbank, P. C.; Liu, J.; Zhai, L.; McCullough, R. D. Regioregular, Head-to-Tail Coupled Poly(3-Alkylthiophenes) Made Easy by the GRIM Method: Investigation of the Reaction and the Origin of Regioselectivity. *Macromolecules* **2001**, *34* (13), 4324–4333.

Chapter 5

Solution Self-Assembly and Seeded Growth of Phosphonium-Capped Poly(di-*n*-hexylfluorene) Homopolymers

Contributions:

Characterization by atomic force microscopy was carried out by Dr. Yuetong Kang. All other work presented in this chapter was performed by Huda Shaikh.

5.1. Abstract

Herein, the preparation of amphiphilic poly(di-*n*-hexylfluorene) (PDHF) homopolymers with a charged phosphonium terminal group, and investigations into the solution self-assembly behaviour of these materials are presented. Crystallization-driven self-assembly (CDSA) of charge-capped PDHF homopolymers led to the formation of either one-dimensional (1D) or two-dimensional (2D) morphologies depending on the self-assembly protocol. Specifically, fiber-like, tape-like, and platelet micelle morphologies are all accessible by careful choice of the selective solvent, the common solvent to selective solvent ratio, and the temperature. Self-assembly in solvent systems with large volume fractions of polar aprotic solvent selective for the charged phosphonium group exclusively yielded 2D platelet micelles, whereas 1D fiber-like micelle formation occurs in solvent systems rich in common solvent. Seeded growth from 1D or 2D seed micelles in fiber- or platelet-forming solvent systems led to the formation of low dispersity, high aspect-ratio micelles. Scarf-like micelles with tassels of controlled length were prepared through the seeded growth of PDHF-based BCP unimers from seeds composed of phosphonium capped-PDHF.

5.2. Introduction

Functional nanoparticles formed through the self-assembly of π-conjugated polymers are highly desirable for a broad range of applications including electronics, biomedical imaging and therapy, sensing and photocatalysis.[1–5] Most reports have focussed on spherical conjugated polymer nanoparticles synthesized via reprecipitation, polymer emulsification, and mini-emulsion polymerization techniques.[6–8] However, one-dimensional (1D) nanowire and two-dimensional (2D) nanosheet architectures are highly desirable for use as active materials in electronic devices.[3,4,9] Block copolymer (BCP) self-assembly in solution offers a versatile platform for the fabrication a variety of functional core-shell nanostructures with different morphologies.[10,11] Although many complex morphologies can be prepared, spherical micelles are the most accessible. For BCPs with amorphous core-forming blocks only a narrow range of conditions can afford morphologically pure micelles with low curvature at the core-corona interface.[12]

In solution, crystallization-driven self-assembly (CDSA) of BCPs with a crystallizable core-forming block can exclusively yield either 1D fiber-like micelles or 2D platelets depending on the block ratio, solvent, temperature, additives and corona-forming block.[13–15] Homogenous nucleation of BCPs in a solvent selective for a corona-forming block occurs randomly to afford kinetically trapped fiber-like micelles or platelets of varied length and area, respectively. Metallopolymers, biodegradable and π-conjugated materials can generate 1D fibers with a crystalline core via this method.[15–17] Addition of solvated BCP (unimer) to 1D crystalline core seed micelles, produced by the sonication of polydisperse fibers formed by CDSA, results in bidirectional epitaxial growth from the exposed crystal faces on the fiber termini. This seeded growth process is termed 'living' CDSA and is analogous to a living covalent polymerization. The fiber termini remain active to the epitaxial growth of added unimer.

For PFS-based materials, 2D rectangular platelets can be obtained through the seeded growth of a 1:1 blend of PFS-based BCP and PFS homopolymer from a 1D cylindrical micelle seed.[18] Additionally, the heteroepitaxial growth of a 1:1 blend of poly(ferrocenyldimethylgermane)-based BCP and homopolymer from 2D rectangular PFS platelets can yield segmented platelets.[19] Recently, we have

shown that charged phosphonium or ammonium groups can be used instead of corona-forming polymer blocks to stabilize the crystalline micelle cores. Charged PFS- and poly(L-lactide) (PLLA)-based materials produced various 2D platelet morphologies, including rectangular, diamond-like, hexagonal shapes, via seeded growth strategies.[20–22] In contrast to these systems, low dispersity 1D fiber-like micelles are formed through the 'living' CDSA of phosphonium-capped poly(fluorene trimethyl carbonate) (PFTMC) or poly(3-hexylthiophene) (P3HT) homopolymers.[23,24]

BCPs with a crystallizable π-conjugated polymer core-forming block are of particular interest in the preparation of 1D nanowires and 2D crystalline lamellae for potential electronic applications. Recently, the 'living' CDSA method has been applied to a wide-range of π-conjugated core-forming blocks such as polythiophenes,[25–27] poly(*p*-phenylenevinylene) (PPV),[28–31] poly(cyclopentenylene-vinylene)[32], polyselenophene[33] and polytellurophene[34]. 'Living' CDSA has also allowed the preparation of low dispersity 1D nanowires with a photoluminescent crystalline poly(di-*n*-hexylfluorene) (PDHF) core (see Chapters 2-4).[35,36] Different types of nanowire-based heterojunctions can be prepared using the PDHF crystalline core as a donor, and incorporating either amorphous or crystalline acceptor polythiophene regions (see Chapter 2).[35,36] The epitaxial growth process enables the formation of a fiber core with near single crystal-like order that allows access to exceptionally long exciton diffusion lengths (> 200 nm).[35] Recently, the self-assembly of π-conjugated BCPs with high core-to-corona block ratios (<1:2) has been investigated.[29,37] 2D square or rectangular platelets were prepared via the self-assembly of PPV and P3HT-based BCPs, respectively. The size and/or aspect ratio of these platelets could be tuned by changing the concentration and the ratio of the polymer blocks.

In Chapters 2-4, studies of the self-assembly of different PDHF-based BCPs were presented that showed 1D fiber-like micelles can be readily prepared through CDSA protocols. We have also demonstrated that for the 1D fibers epitaxial growth occurs in the plane commensurate with π-π stacking between the conjugated backbones of different PDHF chains.[35,36] In this Chapter, investigations into the solution self-assembly behaviour of PDHF homopolymers with a charged phosphonium terminal group are presented. We postulated that the absence of a

large polymeric corona-forming block may facilitate lateral epitaxial growth to yield 2D platelet morphologies rather than fiber-like micelles with a PDHF core. In addition, for the charge-capped PDHF materials, attempts made to control micelle morphology and dimensions via 'living' CDSA protocols are discussed.

5.3. Results and Discussion

5.3.1. Synthesis and Characterisation of PDHF Block Copolymers with Charged Terminal Groups

In previous work, the CDSA behavior of PDHF BCPs with polymeric corona forming blocks, such as poly(ethylene glycol) (PEG) and poly(2-vinylpyridine) (P2VP), was investigated. Highly ordered crystalline nanofibers were prepared where the fiber width corresponds to the extended chain length of the PDHF block, the fiber height is composed of a few layers of PDHF chains (ca. 4) with interdigitated side chains and the fiber long axis corresponds to the π-π stacking direction. Control over fiber length was achieved by using the living CDSA seeded growth method, whereby epitaxial growth of unimer from pre-existing seeds occurs only from the faces associated with the π-π stacking direction. Promoting extensive growth in the direction associated with side-chain interactions to yield 2D assemblies has not been achieved with these materials.

The use of charged terminal groups instead of large polymeric corona-forming blocks has been shown to be successful for promoting 2D growth in PFS- and PLLA-based systems.[20–22] For these materials the charged terminal groups are phosphonium or ammonium species that allow for CDSA to occur in polar solvent mixtures to afford colloidally-stable 2D micelles. Structural characterization has demonstrated that the charged species are distributed on the two largest faces of the resulting platelets. Following on from this work, herein we investigate the self-assembly behavior of PDHF-based homopolymers with charged termini consisting of phosphonium groups in an effort to promote epitaxial growth in the direction of side-chain interactions and subsequently to prepare 2D micelle morphologies. Alkyne-terminated PDHF homopolymers were synthesized by Grignard metathesis polymerization and purified by Soxhlet extraction to give low dispersity products ($Đ_m$ < 1.18) (Figure S5. 3 and Figure S5. 4). Employing a copper azide-alkyne cycloaddition (CuAAc) click reaction with the alkyne-terminated PDHF polymers and (3-azidopropyl)triphenyl phosphonium bromide (Figure S5. 1) afforded the charge-capped polymers which were subsequently purified by silica gel chromatography to give well-defined materials with $Đ_m$ < 1.15 (Figure 5. 1, Figure S5. 3 and Table 5. 1).

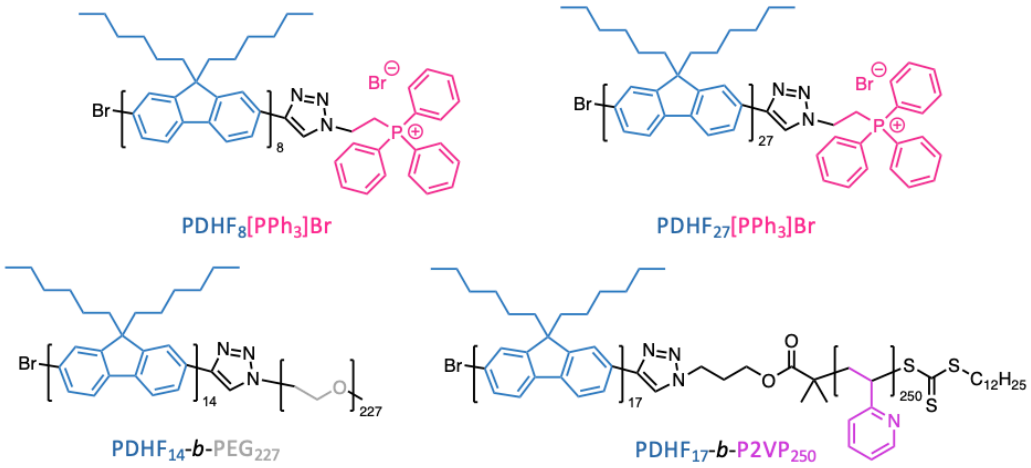

Figure 5. 1: Chemical structures of the polymers used in this investigation. $PDHF_8[PPh_3]Br$, $PDHF_{27}[PPh_3]Br$, $PDHF_{14}$-*b*-PEG_{227} and $PDHF_{17}$-*b*-$P2VP_{250}$.

Table 5. 1: Characterization data for the polymers used in this study.

Material Composition [a, b]	M_n (kDa) [c]	M_w (kDa) [c]	$Đ_m$ [c]
$PDHF_8$ [a]	5.8	6.8	1.17
$PDHF_{27}$ [a]	23.2	26.5	1.14
$PDHF_8[PPh_3]Br$	6.1	7.0	1.14
$PDHF_{27}[PPh_3]Br$	22.9	25.6	1.12
$PDHF_{14}$-*b*-PEG_{227} [b]	29.3	32.4	1.11
$PDHF_{17}$-*b*-$P2VP_{250}$ [b]	14.7	18.3	1.24

Degree of polymerization determined by [a] MALDI-ToF and [b] ^1H NMR. Number-average molecular weight (M_n), weight-average molecular weight (M_w) and molecular mass dispersity ($Đ_m = M_w/M_n$) values determined by [c] GPC (THF containing $[nBu_4N]Br$ (0.1% w/w)) calibrated against polystyrene standards.

5.3.2. Self-assembly of PDHF[PPh3]Br

The solution self-assembly of $PDHF_{27}[PPh_3]Br$ was investigated in mixed solvent systems composed of tetrahydrofuran (THF, common solvent for the PDHF block and the phosphonium end-group) and different polar solvents that are all poor for the PDHF block and may subsequently facilitate crystallization (Table S5. 1). Only small irregular aggregates (<20 nm) were observed in all solvent systems apart from in THF:DMSO mixtures. Heating a suspension of $PDHF_{27}[PPh_3]Br$ polymer in THF:DMSO mixtures to 140 °C for 30 min, followed by slow cooling to 20 °C afforded 2D ribbon-like or platelet micelles by TEM (Figure S5. 5a-c). However, the 2D platelets formed through the self-assembly of

$PDHF_{27}[PPh_3]Br$ possessed limited colloidal stability and the micelle dimensions were limited to below 1 µm in length and 500 nm in width (Figure S5. 5a, c). This suggests that the degree of polymerization of PDHF is too large resulting in rapid self-nucleation in solution. The small phosphonium groups are appear unable to provide sufficient colloidal stability to the resulting micelles in this case leading to aggregation and precipitation over time (Figure S5. 5d).

Next, we explored whether the use of a shorter PDHF block would facilitate the preparation of colloidally stable micelles. The solution self-assembly of $PDHF_8[PPh_3]Br$ was investigated in mixed solvent systems with different ratios of THF (common solvent) to polar solvent. In a typical self-assembly experiment, polar solvent was added dropwise to a solution of $PDHF_8[PPh_3]Br$ in THF at 20 °C until a polymer concentration of 0.2 mg mL^{-1} was reached (Figure 5. 2a). Additionally, a direct dissolution method was also investigated in which a 0.2 mg mL^{-1} suspension of $PDHF_8[PPh_3]Br$ in a mixture of common solvent and poor solvent for the PDHF-core block was heated for 30 min to a temperature just below the boiling point of the solvent mixture before slow cooling (ca. 1 °C min^{-1}) to 20 °C. All samples were aged for 24 h at 20 °C before analysis by TEM after solvent evaporation.

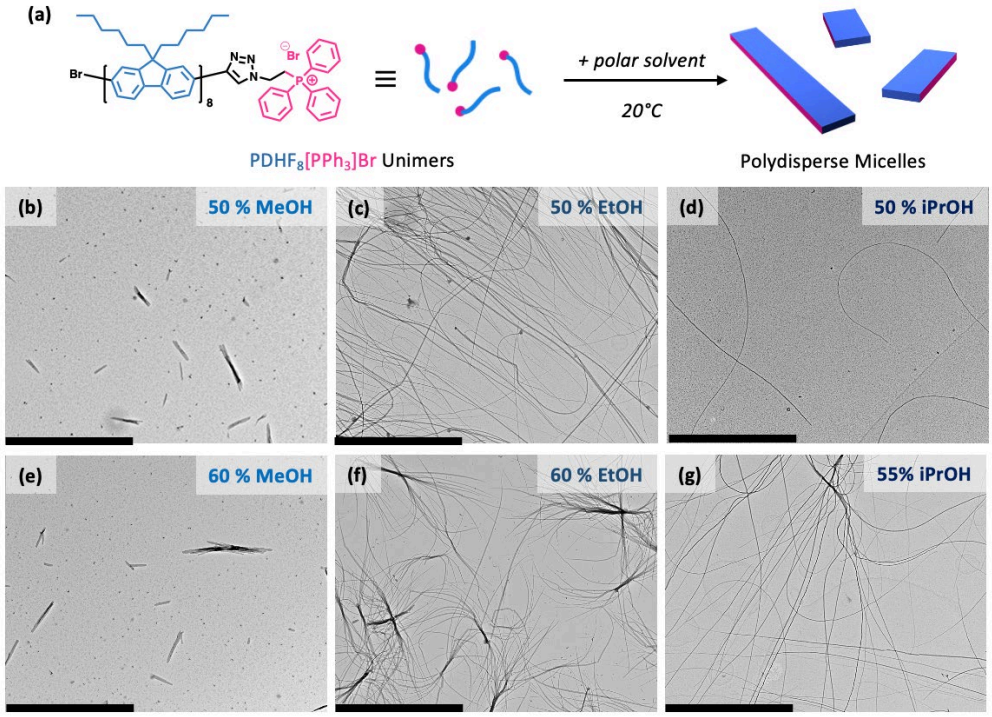

Figure 5. 2: (a) Schematic illustration of the preparation of fiber-like micelles from CDSA of $PDHF[PPh_3]Br$ via poor solvent addition. Self-assembly of $PDHF_8[PPh_3]Br$ in (b) THF:MeOH (1:1), (c) THF:EtOH (1:1), (d) THF:iPrOH (1:1), (e) THF:MeOH (2:3), (f) THF:EtOH (2:3) and (g) THF:iPrOH (9:11). Scale bars: 4 µm.

For the method involving dropwise addition of a poor solvent for PDHF, TEM analysis of samples showed that small spherical micelles (ca. < 20 nm) and irregular ribbon-like micelles (length < 2.5 μm, W_n = 101 nm, W_n/W_w = 1.04, where W_n is the number-average width and W_w is the weight-average width) were formed in THF:MeOH mixtures (Figure 5. 2b, e). In THF:MeCN mixtures, very long (length ca. > 15 μm, W_n = 49 nm, W_n/W_w = 1.09) ribbon-like micelles were observed (Figure S5. 6). A mixture of very long (length ca. > 15 μm) ribbon-like micelles (W_n = 43 nm) and fiber-like micelles (W_n = 21 nm) were observed in THF:EtOH mixtures (W_n = 26 nm, W_n/W_w = 1.16) (Figure 5. 2c, f). Exclusive formation of fiber-like micelles (W_n = 11 nm, W_n/W_w = 1.03) was observed in THF:iPrOH (9:11, v/v) (Figure 5. 2d, g). For all self-assembly experiments in higher contents of polar alcohol solvent (> 60 %), irregular aggregates or fibrous bundles were observed. There was no direct correlation between the difference in solubility parameters of PDHF and the poor solvent, with the widths of the 1D micelles obtained (Table S5. 1). Wider 1D micelles were prepared in THF:MeOH/MeCN mixtures than in THF:EtOH/iPrOH mixtures (Figure S5. 7).

For the THF:iPrOH systems, the direct dissolution method was also attempted to see the influence of employing a heating and slow cooling treatment on the self-assembly of $PDHF_8[PPh_3]Br$. These mixtures were heated to 70 °C for 30 min then slowly cooled to 20 °C and aged for 24 h before analysis by TEM (Figure S5. 8). However, large bundles and clusters of ribbon-like micelles were observed from the direct dissolution method. Fiber-like micelles with uniform fiber core widths (W_n = 11 nm, W_n/W_w = 1.03), prepared by addition of iPrOH at 20 °C to a solution of $PDHF_8[PPh_3]Br$ in THF, are more suitable for seeded growth experiments (vide infra).

In the next series of experiments self-assembly of $PDHF_8[PPh_3]Br$ in solvent mixtures containing a polar aprotic solvent (DMSO) was investigated. Dropwise addition of DMSO to a solution of unimers in THF resulted in either precipitation of the polymer or rapid aggregation into large clusters of aggregates. However, colloidally stable micelles could be prepared by heating a suspension of polymer in THF:DMSO mixtures to 140 °C for 30 min, followed by slow cooling to 20 °C (Figure 5. 3a). After ageing for 24 h, TEM analysis revealed the presence of

different micelle morphologies. At high contents (≥ 45 %) of good solvent for the PDHF-core, bundles of ribbon-like and fiber-like micelles (widths < 600 nm) were formed (Figure 5. 3b, c). Using lower contents (0-35 %) of good solvent for the PDHF-core led to the formation of platelets with a lower aspect-ratio and substantially larger widths (up to ca. 3 μm) (Figure 5. 3d-g).

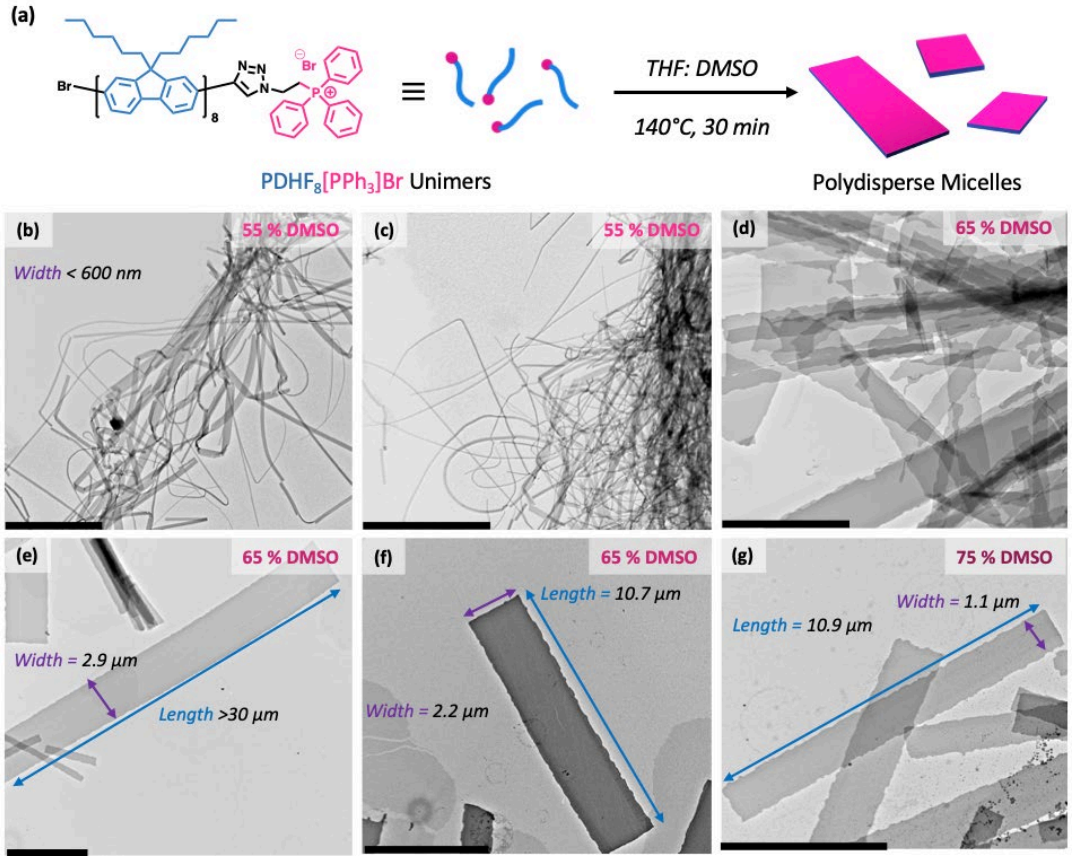

Figure 5. 3: Ribbon-like micelles and rectangular platelet micelles from CDSA of PDHF[PPh_3]Br. Self-assembly of $PDHF_8$[PPh_3]Br in (a)-(b) THF:DMSO (9:11), (c)-(e) THF:DMSO (7:13) and (f) THF:DMSO (1:3). Scale bars: 5 μm.

A mixture of fiber-like micelles and platelets were observed from the self-assembly of $PDHF_8$[PPh_3]Br in THF:DMSO (2:3, v/v), prepared via heating the polymer suspension to 140 °C for 30 min in air, followed by slow cooling to 20 °C and ageing for 24 h (Figure 5. 4c). From this sample the dimensions of the fiber-like micelles and platelets can be analyzed and compared by TEM and atomic force microscopy (AFM) (Figure 5. 4c and d). We have previously shown that the crystalline cores of nanofibers prepared by the CDSA of PDHF-based BCPs are composed of one plane (001) commensurate with the degree of polymerization of the PDHF block.[35,36] In micelles prepared by the CDSA of $PDHF_8$[PPh_3]Br, this plane should equate to the fully extended chain conformation of $PDHF_8$. The

repeat unit length for PDHF is 0.89 nm, a fully extended $PDHF_8$ chain should equate to 7.12 nm.[35,36] We have also shown that π-π stacking interactions between the conjugated polymer chains is commensurate with the largest plane (010) of the self-nucleated PDHF core micelles. The final plane (100) corresponds to layers of PDHF chains packed via alkyl side-chain interactions.

AFM height analysis of the sample revealed that the height of the platelets (ca. 7 nm) was found to be larger than that of the fiber-like micelles (ca. 3 nm) (Figure 5. 4e). The observed height of the platelets is in good agreement with the extended chain length of $PDHF_8$ (7.12 nm), whereas the platelet widths observed are too large (ca. 250 - 400 nm) to correspond to the extended chain length of $PDHF_8$ (Figure 5. 4b). TEM analysis of the widths of the fiber-like micelles (ca. 11 nm) is also similar to the extended chain length of $PDHF_8$ whereas the average height of these fibers from AFM analysis is significantly smaller (ca. 3 nm) (Figure 5. 4a). A schematic illustration of the orientations of the fiber-like micelles and platelets relative to a substrate and their chain packing are depicted in Figure 5.5a-b.

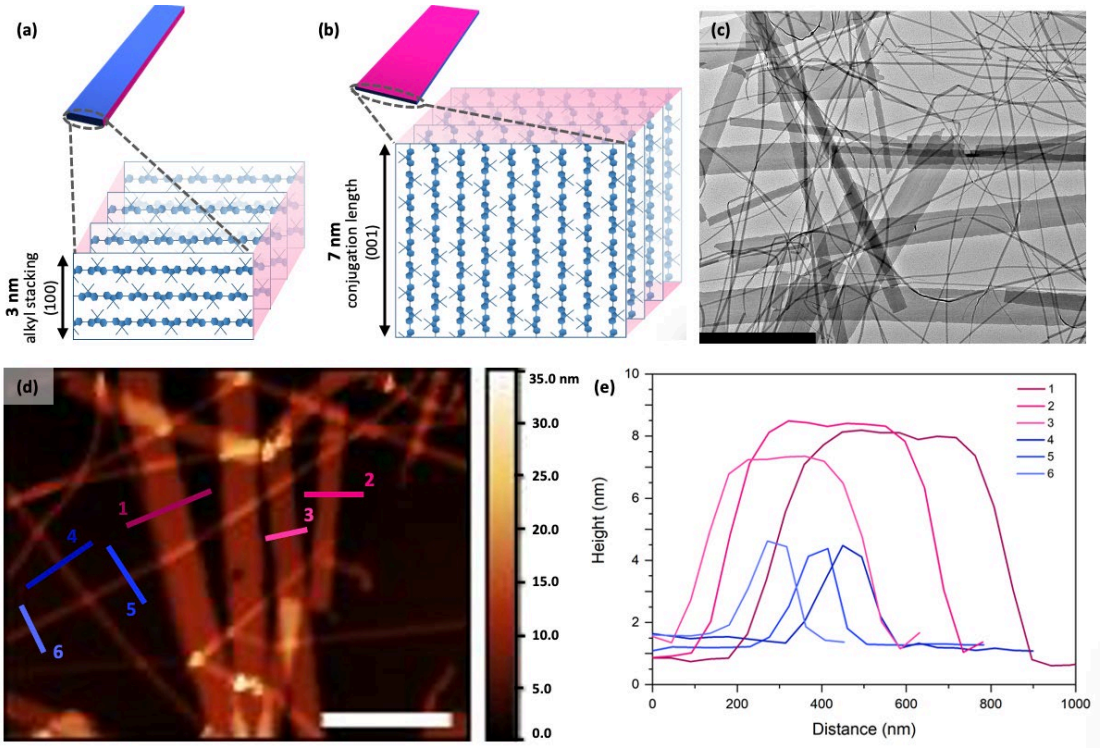

Figure 5. 4: Schematic representation of the different orientations of (a) fiber-like and (b) platelets PDHF micelles relative to a substrate. (c) TEM and (d) AFM height image of fibers and platelets prepared by the CDSA of $PDHF_8[PPh_3]Br$ in THF:DMSO (2:3, v/v) drop cast on to a carbon-coated copper mesh grid or silicon wafer, respectively. (e) Corresponding height traces for the AFM image. The platelet analyses were collected from the pink traces and the fiber analyses from the blue traces. Scale bars: (c) 4 μm and (d) 2 μm.

Next, UV-vis and fluorescence spectroscopy measurements on the different materials were performed. Dissolved $PDHF_8$ displays an absorption maximum (λ_{max}) at 380 nm in THF consistent with the absorption spectra obtained for $PDHF_8[PPh_3]Br$ (Figure S5. 9).[38] Poly(di-*n*-alkylfluorenes) also typically display bright blue emission in solution or in the aggregated state.[39] Normalized fluorescence spectra for nanofibers with a crystalline PDHF core prepared by the CDSA of PDHF-based BCPs typically display a high intensity blue $I_{0\text{-}0}$ vibronic band (λ_{max} = 410-425 nm) (see Chapters 2-4). Fiber-like micelles formed via self-assembly of $PDHF_8[PPh_3]Br$ in THF:iPrOH (9:11, v/v) also exhibit bright blue emission when the PDHF core is excited at 380 nm (Figure 5. 5). However, a significant change in the fluorescence spectrum was detected for $PDHF_8[PPh_3]Br$ platelet micelles in THF:DMSO (7:13, v/v) (Figure 5. 5). An additional broad green emission band with defined vibronic structure was observed (λ_{max} = 488-535 nm) for this sample. Reports on the origin of a green emission band for different types of polyfluorene materials suggest that oxidation of fluorene or strong aggregation of the polymer backbone may be responsible for this phenomenon.[40,41]

Oxidation of the fluorene units into fluorenone species could occur during prolonged exposure to UV irradiation or thermal treatment in air. Annealing poly(di-*n*-alkylfluorenes) in air at high temperatures (≥150 °C) and for prolonged amounts of time (> 2 h) have been shown to result in the formation of the green emission band.[42,43] The self-assembly of $PDHF_8[PPh_3]Br$ into platelet micelles in THF:DMSO (7:13, v/v) was achieved by heating the polymer suspension to 140 °C for 30 min in air followed by slow cooling to 20 °C and ageing for 24 h. Heating the sample for this shorter period and at a lower temperature should not result in oxidation of polyfluorene. Additionally, the absence of a broad absorption peak at 458 nm (λ_{max}) in the UV-vis spectrum of the 2D platelet sample, associated with the n-π* transition of the fluorenone unit,[41] suggests that no significant oxidation has occurred (Figure 5. 5a). Another possible explanation for this observation could be due to the increased aggregation of the polyfluorene chains via side-chain interactions. The cores of the 2D platelets formed via CDSA of $PDHF_8[PPh_3]Br$ exhibit increased alkyl side-chain packing compared to the 1D fibers prepared by CDSA. This might affect the ordering of the polymer backbone which could also be

the origin of the blue-shifted UV-vis absorption maximum observed for the 2D platelets (λ_{max} = 350 nm) versus the 1D fibers (λ_{max} = 370 nm) in THF:iPrOH (9:11, v/v) (Figure 5. 5a).

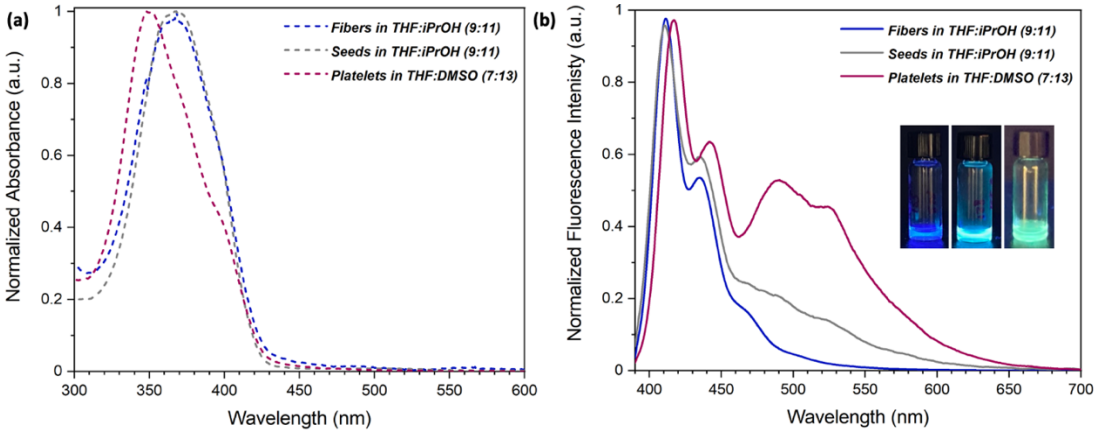

Figure 5. 5: Normalized (a) UV-Vis and (b) photoluminescence spectra of $PDHF_8[PPh_3]Br$ fibers in THF:iPrOH (9:11, v/v) (*blue traces*), seeds prepared by the sonication of fibers at 20 °C in THF:iPrOH (9:11, v/v) (*grey traces*), platelets in THF:DMSO (7:13, v/v) (*pink traces*). λ_{ex} = 380 nm. Inset: Photograph of $PDHF_8[PPh_3]Br$ fibers in THF:iPrOH (9:11, v/v) (*left*), seeds in THF:iPrOH (9:11, v/v) (*middle*) and platelets in THF:DMSO (7:13, v/v) (*right*) under UV light (365 nm).

5.3.3. 1D Seeded growth of $PDHF_8[PPh_3]Br$, $PDHF_{14}$-*b*-PEG_{227}, and $PDHF_{17}$-*b*-$P2VP_{250}$ unimers from $PDHF_8[PPh_3]Br$ seeds

As shown in Chapters 2-4, seeded growth protocols can be used to prepare low dispersity fiber-like micelles of tunable length from the living CDSA of PDHF-based BCPs. Typically, a sample of polydisperse fiber-like micelles, formed via CDSA of a PDHF-based BCP, is subjected to a short period of vigorous sonication. This yields short micelle fragments of low length dispersity (L_w/L_n < 1.2, where L_n is the number-average length and L_w is the weight-average length). On addition of solvated BCP unimer, these fragments (seeds) undergo further epitaxial growth from the terminal crystal faces. Altering the ratio of unimers to seeds allows for the preparation of a range of low dispersity fiber-like micelles with different lengths.

In this Chapter, we aimed to apply this methodology to phosphonium-capped PDHF materials. Polydisperse fiber-like micelles prepared through the self-nucleation of $PDHF_8[PPh_3]Br$ polymer in THF:iPrOH (9:11, v/v) (Figure 5. 2g) were subjected to vigorous sonication for 1 h at 0 °C. The sample was then aged for 24 h at 20 °C before analysis by TEM. Shorter, low dispersity 1D micelles (L_n = 391 nm, L_w/L_n = 1.05) were prepared by this method (Figure S5. 10c). Interestingly, an increase in width and width dispersity was observed for the

micelle fragments (W_n = 31 nm, W_n/W_w = 1.16) obtained after sonication compared to the initial polydisperse 1D micelles (W_n = 11 nm, W_n/W_w = 1.03) (Figure S5. 10b, d). Sonication was also conducted at 20 °C however an increase in micelle width was still observed. This suggests that sonication is responsible for the increase in micelle width and not the cooling of the sample (from 20 °C to 0° C). On annealing at 70 °C (Figure S5. 8) or subjecting to ultrasonication (Figure S5. 10c), some of the fiber-like micelles formed by CDSA at 20 °C appear to bundle or fuse together. Moreover, the fluorescence spectrum of the seed micelles shows the presence of an emission band at 500 – 600 nm, which is absent in the fluorescence spectrum of the initial polydisperse fibers and similar to that of the platelets prepared in THF:DMSO (7:13, v/v) (Figure 5. 5b, Figure S5. 10). The seed micelles were not prepared in DMSO solvent mixtures and the sample was not subjected to a temperature above 30 °C. This suggests that that the emission band at 500 – 600 nm is not caused by oxidation and increased side-chain stacking (as expected as a result of a larger W_n value) is more likely as an alternative explanation of the lower energy emission band. The green emission band has a considerably smaller contribution in the fluorescence spectrum of the seed micelles than in the fluorescence spectrum of the platelets (Figure 5. 5b). The width distribution of the seed sample (W_n = 31, W_n/W_w = 1.16) (Figure S5. 10d) shows that there is a significant number of fiber-like micelles with small widths (< 30 nm) but the population of micelles with larger widths (up to ca. 90 nm) are more likely responsible for the small green emission band observed in the fluorescence spectrum.

Nevertheless, seeded growth of $PDHF_8[PPh_3]Br$ unimers from seed micelles (L_n = 195 nm, L_w/L_n = 1.04) in THF:iPrOH (9:11, v/v) prepared via sonication at 20 °C for 2 h was carried out (Figure 5. 6a-c). Despite the presence of some wider seed micelles, epitaxial growth of the added unimer (4 equivalents of unimer to seeds) occurred uniformly and preferentially in the π-π stacking direction resulting in low dispersity 1D ribbon-like micelles (L_n = 899 nm, L_w/L_n = 1.01) (Figure 5. 6d-e). The obtained micelle length was lower than the theoretical micelle length expected for this seeded growth experiment (ca. 975 nm). This may be the result of a small percentage of added unimer undergoing epitaxial growth from the lateral faces of the micelles.

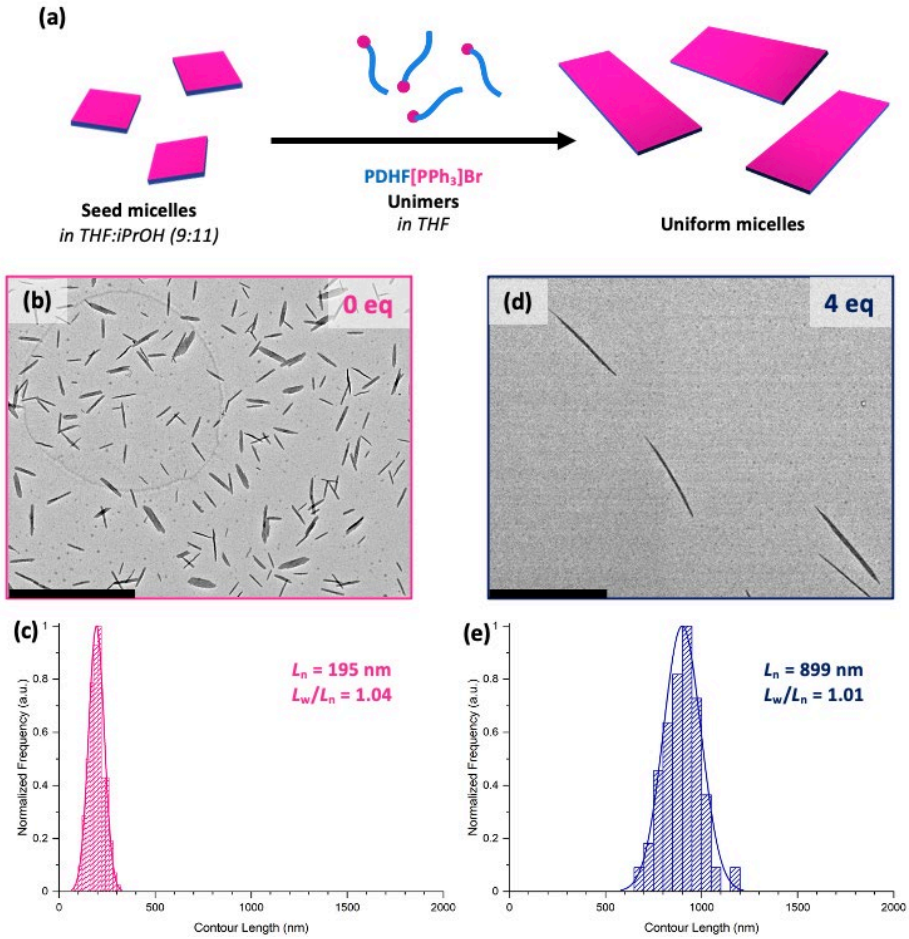

Figure 5. 6: Schematic illustration of the seeded growth protocol employed to prepare low dispersity $PDHF_8[PPh_3]Br$ 1D micelles in THF:iPrOH (9:11, v/v). The unimer was added as a solution in THF. (b) TEM images of $PDHF_8[PPh_3]Br$ seed micelles (L_n= 195 nm, L_w/L_n= 1.04) and (c) corresponding histogram of the contour length distribution. (d) TEM image of low dispersity 1D micelles (L_n= 899 nm, L_w/L_n= 1.01) prepared by the seeded growth of $PDHF_8[PPh_3]Br$ unimer from seed micelles (L_n= 195 nm, L_w/L_n= 1.04) with a m_{unimer}/m_{seed} value of 4 and (e) corresponding histogram of the contour length distribution. Scale bars: 1 μm.

Next, we explored the formation of segmented micelles from the seeded growth of PDHF-based BCP unimers from $PDHF_8[PPh_3]Br$ seed micelles (Figure 5. 7a). In a typical experiment, either $PDHF_{14}$-*b*-PEG_{227} or $PDHF_{17}$-*b*-$P2VP_{250}$ unimers in THF were added in one quick injection to a dilute solution of $PDHF_8[PPh_3]Br$ seed micelles and the sample was aged at 30 °C for 24 h before analysis by TEM. 'Living' CDSA of $PDHF_{14}$-*b*-PEG_{227} or $PDHF_{17}$-*b*-$P2VP_{250}$ materials has been achieved in THF:MeOH (1:1, v/v) or THF:EtOH (1:1, v/v) solvent mixtures (see Chapters 2 and 3). However, $PDHF_8[PPh_3]Br$ micelles appear to the most colloidally stable in THF:iPrOH mixtures. 'Living' CDSA was attempted in all of these solvent mixtures to determine the optimal conditions required to facilitate epitaxial growth of the BCP unimers from $PDHF_8[PPh_3]Br$ seeds. For the seeded

growth experiments, $PDHF_8[PPh_3]Br$ seed micelles (L_n = 97 nm, L_w/L_n = 1.13) prepared in THF:iPrOH (9:11, v/v) were first diluted in THF:MeOH/EtOH/iPrOH (1:1, v/v) solvent mixtures (Figure S5. 12a).

The seeded growth of $PDHF_{14}$-*b*-PEG_{227} BCP from $PDHF_8[PPh_3]Br$ seeds will be discussed first. Multiple 1D fibers, composed of $PDHF_{14}$-*b*-PEG_{227} BCP, were nucleated from the $PDHF_8[PPh_3]Br$ seed micelles in all solvent mixtures. Using a unimer to seed ratio of 10, the seeded growth of $PDHF_{14}$-*b*-PEG_{227} resulted in the formation of low-dispersity ($L_w/L_n \leq 1.05$) fiber arms from the $PDHF_8[PPh_3]Br$ seeds. In THF:MeOH/EtOH mixtures, aggregation of the central $PDHF_8[PPh_3]Br$ seeds was observed resulting in branched micelles with fiber arms of low length dispersity (Figure S5. 11). Individual scarf-like micelles were observed in THF:iPrOH (1:1, v/v), characterized by a wider central segment and narrower fiber arms (tassels) grown exclusively in one dimension (Figure 5. 7b). Although the $PDHF_8[PPh_3]Br$ seeds aggregate in THF:MeOH (1:1, v/v), seeded growth of $PDHF_{14}$-*b*-PEG_{227} resulted in branched supermicelles with low dispersity fiber arms using a unimer-to-seed ratio of 5 (L_n = 471 nm, L_w/L_n = 1.03) and 10 (L_n = 944 nm, L_w/L_n = 1.02) (Figure S5. 12b-c and Figure S5. 13a-b). $PDHF_8[PPh_3]Br$ seeds are better dispersed in THF:iPrOH (1:1, v/v) and epitaxial growth of added $PDHF_{14}$-*b*-PEG_{227} unimer yielded multiple low dispersity fiber arms (Figure S5. 12d-e and Figure S5. 13c-d). However, the tassel lengths obtained from the seeded growth experiments using a unimer-to-seed ratio of 5 (L_n = 539 nm, L_w/L_n = 1.05) and 10 (L_n = 644 nm, L_w/L_n = 1.04) were not significantly different. TEM analysis detected the presence of films that can be attributed to residual unimer aggregation, this suggests that THF:iPrOH solvent mixture is not sufficiently polar to enable complete consumption of unimer via seeded growth (Figure S5. 14).

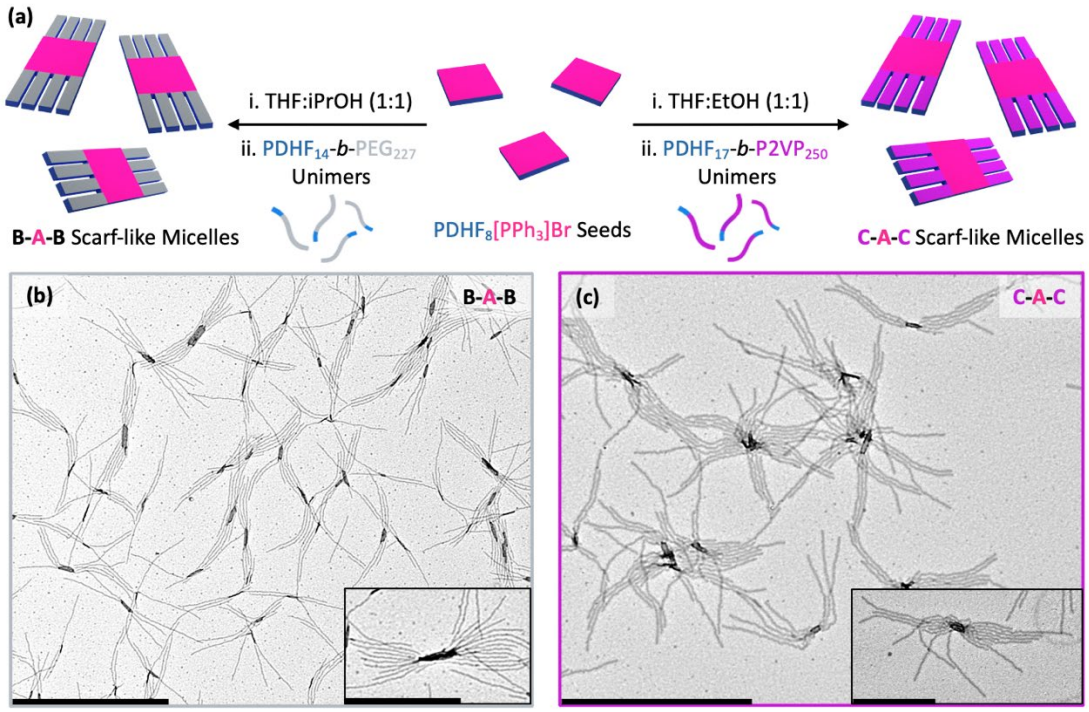

Figure 5. 7: (a) Schematic illustration of the seeded growth of $PDHF_{14}$-*b*-PEG_{227} or $PDHF_{17}$-*b*-$P2VP_{250}$ unimers from $PDHF_8[PPh_3]Br$ seeds. TEM images of branched scarf-like micelles prepared by the seeded growth of (b) $PDHF_{14}$-*b*-PEG_{227} or (c) $PDHF_{17}$-*b*-$P2VP_{250}$ unimers from $PDHF_8[PPh_3]Br$ seeds (L_n= 97 nm, L_w/L_n= 1.13) with a m_{unimer}/m_{seed} value of (b) 10 or (c) 20 in (b) THF:iPrOH (1:1, v/v) or (c) THF:EtOH (1:1, v/v). Scale bars: 2 μm, inset scale bars: 1 μm. A = $PDHF_8[PPh_3]Br$, B = $PDHF_{14}$-*b*-PEG_{227} and C = $PDHF_{17}$-*b*-$P2VP_{250}$.

Furthermore, the addition of $PDHF_{17}$-*b*-$P2VP_{250}$ BCP unimers to $PDHF_8[PPh_3]Br$ seeds also resulted in the formation of branched scarf-like micelles in THF:EtOH (1:1, v/v) (Figure 5. 7c). The tassel lengths of these scarf-like micelles, composed of $PDHF_{17}$-*b*-$P2VP_{250}$ BCP, were found to be linearly dependent on the unimer-to-seed ratio (Figure 5. 8f). Using unimer-to-seed ratios of 10. 20, 30 and 40, resulted in scarf-like micelles with tassel lengths from 362 nm to 1031 nm with low length dispersities ($L_w/L_n \leq 1.05$) (Figure 5. 8 and Figure S5. 15). From these studies we have shown that $PDHF_8[PPh_3]Br$ seeds can be used to nucleate several fiber arms in the presence of added BCP unimer which leads to the formation of branched scarf-like micelles. The length of the fiber arms can be tuned, however the number of arms from each seed micelle varies and is dependent on the width of the seed. Obtaining seeds with monodisperse widths will be essential for controlling the number of fiber arms in these scarf-like micelles. Future work will focus on optimizing the self-assembly conditions to afford scarf-like micelles with a defined number of tassels.

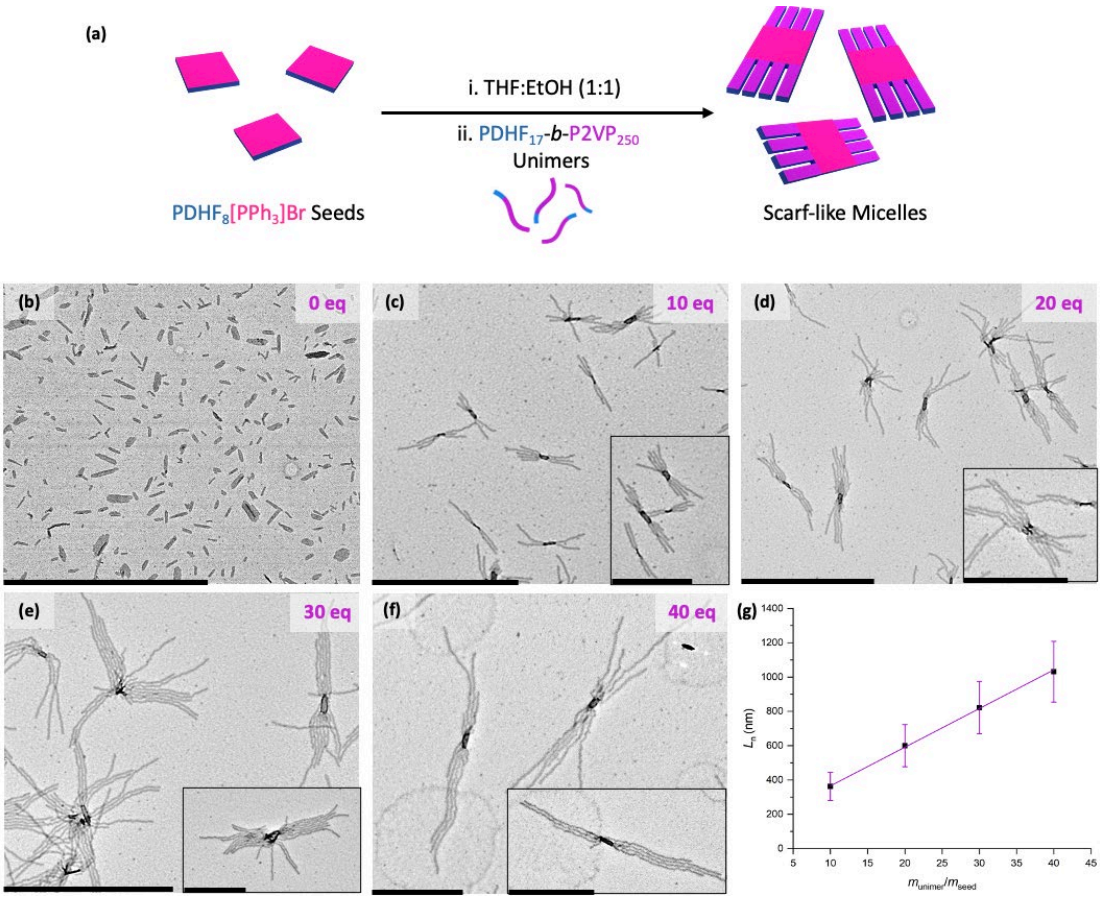

Figure 5. 8: (a) Schematic illustration of the seeded growth of $PDHF_{17}$-*b*-$P2VP_{250}$ unimers from $PDHF_8[PPh_3]Br$ seeds TEM images of branched scarf-like micelles prepared by the seeded growth of $PDHF_{17}$-*b*-$P2VP_{250}$ unimers from $PDHF_8[PPh_3]Br$ seeds (L_n= 97 nm, L_w/L_n= 1.13) with a m_{unimer}/m_{seed} value of (b) 0, (c) 10, (d) 20, (e) 30, and (f) 40 in THF:EtOH (1:1, v/v). Scale bars: (b)-(e) 2 μm and (f) 1 μm, inset scale bars: 1 μm. (g) A plot showing the dependence of fiber tassel length on the unimer-to-seed mass ratio.

5.3.4. Attempted 2D Seeded Growth of $PDHF_8[PPh_3]Br$

Low dispersity 2D morphologies such as rectangular, diamond-like and hexagonal platelets can be prepared by the seeded growth of charge-capped PFS or PLLA homopolymer from 1D fiber-like or 2D platelet seed micelles.[20–22] We therefore attempted to use 'living' CDSA to afford low dispersity platelets with low aspect ratio composed of phosphonium-capped PDHF homopolymer. In section 5.3.2, we have shown that polydisperse 2D platelet micelles can be prepared by the self-nucleation of $PDHF_8[PPh_3]Br$ polymer in THF:DMSO mixtures. Seeded growth experiments for the formation of low dispersity platelets were therefore conducted in THF:DMSO mixtures in an effort to promote 2D epitaxial growth from seed micelles.

Seeded growth was first attempted from seeds prepared by the sonication of polydisperse 2D platelet micelles, formed in THF:DMSO (7:13, v/v), at 20 °C for

1 h. Fragmented 2D seed micelles were obtained with low length dispersity (L_n = 150 nm, L_w/L_n = 1.13) and an area dispersity of 1.50 (A_n = 8.3 x 10^{-3} nm^2, A_w/A_n = 1.50, where A_n is the number average area and A_w is the weight average area) (Figure S5. 16). Similar area dispersities have been observed for 2D seed micelles prepared by the sonication of PFS- based platelets.[20] The broader dispersity obtained for these 2D seeds versus those typically obtained for 1D seeds may be the result of fragmentation occurring along two dimensions. In THF:DMSO mixtures, $PDHF_8[PPh_3]Br$ homopolymer precipitates rapidly at ambient temperatures, so seeded growth experiments were conducted at an elevated temperature to suppress the self-nucleation of added unimer. At 80 °C, 2D seeds remain stable and no significant change in area or length dispersity was detected. An aliquot of dissolved $PDHF_8[PPh_3]Br$ homopolymer in THF was added to the 2D seeds in THF:DMSO (7:13, v/v) at 80 °C and incubated at this temperature for 30 mins before slow cooling to 20 °C. High aspect ratio ribbon-like micelles with a narrower area dispersity compared to that of the seeds were prepared using a unimer-to-seed ratio of 5 (A_n = 47.8 x 10^{-3} nm^2, A_w/A_n = 1.36) (Figure S5. 17). Comparing the L_n and W_n of the seeds (L_n = 150 nm, W_n = 52 nm) to that of the micelles obtained in the seeded growth experiment (L_n = 665 nm, W_n = 68 nm) suggest that epitaxial growth mainly occurred in the π-π stacking direction.

Next we explored the use of low length dispersity 1D seeds for the seeded growth of $PDHF_8[PPh_3]Br$ in THF:DMSO mixtures. 1D seed micelles (L_n = 195 nm, L_w/L_n = 1.04) prepared in THF:iPrOH (9:11, v/v) were diluted with THF:DMSO (7:13, v/v). The resulting seed sample was heated to 80 °C, 10 equivalents of $PDHF_8[PPh_3]Br$ unimers was then added and the sample was incubated at this temperature for 30 mins before slow cooling to 20 °C. Epitaxial growth mainly occurred in the π-π stacking direction as the L_n increased significantly from 195 to 2034 nm but the W_n did not increase substantially (31 nm to 85 nm) (Figure S5. 18). Further attempts at preparing low dispersity 2D platelets involved using higher contents of DMSO (up to 90 %) and/or adding unimers at different temperatures (70 and 100 °C) and ageing at 50 °C for 4 h before slowly cooling to 20 °C. These approaches resulted in the formation of some low dispersity platelet morphologies but also a significant amount of self-nucleated micelles (long polydisperse ribbons) or small irregular aggregates formed through rapid

precipitation of added unimer (Figure S5. 19). From these results, temperature and DMSO content appear to heavily influence the formation of 2D platelets. These conditions need to be optimized further for the realization of pure low dispersity 2D platelets by the seeded growth of charge-capped polyfluorene homopolymers.

5.4. Summary

In this Chapter, we have shown that through the self-assembly of phosphonium-capped PDHF homopolymer a variety of micelle morphologies can be prepared, including fibers, ribbons and platelets. Previously, the self-assembly of crystallizable charge-capped homopolymers has been shown to preferentially form either 2D platelets, in the case of PFS and PLLA materials, or 1D fibers, in the case of PFTMC and P3HT materials. [20–24] In this work we show that the solution self-assembly of charge-capped PDHF in different solvent systems can yield either 1D or 2D micelles. 'Living' CDSA has been achieved to prepare low dispersity 1D micelles from $PDHF_8[PPh_3]Br$ seeds via epitaxial growth of added unimer predominantly in the π-π stacking direction. We have also shown that seeded growth of different PDHF-based BCP unimers from $PDHF_8[PPh_3]Br$ seeds presents an efficient route towards the formation of branched scarf-like micelles with tunable tassel lengths.

Fluorescence spectroscopy revealed that the 2D platelet micelles possessed an additional green emission band unlike the fiber-like micelles formed by self-nucleation of $PDHF_8[PPh_3]Br$. This suggests that the crystal lattice in the PDHF micelle cores of 1D and 2D morphologies may differ. Ongoing work focusses on identifying the origin of this green emission band by verifying whether oxidation of the fluorene units may have occurred or whether there is a difference in the crystalline structure of the 1D versus 2D micelle cores. Single area electron diffraction studies are underway to elucidate the crystal structures in the scarf-like micelles composed of a central 2D segment and 1D fiber arms. Furthermore, future work will also focus on developing a methodology to control the number of fiber arms nucleated from the $PDHF_8[PPh_3]Br$ seeds via optimization of the seed width dispersities and tuning the concentrations used in the seeded growth experiments.

Attempts at preparing lower aspect ratio platelets via 2D seeded growth were unsuccessful. Using solvent systems that favoured the formation of 2D structures through self-nucleation of $PDHF_8[PPh_3]Br$ and using either high aspect ratio 1D seeds or short 2D seeds resulted in the formation of low dispersity 1D ribbon-like micelles. This suggests that epitaxial growth in the direction of π-π stacking interactions occurs on a much faster timescale than growth in the alkyl

chain stacking direction. To promote epitaxial growth in these two dimensions, future work will focus on optimizing the incubation temperature and solvent conditions used for the seeded growth experiments. Aggregation in THF:DMSO mixtures could be monitored via temperature-dependent dynamic light scattering measurements. This might provide some insight into the optimal conditions required to achieve significant epitaxial growth in two dimensions via the 'living' CDSA of charge-capped polyfluorene materials.

5.5. Supporting Information

5.5.1. Materials and Methods

All reagents and solvents used for polymers synthesis were of reagent grade, and unless otherwise stated and were used as received. Solvents for self-assembly were of HPLC grade and filtered using 0.2 μm syringe filters prior to use. The synthesis of $PDHF_{14}$-*b*-PEG_{227} has been reported elsewhere[1] and the synthesis of $PDHF_{17}$-*b*-$P2VP_{250}$ has been described in Chapter 3 and is not reported here.

Nuclear magnetic resonance (NMR). ^1H NMR spectra were taken with a Bruker 500 MHz spectrometer; chemical shifts were referenced to the residual solvent peak ($CHCl_3$, δ = 7.26 ppm).

Gel Permeation Chromatography (GPC). measurements were conducted on Viscotek GPC_{max} equipped with a UV detector operating at 400 nm and a refractometer. Measurements were carried out at 1.0 mL min^{-1} with THF containing [*n*Bu4N]Br (0.1% w/w) as the eluent at 35 ˚C, results were measured against polystyrene standards (Viscotek).

Matrix-Assisted Laser Desorption/Ionization Time-Of-Flight Mass Spectrometry (MALDI-TOF MS). Measurements were conducted on a Bruker Ultraflex II ToF spectrometer under the reflector positive ion regime. Samples were prepared with a 9:1 ratio of *trans*-2-[3-(4- *tert*-butylphenyl)-2-methyl-2-propenylidene]malonitrile matrix (20 mg mL^{-1} in THF) to polymer solution (0.2 mg mL^{-1} in THF), then 5 μL of the sample was deposited onto the sample plate and dried under ambient conditions.

Transmission Electron Microscopy (TEM). Samples were prepared by drop casting 10 μL of the nanofiber solution onto a carbon-coated copper grid (Agar Scientific, mesh size 200). Bright-field TEM micrographs were taken using a JEOL JEM 1011EX microscope operating at 80 kV, equipped with a 11M pixel CCD camera. Micelle length distributions were determined using the software program ImageJ developed at US National Institute of Health. A minimum of 300 micelles are traced to determine their contour length or width and length or width distributions. This data allows for calculation of the number average length (L_n), weight average length (L_w), number average width (W_n), weight average width (W_w), number average area (A_n), weight average area (A_w) for a sample, this is

calculated as shown below (L = length of micelle, W = width of micelle, A = area of micelle, N = number).

$$L_n = \frac{\sum_{i=1}^{n} N_i L_i}{\sum_{i=1}^{n} N_i} \qquad L_w = \frac{\sum_{i=1}^{n} N_i {L_i}^2}{\sum_{i=1}^{n} N_i L_i}$$

$$W_n = \frac{\sum_{i=1}^{n} N_i W_i}{\sum_{i=1}^{n} N_i} \qquad W_w = \frac{\sum_{i=1}^{n} N_i {W_i}^2}{\sum_{i=1}^{n} N_i W_i}$$

$$A_n = \frac{\sum_{i=1}^{n} N_i A_i}{\sum_{i=1}^{n} N_i} \qquad A_w = \frac{\sum_{i=1}^{n} N_i {A_i}^2}{\sum_{i=1}^{n} N_i A_i}$$

Spectroscopic Measurements. UV/vis data were obtained on a Lambda 35 Spectrometer employing glass cells (1 cm x 1 cm) from 200 to 800 nm. Fluorescence data was obtained on a PTI QM40 Spectrofluorometer using an excitation wavelength of λ_{ext} at 380 nm.

5.5.2. Synthesis of alkyne-terminated PDHF

Alkyne-terminated PDHF homopolymers were synthesized by Grignard Metathesis polymerization (GRIM). 2-Bromo-7-iodo-9,9-bis-*n*-hexylfluorene was synthesised according to the reported procedure.[44] In an example polymerization, 2-Bromo-7-iodo-9,9-bis-*n*-hexylfluorene (435 mg, 0.81 mmol) was dissolved in 10 mL of anhydrous THF. The resulting solution was cooled to -20˚C before 1.3 M *i*PrMgCl.LiCl complex (1 eq.) was added dropwise, then the solution was left to stir for 90 min at -78˚C. The activated solution of 2-bromo-7-iodo-9,9-bis-*n*-hexylfluorene monomer was added in one quick injection to a solution of Ni(dppp)Cl_2 (17.5 mg, 0.032 mmol) and anhydrous THF (100 mL) at 0˚C. After 15 mins, 0.5 M ethynylmagnesium bromide (3 mL) was added to the reaction mixture which was then stirred for 1 h. The resultant mixture was then precipitated into methanol affording a pale yellow solid. The polymer was then dissolved in DCM, washed with water several times then with saturated NaCl solution before drying with anhydrous $MgSO_4$. After filtration, the solution was concentrated *in vacuo* before precipitation in cold methanol to afford a bright yellow solid. Further purification by Soxhlet extraction in ethyl acetate followed by collection in chloroform gave the purified polymer as a yellow solid (151 mg, yield: 45 %).

The degree of polymerisation of all PDHF homopolymers was determined by MALDI-TOF MS. Samples were composed of a 9:1 ratio of matrix to polymer

solution (0.2 mg mL^{-1} in THF). The polydispersity (M_w/M_n) was determined by GPC (THF containing [nBu$_4$N]Br (0.1 % w/w).

PDHF$_{27}$-yne

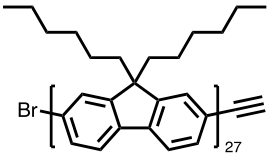

Alkyne-terminated PDHF$_{27}$ was synthesized by the method mentioned above. Yield = 151 mg, 45 %. MALDI-ToF MS: M^+ = 9086 Da, repeat unit weight = 332 amu. GPC (THF containing [nBu$_4$N]Br (0.1 % w/w), 1 mL min^{-1}): M_n = 23.2 kDa, M_w = 26.5 kDa, M_w/M_n = 1.14. ^{1}H NMR (500 MHz, $CDCl_3$) ppm δ = 7.91-7.61 (m, 6 H, C*H* aromatic), 2.13 (m, 4 H, (C*H*$_2$) x 2), 1.22-0.96 (m, 16 H, (C*H*$_2$) x 6) and 0.95-0.77 (m, 10 H, (C*H*$_3$) x 2 and (C*H*$_2$) x 2).

PDHF$_8$-yne

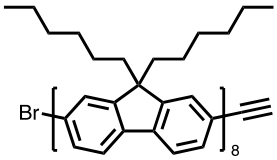

Alkyne-terminated PDHF$_7$ was synthesized by an analogous method to that mentioned above. Yield = 146 mg, 52 %. MALDI-ToF MS: M^+ = 2765 Da, repeat unit weight = 332 amu. GPC (THF containing [nBu$_4$N]Br (0.1 % w/w), 1 mL min^{-1}): M_n = 4.4 kDa, M_w = 5.5 kDa, M_w/M_n = 1.25. ^{1}H NMR (500 MHz, $CDCl_3$) δ (ppm) = 7.91-7.62 (m, 6 H, C*H* aromatic), 2.13 (m, 4 H, (C*H*$_2$) x 2), 1.22-0.96 (m, 16 H, (C*H*$_2$) x 6) and 0.95-0.77 (m, 10 H, (C*H*$_3$) x 2 and (C*H*$_2$) x 2).

5.5.3. Synthesis of (3-azidopropyl)triphenyl phosphonium bromide

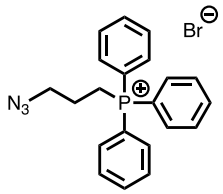

(3-Bromopropyl)triphenyl phosphonium bromide (2 g, 4.29 mmol) and sodium azide (0.56 g, 8.61 mmol) were dissolved in 10 mL of a water: ethanol mixture (1:1 v/v). The resulting mixture, under stirring, was heated to 80°C under reflux for 16 h. After concentrating *in vacuo,* the supersaturated solution was cooled in an ice bath (0°C) for 2 h. The solution was filtered, and the solids washed with ice cold water to afford the product as a white solid. Yield = 1.73 g, 87 %. ^{1}H NMR (500 MHz, $CDCl_3$) ppm δ = 7.89-7.67 (m, 15 H, (C*H*) x 15 - aromatic), 4.03 (m, 2 H, CH_2P^+), 3.84 (t, 2 H, CH_2N_3) and 1.90 (m, 2 H, C$H_2CH_2N_3$).

5.5.4. Synthesis of PDHF homopolymers with a terminal phosphonium end-group

Alkyne- and azido-functionalized materials can be coupled by using a copper-catalyzed azide-alkyne cycloaddition (CuAAC) click reaction.[45] In an example polymerization, alkyne-terminated $PDHF_{27}$ (60 mg, 0.0066 mmol), (3-azidopropyl)triphenyl phosphonium bromide (10 mg, 0.03 mmol) and PMDETA (50 µL, excess) were dissolved in 3 mL of THF and subjected to three consecutive freeze-pump-thaw cycles. CuBr (5 mg, excess) was added to polymer solution (under inert atmosphere). The reaction mixture was heated to 45 ˚C and stirred for 48 h. The solution was then diluted with DCM, washed with water several times then with saturated NaCl solution before drying with anhydrous $MgSO_4$. After filtration, the solution was concentrated *in vacuo*. Residual alkyne-terminated $PDHF_{27}$ was removed by silica gel chromatography (eluent chloroform 100 %), then the charge-capped polymer was collected using chloroform and methanol (9:1, v/v) as the eluent. The pure fractions were concentrated *in vacuo* before precipitation in cold methanol to afford the product as a pale yellow solid (yield: 28 mg, 47 %).

PDHF$_{27}$[PPh$_3$]Br

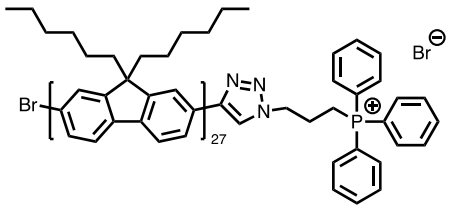

PDHF$_{27}$[PPh$_3$]Br was synthesized by the method mentioned above. Yield = 28 mg, 47 %. GPC (THF containing [*n*Bu$_4$N]Br (0.1 % w/w), 1 mL min^{-1}): M_n = 22.9 kDa, M_w = 25.6 kDa, M_w/M_n = 1.12. ^{1}H NMR (500 MHz, CDCl$_3$) ppm δ = 7.90-7.59 (m, 177 H, C*H* aromatic-PDHF and PPh$_3$) and 2.38-1.91 (m, 108 H, C*H$_2$* x 2-PDHF).

PDHF$_8$[PPh$_3$]Br

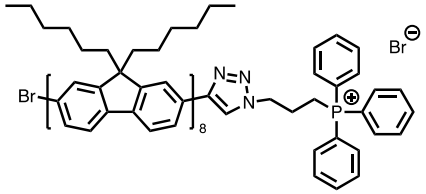

PDHF$_8$[PPh$_3$]Br was synthesized by an analogous method to that mentioned above. Yield = 23 mg, 40 %. GPC (THF containing [*n*Bu$_4$N]Br (0.1 % w/w), 1 mL min^{-1}): M_n = 6.1 kDa, M_w = 7.0 kDa, M_w/M_n = 1.14. ^{1}H NMR (500 MHz, CDCl$_3$) ppm δ = 7.90-7.59 (m, 63 H, C*H* aromatic-PDHF and PPh$_3$) and 2.38-1.91 (m, 32 H, C*H$_2$* x 2-PDHF).

5.5.5. Supplementary Figures

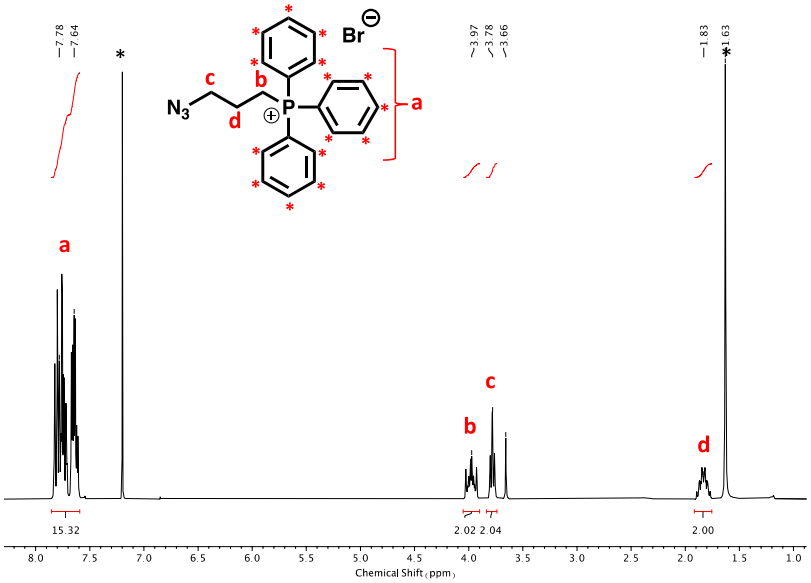

Figure S5. 1: ^{1}H NMR spectrum of (3-azidopropyl)triphenyl phosphonium bromide (500 MHz, $CDCl_3$). $CDCl_3$ (δ = 7.26 ppm) is labelled. $CDCl_3$ (δ = 7.26 ppm) and H_2O (δ = 1.63 ppm) are marked with an *.

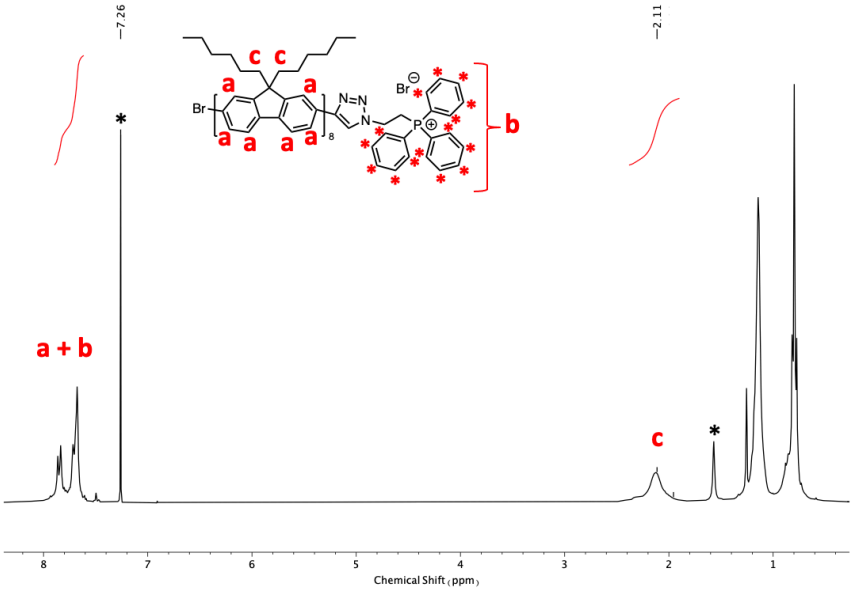

Figure S5. 2: ^{1}H NMR spectrum of $PDHF_8[PPh_3]Br$ (500 MHz, $CDCl_3$). $CDCl_3$ (δ = 7.26 ppm) and H_2O (δ = 1.56 ppm) are marked with an *.

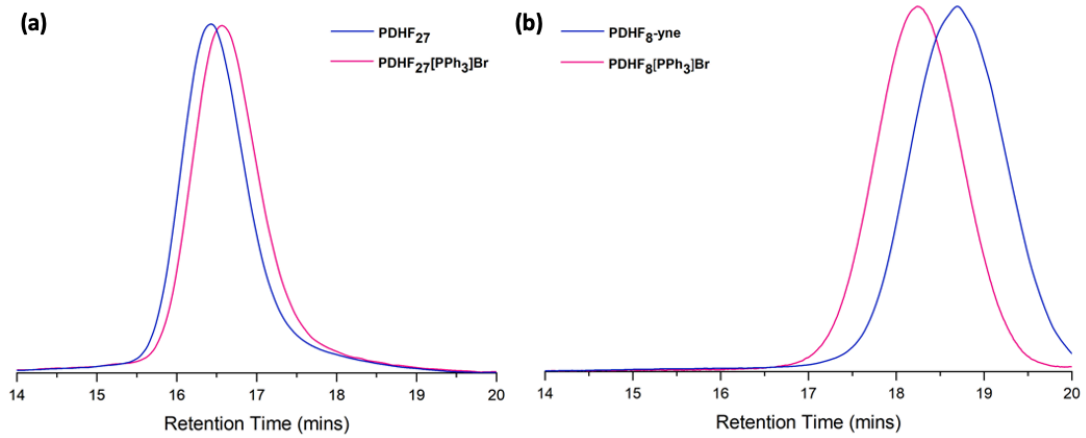

Figure S5. 3: GPC traces (UV response at λ = 380 nm) eluted in THF containing [*n*Bu$_4$N]Br (0.1 % w/w) (1 mL/min) at 35 ˚C of (a) PDHF$_{27}$ homopolymer (blue trace) and PDHF$_{27}$[PPh$_3$]Br (pink trace), and (b) PDHF$_8$ homopolymer (blue trace) and PDHF$_8$[PPh$_3$]Br (pink trace).

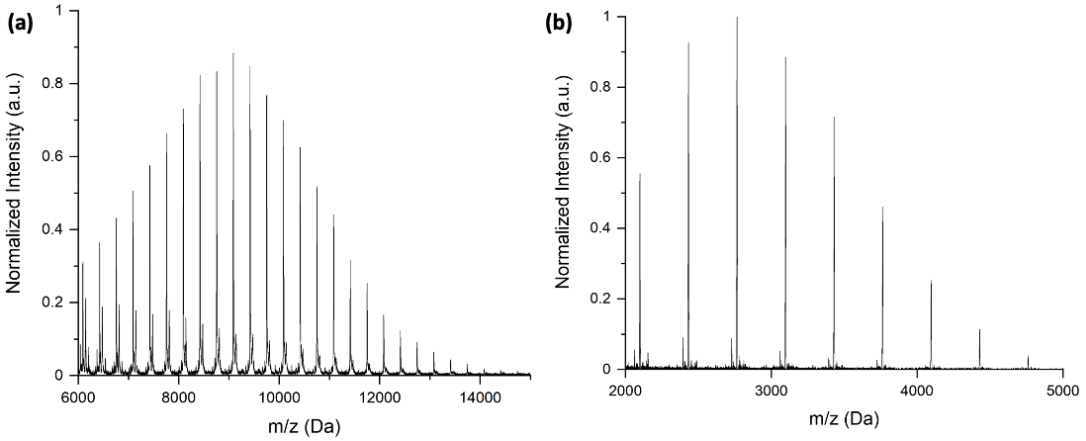

Figure S5. 4: MALDI-ToF mass spectrum of (a) alkyne-capped PDHF$_{27}$, M$^+$ = 9086 Da and (b) alkyne-capped PDHF$_8$, M$^+$ = 2765 Da. The mass of each PDHF repeat unit is 332 g mol^{-1}.

Table S5. 1: Hildebrand solubility parameter of materials and solvents.[46–48]

Material/Solvent	δ (MPa)$^{1/2}$
Poly(di-*n*-alkylfluorenes)	18.6 – 19.0
THF	18.5
Toluene	18.3
iPrOH	23.5
DMF	24.7
MeCN	24.8
EtOH	26.0
DMSO	26.4
MeOH	29.7

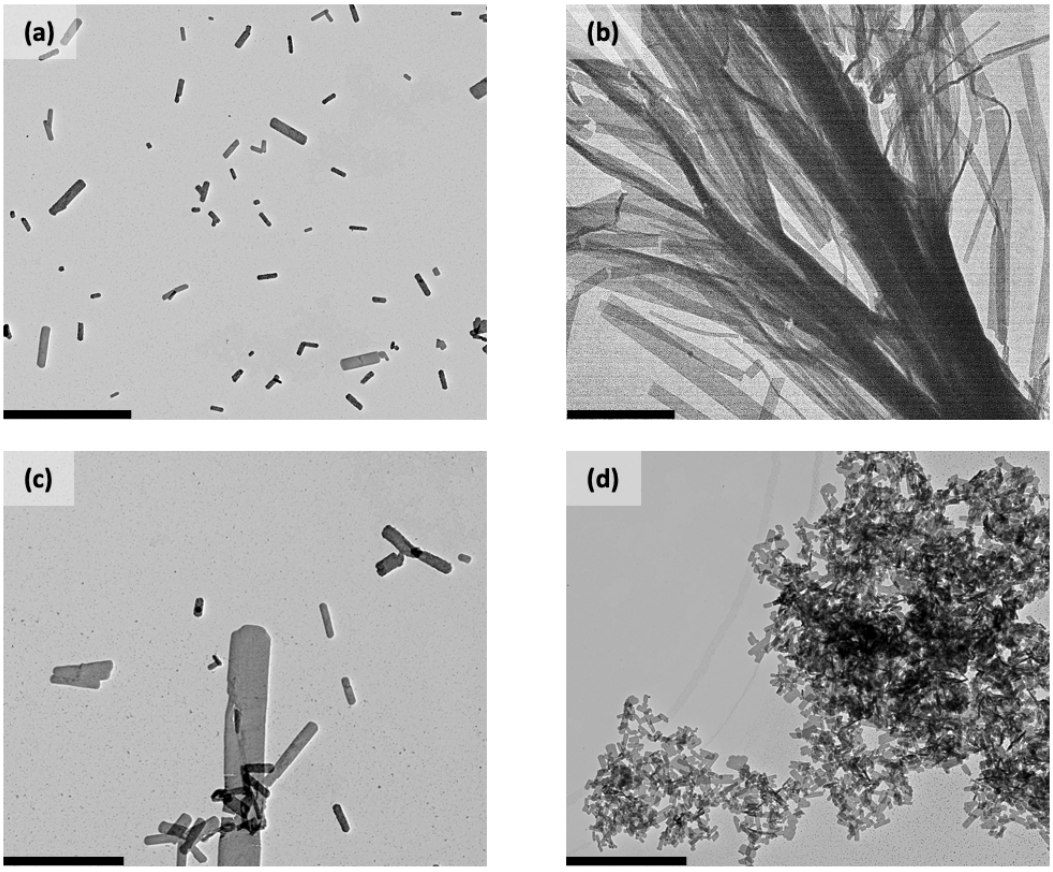

Figure S5. 5: Self-assembly of $PDHF_{27}[PPh_3]Br$ in (a) THF:DMSO (1:9), (b) THF:DMSO (1:1), (c) THF:DMSO (2:3) after 24 h of ageing at 20 °C and in (d) THF:DMSO (1:9) after 7 days of ageing at 20 °C. Scale bars: (a), (b), (d) 2 μm and (b) 1 μm.

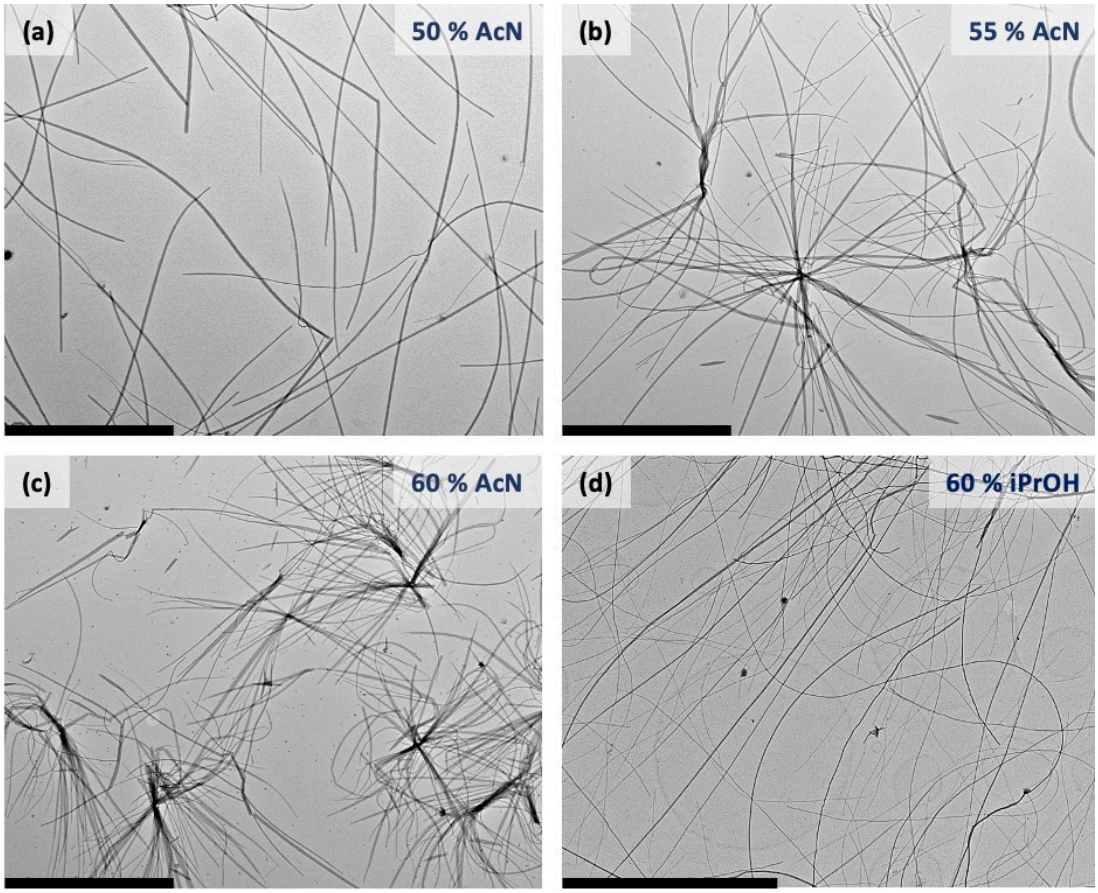

Figure S5. 6: Self-assembly of $PDHF_8[PPh_3]Br$ in (a) THF:AcN (1:1), (b) THF:AcN (9:11), (c) THF:AcN (2:3) and (d) THF:iPrOH (2:3). Scale bars: 4 μm.

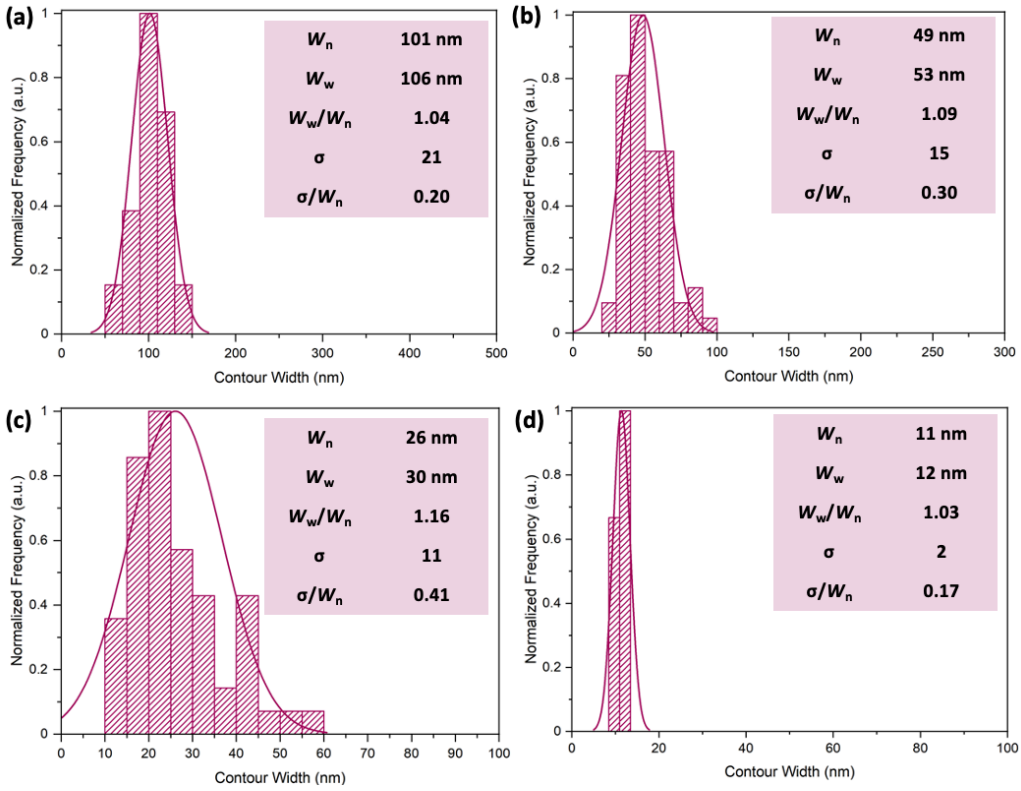

Figure S5. 7: Histograms representing contour width distributions of micelles prepared by the CDSA of $PDHF_8[PPh_3]Br$ in (a) THF:MeOH (1:1, v/v), (b) THF:MeCN (1:1, v/v), (c) THF:EtOH (1:1, v/v) and (d) THF:iPrOH (9:11, v/v). Samples were aged at 20 °C for 24 h before TEM analysis.

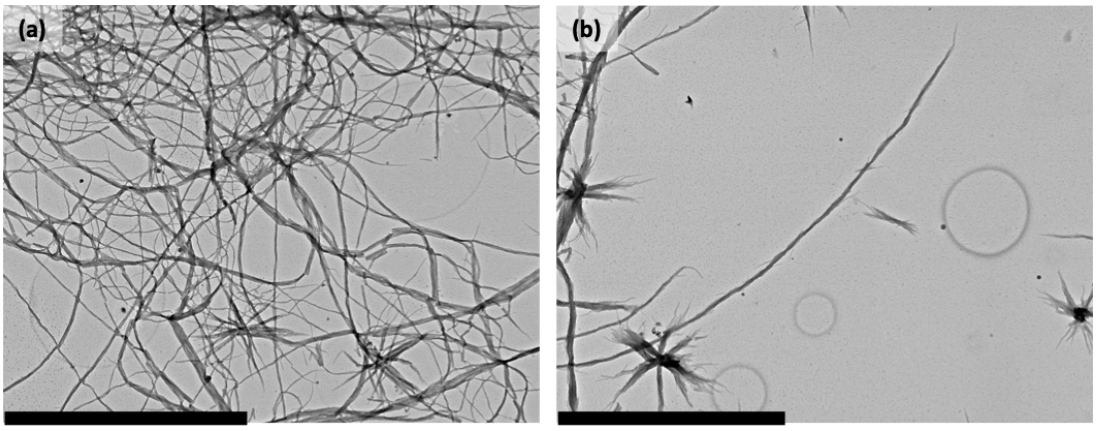

Figure S5. 8: TEM images showing the self-assembly of $PDHF[PPh_3]Br$ in (a) THF:iPrOH (1:1) and (b) THF:iPrOH (9:11) upon heating to 70 °C for 30 min followed by slow cooling to 20 °C and ageing for 1 day before TEM analysis.

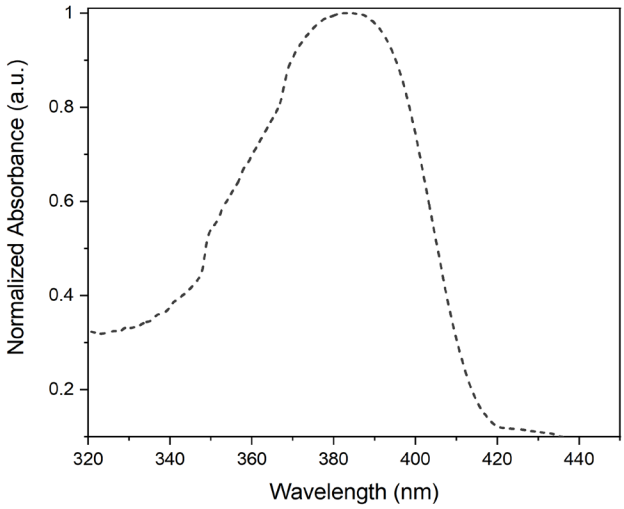

Figure S5. 9: Normalized UV-Vis spectrum of $PDHF_8[PPh_3]Br$ in THF (λ_{max} = 380 nm).

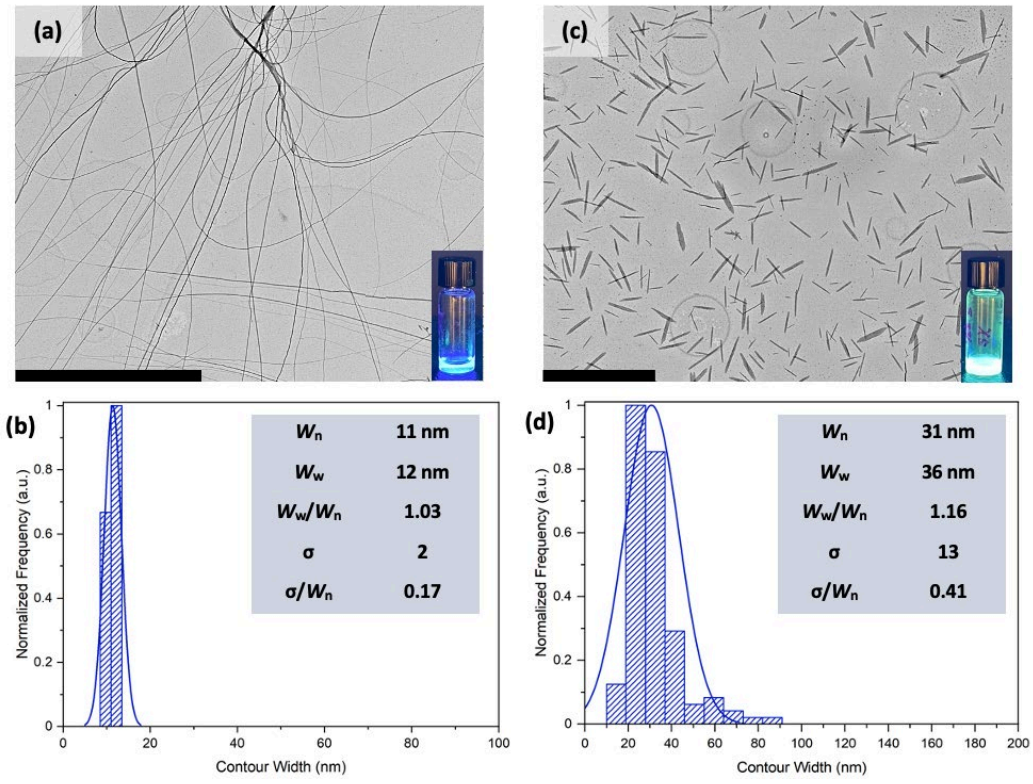

Figure S5. 10: (a) TEM image of micelles prepared by the CDSA of $PDHF_8[PPh_3]Br$ in THF:iPrOH (9:11, v/v) and (b) corresponding histogram representing the contour width distribution. (c) TEM image of seed micelles prepared by the sonication of polydisperse $PDHF_8[PPh_3]Br$ micelles Br in THF:iPrOH (9:11, v/v) and (d) corresponding histogram representing the contour width distribution. Scale bars: (a) 4 µm and (c) 2 µm. TEM image insets: photographs of the self-assembly samples under UV light (365 nm). Sample concentrations: 0.2 mg mL^{-1}

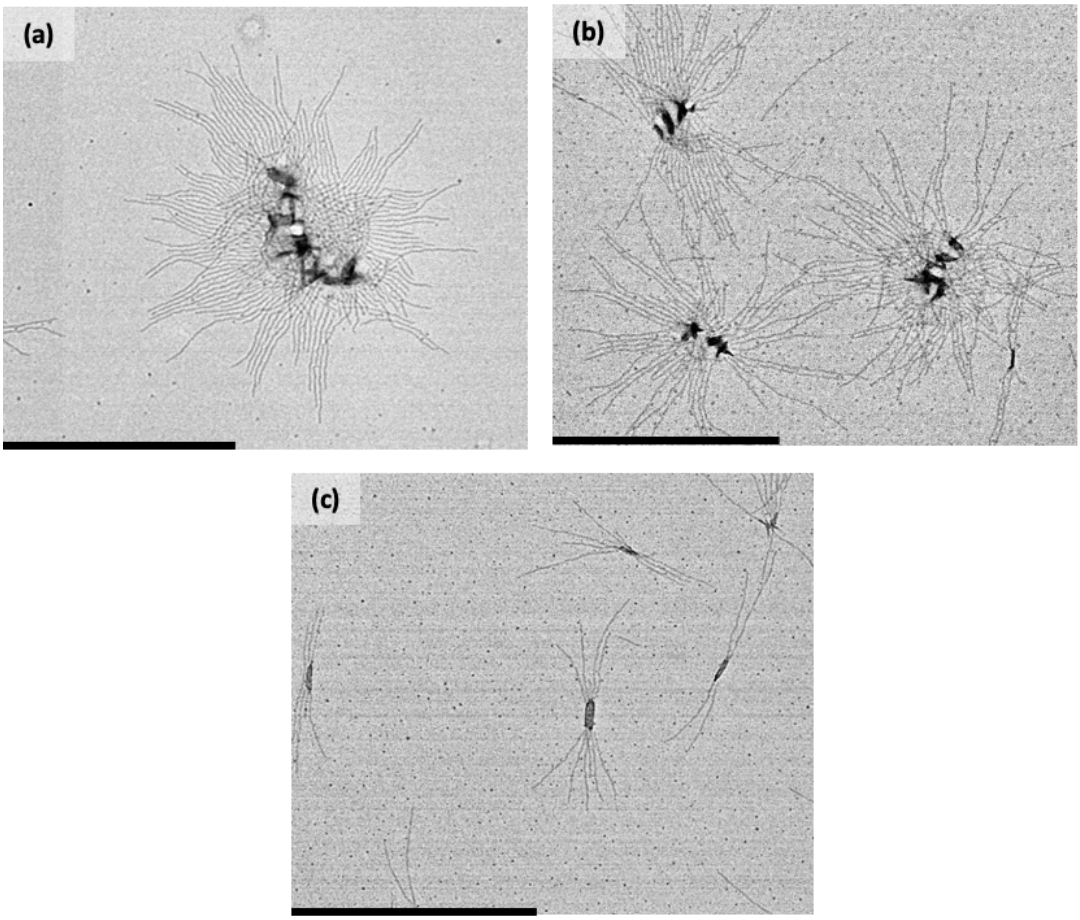

Figure S5. 11: TEM images of branched micelles prepared by the seeded growth of $PDHF_{14}$-*b*-PEG_{227} from $PDHF_8[PPh_3]Br$ seeds with a m_{unimer}/m_{seed} values of 10 in (a) THF:MeOH (1:1, v/v), (b) THF:EtOH (1:1, v/v) and (c) THF:iPrOH (1:1, v/v). Scale bars: 2 μm.

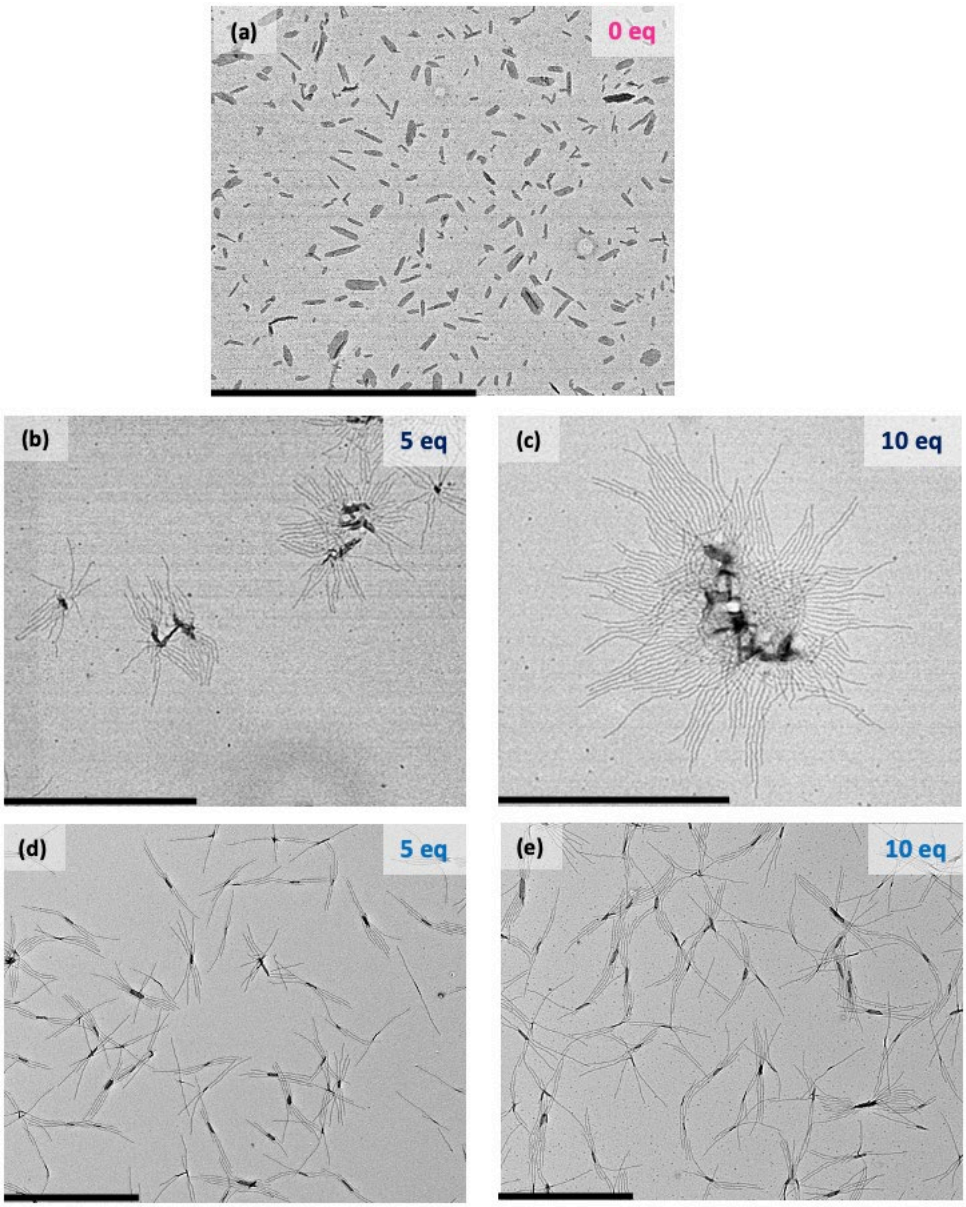

Figure S5. 12: (a) TEM image of seed micelles prepared by the sonication of polydisperse $PDHF_8[PPh_3]Br$ micelles Br in THF:iPrOH (9:11, v/v) (L_n = 97 nm, L_w/L_n = 1.13). TEM image of branched micelles with low dispersity fiber arms prepared by the seeded growth of $PDHF_{14}$-*b*-PEG_{227} unimer from $PDHF_8[PPh_3]Br$ seed micelles in THF:MeOH (1:1, v/v) with a m_{unimer}/m_{seed} value of (b) 5 and (c) 10 or in THF:iPrOH (1:1, v/v) with a m_{unimer}/m_{seed} value of (d) 5 and (e) 10. Scale bars: 2 μm. Fiber arm lengths and dispersities: (b) L_n = 471 nm, L_w/L_n = 1.03, (c) L_n = 944 nm, L_w/L_n = 1.02, (d) L_n = 539 nm, L_w/L_n = 1.05, and (e) L_n = 644 nm, L_w/L_n = 1.04.

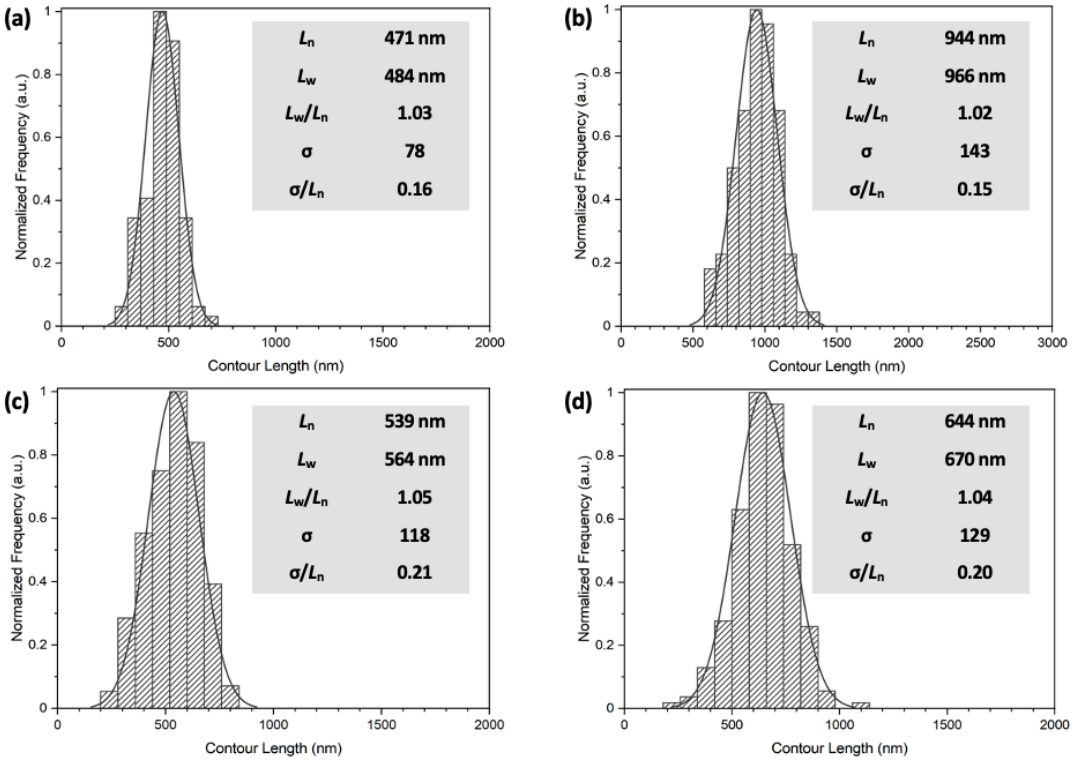

Figure S5. 13: Histograms representing contour length distributions of the fiber tassel arms in branched scarf-like micelles prepared by the seeded growth of $PDHF_{14}$-*b*-PEG_{227} unimers from $PDHF_8[PPh_3]Br$ seeds (L_n= 97 nm, L_w/L_n= 1.13) in THF:MeOH (1:1, v/v) with a m_{unimer}/m_{seed} value of (a) 5 and (b) 10 or in THF:iPrOH (1:1, v/v) with a m_{unimer}/m_{seed} value of (c) 5 and (d) 10.

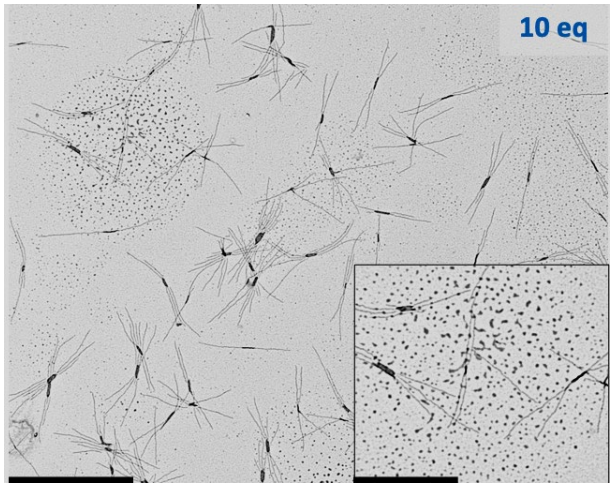

Figure S5. 14: TEM image of branched micelles with low dispersity fiber arms prepared by the seeded growth of $PDHF_{14}$-*b*-PEG_{227} unimer from $PDHF_8[PPh_3]Br$ seed micelles in THF:iPrOH (1:1, v/v) with a m_{unimer}/m_{seed} value of 10. Inset shows the presence of film (unimer). Scale bar: 2 μm, inset: 1 μm.

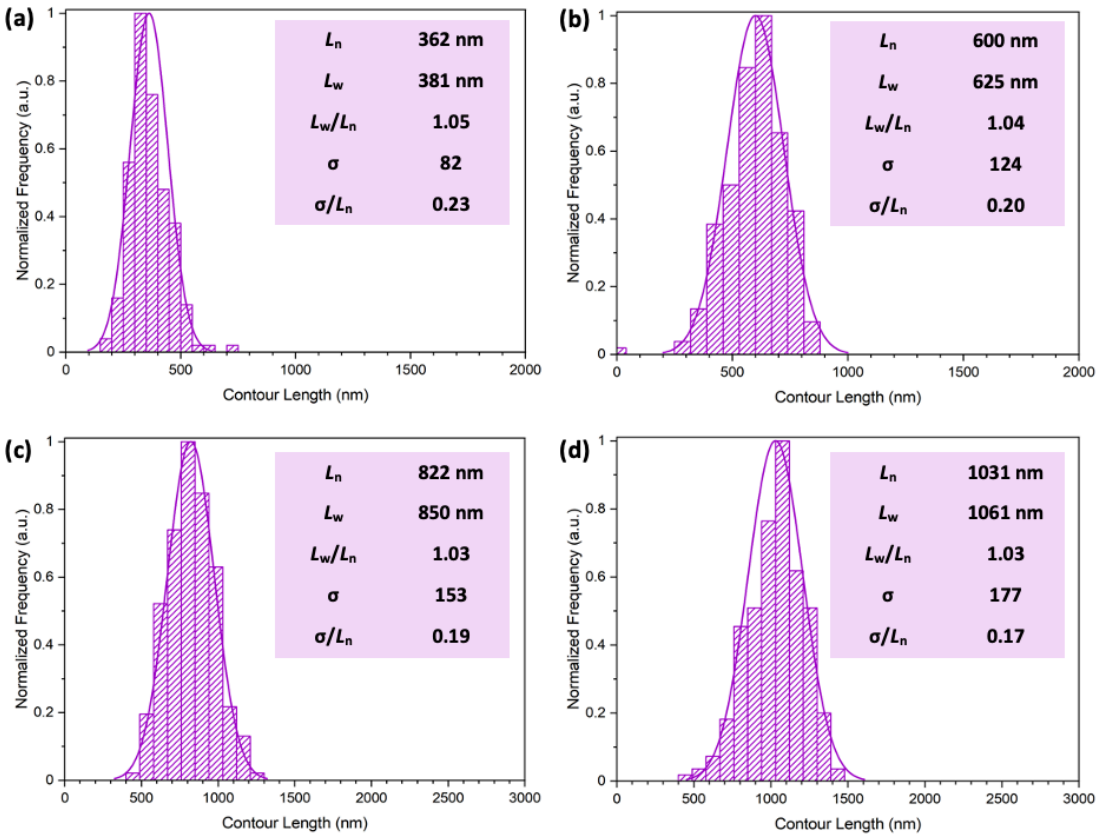

Figure S5. 15: Histograms representing contour length distributions of the fiber tassel arms in branched scarf-like micelles prepared by the seeded growth of $PDHF_{17}$-*b*-$P2VP_{250}$ unimers from $PDHF_8[PPh_3]Br$ seeds (L_n= 97 nm, L_w/L_n= 1.13) with a m_{unimer}/m_{seed} value of (a) 10, (b) 20, (c) 30, and (d) 40 in THF:EtOH (1:1, v/v).

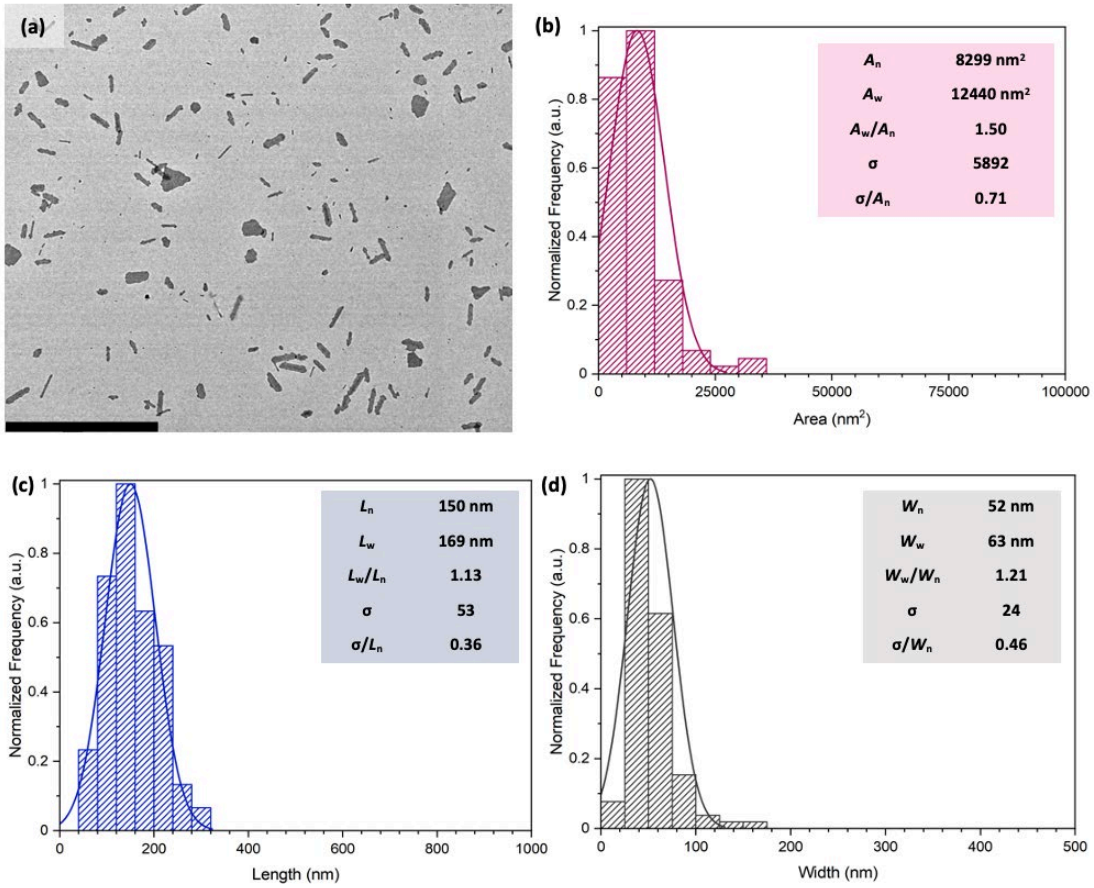

Figure S5. 16: (a) TEM image of seed micelles prepared by the sonication of polydisperse $PDHF_8[PPh_3]Br$ micelles Br in THF:DMSO (7:13, v/v). Corresponding histograms representing the (b) area, (c) length, and (d) width distributions. Scale bar: 2 µm.

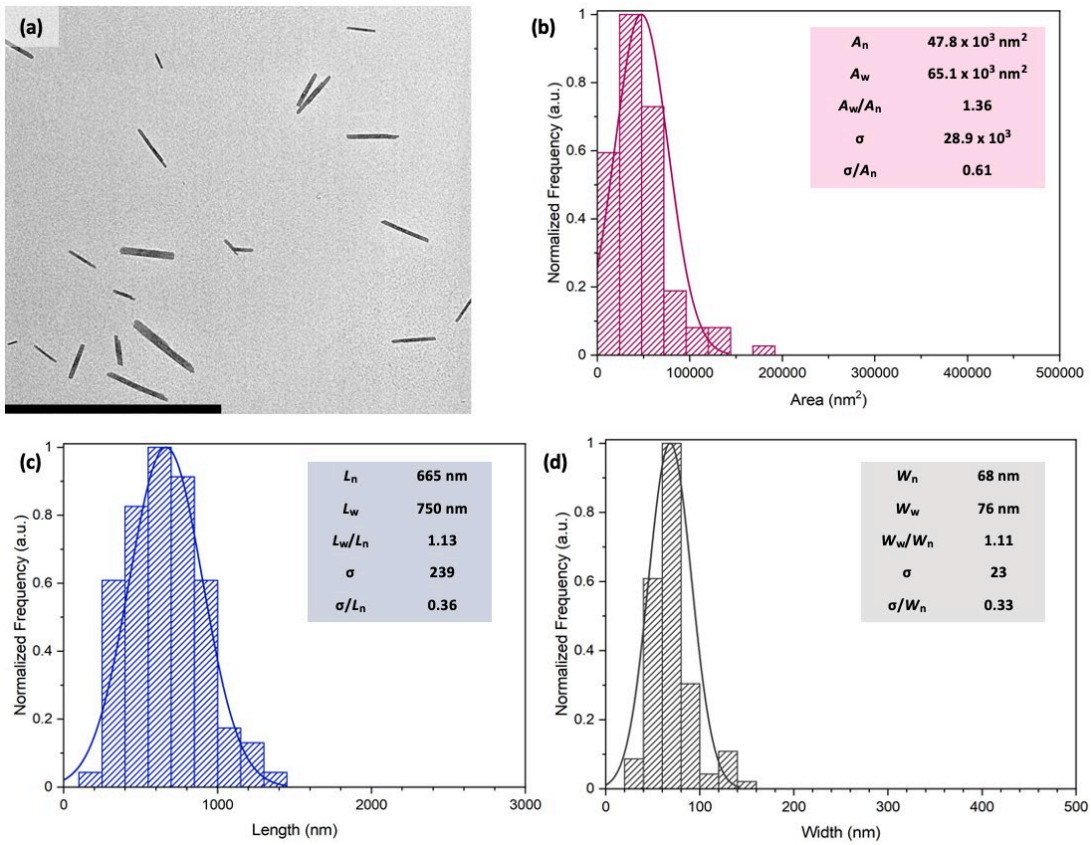

Figure S5. 17: (a) TEM image of ribbon-like micelles prepared by the seeded growth of $PDHF_8[PPh_3]Br$ unimer from 2D seed micelles in THF:DMSO (7:13, v/v) with a m_{unimer}/m_{seed} value of 5. Corresponding histograms representing the (b) area, (c) length, and (d) width distributions. Scale bar: 3 μm.

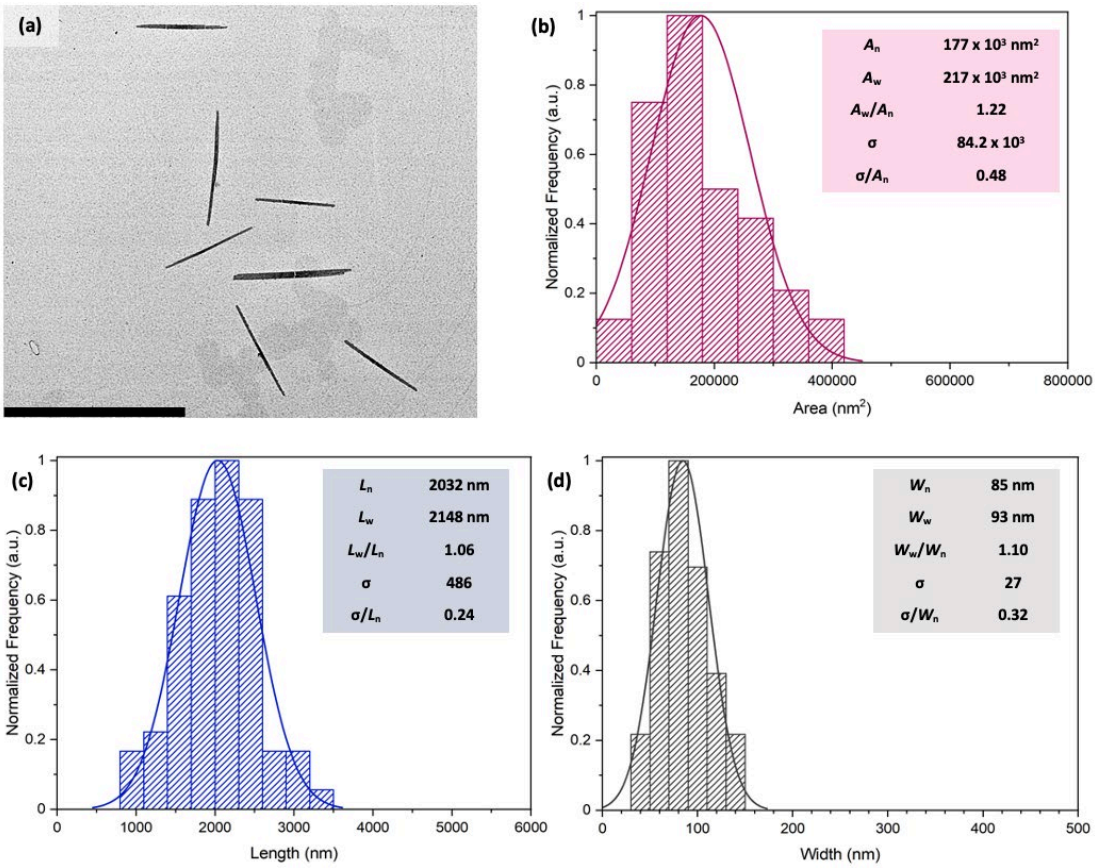

Figure S5. 18: (a) TEM image of ribbon-like micelles prepared by the seeded growth of $PDHF_8[PPh_3]Br$ unimer from 1D seed micelles in THF:DMSO (7:13, v/v) with a m_{unimer}/m_{seed} value of 10. Corresponding histograms representing the (b) area, (c) length, and (d) width distributions. Scale bar: 4 μm.

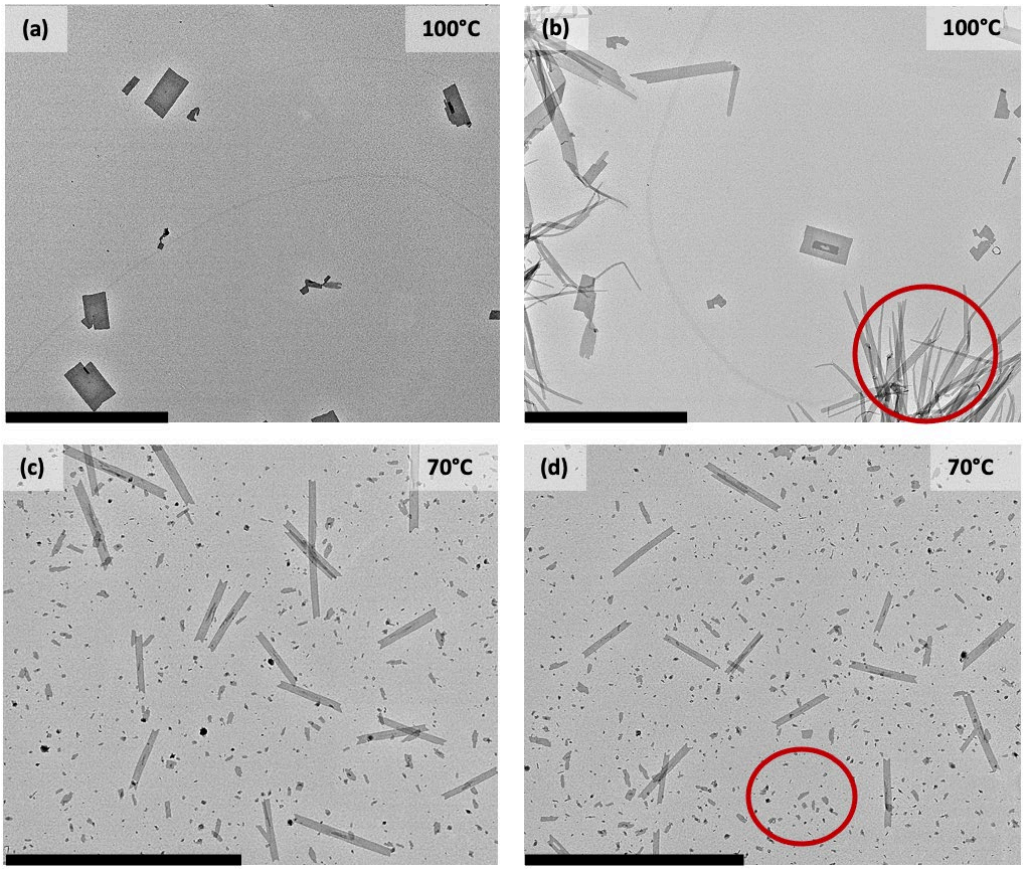

Figure S5. 19: TEM images of micelles prepared by the seeded growth of $PDHF_8[PPh_3]Br$ in THF:DMSO (1:9, v/v) with a m_{unimer}/m_{seed} value of 10. Seed micelles were heated to either (a)-(b) 100 °C or (c)-(d) 70 °C for 30 min, unimer was added and temperature was held for 30 min before slow cooling to 50 °C, aging for 4 h and slow cooling to 20 °C. Scale bars: 4 μm.

5.6. References

(1) Schenning, A. P. H. J.; Meijer, E. W. Supramolecular Electronics; Nanowires from Self-Assembled π-Conjugated Systems. *Chem. Commun.* **2005**, No. 26, 3245–3258.

(2) Günes, S.; Neugebauer, H.; Sariciftci, N. S. Conjugated Polymer-Based Organic Solar Cells. *Chem. Rev.* **2007**, *107* (4), 1324–1338.

(3) Kim, F. S.; Ren, G.; Jenekhe, S. A. One-Dimensional Nanostructures of π-Conjugated Molecular Systems: Assembly, Properties, and Applications from Photovoltaics, Sensors, and Nanophotonics to Nanoelectronics. *Chem. Mater.* **2011**, *23*, 682–732.

(4) Tatum, W. K.; Luscombe, C. K. π-Conjugated Polymer Nanowires: Advances and Perspectives toward Effective Commercial Implementation. *Polym. J.* **2018**, *50*, 659–669.

(5) MacFarlane, L. R.; Shaikh, H.; Garcia-Hernandez, J. D.; Vespa, M.; Fukui, T.; Manners, I. Functional Nanoparticles through π-Conjugated Polymer Self-Assembly. *Nat. Rev. Mater.* **2021**, *6*, 7–26.

(6) Landfester, K.; Montenegro, R.; Scherf, U.; Güntner, R.; Asawapirom, U.; Patil, S.; Neher, D.; Kietzke, T. Semiconducting Polymer Nanospheres in Aqueous Dispersion Prepared by a Miniemulsion Process. *Adv. Mater.* **2002**, *14* (9), 651–655.

(7) Szymanski, C.; Wu, C.; Hooper, J.; Salazar, M. A.; Perdomo, A.; Dukes, A.; McNeill, J. Single Molecule Nanoparticles of the Conjugated Polymer MEH-PPV, Preparation and Characterization by near-Field Scanning Optical Microscopy. *J. Phys. Chem. B* **2005**, *109*, 8543.

(8) Baier, M. C.; Huber, J.; Mecking, S. Fluorescent Conjugated Polymer Nanoparticles by Polymerization in Miniemulsion. *J. Am. Chem. Soc.* **2009**, *131*, 14267–14273.

(9) Tan, C.; Cao, X.; Wu, X. J.; He, Q.; Yang, J.; Zhang, X.; Chen, J.; Zhao, W.; Han, S.; Nam, G. H.; Sindoro, M.; Zhang, H. Recent Advances in Ultrathin Two-Dimensional Nanomaterials. *Chem. Rev.* **2017**, *117*, 6225–6331.

(10) Mai, Y.; Eisenberg, A. Self-Assembly of Block Copolymers. *Chem. Soc. Rev.* **2012**, *41* (18), 5969.

(11) Tritschler, U.; Pearce, S.; Gwyther, J.; Whittell, G. R.; Manners, I. 50th Anniversary Perspective: Functional Nanoparticles from the Solution Self-Assembly of Block Copolymers. *Macromolecules* **2017**, *50* (9), 3439–3463.

(12) Lodge, T. P. Block Copolymers: Past Successes and Future Challenges. *Macromol. Chem. Phys.* **2003**, *204*, 265–273.

(13) Vilgis, T.; Halperin, A. Aggregation of Coil-Crystalline Block Copolymers: Equilibrium Crystallization. *Macromolecules* **1991**, *24*, 2090–2095.

(14) He, W. N.; Xu, J. T. Crystallization Assisted Self-Assembly of Semicrystalline Block Copolymers. *Prog. Polym. Sci.* **2012**, *37*, 1350–1400.

(15) Massey, J. A.; Temple, K.; Cao, L.; Rharbi, Y.; Raez, J.; Winnik, M. A.; Manners, I. Self-Assembly of Organometallic Block Copolymers : The Role of Crystallinity of the Core-Forming Polyferrocene Block in the Micellar Morphologies Formed by Poly (Ferrocenylsilane- b -Dimethylsiloxane) in n -Alkane Solvents. *J. Am. Chem. Soc.* **2000**, *122* (47), 11577–11584.

(16) Petzetakis, N.; Walker, D.; Dove, A. P.; O'Reilly, R. K. Crystallization-Driven Sphere-to-Rod Transition of Poly(Lactide)-b-Poly(Acrylic Acid) Diblock Copolymers: Mechanism and Kinetics. *Soft Matter* **2012**, *8* (28), 7408–7414.

(17) Page, Z.; Kim, J.-K.; Lee, E.; Hayward, R. C.; Hammer, B.; Emrick, T. Hierarchical Helical Assembly of Conjugated Poly(3-Hexylthiophene)- Block -Poly(3-Triethylene Glycol Thiophene) Diblock Copolymers . *J. Am. Chem. Soc.* **2011**, *133* (27), 10390–10393.

(18) Qiu, H.; Gao, Y.; Boott, C. E.; Gould, O. E. C.; Harniman, R. L.; Miles, M. J.; Webb, S. E. D.; Winnik, M. A.; Manners, I. Uniform Patchy and Hollow Rectangular Platelet Micelles from Crystallizable Polymer Blends. *Science.* **2016**, *352* (6286), 697–701.

(19) Nazemi, A.; He, X.; MacFarlane, L. R.; Harniman, R. L.; Hsiao, M. S.; Winnik, M. A.; Faul, C. F. J. J.; Manners, I. Uniform "Patchy" Platelets by Seeded Heteroepitaxial Growth of Crystallizable Polymer Blends in Two Dimensions. *J. Am. Chem. Soc.* **2017**, *139* (12), 4409–4417.

(20) He, X.; Hsiao, M. S.; Boott, C. E.; Harniman, R. L.; Nazemi, A.; Li, X.; Winnik, M. A.; Manners, I. Two-Dimensional Assemblies from Crystallizable Homopolymers with Charged Termini. *Nat. Mater.* **2017**, *16* (4), 481–488.

(21) He, X.; He, Y.; Hsiao, M. S.; Harniman, R. L.; Pearce, S.; Winnik, M. A.; Manners, I. Complex and Hierarchical 2D Assemblies via Crystallization-Driven Self-Assembly of Poly(l -Lactide) Homopolymers with Charged Termini. *J. Am. Chem. Soc.* **2017**, *139* (27), 9221–9228.

(22) Pearce, S.; He, X.; Hsiao, M. S.; Harniman, R. L.; Macfarlane, L. R.; Manners, I. Uniform, High-Aspect-Ratio, and Patchy 2D Platelets by Living Crystallization-Driven Self-Assembly of Crystallizable Poly(Ferrocenyldimethylsilane)-Based Homopolymers with Hydrophilic Charged Termini. *Macromolecules* **2019**, *52* (16), 6068–6079.

(23) Fukui, T.; Garcia-Hernandez, J. D.; MacFarlane, L. R.; Lei, S.; Whittell, G. R.; Manners, I. Seeded Self-Assembly of Charge-Terminated Poly(3-Hexylthiophene) Amphiphiles Based on the Energy Landscape. *J. Am. Chem. Soc.* **2020**, *142*, 15038–15048.

(24) He, X.; Finnegan, J. R.; Hayward, D. W.; MacFarlane, L. R.; Harniman, R. L.; Manners, I. Living Crystallization-Driven Self-Assembly of Polymeric Amphiphiles: Low-Dispersity Fiber-like Micelles from Crystallizable Phosphonium-Capped Polycarbonate Homopolymers. *Macromolecules* **2020**, *53*, 10591–10600.

(25) Patra, S. K.; Ahmed, R.; Whittell, G. R.; Lunn, D. J.; Dunphy, E. L.; Winnik, M. A.; Manners, I. Cylindrical Micelles of Controlled Length with a π-Conjugated Polythiophene Core via Crystallization-Driven Self-Assembly. *J. Am. Chem. Soc.* **2011**, *133* (23), 8842–8845.

(26) Gwyther, J.; Gilroy, J. B.; Rupar, P. A.; Lunn, D. J.; Kynaston, E.; Patra, S. K.; Whittell, G. R.; Winnik, M. A.; Manners, I. Dimensional Control of Block Copolymer Nanofibers with a π-Conjugated Core: Crystallization-Driven Solution Self-Assembly of Amphiphilic Poly(3-Hexylthiophene)-b-Poly(2-Vinylpyridine). *Chem. - A Eur. J.* **2013**, *19* (28), 9186–9197.

(27) Qian, J.; Li, X.; Lunn, D. J.; Gwyther, J.; Hudson, Z. M.; Kynaston, E.; Rupar, P. A.; Winnik, M. A.; Manners, I. Uniform High Aspect Ratio Fiber-like Micelles and Block Co-Micelles with a Crystalline π - Conjugated Polythiophene Core by Self-Seeding. *J. Am. Chem. Soc.* **2014**, *136* (11), 4121–4124.

(28) Shin, S.; Menk, F.; Kim, Y.; Lim, J.; Char, K.; Zentel, R.; Choi, T. L. Living Light-Induced Crystallization-Driven Self-Assembly for Rapid Preparation of Semiconducting Nanofibers. *J. Am. Chem. Soc.* **2018**, *140* (19), 6088–6094.

(29) Han, L.; Wang, M.; Jia, X.; Chen, W.; Qian, H.; He, F. Uniform Two-Dimensional Square Assemblies from Conjugated Block Copolymers Driven by π-π Interactions with Controllable Sizes. *Nat. Commun.* **2018**, *9*, 865.

(30) Tao, D.; Feng, C.; Cui, Y.; Yang, X.; Manners, I.; Winnik, M. A.; Huang, X. Monodisperse Fiber-like Micelles of Controlled Length and Composition with an Oligo(p-Phenylenevinylene) Core via "Living" Crystallization-Driven Self-Assembly. *J. Am. Chem. Soc.* **2017**, *139* (21), 7136–7139.

(31) Tao, D.; Wang, Z.; Huang, X.; Tian, M.; Lu, G.; Manners, I.; Winnik, M. A.; Feng, C. Continuous and Segmented Semiconducting Fiber-like Nanostructures with Spatially Selective Functionalization by Living Crystallization-Driven Self-Assembly. *Angew. Chem. Int. Ed.* **2020**, *59* (21), 8232–8239.

(32) Yang, S.; Kang, S. Y.; Choi, T. L. Morphologically Tunable Square and Rectangular Nanosheets of a Simple Conjugated Homopolymer by Changing Solvents. *J. Am. Chem. Soc.* **2019**, *141* (48), 19138–19143.

(33) Kynaston, E. L.; Nazemi, A.; MacFarlane, L. R.; Whittell, G. R.; Faul, C. F. J.; Manners, I.; Faul, C. F. J. Uniform Polyselenophene Block Copolymer Fiberlike Micelles and Block Co-Micelles via Living Crystallization-Driven Self-Assembly. *Macromolecules* **2018**, *51* (3), 1002–1010.

(34) Hicks, G. E. J. J.; Jarrett-Wilkins, C. N.; Panchuk, J. R.; Manion, J. G.; Seferos, D. S. Oxidation Promoted Self-Assembly of π-Conjugated Polymers. *Chem. Sci.* **2020**, *11* (25), 32–34.

(35) Jin, X.-H.; Price, M. B.; Finnegan, J. R.; Boott, C. E.; Richter, J. M.; Rao, A.; Menke, S. M.; Friend, R. H.; Whittell, G. R.; Manners, I. Long-Range Exciton Transport in Conjugated Polymer Nanofibers Prepared by Seeded Growth. *Science.* **2018**, *360* (6391), 897–900.

(36) Shaikh, H.; Jin, X. H.; Harniman, R. L.; Richardson, R. M.; Whittell, G. R.; Manners, I. Solid-State Donor-Acceptor Coaxial Heterojunction Nanowires via Living Crystallization-Driven Self-Assembly. *J. Am. Chem. Soc.* **2020**, *142* (31), 13469–13480.

(37) Qi, R.; Zhu, Y.; Han, L.; Wang, M.; He, F. Rectangular Platelet Micelles with Controlled Aspect Ratio by Hierarchical Self-Assembly of Poly(3-Hexylthiophene)- b-Poly(Ethylene Glycol). *Macromolecules* **2020**, *53* (15), 6555–6565.

(38) Klaerner, G.; Miller, R. D. Polyfluorene Derivatives: Effective Conjugation Lengths from Well-Defined Oligomers. *Macromolecules* **1998**, *31* (6), 2007–2009.

(39) Scherf, U.; List, E. J. W. Semiconducting Polyfluorenes - Towards Reliable Structure-Property Relationships. *Adv. Mater.* **2002**, *14* (7), 477–487.

(40) Sims, M.; Bradley, D. D. C.; Ariu, M.; Koeberg, M.; Asimakis, A.; Grell, M.; Lidzey, D. G. Understanding the Origin of the 535 Nm Emission Band in Oxidized Poly(9,9-Dioctylfluorene): The Essential Role of Inter-Chain/Inter-Segment Interactions. *Adv. Funct. Mater.* **2004**, *14* (8), 765–781.

(41) Chi, C.; Im, C.; Enkelmann, V.; Ziegler, A.; Lieser, G.; Wegner, G. Monodisperse Oligofluorenes with Keto Defect as Models to Investigate the Origin of Green Emission from Polyfluorenes: Synthesis, Self-Assembly, and Photophysical Properties. *Chem. - A Eur. J.* **2005**, *11* (23), 6833–6845.

(42) Liu, B.; Lin, J.; Lei, Z.; Sun, M.; Xie, L.; Xue, W.; Yin, C.; Zhang, X.; Huang, W. Solvent and Steric Hindrance Effects of Bulky Poly(9,9-Diarylfluorene)s on Conformation, Gelation, Morphology, and Electroluminescence. *Macromol. Chem. Phys.* **2015**, *216* (10), 1043–1054.

(43) Abbel, R.; Wolffs, M.; Bovee, R. A. A.; Van Dongen, J. L. J.; Lou, X.; Henze, O.; Feast, W. J.; Meijer, E. W.; Schenning, A. P. H. J. Side-Chain Degradation of Ultrapure π-Conjugated Oligomers: Implications for Organic Electronics. *Adv. Mater.* **2009**, *21*, 597–602.

(44) Loewe, R. S.; Ewbank, P. C.; Liu, J.; Zhai, L.; McCullough, R. D. Regioregular, Head-to-Tail Coupled Poly(3-Alkylthiophenes) Made Easy by the GRIM Method: Investigation of the Reaction and the Origin of Regioselectivity. *Macromolecules* **2001**, *34* (13), 4324–4333.

(45) Zhang, M.; Rupar, P. A.; Feng, C.; Lin, K.; Lunn, D. J.; Oliver, A.; Nunns, A.; Whittell, G. R.; Manners, I.; Winnik, M. A. Modular Synthesis of Polyferrocenylsilane Block Copolymers by Cu-Catalyzed Alkyne/Azide "Click" Reactions. *Macromolecules* **2013**, *46* (4), 1296–1304.

(46) Hansen, C. H. *Hansen Solubility Parameters: A User's Handbook*, 1st ed.; CRC Press LLC: Florida, 2000.

(47) Menandro, A. S.; Fernandes, J. C.; Olivera, H. P. M.; Peres, L. O. Energy Transfer in Fluorene-Containing Donor/Acceptor Polymer System. *J. Mater Sci: Mater Electron* **2019**, *20*, 16892–16902.

(48) Bradley, D. D. C.; Grell, M.; Long, X.; Mellor, H.; Grice, A. W.; Inbasekaran, M.; Woo, E. P. Influence of Aggregation on the Optical Properties of a Polyfluorene. *Opt. Probes Conjug. Polym.* **1997**, *3145*, 254–259.

Chapter 6

Solution Self-Assembly of Diblock Copolymers with a Crystallizable Poly(di-*n*-octylfluorene) Core-Forming Block with Enhanced β-Phase Content

Contributions:

All results presented in this chapter are the sole work of Huda Shaikh.

6.1. Abstract

In this work, the solution self-assembly of block copolymers (BCPs) with crystallizable poly(di-*n*-octylfluorene) (PDOF) core-forming blocks is presented. PDOF polymer chains can adopt three different structural phases that possess unique chain packing conformations. In particular, octyl side chains can enable planarization of the polymer backbone during aggregation leading to the formation of a highly ordered crystalline phase termed the β-phase. Fabricating PDOF-based nanowires with β-phase regions is beneficial for achieving enhanced photoluminescence and electroluminescence efficiencies. Crystallization-driven self-assembly (CDSA) of PDOF-based BCPs in solution afforded fiber-like micelles with β-phase chain conformations present in the fiber cores. Self-assembly of PDOF-*b*-poly(*N*-isopropylacrylamide) (PDOF-*b*-PNIPAm) formed short fiber-like micelles in mixed solvents systems composed of a mixture of a common solvent for both polymer blocks (add solvent info) and a selective solvent for the PNIPAm block (and solvent info). Increasing the ratio of coronal selective solvent to common solvent correlated with an increase in β-phase content. Attempts to prepare longer fiber-like micelles (L_n > 200 nm) from the solution self-assembly studies of PDOF-*b*-PNIPAm, PDOF-*b*-poly(ethylene glycol) (PDOF-*b*-PEG) and PDOF-*b*-poly(dimethylsiloxane) (PDOF-*b*-PDMS) BCPs were not successful. Studies targeting the use of short fiber-like micelles prepared by homogenous nucleation of PDOF-*b*-PNIPAm to seed the epitaxial growth of solvated BCP unimer were also unsuccessful and resulted in rapid homogenous nucleation of the latter.

6.2. Introduction

Polymorphism describes the ability of materials to adopt different packing motifs in the bulk or aggregated state.[1] Semiconducting materials including conjugated small molecules and polymers possess optical and electronic properties unique to each packing motif.[2–5] Recent research efforts have focussed on understanding these structure-property relationships for the development of enhanced materials for organic electronics.[6]

Polyfluorenes are an extensively studied class of π-conjugated polymers that typically display bright blue emission but possess tunable optoelectronic properties in the form of a copolymer of fluorene units with other conjugated monomers.[7,8] For alkyl-substituted polyfluorenes, three main states with unique chain conformations have been identified: 'glassy', crystalline (also called the α-phase), and the highly ordered crystalline β-phase (Figure 6. 1a). The β-phase consists of a planarized polymer backbone and is characterized by red-shifted absorption and emission spectra (Figure 6. 1c-d).[9] The different chain conformations are influenced by the alkyl sidechain length, solvent medium, and temperature.[10, 11, 5] Exercising control over the formation of the β-phase is key to optimizing the performance of polyfluorene-based light-emitting diodes (LEDs). The fraction of the β-phase has been shown to directly affect the photoluminescence and electroluminescence efficiency.[9] To access the β-phase, self-assembly conditions that enable aggregation and planarization of the polymer backbone are needed. If the side chains along the polymer backbone are too long the polymer will be amorphous. If they are too short then backbone planarization cannot be achieved as the Van der Waals bond energy is not sufficient to overcome steric repulsion (Figure 6. 1b).[11,12]

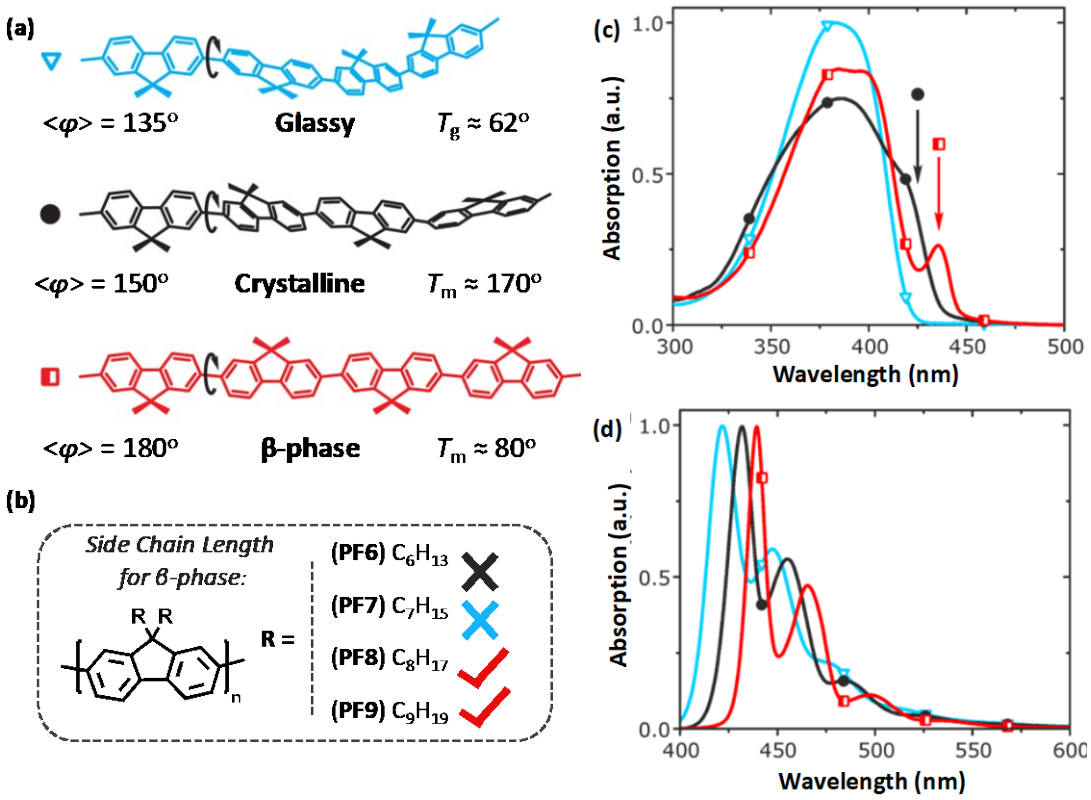

Figure 6. 1: (a) Chemical structures depicting the different chain conformations of poly(di-*n*-alkylfluorenes). (b) β-phase accessibility depending on side-chain length. UV-vis (c) and photoluminescence (d) spectra of different chain conformations of poly(di-*n*-alkylfluorenes) (glassy phase = blue traces; crystalline phase = black traces; β-phase = red traces). Adapted with permission from ref [13].

Improved photoluminescence quantum efficiency (PLQE) and increased emission stability have been observed with materials containing the β-phase. [14,15] The presence of even a small amount of β-phase has been shown to have a positive influence on the overall optoelectronic behaviour of polyfluorene materials. Applications, including as LEDs, transistors and electrically pumped organic lasers, have been investigated.[16–21] Additionally, structure-property relationships have been uncovered which reveal that a higher fraction of the β-phase results in improved PLQE efficiency and hole mobility.[15,22–24] This can be attributed to the increased planarity of the polymer chains that results in increased electronic delocalization therefore a lower energy HOMO-LUMO transition (optical bandgap) compared to the other aforementioned chain conformations[25] The β-phase also has a longer conjugation length and higher degree of order, both of which are favorable properties for enhanced charge carrier transport. As the β-phase regions are also lower in energy than the other chain conformations they can act as low-energy exciton traps to produce a 'self-doped' material.[26,27] The emission

spectrum is often completely dominated by the β-phase, even at low fractions. Efficient energy transfer occurs from the regions with different chain conformations to the β-phase regions.

Synthetic strategies for accessing the β-phase have mainly focussed on controlling the aggregation of poly(di-*n*-octylfluorene) (PDOF) homopolymer by using different solvent mixtures or by employing vapour or thermal treatments.[5,28] Generally the content of β-phase is relatively low (<45 %) and is not the dominant chain conformation.[28,29] Recently the highest content of the β-phase (52 %) has been reported for a PDOF film prepared by inducing aggregation by the addition of 1,8-diiodooctane (up to 4 vol %) to a solution of PDOF in *o*-xylene followed by solvent vapor annealing with *o*-xylene. [30] This vapor treatment enhances the mobility of the polymer chains, increases the time required to form a film and makes it easier for the chains to become ordered therefore enabling access to a higher content of β-phase.

Anisotropic aggregates with β-phase regions are also of particular interest for electronic applications. Nanowires (between 1 – 35 μm in length) with β-phase regions have been prepared by using a melt-assisted template wetting method which involves heating polymer in a porous membrane template (Figure 6. 2).[18,26] The mechanical stress during the filling of the pores in the template assists in inducing β-phase formation. The nanowires showed remarkable Fabry-Pérdot microcavity behaviour (confinement of light to a small region)[31] and optically pumped lasing properties.[18] Recently electrospun PDOF nanofibers have been explored as optical sensors for volatile organic compounds (VOCs).[32] The spun fibers contain PDOF with mainly glassy-phase regions. In the presence of certain VOCs the β-phase content is increased which was characterized by the quenching of the emission of the glassy-phase.

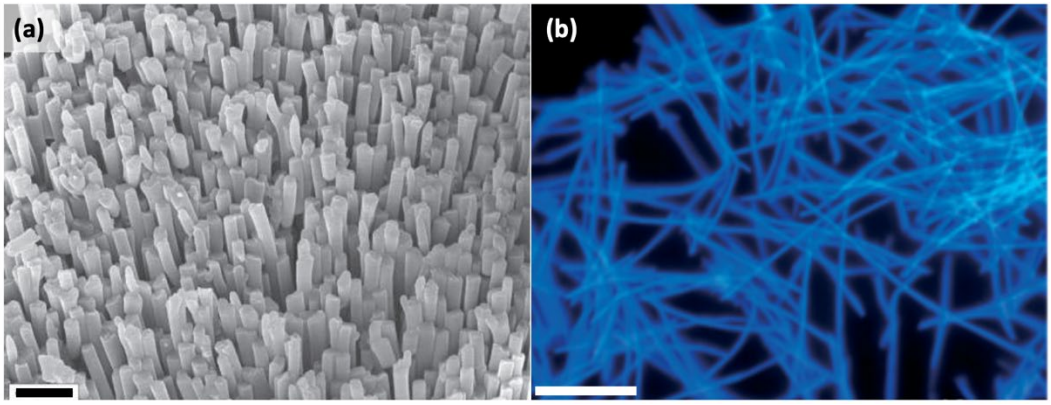

Figure 6. 2: PDOF nanowires with β-phase chain packing prepared by melt-assisted template wetting. (a) SEM image[18] and (b) fluorescence microscopy image of PDOF nanowires.[26] Scale bars: (a) 1 μm and (b) 10 μm.

Polymer-based nanofibers can also be prepared through the solution self-assembly of amphiphilic block copolymers (BCPs).[33] If one of the blocks is able to crystallize, nanoparticles with low curvature at the core-corona interface are favoured. 1D cylindrical micelles can be exclusively formed by targeting certain block ratios and degreed of polymerization. The length of 1D nanostructures containing crystalline cores can be controlled by the seeded growth method termed 'living' crystallization-driven self-assembly (CDSA). [34–43] Segmented nanostructures can be easily prepared by the sequential addition of different BCPs to low dispersity seed micelles using this approach.[44,45] We have recently applied this approach towards the fabrication of low-dispersity nanofibers with poly(di-*n*-hexylfluorene) (PDHF) cores.[46] Segmented fibers with distinct coronal regions were prepared, subsequent transient absorption measurements uncovered exceptionally long-range exciton transport along the fiber core (> 200 nm).[46] Additionally, fluorescent solid-state heterojunction nanowires with an inner donor PDHF core and an outer acceptor core can be prepared by a two-step crystallization method.[47]

In this Chapter, we present studies on the solution self-assembly of PDOF-based BCPs. Previously, we have shown that polyfluorene with hexyl side chains can undergo crystallization-driven self-assembly to form crystalline core nanofibers.[46,47] However this polymer is not able to access the β-phase chain conformation. Exploring the CDSA behavior of polyfluorenes with octyl side chain and controlling the β-phase content could provide a route to optimizing optoelectronic properties of the nanoparticles accessible using solution self-

assembly methods. PDOF-based BCPs were chosen as this is the optimal polyfluorene derivative for accessing the β-phase in the aggregated state.[11,12] These materials are anticipated to exhibit different crystallization kinetics and 'living' CDSA behaviour compared to PDHF BCPs. β-phase packing in the nanoparticles is characterized by UV-vis and fluorescence spectroscopy.

6.3. Results and Discussion

6.3.1. Synthesis and Characterisation of PDOF Block Copolymers

Synthetic methods for preparing poly(di-*n*-hexylfluorene) BCPs (PDHF) described previously in Chapters 2-5 can also be used to synthesize well-defined poly(di-*n*-octylfluorene)-based (PDOF) BCPs. Grignard metathesis polymerization (GRIM) was employed to prepare alkyne-terminated PDOF homopolymer. Copper-catalyzed azide-alkyne cycloaddition click reactions (CuAAc) with the PDOF homopolymer and different azido-terminated corona forming blocks such poly(ethylene glycol) (PEG), poly(*N*-isopropylacrylamide) (PNIPAm) and poly(dimethylsiloxane) (PDMS) were carried out (Scheme 6. 1). Azido-terminated PNIPAm was synthesized by atom transfer radical polymerization (ATRP), azido-terminated PDMS was synthesized by living anionic polymerization, and azido-terminated PEG was synthesized from tosylate-terminated PEG.

Soxhlet extraction was carried out in ethyl acetate followed by methanol to afford an alkyne-terminated PDOF homopolymer with low molar mass dispersity. The PDOF polymer was then collected in chloroform, concentrated *in vacuo* and precipitated into cold MeOH to obtain the purified product. BCPs with a polar corona block (PNIPAm, PEG) were purified via silica gel column chromatography to remove residual PDOF homopolymer. The solid polymers were washed with methanol several times then precipitated into cold methanol to remove residual PNIPAm and PEG homopolymers. PDOF-*b*-PDMS was purified by preparative size exclusion chromatography (SEC) to remove residual homopolymers. Selective precipitation to remove any residual PDMS homopolymer was challenging as the PDOF-*b*-PDMS BCP does not precipitate in good solvents for PDMS such as hexanes and ethyl acetate. Instead the solid polymer was washed repeatedly with cold hexanes to remove residual PDMS. Material characterization was achieved by matrix-assisted laser/desorption/ionization time-of-flight (MALDI-TOF) mass spectrometry, gel permeation chromatography (GPC) and ^{1}H NMR spectroscopy, details are provided in the Supporting Information (Figure S6. 1-S6.2).

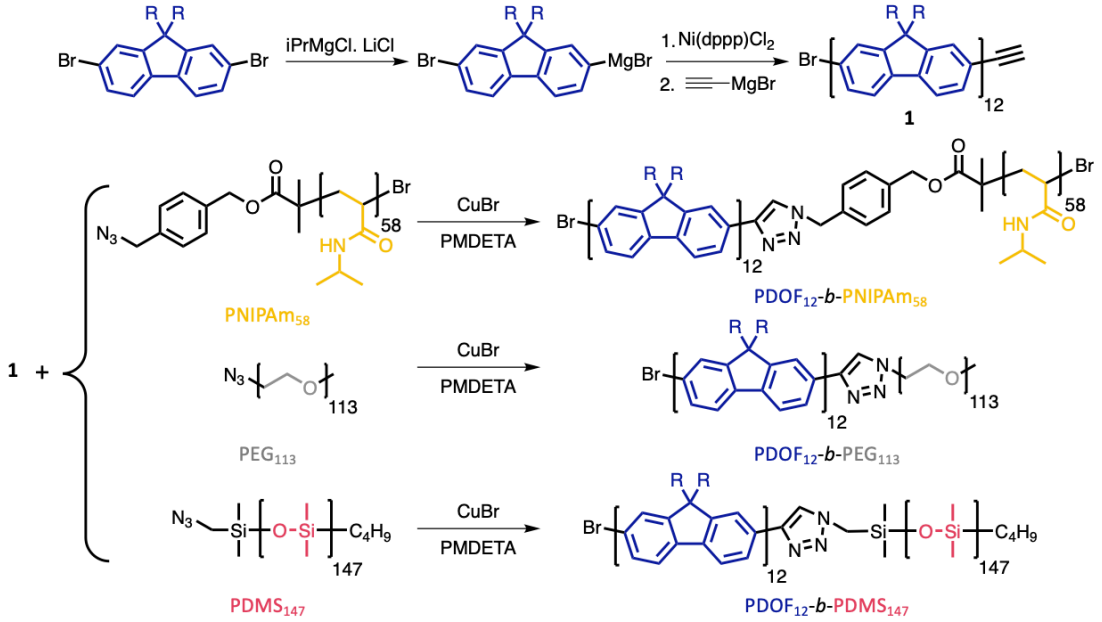

Scheme 6. 1: Synthesis of PDOF-based block copolymers. PDOF$_{12}$-*b*-PNIPAm$_{58}$, PDOF$_{12}$-*b*-PEG$_{113}$ and PDOF$_{12}$-*b*-PDMS$_{200}$. . R = alkyl side chain. iPrMgCl. LiCl = isopropylmagnesium chloride lithium chloride complex solution (turbo grignard). Ni(dppp)Cl$_2$ = dichloro(1,3-bis(diphenylphosphino)propane)nickel. PMDETA = N,N.N',N''.N''-pentamethyldiethylenetriamine.

6.3.2. Self-assembly of PDOF-*b*-PNIPAm

The solution self-assembly of PDOF-*b*-PNIPAm BCP was investigated first. The individual PNIPAm (Hildebrand solubility parameter, δ_{PNIPAm} = 24.8 MPa$^{1/2}$) and PDOF blocks (δ_{PF} = 18.6-19.0 MPa$^{1/2}$) have significant differences in solubility (Table S6. 1). Therefore aggregation of the PDOF block may occur in solvents that are selective for the PNIPAm block, such as polar solvents like isopropanol (iPrOH, δ_{iPrOH} = 23.5 MPa$^{1/2}$), dimethyl sulfoxide (DMSO, δ_{DMSO} = 26.4 MPa$^{1/2}$) and dimethylformamide (DMF, δ_{DMF} = 24.7 MPa$^{1/2}$) (Table S6. 2). An example of a self-assembly protocol is as follows, PNIPAm selective solvent was added dropwise to a solution of PDOF-*b*-PNIPAm in THF or toluene (Tol) to obtain a sample with a polymer concentration of 0.2 mg mL^{-1}. The samples are then heated for 30 min to dissolve the polymer, depending on the solvent system ca. 65-80 °C for MeOH, EtOH, iPrOH and MeCN mixtures, 140°C for DMF and DMSO mixtures. The samples are then cooled to 20 °C slowly and aged for a further 24 h before analysis by transmission electron microscopy (TEM) (Figure 6. 3a).

Typically, in the case of PDHF BCPs with polar corona forming blocks, long crystalline fibers (> 8 μm) can be prepared via CDSA in solvent systems composed of 50 % common solvent (THF, Tol) and 50 % alcohol corona-selective solvent (iPrOH, EtOH, MeOH). However, for PDOF-*b*-PNIPAm, only short fiber-like

micelles (e.g. L_n = 19 nm, L_w/L_n= 1.06, where L_n is the number-average length and L_w is the weight-average length) were observed in Tol:iPrOH (1:1, v/v) (Figure 6. 3b) and Tol:EtOH (1:1, v/v). The electron contrast of these fibers with the background of the carbon-coated grid is very poor compared to that typically observed for crystalline PDHF micelles, which suggests the micelle cores may be amorphous. In Tol:MeOH (1:1, v/v) and Tol:MeCN (1:1, v/v), mixed morphologies were observed, consisting of spherical and short fiber-like micelles (ca. < 50 nm). In mixtures with higher contents of PNIPAm selective solvent (MeCN/iPrOH/EtOH/MeOH) mainly short fiber-like micelles and spherical micelles were observed (Figure 6. 3c). In Tol:DMSO (1:1, v/v), longer lower contrast fibers (L_n = 742 nm, L_w/L_n = 1.12) were observed with a small percentage of higher contrast fibers (ca. < 1%) that appears to have formed upon drying (Figure 6. 3f). Increasing the DMSO content only led to formation of spherical micelles and some short fiber-like micelles (Figure 6. 3g).

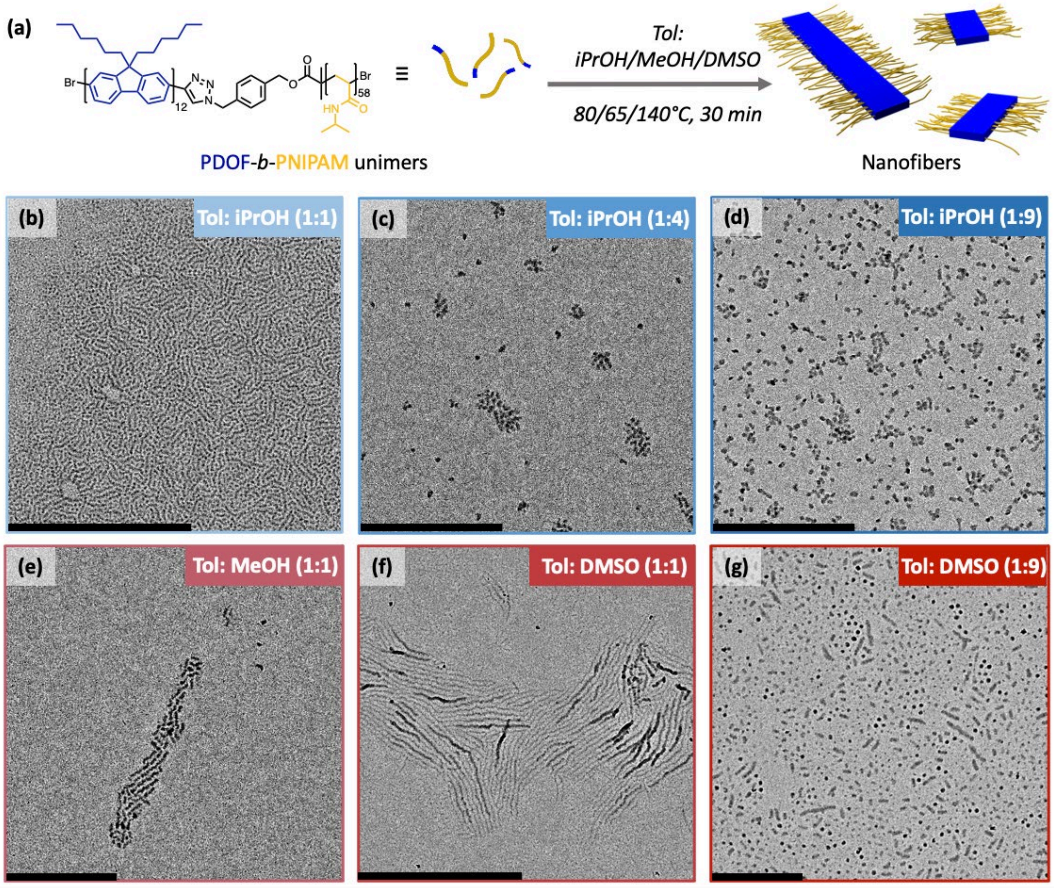

Figure 6. 3: (a) Schematic illustration of the preparation of PDOF-*b*-PNIPAm fiber-like micelles in Tol:iPrOH/MeOH/DMSO mixtures via heating to dissolution (80/65/140 °C) followed by slow cooling to 20 °C. TEM images of PDOF-*b*-PNIPAm fiber-like micelles in (b) Tol: iPrOH (1:1, v/v), (c) Tol: iPrOH (1:4, v/v), (d) Tol: iPrOH (1:9, v/v), (e) Tol:MeOH (1:1, v/v), (f) Tol:DMSO (1:1, v/v) and (g) Tol:DMSO (1:9, v/v). Scale bars: 1 μm.

Exclusive formation of fiber-like micelles was observed in Tol:DMF mixtures (≥ 1:1, v/v). All fibers formed by homogenous nucleation in these solvents systems were short (ca. < 30 nm). From these studies Tol:DMF mixtures appeared to be most promising solvent system to promote fiber formation. Next, the self-assembly protocol was modified in an attempt to promote the formation of longer crystalline fibers by slowing the rate of nucleation and improving crystal growth from nuclei. A sample of PDOF-*b*-PNIPAm at 0.2 mg mL^{-1} in different Tol:DMF mixtures was heated until dissolution at 140°C for 1 h. The samples were then cooled to 110 °C, just below the melting temperature of PDOF (T_m = 120 °C) (Figure S6. 3) and held at this temperature for a further 4 h to induce slow crystallization, before being slowly cooled to 20 °C and ageing for 24 h. Fiber formation was improved under these conditions compared to other solvent systems and protocols, but fiber length was still limited (ca. 20 – 100 nm) (Figure 6. 4 and Figure S6. 4).

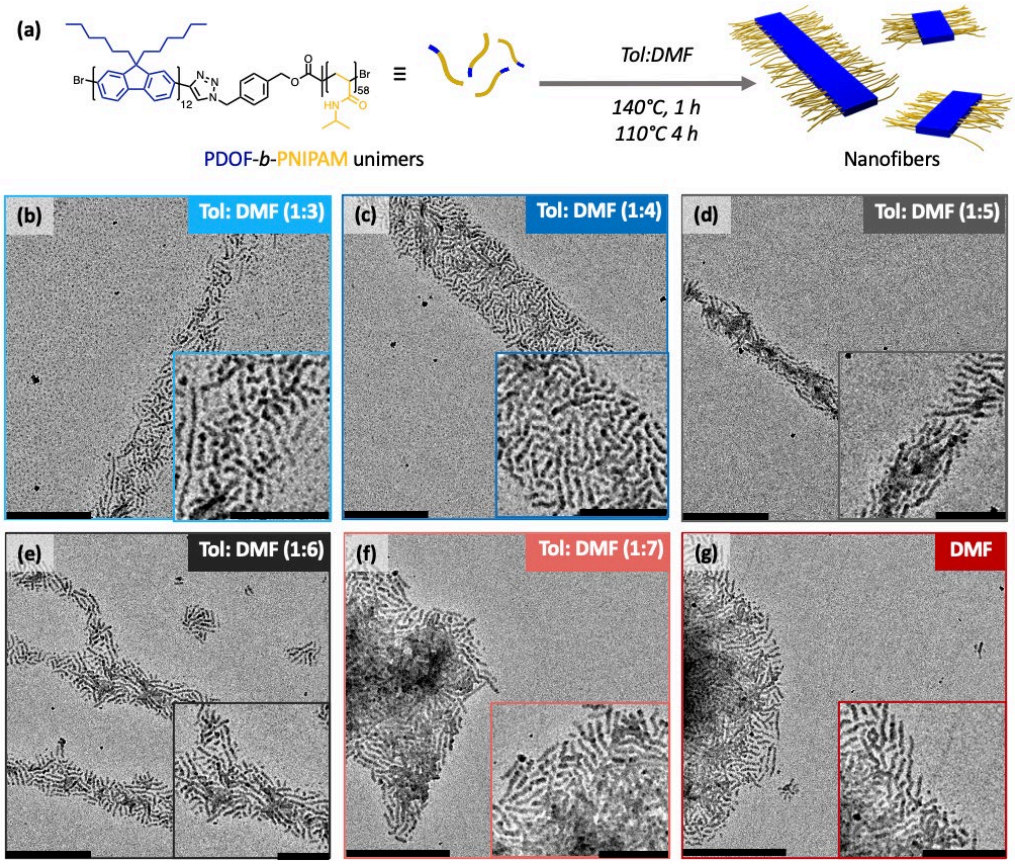

Figure 6. 4: (a) Schematic illustration of the preparation of PDOF-*b*-PNIPAm fiber-like micelles in Tol:DMF mixtures via heating to dissolution (140 °C) followed by an isothermal hold, to help induce crystallization, at 110 °C just below the T_m (120 °C) followed by slow cooling to 20 °C. TEM images of PDOF-*b*-PNIPAm fiber-like micelles in (b) Tol:DMF (1:3, v/v), (c) Tol:DMF (1:4, v/v), (d) Tol:DMF (1:5, v/v), (e) Tol:DMF (1:6, v/v), (f) Tol:DMF (1:7, v/v) and (g) DMF. Scale bars: 500 nm. Inset scale bars: 250 nm.

Next, the self-assembly protocol was modified further in attempt to see whether longer fibers (> 100 nm) can be prepared by a homogenous nucleation of PDOF-*b*-PNIPAm. Similar to the previous protocol described, the first step involves heating the polymer to dissolution in Tol:DMF mixtures at 140 °C for 30 min. Then the samples were cooled to different temperatures below the T_m of PDOF (120 °C), at 70 °C, 90 °C, and 110 °C, held for 4 h at these temperatures, before slow cooling to 20 °C and ageing for 24 h. By incorporating this isothermal hold, we aimed to suppress rapid self-nucleation, which results in short micelles, and to promote elongation. On cooling from 140 °C (corresponding to the molecularly dissolved BCP state) to a temperature below the T_m of PDOF, some self-nucleation would be anticipated. The selected temperature should affect the rate of crystallization, and specifically the relative rates of self-nucleation versus elongation.

TEM analysis revealed that the temperature of the isothermal hold step had an influence on the observed fiber length (Figure 6. 5). The sample that underwent an isothermal hold at 110 °C consisted of very short fiber-like micelles (L_n = 33 nm, L_w/L_n = 1.14) (Figure S6. 7a). Decreasing the temperature of the isothermal hold step to 90 °C (L_n = 83 nm, L_w/L_n = 1.20) and 70 °C (L_n = 111 nm, L_w/L_n = 1.24) produced longer fiber-like micelles (Figure S6. 7b-c). This data provides some information on the conditions required to favour epitaxial growth over self-nucleation of PDOF-*b*-PNIPAm. However, the obtained micelle lengths were still limited (<200 nm).

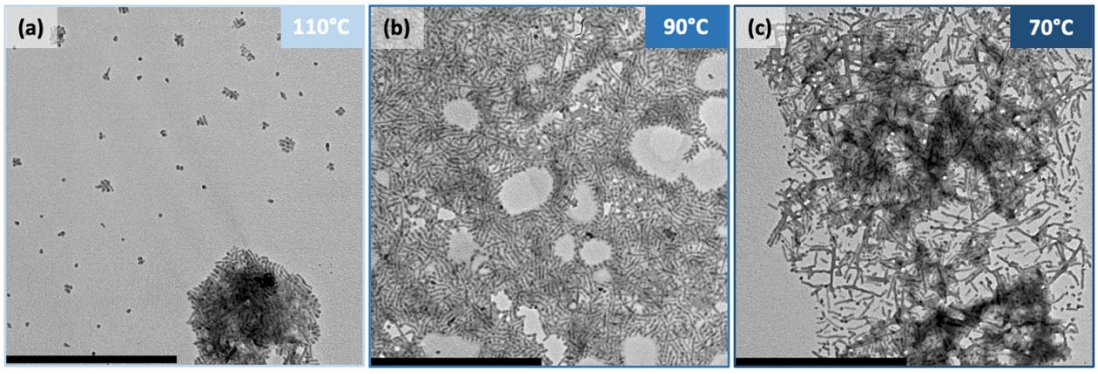

Figure 6. 5: TEM images of PDOF-*b*-PNIPAm fiber-like micelles prepared in Tol:DMF (1:9, v/v) by heating at 140 °C for 30 min, cooling to and held at (a) 110 °C, (b) 90 °C and (c) 70 °C for 4 h before slow cooling to 20 °C and ageing for 24 h.

Low yields of fibers were observed in solvent mixtures composed of high contents of common solvent (≥ 50 %THF/Tol, v/v) at 20 °C. In a further attempt to obtain long fiber-like micelles from the CDSA of PDOF-*b*-PNIPAM, self-assembly was investigated in these solvent mixtures again using a modified protocol. In a typical experiment, after the addition of PNIPAm-selective solvent to a solution of the BCP in THF, the sample was heated to just under the solvent boiling point and then slowly cooled to -20 °C. Short fiber-like micelles were observed in THF:MeCN (5:4, v/v) and in THF:MeOH (5:4, v/v) however no long fibers were detected (Figure S6. 8). Further attempts using different temperatures and solvent mixtures were unsuccessful with respect to the preparation of long fiber-like micelles.

6.3.3. Characterization of β-Phase Behaviour

PDOF-based materials predominantly exhibit the 'glassy' phase, crystalline α-phase or β-phase chain conformations. Self-assembled nanofibers prepared by CDSA of PDOF-*b*-PNIPAm in different Tol:DMF solvent systems were analyzed by UV-vis and fluorescence spectroscopy to characterize the chain packing in the fiber cores. Different amounts of DMF were added to a unimer solution of PDOF-*b*-PNIPAm in toluene. The resulting solutions were heated to 140 °C for 1 h before cooling to 110 °C for 4 h and then cooling to room temperature and ageing for 1 day. From the UV-vis spectra of the nanofibers in solution, characteristic absorption peaks for the glassy-phase (ca. 380 nm) and β-phase (433-435 nm) were observed for all solvent systems that were selective for PNIPAm (Figure 6. 6a). With increasing poor solvent for PDOF (DMF) an increase in the absorption peak intensity for the β-phase conformation was observed relative to the glassy-phase absorption peak.

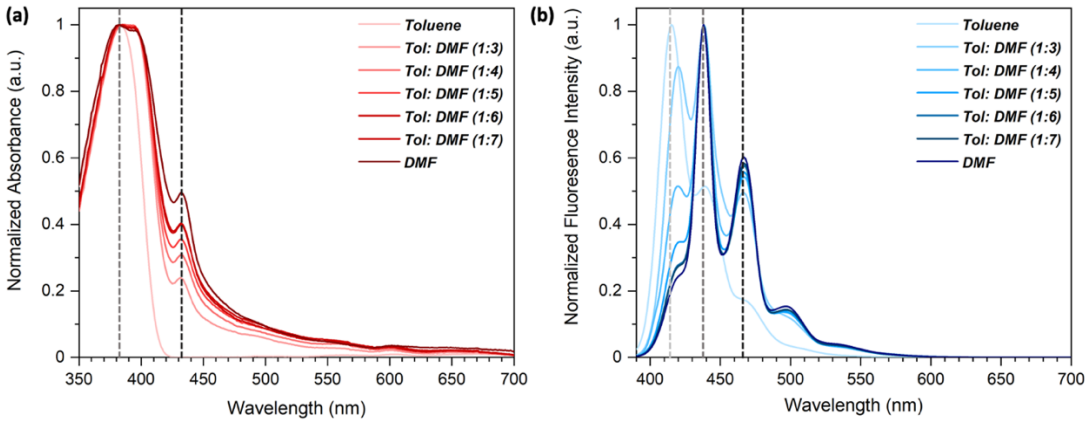

Figure 6. 6: Optical spectroscopy data of $PDOF_{12}$-*b*-$PNIPAm_{58}$ in different ratios of Tol:DMF (v/v). (a) UV-vis and (b) photoluminescence spectra illustrating the change in β-phase content with different amounts of poor solvent for PDOF. From the UV-vis spectra the absorbance for the glassy-phase (A_g, *dark grey line*) and β-phase (A_β, *black line*) are marked. From the photoluminescence spectra the $I_{0\text{-}0}$ vibronic band for the glassy-phase (*light grey line*), $I_{0\text{-}0}$ vibronic band for the β-phase (*dark grey line*) and $I_{0\text{-}1}$ vibronic band for the β-phase (*black line*) are marked.

Analysis by fluorescence spectroscopy revealed a similar trend, increasing β-phase content was observed with increasing amount of poor solvent for the PDOF block (Figure 6. 6b). Compared to the unimer solution in toluene, a slight red-shift is expected for the PDOF $I_{0\text{-}0}$ vibronic band (ca. 410 to 416 nm) in an aggregates state (without β-phase). A significant red-shift in the PDOF $I_{0\text{-}0}$ vibronic band (to ca. 437 - 441 nm) accompanied by a slight increase in the intensity and narrowing of the PDOF $I_{0\text{-}1}$ vibronic band (ca. 467 nm) occurs in the presence of β-phase. These spectral features are a result of an increase in conjugation length, planarization of the PDOF backbone, and the presence of a highly delocalized excited state associated with the β-phase. These spectroscopic trends are enhanced at higher DMF contents.

The percentage of β-phase content (β %) is calculated from Eqn. 1 where the glassy-phase absorbance (A_g) is at 400 nm; β-phase absorbance (A_β) at 433 nm; glassy-phase extinction coefficient (ε_g) is 4.46 and β-phase extinction coefficient (ε_β) is 4.83.[30] Enhancement of β-phase content is observed by increasing the PNIPAm selective and PDOF poor solvent, DMF. Fibers formed in Tol:DMF (1:3, v/v) have 18 % β-phase content this was enhanced up to 32 % for the nanofibers prepared in pure DMF (Figure 6. 7).

$$\beta\ \% = \frac{c_\beta}{c_\beta + c_g} = \frac{A_\beta \times \varepsilon_g}{A_\beta \times \varepsilon_g + A_g \times \varepsilon_\beta} \qquad \text{(Eqn. 1)}$$

Additionally, for the mixed morphology micelles (spherical and fiber-like) prepared in Tol:DMSO mixtures the highest percentage of β-phase content was 24 %, which was observed for all self-assembly samples from Tol:DMSO (1:1, v/v) to (1:9, v/v) (Figure S6. 5). Samples prepared from Tol/THF and mixed alcohol solvent systems also exhibited some β-phase packing with a maximum β-phase content of 26 % observed for micelles formed in THF:iPrOH (1:9, v/v) (Figure S6. 6).

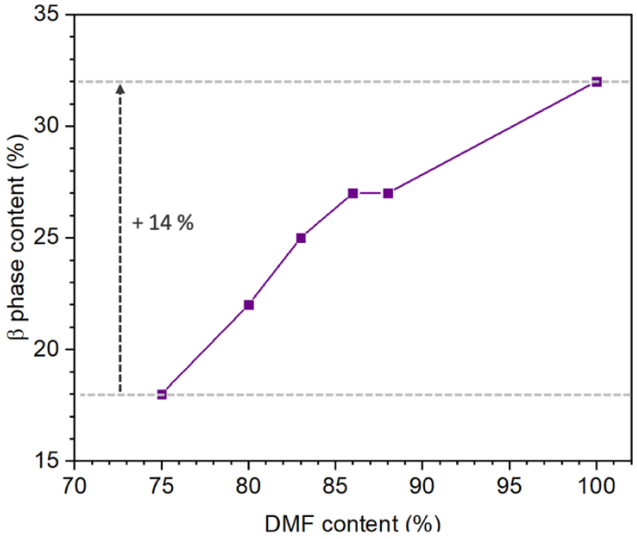

Figure 6. 7: Graph showing the percentage of β-phase content observed in micelles prepared in Tol:DMSO mixtures with varying DMSO content. β-phase content was calculated from Equation 1.

6.3.4. Self-assembly of PDOF-*b*-PEG and PDOF-*b*-PDMS Diblock Copolymers

The use of a different corona-forming block with a more similar solubility to the PDOF segment would be expected to assist in slowing down the rate of nucleation of the core-forming block in solution. Compared to PNIPAm (δ_{PNIPAm} = 24.8 $MPa^{1/2}$), PEG ($\delta_{PEG\ 5k}$ = 21.4 $MPa^{1/2}$) is more similar in solubility to the PDOF core (δ_{PF} = 18.6-19.0 $MPa^{1/2}$) based on the solubility parameters (Table S6. 1). The self-assembly of $PDOF_{12}$-*b*-PEG_{113} was studied in solvent mixtures with different ratios of common solvent for both blocks (THF or toluene) and polar solvent (selective for PEG). Attempts at preparing long fiber-like micelles from the CDSA of $PDOF_{12}$-*b*-PEG_{113} in these solvent mixtures were also unsuccessful. The rapid self-assembly of the BCP in most of these solvent mixtures resulted in the formation of small irregular aggregates or spherical micelles. Some short fiber-like micelles (ca. 30 nm) were observed from self-nucleation in THF:MeOH and THF:iPrOH solvent mixtures (Figure S6. 9).

In an attempt to reduce the rate of nucleation further, we next sought to use a non-polar corona (PDMS). Self-assembly studies of $PDOF_{12}$-*b*-$PDMS_{147}$ BCP were conducted in different solvent systems composed of common solvent for both blocks, such as THF or toluene and solvents that could be selective for the PDMS block (δ_{PDMS} = 15.3 $MPa^{1/2}$), including hexanes (δ_{Hex} = 14.9 $MPa^{1/2}$), cyclohexane (δ_{CH} = 16.8 $MPa^{1/2}$), butyl acetate (δ_{BuOAc} = 17.6 $MPa^{1/2}$) and ethyl acetate (δ_{EtOAc} = 18.1 $MPa^{1/2}$) (Table S6. 2). The majority of solvents studied were not sufficiently selective for the PDMS block and aggregation of the PDOF block (δ_{PF} = 18.6-19.0 $MPa^{1/2}$) was not observed. The only instance some fibrous aggregates were observed was in THF and cyclohexane mixtures. Cyclohexane (CH) was added dropwise (over ca. 2 minutes) to solutions of $PDOF_{12}$-*b*-$PDMS_{147}$ in THF. In THF:CH (3:2, v/v), unimeric species and small spherical aggregates were observed by TEM (Figure S6. 10a). At a slightly higher content of PDMS selective solvent in THF:CH (2:3, v/v) fibrous bundles of ribbon-like structures and small irregular aggregates were detected (Figure S6. 10b). From these observations the small difference in the solubility of PDOF and PDMS coblocks prevents efficient crystallization of the PDOF core block in solvents selective for PDMS.

6.3.5. Attempted Seeded Growth of PDOF Diblock Copolymers

'Living' CDSA protocols typically consist of a sonication step to fragment the long polydisperse fiber-like micelles initially formed by the self-nucleation of BCPs in solution. This generates short micelles of low length dispersity that can seed the epitaxial growth of added unimer. However, seeds can also be generated without the need for sonication through direct self-nucleation in appropriate solvent systems.[37,48,49] Short fibers (L_n < 100 nm) formed by the direct dissolution of $PDOF_{12}$-*b*-$PNIPAM_{58}$ in different solvent mixtures (e.g. toluene/THF:iPrOH/MeOH/DMF mixtures) were observed to have low length dispersity (L_w/L_n < 1.20) and were therefore suitable for use as seed micelles without the need for sonication (Scheme 6. 2a). Rapid self-nucleation of $PDOF_{12}$-*b*-$PNIPAM_{67}$ BCP occurs in these solvent mixtures when the ratio of poor solvent to common solvent is high (> 1:1, v/v). For seeded growth experiments iPrOH was chosen as the selective solvent for PNIPAm. This solvent was expected to be

advantageous for suppressing self-nucleation of the added BCP unimer as the solubility parameter of iPrOH is more similar to that of PDOF than those for the other polar solvents (Table S6. 1 and Table S6. 2).

In an example of a seeded growth experiment, first seed micelles were prepared by adding iPrOH (PNIPAm selective solvent) dropwise to a stirred solution of $PDOF_{12}$-*b*-$PNIPAM_{58}$ at 20 °C in THF (common solvent) until a ratio of 1:9 (v/v) was reached. After ageing for 1 day at 20°C the formation of short low length dispersity fiber-like micelles (L_n = 19 nm, L_w/L_n = 1.05) was observed from TEM analysis (Figure S6. 11b, d). The THF content was then increased to 20 % (v/v) in order to minimise any self-nucleation events during the addition of unimer. BCP unimer in THF was added in one rapid injection to a diluted solution of the seed micelle sample. The resulting sample was aged at 30°C for 24 h before analysis by TEM (Figure S6. 11c). Seeded growth was performed at 30 °C instead of 20 °C as the $PDOF_{12}$-*b*-$PNIPAM_{58}$ unimer solution is more colloidally stable and this should suppress homogenous nucleation further. Although a slight increase in the number-average contour length of the fibers was observed (L_n = 25 nm, L_w/L_n = 1.10) significant self-nucleation of the added unimer was evident. A bimodal contour length distribution was observed, with the lengths of the two different populations of micelles centering at 19 and 27 nm (Figure S6. 11e). From this data we postulate that homogenous nucleation of the added unimer is rapid and is still favoured over epitaxial growth from the termini of the pre-existing seed micelles.

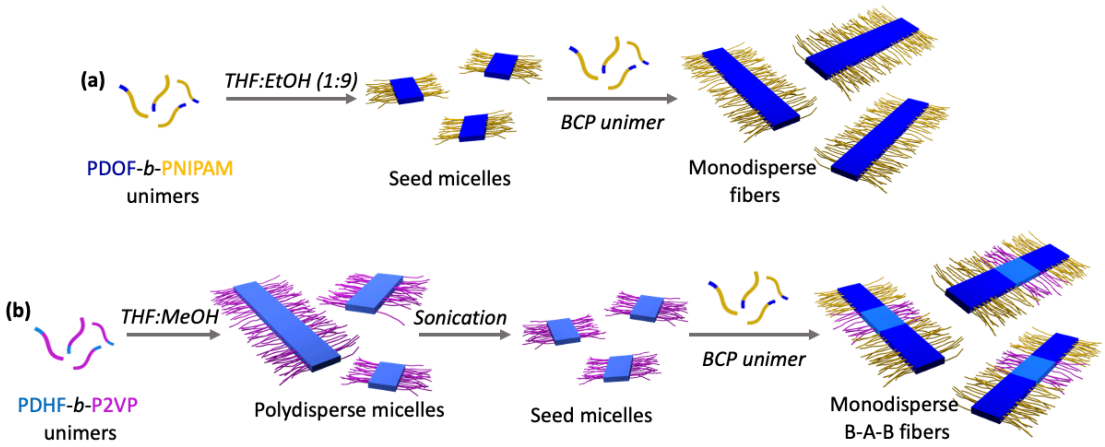

Scheme 6. 2: Schematic representation of the attempted preparation of low dispersity (a) PDOF-*b*-PNIPAm fibers by homoepitaxial seeded growth of PDOF-*b*-PNIPAm unimer from PDOF-*b*-PNIPAm seed micelles and (b) B-A-B nanofibers by heteroepitaxial seeded growth of PDOF-*b*-PNIPAm unimers from PDHF-*b*-P2VP seed micelles. A = PDHF-*b*-P2VP and B = PDOF-*b*-PNIPAm.

We have shown that seeded growth can be applied to a range of PDHF-based BCPs to yield low dispersity fibers. In chapter 3 in particular, we present the preparation of pentablock comicelles by homoepitaxial growth of BCPs with different corona-forming blocks from the termini of PDHF-*b*-P2VP (P2VP = poly(2-vinylpyridine) seed micelles. The wide scope of the 'living' CDSA of PDHF-based materials is encouraging for potential coassembly with other BCPs with different crystallizable core-forming blocks, a process termed heteroepitaxial seeded growth. The preparation of 1D fibers and 2D platelets of controlled dimensions with segmented cores has been achieved via the heteroepitaxial 'living' CDSA of poly(ferrocenyldimethylsilane) (PFDMS) and poly(ferrocenyldimethylgermane) (PFDMG) BCPs.[50–52] Following on from this work we sought to investigate the preparation of fibers with segmented π–conjugated cores by using PDHF-based fibers to seed the growth of PDOF BCP unimers (Scheme 6. 2b).

First, long polydisperse PDHF-based fibers were prepared by adding MeOH dropwise (over ca. 2 minutes) to a solution of $PDHF_{17}$-*b*-$P2VP_{250}$ unimers in THF to reach a 1:1 (v/v) ratio. The polydisperse fibers were then subjected to vigorous sonication for 2 h at 0 °C followed by annealing at 45 °C for 1 h to further increase the crystallinity of the fiber cores and then slow cooling to 20 °C. This resulted in short low dispersity micelles (L_n = 40 nm, L_w/L_n = 1.15) observed by TEM. Longer seed micelles (L_n = 188 nm, L_w/L_n = 1.10) were then prepared by the seeded growth of $PDHF_{17}$-*b*-$P2VP_{250}$ unimer from these short seed micelles (Figure S6. 12b, d).

The seeded heteroepitaxial growth of $PDOF_{12}$-*b*-$PNIPAM_{58}$ BCPs from these $PDHF_{17}$-*b*-$P2VP_{250}$ seeds was attempted. $PDOF_{12}$-*b*-$PNIPAM_{67}$ unimer (unimer-to-seed ratio = 5) in THF was added in one quick injection to a diluted sample of $PDHF_{17}$-*b*-$P2VP_{250}$ seed micelles in THF:MeOH (1:1, v/v) followed by rapid shaking for 10 s and aging at 30 °C for 24 h. TEM analysis of the sample revealed no significant change in the seed micelle lengths (L_n = 170 nm, L_w/L_n = 1.19) but revealed the presence of a population of shorter micelles. Analysis of the sample revealed a bimodal contour length distribution, with the lengths of the two different populations of micelles centering at 80 nm and 200 nm (Figure S6. 12c, e). The lack of micelle growth observed is likely due to the rapid homogenous

nucleation of the PDOF BCP which is favoured over epitaxial growth from the PDHF seed micelle ends. This is further supported by the increase in length dispersity (L_w/L_n = from 1.10 to 1.19) observed and the increase in the standard deviation relative to L_n (σ/L_n = from 0.32 to 0.44). Combined, this data suggests the presence of new shorter fibers formed by self-nucleation and limited epitaxial growth from the seed micelles.

Further attempts to promote homoepitaxial growth (from $PDOF_{12}$-*b*-$PNIPAM_{58}$ seeds) and heteroepitaxial growth (from $PDHF_{17}$-*b*-$P2VP_{250}$ seeds) were unsuccessful. The seeded growth experiments were performed at higher temperatures (30 – 45°C) and in different solvent mixtures with high common solvent contents but homogenous nucleation was not suppressed.

6.4. Summary

For the potential use of polyfluorene-based nanowires in optoelectronic devices, the presence of β-phase regions is desirable. Even at small contents of the β-phase, improved photoluminescence and electroluminescence efficiencies have been reported for polyfluorene materials. [22–24] In this chapter we have presented a new route towards the preparation of β-phase containing nanofibers. Previous synthetic methods for the preparation of β-phase nanofibers include electrospinning and melt or solution-assisted template wetting. From these methods up to 21 % β-phase content was observed in PDOF homopolymer nanowires. Herein, we have applied solution self-assembly protocols to prepare nanofibers from PDOF-based BCPs. β-phase content in the fiber cores was enhanced to up to 32 % by using higher ratios of corona-selective solvent to common solvent. We have shown that low dispersity nanofibers can be prepared by a direct dissolution method. However, the attempted use of 'living' CDSA to prepare low dispersity fibers of tunable lengths via epitaxial seeded growth was unsuccessful.

In future work, the solution self-assembly of PDOF-based BCPs with alternative polymer coronal blocks, such as poly(2-vinylpyridine) or polystyrene and terminal charged groups, such as phosphonium or ammonium-based cations, could be investigated for the preparation of long fiber-like micelles via 'living' CDSA. After optimization of the type of coronal group (including degree of polymerization and core-to-corona block ratio), modified seeded growth or self-seeding protocols could be attempted to try and yield low dispersity nanofibers of different lengths. Potential modifications could include adding seed micelles to a supersaturated solution of unimer at an elevated temperature followed by slow cooling to suppress self-nucleation events.[53]

6.5. Supporting Information

6.5.1. Materials and Methods

All reagents and solvents used for polymers synthesis were of reagent grade, and unless otherwise stated and were used as received. Solvents for self-assembly were of HPLC grade and filtered using 0.2 μm syringe filters prior to use. The synthesis of $PDHF_{17}$-*b*-$P2VP_{250}$ has been reported in Chapter 3 and is not described here. Poly(ethylene glycol) methyl ether tosylate (M_n = 5000 Da) was purchased from Sigma Aldrich and used as received in the synthesis of PEG-azide.

Nuclear magnetic resonance (NMR). ^{1}H NMR spectra were taken with a Varian 400 MHz spectrometer; chemical shifts were referenced to the residual solvent peak ($CHCl_3$, δ = 7.26 ppm).

Gel Permeation Chromatography (GPC). measurements were conducted on Viscotek GPC_{max} equipped with a UV detector operating at 400 nm and a refractometer. Measurements were carried out at 1.0 mL min^{-1} with THF containing [*n*Bu4N]Br (0.1% w/w) as the eluent at 35˚C, results were measured against polystyrene standards (Viscotek).

Matrix-Assisted Laser Desorption/Ionization Time-Of-Flight Mass Spectrometry (MALDI-TOF MS). Measurements were conducted on a Bruker Ultraflex II ToF spectrometer under the reflector positive ion regime. Samples were prepared with a 9:1 ratio of *trans*-2-[3-(4- *tert*-butylphenyl)-2-methyl-2-propenylidene]malonitrile matrix (20 mg mL^{-1} in THF) to polymer solution (0.2 mg mL^{-1} in THF), then 5 μL of the sample was deposited onto the sample plate and dried under ambient conditions.

Transmission Electron Microscopy (TEM). Samples were prepared by drop casting 10 μL of the nanofiber solution onto a carbon-coated copper grid (Agar Scientific, mesh size 200). Bright-field TEM micrographs were taken using a JEOL JEM 1011 EX microscope operating at 80 kV, equipped with a 11M pixel CCD camera. Micelle length distributions were determined using the software program ImageJ developed at US National Institute of Health. A minimum of 300 micelles are traced to determine their contour length and histograms of the length distributions obtained. This data allows for calculation of the number average

length (L_n), weight average length (L_w) for each sample, this is calculated as shown below (L = length of fiber, N = number).

$$L_n = \frac{\sum_{i=1}^{n} N_i L_i}{\sum_{i=1}^{n} N_i} \qquad L_w = \frac{\sum_{i=1}^{n} N_i {L_i}^2}{\sum_{i=1}^{n} N_i L_i}$$

Spectroscopic Measurements. UV/vis data were obtained on a Lambda 35 Spectrometer employing glass cells (1 cm x 1 cm) from 200 to 800 nm. Fluorescence data were obtained on a PTI QM40 Spectrofluorometer using an excitation wavelength of λ_{ext} at 380 nm.

6.5.2. Synthesis of alkyne-terminated PDOF$_{12}$

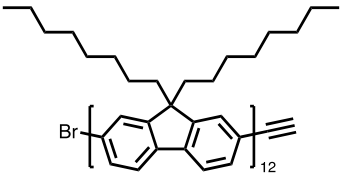

Alkyne-terminated PDOF was synthesized by Grignard Metathesis polymerization (GRIM). 2-Bromo-7-iodo-9,9-bis-*n*-octyllfluorene was synthesised according to the reported procedure.[54] 2-Bromo-7-iodo-9,9-bis-*n*-octylfluorene (700 mg, 1.18 mmol) was dissolved in 10 mL of anhydrous THF. The resulting solution was cooled to -20˚C before 1.3 M *i*PrMgCl.LiCl complex (1 eq.) was added dropwise, then the solution was left to stir for 90 min at -78˚C. The activated solution of 2-bromo-7-iodo-9,9-bis-*n*-octylfluorene monomer was added in one quick injection to a stirring solution of Ni(dppp)Cl_2 (31.8 mg, 0.059 mmol) in anhydrous THF (100 mL) at 0˚C. After 15 mins, 0.5 M ethynylmagnesium bromide (3 mL, excess) was added to the reaction mixture which was then stirred for 1 h. The resultant mixture was then precipitated into MeOH to quench any unreacted Grignard, giving a yellow solid. The polymer was then dissolved in DCM, washed with water several times then with saturated NaCl solution before drying with anhydrous $MgSO_4$. After filtration, the solution was concentrated *in vacuo* before precipitation in MeOH to afford a bright yellow solid. Further purification by Soxhlet extraction in ethyl acetate followed by chloroform gave the purified polymer as yellow solid, yield = 155 mg, 45 %. GPC (THF containing [nBu$_4$N]Br (0.1 % w/w), 1 mL min^{-1}): M_n = 7.6 kDa, M_w = 9.3 kDa, M_w/M_n = 1.22. ^{1}H NMR (500

MHz, $CDCl_3$) ppm δ = 7.62-7.91 (m, 72 H, polyfluorene aromatic), 3.16 (s, 1 H, alkyne), 2.13 (brs, 47 H, polyfluorene-(C*H*$_2$)x2), 0.72-1.31 (m, 363 H, polyfluorene-(C*H*$_2$ x 6) x 2 and (C*H*$_3$) x 2).

6.5.3. Synthesis of azido-functionalized PDMS

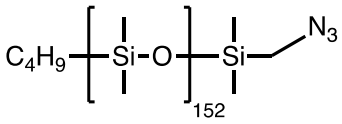

Azido-functionalized PDMS was synthesized by anionic polymerization of hexamethylcyclotrisiloxane as according to literature procedures.[55] Hexamethylcyclotrisiloxane (1.78 g, 8 x 10^{-3} mol) was first dissolved in 8 mL of dry THF. The mixture was then stirred rapidly and nBuLi (1.6 M in cyclohexane) (100 µL, 1.6 x 10^{-4} mol) was added in one quick injection. The reaction was left to stir for 2.5 h at 20°C before being quenched with (bromomethyl)chlorodimethylsilane (0.25 g, excess). The polymer was purified by repeated precipitation into MeOH to afford a clear viscous liquid. Bromo-functionalized PDMS was then converted to azido-functionalized PDMS. To a stirring solution of the polymer (1.44 g, 1.32 x 10^{-4} mol) in 20 mL of THF, sodium azide (160 mg, 2.46 x 10^{-3} mol) and tetrabutylammonium bromide (793 mg, 2.46 x 10^{-3} mol) were added. The resulting solution was stirred for 48 h at 40°C. The solution was then washed with water several times then with saturated NaCl solution before drying with anhydrous $MgSO_4$. After filtration, the solution was concentrated *in vacuo* before precipitation in MeOH to afford azido-functionalized PDMS as a clear viscous liquid, yield = 1.23 g, 85 %. GPC (THF containing [*n*Bu_4N]Br (0.1 % w/w), 1 mL min^{-1}): M_n = 13.2 kDa, M_w = 14.8 kDa, M_w/M_n = 1.12. ^{1}H NMR (400 MHz, $CDCl_3$) ppm δ = 2.74 (s, 2 H, C*H*$_2$N$_3$), 1.27 (m, 4 H, (C*H*$_2$)$_2$CH$_3$), 0.88 (t, 3 H, C*H*$_3$), 0.53 (m, 2 H, C*H*$_2$(CH$_2$)$_2$CH$_3$) and 0.00-0.24 (m, 912 H, C*H*$_3$SiC*H*$_3$).

6.5.4. Synthesis of azido-functionalized PNIPAm

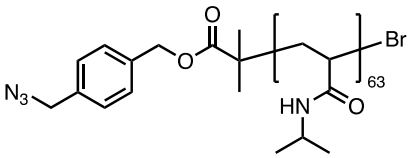

Azido-functionalized PNIPAm was synthesized by atom transfer radical polymerization of *N*-isopropylacrylamide as according to literature procedures.[56] A mixture of *N*-isopropylacrylamide (1 g, 8.83 x 10^{-3} mol), 4-(azidomethyl)benzyl2-bromo-2-methylpropanoate (27.6 mg, 8.83 x 10^{-5} mol), DMF (1 mL) and H_2O (2 mL) was subjected to three consecutive freeze pump thaw cycles. A solution of pre-mixed CuBr (12.7 mg, 8.83 x 10^{-5} mol), Me_6TREN (20.3 mg, 8.83 x 10^{-5} mol) and anhydrous DMF (1 mL) was added in one quick injection to the degassed monomer and initiator mixture under rapid stirring at room temperature. After 10 mins, the reaction was quenched by exposure to air and dilution with THF. The resulting mixture was precipitated in diethyl ether (under vigorous stirring), redissolved into THF and filtered through a basic alumina plug to remove residual copper salts. The solution was concentrated *in vacuo* before repeated precipitation in diethyl ether was carried out to afford azido-functionalized PNIPAm as a white solid, yield = 536 mg, 52 %. GPC (THF containing [nBu$_4$N]Br (0.1 % w/w), 1 mL min^{-1}): M_n = 29.2 kDa, M_w = 34.2 kDa, M_w/M_n = 1.17.

6.5.5. Synthesis of block copolymers via CuAAC click reactions

Homopolymers prepared by different polymerization methods can be coupled by using a copper-catalyzed azide-alkyne cycloaddition (CuAAC) click reaction.[55] This method has been particularly effective at preparing BCPs that contain a π-conjugated polymer block, synthesized via GRIM, and other polymer blocks prepared by living anionic, RAFT and ATRP polymerization techniques.[49,57–60] In a typical procedure alkyne-terminated π-conjugated polymer and azido-terminated homopolymer are dissolved in THF and subjected to three consecutive freeze pump thaw cycles. CuBr (excess) and PMDETA (excess) are premixed in anhydrous THF and then added to the polymer solution.

The reaction mixture is then heated to 45°C and stirred for 48 h. To remove residual copper salts the reaction mixture is then filtered through a basic alumina column. Additional purification steps to remove residual homopolymers are specific to the diblock copolymer and are described below.

PDOF$_{12}$-*b*-PNIPAM$_{58}$

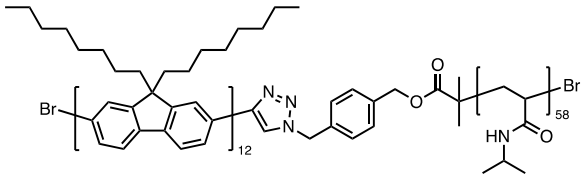

PDOF$_{12}$-*b*-PNIPAm$_{58}$ was synthesized by an analogous method to that mentioned above. Additional purification involved repeated precipitation of a solution of the polymer (in THF) into cold MeOH to remove any residual PNIPAm homopolymer. Residual alkyne-terminated PDOF was removed by silica gel chromatography) eluent chloroform 100 %), then the diblock copolymer was collected using a mixture of chloroform and methanol (9:1, v/v) as the eluent. One of the collected fractions was used for further studies and was precipitated into cold MeOH which gave the final product as a pale yellow solid, yield = 41 mg, 28 %. GPC (THF containing [*n*Bu$_4$N]Br (0.1 % w/w), 1 mL min^{-1}): M_n = 33.2 kDa, M_w = 36.5 kDa, M_w/M_n = 1.10. ^{1}H NMR (400 MHz, $CDCl_3$) ppm δ = 7.65-7.88 (m, 74 H, polyfluorene aromatic), 5.10 (s, 2 H, C*H*$_2$O), 4.00 (brs, 58 H, polynipam-C*H*).

PDOF$_{12}$-*b*-PDMS$_{147}$

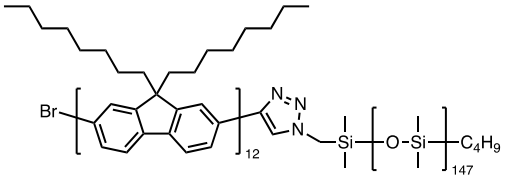

PDOF$_{12}$-*b*-PDMS$_{147}$ was synthesized by an analogous method to that mentioned above. Additional purification involved using preparative size exclusion chromatography (eluent THF) to remove any unreacted homopolymers, yield = 42 mg, 25 %. GPC (THF containing [*n*Bu$_4$N]Br (0.1 % w/w), 1 mL min^{-1}):

M_n = 15.8 kDa, M_w = 18.0 kDa, M_w/M_n = 1.14. ^{1}H NMR (400 MHz, $CDCl_3$) ppm δ = 7.65-7.88 (m, 74 H, polyfluorene aromatic) and 0.00-0.24 (m, 883 H, CH_3SiCH_3).

PDOF$_{12}$-*b*-PEG$_{113}$

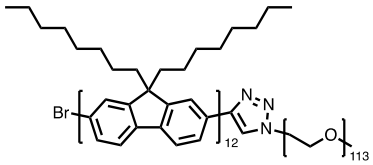

PDOF$_{12}$-*b*-PEG$_{113}$ was synthesized by an analogous method to that mentioned above. Additional purification involved repeated precipitation of a solution of the polymer (in THF) into cold MeOH to remove any residual PEG homopolymer. Residual alkyne-terminated PDOF was removed by silica gel chromatography) eluent chloroform 100 %), then the diblock copolymer was collected using a mixture of chloroform and methanol (9:1, v/v) as the eluent. One of the collected fractions was used for further studies and was precipitated into cold MeOH which gave the final product as a pale yellow solid, yield = 37 mg, 31 %. GPC (THF containing [*n*Bu$_4$N]Br (0.1 % w/w), 1 mL min^{-1}): M_n = 18.5 kDa, M_w = 21.3 kDa, M_w/M_n = 1.15. ^{1}H NMR (500 MHz, $CDCl_3$) ppm δ = 7.65-7.88 (m, 71 H, polyfluorene aromatic), 3.65 (s, 453 H, polyethylene glycol-(CH_2) x 2) and 3.39 (s, 3 H, polyethylene glycol-CH_3).

6.5.6. Supplementary Figures

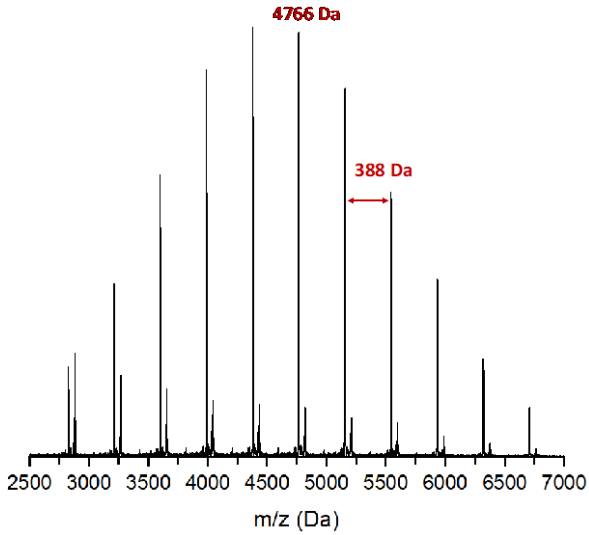

Figure S6. 1: MALDI-TOF mass spectrum of alkyne-capped $PDOF_{12}$. The mass of each PDOF repeat unit is 388 g mol^{-1}.

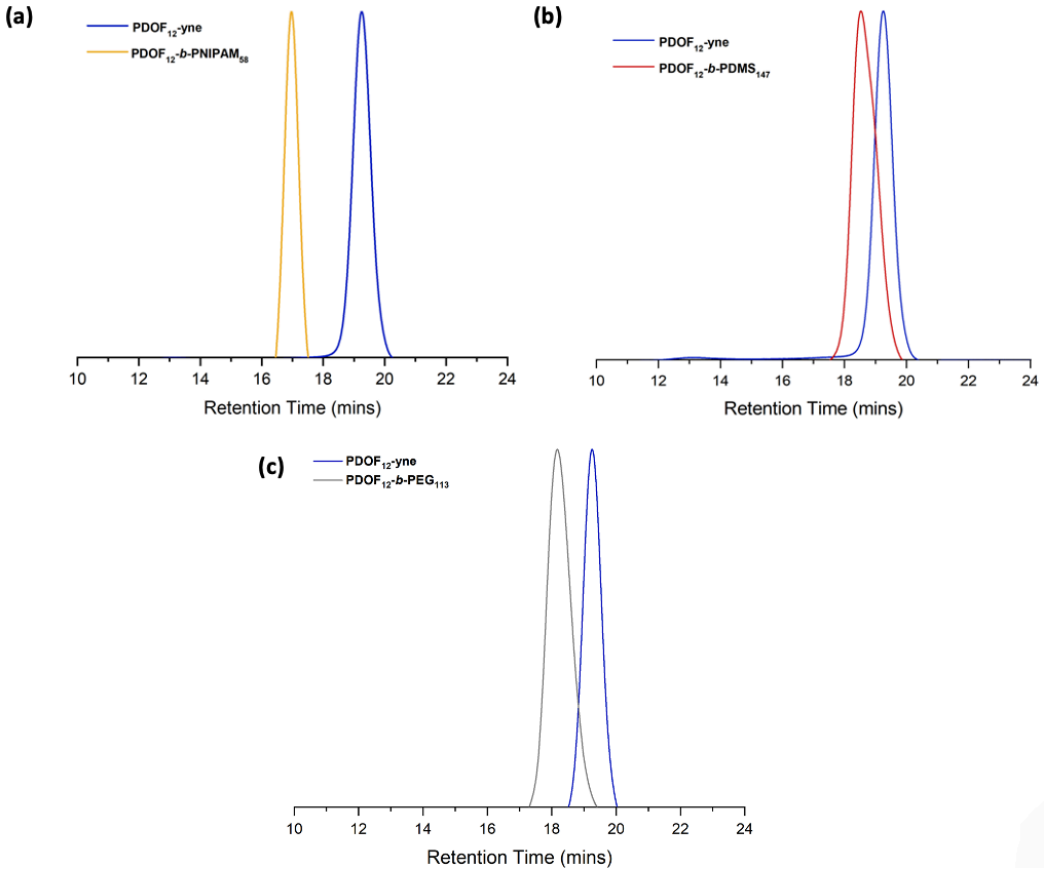

Figure S6. 2: GPC traces (UV response at λ = 380 nm) eluted in THF containing [nBu$_4$N]Br (0.1 % w/w) (1 mL/min) at 35°C of $PDOF_{12}$ homopolymer (blue traces), (a) $PDOF_{12}$-*b*-$PNIPAm_{58}$ (yellow trace),(b) $PDOF_{12}$-*b*-$PDMS_{147}$ (red trace)and (c) $PDOF_{12}$-*b*-PEG_{113} (grey trace).

Table S6. 1: Hildebrand solubility parameter of homopolymers.[61–63]

Polymer	δ (MPa)$^{1/2}$
Poly(di-*n*-octylfluorene)	18.6 – 19.0
Poly(dimethylsiloxane) (PDMS)	15.3
Poly(ethylene glycol) (PEG)	21.4
Poly(*N*-isopropylacrylamide) (PNIPAm)	24.8

Table S6. 2: Hildebrand solubility parameter of solvents.[64]

Solvent	δ (MPa)$^{1/2}$
MeOH	29.7
DMSO	26.4
EtOH	26.0
MeCN	24.8
DMF	24.7
iPrOH	23.5
THF	18.5
Toluene	18.3
EtOAc	18.1
BuOAc	17.6
Cyclohexane	16.8
Decane	15.8
Hexane	14.9

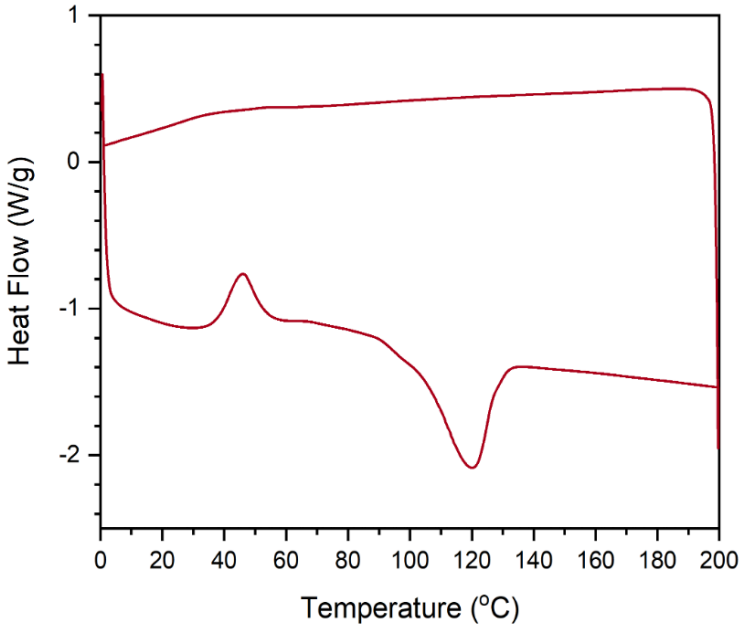

Figure S6. 3: DSC thermograph of $PDOF_{12}$ homopolymer showing the T_c (46°C)and T_m (120°C). Scanning rate = 10°C min^{-1}.

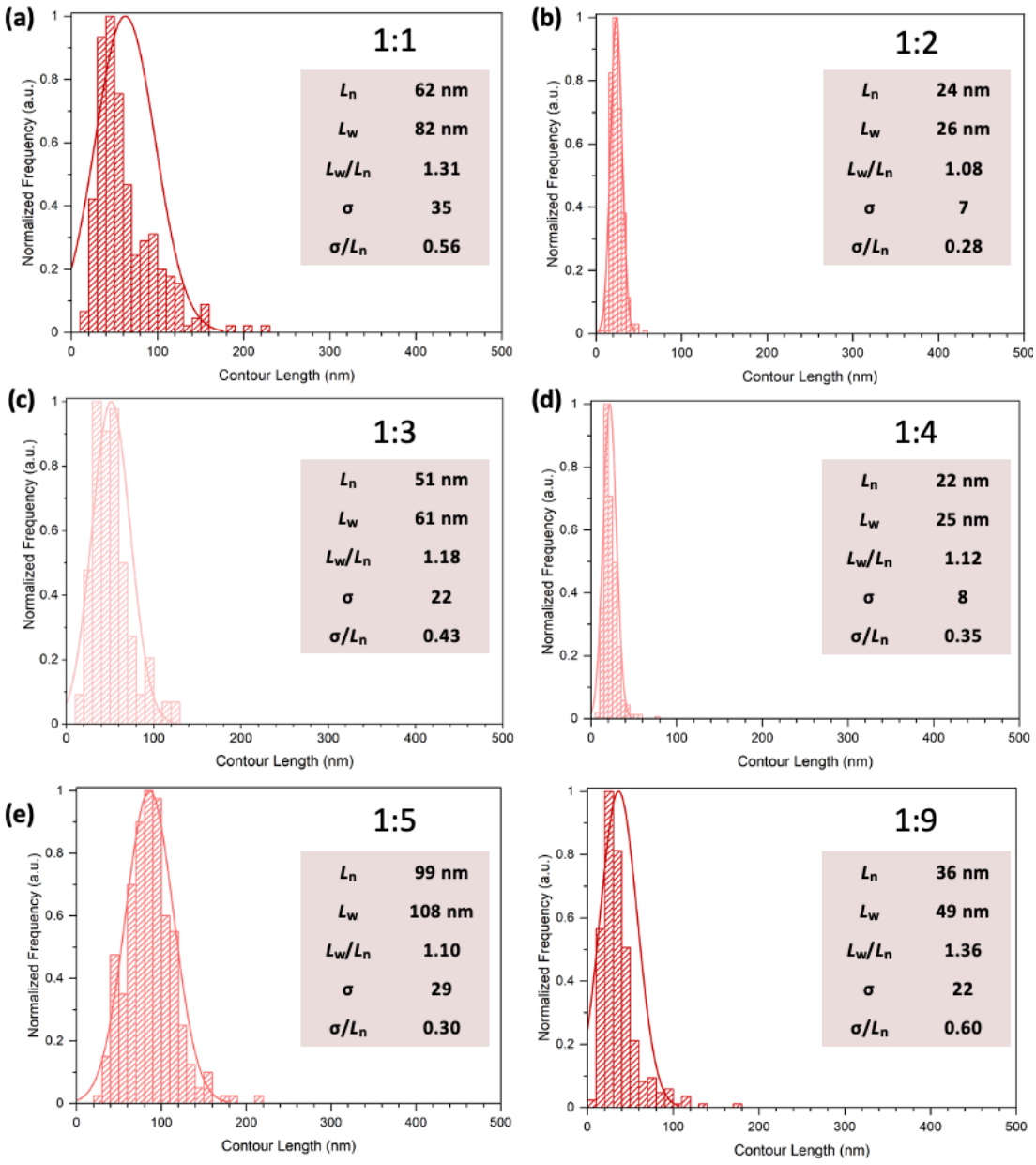

Figure S6. 4: Histograms representing contour length distributions of nanofibers prepared by the CDSA of $PDOF_{12}$-*b*-$PNIPAm_{58}$ in Tol:DMF (a) (1:1, v/v), (b) (1:2, v/v), (c) (1:3, v/v), (d) (1:4, v/v), (e) (1:5, v/v) and (d) (1:9, v/v). Sample were heated to 140°C for 30 min, cooled to and held at 110°C for 4 h before slow cooling to 20°C and ageing for 24 h.

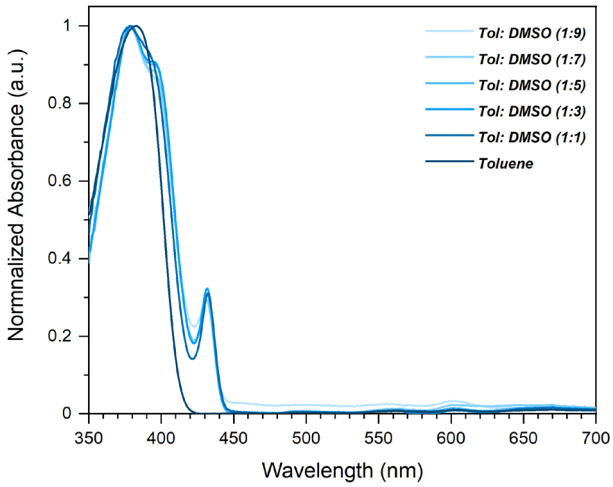

Figure S6. 5: UV-vis spectra of $PDOF_{12}$-*b*-$PNIPAm_{58}$ in different ratios of Tol:DMSO (v/v).

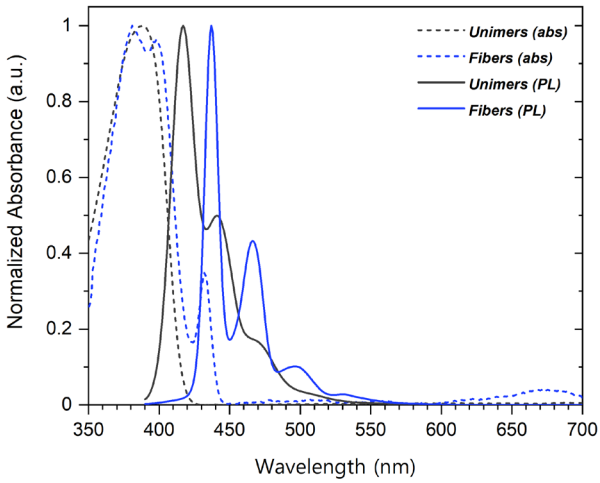

Figure S6. 6: Optical spectroscopy data of $PDOF_{12}$-*b*-$PNIPAm_{58}$ unimers in THF and micelles in THF: iPrOH (1:9, v/v). UV-vis spectra (dashed traces) and photoluminescence spectra (solid traces) of unimers in THF (grey traces) and micelles in THF: iPrOH (1:9,v/v) (blue traces).

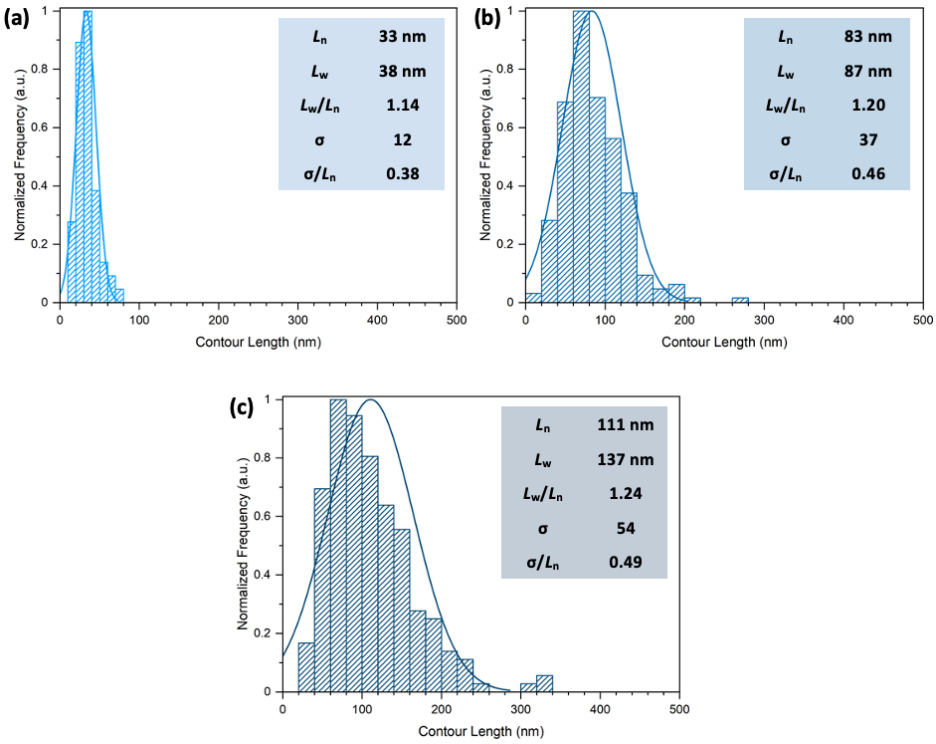

Figure S6. 7: Histograms representing contour length distributions of nanofibers prepared by the CDSA of PDOF$_{12}$-*b*-PNIPAm$_{58}$ in Tol:DMF (1:9, v/v) by heating at 140°C for 30 min, cooling to and held at (a) 110°C, (b) 90°C and (c) 70°C for 4 h before slow cooling to 20°C and ageing for 24 h.

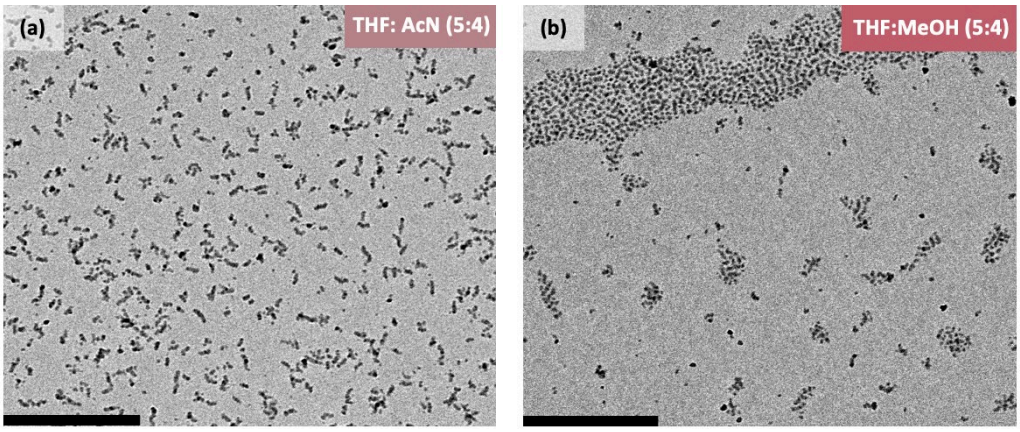

Figure S6. 8: TEM images of PDOF$_{12}$-*b*-PNIPAM$_{58}$ in THF:MeCN (5:4, v/v) and in (b) THF:MeOH (5:4, v/v). Samples were prepared (at 20°C) by adding MeCN/MeOH dropwise to a solution of PDOF-*b*-PNIPAm in THF till a ratio of 5:4 (v/v) ratio. The samples were then cooled to -20°C, aged for 3 h before warming to 20°C and ageing for 24 h.

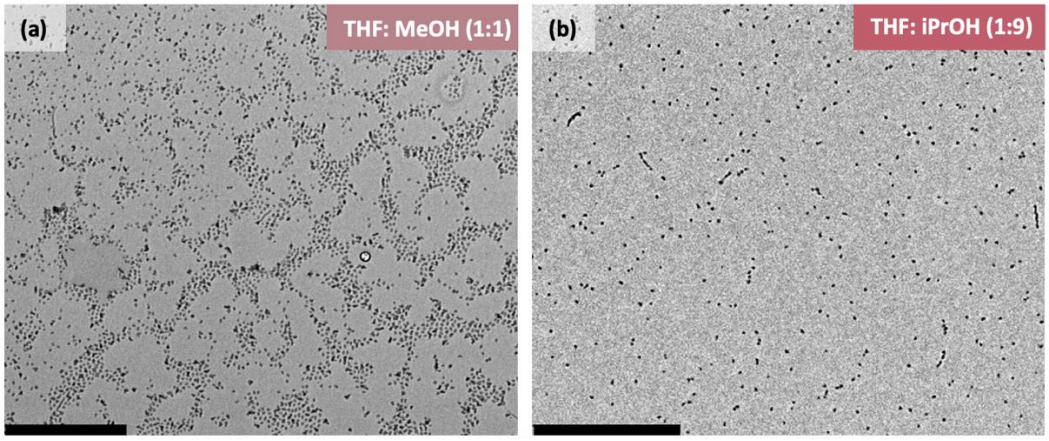

Figure S6. 9: TEM images of $PDOF_{12}$-*b*-PEG_{113} in (a) THF:MeOH (1:1, v/v) and in (b) THF:iPrOH (1:9, v/v).

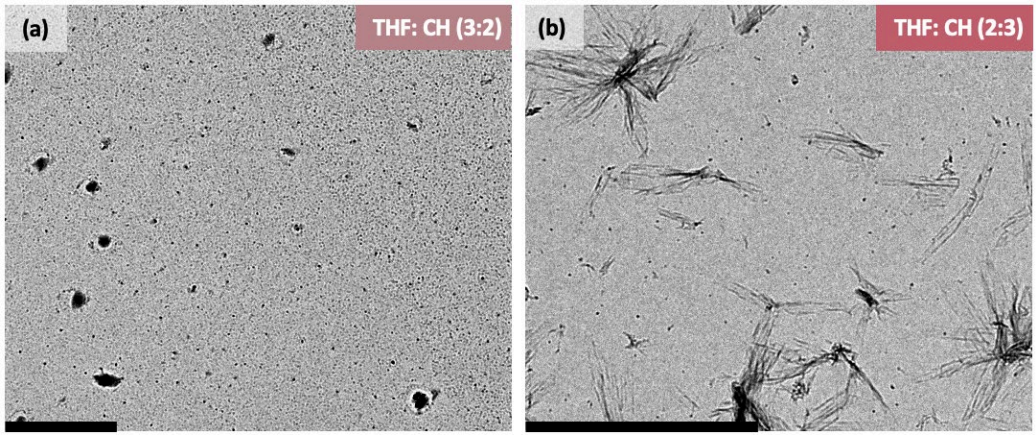

Figure S6. 10: TEM images of $PDOF_{12}$-*b*-$PDMS_{147}$ in (a) THF:CH (3:2, v/v) and in (b) THF:CH (2:3, v/v).

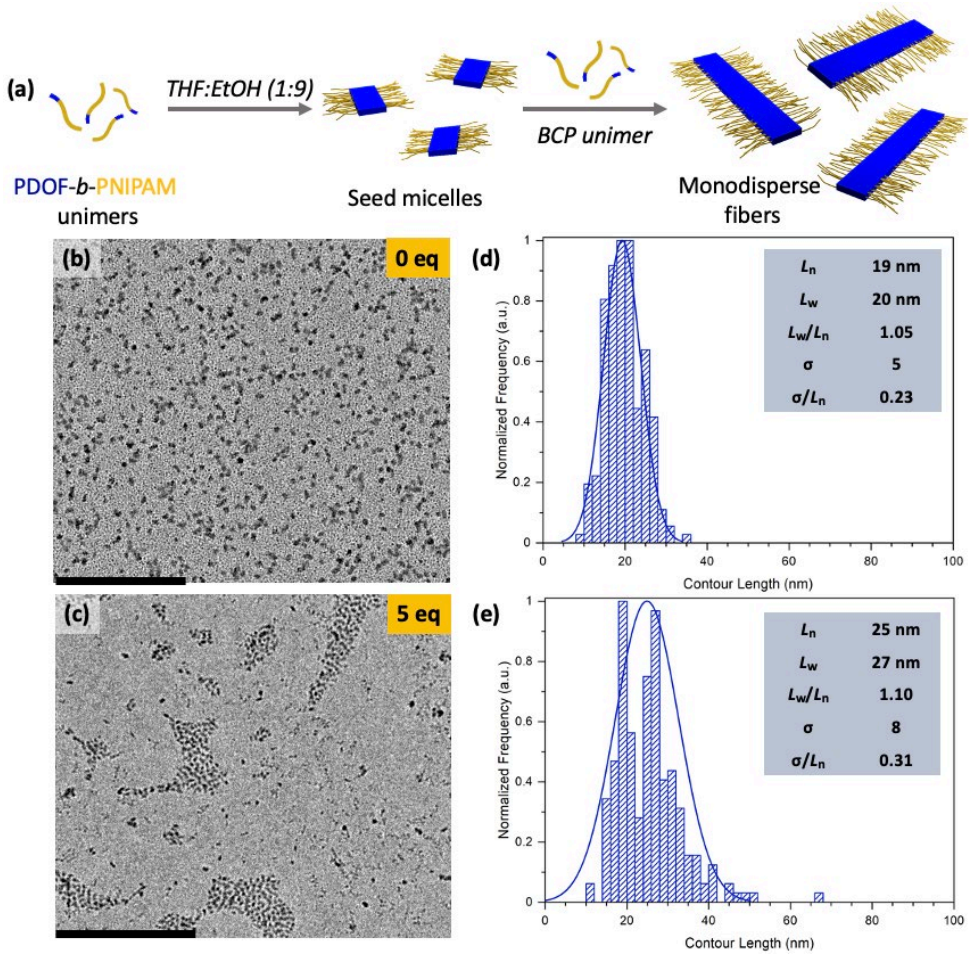

Figure S6. 11: (a) Schematic representation of the attempted preparation of low dispersity $PDOF_{12}$-*b*-$PNIPAm_{58}$ fibers by homoepitaxial seeded growth of $PDOF_{12}$-*b*-$PNIPAm_{67}$ unimer from $PDOF_{12}$-*b*-$PNIPAm_{58}$ seed micelles. TEM image of (b) PDOF-*b*-PNIPAm seed micelles (L_n = 19 nm, L_w/L_n = 1.05) prepared in THF:iPrOH (1:9, v/v) and (d) corresponding histograms representing the contour length distribution of the nanofibers. TEM image of (c) nanofibers (L_n = 25 nm, L_w/L_n = 1.10) prepared by the seeded growth of $PDOF_{12}$-*b*-$PNIPAm_{58}$ unimer from seed micelles (L_n = 19 nm, L_w/L_n = 1.05) in THF:iPrOH (1:4, v/v) and (d) corresponding histograms representing the contour length distribution of the nanofibers. Scale bars: 500 nm.

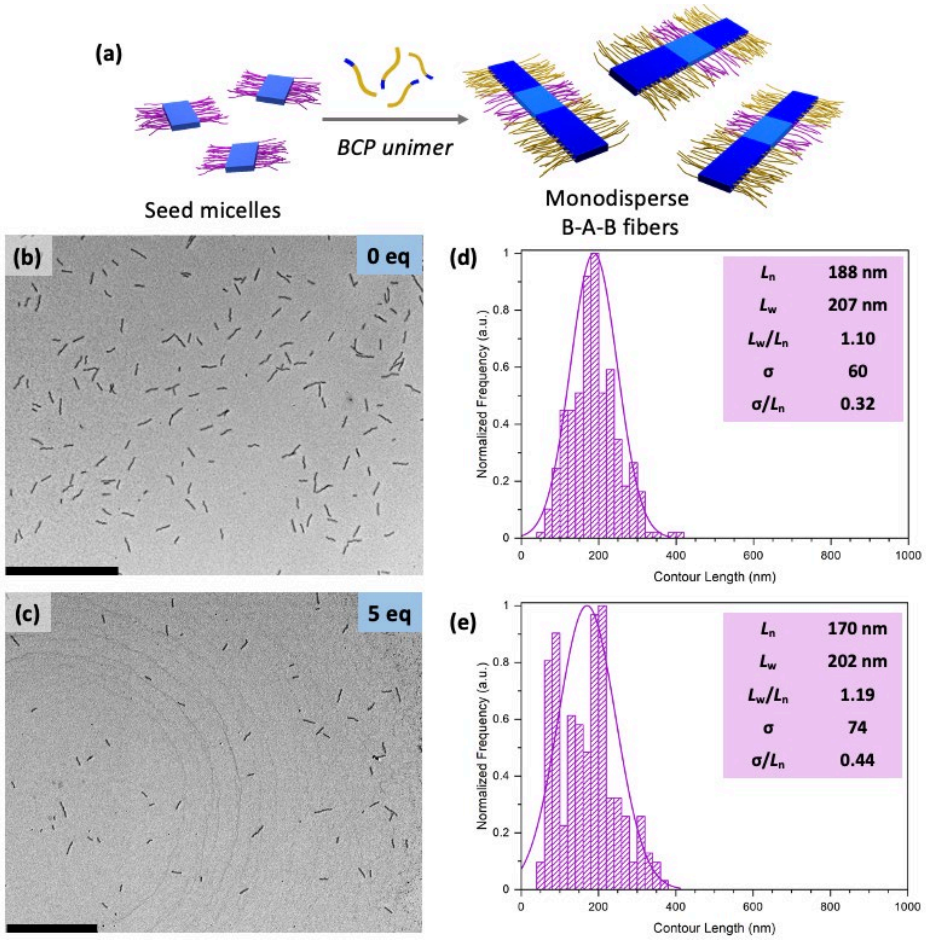

Figure S6. 12: (a) Schematic representation of the attempted preparation of low dispersity B-A-B nanofibers by heteroepitaxial seeded growth of $PDOF_{12}$-*b*-$PNIPAm_{58}$ unimers from $PDHF_{17}$-*b*-$P2VP_{250}$ seed micelles. A = $PDHF_{17}$-*b*-$P2VP_{250}$ and B = $PDOF_{12}$-*b*-$PNIPAm_{58}$. TEM image of (b) $PDHF_{17}$-*b*-$P2VP_{250}$ seed micelles (L_n = 188 nm, L_w/L_n = 1.10) prepared in THF:MeOH (1:1, v/v) and (d) corresponding histograms representing the contour length distribution of the nanofibers. TEM image of (c) nanofibers (L_n = 170 nm, L_w/L_n = 1.19) prepared by the seeded growth of $PDOF_{12}$-*b*-$PNIPAm_{58}$ unimer from $PDHF_{17}$-*b*-$P2VP_{250}$ seed micelles (L_n = 188 nm, L_w/L_n = 1.10) in THF:MeOH (1:1, v/v) and (d) corresponding histograms representing the contour length distribution of the nanofibers. Scale bars: 2 µm.

6.6. References

(1) Threlfall, T. L. Analysis of Organic Polymorphs. A Review. *Analyst* **1995**, *120*, 2435–2460.

(2) Datta, A.; Mohakud, S.; Pati, S. K. Comparing the Electron and Hole Mobilities in the α and β Phases of Perylene: Role of π-Stacking. *J. Mater. Chem.* **2007**, *17*, 1933–1938.

(3) He, T.; Stolte, M.; Burschka, C.; Hansen, N. H.; Musiol, T.; Kälblein, D.; Pflaum, J.; Tao, X.; Brill, J.; Würthner, F. Single-Crystal Field-Effect Transistors of New Cl 2-NDI Polymorph Processed by Sublimation in Air. *Nat. Commun.* **2015**, *6*, 4954.

(4) Poelking, C.; Andrienko, D. Effect of Polymorphism, Regioregularity and Paracrystallinity on Charge Transport in Poly(3-Hexylthiophene) [P3HT] Nanofibers. *Macromolecules* **2013**, *46*, 8941–8956.

(5) Cadby, A. J.; Lane, P. A.; Mellor, H.; Martin, S. J.; Grell, M.; Giebeler, C.; Bradley, D. D. C.; Wohlgenannt, M.; An, C.; Vardeny, Z. V. Film Morphology and Photophysics of Polyfluorene. *Phys. Rev. B - Condens. Matter Mater. Phys.* **2000**, *62* (23), 15604–15609.

(6) Li, M.; Balawi, A. H.; Leenaers, P. J.; Ning, L.; Heintges, G. H. L.; Marszalek, T.; Pisula, W.; Wienk, M. M.; Meskers, S. C. J.; Yi, Y.; Laquai, F.; Janssen, R. A. J. Impact of Polymorphism on the Optoelectronic Properties of a Low-Bandgap Semiconducting Polymer. *Nat. Commun.* **2019**, *10*, 2867.

(7) Kim, D. Y.; Cho, H. N.; Kim, C. Y. Blue Light Emitting Polymers. *Prog. Polym. Sci.* **2000**, *25* (8), 1089–1139.

(8) Leclerc, M. Polyfluorenes: Twenty Years of Progress. *J. Polym. Sci. Part A Polym. Chem.* **2001**, *39* (17), 2867–2873.

(9) Scherf, U.; List, E. J. W. Semiconducting Polyfluorenes - Towards Reliable Structure-Property Relationships. *Adv. Mater.* **2002**, *14* (7), 477–487.

(10) Khan, A. L. T.; Banach, M. J.; Köhler, A. Control of β-Phase Formation in Polyfluorene Thin Films via Franck-Condon Analysis. *Synth. Met.* **2003**, *139* (3), 905–907.

(11) Bright, D. W.; Dias, F. B.; Galbrecht, F.; Scherf, U.; Monkman, A. P. The Influence of Alkyl-Chain Length on Beta-Phase Formation in Polyfluorenes. *Adv. Funct. Mater.* **2009**, *19* (1), 67–73.

(12) Liu, B. B.; Li, T.; Zhang, H.; Ma, T.; Ren, J.; Liu, B. B.; Lin, J.; Yu, M.; Xie, L.; Lu, D. Polyfluorene (PF) Single-Chain Conformation, β Conformation, and Its Stability and Chain Aggregation by Side-Chain Length Change in the Solution Dynamic Process. *J. Phys. Chem. C* **2018**, *122* (26), 14814–14826.

(13) Perevedentsev, A.; Aksel, S.; Feldman, K.; Smith, P.; Stavrinou, P. N.; Bradley, D. D. C. Interplay between Solid State Microstructure and Photophysics for Poly(9,9-Dioctylfluorene) within Oriented Polyethylene Hosts. *J. Polym. Sci. Part B Polym. Phys.* **2015**, *53* (1), 22–38.

(14) Lu, H. H.; Liu, C. Y.; Chang, C. H.; Chen, S. A. Self-Dopant Formation in Poly(9,9-Di-n-Octylfluorene) via a Dipping Method for Efficient and Stable Pure-Blue Electroluminescence. *Adv. Mater.* **2007**, *19* (18), 2574–2579.

(15) Perevedentsev, A.; Chander, N.; Kim, J. S.; Bradley, D. D. C. Spectroscopic Properties of

Poly(9,9-Dioctylfluorene) Thin Films Possessing Varied Fractions of β-Phase Chain Segments: Enhanced Photoluminescence Efficiency via Conformation Structuring. *J. Polym. Sci. Part B Polym. Phys.* **2016**, *54* (19), 1995–2006.

(16) Misaki, M.; Ueda, Y.; Nagamatsu, S.; Chikamatsu, M.; Yoshida, Y.; Tanigaki, N.; Yase, K. Highly Polarized Polymer Light-Emitting Diodes Utilizing Friction-Transferred Poly(9,9-Dioctylfluorene) Thin Films. *Appl. Phys. Lett.* **2005**, *87* (24), 243503.

(17) Rothe, C.; Galbrecht, F.; Scherf, U.; Monkman, A. The β-Phase of Poly(9,9-Dioctylfluorene) as a Potential System for Electrically Pumped Organic Lasing. *Adv. Mater.* **2006**, *18* (16), 2137–2140.

(18) O'Carroll, D.; Lieberwirth, I.; Redmond, G. Microcavity Effects and Optically Pumped Lasing in Single Conjugated Polymer Nanowires. *Nat. Nanotechnol.* **2007**, *2* (3), 180–184.

(19) Qian, J.; Lu, Y.; Chia, A.; Zhang, M.; Rupar, P. A.; Gunari, N.; Walker, G. C.; Cambridge, G.; He, F.; Guerin, G.; Manners, I.; Winnik, M. A. Self-Seeding in One Dimension : A Route to Uniform Fiber-like Nanostructures from Block Copolymers with a Crystallizable Core-Forming Block. *ACS Nano* **2013**, *7* (5), 3754–3766.

(20) Zhang, X.; Hu, Q.; Lin, J.; Lei, Z.; Guo, X.; Xie, L.; Lai, W.; Huang, W. Efficient and Stable Deep Blue Polymer Light-Emitting Devices Based on β-Phase Poly(9,9-Dioctylfluorene). *Appl. Phys. Lett.* **2013**, *103* (15), 153301.

(21) Chua, L. L.; Zaumseil, J.; Chang, J. F.; Ou, E. C. W.; Ho, P. K. H.; Sirringhaus, H.; Friend, R. H. General Observation of N-Type Field-Effect Behaviour in Organic Semiconductors. *Nature* **2005**, *434*, 194–199.

(22) Wohlgenannt, M.; Jiang, X. M.; Vardeny, Z. V.; Janssen, R. A. J. Conjugation-Length Dependence of Spin-Dependent Exciton Formation Rates in [Formula Presented]-Conjugated Oligomers and Polymers. *Phys. Rev. Lett.* **2002**, *88* (19), 197401.

(23) Becker, K.; Lupton, J. M. Dual Species Emission from Single Polyfluorene Molecules: Signatures of Stress-Induced Planarization of Single Polymer Chains. *J. Am. Chem. Soc.* **2005**, *127* (20), 7306–7307.

(24) Chen, L.; Zhu, L.; Shuai, Z. Singlet - Triplet Splittings and Their Relevance to the Spin-Dependent Exciton Formation in Light-Emitting Polymers: An EOM/CCSD Study. *J. Phys. Chem. A* **2006**, *110* (50), 13349–13354.

(25) Grell, M.; Bradley, D. D. C.; Ungar, G.; Hill, J.; Whitehead, K. S. Interplay of Physical Structure and Photophysics for a Liquid Crystalline Polyfluorene. *Macromolecules* **1999**, *32* (18), 5810–5817.

(26) O'Carroll, D.; Iacopino, D.; O'Riordan, A.; Lovera, P.; O'Connor, É.; O'Brien, G. A.; Redmond, G. Poly(9,9-Dioctylfluorene) Nanowires with Pronounced β-Phase Morphology: Synthesis, Characterization, and Optical Properties. *Adv. Mater.* **2008**, *20* (1), 42–48.

(27) Ling, H.; Lin, J.; Yi, M.; Liu, B.; Li, W.; Lin, Z.; Xie, L.; Bao, Y.; Guo, F.; Huang, W. Synergistic Effects of Self-Doped Nanostructures as Charge Trapping Elements in Organic Field Effect Transistor Memory. *ACS Appl. Mater. Interfaces* **2016**, *8*, 18969–18977.

(28) Peet, J.; Brocker, E.; Xu, Y.; Bazan, G. C. Controlled β-Phase Formation in Poly(9,9-Di-n-Octylfluorene) by Processing with Alkyl Additives. *Adv. Mater.* **2008**, *20* (10), 1882–1885.

(29) Li, X.; Bai, Z.; Liu, B.; Li, T.; Lu, D. From Starting Formation to the Saturation Content of the

β-Phase in Poly(9,9-Dioctylfluorene) Toluene Solutions. *J. Phys. Chem. C* **2017**, *121* (27), 14443–14450.

(30) Liu, Y. Di; Zhang, Q.; Yu, X. H.; Liu, J. G.; Han, Y. C. Increasing the Content of β Phase of Poly(9,9-Dioctylfluorene) by Synergistically Controlling Solution Aggregation and Extending Film-Forming Time. *Chinese J. Polym. Sci. (English Ed.* **2019**, *37*, 664–673.

(31) Vahala, K. J. Optical Microcavities. *Nature* **2003**, *424*, 839–846.

(32) Terra, I. A. A.; Sanfelice, R. C.; Valente, G. T.; Correa, D. S. Optical Sensor Based on Fluorescent PMMA/PFO Electrospun Nanofibers for Monitoring Volatile Organic Compounds. *J. Appl. Polym. Sci.* **2018**, *135* (14), 46128.

(33) MacFarlane, L. R.; Shaikh, H.; Garcia-Hernandez, J. D.; Vespa, M.; Fukui, T.; Manners, I. Functional Nanoparticles through π-Conjugated Polymer Self-Assembly. *Nat. Rev. Mater.* **2021**, *6*, 7–26.

(34) Wang, X.; Guerin, G.; Wang, H.; Wang, Y.; Manners, I.; Winnik, M. A. Cylindrical Block Copolymer Micelles and Co-Micelles of Controlled Length and Architecture. *Science.* **2007**, *317* (5838), 644–647.

(35) Boott, C. E.; Gwyther, J.; Harniman, R. L.; Hayward, D. W.; Manners, I. Scalable and Uniform 1D Nanoparticles by Synchronous Polymerization, Crystallization and Self-Assembly. *Nat. Chem.* **2017**, *9* (8), 785–792.

(36) Schöbel, J.; Karg, M.; Rosenbach, D.; Krauss, G.; Greiner, A.; Schmalz, H. Patchy Wormlike Micelles with Tailored Functionality by Crystallization-Driven Self-Assembly: A Versatile Platform for Mesostructured Hybrid Materials. *Macromolecules* **2016**, *49* (7), 2761–2771.

(37) Schmelz, J.; Karg, M.; Hellweg, T.; Schmalz, H. General Pathway toward Crystalline-Core Micelles with Tunable Morphology and Corona Segregation. *ACS Nano* **2011**, *5* (12), 9523–9534.

(38) Tao, D.; Feng, C.; Cui, Y.; Yang, X.; Manners, I.; Winnik, M. A.; Huang, X. Monodisperse Fiber-like Micelles of Controlled Length and Composition with an Oligo(p-Phenylenevinylene) Core via "Living" Crystallization-Driven Self-Assembly. *J. Am. Chem. Soc.* **2017**, *139* (21), 7136–7139.

(39) Arno, M. C.; Inam, M.; Coe, Z.; Cambridge, G.; Macdougall, L. J.; Keogh, R.; Dove, A. P.; O'Reilly, R. K. Precision Epitaxy for Aqueous 1D and 2D Poly(ϵ -Caprolactone) Assemblies. *J. Am. Chem. Soc.* **2017**, *139* (46), 16980–16985.

(40) Yang, S.; Choi, T. L. Rapid Formation and Real-Time Observation of Micron-Sized Conjugated Nanofibers with Tunable Lengths and Widths in 20 Minutes by Living Crystallization-Driven Self-Assembly. *Chem. Sci.* **2020**, *11* (32), 8416–8424.

(41) Hicks, G. E. J. J.; Jarrett-Wilkins, C. N.; Panchuk, J. R.; Manion, J. G.; Seferos, D. S. Oxidation Promoted Self-Assembly of π-Conjugated Polymers. *Chem. Sci.* **2020**, *11* (25), 32–34.

(42) Qi, R.; Zhu, Y.; Han, L.; Wang, M.; He, F. Rectangular Platelet Micelles with Controlled Aspect Ratio by Hierarchical Self-Assembly of Poly(3-Hexylthiophene)- b-Poly(Ethylene Glycol). *Macromolecules* **2020**, *53* (15), 6555–6565.

(43) Shin, S.; Menk, F.; Kim, Y.; Lim, J.; Char, K.; Zentel, R.; Choi, T. L. Living Light-Induced Crystallization-Driven Self-Assembly for Rapid Preparation of Semiconducting Nanofibers. *J. Am. Chem. Soc.* **2018**, *140* (19), 6088–6094.

(44) Wang, H.; Lin, W.; Fritz, K. P.; Scholes, G. D.; Winnik, M. A.; Manners, I. Cylindrical Block Co-Micelles with Spatially Selective Functionalization by Nanoparticles. *J. Am. Chem. Soc.* **2007**, *129* (43), 12924–12925.

(45) Mann, S.; Manners, I.; Patil, A. J.; Winnik, M. A.; Manners, I.; Wang, H.; Liu, K.; Petrov, S. Fabrication of Continuous and Segmented Polymer/ Metal Oxide Nanowires Using Cylindrical Micelles and Block Comicelles as Templates. *Adv. Mater.* **2009**, *21* (18), 1805–1808.

(46) Jin, X.-H.; Price, M. B.; Finnegan, J. R.; Boott, C. E.; Richter, J. M.; Rao, A.; Menke, S. M.; Friend, R. H.; Whittell, G. R.; Manners, I. Long-Range Exciton Transport in Conjugated Polymer Nanofibers Prepared by Seeded Growth. *Science.* **2018**, *360* (6391), 897–900.

(47) Shaikh, H.; Jin, X. H.; Harniman, R. L.; Richardson, R. M.; Whittell, G. R.; Manners, I. Solid-State Donor-Acceptor Coaxial Heterojunction Nanowires via Living Crystallization-Driven Self-Assembly. *J. Am. Chem. Soc.* **2020**, *142* (31), 13469–13480.

(48) Massey, J. A.; Temple, K.; Cao, L.; Rharbi, Y.; Raez, J.; Winnik, M. A.; Manners, I. Self-Assembly of Organometallic Block Copolymers: The Role of Crystallinity of the Core-Forming Polyferrocene Block in the Micellar Morphologies Formed by Poly(Ferrocenylsilane-b-Dimethylsiloxane) in n-Alkane Solvents. *J. Am. Chem. Soc.* **2000**, *122* (47), 11577–11584.

(49) Kynaston, E. L.; Nazemi, A.; MacFarlane, L. R.; Whittell, G. R.; Faul, C. F. J.; Manners, I.; Faul, C. F. J. Uniform Polyselenophene Block Copolymer Fiberlike Micelles and Block Co-Micelles via Living Crystallization-Driven Self-Assembly. *Macromolecules* **2018**, *51* (3), 1002–1010.

(50) Gädt, T.; Ieong, N. S.; Cambridge, G.; Winnik, M. A.; Manners, I. Complex and Hierarchical Micelle Architectures from Diblock Copolymers Using Living, Crystallization-Driven Polymerizations. *Nat. Mater.* **2009**, *8* (2), 144–150.

(51) Nazemi, A.; He, X.; MacFarlane, L. R.; Harniman, R. L.; Hsiao, M. S.; Winnik, M. A.; Faul, C. F. J. J.; Manners, I. Uniform "Patchy" Platelets by Seeded Heteroepitaxial Growth of Crystallizable Polymer Blends in Two Dimensions. *J. Am. Chem. Soc.* **2017**, *139* (12), 4409–4417.

(52) Oliver, A. M.; Gwyther, J.; Boott, C. E.; Davis, S.; Pearce, S.; Manners, I. Scalable Fiber-like Micelles and Block Co-Micelles by Polymerization-Induced Crystallization-Driven Self-Assembly. *J. Am. Chem. Soc.* **2018**, *140* (51), 18104–18114.

(53) MacFarlane, L. R.; Fukui, T.; Vespa, M.; Manners, I. Improvements to the Seeded Growth of π-Conjugated Block Copolymers: Formation of Hierarchical Assemblies of Greater Control. *Manuscr. Prep.*

(54) Loewe, R. S.; Ewbank, P. C.; Liu, J.; Zhai, L.; McCullough, R. D. Regioregular, Head-to-Tail Coupled Poly(3-Alkylthiophenes) Made Easy by the GRIM Method: Investigation of the Reaction and the Origin of Regioselectivity. *Macromolecules* **2001**, *34* (13), 4324–4333.

(55) Zhang, M.; Rupar, P. A.; Feng, C.; Lin, K.; Lunn, D. J.; Oliver, A.; Nunns, A.; Whittell, G. R.; Manners, I.; Winnik, M. A. Modular Synthesis of Polyferrocenylsilane Block Copolymers by Cu-Catalyzed Alkyne/Azide "Click" Reactions. *Macromolecules* **2013**, *46* (4), 1296–1304.

(56) Zhou, H.; Lu, Y.; Zhang, M.; Guerin, G.; Manners, I.; Winnik, M. A. PFS-b-PNIPAM: A First Step toward Polymeric Nanofibrillar Hydrogels Based on Uniform Fiber-Like Micelles. *Macromolecules* **2016**, *49* (11), 4265–4276.

(57) Qian, J.; Li, X.; Lunn, D. J.; Gwyther, J.; Hudson, Z. M.; Kynaston, E.; Rupar, P. A.; Winnik, M.

A.; Manners, I. Uniform High Aspect Ratio Fiber-like Micelles and Block Co-Micelles with a Crystalline π - Conjugated Polythiophene Core by Self-Seeding. *J. Am. Chem. Soc.* **2014**, *136* (11), 4121–4124.

(58) Tao, D.; Feng, C.; Lu, Y.; Cui, Y.; Yang, X.; Manners, I.; Winnik, M. A.; Huang, X. Self-Seeding of Block Copolymers with a π-Conjugated Oligo(p -Phenylenevinylene) Segment: A Versatile Route toward Monodisperse Fiber-like Nanostructures. *Macromolecules* **2018**, *51* (5), 2065–2075.

(59) Urien, M.; Erothu, H.; Cloutet, E.; Hiorns, R. C.; Vignau, L.; Cramail, H. Poly(3-Hexylthiophene) Based Block Copolymers Prepared by "Click" Chemistry. *Macromolecules* **2008**, *41* (19), 7033–7040.

(60) Smith, K. A.; Lin, Y. H.; Dement, D. B.; Strzalka, J.; Darling, S. B.; Pickel, D. L.; Verduzco, R. Synthesis and Crystallinity of Conjugated Block Copolymers Prepared by Click Chemistry. *Macromolecules* **2013**, *46* (7), 2636–2645.

(61) Perevedentsev, A.; Stavrinou, P. N.; Bradley, D. D. C.; Smith, P. Solution-Crystallization and Related Phenomena in 9,9-Dialkyl-Fluorene Polymers. I. Crystalline Polymer-Solvent Compound Formation for Poly(9,9-Dioctylfluorene). *J. Polym. Sci. Part B Polym. Phys.* **2015**, *53*, 1481–1491.

(62) Özdemir, C.; Güner, A. Solubility Profiles of Poly(Ethylene Glycol)/Solvent Systems, I: Qualitative Comparison of Solubility Parameter Approaches. *Eur. Polym. J.* **2007**, *43*, 3068–3093.

(63) Poly(dimethylsiloxane) https://polymerdatabase.com/polymers/Polydimethylsiloxane.html (accessed Feb 24, 2021).

(64) Barton, A. F. M. *Handbook of Solubility Parameters and Other Cohesion Parameters*; CRC Press LLC, 1991.

Chapter 7

Conclusions, Future Work and Outlook

7.1. Conclusions

Work presented in this thesis has demonstrated the scope and versatility of the crystallization-driven self-assembly (CDSA) of polyfluorene-containing polymers. It has been demonstrated that a variety of different nanoscale heterojunction styles can be constructed. Crystalline poly(di-*n*-hexylfluorene) was used as a donor material and compromised the core of the nanofibers. Solid-state heterojunctions were fabricated with crystalline polymeric acceptor regions located coaxially along the fiber core or at different points in segmented fibers. It has also been shown that hybrid heterojunction conjugates can be easily constructed via attachment of quantum dots or rods to functional coronal regions on segmented PDHF nanofibers. Efficient energy funneling through the fiber core towards the attached quantum rods on the fiber termini was realized. Detailed transient absorption measurements revealed that this energy funneling led to a 4-fold enhancement in the emission of the acceptor-based quantum rods. Additionally, the high energy transfer efficiency (70 %) in this hybrid system is very promising and opens up a facile route towards preparing a variety of different hybrid materials. Modification of the conjugated polymer core-forming block and the attached nanoparticles should enable the construction of a wide range of nanoscale heterojunction materials with tunable optical and/or electronic properties.

In the latter Chapters of this thesis the preparation of other micelle morphologies and core-forming blocks has been demonstrated. For the first time the formation of large 2D platelet micelles and one-handed helical micelles

through the CDSA of amphiphilic polyfluorene materials has been demonstrated. These morphologies may offer different electronic properties to the 1D nanofiber morphology. Finally, we show that CDSA also enables enhancement of the content of the highly ordered β-phase when compared to other techniques for the preparation of polyfluorene nanofibers.

All these results demonstrate the advantages of the CDSA method for the fabrication of a variety of precisely ordered nanomaterials with desirable structural, chemical and electronic properties. Ultimately, for the use of these materials in applications we need to expand the scope of materials that we can use as the crystallizable core-forming block.

7.2. Future Work

Following on from the results presented in this thesis a number of future research directions could be pursued and are outlined below:

7.2.1. Investigations of Low Bandgap and N-Type π-Conjugated Polymers for CDSA

During the development of functional materials through the CDSA of π-conjugated polymers, our group and multiple other groups have focussed on p-type polymers amongst which polythiophenes, polyfluorenes and poly(*p*-phenylenevinylene) are the most studied. We have shown that fibers with a p-type crystalline core exhibit modest charge-carrier mobilities and exceptional exciton diffusion properties.[1,2] In Chapter 2, we reported a route towards fabricating solid-state heterojunction nanowires. We use a proof-of-concept system with two different p-type conjugated polymers. For the realization of high-performance electronic devices based on nanowires prepared by CDSA we need to consider other semiconducting conjugated polymers. Future research efforts will focus on preparing fibers with crystalline cores from the CDSA of n-type conjugated polymers and subsequently p-n heterojunction nanostructures. The main challenge for this research direction is the synthesis and purification of low molar mass dispersity n-type polymers, an essential prerequisite for living CDSA. Pyridine flanked diketopyrrolopyrrole-based conjugated polymers are attractive potential candidates for the realization of n-type crystalline core nanofibers with

exceptionally high electron mobility (up to ca. 2.45 $cm^2 V^{-1} s^{-1}$).[3,4] The origin of this desirable electron transport behaviour was attributed to the high crystallinity of the polymer. If fibers with an n-type crystalline core can be prepared via CDSA we could fabricate n-channel organic field effect transistors or all-polymer photovoltaic cells composed of p-type and n-type crystalline fibers.[5]

7.2.2. 2D Seeded Growth of π-Conjugated Polymeric Amphiphiles

In Chapter 5, large 2D platelets with a PDHF core formed via CDSA was presented. Seeded growth experiments in solvent systems suitable for the formation of platelets via self-nucleation showed that epitaxial growth preferentially occurs in one direction (plane associated with π-π stacking). Future work could focus on further optimization of the seeded growth protocol to promote lateral epitaxial growth from seed micelles. The rate of epitaxial growth in the π-π stacking plane needs to be similar to that in the alkyl side-chain stacking plane for the realization of 2D platelets of controlled size and tunable areas. Ongoing and future work will also focus on investigating the exciton diffusion properties of the 2D PDHF platelets. These materials could be useful for light harvesting applications if we can find an optimal route to integrate the micelles into photovoltaic devices (vide infra).

7.2.3. Further Investigations into Heterojunction Conjugates

In Chapter 3, we show that quantum nanostructures can be attached via electrostatic interactions to quaternized polyfluorene coronal regions in fiber-like micelles with PDHF crystalline cores. On excitation of the PDHF core, the absorbed energy can be funneled to the attached quantum rods. This methodology can also be applied to the scarf-like micelles prepared in Chapter 5. Quantum nanostructures could be attached to the central 2D seed composed of the charge-capped PDHF homopolymer. Energy could be funneled through the multiple tassels (antennae) towards the central segment and then transfer to nanoparticles attached via electrostatic interactions. These scarf-like micelles could also be the ideal type of architecture for the preparation of conjugated polymer-based micelle brushes from a surface.[6] Attachment of the flat 2D seed to a substrate via electrostatic interactions and using seeded growth to grow multiple antennae from a single seed could be explored in future work.

Furthermore, ongoing work is also focussed on combining the optical properties of magnetic nanoparticles (plasmonics) or up-converting nanoparticles with the exceptional energy funneling properties of nanofibers prepared by CDSA. Hybrid plasmonic materials are particularly attractive for the conversion of electromagnetic radiation into electric current.[7] Plasmonic metal nanoparticles can convert radiation into electron-holes and the semiconducting conjugated nanofiber could extract the hot carriers. Such a system is desirable for photovoltaic and photodetection applications.

7.2.4. Development of Chiral Hybrid Plasmonic Materials

In Chapter 4, we present a route towards the formation of helical fibers with controlled lengths and handedness. The uniform helical nanofibers presented were composed of a PDHF core, chiral conjugated (*S*-) poly(di-*n*-(3,7-dimethyoctane)fluorene) ((*S*-) PDCF) coronal regions, and poly(*N*-isopropylacrylamide) (PNIPAm) polar coronal regions. Attachment of metallic nanoparticles (NPs) to these fibers could be facilitated by non-covalent interactions with the (*S*-)/(*R*-) PDCF block (Figure 7. 1a). The twisted conformation of the nanofiber could act as a scaffold for the helical arrangement of metallic nanoparticles (Figure 7. 1b) [8–10] This work could pave the way towards the preparation of precisely ordered chiral hybrid plasmonic materials. Resonant interactions between the neighbouring metallic NPs arranged in a helical conformation should result in a significantly enhanced chiral optical response.

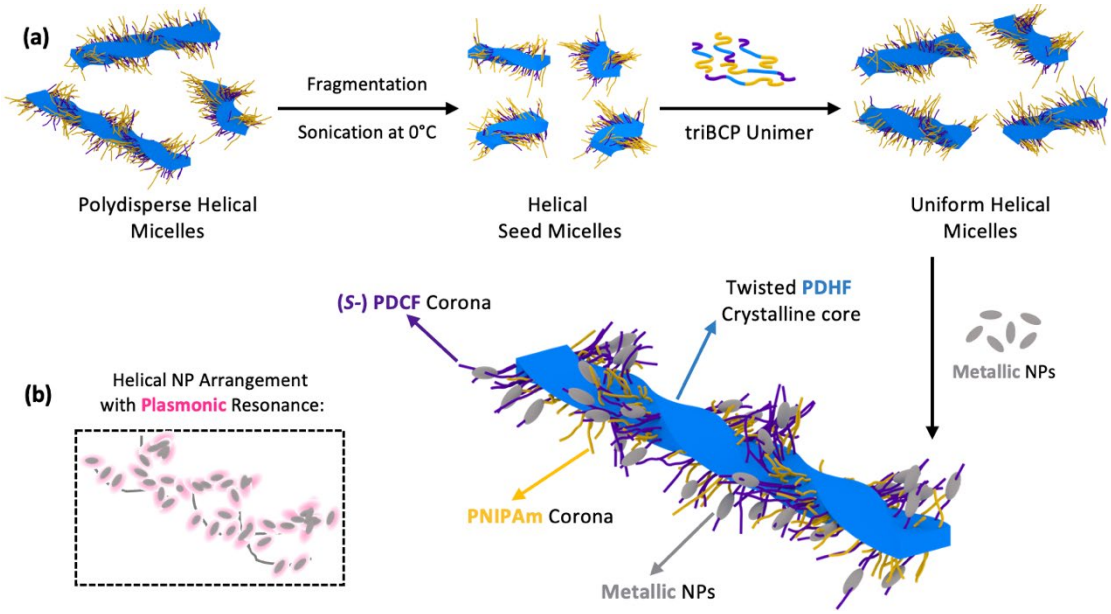

Figure 7. 1: (a) Schematic representation of the preparation of metal nanoparticle-1D helical conjugated nanofiber hybrid. (b) Illustration of the helical arrangement of metallic nanoparticle (NP) templated by the nanofiber. Plasmonic resonance exhibited by the metallic NPs is depicted by the pink regions

7.2.5. Integration of Nanowires Prepared by Living CDSA into Electronic Devices

Previously, the integration of polythiophene-based nanofibers prepared by CDSA into a field effect transistor device has been shown.[1] Results based on this work indicated that future research will need to focus on the efficient attachment of fibers to a substrate in order to achieve desirable device performance. In this thesis and in previous work it has been demonstrated that we can exercise remarkable control over the structure of fibers prepared by living CDSA. The next major research goal in this field is to optimize device fabrication using these materials. Preliminary work could focus on the attachment of π-conjugated nanofibers to a silicon substrate, similar to what has been already achieved for PFS-based micelles.[6] This methodology should provide an efficient route to the energetic coupling of nanofibers with electrode layers.

7.3. Outlook

Living CDSA presents an exciting route towards the fabrication of advanced nanomaterials with precisely controlled dimensions. Such materials possess advantageous properties that could meet the needs of emerging technological applications.[11] Current limitations include the scope of the crystallizable core-forming block and the heteroepitaxial seeded growth process. Although several different functional materials have been investigated including a variety of semiconducting and biodegradable polymers we need to continue investigating other functional core-forming blocks in order to use these nanomaterials for real-world applications. Finally, the construction of size- and shape-controlled nanostructures via living CDSA will continue to be important in material design for applications in areas such as therapeutics, bioimaging, electronics, and photocatalysis.[1,12,13]

7.4. References

(1) Li, X.; Wolanin, P. J.; Macfarlane, L. R.; Harniman, R. L.; Qian, J.; Gould, O. E. C.; Dane, T. G.; Rudin, J.; Cryan, M. J.; Schmaltz, T.; Frauenrath, H.; Winnik, M. A.; Faul, C. F. J.; Manners, I. Uniform Electroactive Fibre-like Micelle Nanowires for Organic Electronics. *Nat. Commun.* **2017**, *8*, 15909.

(2) Jin, X.-H.; Price, M. B.; Finnegan, J. R.; Boott, C. E.; Richter, J. M.; Rao, A.; Menke, S. M.; Friend, R. H.; Whittell, G. R.; Manners, I. Long-Range Exciton Transport in Conjugated Polymer Nanofibers Prepared by Seeded Growth. *Science.* **2018**, *360* (6391), 897–900.

(3) Li, W.; Hendriks, K. H.; Wienk, M. M.; Janssen, R. A. J. Diketopyrrolopyrrole Polymers for Organic Solar Cells. *Acc. Chem. Res.* **2016**, *49*, 78–85.

(4) Guo, K.; Bai, J.; Jiang, Y.; Wang, Z.; Sui, Y.; Deng, Y.; Han, Y.; Tian, H.; Geng, Y. Diketopyrrolopyrrole-Based Conjugated Polymers Synthesized via Direct Arylation Polycondensation for High Mobility Pure n-Channel Organic Field-Effect Transistors. *Adv. Funct. Mater.* **2018**, *28*, 1801097.

(5) Zhao, X.; Zhan, X. Electron Transporting Semiconducting Polymers in Organic Electronics. *Chem. Soc. Rev.* **2011**, *40*, 3728–3743.

(6) Cai, J.; Li, C.; Kong, N.; Lu, Y.; Lin, G.; Wang, X.; Yao, Y.; Manners, I.; Qiu, H. Tailored Multifunctional Micellar Brushes via Crystallization-Driven Growth from a Surface. *Science.* **2019**.

(7) Pescaglini, A.; Iacopino, D. Metal Nanoparticle-Semiconductor Nanowire Hybrid Nanostructures for Plasmon-Enhanced Optoelectronics and Sensing. *J. Mater. Chem. C* **2015**, *3*, 11785–11800.

(8) Kim, Y. J.; Cho, C. H.; Paek, K.; Jo, M.; Park, M. K.; Lee, N. E.; Kim, Y. J.; Kim, B. J.; Lee, E. Precise Control of Quantum Dot Location within the P3HT-b-P2VP/QD Nanowires Formed by Crystallization-Driven 1D Growth of Hybrid Dimeric Seeds. *J. Am. Chem. Soc.* **2014**, *136* (7), 2767–2774.

(9) Hentschel, M.; Schäferling, M.; Duan, X.; Giessen, H.; Liu, N. Chiral Plasmonics. *Sci. Adv.* **2017**, *3*, e1602735.

(10) Cheng, G.; Xu, D.; Lu, Z.; Liu, K. Chiral Self-Assembly of Nanoparticles Induced by Polymers Synthesized via Reversible Addition-Fragmentation Chain Transfer Polymerization. *ACS Nano* **2019**, *13*, 1479–1489.

(11) Macfarlane, L. R.; Zhao, C.; Cai, J.; Qiu, H.; Manners, I. Emerging Applications for Living Crystallization-Driven Self-Assembly. *Chem. Sci.* **2021**, Accepted Manuscript.

(12) Tian, J.; Zhang, Y.; Du, L.; He, Y.; Jin, X. H.; Pearce, S.; Eloi, J. C.; Harniman, R. L.; Alibhai, D.; Ye, R.; Phillips, D. L.; Manners, I. Tailored Self-Assembled Photocatalytic Nanofibres for Visible-Light-Driven Hydrogen Production. *Nat. Chem.* **2020**, *12*, 1150–1156.

(13) Street, S. T. G.; He, Y.; Jin, X. H.; Hodgson, L.; Verkade, P.; Manners, I. Cellular Uptake and Targeting of Low Dispersity, Dual Emissive, Segmented Block Copolymer Nanofibers. *Chem. Sci.* **2020**, *11*, 8394–8408.